

Faculty Profile

Dr. SACHIN SHIVAJI PUJARI

Assistant Professor

Department of Physics,

Yashwantrao Chavan Warana Mahavidyalaya,
Warananagar, Tal. Panhala Dist. Kolhapur- 416113

Email: spujari164@gmail.com

Contact: +91 8855992962



Google Scholar: <https://scholar.google.co.in/citations?user=ZfPv0I0AAAAJ&hl=en>

ResearchGate: <https://www.researchgate.net/profile/Sachin-Pujari>

Educational Qualification

Sr. No	Name of Degree	Name of University	Subject	Class Obtained	Year	Page No.
1.	B. Sc.	Shivaji University, Kolhapur	Physics	I st	2013	7
2.	M. Sc.	Savitribai Phule Pune University, Phule	Physics	I st	2015	8
3.	Ph.D.	D. Y. Patil Education Society, Kolhapur	Research in Methodology and Thin Film Technology	-	2022	9

Research And Training Portfolio

A) Research

II Publications:

I. Book (International-01) and Chapter Writing (International-01)

Sr. No.	Name of Book	Name of Chapter	Name of Publisher	ISBN	Year	DOI	Page No.
1.	Transition metal phosphate for supercapacitor application	-	LAP LAMBERT Academic Publishing	978-620-5-64147-7	2023	https://www.barnesandnoble.com/w/transition-metal-phosphate-for-supercapacitor-application-sachin-pujari/1143126181	10
2.	Chemically Deposited Metal Chalcogenide-based Carbon Composites for Versatile Applications	1D, 2D, and 3D Structured Metal Chalcogenides for Supercapacitor Application	Springer, Chem	978-3-03123401-9	2023	https://doi.org/10.1007/978-3-031-23401-9_2	11

II. International Research Paper Published in Scopus Indexed Journals

Sr. No.	Title of Research Paper	Name of Journal	Name of Publisher	Year	Impact Factor	DOI	Page No.
1.	Hydrothermally synthesized nickel copper phosphate thin film cathodes for high performance hybrid supercapacitor devices	Journal of Energy Storage	Elsevier	2022	9.4	https://doi.org/10.1016/j.est.2022.105037	12
2.	A binder-free facile synthetic approach for amorphous, hydrous nickel copper phosphate thin film electrode preparation and its application as a highly stable cathode for hybrid asymmetric supercapacitors	Sustainable Energy & Fuels	RSC	2022	5.6	https://doi.org/10.1039/D2SE00978A	27
3.	Amorphous, hydrous nickel phosphate thin film electrode prepared by SILAR method as a highly stable cathode for hybrid asymmetric supercapacitor	Synthetic Metals	Elsevier	2021	4.4	https://doi.org/10.1016/j.synthmet.2021.116876	40

4.	Highly sensitive hydrothermally prepared nickel phosphate electrocatalyst as non-enzymatic glucose sensing electrode	Journal of Porous Materials	Springer	2020	2.6	https://doi.org/10.1007/s10934-020-01000-0	52
5.	Facile synthesis of microstrip-like copper phosphate hydroxide thin films for supercapacitor applications	Journal of Electronic Materials	Springer	2020	2.1	https://doi.org/10.1007/s11664-020-08095-w	67
6.	Growth dynamics-dependent chemical approach to accomplish nanostructured cobalt vanadium oxide thin film electrodes with controlled surface area for high-performance solid-state hybrid supercapacitor devices	Energy Technology	John Wiley & Sons	2023	4.14	https://doi.org/10.1002/ente.202300400	79
7.	Development of binder-free, amorphous nickel vanadate cathodes by SILAR method for hybrid supercapacitors: Exploiting surface area by monitoring growth rate	Journal of Energy Storage	Elsevier	2023	9.4	https://doi.org/10.1016/j.est.2023.108417	95
8.	Dual functional SILAR deposited NiWO ₄ electrocatalyst for non-enzymatic glucose sensing and hydrogen evolution reaction	Applied Physics A Materials Science & Processing	Springer	2023	2.7	https://doi.org/10.1007/s00339-023-06798-5	111
9.	Cobalt doped iron phosphate thin film: An effective catalyst for electrochemical water splitting	Journal of Alloys and Compounds	Elsevier	2021	6.2	https://doi.org/10.1016/j.jallcom.2021.160914	123
10.	Regulated micro-leaf like nickel pyrophosphate as a cathode electrode for asymmetric supercapacitor	Synthetic Metals	Elsevier	2020	4.4	https://doi.org/10.1016/j.synthmet.2019.116224	132
11.	Effect of phosphate (anion) precursor on structural and morphology behavior of nickel phosphate thin films and its supercapacitive performance	Materials Science & Engineering B	Elsevier	2020	3.6	https://doi.org/10.1016/j.mseb.2020.114641	145
12.	Hydrothermally synthesized iron phosphate hydroxide thin film electrocatalyst for electrochemical water splitting	Electrochimica Acta	Elsevier	2019	6.6	https://doi.org/10.1016/j.electacta.2019.06.162	155

13.	Enhanced energy density of all-solid-state asymmetric supercapacitors based on morphologically tuned hydrous cobalt phosphate electrode as cathode material	ACS Sustainable Chemistry & Engineering	ACS	2019	8.4	https://doi.org/10.1021/acsuschemeng.9b00504	166
14.	Single-pot hydrothermal synthesis of manganese phosphate microrods as a cathode material for highly stable flexible solid-state symmetric supercapacitors	Synthetic Metals	Elsevier	2020	4.4	https://doi.org/10.1016/j.synthmet.2020.116446	180
15.	Intercalation type pseudocapacitive clustered nanoparticles of nickel-cobalt phosphate thin films synthesized via electrodeposition as a cathode for high performing hybrid supercapacitor devices	Journal of Materials Chemistry A	RSC	2022	11.9	https://doi.org/10.1039/D2TA00761D	193
16.	Hydrous and amorphous cobalt phosphate thin-film electrodes synthesized by the SILAR method for high-performing flexible hybrid energy storage devices	Energy Fuels	ACS	2022	5.3	https://doi.org/10.1021/acs.energyfuels.2c02202	210

III. Indian Patents (Granted 02)

Sr. No.	Title of invention	Application No	Filing Date	Granted Date	Page No.
1.	Amorphous nickel phosphate thin film electrode by chemical method for supercapacitor application	202021041651	25/09/2020	28/04/2023	226
2.	A chemical synthesis process for cobalt-iron phosphate and used as electrocatalyst thereof	202221021487	11/04/2022	04/09/2023	227

IV. State level / National level / International level conferences/ seminars Attended & research Paper Presented

1) Research Paper Presented (01)

Sr. No.	Title	Organize Institutes	International/ National/Regional	Date	Page No.
1.	The University Anveshan-2018	D. Y. Patil Education Society, Kolhapur	Regional	5-12-2018	228

2) Research Seminar Attended (04)

Sr. No.	Title	Organize Institutes	International/ National/Regional	Date	Page No.
1.	Novel Applications of Nanomaterials	Dr. N. D. Patil Mahavidyalaya, Malkapur	International Web-Seminar	18-07-2020	229
2.	Modern Approaches in Sciences	K. N. Bhise Arts, Commerce and Vinayakrao Patil Science	International Web-Seminar	28-01-2019	230
3.	Recent Trends in Nanostructured Materials Based Devices and Their Applications	D. P. Bhosale College, Koregaon	National	18-07-2020	231
4.	Emerging Nano Materials for Renewable Energy	Sanjay Ghodawat University	National	26-12-2020	232

3) Research Conference Attended (05)

Sr. No.	Title	Organize Institutes	International/ National/Regional	Date	Page No.
1.	Advanced Materials Synthesis, Characterization and Applications	Department of Physics, Savitribai Phule Pune University	National	14-12-2018	233
2.	Physics of Material and Materials Based Device Fabrication	Department of Physics, Shivaji University	International	10-11-2019	234
3.	Smart Materials and Nanotechnology	SKN Sinhgad College of Engineering, Pandharpur	International	02-01-2020	235
4.	Advanced Nanostructured Materials for Energy Generation, Storage and Smart Applications	Shardabai Pawar Mahila Arts, Commerce and Science College, Shardanagar, Baramati	International Web-Conference	09-10-2020	236
5.	Engineered Science 2020	Prof. C. D. Lokhande Endowment Charitable Trust	Asian e-Conference	05-12-2020	237

4) Research Workshop Attended (02)

Sr. No.	Title	Organize Institutes	International/ National/Regional	Date	Page No.
1.	Intellectual Property Rights	D. P. Bhosale College, Koregaon	National e-Workshop	12-08-2022	238
2.	Biodiversity Conservation and Biodiversity Act 2002	D. Y. Patil Education Society, Kolhapur	Regional	15-02-2019	239

5) Research Webinar Attended (02)

Sr. No.	Title	Organize Institutes	International/ National/Regional	Date	Page No.
1.	Density Functional Theory- In the Absence of Spectrometers	Shri Kadasiddheswar Arts College, Hubballi	National	22-07-2020	240
2.	Emerging Trends and Clinical Challenges in Cancer Treatment	D. Y. Patil Education Society, Kolhapur	Regional	04-02-2021	241

6) Training Programme Attended (01)

Sr. No.	Title	Organize Institutes	International/ National/Regional	Date	Page No.
1.	National Intellectual Property	Intellectual Property Office, India	National	12-08-2022	242

Shivaji University, Kolhapur



the Chancellor, Vice-Chancellor and
Members of the Management Council on
the recommendation of the Academic Council certify that

Pujari Sachin Shivaji
Mother's Name - Chaya
has passed the



Bachelor of Science

Examination in the Subject

Physics

with First Class

in the year April 2013.

*The said degree has been conferred on him
at Kolhapur in the Winter Session
of the year two thousand fourteen.*

In Testimony *whereof are set the seal of the
University and the signatures of the
Registrar and the Vice-Chancellor.*

Registrar



Vice-Chancellor



Savitribai Phule Pune University

(formerly University of Pune)

We, the Chancellor, the Vice Chancellor and the Members of the Management Council and the Academic Council of the Savitribai Phule Pune University certify that
Pujari Sachin Shivaji, Mother's Name: Chaya
of New Arts, Science & Commerce College, Ahmednagar having been examined in Physics and found duly qualified for the degree of
Master of Science
and placed in the B Grade in April 2015. The said degree has been conferred on him. In testimony whereof is set the seal of the said University.

सावित्रीबाई फुले पुणे विद्यापीठ

(पूर्वीचे पुणे विद्यापीठ)

आम्ही, सावित्रीबाई फुले पुणे विद्यापीठाचे कुलपति, कुलगुरु आणि व्यवस्थापन परिषद व विद्या परिषद सदस्य, प्रमाणित करितो की,

पुजारी सचिन शिवाजी, आईचे नाव: छाया

हे न्यू कला, विज्ञान आणि वाणिज्य महाविद्यालय, अहमदनगर येथून बी श्रेणीत एप्रिल २०१५ मध्ये भौतिकशास्त्र विषय घेऊन

विज्ञान पारंगत

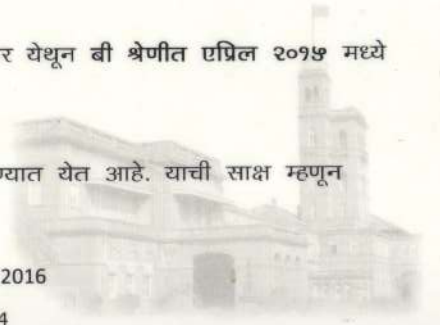
पदवी परीक्षा उत्तीर्ण झाल्याबद्दल त्यांना ही पदवी प्रदान करण्यात येत आहे. याची साक्ष म्हणून विद्यापीठाची अधिकृत मुद्रा येथे अंकित करण्यात येत आहे.



Vice Chancellor

30th December 2016

SC16-01584





D.V. Patil Education Society,
Kolhapur

Institution Deemed to be University
(Declared u/s 3 of the UGC Act 1956 by GOI)

2018000355



WE the Chancellor, Vice - Chancellor and
Members of the Board of Management,
on the recommendation of the Academic Council,
certify that

Doctor of Philosophy

(Physics)

has been conferred upon him at the convocation held
on 24th day of the month of February in the Year
Two Thousand Twenty Three.

on

Pujari Sachin Shivaji

In Testimony whereof are set the Seal of the University
and the Signatures of the Registrar and the
said Vice - Chancellor

Registrar



Vice - Chancellor

Transition metal phosphate (TMP) based materials are developing as advanced type electrode materials for hybrid supercapacitors (SCs) due to their unprecedented conductivity, and rich redox activity. Attracted by these fabulous physicochemical characteristics of metal phosphates, binder-free nickel copper (Ni-Cu) phosphate thin films with Ni-Cu composition variation were directly grown on stainless steel (SS) substrate via hydrothermal and SILAR methods. The composition of nickel and copper ratio varied to achieve better results by using synergy among them. Binder-free and adherent thin films of nickel copper phosphate were characterized by various physico-chemical methods. The best performing nickel copper phosphate electrodes were used for the fabrication of asymmetric (Ni-Cu Phosphate//rGO) aqueous (1 M KOH electrolyte) and solid state device (SSD) (PVA-KOH gel electrolyte). Moreover, SSD brightens a panel of 201 red light-emitting diodes (LEDs) illustrating its commercial practicability to next-generation hybrid energy storage devices.



Sachin Pujari
Umakant Patil



Dr. Sachin Pujari studied master of physics at New Arts College, Ahmednagar, and received a Doctorate degree in 2022 from D. Y. Patil Education Society, Kolhapur, India under the supervision of Dr. U. M. Patil. His research interests currently focus on metal phosphates for energy conversion/storage devices

Transition metal phosphate for supercapacitor application

Electrochemical properties of hydrothermally and SILAR deposited nickel copper phosphate thin films

Sachin Pujari, Umakant Patil



LAP
LAMBERT
Academic Publishing

1D, 2D, and 3D Structured Metal Chalcogenides for Supercapacitor Application

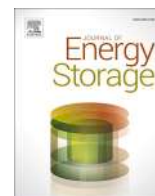
S. S. Kumbhar, S. J. Marje, V. V. Patil, S. B. Bhosale, S. S. Pujari, J. L. Gunjekar, C. D. Lokhande, and U. M. Patil

Abbreviations

1D	One dimensional	7
2D	Two dimensional	8
3D	Three dimensional	9
AB	Acetylene black	10
CBD	Chemical bath deposition	11
CC	Carbon cloth	12
CV	Cyclic voltammetry	13
EDLC	Electric double-layer capacitor	14
EIS	Electrochemical impedance spectroscopy	15
FESEM	Field emission scanning electron microscopy	16
GCD	Galvanostatic charge-discharge	17
GO	Graphene oxide	18
NG	N-doped graphene	19
NMC	Nitrogen-doped mesoporous carbon	20
NWs	Nanowires	21
PANI	Polyaniline	22
Pt	Platinum	23
rGO	Reduced graphene oxide	24
TEM	Transmission electron microscopy	25

S. S. Kumbhar · S. J. Marje · V. V. Patil · S. B. Bhosale · S. S. Pujari · J. L. Gunjekar
C. D. Lokhande · U. M. Patil (✉)
Centre for Interdisciplinary Research, D. Y. Patil Education Society, Kolhapur, India

© The Author(s), under exclusive license to Springer Nature Switzerland AG 2023
F. I. Ezema et al. (eds.), *Chemically Deposited Metal Chalcogenide-based Carbon Composites for Versatile Applications*, https://doi.org/10.1007/978-3-031-23401-9_2



Research Papers

Hydrothermally synthesized nickel copper phosphate thin film cathodes for high-performance hybrid supercapacitor devices

Sachin S. Pujari^a, Sujit A. Kadam^b, Yuan-Ron Ma^b, Satish B. Jadhav^a, Sambhaji S. Kumbhar^a, Shradha B. Bhosale^a, Jayavant L. Gunjekar^a, Chandrakant D. Lokhande^a, Umakant M. Patil^{a,*}

^a Centre for Interdisciplinary Research, D. Y. Patil Education Society, Kasaba Bawada, Kolhapur 416 006, India

^b Department of Physics, National Dong Hwa University, Hualien 97401, Taiwan



ARTICLE INFO

Keywords:

Concentration variation
Microplates
Microrods
Nickel copper phosphate
Hydrothermal method
Hybrid energy storage devices
Thin film electrode

ABSTRACT

Transition metal phosphate (TMP) based materials are developing as advanced type electrode materials for hybrid supercapacitors (SCs) due to their unprecedented conductivity, and rich redox activity. Attracted by these fabulous physicochemical characteristics of metal phosphates, binder-free nickel copper (Ni-Cu) phosphate thin films directly grown on stainless steel (SS) substrate by hydrothermal method. The morphological alteration from microplates like nickel phosphate to microrods like copper phosphate is detected with increasing copper content in Ni-Cu phosphate thin films. The optimal 1:1 ratio of nickel and copper in Ni-Cu phosphate ($\text{Ni}_{1.62}\text{Cu}_{1.35}(\text{PO}_4)_2 \cdot \text{H}_2\text{O}$) thin film illustrates high specific capacitance (C_s) (capacity (C_c)) of 711 F g^{-1} (355.5 C g^{-1}) at 1.5 A g^{-1} . More significantly, a hybrid aqueous SC (HASC) and all-solid-state SC (HASSC) electrochemical energy storage devices (ESDs) have been fabricated. The HASC device showed superior C_s (85 F g^{-1} at 0.8 A g^{-1}) with specific energy (SE) of 30 Wh kg^{-1} at 1.27 kW kg^{-1} specific power (SP). Additionally, HASSC device offers a higher C_s (52 F g^{-1} at 0.6 A g^{-1}) with 18.53 Wh kg^{-1} SE at 1.64 kW kg^{-1} SP. Also, both HASC and HASSC devices exhibit excellent long-term durability of 84.81 and 80.83 %, respectively, after 5000 GCD cycles. Moreover, HASSC device brightens a panel of 201 red light-emitting diodes (LEDs) illustrating its commercial practicability to next-generation hybrid energy storage devices.

1. Introduction

High-performance electrochemical energy storage devices (ESDs) (e. g., supercapacitors (SCs) and batteries) are acquiring increasing focus from researchers in the industrial field as well as fundamental scientific research [1]. The SC as steady and reversible ESDs has become the most favourable commercial device [2]. Unlike batteries, SCs possess high specific power (SP) and long cycle lifespan that make them promising candidates where (a) peak power demands and (b) maintenance-free ESDs are necessary [3]. A unique scheme to improve the specific energy (SE) of a SC is the usage of electrolytes with a wide working voltage window and a high specific capacitance (C_s) electrode (since $E = 0.5 \text{ CV}^2$) [1,4]. Remarkably, hybrid SC can offer both high SE and excellent SP, ideally suitable for many emerging applications such as smart grids, portable electronics, and electric vehicles [5]. The electrochemical behaviours of hybrid devices depends characteristics of the electrode materials (porosity, surface area and conductivity) and sensitively on

the structures, particularly with the negative electrode materials (carbon based materials) [6,7]. Hence, the design and construction of novel advanced electrode materials along with unique functionalities and structural properties are critical to attaining breakthroughs in the improvement of high-performance hybrid devices [8].

Till today, the various types of cathode materials have been examined for SCs including conducting polymers (polypyrrole, polyaniline, etc.) and transition metal oxides/sulfides/hydroxide. Out of these electrode materials, currently, TMPs have been fascinating enormous attention for several applications including energy conversion, sensors, magnetic devices, and ESDs owing to their metalloid characteristics [9]. Especially, TMPs with the qualities of outstanding redox activity, high conductivity, environmental compatibility, earth abundance, sustainability is more advantageous for ESDs and have been recognized as competitive alternates for conventional metal oxide and hydroxide along with conducting polymers-based electrodes [10]. Basically, PO_4^{3-} polyhedral anions along with a zeolite structure are much more

* Corresponding author.

E-mail address: umakant.physics84@gmail.com (U.M. Patil).

favourable than those of phosphides, sulphides and oxides counterparts owing to the lower electronegativity of P atom, aimed to remarkable electronic properties [11]. Compared with other pseudocapacitive materials, TMPs possess highly desirable electrical conductivity (quick reaction dynamics, naturally effective redox activity, rapid electron transport), and also offer tuneable meso- and nano-structures to enhance access of electrolytic ions, which is beneficial in SCs [12,13].

The mixed metal compositions have been examined as a cathode material in hybrid SCs, since mixed metal compounds can reveal high SE than single metal compounds because of the synergetic effect among two metal cation species [14]. Presently, some attention has been paid to the binary TMPs owing to their high electrochemical activities, when serving as electrode materials in SCs. Specifically, in TMPs metals like, Ni, Cu and Co, can provide multiple oxidation states, which demonstrates pseudocapacitive behaviour. Hence, researchers have been developing numerous TMPs, such as $\text{Ni}_3(\text{PO}_4)_2$ [15], $\text{Cu}_2(\text{PO}_4)(\text{OH})$ [16] and $\text{Co}_3(\text{PO}_4)_2$ [17] and used as a cathode in hybrid ESDs. Particularly, nickel phosphate and copper phosphate are favourable electrode materials for SCs owing to their low cost as well as richer redox reactions [16,18,19]. However, pristine nickel phosphate has some limitations, such as poor rate capability [20] along with slow ion transfer rate [21], and copper phosphate demonstrates low C_s . Hence, nickel phosphate and copper phosphate combination can resolve these shortcomings and offer an efficient approach to perform higher supercapacitive performance (durability, SE and C_s). The combined advantages of nickel-copper (Ni-Cu) phosphate can exhibit superior electrochemical performance in SC applications. Moreover, the studies on Ni-Cu phosphate thin film synthesis by using hydrothermal method for SC application have been not investigated yet.

Considering the interplay and synergy matrix effect of bimetallic phosphates, the binder-free Ni-Cu phosphate thin films are prepared for the first time by using one-step hydrothermal method with various ratios of nickel and copper molar concentration and investigated for SC application. The impact of molar composition on morphological and structural characteristics is investigated and analysed. The electrochemical capacitive performance of Ni-Cu phosphate electrodes was

tested in a 1 M KOH electrolyte. Moreover, the HASC device (NCP-3//KOH//rGO) and HASSC (NCP-3//PVA-KOH//rGO) devices were constructed using the highest performing Ni-Cu phosphate thin films as a cathode and rGO as an anode. The combined influence of both types (pseudocapacitive and EDLC) electrodes at the hybrid supercapacitor device are examined and described herein.

2. Experimental section

2.1. Preparation of nickel copper phosphate thin films

In the Ni-Cu phosphate material synthesis, $\text{NiSO}_4 \cdot 6\text{H}_2\text{O}$, $\text{CuSO}_4 \cdot 5\text{H}_2\text{O}$, and KH_2PO_4 were used as a source of nickel, copper, and phosphate, respectively. For the controlled reaction procedure, urea is added as a hydrolyzing agent in the chemical bath. Initially, $\text{NiSO}_4 \cdot 6\text{H}_2\text{O}$ (0.033 M), $\text{CuSO}_4 \cdot 5\text{H}_2\text{O}$ (0.033 M) and KH_2PO_4 (0.066 M) sources were dissolved in 50 ml of DDW along with urea (0.075 M). The prepared mixture was stirred intensely till the formation of a homogeneous solution, and then it was utilized for further Ni-Cu phosphate preparation. The Ni and Cu content is varied by altering molar composition as 0.033:0 (1:0), 0.024:0.008 (0.75:0.25), 0.016:0.016 (0.50:0.50), 0.008:0.024 (0.25:0.75) and 0:0.033 (0:1) M in chemical bath and named as H-NCP-1, H-NCP-2, H-NCP-3, H-NCP-4, and H-NCP-5, respectively. In prepared solution baths with different Ni and Cu molar ratios (as mentioned above), best cleaned SS substrates were dipped vertically. After dipping the substrate, the solution baths were put into a hydrothermal autoclave and kept at a stable 388 K temperature for 60 min as displayed in schematic Fig. 1. After continuous 60 min heating, the reaction bath was removed from hydrothermal autoclave and deposited substrates were taken out from solution. The substrates with deposited material rinsed several times in DDW for removal of loosely bonded particles from the surface and dried at ambient conditions. The prepared Ni-Cu phosphate electrodes on SS substrate were directly employed for physicochemical characterizations. The deposited mass of Ni-Cu phosphate material with various nickel:copper ratio is analysed by weight difference method (Fig. S1) (see ESI). For samples H-

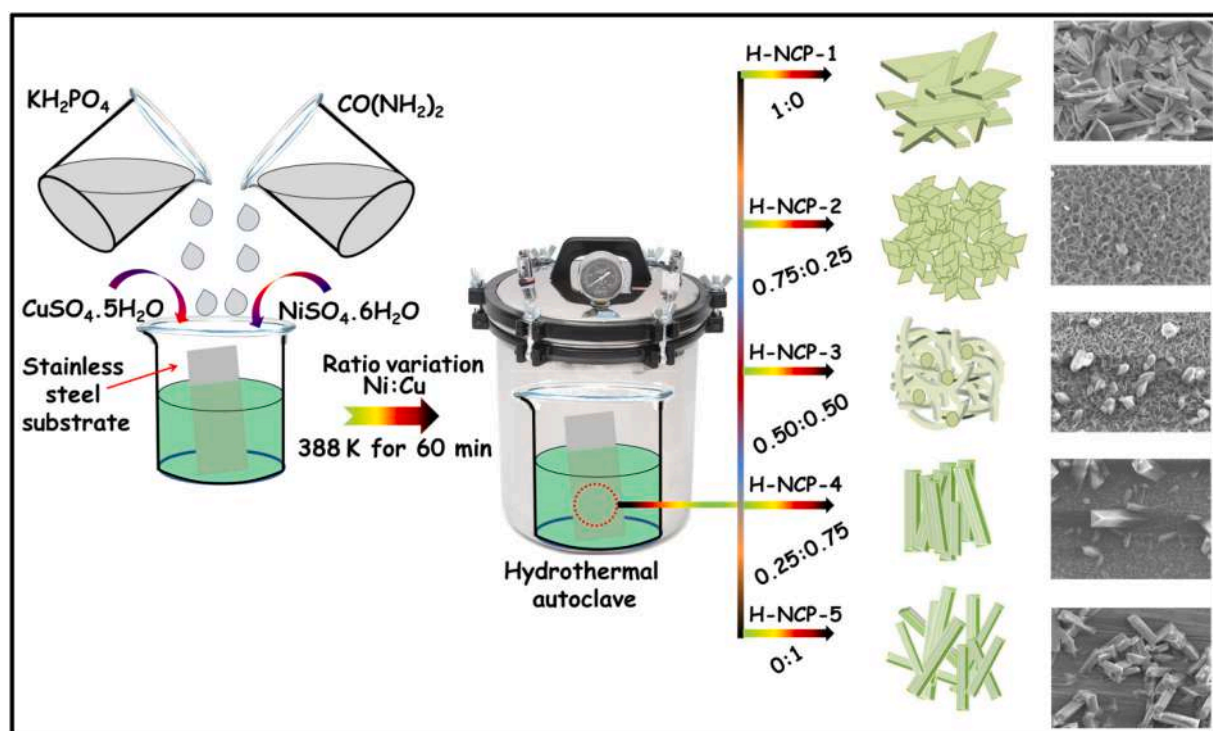


Fig. 1. Schematic illustration of Ni-Cu phosphate thin films deposition by hydrothermal method at various nickel and copper molar ratio.

NCP-1, H-NCP-2, H-NCP-3, H-NCP-4, and H-NCP-5, the deposited mass per unit area is 0.65, 0.67, 0.70, 0.71, and 0.73 mg cm⁻², respectively. It is noted that, the increasing concentration of copper gradually increases the mass of thin films, which may be owing to the little faster growth kinetics of copper than nickel phosphate.

2.2. Preparation of reduced graphene oxide (rGO) electrode

The rGO was synthesized by using Hummers method from graphite flakes [22]. Then, the achieved graphene oxide (GO) slurry was reduced by employing hydrothermal technique (453 K for 14 h) and freeze-dried to maintain a porous structure with a large surface area. Further, the rGO electrode was made as follows: 75 wt% of well-synthesized rGO powder, 20 wt% of carbon black (CB), and 5 % polyvinylidene difluoride (PVDF) in *N*-methyl-2-pyrrolidone (NMP) were added to constitute a uniform slurry. Then, the achieved slurry was laminated on the SS substrate (area 2 cm²) and dried at 328 K for 3 h. Prepared rGO electrode was utilized to probe electrochemical capacitive investigation and construction of hybrid SC devices.

2.3. Hybrid device fabrication

In the present work, the PVA-KOH gel electrolyte is prepared as discussed in our earlier report [17]. In constructing a hybrid device, Ni-Cu phosphate served as a cathode electrode and rGO served as an anode electrode along with gel electrolyte. To achieve better performance of the device, charge balance between anode and cathode is crucial and it is achieved by mass balance of both electrodes according to Eq. (6). The mass balance ratio is found to be 0.44:1, where mass loading of H-NCP-3 electrode is 0.51 mg cm⁻² and rGO is 1.16 mg cm⁻². Positive and negative electrodes were painted herewith the gel electrolyte to develop a thin layer and dried at ambient temperature. Later together the electrodes were sandwiched over each other in such a way that the electroactive surface of both the electrodes was facing each other. After the whole assembly was packed in the insulating tape to avoid any contamination. Furthermore, the constructed device was pressed under a hydraulic pressure at 0.7-ton pressure for 12 h to enhance the interfacial interaction of gel electrolyte among both electrodes. The constructed devices were packed in a plastic box and examined for the electrochemical capacitive study.

2.4. Characterization techniques

The structural characterization of the Ni-Cu phosphate thin films were examined by XRD from Rigaku miniflex-600 with Cu K α ($\lambda = 0.15406$ nm) in the 2θ range of 10–80°. The FT-IR spectra were recorded by an FT-IR 4600 type-A instrument using a KBr pellet at ambient temperature for the detection of functional groups in Ni-Cu phosphate thin films. The XPS (K-alpha XPS System, Thermo Fisher Scientific, U.K.) was analysed for identifying oxidation states and chemical composition of Ni-Cu phosphate thin film. The surface area and porosity were measured from BET analysis using (Belsorp II mini) instrument. The FE-SEM (JSM-6500F, JEOL) was utilized to examine the surface morphology of prepared material and EDS (Oxford, X-max) was used to observe elemental analysis. All electrochemical activities were evaluated by using the ZIVE MP1 multichannel electrochemical workstation.

2.5. Electrochemical measurements

ZIVE MP1 electrochemical workstation was used to study the electrochemical properties of Ni-Cu phosphate electrodes in 1 M KOH electrolyte at the ambient conditions. The standard three-electrode system was configured, where Ni-Cu phosphate electrodes were act as a working, platinum sheet as the counter and the mercury/mercury oxide (Hg/HgO) employed as the reference electrodes. The utilized geometrical area in electrochemical measurements of working and

counter electrodes was ~ 1 cm \times 1 cm. Moreover, the examination of electrochemical capacitive performance of hybrid devices was carried out by using a two-electrode system.

The electrochemical properties of the Ni-Cu phosphate material were studied by conducting cyclic voltammetry (CV), galvanostatic charge-discharge (GCD) and cycling stability. The electrochemical impedance spectroscopy (EIS) was conducted in the frequency range from 100 kHz to 100 mHz at 10 mV amplitude and fitted well suitable equivalent circuit utilizing ZView impedance software. Specific capacity (C_c), C_s and energy efficiency (EE) of the Ni-Cu phosphate sample was estimated from the GCD tests as per following equations,

$$C_c = \frac{I \times \Delta t}{m} \quad (\text{C g}^{-1}) \quad (1)$$

$$C_s = \frac{I \times \Delta t}{m \times \Delta V} \quad (\text{F g}^{-1}) \quad (2)$$

$$EE = \frac{I_{dis} \int_{t_1}^{t_2} V_{dis} dt}{I_{ch} \int_0^t V_{ch} dt} \times 100 \quad (3)$$

where m denotes the mass of electroactive material (g), Δt denotes the discharge time (s), I denotes the applied current (A g^{-1}), ΔV denotes the potential range (V), I_{dis}/I_{ch} are the respective discharge/charge currents, V_{dis}/V_{ch} are the discharge/charge cell voltages, $\int_{t_1}^{t_2}$ denotes discharging time and \int_0^t denotes charging time.

The SE and SP of the HASC and HASSC devices were calculated by using Eqs. (4) and (5), respectively as,

$$SE = \frac{0.5 \times C_s \times (\Delta V)^2}{3.6} \quad (\text{Wh kg}^{-1}) \quad (4)$$

$$SP = \frac{E \times 3.6}{\Delta t} \quad (\text{kW kg}^{-1}) \quad (5)$$

where ΔV denotes potential windows (V/Hg/HgO) as well as Δt denotes discharging time (s). The optimum mass ratio of the cathode material (m_+) and anode electrode material (m_-) is calculated according to charge balance equation as,

$$\frac{m_+}{m_-} = \frac{C_- \times \Delta V_-}{C_+ \times \Delta V_+} \quad (6)$$

where, $C_{(+ \text{ or } -)}$ and $\Delta V_{(+ \text{ or } -)}$ are C_s and potential window of the cathode and anode electrodes, respectively.

3. Results and discussion

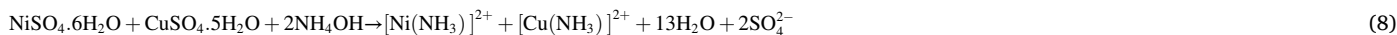
3.1. Nickel-copper phosphate thin film formation mechanism

Hydrothermally synthesized Ni-Cu phosphate material strongly depends on the controlled precipitation via direct heating under enclosed conditions and the development of solid-state through the conversion of supersaturated phase to saturated phase of a solution [19]. Two significant steps contribute to the film formation process, the initial one is nucleation monitored by the second one of crystal growth. During the process of thin film formation, on the surface of a substrate, the growth of material is followed by nucleation, coalescence, and stacking [17,23]. The deposition of Ni-Cu phosphate thin films is executed for different molar ratios (H-NCP-1, H-NCP-2, H-NCP-3, H-NCP-4, and H-NCP-5) of nickel and copper by using a hydrothermal method, and urea is utilized as a hydrolyzing agent in the synthesis process. When the reaction bath is heated at 363 K temperature, then urea decomposes delicately producing CO_2 and NH_3 as [24,25].



According to the Eq. (7), released NH_4^+ ions complexes the Ni^{2+} and Cu^{2+} ions in solution and forms $\text{Ni}(\text{NH}_3)_2^{2+}$ of $\text{Cu}(\text{NH}_3)_2^{2+}$ (Eq. 8). This

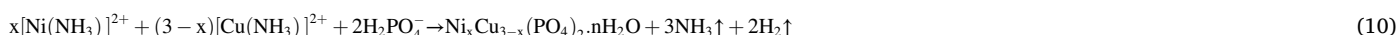
metal amine complex gradually releases $\text{Ni}^{2+}/\text{Cu}^{2+}$ ions, which inhibits fast nucleation and controls the reaction rate, subsequently producing homogeneous nucleation in the solution and heterogeneous on substrate surface.



Also, KH_2PO_4 decomposes as given below,



Finally, $\text{Ni}^{2+}/\text{Cu}^{2+}$ ions from nickel/copper complex and H_2PO_4^- ions from phosphate precursor react with each other and produces $\text{Ni}_x\text{Cu}_{3-x}(\text{PO}_4)_2 \cdot n\text{H}_2\text{O}$ solid state thin film, as per following reaction,



Reaction temperature (388 K) and reaction time (1 h) were optimized for the uniform deposition of material on SS substrate as shown in Fig. 1.

3.2. Structural and morphological analysis

XRD patterns of Ni-Cu phosphate (H-NCP-1 to H-NCP-5) electrodes are exhibited in Fig. 2 (a). The H-NCP-1 and H-NCP-5 are XRD patterns of pristine nickel phosphate and copper phosphate electrodes, respectively. The sample H-NCP-1 (indicated as “●” in Fig. 2 (a)) affirms the formation of $\text{Ni}_3(\text{PO}_4)_2 \cdot 8\text{H}_2\text{O}$ (JCPDS-033-0951) with planes ascribed to the (1 1 0), (0 2 0), (2 0 0), (0 1 1), (1 3 0), (1 0 1), (0 3 1), ($\bar{3}$ 0 1), ($\bar{3}$ 2 1), (1 4 1), ($\bar{1}$ 1 0), ($\bar{2}$ 5 1), ($\bar{2}$ 2 0), and (0 8 0) lattices. Also, the sample H-NCP-5 (indicated as “▲” in Fig. 2 (a)) confirms the formation of $\text{Cu}_3(\text{PO}_4)_2$ (JCPDS-01-070-0494) with planes corresponding to the (0 0 1), (0 1 0), ($\bar{1}$ 0 1), (0 1 2), (1 2 1), ($\bar{1}$ 0 2), (2 1 0), ($\bar{2}$ 1 1), (2 3 2) and ($\bar{3}$ $\bar{2}$ 1). Crystal planes and detected peaks represent the creation of

monoclinic crystal structure of prepared nickel phosphate and copper phosphate in H-NCP series. The peaks noted with an asterisk (*) are recognized to the SS substrate. It can be noticed that, the diffraction peaks relate to nickel phosphate are more prominent in H-NCP-2 than

other samples electrode, where nickel concentration is more than copper in Ni-Cu phosphate films. Moreover, peaks related to copper phosphate are more dominant than nickel phosphate in samples H-NCP-4, due to higher concentration of copper. Intensity of peaks corresponding to nickel phosphate decreases with decreases in concentration of nickel in Ni-Cu phosphate sample and thus, XRD results affirm the formation of Ni-Cu phosphate thin film form on SS substrate. The obtained XRD patterns exhibits sharp intensity peak implies that, Ni-Cu phosphate thin films are highly crystalline. Moreover, well crystallinity of Ni-Cu phos-

phate may favourable for improving the electrochemical performance by providing excellent electrochemical conductivity [26].

FT-IR spectroscopic investigation was performed to examine the molecular chemical bonds and functional groups present in the synthesized H-NCP thin films. Fig. 2 (b) reveals the characteristic peak at 559 cm^{-1} originated from metal-oxygen bonding of Ni—O in H-NCP-1 sample [27] and peak at 620 cm^{-1} reveals Cu—O bonding in H-NCP-5 thin film [28,29]. The vibrational bands of PO_4^{3-} anion are noticed around wavenumbers of 750 cm^{-1} [30,31]. The peak positions at 1003, 1049 and 1134 cm^{-1} are attributed to symmetric stretching vibration of P—O, and antisymmetric stretching of PO_4^{3-} [32–34]. The absorption peak of 1361 cm^{-1} reveals bending mode of H—O—P bond [35]. The peak of 1593 to 1698 cm^{-1} illustrates H—O—H bending vibration of structural water form H-NCP series samples. Also, the broad band from 3004 to 3387 cm^{-1} signifies the O—H stretching from adsorbed water in the synthesized material [36,37]. The prepared samples denote almost similar range of peaks which confirms occurrence of similar chemical bonds present in the Ni-Cu phosphate material and affirms presence of

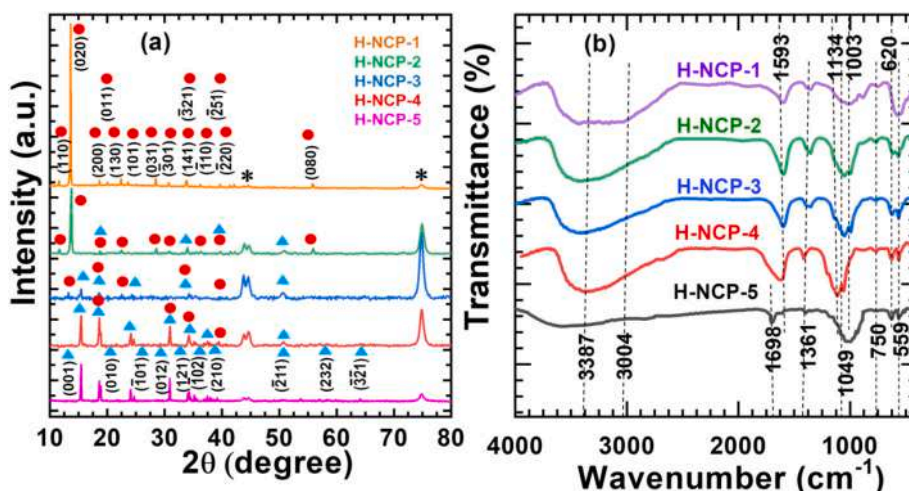


Fig. 2. (a) XRD patterns of Ni-Cu phosphate (H-NCP series) thin films, (b) FTIR spectra of as-prepared Ni-Cu phosphate thin films series.

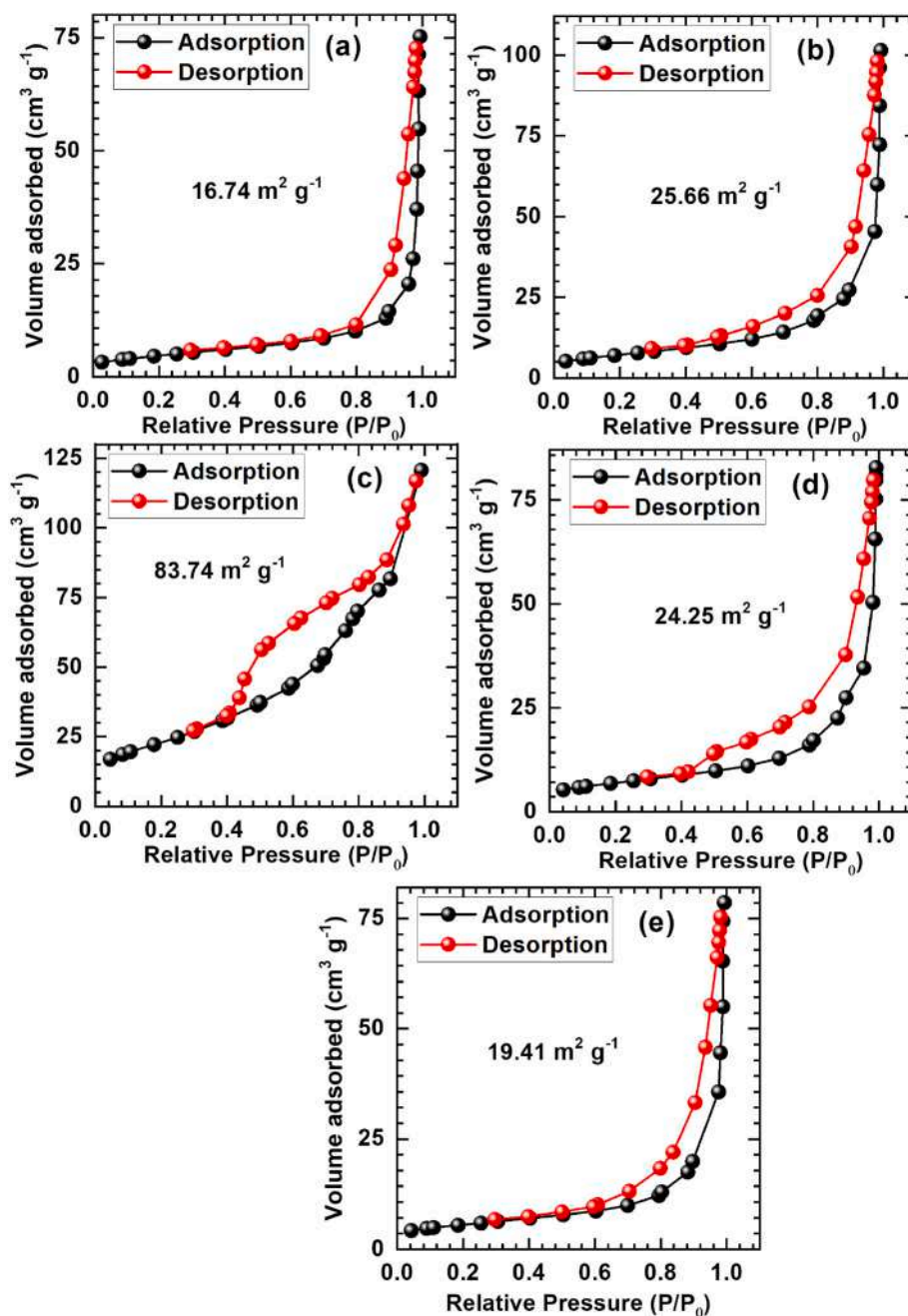


Fig. 3. Nitrogen adsorption-desorption isotherm of samples (a) H-NCP-1, (b) H-NCP-2, (c) H-NCP-3, (d) H-NCP-4 and (e) H-NCP-5.

structural water in the prepared Ni-Cu phosphate thin film samples. The FT-IR investigation indicates successful synthesis of the hydrous Ni-Cu phosphate thin films.

The N_2 adsorption-desorption experiments were executed for the analysis of specific surface area and pore characteristics of H-NCP series samples, as depicted in Fig. 3 (a–e). The detected isotherms of H-NCP series sample reveal a type III isotherm with H3 type hysteresis loop except for sample H-NCP-3, which exhibits hysteresis of type IV isotherm and H2 type of physisorption [38]. The type III isotherm represents most likely macroporous structural of material, and a lower energy of adsorption, whereas, type IV isotherm indicates characteristic property of mesoporous material [39]. A typical H3 type hysteresis loop of H-Ni-Cu phosphate series samples represent plate-like particles generating slit-shaped pores. On the other hand, H2 type hysteresis loop of H-NCP-3 (c) sample represents well-ordered pores with narrow as well as wide portions due to interconnecting channels [39,40].

Accordingly, BET surface area were calculated as the 16.74, 25.66, 83.74, 24.25 and 19.41 $m^2 g^{-1}$ for samples H-NCP-1, H-NCP-2, H-NCP-3, H-NCP-4 and H-NCP-5, respectively.

The BET results reveal that, H-NCP electrode with optimum composition of Ni and Cu (50:50), exhibits large surface area of 83.74 $m^2 g^{-1}$. The obtained high surface area can assists more active sites for electrochemical interactions with electrolyte ions and it is convenient for energy storage application. The average pore size distribution of H-NCP series is shown in Fig. S2 (see ESD). Average pore diameters of 26.83, 23.79, 8.90, 24.03 and 20.76 nm are found for samples H-NCP-1, H-NCP-2, H-NCP-3, H-NCP-4 and H-NCP-5, respectively. This macro and mesoporosity along with higher surface area of the electrodes is beneficial for electrochemical capacitive performance.

The chemical environment and composition of the elements are investigated by employing XPS analysis. The survey spectrum of XPS for sample H-NCP-3 (Fig. 4 (a)) displays existence of Ni, Cu, P and O

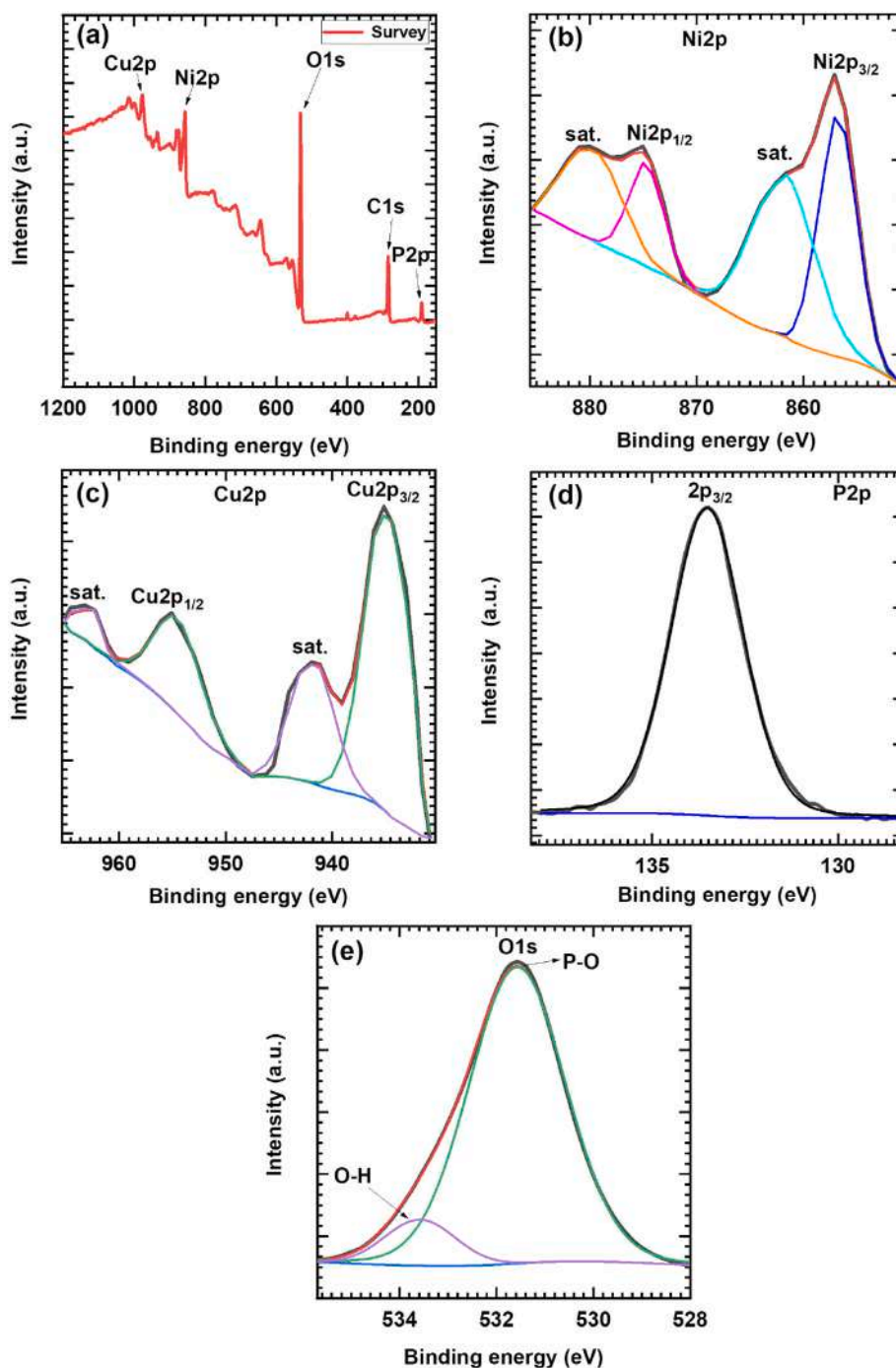


Fig. 4. XPS complete survey spectra (a) and the corresponding (b) Ni2p, (c) Cu2p, (d) P2p and (e) O1s of the sample H-NCP-3.

elements. The Ni2p XPS spectrum in shown Fig. 4 (b) exhibits two peaks at 874.6 and 856.90 eV corresponding to Ni2p_{1/2} and Ni2p_{3/2}, respectively which are characteristic to Ni²⁺ states with satellite peaks at 861.7 and 879.9 eV are attributed to Ni³⁺ placed at the surface [26,41,42]. For the XPS spectrum of Cu2p region (Fig. 4 (c)), the peak at 935.0 eV binding energy corresponds to Cu2p_{3/2} along with satellite peak at 941.9 eV binding energy, signifies presence of Cu⁺ [43]. Similarly, the intense peak at 955.1 eV binding energy implies Cu2p_{1/2} and the satellite peak at 963.3 eV reveal Cu²⁺ oxidation state [44]. The P2p spectrum reveals a peak at 133.5 eV is due to 2P_{3/2} state, which represent P—O bonding (Fig. 3 (d)), and confirms pentavalent state of phosphorous (PO₄³⁻) [45,46]. Fig. 4 (e) displays the spectrum of O1s which deconvoluted into two peaks at 530.9 and 532.2 eVs attributed to strong

P—O and minute amount of O—H which reaffirms hydrous nature of H-NCP-3 thin film [47].

The change in microstructure of Ni-Cu phosphate thin film electrodes is visualized by FE-SEM images, owing to the ratio variation of Ni:Cu in synthesis process. The SEM micrographs of Ni-Cu phosphate thin film electrodes at two different magnifications (X500 and X2000) are depicted in Fig. 5 (a1–e2). The FE-SEM pictures of H-NCP-1 for pristine nickel phosphate displayed in Fig. 5 (a1, a2), indicates microplates like architecture consisting of irregular shapes with average length of 12.23 μm and average thickness of about 1.4 μm. FE-SEM morphology of H-NCP-2 sample is shown in Fig. 5 (b1, b2), the increased concentration of copper in H-NCP-2 thin film exhibits change in morphology from dense microplates like network to microflower with interconnected

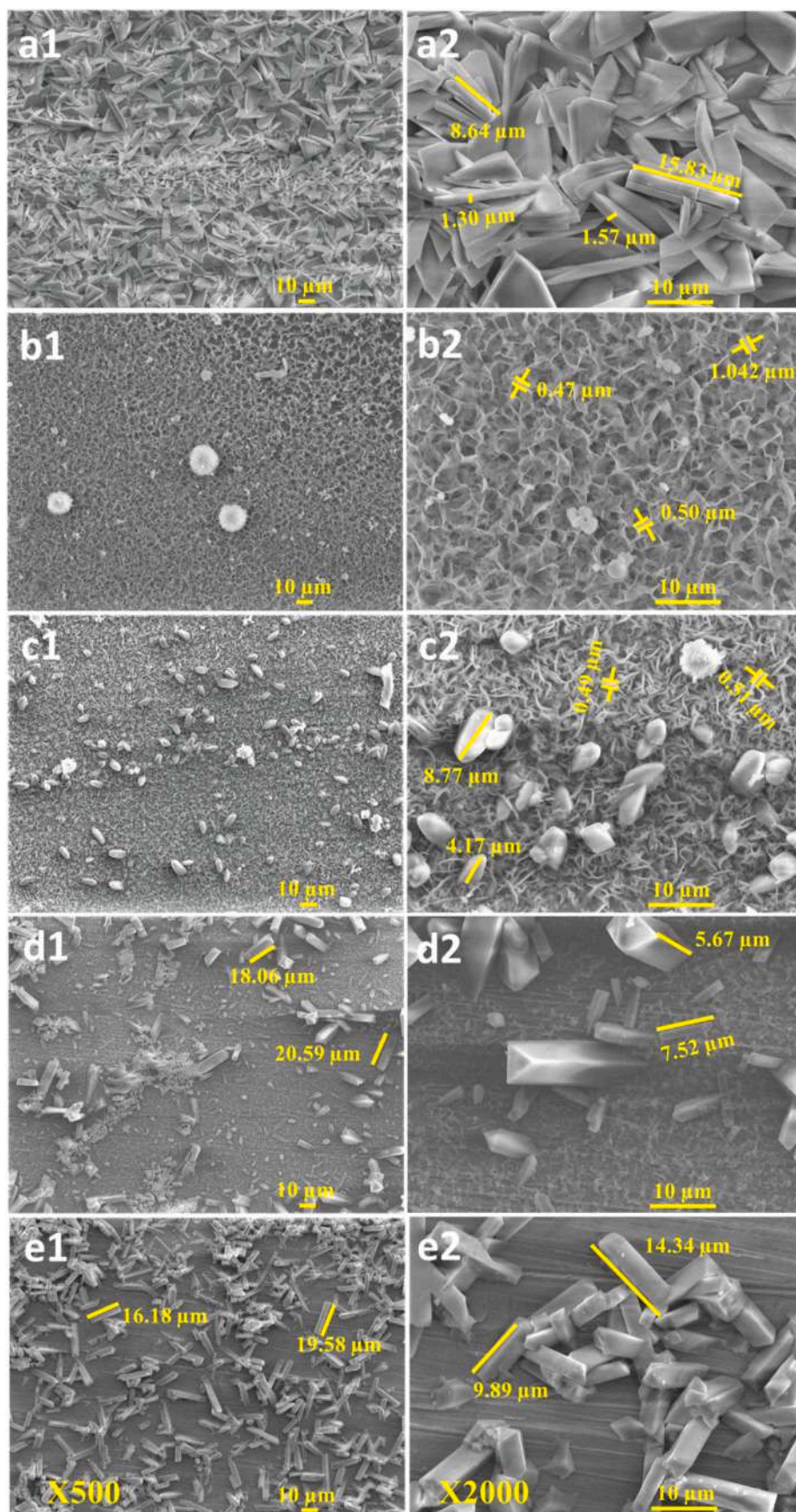


Fig. 5. FE-SEM images of Ni-Cu phosphate electrodes: (a1, a2) H-NCP-1, (b1, b2) H-NCP-2, (c1, c2) H-NCP-3, (d1, d2) H-NCP-4, and (e1, e2) H-NCP-5 at different magnifications of X500 and X2000.

microflakes like structure. It is observed that, the microflakes are interconnected with each other and microflowers are over grown on the surface of interconnected microflakes with an average thickness of 0.67 μm . Further increase in the content of copper for H-NCP-3 thin film sample shows the microflakes like morphology with some individually overgrown microrods as displayed in Fig. 5 (c1, c2). Also, these microflakes are connected to each other forming into interconnected networks. The average thickness of flakes is 0.50 μm which is less than observed for H-NCP-2 sample. The interconnected flakes like network of H-NCP-3 can give enough space for diffusion of electrolyte ions, which is highly desirable for SC electrodes [48]. Fig. 5 (d1, d2) displays a microrod-like morphology with an average thickness of 6.59 μm over microflakes with further increase of Cu concentration in H-NCP-4 thin film sample. The sample H-NCP-5 of pure copper phosphate exhibited in Fig. 5 (e1, e2) represents uneven structured microrods with an average

length of 12.11 μm . The surface morphologies of H-NCP series thin films demonstrate conversion of microplates to microflakes to microrod like structure upon Ni:Cu composition variation in Ni-Cu phosphate thin films. Such a change in microplates to microrods like morphology can allow faster charge transport and rapid ion accessibility during an electrochemical reaction [49].

The chemical composition of Ni:Cu phosphate executed by EDS study and shown in Fig. S3 (see ESI). For sample H-NCP-1 exhibits Ni, P and O elements, and affirms formation of nickel phosphate. Similarly, the H-NCP-5 sample exhibits Cu, P and O elements and affirms formation of copper phosphate. The other samples (H-NCP-2 to H-NCP-4) exhibit nickel, copper, phosphorous also oxygen elements in the EDS analysis without any other impurity, which confirm successful preparation of Ni-Cu phosphate material in thin film form. The observed atomic ratios of Ni:Cu (H-NCP-1 to H-NCP-5) electrodes along with experimental ratios

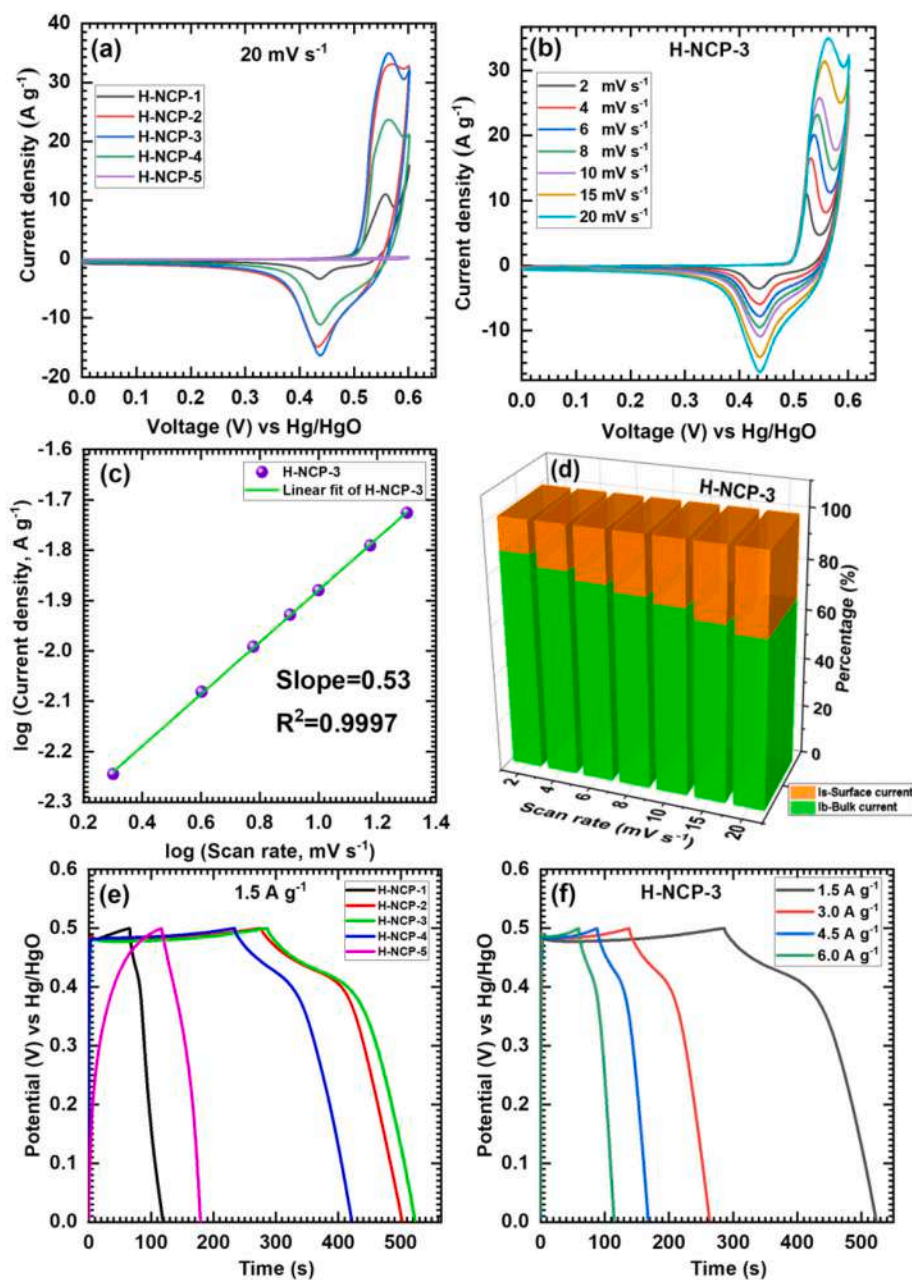


Fig. 6. Electrochemical properties of H-NCP electrodes (a) comparative CV plots at scan rate of 20 mV s^{-1} , (b) CV curves of H-NCP-3 electrodes at scan rates from 2 to 20 mV s^{-1} , (c) plot of $\log(\text{peak currents})$ vs $\log(\text{scan rate})$ for electrode H-NCP-3, (d) plots of current contribution of battery type and capacitive type processes of H-NCP-3 electrode, (e) comparative GCD plots at current density of 1.5 A g^{-1} , (f) GCD curves of H-NCP-3 electrodes at current densities from 1.5 to 6.0 A g^{-1} .

are provided in Table S1 and it affirms a change in Ni:Cu composition in Ni-Cu phosphate material, according to experimental molar variation. The SEM and EDS results confirm Ni:Cu ratio variation influence to the morphological alteration of Ni-Cu phosphate material.

4. Electrochemical analysis of nickel copper phosphate thin films

The morphology alteration caused by molar ratio variation of nickel and copper in Ni-Cu phosphate and its effect on supercapacitive performance was examined in electrochemical cell of three electrode system. The CV curves of H-NCP series electrodes are measured in optimized potential range of 0 to 0.6 V (vs Hg/HgO), as shown in Fig. S4 (a) (see ESI). The comparative CV curves of H-NCP series electrodes at 20 mV s⁻¹ scan rate are revealed in Fig. 6 (a). The area under CV curve of H-NCP-3 (Fig. 6 (b)) electrode is higher than nickel phosphate (H-NCP-1), copper phosphate (H-NCP-5) and other Ni-Cu phosphate (H-NCP-2, H-NCP-4) electrodes as shown in Fig. S4 (see ESI). The microstructure of interconnected microflakes in H-NCP-3 sample reveal higher current area under the curve than microplates and microrods like structure may be due to high surface area offered by large number of pores created in interconnected structure.

The CV curves of H-NCP-3 electrode at different scan rates from 2 to 20 mV s⁻¹ are displayed in Fig. 6 (b) and CV for reaming electrodes are provided in Fig. S4 (a) (see ESI). The nickel phosphate electrode (H-NCP-1) and copper phosphate electrodes (H-NCP-5) show well-established redox peaks (Fig. S4 (b) and (e)) (see ESI) confirm pseudocapacitive nature of material. Increasing copper content affects the morphology that ultimately influence on the electrochemical performance in terms of area under CV curves. The change of CV curve nature from nickel phosphate to copper phosphate electrode (H-NCP-1 to H-NCP-5) is very clearly noticeable in the Fig. S4 from (b) to (e) (see ESI). Area under the CV curve increases for each sample with increasing scan rates from 2 to 20 mV s⁻¹, which exhibits the voltammetric current is directly proportional to the scan rate. Furthermore, the reaction kinetics of CV curves was obtained by using power's law expressed as follows;

$$i_p = av^b \quad (11)$$

where, i_p denotes peak current, a and b are adjustable factors, v denotes scan rate, while b denotes determined values. The graph of $\log(i)$ vs $\log(v)$ is used to calculate b value from slope of graph, where, if b is near to 0.5, the diffusion-controlled charge storage process is dominant, while b is near to 1 represent the non-diffusion-controlled process [50]. The calculated b -value of sample H-NCP-3 is 0.53, as shown in Fig. 6 (c). The prepared H-NCP-1, H-NCP-2, H-NCP-4, and H-NCP-5 electrodes exhibit b values of 0.52, 0.50, 0.51, and 0.76, respectively as shown in Fig. S5 (see ESI). The values of b for H-Ni-Cu phosphate series electrodes are between 0.5 and 1, illustrating both (diffusive as well as capacitive) processes are responsible for charge storage. To evaluate the distinct influence of battery process (diffusion controlled) as well as surface pseudocapacitive (non-diffusion controlled), modified Power's law is used as expressed in following equation.

$$I_p = I_s v + I_b v^{1/2} \quad (12)$$

where, I_p denote peak current density, $I_s v$ denote pseudo-capacitive process (I_{surface}), $I_b v^{1/2}$ represent bulk process (I_{bulk}) and v is the scan rate [16]. Distribution of current density from pseudo-capacitive (I_{surface}) as well as battery-like (I_{bulk}) process for all five Ni-Cu phosphate thin films electrodes calculated using above equation and expressed in Fig. S6 (see ESI). It depicts that, with increasing scan rate the distribution from pseudocapacitive process increases, which concludes that capacitive process is dominant at high scan rate and diffusive process is predominant at low scan rate and so, the active material demonstrate battery like behaviour at low scan rate. At lower scan rate, due to more time available for the diffusion process, electrolytic ions get accessibility

in inner surface of the material which improves the utilization of electrode material and store more charges and vice versa. The H-NCP-5 electrode (copper phosphate) shows highest capacitive contribution (24 %) than the other samples at scan rate of 2 mV s⁻¹ (Fig. S6 (d) (see ESI)). Conversely, the nickel phosphate electrode (H-NCP-1) shows comparatively less surface capacitive current contribution (~10 %) in total current at scan rate of 2 mV s⁻¹ (Fig. S6 (a) (see ESI)). The H-NCP-3 electrode shows (Fig. 6 (d)) surface moderate capacitive current contribution of ~13 % and other sample reveals different values of current contribution owing to different chemical compositions (nickel and copper) and morphology.

The synthesized H-NCP series electrodes are further studied by performing GCD measurements in the optimized potential of 0.0 to 0.5 V (vs Hg/HgO) and comparative GCD plots of all H-NCP electrodes at a current density of 1.5 A g⁻¹ are exhibited in Fig. 6 (e). The GCD plots of H-NCP-3 electrode at various current densities are exhibited in Fig. 6 (f), and GCD plots of other H-NCP series electrodes are given in Fig. S7 (a-d) (see ESI). The nickel phosphate (H-NCP-1) and copper phosphate (H-NCP-5) electrodes show distinct nature of charge-discharge curve as shown in Fig. S7 (see ESI). The quasi-triangular (non-linear) profile of the GCD plots exhibits the intercalation pseudo-capacitive nature of Ni-Cu phosphate material [51,52]. The iR drop at the discharge curve is very negligible and it is found in the range of ~0.005 to 0.02 V/Hg/HgO for current densities from 1.5 to 6.0 A g⁻¹. Such a low iR drop suggests excellent electrochemical conductivity of Ni-Cu phosphate thin film electrodes, and it is attributed to the binder-free synthesis by the hydrothermal method. We have calculated the energy efficiency (Eq. (3)) and the maximum energy efficiency value of 82.8 % is obtained for H-NCP-3 electrode at 1.5 A g⁻¹ current density.

The H-NCP-3 (Fig. 6 (f)) electrode with optimum Ni:Cu ratio shows high discharging time and reveal high charge storing capacity than other Ni-Cu phosphate electrodes. The C_s is calculated from GCD curves for H-NCP series electrodes using the Eq. (2) and shown in Fig. 7 (a). The H-NCP-3 electrode displays maximum C_s value of 711 F g⁻¹ (355.5 C g⁻¹) at a current density of 1.5 A g⁻¹ and maintain C_s of 672 F g⁻¹ (336 C g⁻¹) at current density of 6.0 A g⁻¹ confirms good capacitive retention (85 %) even at high current density as displays in Fig. 7 (a). Similarly, the H-NCP-1, H-NCP-2, H-NCP-4 and H-NCP-5 thin film electrodes show maximum C_s value of 159, 672, 555 and 185 F g⁻¹, respectively at 1.5 A g⁻¹ current density as shown in Fig. 7 (a) and the C_s values calculated at various current densities from 1.5 to 6.0 A g⁻¹ are plotted in Fig. S8 (see ESI). It indicated that, C_s value decreases at high current density because of quick charging-discharging rate. Conversely, large exertion of active material is feasible at lower current density which results in the high capacitance values, owing to more penetration time available for electrolytic ions to access inner surface of the material [53]. The well electrochemical capacitive behaviour of H-NCP-3 electrode is originated from synergistic influence of nickel and copper species (50:50 ratio) and high surface area offered by interconnected flakes-like morphology.

Electrochemical cycling stability is crucial parameter for the SC application. The electrochemical stability of H-NCP-3 electrode was examined for 4000 GCD cycles at current density of 11.5 A g⁻¹ and exhibited in Fig. 7 (b). The H-NCP-3 electrode shows 88.5 % capacitive retention over 4000 GCD cycles. The GCD plots of first and last 5 cycles are presented as inset (A and B) of Fig. 7 (b). The reduction in charge-discharge time is noticed in final GCD cycles (inset Fig. 7 (b)) and such, decrease in capacitance after 4000 cycle is observed may be due to the loss of minute active material by the dissolution or detachment during the early charging-discharge cycles [54]. The XRD, XPS and FE-SEM analysis of nickel copper phosphate (H-NCP-3) sample was carried out after the stability test. As mentioned in the XRD analysis, the before stability H-NCP-3 sample displays crystalline nature due to the formation of interconnected microflakes of nickel copper phosphate material. Moreover, the XRD patterns of H-NCP-3 samples for the before and after stability test seem almost similar, as shown in Fig. S9 (a) (see ESI). There is a minor change in XRD pattern of the H-NCP-3 sample after stability.

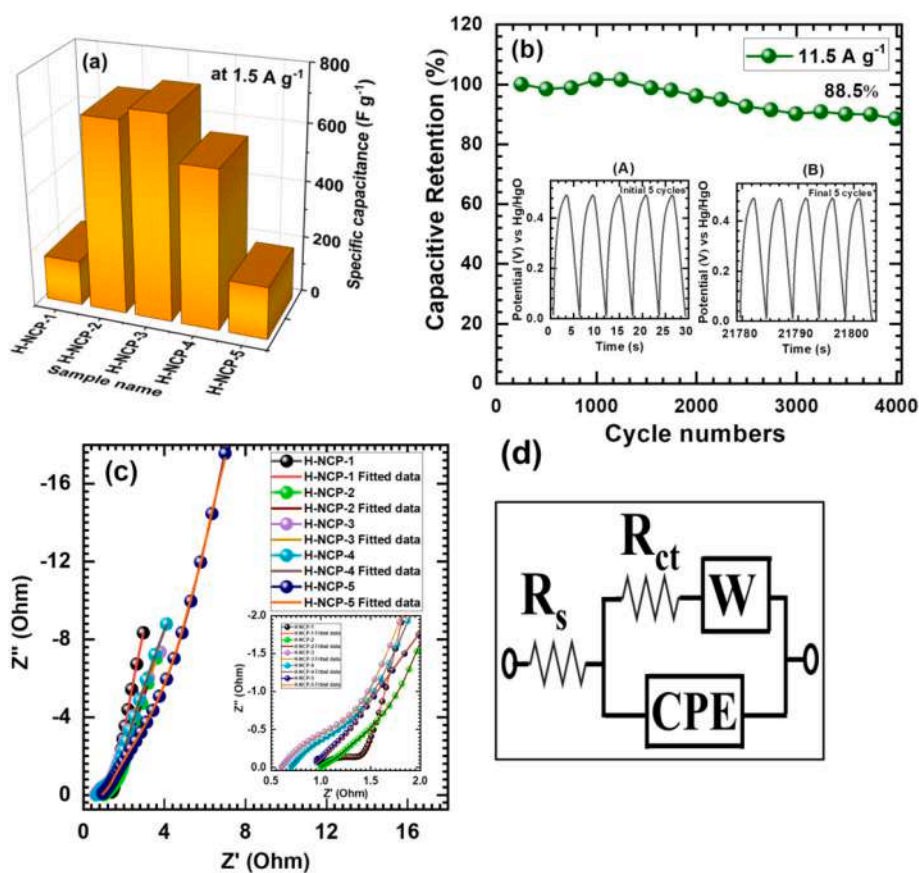


Fig. 7. (a) Specific capacitance at current density of 1.5 A g^{-1} of H-NCP electrodes (H-NCP-1 to H-NCP-5), (b) Capacitive retention vs cycle number plot of H-NCP-3 electrode at 11.5 A g^{-1} current density for 4000 cycles (inset: GCD plots of (A) first and (B) last 5 cycles). (c) Nyquist plots of H-NCP electrodes (H-NCP-1 to H-NCP-5) and (d) the fitted equivalent circuit.

Upon matching, it is confirmed that the most intense peaks of H-NCP-3 sample (before and after stability) match perfectly with $\text{Ni}_3(\text{PO}_4)_2 \cdot 8\text{H}_2\text{O}$ (JCPDS: 00-033-0951) and $\text{Cu}_3(\text{PO}_4)_2$ (JCPDS-01-070-0494). Most of the peaks of H-NCP-3 sample match with the peaks present in the $\text{Ni}_3(\text{PO}_4)_2 \cdot 8\text{H}_2\text{O}$ and $\text{Cu}_3(\text{PO}_4)_2$, confirming the relatively stable nature of nickel copper phosphate thin film electrode prepared by hydrothermal method. Moreover, to investigate the structural stability of nickel copper phosphate electrodes, the XPS analysis of nickel copper phosphate (H-NCP-3) electrodes before and after the stability test was carried out (Fig. S9 (b)). In the XPS analysis of H-NCP-3 electrode, it is observed that the valence states of Ni and Cu sites are slightly changed because of oxidation/reduction of cations after stability. In Ni2p spectra (Fig. S9 (b (i))), the Ni^{3+} state is slightly suppressed after stability and shows a little increase in Ni^{2+} state (855.2 and 872.8 eV), which is evident in the transition of Ni states from Ni^{3+} to Ni^{2+} after the stability [26,41,42]. Similarly, oxidation in valence states of Cu cation is observed in Cu2p region, as presented in Fig. S9 (b (ii)), which demonstrates oxidation from Cu^+ to Cu^{2+} (934.2 and 954.3 eV) [43,44]. Moreover, the satellite peak at 940.2 and 943.1 reveals Cu^{2+} oxidation state of Cu cations, which further confirms the partially filled d-orbital of divalent copper (Cu^{2+}) [43,44]. Also, a slight change in Cu2p and Ni2p binding energies after stability material confirms a similar transformation of valence states of Cu and Ni cations. However, the major intensity decrement of P2p (phosphorous) spectra is observed after stability (Fig. S9 (b (iii))), which shows the pentavalent state of phosphorous is diminished near the surface of electrode material. Moreover, an extra metal-oxygen bond (M-O) is observed after the stability in O1s spectra, as shown in Fig. S9 (b (iv)). These transformations of valence states of cations and the appearance of M-O bonding confirms the insertion and extraction of OH^- ions in the material during the charge-discharge process. The

overall observed changes in the XPS study state that the vacancy sites of $(\text{PO}_4)_3$ are occupied by the intercalated hydroxyl ions during charge and deintercalated from their accommodated positions upon undergoing the discharge process.

Furthermore, to examine the morphological change of nickel copper phosphate electrodes, FE-SEM analysis (at different magnifications) of nickel copper phosphate (H-NCP-3) electrodes before and after long-term cyclic stability test was carried out (Fig. S9 (c)). It is clearly observed that the microflakes like morphology is not much disturbed and looks similar to before and after cycling (Fig. S9 (c (i, iii))). At higher magnification of SEM images (Fig. S9 (c (ii, iv))), the external surface of H-NCP-3 microflakes seems plane after cycling, where the overgrown particles have vanished. The surface of microflakes is clearly observed, which further confirms of sustainability of morphology after several cycling (presented in Fig. S9 (c (i, iii))). The small change in surface morphology without degrading microflakes like structure displaying good electrolyte ion interaction and the stable morphology of the material. Less damage in microstructure of microflakes proves excellent electrochemical cyclic stability of nickel copper phosphate (H-NCP-3) thin film electrode. Conclusively, XRD, XPS and FESEM analysis of Ni-Cu phosphate thin film electrode after stability test illustrates that the crystalline phase and interconnected microflakes like morphology are relatively stable and can sustain strain and stress upon the intercalation of OH^- ions during charging and discharging, and suggests that binder free Ni-Cu phosphate thin film electrodes are suitable for energy storage application. Also, it is found that, the achieved supercapacitive performance for Ni-Cu phosphate electrodes is higher by means of C_s and durability compared to pristine nickel and copper phosphate/pyrophosphate based materials reported previously, as given in Table S2 (see ESI).

The measured electrochemical impedance quantitatively examines the characteristics of thin film electrodes and electrolytes and interfacial contact between them. The Nyquist plots of H-NCP series electrodes are presented in Fig. 7 (c). Typically, all Nyquist plots display two different portions: the semi-circle in high-frequency portion indicates solution resistance (R_s) and charge transfer resistance (R_{ct}), the middle frequency portion related with diffusion-controlled process denoted by Warburg element (W), and the low-frequency (straight line) part shows the capacitive behaviour of electrode [55,56]. An equivalent circuit is shown in Fig. 7 (d) and the fitted factors of equivalent circuit are given in Table S3 (see ESI). The R_s and R_{ct} represent interface resistance along with constant phase element (CPE) exhibit general imperfect capacitor (when $n = 1$ and $Q = C$) recognized to semi-infinite diffusion charges [57]. The R_s values for H-NCP-1, H-NCP-2, H-NCP-3, H-NCP-4 and H-NCP-5 electrodes are found to be 0.81, 0.98, 0.59, 0.68, and 0.90 $\Omega \text{ cm}^{-2}$, respectively, and the R_{ct} values are 1.73, 5.33, 1.60, 2.80, and 3.50 $\Omega \text{ cm}^{-2}$, respectively. The smaller values of R_s and R_{ct} for H-NCP series thin films indicate a good attachment (binder-free) of active material with current collector (SS substrate) and the spontaneous electrochemical reaction among the electrolyte and active electrode material. Also, it reveals good ionic conductivity of electrolyte and very

low R_{ct} value of material which lead to a high capacitance of H-NCP-3 electrode.

4.1. Hybrid aqueous supercapacitor (HASC) device

Improved working voltage range and higher SE is the vital benefits of a hybrid SC device so herein HASC device is fabricated. To evaluate practical feasibility of Ni-Cu phosphate electrode (H-NCP-3) in hybrid device, a two-electrode system executed by constructing HASC device in 1 M KOH. The HASC device was fabricated by incorporation of best achieved Ni-Cu phosphate electrode (H-NCP-3) and rGO electrode as cathode and anode electrode, respectively. The schematic of the as fabricated HASC device is illustrated in Fig. 8 (a). The electrochemical study and characterization of rGO electrode (anode) are provided in supporting information (Fig. S10) (see ESI). Fig. 8 (b) displays the CV plots of rGO and H-NCP-3 electrodes within distinct potential windows at a 50 mV s^{-1} scan rate in a 1 M KOH. Fig. 8 (c) demonstrates that the two individual pseudocapacitive electrodes with a balanced combination can achieve an extensive operating voltage in the HASC device. The voltage of HASC device was optimized within the range of 1.2–1.7 V by CV analysis, as revealed in Fig. S11 (a) (see ESI). The quasi-rectangular

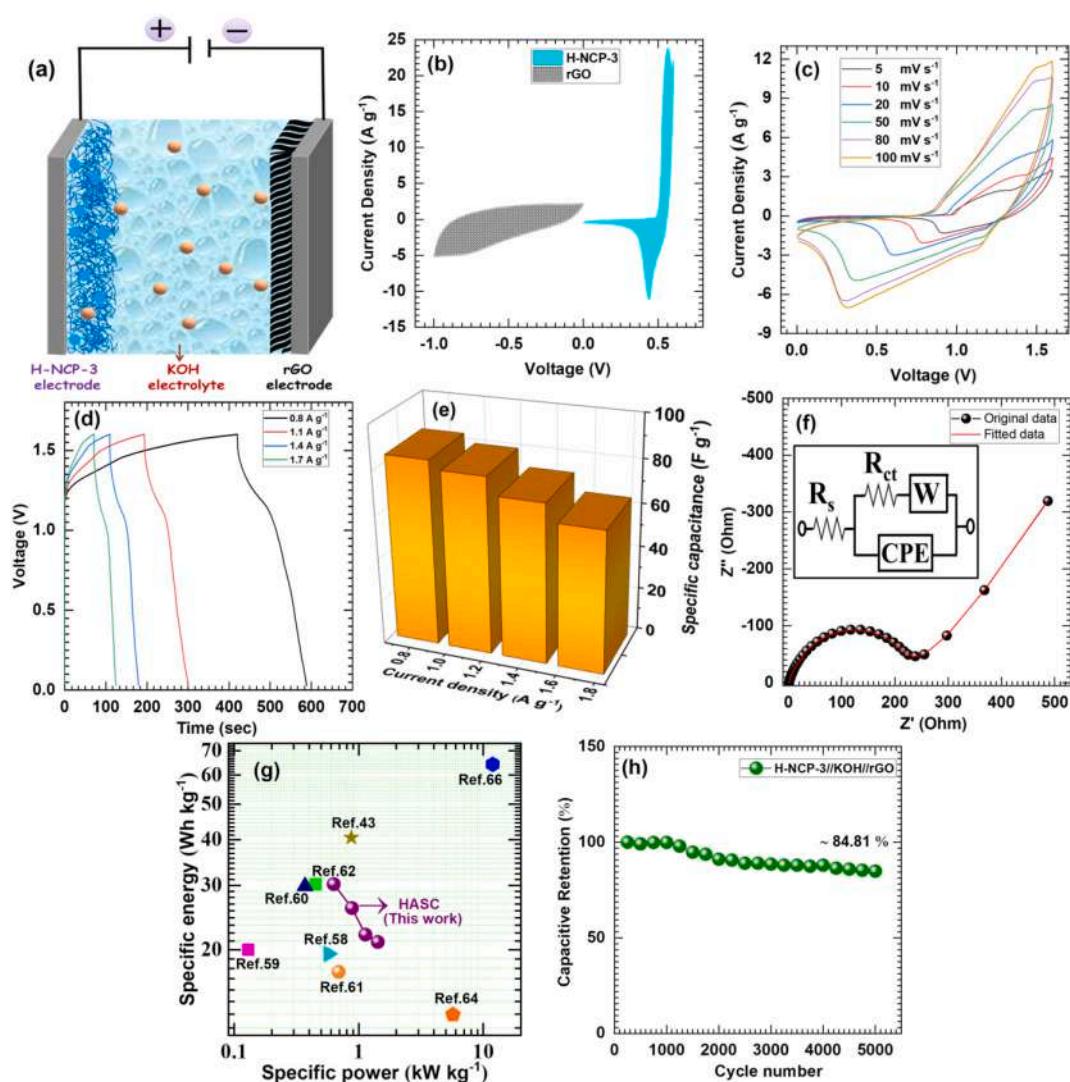


Fig. 8. (a) Schematic illustration of process to construct the HASC device, (b) The electrode CV curves for the rGO and H-NCP-3 electrode at a scan rate of 50 mV s^{-1} , (c) the CV and (d) GCD curves for the HASC device at different scan rates (5–100 mV s^{-1}) and current densities (0.8–1.7 A g^{-1}), respectively, (e) a plot of C_s with employed current densities for HASC device, (f) Nyquist plot for HASC device and the inset shows equivalent circuit for fitted data, (g) Ragone plot of HASC device with available literature, (h) a plot of capacitive retention versus cycle number for HASC device.

nature of CV plots are achieved up to voltage within 0 to 1.6 V and thereafter, sudden increase in cathodic current is observed in CV profiles, signifying the corrosion of the electrode material and decomposition of the electrolyte can lead to irreversible electrochemical reactions.

Furthermore, the GCD curves of the HASC device at various voltages (+1.2–1.7 V) are exhibited in Fig. S11 (b) (see ESI). At a voltage of +1.6 V, HASC device exhibits well GCD performance. Also, Fig. 7 (d) reveals the GCD curves within a 0.0 to +1.6 V voltage range at 0.8–1.7 A g⁻¹ current densities. The C_s (displayed in Fig. 8 (e)) of the HASC device calculated by using the discharge times according to Eq. (2) and maximum C_s of 85 F g⁻¹ is obtained at a current density of 0.8 A g⁻¹.

Electrochemical impedance analyses of HASC device are presented in Fig. 8 (f). Nyquist plot with fitted equivalent circuit as shown in Fig. 8 (f) for HASC device. From the fitting circuit, equivalent series resistance (R_s) and charge transfer resistance (R_{ct}) of the HASC device are estimated to be 1.05 and 247.3 Ω cm⁻². A less R_s signifying electrochemical interaction in among the electrode material as well as the electrolyte ions. Also, in equivalent circuit W (4.49 Ω) and CPE (0.82 mF) are Warburg impedance and general imperfect capacitor when n = 0.84, respectively, where the CPE represent an imperfect capacitor owing to semi-infinite diffusion of ions [57]. Furthermore, SE and SP are crucial factors for a hybrid SCs. Fig. 8 (g) displays the comparative Ragone plot of the HASC device and it demonstrate maximum SE of 30.22 Wh kg⁻¹ at a SP of 0.63 kW kg⁻¹. Also, the SE of 21 Wh kg⁻¹ is retained even at high SP of 1.42 kW kg⁻¹. The superior SE and SP values are the outcomes of rational combination of cathode with the synergy of Ni-Cu phosphate and anode of rGO electrode. The cycling performance of HASC device at a current density of 3 A g⁻¹ is presented in Fig. 8 (h). The HASC device displays 84.81 % capacitive retention over 5000 cycles, displaying

superior reversibility of the HASC device. All of above tests exhibits that the HASC device with favourable cycling stability as well as excellent SE and SP has a great potential application as the hybrid SCs.

4.2. Hybrid all solid-state supercapacitor (HASSC) device

Last few years, significant demand for portable electronics such as roll-up-displays, mobile phones, wearable electronics, etc. have special requirements of HASSC device as the latest ESDs due their facile fabrication, cheap cost packaging, lightweight, compatibility and smaller size. In this regard, Ni-Cu phosphate electrode based HASSC device was constructed using PVA-KOH gel electrolyte as demonstrated in schematic Fig. 9 (a) and probed its applicability. The HASSC device was assembled with H-NCP-3 (Ni_{1.62}Cu_{1.35}(PO₄)₂) as a cathode and rGO selected as an anode with gel electrolyte; its SC performance were probed using CV, GCD, and EIS study. The CV curves of the HASSC device are estimated at various voltage range (+1.2 to +1.7 V), as displayed in Fig. S12 (a) (see ESI) at a 20 mV s⁻¹ fixed scan rate. However, a fabricated HASSC device shows a quasi-rectangular nature of CV curve in the voltage range 0 to 1.6 V. Hence, the HASSC device is examined within 0–1.6 V at scan rates from 5 to 100 mV s⁻¹ and depicted in Fig. 9 (b). The show CV curves maintain their nature at various scan rates, indicating better capacitive characteristics of the device. The GCD plots of the HASSC device at voltage range of +1.2–1.7 V at 2.0 A g⁻¹ are displayed in Fig. S12 (b) (see ESI). In the voltage range 0–1.6 V, the HASSC device exhibits well GCD performance. Fig. 9 (c) exhibits GCD curves of the HASSC device at 0.6–2.7 A g⁻¹ current densities. Non-linear behaviour of GCD curves affirms the typical diffusion-controlled charge storage mechanism of pseudocapacitive (H-NCP-3) electrode. The HASSC device

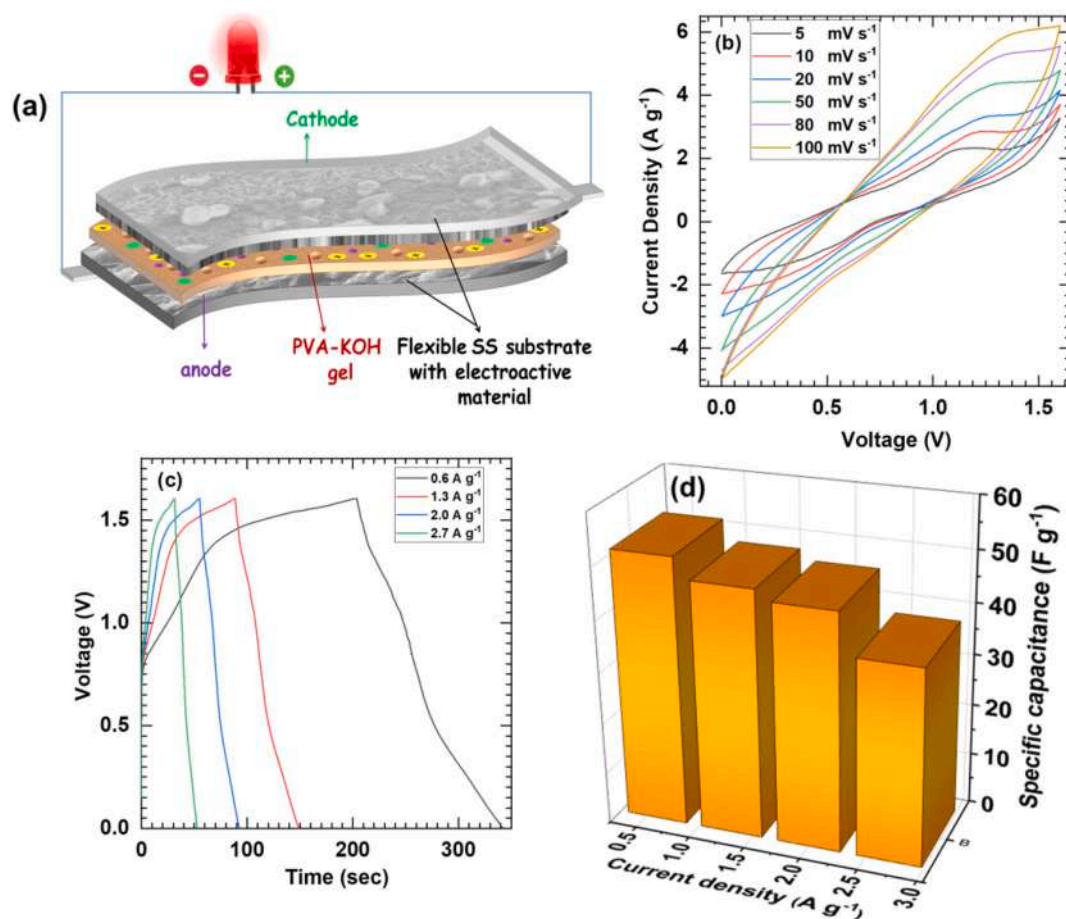


Fig. 9. (a) Schematic illustration of assembled HASSC device, (b) the CV and (c) GCD curves for the HASSC device at different scan rates (5–100 mV s⁻¹) and current densities (0.6–2.7 A g⁻¹), respectively, (d) a plot of C_s with employed current density for HASSC device.

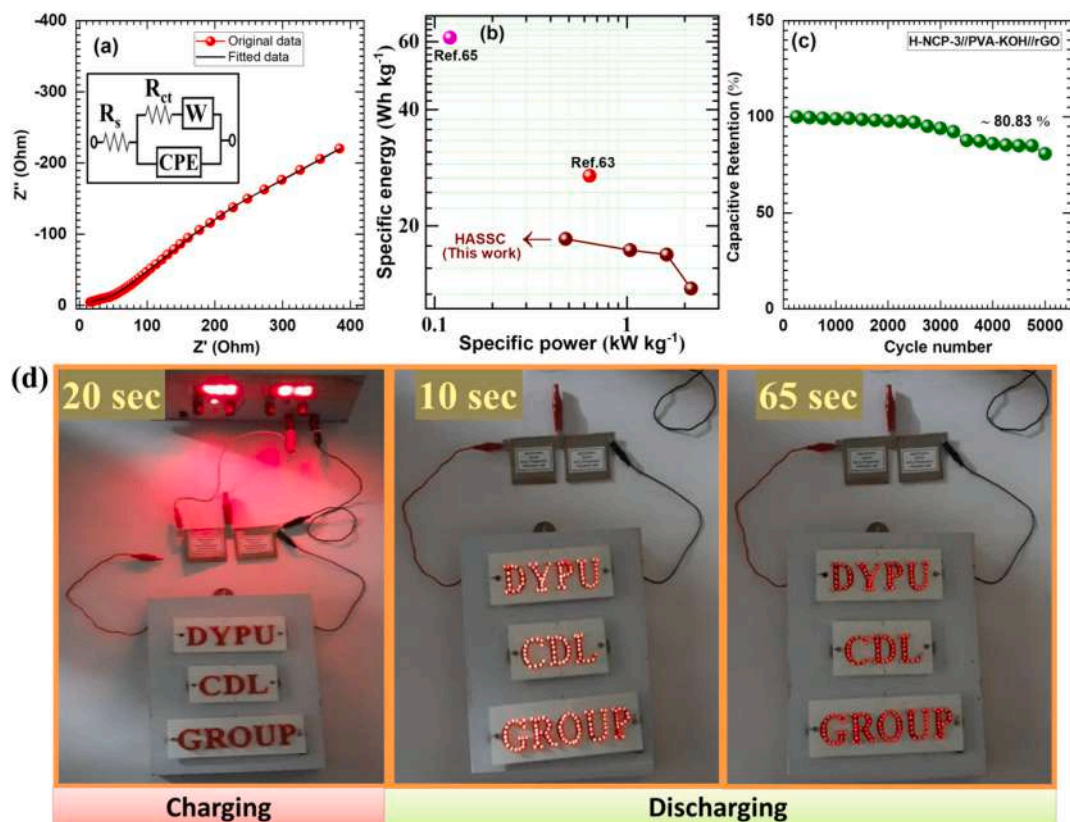


Fig. 10. (a) Nyquist plot for HASSC device and the inset displays equivalent circuit for fitted data, (b) Ragone plot of HASSC device with available literature, (c) a plot of capacitive retention versus cycle number for HASSC device, (d) Digital photographs of device demonstration of HASSC device with glowing panel of 201 red LEDs panel at different time periods. (For interpretation of the references to colour in this figure legend, the reader is referred to the web version of this article.)

exhibited maximum C_s of 52 F g^{-1} at current density of 0.6 A g^{-1} as displayed in Fig. 9 (d).

Fig. 10 (a) shows Nyquist plot of the HASSC device and inset shows fitted equivalent circuit. The low values of R_s ($6.33 \text{ } \Omega$) and R_{ct} ($17.3 \text{ } \Omega$) of HASSC device suggest the facile electrochemical interaction among electrolyte and electrode material. Also in equivalent circuit, W ($0.20 \text{ } \Omega$) and CPE (0.50 mF , $n = 0.84$) are Warburg impedance and general imperfect capacitor. Fig. 10 (b) shows a comparative Ragone plot of the HASSC device, which displays that the HASSC device has achieved the maximum SE of 18.53 Wh kg^{-1} at SP of 0.47 kW kg^{-1} . The stability test of the HASSC device is examined for 5000 GCD cycles at current density of 4.8 A g^{-1} , and 80.83 % retention is achieved as illustrate in Fig. 10 (c). The HASSC device displays long-term stability as well as good interaction between electrode and electrolyte ions. Fig. 10 (d) illustrate the practical applicability of the HASSC device, illumination of red LED panel is executed using two series connected HASSC devices. Two series connected HASSC devices operated at voltage of $+3.2 \text{ V}$ for 20 s and then discharged through a LED panel of 201 parallel connected LEDs. More strikingly, the HASSC device can glow the LED panel (201) for 65 s. The present demonstration of HASSC device proposes that it is a favourable hybrid ESD and can be utilize in portable electronic.

According to literature survey, there have not yet been studies on Ni-Cu phosphate material based hybrid ESDs and therefore, hereby the obtained performance of HASC and HASSC devices is compared with other metal phosphate based devices by means of SE, SP and stability, as given in Table S4 (see ESI). For example, Mirghni et al. [58] constructed $\text{NaNi}_4(\text{PO}_4)_3/\text{GF}/\text{AC}$ device in a 2 M NaNO_3 electrolyte and it shows SE of 19.5 Wh kg^{-1} at a SP of 0.57 kW kg^{-1} . An $\text{AC}||\text{NaNiPO}_4$ based asymmetric SC device was constructed by Senthilkumar et al. [59], which exhibits the SE of 20 Wh kg^{-1} and a SP of 0.13 kW kg^{-1} . Also, a $\text{NaNi}_{0.33}\text{Co}_{0.67}\text{PO}_4 \cdot \text{H}_2\text{O}/\text{AC}$ device constructed by Liu et al. [60]

revealed an SE of 29.85 Wh kg^{-1} and 0.374 kW kg^{-1} SP. Gu et al. [61] constructed $\text{Ni-CoP}@C/\text{CNT}/\text{GO}$ based SC and it exhibits an SP of 17.4 Wh kg^{-1} and SP of 0.69 kW kg^{-1} . Wang et al. [62] assembled $\text{T-Nb}_2\text{O}_5@/\text{Ni}_2\text{P}/\text{AC}$ asymmetric SC that presents a maximum SE of 30.2 Wh kg^{-1} and SP of 0.45 kW kg^{-1} . Lan et al. [63] fabricated $\text{NiCoP}/\text{NF}/\text{AC}$ asymmetric device, which exhibits SE of 27 Wh kg^{-1} at a SP of 0.64 kW kg^{-1} . Li et al. [64] demonstrate $\text{AC}/\text{Ni-P}/\text{NiCo}_2\text{O}_4$ asymmetric SC and the SC exhibit maximum SE 13.3 Wh kg^{-1} at a SP 5.7 kW kg^{-1} . Andikaey et al. [65] constructed an asymmetric SC device of $\text{FeCoCuP}/\text{AC}$. The $\text{FeCoCuP}/\text{AC}$ device exhibits maximum SE of 61.5 Wh kg^{-1} and a high SP of 1201.7 W kg^{-1} . H. Sharkawy et al. [43] assembled hybrid $\text{Ni-Cu-P}/\text{NF}/\text{AC}$ SC device and reported a high SE of 40.5 Wh kg^{-1} at 875 W kg^{-1} SP. Furthermore, Alzaid et al. [66] assembled $\text{Ni}_{0.75}\text{Mn}_{0.25}(\text{PO}_4)_2/\text{AC}$ device which shows remarkable SE of 64.2 Wh kg^{-1} and SP of $11,896 \text{ W kg}^{-1}$. Various electroactive materials based on Ni, Cu, P delivered different charge storage properties with enhanced electrochemical activities. The reported energy densities for $\text{T-Nb}_2\text{O}_5@/\text{Ni}_2\text{P}/\text{NF}$, $\text{FeCoCuP}/\text{NF}$, $\text{Ni-Cu-P}/\text{NF}$, and $\text{Ni}_{0.75}\text{Mn}_{0.25}(\text{PO}_4)_2/\text{NF}$ devices are little higher than current work, which may be owing to the usage of Ni-foam (NF) as a current collector. In this study, SS is employed as a current collector, which does not involve in the redox reaction and contribute in capacitance. Hence, the obtained SE and SP are ultimately delivered by the Ni-Cu phosphate material in present work. The HASC and HASSC devices display high performance which is ascribed to the several benefits delivered by Ni-Cu phosphate-based cathode such as, the microflakes like morphology, synergistic impact among bimetals and binder-free preparation of Ni-Cu phosphate thin film electrodes.

5. Conclusions

In this study, Ni-Cu phosphate thin films are successfully prepared on SS substrate with variation in nickel and copper content by utilizing single-step hydrothermal method. The XRD analysis affirms the monoclinic crystal structure, and XPS study and FTIR spectroscopy denote the hydrous nature of Ni-Cu phosphate ($\text{Ni}_{3-x}\text{Cu}_x(\text{PO}_4)_2 \cdot n\text{H}_2\text{O}$) thin films. The molar variation (Ni and Cu content) affects the reaction kinetics, eventually changing the morphology of microplates to microrods via microflakes and offers distinct surface area with numerous electroactive sites. The optimum Ni and Cu ratio (~1:1) in Ni-Cu phosphate ($\text{Ni}_{1.62}\text{Cu}_{1.35}(\text{PO}_4)_2 \cdot \text{H}_2\text{O}$) thin film electrode exhibit maximum C_s (C_s) of 711 F g^{-1} (355.5 C g^{-1}) at a current density of 1.5 A g^{-1} owing to high surface area ($83.74 \text{ m}^2 \text{ g}^{-1}$) and low EIS. Furthermore, the HASC device delivers a maximum C_s of 85 F g^{-1} with a high SE of 30.22 Wh kg^{-1} at SP of 0.63 kW kg^{-1} . Also, the HASSC device displayed a C_s value of 52.12 F g^{-1} with a SE of 18.53 Wh kg^{-1} at 1.64 kW kg^{-1} SP. Moreover, HASC and HASSC devices demonstration better cyclic durability of 84.81 and 80.83 % after 5000 cycles. These superior electrochemical features and practical applicability of fabricated devices suggesting a great potential of Ni-Cu phosphate thin film electrodes as cathode in enlarging the era of portable electronics.

CRedit authorship contribution statement

Mr. S. S. Pujari carried out an investigation and formal analysis, data curation, and original draft writing, Mr. S. A. Kadam and Prof. Y-R Ma provided resources and formal analysis. Mr. S. B. Jadhav, Mr. S. S. Kumbhar, Ms. S. B. Bhosale, Dr. J. L. Gunjekar and Prof. C. D. Lokhande carried out modification, creation, and presentation and visualization of the manuscript. Dr. U. M. Patil carried out funding acquisition, administration, supervision, manuscript editing. All persons made substantial contributions to the work reported in the manuscript.

Declaration of competing interest

The authors declare that they have no known competing financial interests or personal relationships that could have appeared to influence the work reported in this paper.

Acknowledgement

Authors are thankful to D. Y. Patil Education Society, Kasaba Bawada, Kolhapur for financial support through research projects sanction No. DYPES/DU/R&D/3109 and DST-FIST analytical Instrumental Laboratory Jaysingpur College, Jaysingpur for characterization facilities.

Appendix A. Supplementary data

Supplementary data to this article can be found online at <https://doi.org/10.1016/j.est.2022.105037>.

References

- [1] K. Krishnamoorthy, P. Pazhamalai, V. Mariappan, S. Manoharan, D. Kesavan, S.-J. Kim, Two-dimensional siloxane-graphene heterostructure-based high-performance supercapacitor for capturing regenerative braking energy in electric vehicles, *Adv. Funct. Mater.* 31 (2020) 2008422.
- [2] G. Li, Y. Li, J. Deng, H. Lin, X. Hou, L. Jia, Ultrahigh rate capability supercapacitors based on tremella-like nitrogen and phosphorus co-doped graphene, *Mater. Chem. Front.* 4 (2020) 2704–2715.
- [3] S. Manoharan, K. Krishnamoorthy, A. Sathyaseelan, S.-J. Kim, High-power graphene supercapacitors for the effective storage of regenerative energy during the braking and deceleration process in electric vehicles, *Mater. Chem. Front.* 5 (2021) 6200–6211.
- [4] D. Cui, H. Li, M. Li, C. Li, L. Qian, B. Zhou, B. Yang, Boron-doped graphene directly grown on boron-doped diamond for high-voltage aqueous supercapacitors, *ACS Appl. Energy Mater.* 2 (2019) 1526–1536.
- [5] S. Dai, Y. Bai, W. Shen, S. Zhang, H. Hu, J. Fu, X. Wang, C. Hu, M. Liu, Core-shell structured $\text{Fe}_2\text{O}_3/\text{Fe}_3\text{C}/\text{C}$ nanochains and Ni-Co carbonate hydroxide hybridized microspheres for high-performance battery-type supercapacitor, *J. Power Sources* 482 (2021), 228915.
- [6] W. Shen, J. Zang, H. Hu, J. Xu, Z. Zhang, R. Yan, S. Dai, Controlled synthesis of $\text{KCu}_7\text{S}_4/\text{rGO}$ nanocomposites for electrochemical energy storage, *Mater. Des.* 195 (2020), 108992.
- [7] K. Krishnamoorthy, M.S.P. Sudhakaran, P. Pazhamalai, V. Mariappan, Y. Mok, S.-J. Kim, Highly efficient 2D siloxane coated Ni foam catalyst for methane dry reforming and an effective approach to recycle spent catalyst towards energy storage application, *J. Mater. Chem. A* 7 (2019) 18950–18958.
- [8] S. Dai, Z. Zhang, J. Xu, W. Shen, Q. Zhang, X. Yang, T. Xu, D. Dang, H. Hu, B. Zhao, Y. Wang, C. Qu, J. Fu, X. Li, C. Hu, M. Liu, In situ Raman study of nickel bicarbonate for high-performance energy storage device, *Nano Energy* 64 (2019), 103919.
- [9] A. Agarwal, B. Sankapal, Ultrathin $\text{Cu}_2\text{P}_2\text{O}_7$ nanoflakes on stainless steel substrate for flexible symmetric all-solid-state supercapacitors, *Chem. Eng. Sci.* 422 (2021), 130131.
- [10] X. Li, A. Elshahawy, C. Guan, J. Wang, Metal phosphides and phosphates-based electrodes for electrochemical supercapacitors, *Small* 13 (2017) 1701530.
- [11] R. Murugavel, A. Choudhury, M.G. Walawalkar, R. Pothiraja, C.N.R. Rao, Metal complexes of organophosphate esters and open-framework metal phosphates: synthesis, structure, transformations, and applications, *Chem. Rev.* 108 (2008) 3549–3655.
- [12] T. Li, S. Kaercher, P. Roesky, Synthesis, structure and reactivity of rare-earth metal complexes containing anionic phosphorus ligands, *Chem. Soc. Rev.* 43 (2014) 42–57.
- [13] S. Kumar, G. Saeed, L. Zhu, K. Hui, N. Kim, J. Lee, 0D to 3D carbon-based networks combined with pseudocapacitive electrode material for high energy density supercapacitor: a review, *Chem. Eng. Sci.* 403 (2021), 126352.
- [14] C. Yuan, H. Wu, Y. Xie, X. Lou, Mixed transition-metal oxides: design, synthesis, and energy-related applications, *Angew. Chem.* 53 (2014), 1788–1504.
- [15] F. Omar, A. Numan, N. Duraisamy, S. Bashir, K. Ramesh, S. Ramesh, Ultrahigh capacitance of amorphous nickel phosphate for asymmetric supercapacitor applications, *RSC Adv.* 6 (2016) 76298–76306.
- [16] S. Pujari, S. Kadam, Y.-R. Ma, P. Katkar, S. Marje, S. Khalate, A. Lokhande, U. Patil, Facile synthesis of microstrip-like copper phosphate hydroxide thin films for supercapacitor applications, *J. Electron. Mater.* 59 (2020) 3890–3901.
- [17] P. Katkar, S. Marje, S. Pujari, S. Khalate, A. Lokhande, U. Patil, Enhanced energy density of all-solid-state asymmetric supercapacitors based on morphologically tuned hydrous cobalt phosphate electrode as cathode material, *ACS Sustain. Chem. Eng.* 7 (2019) 11205–11218.
- [18] S. Pujari, V. Patil, A. Patil, V. Parale, H.-H. Park, J. Gunjekar, C. Lokhande, U. Patil, Amorphous, hydrous nickel phosphate thin film electrode prepared by SILAR method as a highly stable cathode for hybrid asymmetric supercapacitor, *Synth. Met.* 280 (2021), 116876.
- [19] S. Marje, P. Katkar, S. Pujari, S. Khalate, P. Deshmukh, U. Patil, Effect of phosphate (anion) precursor on structural and morphology behavior of nickel phosphate thin films and its supercapacitive performance, *Mater. Sci. Eng. B* 261 (2020) 114641–114650.
- [20] J.-J. Li, M.-C. Liu, L.-B. Kong, D. Wang, Y.-M. Hu, W. Han, L. Kang, Advanced asymmetric supercapacitors based on $\text{Ni}_3(\text{PO}_4)_2/\text{GO}$ and $\text{Fe}_2\text{O}_3/\text{GO}$ electrodes with high specific capacitance and high energy density, *RSC Adv.* 5 (2015) 41721–41728.
- [21] A. Mirghni, M. Madito, K. Oyedotun, T. Masikhwa, N. Ndiaye, S. Ray, N. Manyala, A high energy density asymmetric supercapacitor utilizing a nickel phosphate/graphene foam composite as the cathode and carbonized iron cations adsorbed onto polyaniline as the anode, *RSC Adv.* 8 (2018) 11608–11621.
- [22] D. Marciano, D. Kosynkin, J. Berlin, A. Sinitskii, Z. Sun, A. Slesarev, L. Alemany, W. Lu, J. Tour, Improved synthesis of graphene oxide, *ACS Nano* 4 (2010) 4806–4814.
- [23] Y. Cui, X. Zhao, R. Guo, Improved electrochemical performance of $\text{La}_0.7\text{Sr}_0.3\text{MnO}_3$ and carbon co-coated LiFePO_4 synthesized by freeze-drying process, *Electrochim. Acta* 55 (2010) 922–926.
- [24] G. Gund, D. Dubal, S. Jambure, S. Shinde, C. Lokhande, Temperature influence on morphological progress of $\text{Ni}(\text{OH})_2$ thin films and its subsequent effect on electrochemical supercapacitive properties, *J. Mater. Chem. A* 1 (2013) 4793–4803.
- [25] G. Cai, J. Tu, D. Zhou, L. Li, J. Zhang, X. Wang, C. Gu, The direct growth of a WO_3 nanosheet array on a transparent conducting substrate for highly efficient electrochromic and electrocatalytic applications, *CrystEngComm* 16 (2014) 6866–6872.
- [26] N. Padmanathan, H. Shao, K. Razeeb, Multifunctional nickel phosphate nano/microflakes 3d electrode for electrochemical energy storage, nonenzymatic glucose, and sweat pH sensors, *ACS Appl. Mater. Interfaces* 10 (2018) 8599–8610.
- [27] U. Patil, J. Sohn, S. Kulkarni, S. Lee, H. Park, K. Gurav, J. Kim, S. Jun, Enhanced supercapacitive performance of chemically grown cobalt-nickel hydroxides on three-dimensional graphene foam electrodes, *ACS Appl. Mater. Interfaces* 6 (2014) 2450–2458.
- [28] Y. Zhao, J. Wang, H. Chen, T. Pan, J. Zhang, C. Cao, Different additives-substituted α -nickel hydroxide prepared by urea decomposition, *Electrochim. Acta* 50 (2004) 91–98.
- [29] S. Navale, V. Mali, S. Pawar, R. Mane, M. Naushad, F. Stadler, V. Patil, Electrochemical supercapacitor development based on electrodeposited nickel oxide film, *RSC Adv.* 5 (2015) 51961–51965.

- [30] B. Ameri, S. Davarani, R. Roshani, H. Moazami, A. Tadjarodi, A flexible mechanochemical route for the synthesis of copper oxide nanorods/nanoparticles/nanowires for supercapacitor applications: the effect of morphology on the charge storage ability, *J. Alloys Compd.* 695 (2017) 114–123.
- [31] N. Prokopchuk, V. Kopilevich, L. Voitenko, Preparation of double nickel (II) cobalt (II) phosphates with controlled cationic composition, *Russ. J. Appl. Chem.* 81 (2008) 386–391.
- [32] S. Kullyakool, C. Danvirutai, K. Siriwigong, P. Noisong, Determination of kinetic triplet of the synthesized $\text{Ni}_3(\text{PO}_4)_2 \cdot 8\text{H}_2\text{O}$ by non-isothermal and isothermal kinetic methods, *J. Therm. Anal. Calorim.* 115 (2014) 1497–1507.
- [33] P. Noisong, C. Danvirutai, T. Srithanratana, B. Boonchom, Synthesis, characterization and non-isothermal decomposition kinetics of manganese hypophosphate monohydrate, *Solid State Sci.* 10 (2008) 1598–1604.
- [34] H. Wen, M. Cao, G. Sun, W. Xu, D. Wang, X. Zhang, C. Hu, Hierarchical three-dimensional cobalt phosphate microarchitectures: large-scale solvothermal synthesis, characterization, and magnetic and microwave absorption properties, *J. Phys. Chem. C* 112 (2008) 15948–15955.
- [35] P. Katkar, S. Marje, S. Kale, A. Lokhande, C. Lokhande, U. Patil, Synthesis of hydrous cobalt phosphate electrocatalysts by a facile hydrothermal method for enhanced oxygen evolution reaction: effect of urea variation, *CrystEngComm* 21 (2019) 884–893.
- [36] B. Liang, Y. Chen, J. He, C. Chen, W. Liu, Y. He, X. Liu, N. Zhang, V. Roy, Controllable fabrication and tuned electrochemical performance of potassium Co-Ni phosphate microplates as electrodes in supercapacitors, *ACS Appl. Mater. Interfaces* 10 (2018) 3506–3514.
- [37] P. Katkar, S. Marje, S. Pujari, S. Khalate, P. Deshmukh, U. Patil, Single-pot hydrothermal synthesis of manganese phosphate microrods as a cathode material for highly stable flexible solid-state symmetric supercapacitors, *Synth. Met.* 267 (2020), 116446.
- [38] K. Sing, D. Everett, R. Haul, L. Moscou, R. Pierotti, J. Rouquerol, T. Siemieniowska, International union of pure and applied chemistry: reporting physisorption data for gas/solid systems with special reference to the determination of surface area and porosity, *Pure Appl. Chem.* 57 (1985) 603–619.
- [39] J.B. Condon, in: *Surface Area And Porosity Determinations by Physisorption: Measurements And Theory*, Elsevier, Amsterdam, 2006, pp. 6–14.
- [40] J. Gunjekar, T. Kim, H. Kim, I. Kim, S. Hwang, Mesoporous layer-by-layer ordered nanohybrids of layered double hydroxide and layered metal oxide: highly active visible light photocatalysts with improved chemical stability, *J. Am. Chem. Soc.* 133 (2011) 14998–15007.
- [41] X. Peng, H. Chai, Y. Cao, Y. Wang, H. Dong, D. Jia, W. Zhou, Facile synthesis of cost-effective $\text{Ni}_3(\text{PO}_4)_2 \cdot 8\text{H}_2\text{O}$ microstructures as a supercapattery electrode material, *Water. TodayEnergy* 7 (2018) 129–135.
- [42] W. Bian, Y. Huang, X. Xu, M. Din, G. Xie, X. Wang, Iron hydroxide-modified nickel hydroxylphosphate single-wall nanotubes as efficient electrocatalysts for oxygen evolution reactions, *ACS Appl. Mater. Interfaces* 10 (2018) 9407–9414.
- [43] H. Sharkawy, D. Sayed, A. Dhmees, R. Aboushahba, N. Allam, Facile synthesis of nanostructured binary ni-cu phosphides as advanced battery materials for asymmetric electrochemical supercapacitors, *ACS Appl. Energy Mater.* 3 (2020) 9305–9314.
- [44] Y.-C. Chen, Z.-B. Chen, Y.-G. Lin, Y.-K. Hsu, Synthesis of copper phosphide nanotube arrays as electrodes for asymmetric supercapacitors, *ACS Sustain. Chem. Eng.* 5 (2017) 3863–3870.
- [45] S. Marje, S. Pujari, S. Khalate, V. Patil, V. Parale, T. Kim, H. Park, J. Gunjekar, C. Lokhande, U. Patil, Intercalation type pseudocapacitive clustered nanoparticles of nickel-cobalt phosphate thin films synthesized via electrodeposition as a cathode for high performing hybrid supercapacitor devices, *J. Mater. Chem. A* 10 (2022) 11225–11237.
- [46] D. Wang, Y. Xu, W. Sun, X. Guo, L. Yang, F. Wang, Z. Yang, Ultrasonic treatment of $\text{Co}_7(\text{PO}_4)_2(\text{HPO}_4)_4$ using NMP for supercapacitors and oxygen evolution reaction, *Electrochim. Acta* 337 (2020), 135827.
- [47] X. Wang, H. Jian, Q. Xiao, S. Huang, Ammonium nickel phosphate on nickel foam with a Ni^{3+} -rich surface for ultrasensitive nonenzymatic glucose sensors, *Appl. Surf. Sci.* 459 (2018) 40–47.
- [48] K. Malaie, M.R. Ganjali, T. Alizadeh, P. Norouzi, Simple electrochemical preparation of nanoflake-like copper oxide on Cu-plated nickel foam for supercapacitor electrodes with high areal capacitance, *J. Mater. Sci. Mater. Electron.* 28 (2017) 14631–14637.
- [49] K. Sankar, Y. Seo, S. Lee, S. Jun, Redox additive-improved electrochemically and structurally robust binder-free nickel pyrophosphate nanorods as superior cathode for hybrid supercapacitors, *ACS Appl. Mater. Interfaces* 10 (2018) 8045–8056.
- [50] M. Sathiyaa, A. Prakash, K. Ramesha, J. Tarascon, A. Shukla, V_2O_5 -anchored carbon nanotubes for enhanced electrochemical energy storage, *J. Am. Chem. Soc.* 133 (2011) 16291–16299.
- [51] S. Kandalkar, H. Lee, S. Seo, K. Lee, C. Kim, Cobalt-nickel composite films synthesized by chemical bath deposition method as an electrode material for supercapacitors, *J. Mater. Sci.* 46 (2011) 2977–2981.
- [52] F. Omar, A. Numan, S. Bashir, N. Duraisamy, R. Vikneswaran, Y. Loo, K. Ramesh, S. Ramesh, Enhancing rate capability of amorphous nickel phosphate supercapattery electrode via composition with crystalline silver phosphate, *Electrochim. Acta* 273 (2018) 216–228.
- [53] J. Cherusseria, K. Kar, Ultra-flexible fibrous supercapacitors with carbon nanotube/polypyrrole brush-like electrodes, *J. Mater. Chem. A* 4 (2016) 9910–9922.
- [54] Y.-K. Hsu, Y.-C. Chen, Y.-G. Lin, Synthesis of copper sulfide nanowire arrays for high-performance supercapacitors, *Electrochim. Acta* 139 (2014) 401–407.
- [55] B. Xie, Y. Chen, M. Yu, X. Shen, H. Lei, T. Xie, Y. Zhang, Y. Wu, Carboxyl-assisted synthesis of nitrogen-doped graphene sheets for supercapacitor applications, *Nanoscale Res. Lett.* 10 (2015) 332.
- [56] J. Xiao, S. Yang, S., Bio-inspired synthesis of NaCl-type $\text{Co}_x\text{Ni}_{1-x}\text{O}$ ($0 < x < 1$) nanorods on reduced graphene oxide sheets and screening for asymmetric electrochemical capacitors, *J. Mater. Chem.* 22 (2012) 12253–12262.
- [57] P. Deshmukh, S. Pusawale, V. Jamadade, U. Patil, C. Lokhande, Microwave assisted chemical bath deposited polyaniline films for supercapacitor application, *J. Alloy. Compd.* 509 (2011) 5064–5069.
- [58] A. Mirghni, K. Oyedotun, O. Olaniyan, B. Mahmoud, N. Sylla, N. Manyala, Electrochemical analysis of na-ni bimetallic phosphate electrodes for supercapacitor applications, *RSC Adv.* 9 (2019) 25012–25021.
- [59] B. Senthilkumar, K. Sankar, L. Vasylechko, Y.-S. Lee, R. Selvan, Synthesis and electrochemical performances of maricite- NaMPO_4 ($M = \text{Ni, Co, Mn}$) electrodes for hybrid supercapacitors, *RSC Adv.* 4 (2014) 53192–53200.
- [60] M. Liu, N. Shang, X. Zhang, S. Gao, C. Wang, Z. Wang, Microwave synthesis of sodium nickel-cobalt phosphates as high-performance electrode materials for supercapacitors, *J. Alloys Compd.* 791 (2019) 929–935.
- [61] J. Gu, Li Sun, Y. Zhang, Q. Zhang, X. Li, H. Si, Y. Shi, C. Sun, Y. Gong, Y. Zhang, MOF-derived Ni-doped $\text{CoP}@C$ grown on CNTs for high-performance supercapacitors, *Chem. Eng. Sci.* 385 (2020), 123454.
- [62] F. Wang, H. Lei, H. Peng, J. Zhou, R. Zhao, J. Liang, G. Ma, Z. Lei, Interlaced nickel phosphide nanoflakes wrapped orthorhombic niobium pentoxide nanowires array for sustainable aqueous asymmetric supercapacitor, *Electrochim. Acta* 325 (2019), 134934.
- [63] Y. Lan, H. Zhao, Y. Zong, X. Li, Y. Sun, J. Feng, Y. Wang, X. Zheng, Y. Du, Phosphorization boosts the capacitance of mixed metal nanosheet arrays for high performance supercapacitor electrodes, *Nanoscale* 10 (2018) 11775–11781.
- [64] X. Li, R. Ding, L. Yi, W. Shi, Q. Xu, E. Liu, Mesoporous Ni-P@ NiCo_2O_4 composite materials for high performance aqueous asymmetric supercapacitors, *Electrochim. Acta* 222 (2016) 1169–1175.
- [65] Z. Andikaey, A. Ensafi, B. Rezaei, Iron-doped cobalt copper phosphide/phosphate composite with 3D hierarchical flower-like structures as electrodes for hybrid supercapacitors, *Electrochim. Acta* 393 (2021), 139061.
- [66] M. Alzaid, M. Iqbal, S. Alam, N. Almoisheer, A. Afzal, S. Aftab, Binary composites of nickel-manganese phosphates for supercapattery devices, *J. Energy Storage* 33 (2021), 102020.



Cite this: DOI: 10.1039/d2se00978a

A binder-free facile synthetic approach for amorphous, hydrous nickel copper phosphate thin film electrode preparation and its application as a highly stable cathode for hybrid asymmetric supercapacitors†

Sachin S. Pujari,^a Sujit A. Kadam,^b Yuan-Ron Ma,^b Satish B. Jadhav,^a Sambhaji S. Kumbhar,^a Shraddha B. Bhosale,^a Vinod V. Patil,^{ac} Jayavant L. Gunjekar,^b Chandrakant D. Lokhande^a and Umakant M. Patil^{b*}

Currently, amorphous, hydrous compounds are receiving much attention as electrodes in hybrid supercapacitors (S.C.s) as they offer extraordinary electrochemical efficiency because of disorder in their structure and an excellent electrochemical interface. In this study, a simple, cost-effective and binder-free synthetic SILAR method is used for preparing amorphous, hydrous nickel copper phosphate (NCP-S) thin film on a stainless steel substrate (S.S.). The amorphous, hydrous NCP-S thin films exhibit mesoporous, clustered spherical particle-like morphology. The optimal ratio (1 : 1) of nickel and copper in the NCP-S ($\text{Ni}_{1.56}\text{Cu}_{1.44}(\text{PO}_4)_2 \cdot \text{H}_2\text{O}$) material gives a high specific capacitance (C_s) (capacity) of 750 F g^{-1} (412.50 C g^{-1}) at 1.0 A g^{-1} . More significantly, hybrid asymmetric aqueous S.C. (HAASC) and hybrid all-solid-state asymmetric S.C. (HASASC) electrochemical energy storage devices (ESDs) have been fabricated using NCP-S as a cathode and rGO as an anode. The HAASC device showed a superior C_s (95.62 F g^{-1} at 3.0 A g^{-1}) with specific energy (S.E.) of 34 W h kg^{-1} at 2.40 kW kg^{-1} specific power (S.P.). Additionally, the HASASC device offers higher C_s (37.62 F g^{-1} at 0.7 A g^{-1}) with $13.51 \text{ W h kg}^{-1}$ S.E. at 0.55 kW kg^{-1} S.P. Also, both devices exhibit excellent long-term durability (94.11 and 93.81%, respectively, after 5000 GCD cycles). The amorphous, hydrous structures clearly indicate excellent accessibility of ions and stability of electrodes, which is favourable for the hybrid S.C.s. These remarkable supercapacitive results promise the application of amorphous NCP-S as a cathode in commercialized hybrid energy storage systems.

Received 17th July 2022
Accepted 10th November 2022

DOI: 10.1039/d2se00978a

rsc.li/sustainable-energy

1. Introduction

Supercapacitors (S.C.s) have attracted extensive attention among all energy storage devices (ESDs) due to their unique properties, which include long cycling durability, high-power capability, ease of operation and wide working temperature

range. Owing to such excellent properties, they are found to be more favourable ESDs for modern electronic applications in energy regeneration and hybrid electric vehicles, weight leveling, and aerospace industries.^{1–3} Nevertheless, the surface-controlled electrochemical reactions of S.C.s restrict the charge transfer process near and on the electrode surface,

^aCentre for Interdisciplinary Research, D. Y. Patil Education Society, (Deemed to be University), Kasaba Bawada, Kolhapur-416 006, M.S., India. E-mail: Umakant.physics84@gmail.com

^bDepartment of Physics, National Dong Hwa University, Hualien-97401, Taiwan

^cSchool of Chemical Sciences, Punyashlok Ahilyadevi Holkar Solapur University, Solapur 413255, India

† Electronic supplementary information (ESI) available: Formulae for calculation, mass deposition graph, pore size distribution curves of the NCP-S series samples, EDS spectra of the NCP-S series samples, the CV graphs of NCP-S1, NCP-S2, NCP-S4 and NCP-S5 electrodes, pseudocapacitive (surface current) and battery type (bulk current) current density contribution graph at various scan rates for NCP-S1, NCP-S2, NCP-S4 and NCP-S5 electrodes, the GCD curves of NCP-S1, NCP-S2, NCP-S4 and NCP-S5 electrodes, the specific

capacitance of the NCP-S series electrodes at various current densities, XPS study of the NCP-S3 sample before and after stability testing, the structural and electrochemical study of the rGO electrode, the CV and GCD curves of the HAASC device in different potential windows, schematic of HASASC device fabrication, the CV and GCD curves of the HASASC device in different potential windows, compositions of nickel and copper precursors, experimental and observed nickel and copper atomic ratios in NCP-S series thin films, comparison of various amorphous nickel copper phosphate/pyrophosphate based electrodes, EIS fitted circuit parameters of the NCP-S series electrodes, and comparison of electrochemical performance for HAASC and HASASC devices with previous metal phosphate based devices. See DOI: <https://doi.org/10.1039/d2se00978a>

resulting in less energy storage capability than for the recent lithium-ion batteries.^{4,5} Therefore, upcoming modifications in the S.C. field are on achieving a high specific energy (S.E.) value while sustaining additional features such as specific power (S.P.), cycle lifespan and fabrication cost. The most impressive way to recognize S.C.s with improved S.E. is to fabricate hybrid asymmetric S.C.s using separate cathode and anode electrode materials with different operating potentials in the same electrolyte.^{6–8} Typically, hybrid S.C.s are constructed utilizing redox-active materials as a cathode (high S.E.) and carbon-based materials as anode (high S.P.) electrodes. However, detecting suitable cathode and anode materials that can enhance the S.C. energy storage capability in terms of S.E. with maintained S.P. is crucial.

So far, transition metal phosphates (TMPs) have been widely employed as a potential cathode electrode in hybrid S.C.s; besides this application, they are used in photocatalytic reactions,⁹ electrocatalytic water splitting,¹⁰ and rechargeable batteries.¹¹ As counterparts to transition metal carbides, nitrides, oxides or hydroxides, TMPs have arisen as decent mechanically steady and hard and good conductors for electricity and heat.¹² Open-framework-like structures along with interstitial spaced and enormous channels endow them with excellent ionic conductivity, facile ion/electrolyte mass transport, high ductility with various stoichiometries, good access to active sites for ion intercalation and excellent charge storage capacity. Moreover, strong P–O covalent bonds offer high structural strength and stabilize the lattice oxygen similarly in the highly charged state, hence promising long lifespan and safety in hybrid S.C.s.^{13,14} Thus, rich redox activity and the distinctive structure of TMPs make them favourable cathodes for ESDs. Furthermore, various TMPs have been introduced as electrode materials in hybrid S.C.s due to their metalloid properties and phosphorus that boost charge transportation during electrochemical reactions. Inspired by these fascinating features, various binary transition metal phosphates/phosphides/pyrophosphates of Co–Mn,^{15,16} Ni–Mn,^{17,18} Ni–Co,^{19,20} and Ni–Cu^{21,22} along with several morphologies as well as crystallinities have been explored towards hybrid S.C. application. Among these TMPs, nickel–copper phosphate is desired to be an ideal rival to traditional Co or Ni phosphates, as metallic Cu reveals higher intrinsic conductivity than those of nickel and cobalt, which will enhance the high electron transport rate.²³ Still, the performance of nickel–copper phosphate in the energy storage field has not been explored.

Recently, researchers reported that the amorphous and hydrous structure of compounds reveals superior electrochemical activities with improved lifespan than their crystalline or bulk counterparts owing to the reduced and disordered structure, which reduces ion diffusion lengths.²⁴ The remarkable nature of amorphous compounds is a disorder in structure. Furthermore, amorphous materials dominate in the context of unsaturated atoms ligands and effective faradaically active sites comparable to their crystalline counterparts.²⁵ These features promote the charge storage process in the material. Wang *et al.* reported that amorphous barium nickel phosphate prepared using the cation-exchange reaction method exhibits good

electrochemical properties with C_s of 1058 F g⁻¹ and higher surface area (64.8 m² g⁻¹) than that of its crystalline counterpart.²⁶ Moreover, Xi *et al.* described the higher electrochemical performance of ultrathin amorphous cobalt phosphate nanowires (C_s 1174 F g⁻¹) than the corresponding crystalline compound.²⁷ Chen *et al.* synthesized amorphous vanadyl phosphate (VOPO₄)/graphene composites by a hydrothermal method.²⁸ Pang *et al.* prepared amorphous nickel pyrophosphate microstructures using calcination of the ammonium nickel phosphate hydrate.²⁹ Omar *et al.* prepared a nickel phosphate (Ni₃(PO₄)₂) material using a sonochemical strategy.³⁰ Agarwal *et al.* reported SILAR synthesized Cu₂P₂O₇ nanoflakes.³¹ Agarwal *et al.* synthesized cobalt phosphate by a chemical method.³² Marje *et al.* reported that binder-free amorphous nickel phosphate offers a higher C_s (1031 F g⁻¹) value than its crystalline counterpart.³³ Hence, the reduced electrical conductivity of amorphous compounds can be the main barrier in attaining high electrochemical performance. Such a barrier can be eliminated by developing direct growth or reproducing binder-free electrodes of an amorphous compound on a conductive substrate.

To date, various processing techniques have been used for the synthesis of metal phosphates, such as hydrothermal,^{34,35} co-precipitation,³⁶ solid-state reaction,³⁷ and various other methods.^{38,39} However, these methods include post-annealing treatment, high temperatures, toxic gases, and time-consuming reaction, which altogether hinder their commercialization in the real world. Conversely, the SILAR method is an efficient substitute for synthesizing amorphous nickel copper phosphate (NCP-S) material in thin film form because of its simplicity, less-time-consuming nature and cost-effectiveness. Yet, no work has been reported on the SILAR synthesis of NCP-S thin films.

Herein, for the first time, binder-free amorphous NCP-S thin films were prepared on a conducting S.S. substrate using an industry scalable and simple SILAR method at ambient temperature and their potential in asymmetric hybrid S.C.s was explored. Furthermore, the physicochemical characterization of the synthesized binder-free NCP-S thin films was examined by various techniques to determine the nature of the materials for electrochemical analysis. Moreover, aqueous and hybrid asymmetric devices were successfully constructed in 1 M aqueous KOH and polymer gel electrolytes, respectively, using the best-performing amorphous NCP-S as the cathode electrode and rGO as the anode.

2. Experimental section

2.1 Preparation of amorphous nickel copper phosphate thin films

Amorphous NCP-S thin film electrodes were synthesized by the SILAR method, as shown schematically in Fig. 1(a), which reveals the SILAR method using a three-beaker system at ambient temperature. The S.S. substrates were first wiped with acetone and smoothed with polish paper before ultrasonication in DDW. Varying concentration solutions of nickel sulphate (0.0333–0.0249 M) and copper sulphate (0.0249–0.0333

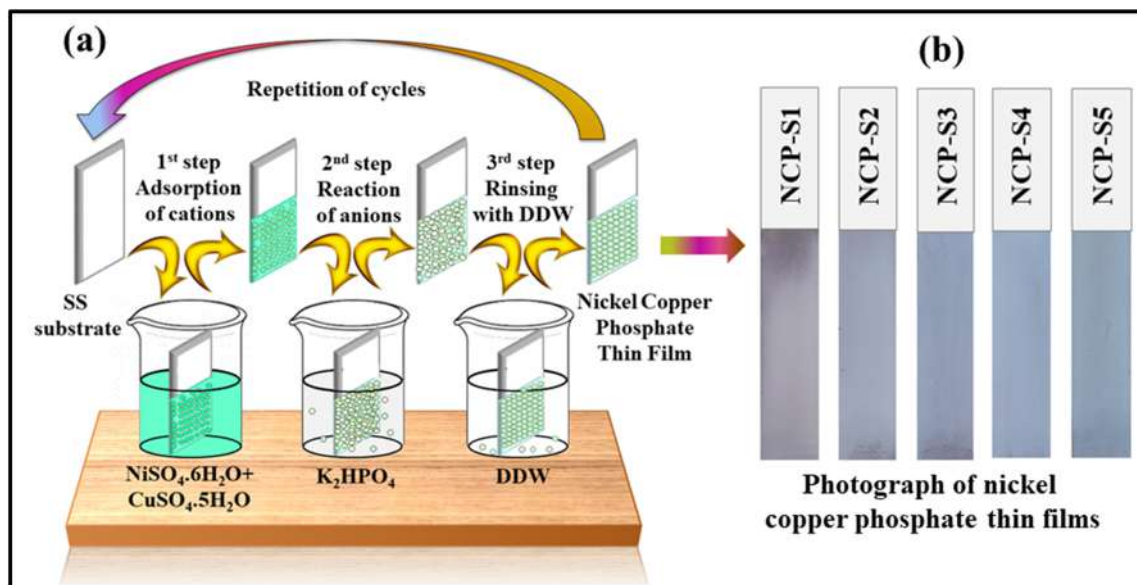


Fig. 1 (a) Illustration of NCP-S thin film deposition by the SILAR method. (b) Photograph of SILAR synthesized NCP-S thin films with different concentrations of nickel and copper.

M) (serving as the source of Ni^{2+} and Cu^{2+} ions) were prepared by dissolving stoichiometric amounts of $\text{NiSO}_4 \cdot 6\text{H}_2\text{O}$ and $\text{CuSO}_4 \cdot 5\text{H}_2\text{O}$ in 50 ml DDW, which served as the cationic precursor source. 0.075 M dipotassium hydrogen orthophosphate was dissolved in 50 ml DDW, serving as the anionic precursor source (source of PO_4^{3-} ions). Detailed proportions of nickel (Ni) and copper (Cu) precursors used experimentally are provided in Table S1 (see the ESI[†]), for deposition of NCP-S materials. In a typical synthesis, the precleaned S.S. substrate was sequentially dipped in the cationic and anionic solutions for 10 s each. After that, the substrate was rinsed in DDW for 20 s. At ambient temperature, 70 such cycles were repeated to ensure a uniform deposition of amorphous NCP-S on the S.S. substrate material.

The adsorption, reaction, and rinsing time in this experiment are optimized by some trials to obtain a uniform and adherent film on the substrate. After 70 deposition cycles, light blue-colored thin films were obtained on the surface of S.S. substrates as displayed in Fig. 1(b). The thin film electrodes prepared by using different compositions of Ni and Cu precursors are denoted as NCP-S1, NCP-S2, NCP-S3, NCP-S4, and NCP-S5 (given in Table S1 (see the ESI[†])).

2.2 Synthesis of the reduced graphene oxide (rGO) electrode

The G.O. was made by using a (top-down approach) modified Hummers method⁴⁰ and further, the rGO was synthesized by reducing the G.O. by the hydrothermal method (458 K for 12 h) and freeze-dried to retain porosity with large surface area. Furthermore, the rGO (negative) electrode made by using the as-synthesized rGO powder (75 wt%), carbon black (C.B.) (20 wt%) and polyvinylidene difluoride (PVDF) (5%) in *N*-methyl-2-pyrrolidone (NMP) was utilized to make a uniform slurry. Then, the achieved slurry was laminated on the S.S. substrate

(area 2 cm²) and dried at 333 K for 2 h. The synthesized rGO electrode was used as an anode in the asymmetric hybrid device fabrication.

2.3 Preparation of polymer gel electrolyte

To make the solid state device (SSD), polyvinyl alcohol (PVA) and KOH were utilized for the preparation of a gel electrolyte. Initially, 2 g PVA was taken in 20 ml DDW and dissolved at a 363 K temperature under constant stirring until the solution became transparent and clear. After that, 1 M KOH solution (in 10 ml of DDW) was dissolved in PVA solution and rigorously stirred until the appearance of the solution became viscous, clear and uniform.⁴¹ The viscous as well as transparent gel (PVA-KOH) was utilized as the gel electrolyte and separator in SSD fabrication.

2.4 Characterization techniques

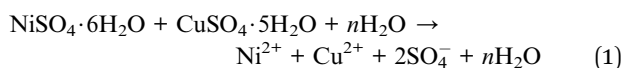
The structural characterization of the NCP-S thin films was carried out by XRD using a Rigaku MiniFlex-600 with Cu K α radiation ($\lambda = 0.15406$ nm) in the 2θ range of 10–80°. The FT-IR spectra were recorded using an FT-IR 4600 type-A instrument using a KBr pellet at ambient temperature for the detection of functional groups. XPS (K-alpha XPS system, Thermo Fisher Scientific, UK) was carried out to determine the oxidation states and chemical composition of the NCP-S thin film. The surface area and porosity were measured *via* a BET investigation using a Belsorp-mini II instrument. FE-SEM (JSM-6500F, JEOL) was employed to examine the surface architecture of the prepared material and EDS (Oxford, X-max) was used for elemental analysis. All supercapacitive properties were estimated by using ZIVE MP1 multichannel electrochemical equipment. The prepared NCP-S thin films were employed as a working electrode, with a platinum sheet and mercury/mercury oxide (Hg/

HgO) as a counter and reference electrode. The electrochemical properties of the prepared thin film electrodes were examined using cyclic voltammetry (CV), galvanostatic charge–discharge (GCD) and electrochemical impedance spectroscopy (EIS). The formulae used for electrochemical performance assessment in three and two electrode systems are provided in the ESI.†

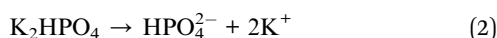
3. Results and discussion

3.1 Amorphous nickel copper phosphate thin film formation mechanism

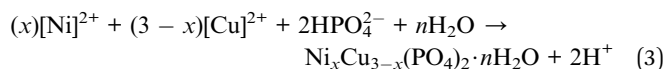
Amorphous NCP-S thin films were developed on the S.S. substrate by adsorption as well as reaction among cations and anions on the S.S. surface (as displayed schematically in Fig. 1(a)). In brief, in a three beaker SILAR system, the first beaker contains a mixture of nickel sulphate and copper sulphate ($\text{NiSO}_4 \cdot 6\text{H}_2\text{O}/\text{CuSO}_4 \cdot 5\text{H}_2\text{O}$) aqueous solution with different compositions as a cationic precursor. Then, the adsorbed cations react with anions from the precursor (K_2HPO_4) in the second beaker. Moreover, DDW in the third beaker is utilized for rinsing purposes. The reaction mechanism for amorphous NCP-S thin film development by the SILAR method is as follows: a thin layer of $\text{Ni}^{2+}/\text{Cu}^{2+}$ ions become adsorbed on the S.S. substrate while dipping the substrate in a cationic precursor solution (kept at room temperature).



An anionic precursor of K_2HPO_4 dissociates as per eqn (2),



Furthermore, the reaction that occurred after dipping of the wet substrate in the K_2HPO_4 anionic solution, where a chemical reaction between HPO_4^{2-} and adsorbed $\text{Ni}^{2+}/\text{Cu}^{2+}$ ions leads to the deposition of an adherent NCP-S layer, is



Thus, the thin film of $\text{Ni}_x\text{Cu}_{3-x}(\text{PO}_4)_2 \cdot n\text{H}_2\text{O}$ is developed by the layer-by-layer growth mechanism, where film growth occurs by the nucleation of the ions at the nucleation middle on the immersed surface of the S.S. substrate. The weight of amorphous NCP-S on the S.S. substrate was measured by the gravimetric mass difference method (Fig. S1, see the ESI†). The deposited mass of material for electrodes NCP-S1, NCP-S2, NCP-S3, NCP-S4, and NCP-S5 is 1.22, 1.10, 0.90, 1.02, and 1.12 mg cm^{-2} , respectively.

3.2 Structural and morphological analysis

The crystallinity of NCP-S1 to NCP-S5 electrodes was examined by XRD analysis and the results are displayed in Fig. 2(a). The amorphous phase of the as-prepared nickel copper phosphate is observed, since no significant diffraction peaks were observed in the XRD patterns. The peaks represented as ‘S.S.’ are related

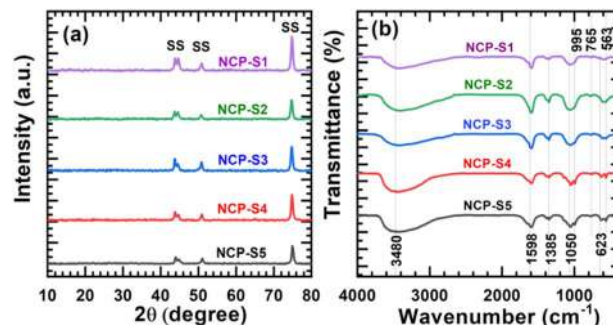


Fig. 2 (a) XRD patterns of NCP-S series thin films. (b) FT-IR spectra of NCP-S thin films (NCP-S1 to NCP-S5).

to the stainless steel substrate. The absence of diffraction peaks from the XRD patterns of the NCP-S series electrodes indicates creation of the amorphous phase of the material. With NCP-S it is feasible to improve the electrochemical activities due to large active sites being obtained owing to the irregular structure of the material. Such amorphous structure of the material can provide facile access to ions for storage in the nickel copper phosphate material and permits a continuous redox reaction on the surface, aimed at enhancing the performance compared to crystalline structures.^{42,43} The presence of chemical bonding in the prepared electrodes was studied by FT-IR analysis. The FT-IR spectra of NCP-S series thin films were examined in the range of 4000–400 cm^{-1} and are presented in Fig. 2(b). The characteristic peaks at 563 and 623 cm^{-1} are ascribed to metal–oxygen bonding in the obtained thin films.^{21,44} The observed peak at 765 cm^{-1} is ascribed to P–O–P linkage.^{15,33} The symmetric and asymmetric (P–O) vibrational mode of PO_4^{3-} anions is confirmed by peaks observed at wavenumbers of 995 and 1050 cm^{-1} .¹⁷ The peak at 1385 cm^{-1} can be assigned to H–O–P bending mode vibrations⁴⁵ and the absorption peak at 1598 cm^{-1} to water molecules (H–O–H). Moreover, a wide band at 3480 cm^{-1} is observed due to the O–H stretching vibration mode from structural water molecules captured in the material during SILAR synthesis.²¹ The FT-IR spectra reveal the characteristic properties of nickel, copper, phosphate and structural water molecule bonding, which indicates the successful formation of the hydrous NCP-S material.

Fig. 3 shows the surface area and pore size (Fig. S2 (see the ESI†)) distribution of the NCP-S series samples examined using N_2 adsorption–desorption isotherms. The obtained isotherms of samples (a) NCP-S1, (b) NCP-S2, (c) NCP-S3, (d) NCP-S4, and (e) NCP-S5 reveal a type III isotherm along with an H3 type hysteresis loop which signifies a lower energy of adsorption and characteristic features of mesoporous-like material.⁴⁶ Using the BET equation, the surface areas were calculated to be 23.77, 36.91, 37.30, 16.02 and 17.09 $\text{m}^2 \text{g}^{-1}$ for samples NCP-S1, NCP-S2, NCP-S3, NCP-S4 and NCP-S5, respectively. The distribution of pore size of the NCP-S series samples is revealed in Fig. S2 (see the ESI†). An average pore diameter of 28.82, 21.49, 18.48, 27.90 and 25.67 nm is obtained for samples NCP-S1, NCP-S2, NCP-S3, NCP-S4 and NCP-S5, respectively, which is attributed to the mesoporous structure of the prepared materials. The

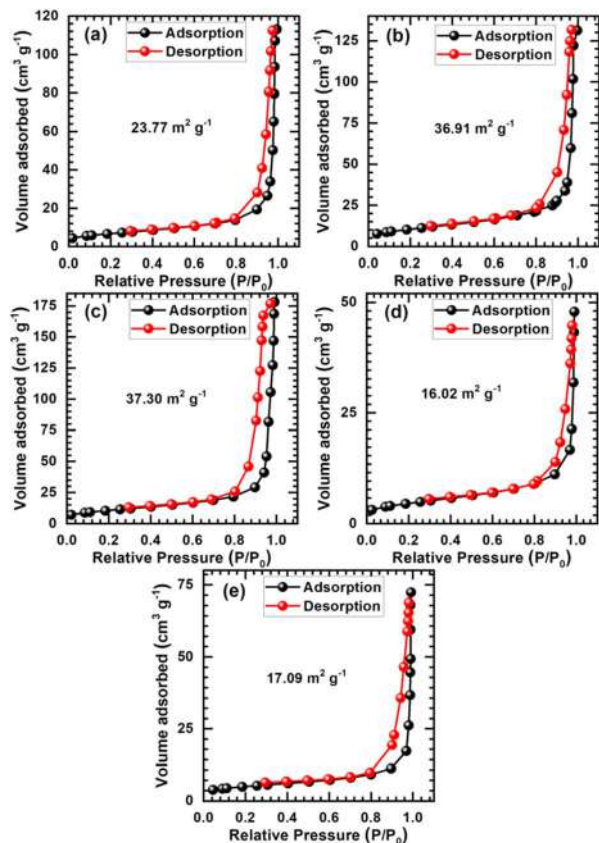


Fig. 3 Nitrogen adsorption–desorption isotherm of samples (a) NCP-S1, (b) NCP-S2, (c) NCP-S3, (d) NCP-S4 and (e) NCP-S5.

amorphous NCP-S thin film exhibits mesoporous like structures as well as providing maximum surface area and numerous mesoporous channels which may allow facile access to the electrolyte within the material.

The surface information and valence states of elements in the SILAR deposited NCP-3 thin film sample were further examined by XPS and the results are presented in Fig. 4. The existence of Ni, Cu, P and O elements was identified from a survey scan of the NCP-S3 electrode (Fig. 4(a)). Fig. 4 (b–e) exhibit the high resolution emission spectra of Ni 2p, Cu 2p, P 2p and O 1s, respectively. In the Ni 2p spectra (Fig. 4(b)), the peak for Ni 2p_{1/2} located at 875.9 eV and for Ni 2p_{3/2} at 858.4 eV in association with the two satellite peaks at 880.1 and 862.6 eV can be attributed to nickel species with the chemical states of Ni²⁺ and Ni³⁺ at the surface of the material.⁴⁷ In the Cu 2p spectra (Fig. 4(c)), the peaks situated at 956.5 and 934.3 eV are from Cu 2p_{1/2} and Cu 2p_{3/2} associated with two satellite peaks at 963.1 and 943.9 eV and can be attributed to copper phosphate with the chemical states of Cu²⁺ and Cu³⁺.²⁴ The P 2p XPS spectra (Fig. 4(d)) of the P element reveal one peak at 134.8 eV, confirming the pentavalent state of phosphorus (PO₄³⁻).⁴⁸ Further, the O 1s band (Fig. 4(e)) was deconvoluted into two peaks at 534.7 and 532.8 eV attributed to metal–oxygen molecules and the O–H group from adsorbed water, respectively.^{49,50} The XPS results confirm the successful synthesis of hydrous Ni–Cu phosphate in thin film form.

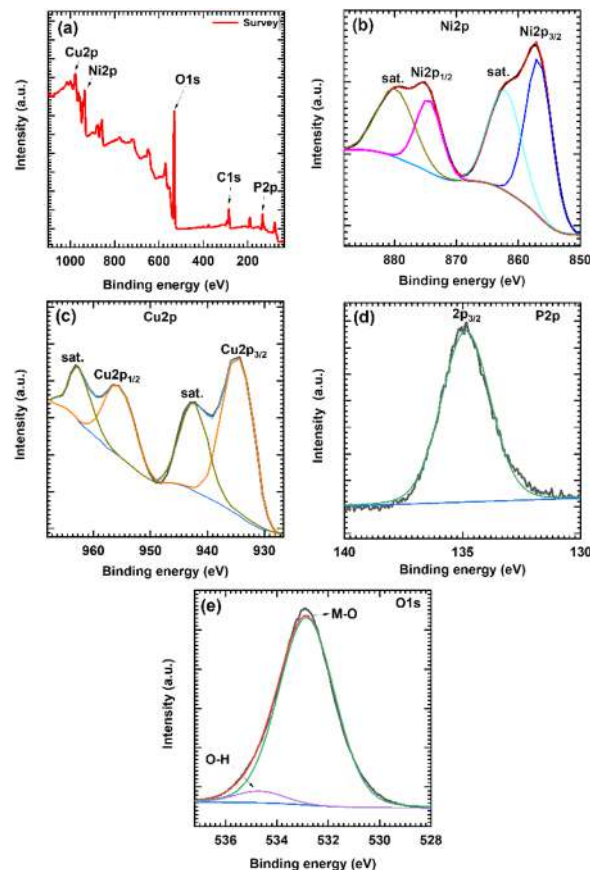


Fig. 4 XPS profile of the NCP-S thin film: (a) complete survey spectrum, and Ni 2p (b), Cu 2p (c), P 2p (d) and O 1s (e) spectra for sample NCP-S3.

FE-SEM investigation was utilized for the surface morphology analysis of SILAR deposited NCP-S thin films. Fig. 5 displays the morphologies of SILAR deposited thin films at different magnifications ($\times 30\,000$ and $\times 100\,000$). The morphological evolution is observed from samples NCP-S1 to NCP-S5 due to variations in nickel and copper composition. The FE-SEM images in Fig. 5 reveal a porous morphology consisting of a spherical particle-like structure of NCP-S material. The FE-SEM images of pristine nickel phosphate (NCP-S1) exhibited in Fig. 5(A1 and A2) reveal that the sample consists of an agglomerated spherical particle-like structure having an average particle size of 110 nm. Moreover, with an increase of copper content in the NCP-S2 sample (Fig. 5(B1 and B2)), a spherical particle-like morphology is detected with an average particle size of 135 nm. Moreover, the sample (NCP-S3) with the same concentration (50 : 50) of nickel and copper phosphate displayed in Fig. 5(C1 and C2) reveals inter-connected spherical particles with an average particle size of 86.50 nm with a comparatively compact structure. Further, increasing the copper concentration (NCP-S4), the morphology revealed a porous network of particles having an average particle size of 115 nm, as shown in Fig. 5(D1 and D2). The pristine copper phosphate sample (NCP-S5) displayed in Fig. 5(E1 and E2) depict an aggregated particle-like structure along with an

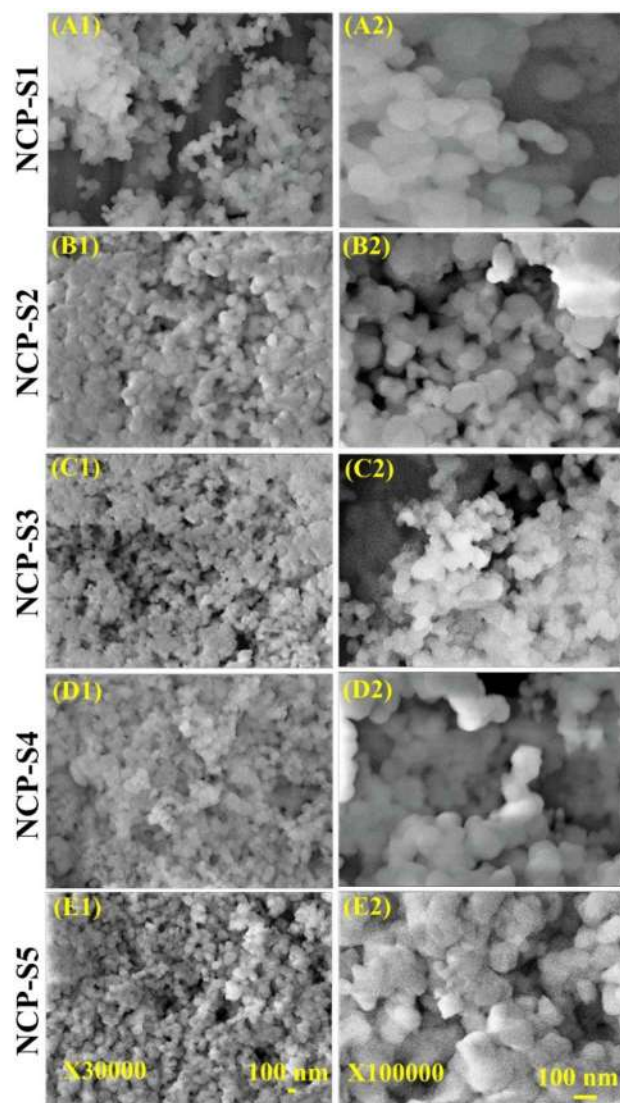


Fig. 5 FE-SEM images of NCP-S electrodes: (A1 and A2) NCP-S1, (B1 and B2) NCP-S2, (C1 and C2) NCP-S3, (D1 and D2) NCP-S4, and (E1 and E2) NCP-S5 at different magnifications ($\times 30\,000$ and $\times 100\,000$).

average particle size of 104 nm. At lower magnification (Fig. 5(A1–E1)), the as-prepared (NCP-S series) samples seem to have uniform, dense, compact and well-covered particles over a substrate. A spherical particle-like structure may exhibit a more porous surface area, which can result in a maximum capacitance value by providing a large number of electroactive sites. At higher magnification, numerous uniform spherical particles possess loosely packed structures (Fig. 5(A2–E2)), which are favourable for the accessibility of electrolyte ions to active materials, which can offer excellent capacitance retention at high charge–discharge rates.

Elemental mapping of the NCP-S series thin film samples was carried out using EDS analysis and is presented in Fig. S3(a–e) (see the ESI†). The presence of Ni, Cu, P and O elements in the prepared samples NCP-S2 to NCP-S4 confirms the successful deposition of the nickel copper phosphate material on the S.S. substrate in thin film form *via* the SILAR deposition method.

Also, the absence of copper in NCP-S1 and nickel in NCP-S5 samples confirms the formation of pristine nickel phosphate and copper phosphate materials, respectively. The experimental and observed nickel/copper ratios for the NCP-S series samples are provided in Table S2 (see the ESI†). It is found that the experimental and observed ratios of nickel and copper contents in the samples are very similar, which further confirms the formation of $\text{Ni}_x\text{Cu}_{3-x}(\text{PO}_4)_2 \cdot n\text{H}_2\text{O}$ ($0 < x < 3$) in NCP-S series thin films.

3.3 Electrochemical analysis of amorphous nickel copper phosphate (NCP-S) thin films

In the amorphous NCP-S material, the variation of the Ni : Cu ratio and its effect on electrochemical capacitive performance is examined by assembling a half test cell. Fig. 6(a) exhibits the comparative CV plots of the NCP-S series electrodes in 1 M KOH electrolyte at a scan rate of 20 mV s^{-1} in the potential range of 0–0.65 V (vs. Hg/HgO). The CV plot of the NCP-S3 electrode,

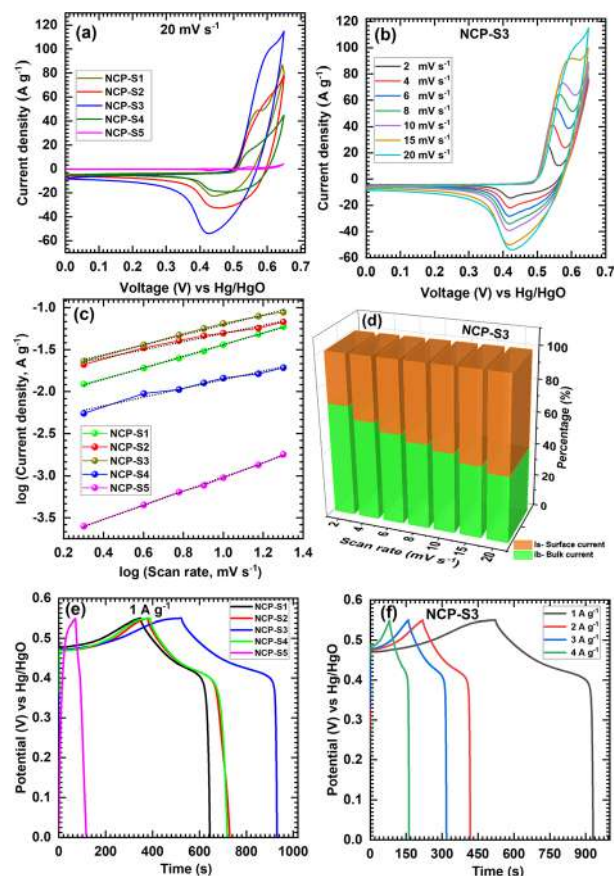


Fig. 6 (a) The comparative CV curves of the NCP-S series electrodes at a 20 mV s^{-1} scan rate, (b) the CV curves at different scan rates from 2 to 20 mV s^{-1} for sample NCP-S3, (c) plot of \log peak currents (A g^{-1}) vs. the \log scan rate (mV s^{-1}) for NCP-S1, NCP-S2, NCP-S3, NCP-S4 and NCP-S5 electrodes, (d) graphs of calculated pseudocapacitive (surface current) and battery type (bulk current) contribution to current density at various scan rates (2 to 20 mV s^{-1}) for the NCP-S3 electrode, (e) the comparative GCD profiles of the NCP-S series electrodes at a current density of 1 A g^{-1} and (f) GCD profiles at different current densities ranging from 1 to 4 A g^{-1} for the NCP-S3 electrode.

compared with other NCP-S series thin film electrodes, encloses a larger area under the CV, reflecting its higher charge storing ability. The amorphous NCP-S electrodes reveal well-established redox peaks that confirm the pseudocapacitive behaviour of thin films. The insertion of OH⁻ ions from the electrolyte to the amorphous NCP-S material takes place at charging and deinsertion during discharging. The CV curves of the NCP-S3 electrode at different scan rates ranging from 2 to 20 mV s⁻¹ are presented in Fig. 6(b), and CV plots of other NCP-S series thin film electrodes are supplied in Fig. S4 (see the ESI†). The alteration of CV nature is distinctly observed from amorphous nickel phosphate to amorphous copper phosphate electrodes (NCP-S1 to NCP-S5) (Fig. S4(a-d)) (see the ESI†). The scan rate dependent CV curves indicate that the area under the CV curves increases with increasing scan rates, indicating that the voltammetry current is proportional to the scan rate, which confirms the pseudocapacitive nature of the prepared NCP-S series electrodes.⁵¹

A charge kinetic investigation was performed to examine the charge storage mechanisms of the NCP-S series thin film electrodes. The charge stored in the electrode can be a result of the combination of two mechanisms (diffusion-controlled and capacitive components) and it is analyzed with the help of the power law using scan rate dependent CV curves and can be represented as follows,

$$i_p = av^b \quad (4)$$

where i_p denotes peak current, a and b denote adjustability factors, and v is the scan rate. The b value of the NCP-S series electrodes is estimated from the slope of the graph of $\log(i)$ vs. $\log(v)$ ⁵² as displayed in Fig. 6(c). The graph illustrates that the b values of NCP-S1, NCP-S2, NCP-S3, NCP-S4, and NCP-S5 electrodes are 0.68, 0.51, 0.59, 0.52 and 0.84, respectively as displayed in Fig. 6(c). The values of b for the NCP-S series electrodes range from 0.5 to 1 (ref. 53), which indicates that both (capacitive and diffusive) processes lead to charge storage in thin film electrodes. To recognize the individual contribution of the capacitive and diffusion-controlled processes, a modified power law can be used as expressed in the following equation.

$$I_p = C_s v + C_b v^{1/2} \quad (5)$$

where I_p represents peak current, v is the scan rate, and $C_s v$ and $C_b v^{1/2}$ denote the charge contribution to current density from capacitive (I_{surface}) and diffusion-controlled processes (I_{bulk}).⁴¹ For NCP-S3 thin film electrodes the current contribution (I_{surface} and I_{bulk}) at different scan rates of 2–20 mV s⁻¹ is expressed in Fig. 6(d). The current contribution of I_{surface} and I_{bulk} for the NCP-S series electrodes is calculated at various scan rates and presented in Fig. S5 (see the ESI†). It is noted that the capacitive contribution is more for high scan rates and more diffusive at low scan rates. Also, other electrodes display different current contribution values due to different concentrations of nickel and copper in the material. The NCP-S3 electrode offers ~58% capacitive current contribution at a 20 mV s⁻¹ scan rate (Fig. 6(d)) and it is higher than for nickel phosphate (NCP-S1)

(~42%) and copper phosphate (NCP-S5) (~46%) electrodes (Fig. S5(a and d)) (see the ESI†).

The GCD analysis was executed within the optimized potential window of 0–0.55 V (vs. Hg/HgO) and comparative GCD plots of all NCP-S electrodes at a current density of 1.5 A g⁻¹ are exhibited in Fig. 6(e). In a comparative study, the NCP-S3 electrode reveals larger charging and discharging time than other electrodes. The GCD curves of other NCP-S series electrodes at various current densities from 1 to 4 A g⁻¹ are given in Fig. S6(a-d).† Non-linear discharging curves of the NCP-S series electrodes exhibit deep ion intercalation and redox reaction, which indicates the pseudocapacitive nature of the material.⁵⁴ GCD analysis concludes that the NCP-S3 electrode gives a higher charge–discharge response which may be due to the large surface area offered by the nanostructure and optimum composition of nickel and copper. From the GCD graph, the C_s of the NCP-S series electrodes are calculated and plotted in Fig. S7.† The NCP-S3 electrode displays higher discharging time that accounts for the high C_s of 750 F g⁻¹ at a 1 A g⁻¹ current density compared to other electrodes and it decreases down to 618 F g⁻¹ at a 4 A g⁻¹ current density. Similarly, the NCP-S1, NCP-S2, NCP-S4 and NCP-S5 thin film electrodes offer maximum C_s of 540, 640, 594, and 83 F g⁻¹, respectively at a 1 A g⁻¹ current density as presented in Fig. 7(a). The achieved performance of the NCP-S electrodes is comparable with that of other phosphate/pyrophosphate based materials owing to the substrate, method of deposition and capacitance, given in Table S3 (see the ESI†). The decrement in C_s is noted with respect to an increase in current density owing

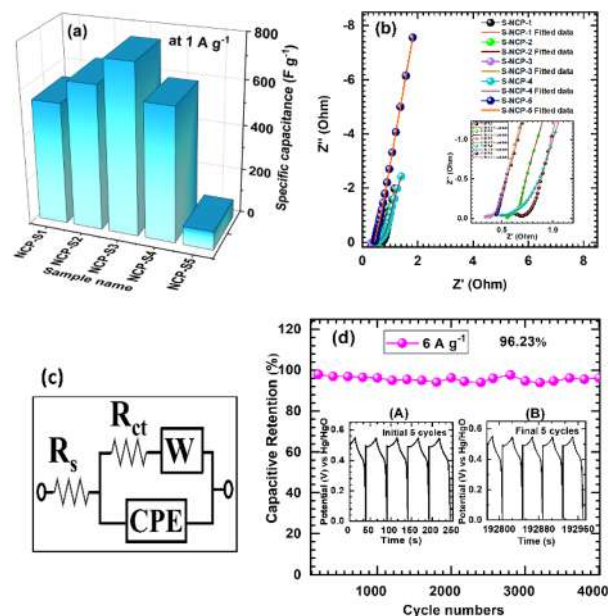


Fig. 7 (a) C_s (F g⁻¹) of NCP-S electrodes (NCP-S1 to NCP-S5) at a current density of 1.0 A g⁻¹, (b) Nyquist plots of NCP-S thin film electrodes (NCP-S1 to NCP-S5) and (c) the fitted circuit for the EIS data. (d) Capacitance retention (%) vs. cycle number plot of the NCP-S3 electrode at a current density of 6 A g⁻¹ for 4000 cycles (inset: GCD plots of (A) the first and (B) last 5 cycles).

to shorter time for electrochemical reaction with the nano-structure by electrolytic ions at higher current density.⁵⁵ At the same time, the longer interaction of electrolyte ions with the inner and outer surface of the electrode material at lower charge–discharge rates gives high C_s values.⁵⁶ The superior electrochemical pseudocapacitive behaviour of the NCP-S3 electrode originates from the synergistic influence of nickel and copper species (50 : 50 ratio) and high surface area offered by the interconnected spherical particle-like morphology.

The EIS technique is employed to examine the ion transfer and electrochemical conductivities of the electrodes. The Nyquist plots for EIS measurements for the NCP-S series electrodes are presented in Fig. 7(b). The EIS analysis was conducted in the region of 100 kHz to 100 MHz at 10 mV amplitude and fitted to a suitable equivalent circuit utilizing ZView impedance software, as displayed in Fig. 7(c). The values of fitted parameters of the equivalent circuit are tabulated in Table S4.† The lower values of R_s (0.55, 0.45, 0.33, 0.48 and 0.38 Ω) and R_{ct} (0.70, 1.04, 0.38, 0.87 and 1.20 Ω) are obtained for the NCP-S series electrodes. The small values of R_s (0.33 Ω) and R_{ct} (0.38 Ω) for the NCP-S3 thin film electrode denote a good attachment of the binder-free active material with the substrate and the spontaneous electrochemical reaction between the electrolyte and active electrode material. From Fig. 7(d), the NCP-S3 electrode shows 96.23% capacitance retention over 4000 GCD cycles at a current density of 6 A g⁻¹, and the GCD curves of the initial (A) and final (B) 5 cycles are revealed as an inset of Fig. 7(d). The decrease in capacitance is noted because of the minute depletion of active material from the surface after several charge–discharge cycles. Moreover, to examine the structural durability of nickel copper phosphate electrodes, the XPS study of nickel–copper phosphate (NCP-S3) electrodes is performed before as well as after the stability test (Fig. S8†). In the XPS analysis of the NCP-S3 electrode, it is noted that the valence states of Ni and Cu sites are slightly inter-changed due to oxidation/reduction of cations after stability testing. In the Ni 2p spectra (Fig. S8(a)†), the Ni³⁺ state is barely suppressed after the stability test and exhibits a slight increase in Ni²⁺ state (855.3 and 872.9 eV), which is apparent in the Ni³⁺ to Ni²⁺ transition of Ni states after the stability test.¹⁹ Similarly, oxidation in the valence states of the Cu cation is detected in the Cu 2p region, as revealed in Fig. S8(b),† which illustrates oxidation from Cu³⁺ to Cu²⁺ (933.8 and 953.5 eV).²² Also, a minute change in Cu 2p and Ni 2p binding energies after the stability test confirms a similar transformation of valence states of Cu and Ni cations. The slight shift and decrease in intensity of the P 2p (phosphorus) spectra observed after the stability test confirm the diminishing of the phosphorus pentavalent states near the surface of the electrode (Fig. S8(c)†). Furthermore, a slight shift of M–O and O–H bonds in the O 1s spectra towards lower binding energy, as shown in Fig. S8(d),† confirms the insertion and extraction of hydroxyl ions (OH⁻) during the charge–discharge process. The overall XPS analysis states that the intercalated hydroxyl ions utilize the vacancy sites of (PO₄)₃ in the process of charging and deintercalating from their accommodated positions upon discharging.

3.4 Hybrid asymmetric aqueous supercapacitor (HAASC) device

In order to further study the nano-structured electrodes for practical application, an HAASC device was constructed, where the NCP-S3 (Ni_{1.56}Cu_{1.44}(PO₄)₂·H₂O) electrode as a cathode and rGO electrode as an anode are utilized and estimated by a full test cell using a 1 M KOH electrolyte. The schematic representation of the as-fabricated HAASC device is illustrated in Fig. 8(a). To sustain charge storage equilibrium between the positive and negative thin film electrodes in an HAASC device, the required weight ratio of amorphous NCP-S3 and rGO electrodes is found to be 0.38 : 1. Using a three-electrode system, the NCP-S3 and rGO electrodes function in a distinct voltage range that is favourable for enhancing the voltage range of the HAASC device. The supercapacitive properties and characterization of the rGO electrode are provided in Fig. S9 (see the ESI†). The working potential limit for NCP-S3 is 0–0.65 V (*vs.* Hg/HgO) whereas the rGO potential range is –1 to 0 V (*vs.* Hg/HgO) as revealed in Fig. 8(b). The HAASC device was examined at a fixed 50 mV s⁻¹ scan rate in the range of 0 to 1.2–1.7 V and the results are exhibited in Fig. S10(a) (see the ESI†). Upon increasing the operating voltage window from 1.2 to 1.7 V, the current contribution of the CV curve increases. The quasi-rectangular nature of the CV loop is achieved up to a voltage limit of 0 to 1.6 V. Thereafter, an abrupt increase in current is noted owing to the polarization phenomenon at 1.7 V, which may be contributing to the irreversible reaction. Thus, the 0–1.6 V

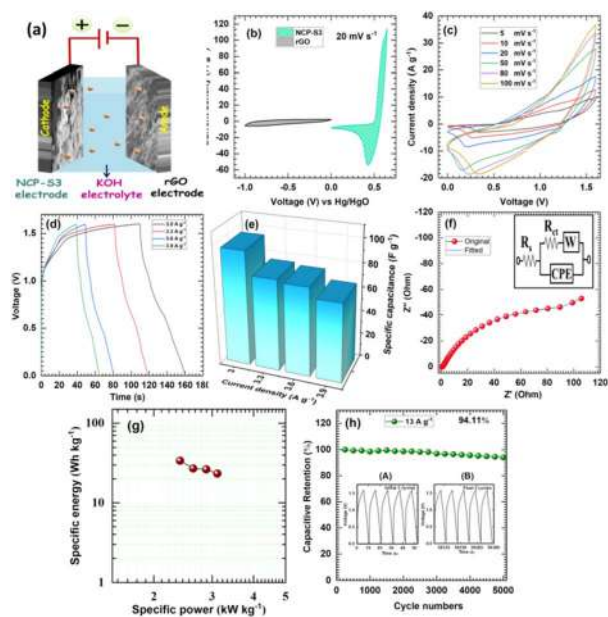


Fig. 8 (a) Diagram illustrating the process of assembling the HAASC device, (b) three-electrode CV plots for the rGO and NCP-S3 electrodes at a scan rate of 50 mV s⁻¹, (c) the CV and (d) GCD plots for the HAASC device at different scan rates (5–100 mV s⁻¹) and current densities (3.0–3.9 A g⁻¹), respectively, (e) a plot of C_s with employed current density for the HAASC device, (f) Nyquist plot for the HAASC device and the inset displays the equivalent circuit for fitted data, (g) Ragone plot of the HAASC device, and (h) a plot of capacitance retention (%) vs. cycle number for the HAASC device.

voltage range is selected for electrochemical examination of the HAASC device. The CV curves of the HAASC device at different scan rates ranging from 5 to 100 mV s^{-1} are exhibited in Fig. 8(c). The device displays a similar and reversible shape of CV curves with good rate capability at various sweep rates.³²

The GCD measurements of the HAASC device in different voltage ranges (1.2 to 1.7 V) at a 3.6 A g^{-1} current density are given in Fig. S10(b) (see the ESI†). The GCD plot displays the good performance within the voltage range of 0 to 1.6 V by showing the symmetric charge–discharge nature. Hence, from CV and GCD studies, the operating voltage range of 0 to 1.6 V was selected for the HAASC and applied for further analysis. The GCD plots of the HAASC device at various current densities ranging from 3.0 to 3.9 A g^{-1} are presented in Fig. 8(d). The non-linear GCD plots are detected for the HAASC device. The C_s of HAASC devices evaluated from GCD measurements are shown in Fig. 8(e). The HAASC device achieves a highest C_s of 95.62 F g^{-1} at a current density of 3.0 A g^{-1} and it decreases down to 65.81 F g^{-1} at a 3.9 A g^{-1} current density as depicted in Fig. 8(e). The small decrement of capacitance at higher current density suggests the excellent rate capability of the HAASC device. The C_s of the device decreases with increasing current density, due to the inadequate electrode–electrolyte interface at higher current density.^{33,34}

The properties of charge transfer kinetics in the HAASC device were investigated by EIS analysis. The Nyquist plot of the HAASC device is revealed in Fig. 8(f) and the equivalent circuit is depicted as inset of the figure. Low R_s (0.87Ω) and R_{ct} (96.92Ω) values are observed owing to the excellent electrochemical charge transfer kinetics. Also, the values of W and CPE are 0.811 mF and 0.205Ω , respectively. The mutual nature of both electrodes (NCP-S and rGO) is responsible for the better electrochemical performance of the HAASC with the enhanced operating voltage range, C_s and S.E. The S.E. and S.P. are two essential parameters in the S.C. performance analysis. The S.E. and S.P. of the HAASC device are calculated and exhibited in Fig. 8(g). The S.E. of the HAASC reached up to 34 Wh kg^{-1} with an S.P. of 2.40 kW kg^{-1} . Moreover, the S.E. remained at 23.39 Wh kg^{-1} at a high S.P. of 3.11 kW kg^{-1} , which indicates the high rate capability of the device. The asymmetric device with two different EDLC and pseudocapacitive materials exhibits an improved working potential window and S.E. and S.P.

The cycling stability of the HAASC device was studied by testing for 5000 continuous GCD cycles at a current density of 13 A g^{-1} (Fig. 8(h)). The capacitance retention with respective cycles is plotted in Fig. 8(h) and the GCD plots of the initial (A) and final (B) 5 cycles are depicted as an inset of the figure. The HAASC device demonstrates an excellent 94.11% capacitance retention after 5000 GCD cycles. The HAASC device shows a decrement in the C_s in the initial cycles followed by an increase in C_s owing to the expansion of the electrochemically active volume of the material due to intercalation and deintercalation of ions after many GCD cycles. The amorphous nature with superior capacitance of the HAASC device encourages further usage of SILAR deposited amorphous NCP-S thin films and rGO electrodes in the hybrid solid state energy storage device application.

3.5 Hybrid all-solid-state asymmetric supercapacitor (HASASC) device

Improving the energy storing capability of S.C.s is essential to expand their feasibility at the commercial level. Drawing inspiration from this, researchers are attempting to enhance the advancement of electrode materials, flexible design and electrolytes to boost the charge storing ability of the HASASC device by keeping its fundamental characteristics. Therefore, an HASASC device is fabricated, which offers many advantages, such as low cost packing, wide working voltage range, and ease of handling owing to lightweight and leakage-free fabrication.⁵⁷ The HASASC device is fabricated using amorphous NCP-S3 and rGO as cathode and anode electrodes, respectively, in PVA–KOH gel electrolyte, as shown in the schematic displayed in Fig. 9(a). An HASASC device was fabricated employing large area ($5 \times 5 \text{ cm}^2$) amorphous NCP-S3 and rGO electrodes. Furthermore, those two electrodes were painted with PVA–KOH gel to form a thin layer of electrolyte and dried in an ambient environment. After drying, the edges of the electrodes were enclosed with insulating tape to inhibit any shortening through the electrode sides. The gel electrolyte was again painted on the surface of the active material to ensure proper contact between the electrode and electrolyte. Later, both electrodes were assembled to form an SSD with the gel electrolyte. The assembled HASASC was further packed with transparent plastic strips. Lastly, the prepared device was pressed under a 1 ton pressure for 12 h to increase the interfacial contact between the active electrode materials and gel electrolyte. Thus, the HASASC device was successfully fabricated by the aforementioned steps shown in Fig. S11 (see the ESI†).

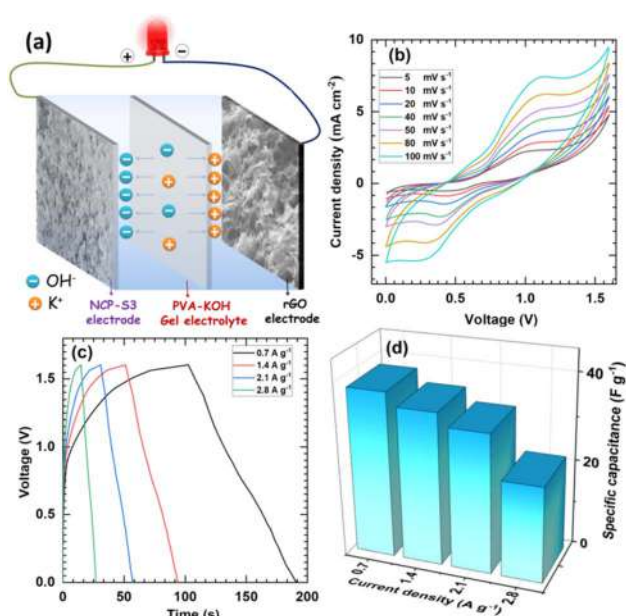


Fig. 9 (a) Diagram illustrating the process of making the HASASC device, (b) the CV and (c) GCD curves for the HASASC device at different scan rates (5 – 100 mV s^{-1}) and current densities (0.7 – 2.8 A g^{-1}), respectively, and (d) a plot of C_s with the employed current density for the HASASC device.

The HASASC device CV and GCD plots optimized in various voltage windows of 0 to 1.2–1.7 V were estimated at a 50 mV s^{-1} scan rate and 2.8 A g^{-1} current density as displayed in Fig. S12(a and b) (see the ESI†). From the CV as well as GCD analysis, the voltage range of 0 to 1.6 V is selected for electrochemical analysis of the HASASC device. Fig. 9(b) displays the CV curves of the HASASC device at various scan rates from 5 to 100 mV s^{-1} . The profile of the CV curve reveals a larger area under the curve with perfect pseudocapacitive behaviour of the HASASC device. All the CV plots maintain their profile irrespective of sweep rate, signifying the capacitive behaviour of the HASASC device. The GCD curves of the HASASC device at different current densities ranging from 0.7 to 2.8 A g^{-1} are shown in Fig. 9(c) and the non-linear charge–discharge profile illustrates a better electrochemical capacitive behaviour based on reversible redox reactions. Fig. 9(d) displays the C_s of the HASASC device analyzed from the GCD profile and the device attains a C_s of 37.62 F g^{-1} at a current density of 0.7 A g^{-1} , and up to 22.75 F g^{-1} is retained at a current density of 2.8 A g^{-1} .

The Nyquist plot for the HASASC device was studied by using EIS analysis and is exhibited in Fig. 10(a) with an equivalent circuit in the inset of the figure. The low values of R_s (0.24Ω) and R_{ct} (144Ω) are attributed to the superior ionic conductivity of the gel electrolyte and compatibility of the binder-free electrode material. The W and CPE are found to be 0.28Ω and 0.568 mF , respectively in the equivalent circuit.

The Ragone plot of the HASASC device is presented in Fig. 10(b) and the fabricated device delivered the highest S.E. of $13.51 \text{ W h kg}^{-1}$ with an S.P. of 0.55 kW kg^{-1} , and maintained

7.82 W h kg^{-1} S.E. at a maximum S.P. of 2.16 kW kg^{-1} . This result illustrates enhanced S.E. and good rate capability of the HASASC device that may have originated from the good C_s and broad working voltage range. Furthermore, the electrochemical cycling stability of the HASASC device is examined by taking the GCD over 5000 cycles at a fixed current density of 8 A g^{-1} (Fig. 10(c)). The HASASC device delivers 93.81% capacitance retention over 5000 cycles, suggesting the good electrochemical reversibility and extensive lifespan of the device, ascribed to the utilization of the gel electrolyte. To demonstrate the practical applicability of the HASASC device, the illumination of the LED (201) panel is executed using two serially joined HASASC devices, as displayed in Fig. 10(d). First, two serially joined HASASC devices were charged at $+3.2 \text{ V}$ for 30 s and then discharged through a LED panel. More remarkably, the HASASC device can light up the LED panel for almost 125 s. The digital pictures of the shining LED panel at various time intervals are displayed in Fig. 10(d). The initial bright shining of LED lights denotes the eminent power output performance, thus offering the fabulous competency of the developed HASASC device.

According to a literature survey, there have not yet been studies on nickel copper phosphate material based asymmetric hybrid devices, except our work reported earlier on synthesis of microflakes of nickel copper phosphate⁵⁸ and therefore, hereby, the obtained performance of the HAASC and HASASC devices is compared with earlier metal phosphate based devices by means of S.P., S.E. and stability tests, and given in Table S5 (see the ESI†). Also, the corresponding Ragone plot of the HAASC and HASASC devices with comparative literature reports is plotted in

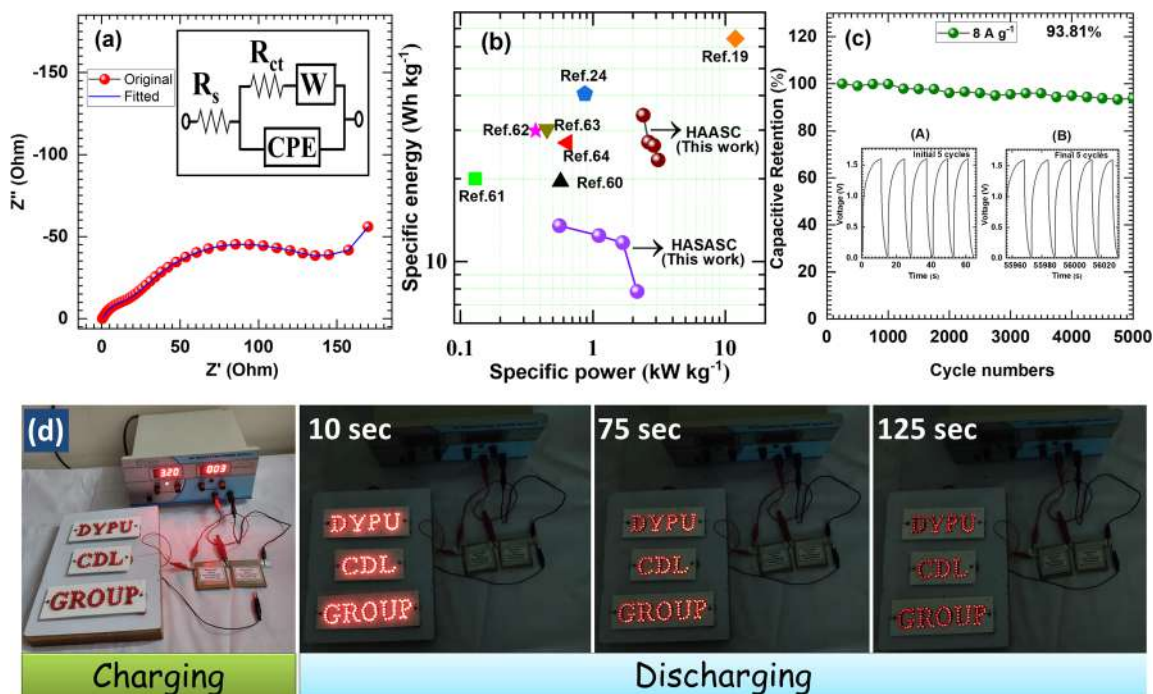


Fig. 10 (a) Nyquist plot for the HASASC device and the inset reveals the equivalent circuit for the fitted data, (b) Ragone plot of the HASASC device, (c) a plot of capacitance retention (%) vs. cycle number for the HASASC device, and (d) digital photographs for demonstration of the HASASC device with a glowing panel of 201 red LEDs at distinct time periods.

Fig. 10(b). For example, Andikaey *et al.*⁵⁹ reported an asymmetric FeCoCuP//AC device and shows an S.E. of 61.5 W h kg⁻¹ and a high S.P. of 1201.7 W kg⁻¹. Mirghni *et al.*⁶⁰ constructed a NaNi₄(PO₄)₃/GF//AC device and reported an S.E. of 19.5 W h kg⁻¹ at a S.P. of 0.57 kW kg⁻¹. An AC||NaNiPO₄ SC was reported by Senthilkumar *et al.*⁶¹ which exhibited an S.E. of 20 W h kg⁻¹ and an S.P. of 0.13 kW kg⁻¹. Also, a NaNi_{0.33}Co_{0.67}PO₄·H₂O//AC device constructed by Liu *et al.*⁶² revealed an S.E. of 29.85 W h kg⁻¹ and 0.374 kW kg⁻¹ S.P. H. Sharkawy *et al.*²⁴ reported a hybrid Ni–Cu–P/NF//AC device which exhibited a high S.E. of 40.5 W h kg⁻¹ at 875 W kg⁻¹ S.D. Wang *et al.*⁶³ assembled a T-Nb₂O₅@Ni₂P//AC asymmetric S.C. that shows an S.E. of 30.2 W h kg⁻¹ and S.P. of 0.45 kW kg⁻¹. Furthermore, Alzaid *et al.*¹⁹ reported an Ni_{0.75}Mn_{0.25}(PO₄)₂//AC device which shows an S.E. of 64.2 W h kg⁻¹ and S.P. of 11 896 W kg⁻¹. Lan *et al.*⁶⁴ fabricated a NiCoP@NF//AC device which exhibits an S.E. of 27 W h kg⁻¹ at a S.P. of 0.64 kW kg⁻¹. The reported FeCoCuP/NF, T-Nb₂O₅@Ni₂P/NF, Ni_{0.75}Mn_{0.25}(PO₄)₂/NF and Ni–Cu–P/NF based hybrid devices exhibit slightly higher S.E. than those in the present work, which may be owing to the usage of Ni-foam (N.F.) as a current collector. Also, various electroactive materials (like Ni, Cu, and P) delivered different charge storage properties for enhancement in electrochemical activities. In this study, S.S. is employed as a current collector, which does not participate in the redox reaction and the achieved S.E. and S.P. are delivered solely by the active material (NCP).

In summary, the amorphous, hydrous and mesoporous NCP-S thin film delivers a higher specific surface area, less impedance (R_s and R_{ct}) owing to binder-free synthesis and speedy charge delivery in redox reaction.^{65–68} In the amorphous material, electrolytic ions freely diffuse because of the defect-rich structure, which is favourable to accessing more electroactive material.⁶⁹ Additionally, the amorphous NCP-S material offered excellent cycling stability relative to the crystalline phase since the amorphous phase does not show changes in strain while charging and discharging.⁷⁰ Hence, in the present work, the achieved amorphous, hydrous material uniquely delivers high S.E. and S.P. due to the mesoporous structure and amorphous spherical particles. The HAASC and HASASC devices display high performance which is attributed to the several benefits delivered by the amorphous nickel copper phosphate cathode, such as spherical particle-like morphology, mesoporous and hydrous nature, synergistic impact of the metal (Ni : Cu) phosphate, and binder-free preparation of the Ni_{1.56}Cu_{1.44}(PO₄)₂·H₂O thin film electrode.

4. Conclusions

In this report, an amorphous NCP-S thin film (binder-free approach) electrode was prepared on an S.S. substrate employing a facile SILAR method at ambient temperature and applied as a cathode material in a hybrid S.C. A facile SILAR method allows binder-free synthesis of an amorphous, hydrous Ni_{3–x}Cu_x(PO₄)₂·nH₂O material with selective Ni : Cu composition variation. The mesoporous, amorphous composition, spherical particles with Ni : Cu composition of 1 : 1 deliver a higher specific capacitance (C_s) (capacity) of 750 F g⁻¹ (412.50

C g⁻¹). The spherical particle-like morphology as well as the amorphous nature of the Ni_{1.56}Cu_{1.44}(PO₄)₂·H₂O thin film electrode exhibit high performance owing to lesser diffusion pathways and extra electroactive sites (37.30 m² g⁻¹) for electrolyte ion penetration. Furthermore, the constructed HAASC device delivers a C_s of 95 F g⁻¹ along with a higher S.E. of 34 W h kg⁻¹ at an S.P. of 2.40 kW kg⁻¹. Also, the HASASC device displayed a C_s value of 37.62 F g⁻¹ with an S.E. of 13.51 W h kg⁻¹ at 0.55 kW kg⁻¹ S.P. Moreover, the HAASC and HASASC devices demonstrated outstanding cycling durability of 94.11% and 93.81% capacitance retention after 5000 cycles. Such an inexpensive, binder-free, facile SILAR synthetic approach and high performance of the amorphous Ni_{1.56}Cu_{1.44}(PO₄)₂·H₂O spherical particle-like structured cathode paves a novel way to a bright future for practical production of high-energy hybrid devices.

Author contributions

Dr S. S. Pujari carried out the investigation and formal analysis, data curation, and original draft writing. Mr S. A. Kadam and Prof. Y.-R. Ma provided resources and formal analysis. Mr S. B. Jadhav, Mr S. S. Kumbhar, Ms. S. B. Bhosale, Mr V. V. Patil, Dr J. L. Gunjekar and Prof. C. D. Lokhande carried out modification, creation, and presentation and visualization of the manuscript. Dr U. M. Patil carried out funding acquisition, administration, supervision, and manuscript editing. All authors made substantial contributions to the work reported in the manuscript.

Conflicts of interest

There are no conflicts of interest to declare.

Acknowledgements

Authors are thankful to D. Y. Patil Education Society, Kasaba Bawada, Kolhapur for financial support through research projects sanction No. DYPES/DU/R&D/2022/2353 and DST-FIST Analytical Instrumentation Laboratory, Jaysingpur College, Jaysingpur for characterization facilities. Also, authors are thankful to the Department of Science and Technology, India-Innovation in Science Pursuit for Inspired Research (DST-INSPIRE) for financial support through research project sanction no. DST/INSPIRE/04/2016/000260 and Mahatma Jyotiba Phule Research & Training Institute (MAHAJYOTI), Nagpur, Government of Maharashtra, India awarded Junior Research Fellowship (JRF) program-2021.

References

- 1 M. El-Kady, M. Ihns, M. Li, J. Y. Hwang, M. F. Mousavi, L. Chaney, A. Lech and R. Kaner, *Proc. Natl. Acad. Sci. U. S. A.*, 2015, **112**, 4233–4238.
- 2 D. Dubal, N. Chodankar, D.-H. Kim and P. Gomez-Romero, *Chem. Soc. Rev.*, 2018, **47**, 2065–2129.
- 3 C. Wang, F. Liu, J. Chen, Z. Yuan, C. Liu, X. Zhang, M. Xu, L. Wei and Y. Chen, *Energy Storage Mater.*, 2020, **32**, 448–457.

- 4 D. Dubal, O. Ayyad, V. Ruiz and P. Gómez-Romero, *Chem. Soc. Rev.*, 2015, **44**, 1777–1790.
- 5 P. Simon, Y. Gogotsi and B. Dunn, *Science*, 2014, **343**, 1210–1211.
- 6 Y. Zhang, H. Hu, Z. Wang, B. Luo, W. Xing, L. i. Li, Z. Yan and L. Wang, *Nano Energy*, 2020, **68**, 104226.
- 7 N. Chodankar, H. Pham, A. Nanjundan, J. F. S. Fernando, K. Jayaramulu, D. Golberg, Y.-K. Han and D. Dubal, *Small*, 2020, **16**, 2002806.
- 8 H. Liu, K.-S. Moon, J. Li, Y. Xie, J. Liu, Z. Sun, L. Lu, Y. Tang and C.-P. Wong, *Nano Energy*, 2020, **77**, 105058.
- 9 R. Shen, J. Xie, X. Lu, X. Chen and X. Li, *ACS Sustainable Chem. Eng.*, 2018, **6**, 4026–4036.
- 10 L. Zhang, C. Chang, C.-W. Hsu, C.-W. Chang and S.-Y. Lu, *J. Mater. Chem. A*, 2017, **5**, 19656–19663.
- 11 F. Gillot, S. Boyanov, L. Dupont, M.-L. Doublet, M. Morcrette, L. Monconduit and J.-M. Tarascon, *Chem. Mater.*, 2005, **17**, 6327–6337.
- 12 S. T. Oyama, P. Clark, X. Wang, T. Shido, Y. Iwasawa, S. Hayashi, J. M. Ramallo-Lopez and F. G. Requejo, *J. Phys. Chem. B*, 2002, **106**, 1913–1920.
- 13 N. Wulan Septiani, Y. Kaneti, K. Fathoni, J. Wang, Y. Ide, B. Yulianto, H. Dipojono Nugrah, A. Nanjundan, D. Golberg, Y. Bando and Y. Yamauchi, *Nano Energy*, 2020, **67**, 104270.
- 14 Y. Fang, J. Zhang, L. Xiao, X. Ai, Y. Cao and H. Yang, *Adv. Sci.*, 2017, **4**, 1600392.
- 15 P. Katkar, S. Marje, V. Parale, C. Lokhande, J. Gunjekar, H. Park and U. Patil, *Langmuir*, 2021, **37**, 5260–5274.
- 16 H. Liu, M. Zhang, T. Ma, Y. Wang, Z. Song, A. Wang and Z. Huang, *Chem. Eng. J.*, 2021, **238**, 116613.
- 17 M. Alzaid, M. Iqbal, S. Alam, N. Almoisheer, A. Afzal and S. Aftab, *J. Energy Storage*, 2021, **33**, 102020.
- 18 S. Alam and M. Iqbal, *Ceram. Int.*, 2021, **47**, 11220–11230.
- 19 S. Marje, V. Patil, V. Parale, H. Park, P. Shinde, J. Gunjekar, C. Lokhande and U. Patil, *Chem. Eng. J.*, 2022, **429**, 132184.
- 20 J. Huang, Y. Xiong, Z. Peng, L. Chen, L. Wang, Y. Xu, L. Tan, K. Yuan and Y. Chen, *ACS Nano*, 2020, **14**, 14201–14211.
- 21 L. Naderi and S. Shahrokhian, *Chem. Eng. J.*, 2020, **392**, 124880.
- 22 H. Sharkawy, D. Sayed, A. Dhmees, R. Aboushahba and N. Allam, *ACS Appl. Energy Mater.*, 2020, **3**, 9305–9314.
- 23 S. Moosavifard, S. Kaverlavani, J. Shamsi and A. Bakouei, *J. Mater. Chem. A*, 2017, **5**, 18429.
- 24 Q. Yu, B. Aguila, J. Gao, P. Xu, Q. Chen, J. Yan, D. Xing, Y. Chen, P. Cheng, Z. Zhang and S. Ma, *Chem.–Eur. J.*, 2019, **25**, 5611–5622.
- 25 J. Li, N. Dudney, X. Xiao, Y.-T. Cheng, C. Liang and M. Verbrugge, *Adv. Energy Mater.*, 2015, **5**, 1401627.
- 26 T. Wang, Q. Hao, J. Liu, J. Zhao, J. Bell and H. Wang, *RSC Adv.*, 2016, **6**, 45986–45992.
- 27 Y. Xi, B. Dong, Y. Dong, N. Mao, L. Ding, L. Shi, R. Gao, W. Liu, G. Su and L. Cao, *Chem. Mater.*, 2016, **28**, 1355–1362.
- 28 N. Chen, J. Zhou, Q. Kang, H. Ji, G. Zhu, Y. Zhang, S. Chen, J. Chen, X. Feng and W. Hou, *J. Power Sources*, 2017, **344**, 185–194.
- 29 H. Pang, Y.-Z. Zhang, Z. Run, W.-Y. Lai and W. Huang, *Nano Energy*, 2015, **17**, 339–347.
- 30 F. Omar, A. Numan, N. Duraisamy, S. Bashir, K. Ramesh and S. Ramesh, *RSC Adv.*, 2016, **6**, 76298–76306.
- 31 A. Agarwal, S. Majumder and B. Sankapal, *Chem. Eng. J.*, 2021, **422**, 130131.
- 32 A. Agarwal and B. Sankapal, *Int. J. Energy Res.*, 2021, **46**, 6177–6196.
- 33 S. Marje, P. Katkar, S. Pujari, S. Khalate, P. Deshmukh and U. Patil, *Mater. Sci. Eng., B*, 2020, **261**, 114641.
- 34 M. Liu, J. Li, Y. Hu, Q. Yang and L. Kang, *Electrochim. Acta*, 2016, **201**, 142–150.
- 35 P. Katkar, S. Marje, S. Pujari, S. Khalate, P. Deshmukh and U. Patil, *Synth. Met.*, 2020, **267**, 116446.
- 36 J. Theerthagiri, K. Thiagarajan, B. Senthilkumar, Z. Khan, R. A. Senthil, P. Arunachalam, J. Madhavan and M. Ashokkumar, *ChemistrySelect*, 2017, **2**, 201–210.
- 37 Q. Liu, H. He, Z.-S. Chao, J. Xie and E. Ruchenstein, *New J. Chem.*, 2012, **36**, 139–147.
- 38 P. Mei, Y. V. Kaneti, M. Pramanik, T. Takei, O. Dag, Y. Sugahara and Y. Yamauchi, *Nano Energy*, 2018, **52**, 336–344.
- 39 N. Duraisamy, N. Arshid, K. Kandiah, J. Iqbal, P. Arunachalam, G. Dhanaraj, K. Ramesh and S. Ramesh, *J. Mater. Sci.: Mater. Electron.*, 2019, **30**, 7435–7446.
- 40 D. Marcano, D. Kosynkin, J. Berlin, A. Sinitskii, Z. Sun, A. Slesarev, L. B. Alemany, W. Lu and J. M. Tour, *ACS Nano*, 2010, **4**, 4806–4814.
- 41 P. Katkar, S. Marje, S. Pujari, S. Khalate, A. Lokhande and U. Patil, *ACS Sustainable Chem. Eng.*, 2019, **7**, 11205–11218.
- 42 A. Davies and A. Yu, *Can. J. Chem. Eng.*, 2011, **89**, 1342–1357.
- 43 S. Marje, S. Pujari, S. Khalate, V. Patil, V. Parale, T. Kim, H. Park, J. Gunjekar, C. Lokhande and U. Patil, *J. Mater. Chem. A*, 2022, **10**, 11225–11237.
- 44 B. Ameri, S. Davarani, R. Roshani, H. Moazami and A. Tadjarodi, *J. Alloys Compd.*, 2017, **695**, 114–123.
- 45 D. Wang, Y. Xu, W. Sun, X. Guo, L. Yang, F. Wang and Z. Yang, *Electrochim. Acta*, 2020, **337**, 135827.
- 46 J. B. Condon, *Surface Area and Porosity Determinations by Physisorption Measurements and Theory*, Elsevier, Amsterdam, 2006, pp. 6–14.
- 47 H. Pang, C. Wei, Y. Ma, S. Zhao, G. Li, J. Zhang, J. Chen and S. Li, *Chempluschem*, 2013, **78**, 546–553.
- 48 J. Li, M. Liu, L. Kong, D. Wang, Y. Hu, W. Han and L. Kang, *RSC Adv.*, 2015, **5**, 41721–41728.
- 49 M. Jiang, J. Li, J. Li, Y. Zhao, L. Pan, Q. Cao, D. Wang and Y. Du, *Nanoscale*, 2019, **11**, 9654–9660.
- 50 C. Mu, D. Butenko, I. Odynets, I. Zatovsky, J. Li, W. Han and N. Klyui, *Dalton Trans.*, 2020, **49**, 8226–8237.
- 51 X. Bai, Q. Liu, Z. Lu, J. Liu, R. Chen, R. Li, D. Song, X. Jing, P. Liu and J. Wang, *ACS Sustainable Chem. Eng.*, 2017, **5**, 9923–9934.
- 52 M. Sathiyaa, A. S. Prakash, K. Ramesha, J.-M. Tarascon and A. K. Shukla, *J. Am. Chem. Soc.*, 2011, **133**, 16291–16299.
- 53 N. Chodankar, I. Bagal, S. Ryu and D. Kim, *Chem. Eng. J.*, 2019, **362**, 609–618.

- 54 K. Sankar, Y. Seo, S. Lee and S. Jun, *ACS Appl. Mater. Interfaces*, 2018, **10**, 8045–8056.
- 55 F. Butt, M. Tahir, C. Cao, F. Idress, R. Ahmed, W. Khan, Z. Ali, N. Mohmood, M. Tanveer, A. Mohmood and I. Aslam, *ACS Appl. Mater. Interfaces*, 2014, **16**, 13635–13641.
- 56 J. Cherusseria and K. Kar, *J. Mater. Chem. A*, 2016, **4**, 9910–9922.
- 57 S. Karade, D. Dubal and B. Sankapal, *ChemistrySelect*, 2017, **2**, 10405–10412.
- 58 S. Pujari, S. Kadam, Y.-R. Ma, S. Jadhav, S. Kumbhar, S. Bhosale, J. Gunjekar, C. Lokhande and U. Patil, *J. Energy Storage*, 2022, **52**, 105037.
- 59 Z. Andikaey, A. Ensafi and B. Rezaei, *Electrochim. Acta*, 2021, **393**, 139061.
- 60 A. Mirghni, K. Oyedotun, O. Olaniyan, B. Mahmoud, N. Sylla and N. Manyala, *RSC Adv.*, 2019, **9**, 25012–25021.
- 61 B. Senthilkumar, K. Sankar, L. Vasylechko, Y.-S. Lee and R. Selvan, *RSC Adv.*, 2014, **4**, 53192–53200.
- 62 M. Liu, N. Shang, X. Zhang, S. Gao, C. Wang and Z. Wang, *J. Alloys Compd.*, 2019, **791**, 929–935.
- 63 F. Wang, H. Lei, H. Peng, J. Zhou, R. Zhao, J. Liang, G. Ma and Z. Lei, *Electrochim. Acta*, 2019, **325**, 134934.
- 64 Y. Lan, H. Zhao, Y. Zong, X. Li, Y. Sun, J. Feng, Y. Wang, X. Zheng and Y. Du, *Nanoscale*, 2018, **10**, 11775–11781.
- 65 M. Javed, H. Lei, Z. Wang, B.-T. Liu, X. Cai and W. Mai, *Nano Energy*, 2020, **70**, 104573.
- 66 M. Javed, S. Shah, T. Najam, S. Siyal, S. Hussain, M. Saleem, Z. Zhao and W. Mai, *Nano Energy*, 2020, **77**, 105276.
- 67 M. Javed, N. Shaheen, S. Hussain, J. Li, S. Shah, Y. Abbas, M. Ahmad, R. Raza and W. Mai, *J. Mater. Chem. A*, 2019, **7**, 946–957.
- 68 M. Javed, S. Shah, S. Hussain, S. Tan and W. Mai, *Chem. Eng. J.*, 2020, **382**, 122814.
- 69 J. Chen, J. Xu, S. Zhou, N. Zhao and C.-P. Wong, *Nano Energy*, 2016, **21**, 145–153.
- 70 R. Yi, J. Feng, D. Lv, M. Gordin, S. Chen, D. Choi and D. Wang, *Nano Energy*, 2013, **4**, 498–504.



Amorphous, hydrous nickel phosphate thin film electrode prepared by SILAR method as a highly stable cathode for hybrid asymmetric supercapacitor

Sachin S. Pujari^a, Vinod V. Patil^a, Akash S. Patil^a, Vinayak G. Parale^b, Hyung-Ho Park^b, Jayavant L. Gunjekar^a, Chandrakant D. Lokhande^a, Umakant M. Patil^{a,*}

^a Centre for Interdisciplinary Research, D. Y. Patil Education Society, Kasaba Bawada, Kolhapur 416 006, India

^b Department of Materials Science and Engineering, Yonsei University, 50 Yonsei-ro, Seodaemun-gu, Seoul 03722, South Korea

ARTICLE INFO

Keywords:

Amorphous materials
Particles cluster
Nickel phosphate
SILAR method
Hybrid Supercapacitor
Thin film electrode

ABSTRACT

To achieve higher supercapacitive performance of active material, several materials with precise structures and properties have been prepared using different chemical synthesis methods. Recently, amorphous materials are gaining much attention as an electrode in supercapacitor application as it provides superior electrochemical properties due to disorder in structure. So, in this investigation, a facile, binder free successive ionic layer adsorption and reaction (SILAR) method is adopted for the preparation and deposition of amorphous, hydrous nickel phosphate thin films on stainless steel substrates. The amorphous nickel phosphate shows mesoporous, clusters of particles like morphology. In the electrochemical study, the amorphous, hydrous nickel phosphate electrode demonstrates a superior specific capacitance of 1700 F g^{-1} (specific capacity- 814 C g^{-1}) at 0.5 mA cm^{-2} current density along with excellent capacitive retention (96.55%) and coulombic efficiency (98.62%) over 5000 cycles. Furthermore, fabricated hybrid supercapacitor device using the nickel phosphate as cathode and reduced graphene oxide as anode exhibits specific capacitance of 113.5 F g^{-1} at 3 mA cm^{-2} current density with a high 40.37 Wh kg^{-1} energy density at 1.689 kW kg^{-1} power density alongwith excellent cyclic stability (95.09% retention after 5000 cycles). The obtained results illustrate that the amorphous, hydrous nature of nickel phosphate is a beneficial and superior choice as a cathode material in high-performing hybrid asymmetric supercapacitor devices.

1. Introduction

Electrochemical supercapacitors have recently gained much attention as superior electrochemical energy storage devices due to their high power density and exceptional stability. Generally, stored electrical energy in supercapacitors is based on two primary electrochemical double-layer capacitance and pseudocapacitance mechanisms. EDLC based supercapacitor exhibits excellent stability and high power, since charge storing proceeds physically via ions adsorption/desorption inside carbon-based materials; however, these materials suffer from low energy density [1]. The pseudocapacitive capacitance originates electrochemically either via redox reactions (e.g., metal oxides/hydroxides/phosphate) or through ion intercalation (e.g., conducting polymers) [2–5]. Further, pseudocapacitor is divided into three types such as intrinsic, intercalation, and extrinsic pseudocapacitor. In

intrinsic pseudocapacitor, charges are stored by double layer and surface redox mechanism on the surface of a material or near the material surface. In intercalation type, pseudocapacitor charge stores through intercalation of electrolytic ion in interplanar space or tunnels. However, in extrinsic pseudocapacitors, battery-type materials exhibit pseudocapacitive behavior with a reduction in their crystallinity or morphology (nanomaterials) [6]. Besides the excellent energy density of pseudocapacitive materials, they suffer from poor stability and less power density.

Transition metal sulfides/oxide/hydroxide and phosphates have been comprehensively explored as pseudocapacitive material for energy storage devices because of their abundant resources and electrochemical activity [7,8]. Among various pseudocapacitive materials, the excellent electrical conductivity of metal phosphate executes a rapid charge transfer, and it is beneficial for supercapacitor [9,10]. Also, the

* Corresponding author.

E-mail address: umakant.physics84@gmail.com (U.M. Patil).

<https://doi.org/10.1016/j.synthmet.2021.116876>

Received 11 June 2021; Received in revised form 19 July 2021; Accepted 3 August 2021

Available online 12 August 2021

0379-6779/© 2021 Elsevier B.V. All rights reserved.

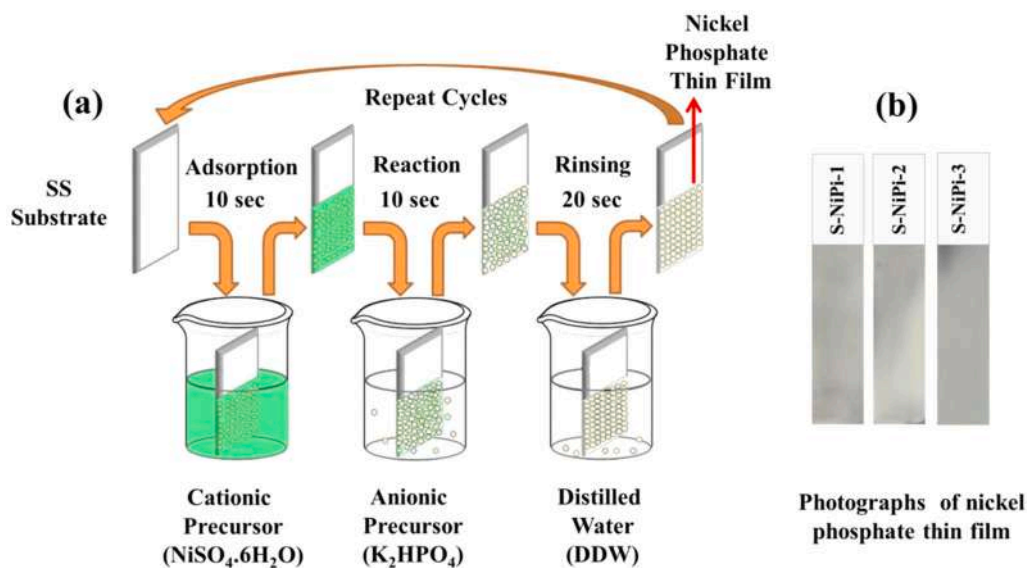


Fig. 1. (a) The schematic representation of SILAR method for the preparation of nickel phosphate thin film electrodes, (b) photograph of nickel phosphate thin films prepared at different molar ratio.

transition metal phosphates demonstrate superior charge/ion conductivity since they have an open framework, including cavities and large solid channels. Moreover, chemically stable P-O covalent bond in metal phosphate exhibits excellent stable structure of material, which is a prime prerequisite of electrochemical energy storage devices [11]. Up to now, various chemical methods were employed for the synthesis of nickel phosphate materials with different microstructure such as, calcination [12,13], hydrothermal [14–20] sonochemical [21,22], co-precipitation [23,24] microwave assisted [25] and chemical bath deposition [26] and utilized in an energy storage devices. Different synthetic approaches provide various morphologies of crystalline nickel phosphate such as nano-microspheres, nano-microrod, nanowire, microflower, micro leaf-like, etc. Eventually, these morphologies display distinct electrochemical capacitive performance.

Recently, researchers noted and reported that the amorphous hydrous phase of materials exhibits excellent pseudocapacitive performance with enhanced stability than their bulk or crystalline counterparts due to the disorder and decreased ion diffusion lengths [27]. Marje et al. noted that the chemically deposited amorphous nickel phosphate delivers maximum specific capacitance than that of crystalline [26]. However, the poor electrical conductivity of amorphous material can be a major hurdle in achieving the high capacitive performance of the electrode. Such a hurdle can be overcome by the preparation of binder-free electrodes or the direct growth of amorphous material over a conductive substrate. Amongst the earlier reports, only Shankar et al. [18] and Marje et al. [9] used a binder-free approach for the deposition of $\text{Ni}_2\text{P}_2\text{O}_7$ on the substrate using chemical bath deposition and hydrothermal method, respectively. Therefore, the present research is directed in search of a facile and reliable synthetic approach to prepare binder-free amorphous materials over conductive substrates. The successive ionic layer adsorption and reaction (SILAR) method is a facile synthetic approach for the preparation of amorphous/nanocrystalline materials over substrate since this method allows abruptness of material growth while deposition and can restricts crystalline growth of material. Compared to other methods, the SILAR method is a simple, less time-consuming and less expensive method for the deposition of metal phosphate thin films [28]. Moreover, to the best of our knowledge, this facile synthetic approach (SILAR) has not been investigated yet for the binder-free synthesis of nickel phosphate thin film.

In present work, the SILAR method has been employed for the first time to synthesize binder-free nickel phosphate thin films on stainless

steel (SS) substrate. The electrochemical capacitive performance of amorphous, hydrous nickel phosphate thin film electrodes is studied in 1 M KOH electrolyte. Also, excellent performing nickel phosphate thin film was employed (cathode) to fabricate hybrid asymmetric devices accompanied by reduced graphene oxide (as an anode). The capacitive accomplishments were examined and reported herein.

2. Experimental section

2.1. Preparation of nickel phosphate thin films

The binder-free nickel phosphate thin films were synthesized by the facile SILAR method. SILAR method is the facile synthetic approach for the preparation of amorphous/nanocrystalline materials on a substrate, which is established on the subsequent accumulation of cation and reaction with anions over substrate surface from separately placed precursor's solution. A modified three-beaker SILAR system (shown in Fig. 1(a)) was employed to synthesize nickel phosphate thin films at room temperature (300 K). Different molar compositions of nickel sulphate ($\text{NiSO}_4 \cdot 6\text{H}_2\text{O}$) and di-potassium hydrogen orthophosphate (K_2HPO_4) were prepared separately by dissolving in 50 ml of double distilled water (DDW). The molar ratios of $\text{NiSO}_4 \cdot 6\text{H}_2\text{O}$ (used as cationic precursor solution) and K_2HPO_4 (used as anionic precursor solution) ($\text{NiSO}_4 \cdot 6\text{H}_2\text{O}:\text{K}_2\text{HPO}_4$) were varied in the synthesis process as 0.66:0.34, 0.5:0.5, and 0.34:0.66, and indicated as S-NiPi-1, S-NiPi-2, and S-NiPi-3, respectively. Three steps are implemented for the deposition of nickel phosphate thin films in the SILAR method. H_2O) Initially, SS substrate dipped in cationic precursor solution for 10 s to adsorb nickel ions on the surface of the substrate. Then in second step, the substrate was dipped for 10 s in an anionic precursor solution (K_2HPO_4) for reaction purpose. In the final step, the substrate was rinsed in DDW for 20 s to remove un-reacted and un-adsorbed species from the surface of SS substrate. The whole three-step procedure is the single SILAR cycle, and it is schematically displayed in Fig. 1(a). Similar 80 SILAR cycles were continued to achieve an optimal thickness of nickel phosphate thin film on the SS substrate. The obtained greenish-white colored thin films (shown in Fig. 1(b)) were dried at ambient temperature, and all preparative parameters are tabulated and given in Table S1 (see ESI). Furthermore, these thin films were directly used for different characterization and electrochemical capacitive testing.

2.2. Preparation of reduced graphene oxide (rGO) electrode

For the preparation of rGO, primarily graphene oxide (GO) was prepared using Hummer's method [29]. Then, the obtained GO solution was reduced hydrothermally (453 K for 12 h) and freeze-dried to achieve a high surface area with a porous structure. The rGO electrode was prepared as follows: 75 wt% of as-prepared rGO material, 20 wt% of carbon black, and 5% polyvinylidene fluoride (PVDF) in N-methyl 2-pyrrolidone (NMP) were used to make a homogeneous slurry. The obtained slurry was covered on a SS substrate ($1 \times 1 \text{ cm}^{-2}$ area) and dried up in an oven at 333 K for 2 h. As-prepared rGO electrode was employed as an anode in the hybrid asymmetric supercapacitor device.

2.3. Characterization techniques

The crystal structure of the prepared thin films was examined using an X-ray powder diffractometer (XRD, Mini Flex 600, Cu K α characteristic radiation at $\lambda = 1.54 \text{ \AA}$; Rigaku). The chemical bonding and functional groups present in the prepared material were analyzed by employing a 4600 type-A Fourier transform infrared (FT-IR) instrument. The pore size distribution and surface area are evaluated from (BJH) analysis and Brunauer–Emmett–Teller (BET) technique (Belsorp II mini). The elemental composition and surface morphology of thin films were investigated using energy-dispersive x-ray spectroscopy (EDS) and field-emission scanning electron microscopy (FE-SEM, JSM-6500F, JEOL).

2.4. Electrochemical measurements

The electrochemical properties of nickel phosphate thin film electrodes were investigated by employing ZIVE MP1 multichannel electrochemical workstation. The electrochemical capacitive performance of the electrodes was probed in 1 M KOH electrolyte using a three-electrode system at the ambient environment, where S-NiPi series electrodes (area $\sim 1 \text{ cm}^2$) served as a working electrode, the mercury/mercury oxide (Hg/HgO) was utilized as the reference electrode and a platinum plate (area $\sim 1 \text{ cm}^2$) as the counter electrode. The supercapacitive performance of the electroactive material was determined by cyclic voltammetry (CV), electrochemical impedance spectroscopy (EIS), and galvanostatic charge-discharge (GCD). The specific capacity (C g^{-1}) and specific capacitance (F g^{-1}) of the S-NiPi series sample was evaluated from the GCD curves using the following equation,

$$C_s = \frac{I \times \Delta t}{m} (\text{Cg}^{-1}) \quad (1)$$

$$C_s = \frac{I \times \Delta t}{m \times \Delta V} (\text{Fg}^{-1}) \quad (2)$$

Where m , Δt , I , and ΔV represent the mass of active substance (g), discharge time (s), current density (mA cm^{-2}), and potential window (V). The energy density (E , Wh kg^{-1}) and power density (P , kW kg^{-1}) of the supercapacitor were calculated from GCD tests using Eqs. (3) and (4), respectively as,

$$E = \frac{0.5 \times C_s \times (\Delta V)^2}{3.6} (\text{Wh kg}^{-1}) \quad (3)$$

$$P = \frac{E \times 3.6}{\Delta t} (\text{kW kg}^{-1}) \quad (4)$$

Where Δt exhibits discharge time (s) and ΔV represents (V/Hg/HgO) a potential window. EIS was evaluated at the open-circuit potential in the range of 100 kHz to 100 mHz at 10 mV amplitude. The electrochemical characteristics of the asymmetric device were examined by constructing a two-electrode system combining a nickel phosphate thin film and rGO as a positive electrode (cathode) and the negative electrode (anode), respectively. To achieve the best supercapacitive performance of the hybrid asymmetric devices, the charges of anode and cathode were balanced by the theory of mass balance using the equation as,

$$\frac{m_+}{m_-} = \frac{C_- \times \Delta V_-}{C_+ \times \Delta V_+} \quad (5)$$

Where $m_{(+ \text{ or } -)}$, $\Delta V_{(+ \text{ or } -)}$ and $C_{(+ \text{ or } -)}$ are the mass of active substance (g), potential window (V) and specific capacitance (F g^{-1}) of the positive and negative electrode, respectively.

3. Results and discussions

3.1. Nickel phosphate thin film formation mechanism

Nickel phosphate thin films are prepared on the SS substrate via electrostatic adsorption of cations as well as a reaction between anions and cations over the surface of SS substrate (as shown in schematic Fig. 1 (a)). In brief, a three-beaker arrangement was used, where the first beaker contains an aqueous solution of nickel sulphate ($\text{NiSO}_4 \cdot 6\text{H}_2\text{O}$) as a cationic precursor. When the well-cleaned SS substrate is dipped in

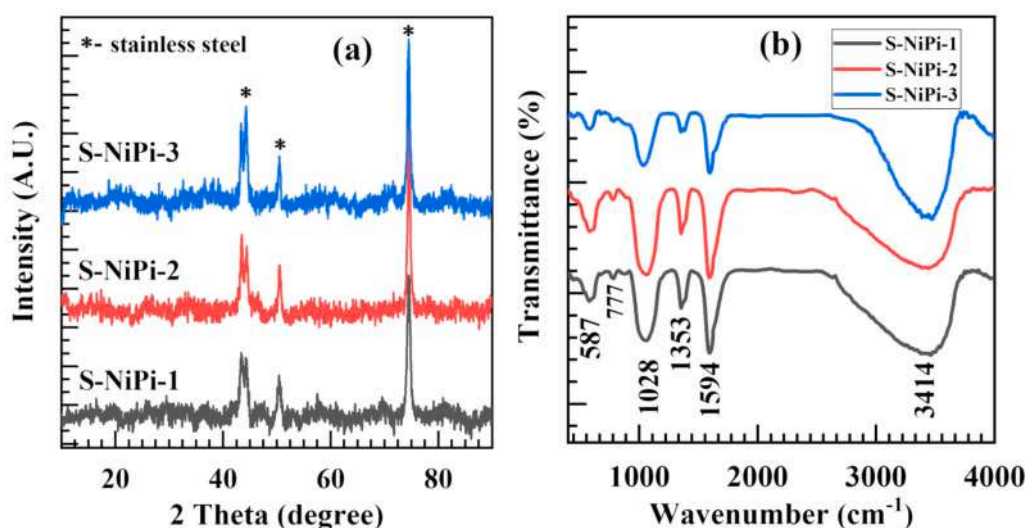


Fig. 2. (a) XRD patterns (b) FT-IR spectra of S-NiPi-1, S-NiPi-2 and S-NiPi-3 electrode.

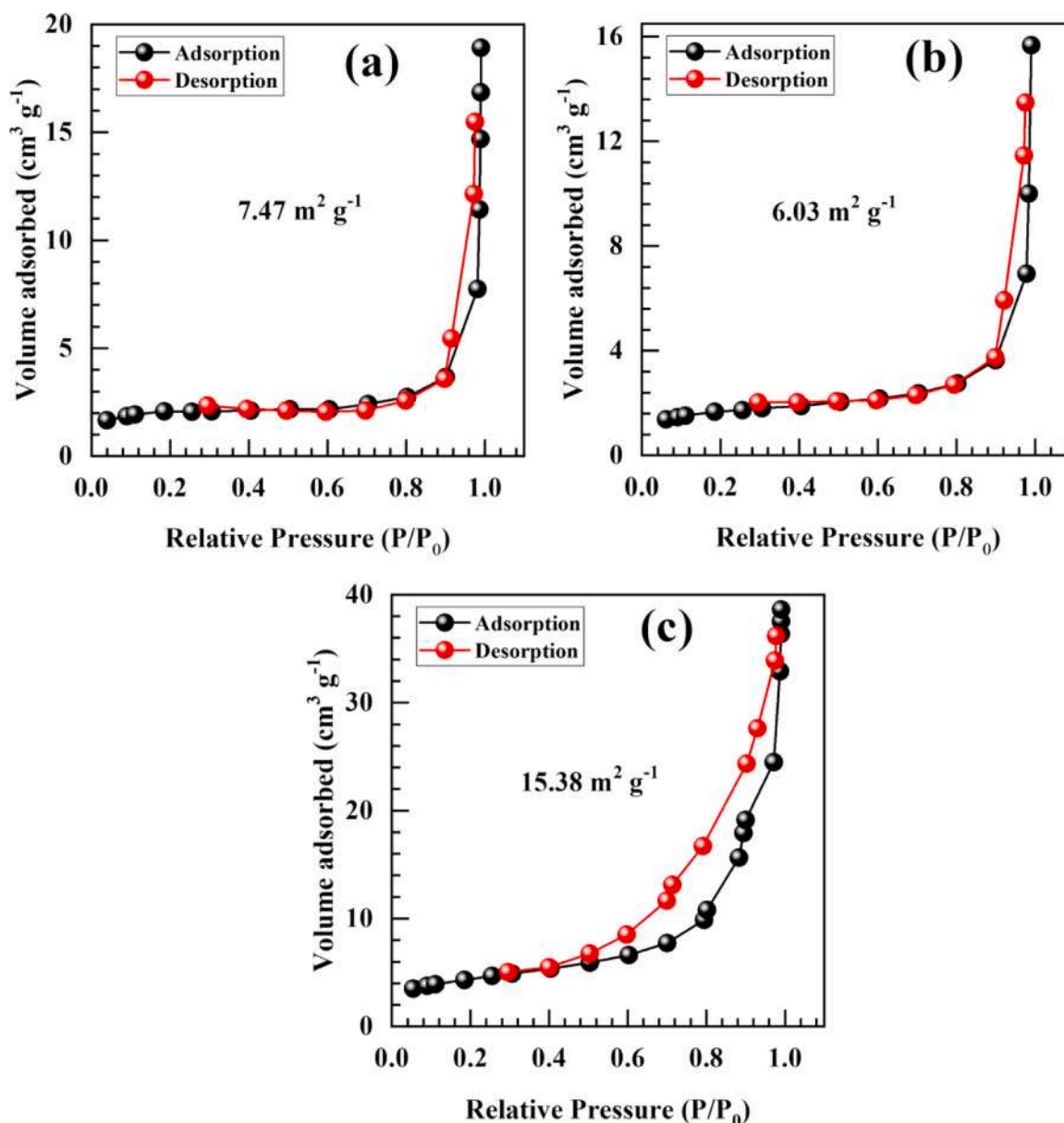


Fig. 3. BET surface area evaluation of sample (a) NiPi-1, (b) S-NiPi-2 and (c) S-NiPi-3.

cationic precursor solution for 10 s, the Ni²⁺ ions get adsorbed at nucleation centers over SS substrate surface because of attractive forces (electrostatic or Van-der Waals or cohesive forces) between SS substrate and nickel species. Then the adsorbed ions react with anions (HPO₄²⁻) from anionic precursor (K₂HPO₄) in the second beaker. Furthermore, DDW in the third beaker was employed for rinsing purpose, where unreacted or loosely bounded molecules detach from the surface.

The reaction mechanism for nickel phosphate thin film formation via the SILAR method is as; a thin layer of Ni²⁺ ions gets adsorbed on SS substrate when the substrate is dipped in a cationic precursor (kept at the ambient condition).

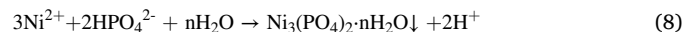


Also, an anionic precursor of dipotassium hydrogen orthophosphate dissociates as per Eq. (7).



Furthermore, the reaction performed by immersion of wet substrate consisting of Ni²⁺ ions layer on surface in the solution of K₂HPO₄ anionic

precursor, in which a chemical reaction among HPO₄²⁻ and adsorbed Ni²⁺ ions lead to the deposition of adherent nickel phosphate monolayer on a substrate as per the following reaction.



Thus, the thin film is deposited through the ion-by-ion growth mechanism, where film deposition occurs by the nucleation of ions at the nucleation centre on the dipped surface of a substrate. Further, the growth of material over substrate surface occurs through coalescence and stacking of particles. Accordingly, the binder-free, well adherent, and uniform nickel phosphate thin film deposited on SS substrate. The molar ratios of anionic and cationic precursors varied in the synthesis process of nickel phosphate to optimize the phase of the material. Upon varying the composition of anionic precursor, the mass of deposited material varied as 0.34, 0.40, and 0.25 mg cm⁻² for S-NiPi-1, S-NiPi-2, and S-NiPi-3 samples, respectively. It is found that the increase in anionic precursor leads to an increase in reaction rate and resulted in to increase in deposited mass of the material from S-NiPi-1 to S-NiPi-2 sample.

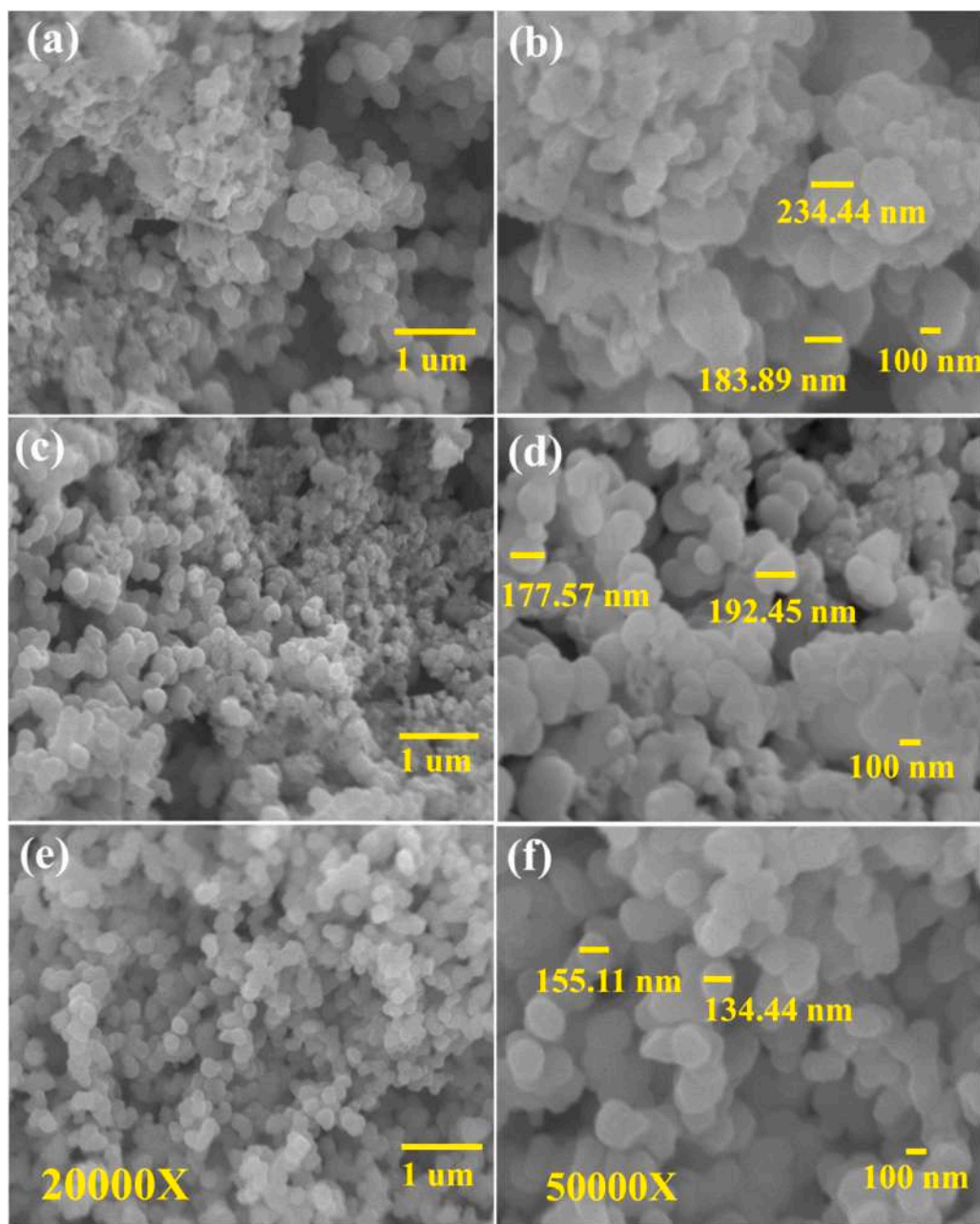


Fig. 4. FE-SEM pictures of prepared sample S-NiPi-1 (a, b), S-NiPi-2 (c, d) and S-NiPi-3 (e, f) at various magnifications of 20,000X and 50,000X.

3.2. X-ray diffractometer, FT-IR, BET study

The structural investigation of nickel phosphate thin films was executed by X-ray diffractometer (XRD) and displayed in Fig. 2(a). The XRD pattern does not show any diffraction peak instead of SS peaks represented by the symbol (*). The absence of diffraction peak from the S-NiPi series thin film electrode suggests the formation of amorphous material. The amorphous phase of material is feasible to achieve enhanced electrochemical activities since the irregular structure can provide large active sites and extended extrinsic pseudocapacitive performance [30]. Also, such an amorphous structure of the material can provide improved stability since sluggish intercalation/deintercalation of electrolytic ions in crystalline material renders its stability [31].

The FTIR spectra of nickel phosphate thin films (Fig. 2(b)) were probed in the range of 400–4000 cm^{-1} . The vibration mode of Ni–O bond is credited to the peak on 587 cm^{-1} [26] and the stretching mode of P–O–P linkages is assigned to 777 cm^{-1} [32]. The peak positioned at

1028 cm^{-1} belongs to PO_4^{3-} vibrational mode. The water molecules (H–O–H) bending vibrational mode appeared at 1353 and 1594 cm^{-1} [33]. Also, the -OH bond from adsorbed water is accredited to the broad peak near 3414 cm^{-1} . As results illustrated in Fig. 2(b), no significant change is observed in FTIR spectra of S-NiPi-1, S-NiPi-2, and S-NiPi-3 electrodes upon cationic and anionic concentration variation. The FTIR results demonstrate that the structural water content exists in synthesized material and the formation of hydrous nickel phosphate thin film over SS substrate.

The porosity and surface area of nickel phosphate thin film is examined by BET analysis. Fig. 3(a)–(c) displays the isotherms of N_2 -adsorption-desorption (at 77 K liquid nitrogen) for nickel phosphate thin films. According to the International Union of Pure and Applied Chemistry (IUPAC) classification, the nickel phosphate thin films displayed a type III isotherm with a hysteresis loop of H3 type. Type III isotherm and H3 type hysteresis loop depict characteristic property of a mesoporous structure created by aggregated particles [34,35]. The

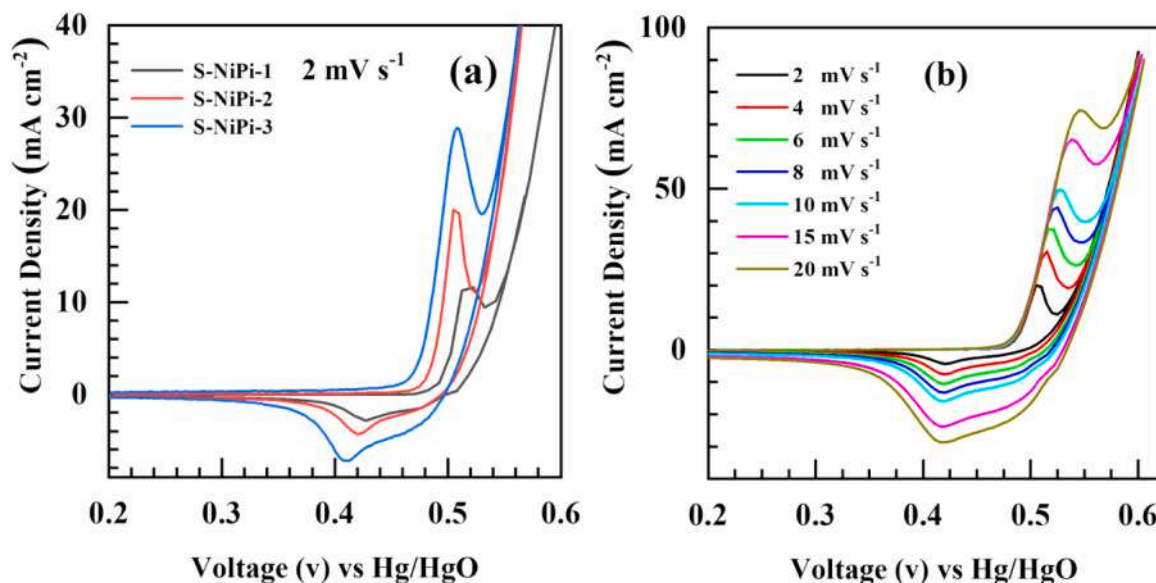


Fig. 5. (a) Comparative CV curves of nickel phosphate electrodes (S-NiPi-1, S-NiPi-2 and S-NiPi-3) at scan rate of 2 mV s^{-1} and (b) CV curves of S-NiPi-3 electrode at various scan rates from 2 to 20 mV s^{-1} .

specific surface area evaluation is analyzed to be 7.47, 6.03, and $15.38 \text{ m}^2 \text{ g}^{-1}$ for samples S-NiPi-1, S-NiPi-2, and S-NiPi-3, respectively. The corresponding distribution of pore size was analyzed by utilizing Barrett–Joyner–Halenda (BJH) technique from the desorption section of isotherm and presented in Fig. S1 (see ESI). The pore size distribution plot indicates an average pore diameter of 14.31, 15.92, and 15.12 nm for sample S-NiPi-1, S-NiPi-2, and S-NiPi-3 respectively, which ascribed to the mesoporous structure of accumulated particles. The mesoporous morphology of thin film electrodes gives rise to the high surface area as well as several channels provide easy access to the electrolyte in the interior of electrode material [36].

3.3. Morphological analysis

The surface morphology of as-synthesized nickel phosphate thin films is examined via FE-SEM. The FE-SEM images of nickel phosphate thin films at two different magnifications (50,000X and 20,000X) are exhibited in Fig. 4(a)–(f). The low magnification (20,000X) FE-SEM image (Fig. 4(a), (c), (e)) of nickel phosphate shows uniformly and densely packed particle-like architecture covered over the SS substrate surface. Also, these particles are randomly distributed on the surface of substrate and created multiple voids and large pores (cavities). Such cavities and voids can offer efficient ways and the lowest diffusion length for ionic easy access. The SEM images at higher magnification (50,000X) shown in Fig. 4(b, d, and f) demonstrate accumulated particles with distinct particles size having an average diameter of 209.6, 185.1, 144.7 nm for sample S-NiPi-1, S-NiPi-2, and S-NiPi-3, respectively. Such smaller particle size of nickel phosphate can give a high electroactive surface area and achieves maximum capacitance through the mesoporous structure. The variation in particle size is observed with variation in precursors concentration due to the alteration in growth kinetics in the SILAR method. It is found that the average particle size reduces with an increase in phosphate precursor concentration, and at the molar composition of 1:2, the prepared thin film shows the smallest size of particles ($\sim 144.7 \text{ nm}$). With an increase in phosphate concentration, the reaction kinetics increases and results in forming a stable phase of the material, which restricts the growth of particles. Moreover, such a porous network with aggregated particles like morphology of nickel phosphate is favourable for energy storage applications.

Elemental investigation of amorphous nickel phosphate thin film was analyzed by EDS, and the outcomes are depicted in S2 (see ESI (a-

c)). The atomic ratio of nickel to phosphorus (Ni:P) was 1:1.61, 1:1.71, and 1:1.72 for samples S-NiPi-1, S-NiPi-2, and S-NiPi-3, respectively. It is observed that phosphorous content increases in thin film with an increase in phosphate precursor concentration. The elemental composition of nickel and phosphorus is quite similar in S-NiPi-2, and S-NiPi-3 samples that attribute to the saturation of phosphate content and confirm the ratio of 1:2 is sufficient to obtain nickel phosphate thin films. Moreover, Ni, P and O elements in the material confirm that the obtained material is hydrous nickel phosphate thin film.

4. Electrochemical study of nickel phosphate thin film

The supercapacitive properties of S-NiPi series electrodes are investigated by a three-electrode cell configuration in a 1 M KOH electrolyte. Fig. 5(a) illustrates comparative CV curves of nickel phosphate thin films between +0.2–0.60 V (vs Hg/HgO) potential range at a scan rate of 2 mV s^{-1} . The S-NiPi-3 electrodes indicate maximum current under the curve than S-NiPi-1 and S-NiPi-2 electrodes. The amorphous nature and particle-like morphology of the NiPi-3 sample provide a high surface area and exhibit enhanced electrochemical performance in terms of current response in the CV curve. The CV curves at scan rates from 2 to 20 mV s^{-1} for the S-NiPi-3 electrode are presented in Fig. 5(b). In CV curves, a current area under the curve increases with an increase in scan rate, and obtained redox peaks attribute to the pseudocapacitive nature of material [37]. The CV curves of S-NiPi-1 and S-NiPi-2 electrodes at scan rates from 2 to 20 mV s^{-1} are provided in Fig. S3 (see ESI).

The charge storage kinetics of prepared nickel phosphate thin film electrodes are examined by using power's law. The correlation between scan rate and peak current density can be represented by following power's law as,

$$i_p = av^b \quad (9)$$

Where i_p denotes peak current density, a and b are adjustable factors and v is scan rate. The slope (linear fit) of the current [$\log(i)$] versus scan rate [$\log(v)$] plot represents the b values. The b value represents two distinct charge storage processes as, when b is 0.5 and 1, then the electrochemical process is diffusive and capacitive, respectively [38,39]. In the present analysis, b values are evaluated from cathodic peak regimes and found to be 0.56, 0.65, and 0.51 for the S-NiPi-1, S-NiPi-2, and S-NiPi-3 electrode, respectively (Fig. 6(a)), which indicate that both

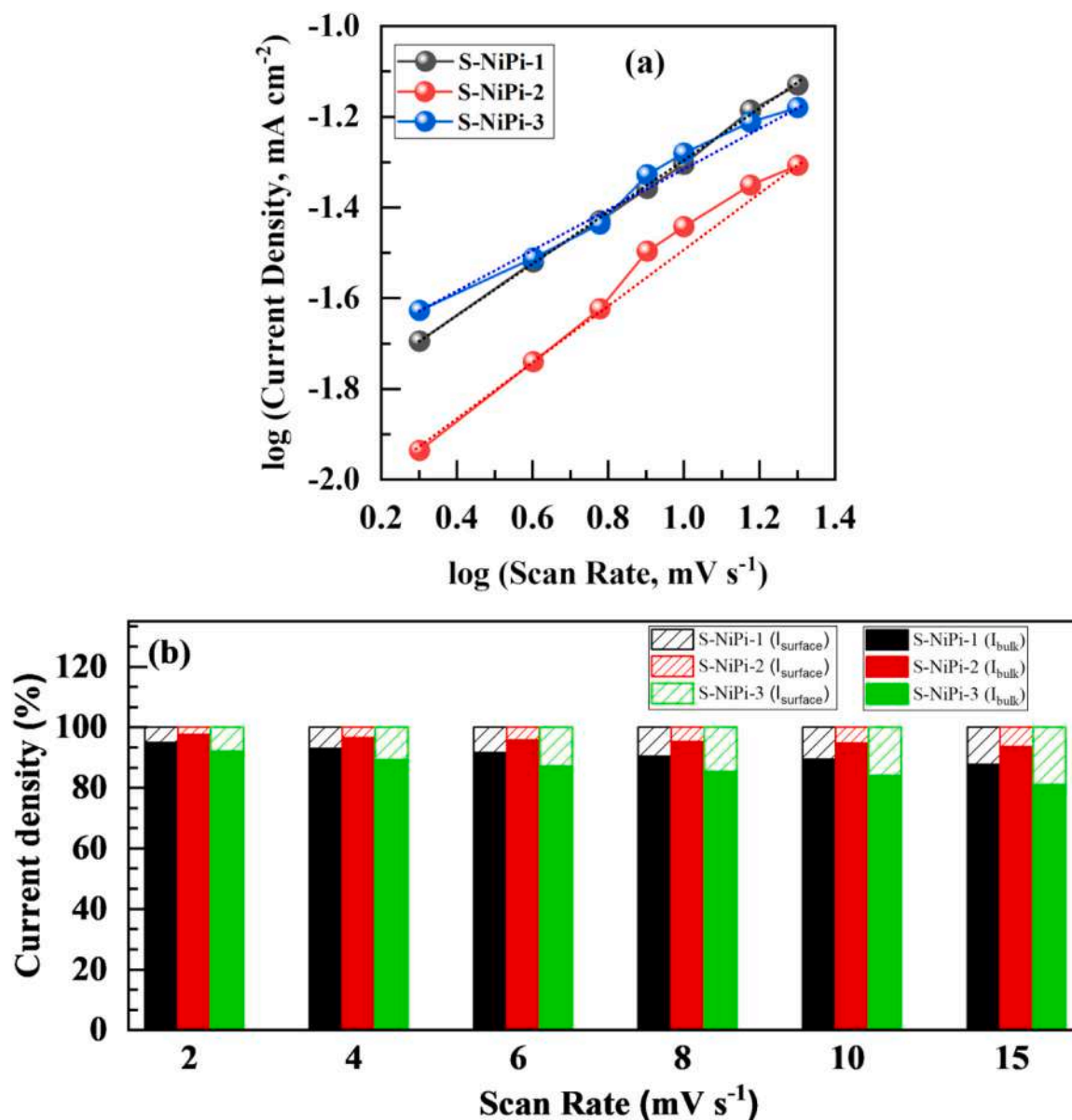


Fig. 6. (a) Plots of log (current density, mA cm⁻²) versus log (scan rate, mV s⁻¹) for S-NiPi series electrodes, (b) contribution of battery type (bulk current) and capacitive type (surface current) current density at various scan rates (2–20 mV s⁻¹) for S-NiPi series electrodes.

(diffusive and capacitive) processes are contributed for charge storage in the electrode materials. To identify the individual contribution of surface pseudo-capacitive and battery process by using modified Power's law expressed as,

$$I_p = C_s \nu + C_b \nu^{1/2} \quad (10)$$

Where I_p represents peak current density, ν is the scan rate and $C_s \nu$ and $C_b \nu^{1/2}$ illustrate current contributions from surface pseudo-capacitive (I_{surface}) and bulk process (I_{bulk}), respectively [40]. Corresponding Fig. 6(b) displays the contribution of current density from the surface pseudo-capacitive (I_{surface}) and battery-like (I_{bulk}) process for nickel phosphate thin film electrodes at various scan rates from 2 to 20 mV s⁻¹. At a low scan rate current, it is noted that current is contributed moderately from the surface pseudo-capacitive process and mostly from the battery-like process. In the case of S-NiPi-1, the contribution of I_{surface} increases from 5% to 15%, whereas the contribution of I_{bulk} decreases from 95% to 85%. The contribution of I_{surface} increases from 3% to 8%, whereas the contribution of I_{bulk} decreases from 97% to 92% in

sample S-NiPi-2. However, the contribution of I_{surface} increases from 8% to 22%, whereas the contribution of I_{bulk} decreases from 92% to 78% for S-NiPi-3 sample. Additionally, S-NiPi-3 exhibits a higher contribution of I_{surface} , indicating the high porosity of material that permits the passage for electrolyte ions and execute surface redox reactions.

Fig. 7(a) displays relative GCD curves of nickel phosphate electrodes within 0 to + 0.50 V (vs Hg/HgO) potential range at current density of 0.5 mA cm⁻². Likewise CV analysis, the non-linear discharge in every curve demonstrates pseudocapacitive and diffusion-controlled charge storage mechanism of the nickel phosphate electrodes. The S-NiPi-3 electrode exhibits a large discharge time as compared with S-NiPi-1 and S-NiPi-2 electrodes. The GCD analysis of S-NiPi-3 electrode at 0.5–4 mA cm⁻² current densities is displayed in Fig. 7(b). Similarly, the GCD curves of S-NiPi-1 and S-NiPi-2 electrodes at 0.5–4 mA cm⁻² current densities are provided in Fig. S4 (a–b) (see ESI). As an increase in the current density, the discharge time decreases because of less time available for interaction between electrode and electrolyte at the higher current density. Moreover, the bell-shaped symmetric charge-discharge profile indicates pseudocapacitive property and good supercapacitive

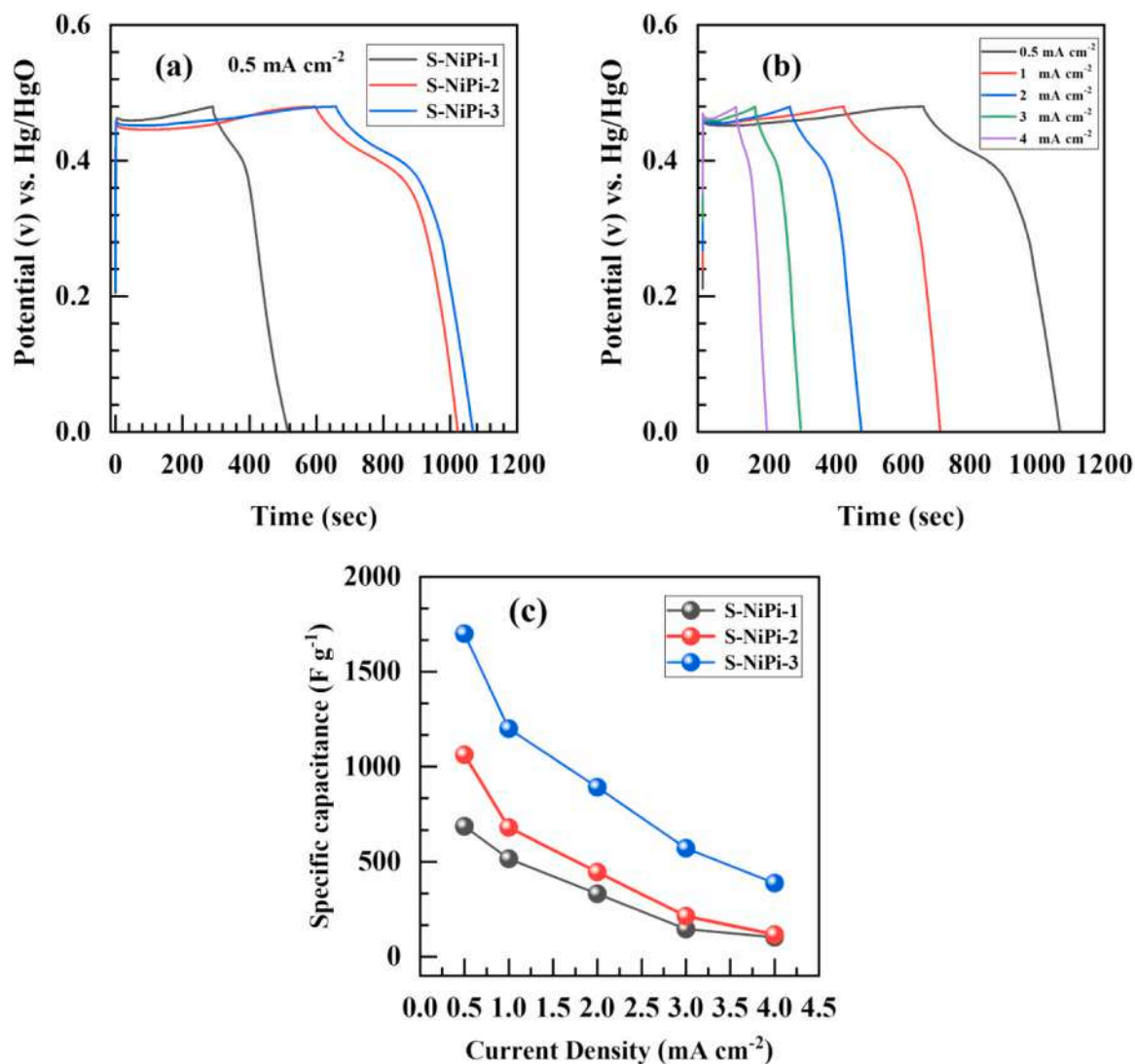


Fig. 7. (a) Comparative GCD curves of nickel phosphate electrodes (S-NiPi-1, S-NiPi-2 and S-NiPi-3) at current density of 0.5 mA cm^{-2} and (b) GCD curve of S-NiPi-3 electrode at various current densities from 0.5 mA cm^{-2} to 4 mA cm^{-2} and (c) specific capacitance versus current density graph for S-NiPi-1, S-NiPi-2 and S-NiPi-3 electrodes.

behavior of the electrode [41]. The specific capacitance calculated from the GCD curve for S-NiPi-1, S-NiPi-2, and S-NiPi-3 electrodes are 686, 1062, and 1700 F g^{-1} , respectively, at 0.5 mA cm^{-2} current density. The obtained performance of nickel phosphate electrodes is compared with previous work by means of crystal structure, morphology, capacitance, and stability and is provided in Table S2 (see ESI). Some previous work [18,20,21,23] reported higher specific capacitance than present work, probably due to the employment of the nickel foam (NF) as a current receiver, which participates in an electrochemical reaction as well as assists to enhance the performance of the whole electrode by including self-capacitance [42]. Nevertheless, in the present work, SS substrate is utilized as a current collector to synthesis nickel phosphate thin film and does not participate in the electrochemical reactions since it is quite stable in the alkaline medium than nickel foam. Therefore, obtained capacitive performance in the present work is solely served by nickel phosphate material.

EIS analysis was carried out to examine the resistance and capacitive characteristics of the amorphous nickel phosphate electrodes in the 100 kHz to 100 mHz frequency range at open circuit potential. The Nyquist plots of S-NiPi-1, S-NiPi-2, and S-NiPi-3 electrodes are demonstrated in Fig. 8, inset display fitted equivalent circuit using ZView-impedance software, and the tailored parameters of equivalent circuit

are provided in Table S3 (see ESI). In the Nyquist plot, the high-frequency portion (semicircle) indicates the interfacial processes, the middle frequency portion is associated with a diffusion-controlled process, and the low-frequency (straight line) portion indicates the capacitive behavior of the material. The initial point/intersection of the semicircle represents solution resistance (R_s), the approximate closing point of the semicircle indicates the resistance of charge transfer kinetics (R_{ct}), and the straight-line at the lower frequency region indicates Warburg diffusion resistance (W). In an equivalent circuit, R_s and R_{ct} interface resistance with CPE exhibits a general imperfect capacitor (when $n = 1$ and $Q = C$) ascribed to semi-infinite diffusion charges [43]. The solution resistances are found to be 0.56, 0.66, and 0.46Ω , respectively. Also, the charge transfer resistances of 1.12, 1.03, and 0.58Ω are obtained for S-NiPi-1, S-NiPi-2, and S-NiPi-3 electrodes, respectively. The smaller values of R_s and R_{ct} indicate easy diffusion of electrolyte in the amorphous structure of material and inclusive utilization of particle like morphology of nickel phosphate electrodes.

Electrochemical cycling stability of working electrode is an important aspect for its utilization in the supercapacitor. Fig. 9 displays the cyclic stability and coulombic efficiency of the best-performed electrode (S-NiPi-3) tested at 4 mA cm^{-2} current density for 5000 cycles. Nickel phosphate electrode exhibited excellent cyclic stability by sustaining

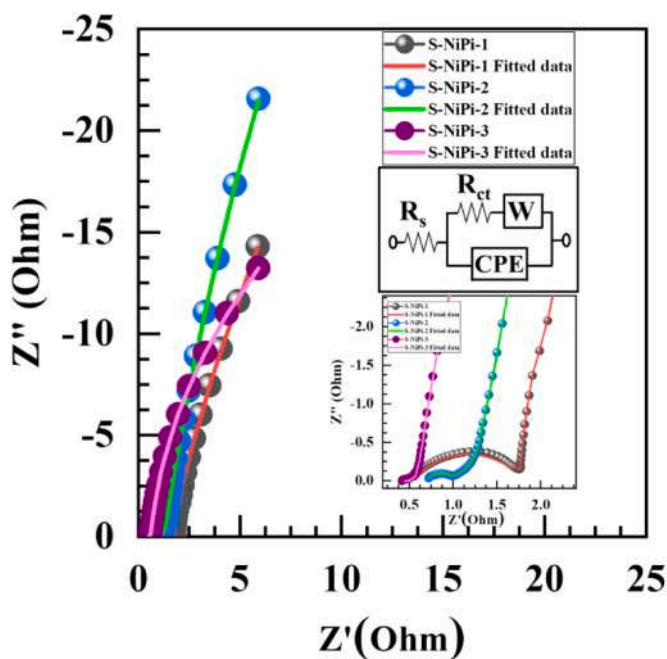


Fig. 8. Nyquist plots of S-NiPi-1, S-NiPi-2 and S-NiPi-3 electrodes (inset: equivalent circuit for fitted data).

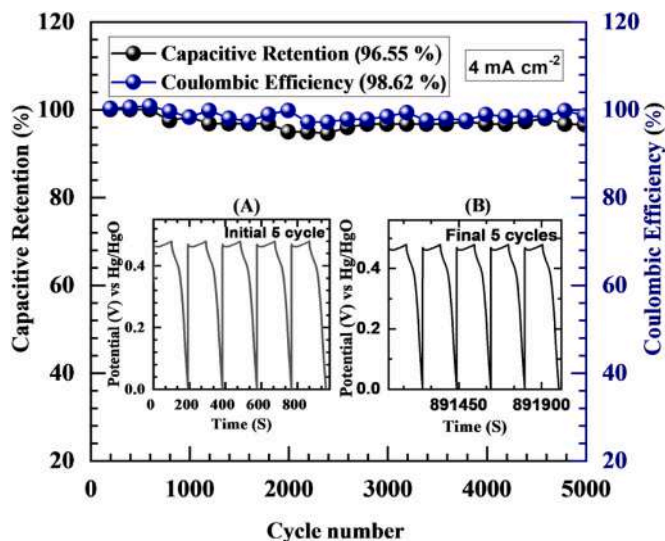


Fig. 9. Stability and coulombic efficiency of nickel phosphate electrode (S-NiPi-3) for 5000 cycles at current density of 4 mA cm^{-2} . (Inset: the GCD curves of the first (A) and last (B) 5 GCD cycles).

capacitive retention of 96.55% and coulombic efficiency is found to be 98.62% over 5000 GCD cycles. The potential vs time curves of the first (A) and last (B) five GCD cycles are presented in inset of Fig. 9. Initial and final GCD cycles display symmetric potential-time response. The long-term cyclic stability of S-NiPi-3 electrode is credited to the amorphous nature and porous surface morphology of material since such an amorphous structure can efficiently sustain swelling and diffusion of electrolytic ions than its crystalline and bulk counterpart.

4.1. Aqueous hybrid asymmetric supercapacitor device (AHASD)

To an additional investigation of hydrous, amorphous, particle like structured nickel phosphate electrode for feasible application in

supercapacitors, a hybrid asymmetric supercapacitor device (AHASD) was constructed by using nickel phosphate as a positive electrode (cathode) and rGO as the negative electrode (anode). Supercapacitive analysis of rGO electrode was executed in 1 M KOH electrolyte. The CV test of rGO electrode at various scan rates from 5 to 100 mV s^{-1} in the optimized potential range of 0 to -1 V (vs Hg/HgO) depicted in Fig. S5 (a) (see ESI). The CV curve of rGO electrode demonstrates a nearly rectangular nature, and the absence of a redox peak proves the electric double layer capacitive nature of rGO material. Also, it was verified by linear GCD plots of rGO electrode shown in Fig. S5(b) (see ESI). The EIS plot along with the fitted circuit (Fig. S5 (c) (see ESI)) for the rGO electrode represents a semicircle in the high-frequency region and a straight line in the low-frequency region. The initial point of the semicircle is attributed to solution resistance ($R_s = 0.48 \Omega$) and the value of semicircle diameter is an electron transfer resistance ($R_{ct} = 47.61 \Omega$), which is responsible for the exclusive electrochemical resistivity of the rGO electrode. The CV graph of rGO electrode and amorphous nickel phosphate electrode (S-NiPi-3) in different potential ranges at 50 mV s^{-1} scan rate is displayed in Fig. 10(a). Fig. 10(a) indicates two individual pseudocapacitive electrodes with practical integration can obtain a wide operating potential window for a hybrid device. Enhanced operating potential window and high energy density are the main benefits of constructing AHASD. To achieve better outcomes of AHASD, mass balancing between two electrodes is essential since both electrodes depict distinct capacitive performance. So, the mass balance among positive and negative electrodes is calculated using the charge balance theory (Eq. 5). To maintain charge storage equilibrium between positive and negative electrode in an AHASD, the weight ratio of nickel phosphate (S-NiPi-3) and rGO electrode is obtained as 0.352:1. The voltage range of AHASD is optimized by performing CV analysis in different (1.2–1.6 V) voltage range at 50 mV s^{-1} scan rate as displayed in Fig. S6 (a) (see ESI). The AHASD does not exhibit a change in redox peaks in CV analysis, but after a 1.6 V slight increase in current is detected at the end of the CV curve, which signifies oxygen evolution reaction [44,45]. Hence, the voltage limit of 0–1.6 V is optimized for AHASD. In a similar way, voltage range (1.2–1.6 V at 4 mA cm^{-2}) for GCD analysis is optimized as revealed in Fig. S6(b). Both CV and GCD analysis confirms the optimum voltage limit for AHASD is 1.6 V. Fig. 10(b) exhibits CV curves of S-NiPi-2//KOH//rGO AHASD at various scan rates from 5 to 100 mV s^{-1} . Good reversibility of AHASD was observed within the voltage range of 0.0–1.6 V at various scan rates. Fig. 10(c) revealed GCD profiles of prepared AHASD in the voltage range of 0.0–1.6 V at different current densities from 3 to 4.5 mA cm^{-2} . The specific capacitance of AHASD was calculated using Eq. (2) and shown in Fig. 10(c) from the GCD profile. The AHASD delivered a high specific capacitance of 113 F g^{-1} at 3 mA cm^{-2} current density. It is observed that, as applied current density increased, the discharge time of the AHASD device decreased, and it indicates that the specific capacitance of the device decreases with an increase in current density because of inadequate electrode-electrolyte interaction at high current density (Fig. 10(d)). The power and energy density of the AHASD are prominent factors for analyzing its feasibilities for practical application. Based on active materials of positive and negative electrodes, power and energy density are calculated using Eqs. (3) and (4). The AHASD device achieved the highest energy density of 40.37 Wh kg^{-1} at a power density of 1.68 kW kg^{-1} . Specific capacitance, energy, and power density of AHASD device with comparative literature survey are presented in Table S4 (see ESI) [9,15–26]. Also, the corresponding Ragone plot of AHASD device with comparative literature is plotted in Fig. 11(a). Only a few articles [18, 21, 23, 24, and 26] reported little higher energy density values than the present study for the devices based on nickel phosphate; however, in most works, nickel foam (NF) was used as a current collector. Nickel foam promotes the entire capacitive performance of electrode as well as a device since it includes self-capacitance originated from the conversion of surface Ni atom to NiO during charging-discharging [42]. Moreover, the AHASD device exhibits

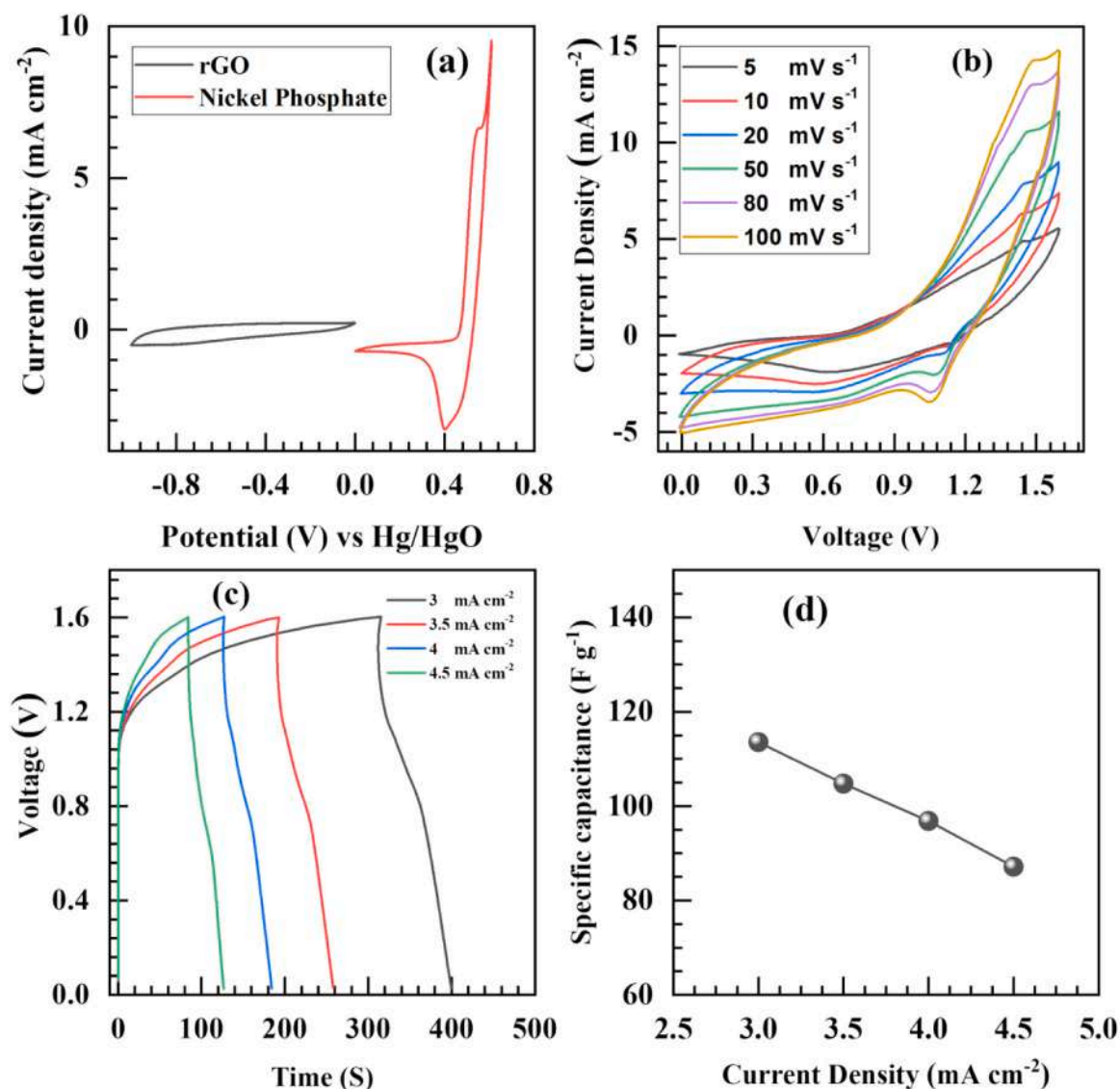


Fig. 10. (a) CV plots of rGO and nickel phosphate thin film electrodes (S-NiPi-3) at scan rate of 20 mV s⁻¹, (b) CV plots of AHASD at various scan rates from 5 to 100 mV s⁻¹, (c) GCD plots of AHASD at various current densities (3–4.5 mA cm⁻²) and (d) plot of specific capacitance versus current densities of AHASD.

excellent stability (~95%) along with competitive energy density and power density than all other supercapacitor devices based on crystalline nickel phosphate electrodes, which underlines the utilization of amorphous nickel phosphate electrode in hybrid supercapacitor device fabrication.

EIS evaluation (Fig. 11(b)) of AHASD is conducted in the frequency range of 100 kHz to 100 mHz at open circuit voltage. The Nyquist plot of AHASD device exhibits R_s and R_{ct} values of 0.9 and 114 Ω , respectively, and the CPE exhibits an imperfect capacitor ascribed to semi-infinite diffusion charges [43]. The hybrid asymmetric device with rGO and mesoporous nickel phosphate electrodes promotes the facile ion transport and enhances the electrochemical capacitance of the device. The cycling stability and coulombic efficiency of the AHASD device were examined for 5000 cycles at 12 mA cm⁻² current density and presented in Fig. 12. The primary (A) and final (B) 5 GCD cycles are displayed in the insets of Fig. 12. Similar GCD nature is observed for initial and final cycles which demonstrate good cyclic stability of AHASD. The AHASD revealed excellent capacitive retention of 95.09% and coulombic efficiency is found to be 97.91% over 5000 GCD cycles, demonstrating excellent cycling stability of the device.

Overall amorphous nature, the mesoporous structure of nickel

phosphate thin film offers a large surface area and low electrochemical resistance (R_s and R_{ct}) for rapid charge transfer in electrochemical reaction. Also, the amorphous nickel phosphate material has a number of defects that may provide exclusive electrochemical and physical properties and deliver the best electrochemical performance [46]. Due to the defect-rich structure, the electrolytic ions freely diffuse in amorphous material, which is beneficial to access more active material [47]. Moreover, amorphous material proposed long-term durability as compared to the crystalline structure since the amorphous structure does not exhibit changes in strain while charging/discharging [48]. Therefore, amorphous particles and mesoporous structure of nickel phosphate deliver high capacitive performance by means of high energy and power density with excellent stability.

5. Conclusions

In the present work, SILAR (binder-free synthetic approach) method successfully utilized to prepare amorphous, hydrous nickel phosphate thin film electrodes. The mesoporous, amorphous, hydrous nickel phosphate particles offer the maximum specific capacity of 814 C g⁻¹ (specific capacitance ~1700 F g⁻¹) with more excellent cyclic stability

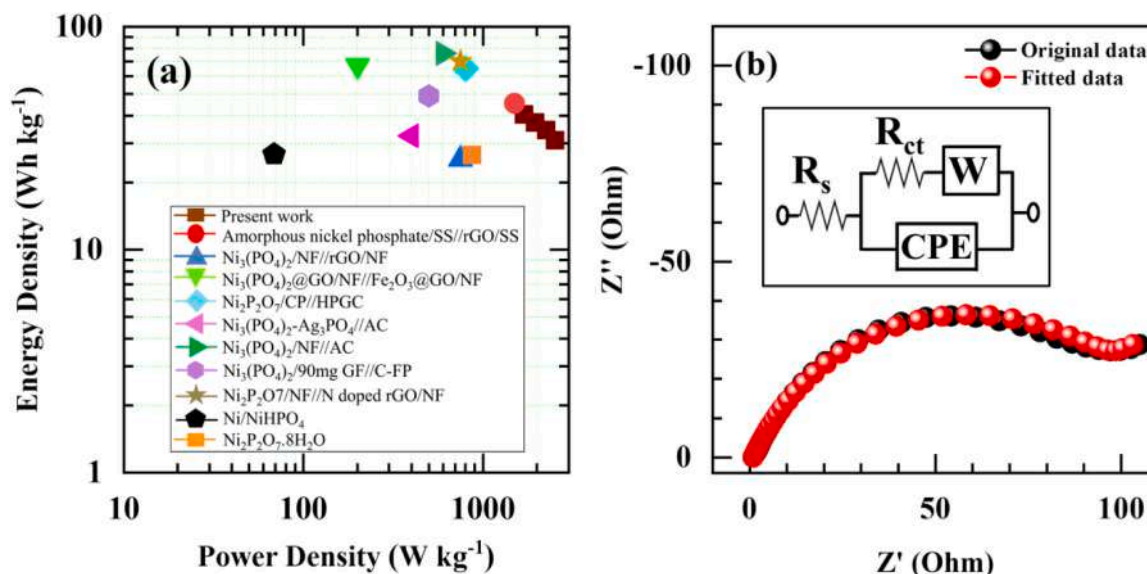


Fig. 11. (a) Ragone plot of AHASD with comparative data and (b) Nyquist plot of AHASD (inset; the equivalent circuit for fitted data).

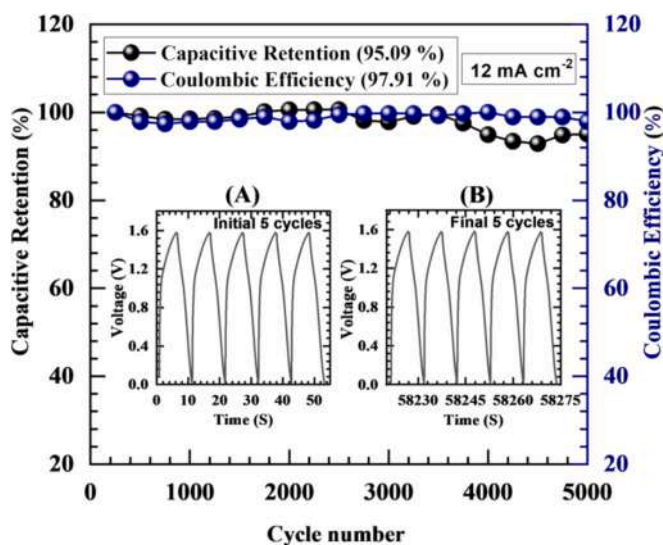


Fig. 12. Stability and coulombic efficiency of AHASD for 5000 cycles at current density of 12 mA cm^{-2} . (Inset: the GCD curves of the first (A) and last (B) 5 GCD cycles).

of 96.55% and coulombic efficiency (98.62%) after 5000 cycles. The amorphous nature and particle-like morphology exhibit smaller diffusion paths and more active sites for the electrolyte ions penetration and resulted in the utilization of high surface area of active material. Furthermore, fabricated asymmetric supercapacitor device delivers specific capacitance of 113.55 F g^{-1} at current density of 3 mA cm^{-2} with an energy density of 40.37 Wh kg^{-1} at a power density of 1.689 kW kg^{-1} along with impressively high cyclic stability (95.09%) and coulombic efficiency (97.91%) after 5000 cycles. The obtained results indicate that amorphous, hydrous nickel phosphate is a highly advantageous candidate in asymmetric hybrid supercapacitors for practical applications and SILAR method is the best synthetic approach to prepare binder-free, amorphous, mesoporous metal phosphate materials in thin film form.

CRediT authorship contribution statement

Mr. S. S. Pujari carried out an investigation and formal analysis, data curation, and original draft writing, Dr. V. G. Parale and Prof. H-H. Park provided resources and formal analysis. Mr. V. V. Patil, Mr. A. S. Patil, Dr. J. L. Gunjekar and Prof. C. D. Lokhande carried out modification, creation, and presentation and visualization of the manuscript. Dr. U. M. Patil carried out funding acquisition, administration, supervision, manuscript editing. All persons made substantial contributions to the work reported in the manuscript.

Declaration of Competing Interest

The authors declare that they have no known competing financial interests or personal relationships that could have appeared to influence the work reported in this paper.

Acknowledgement

Authors are thankful to D. Y. Patil Education Society, Kasaba Bawada, Kolhapur for financial support through research project sanction No. DYPES/DU/R&D/3109 and HHP and VGP announce that this work was supported by the National Research Foundation of Korea (NRF) grant funded by the Korean government (MSIT) (No. 2020R1A5A1019131). Also this research is supported by Science and Engineering Board (SERB), Department of Science and Technology, Government of India, New Delhi, through sanction number CRG/2019/005730.

Appendix A. Supporting information

Supplementary data associated with this article can be found in the online version at [doi:10.1016/j.synthmet.2021.116876](https://doi.org/10.1016/j.synthmet.2021.116876).

References

- [1] D. El-Gendy, N. Abdel Ghany, E. Foad El Sherbini, N. Allam, Adenine-functionalized spongy graphene for green and high-performance supercapacitors, *Sci. Rep.* 7 (2017) 43104, <https://doi.org/10.1038/srep43104>.
- [2] L. Xing, K.-J. Huang, L.-X. Fang, Preparation of layered graphene and tungsten oxide hybrids for enhanced performance supercapacitors, *Dalton Trans.* 45 (2016) 17439–17446, <https://doi.org/10.1039/C6DT03719D>.

- [3] W. Chen, R. Rakhi, H. Alshareef, Capacitance enhancement of polyaniline coated curved-graphene supercapacitors in a redox-active electrolyte, *Nanoscale* 5 (2013) 4134–4138, <https://doi.org/10.1039/C3NR00773A>.
- [4] Z. Wen, W. She, Y. Li, R. Che, Paramesium-like α -MnO₂ hierarchical hollow structures with enhanced electrochemical capacitance prepared by a facile dopamine carbon-source assisted shell-swelling etching method, *J. Mater. Chem. A* 2 (2014) 20729–20738, <https://doi.org/10.1039/C4TA04312J>.
- [5] J. Xu, T. Xiao, X. Tan, P. Xiang, L. Jiang, D. Wu, J. Li, S. Wang, A new asymmetric aqueous supercapacitor: Co₃O₄/Co₂O₄@polypyrrole, *J. Alloy. Compd.* 706 (2017) 351–357, <https://doi.org/10.1016/j.jallcom.2017.02.253>.
- [6] V. Augustyn, P. Simon, B. Dunn, Pseudocapacitive oxide materials for high-rate electrochemical energy storage, *Energy Environ. Sci.* 7 (2014) 1597–1614, <https://doi.org/10.1039/C3EE44164D>.
- [7] K. Trzcinski, A. Lisowska-Oleksiak, Electrochemical characterization of a composite comprising PEDOT/PSS and N doped TiO₂ performed in aqueous and non-aqueous electrolytes, *Synth. Met.* 209 (2015) 399–404, <https://doi.org/10.1016/j.synthmet.2015.08.026>.
- [8] S. Peng, L. Fan, C. Wei, X. Liu, H. Zhang, W. Xu, J. Xu, Flexible polypyrrole/copper sulfide/bacterial cellulose nanofibrous composite membranes as supercapacitor electrodes, *Carbohydr. Polym.* 157 (2017) 344–352, <https://doi.org/10.1016/j.carbpol.2016.10.004>.
- [9] S. Marje, P. Katkar, S. Pujari, S. Khalate, A. Lokhande, U. Patil, Regulated micro-leaf like nickel pyrophosphate as a cathode electrode for asymmetric supercapacitor, *Synth. Met.* 259 (2020), 116224, <https://doi.org/10.1016/j.synthmet.2019.116224>.
- [10] Z. Xiao, Y. Bao, Z. Li, X. Huai, M. Wang, P. Liu, L. Wang, Construction of hollow cobalt–nickel phosphate nanocages through a controllable etching strategy for high supercapacitor performances, *ACS Appl. Energy Mater.* 2 (2019) 1086–1092, <https://doi.org/10.1021/acsaem.8b01627>.
- [11] X. Li, A. Elshahawy, C. Guan, J. Wang, Metal phosphides and phosphates-based electrodes for electrochemical supercapacitors, *Small* 13 (2017), 1701530, <https://doi.org/10.1002/smll.201701530>.
- [12] M. Pramanik, R. Salunkhe, M. Imura, Y. Yamauchi, Phosphonate-derived nanoporous metal phosphates and their superior energy storage application, *ACS Appl. Mater. Interfaces* 8 (2016) 9790–9797, <https://doi.org/10.1021/acsaami.6b01012>.
- [13] H. Pang, Y. Zhang, Z. Runa, W. Lai, W. Huang, Amorphous nickel pyrophosphate microstructures for high-performance flexible solid-state electrochemical energy storage devices, *Nano Energy* 17 (2015) 339–347, <https://doi.org/10.1016/j.nanoen.2015.07.030>.
- [14] J. Zhao, H. Pang, J. Deng, Y. Ma, B. Yan, X. Li, S. Li, J. Chena, W. Wang, Mesoporous uniform ammonium nickel phosphate hydrate nanostructures as high performance electrode materials for supercapacitors, *CrystEngComm* 15 (2013) 5950–5955, <https://doi.org/10.1039/C3CE40712H>.
- [15] J. Zhao, S. Wang, Z. Run, G. Zhang, W. Du, H. Pang, Hydrothermal synthesis of nickel phosphate nanorods for high-performance flexible asymmetric all-solid-state supercapacitors, *Part. Part. Syst. Charact.* 32 (2015) 880–885, <https://doi.org/10.1002/ppsc.201500005>.
- [16] Z. Wang, F. Chen, P. Kannan, S. Ji, H. Wang, Nickel phosphate nanowires directly grown on Ni foam as binder-free electrode for pseudocapacitors, *Mater. Lett.* 257 (2019), 126742, <https://doi.org/10.1016/j.matlet.2019.126742>.
- [17] Y. Gao, J. Zhao, Z. Run, G. Zhang, H. Pang, Microporous Ni₁₁(HPO₃)₈(OH)₆ nanocrystals for high-performance flexible asymmetric all solid-state supercapacitors, *Dalton Trans.* 43 (2014) 17000–17005, <https://doi.org/10.1039/C4DT02831G>.
- [18] K. Sankar, Y. Seo, S. Lee, S. Jun, Redox additive-improved electrochemically and structurally robust binder-free nickel pyrophosphate nanorods as superior cathode for hybrid supercapacitors, *ACS Appl. Mater. Interfaces* 10 (2018) 8045–8056, <https://doi.org/10.1021/acsaami.7b19357>.
- [19] A. Mirghani, M. Madito, K. Oyedotun, T. Masikhwa, N. Ndiaye, S. Ray, N. Manyala, A high energy density asymmetric supercapacitor utilizing a nickel phosphate/graphene foam composite as the cathode and carbonized iron cations adsorbed onto polyaniline as the anode, *RSC Adv.* 8 (2018) 11608–11621, <https://doi.org/10.1039/C7RA12028A>.
- [20] J. Yang, J. Tan, D. Ma, Nickel phosphate molecular sieve as electrochemical capacitors material, *J. Power Sources* 260 (2014) 169–173, <https://doi.org/10.1016/j.jpowsour.2014.03.033>.
- [21] F. Omar, A. Numan, N. Duraisamy, S. Bashir, K. Ramesh, S. Ramesh, Ultrahigh capacitance of amorphous nickel phosphate for asymmetric supercapacitor applications, *RSC Adv.* 6 (2016) 76298–76306, <https://doi.org/10.1039/C6RA15111F>.
- [22] F. Omar, A. Numan, S. Bashir, N. Duraisamy, R. Vikneswaran, Y. Loo, K. Ramesh, S. Ramesh, Enhancing rate capability of amorphous nickel phosphate supercapattery electrode via composition with crystalline silver phosphate, *Electrochim. Acta* 273 (2018) 216–228, <https://doi.org/10.1016/j.electacta.2018.03.136>.
- [23] B. Senthilkumar, Z. Khan, S. Park, K. Kim, H. Ko, Y. Kim, Highly porous graphitic carbon and Ni₂P₂O₇ for a high performance aqueous hybrid supercapacitor, *J. Mater. Chem. A* 3 (2015) 21553–21561, <https://doi.org/10.1039/C5TA04737D>.
- [24] J. Li, M. Liu, L. Kong, D. Wang, Y. Hu, W. Han, L. Kang, Advanced asymmetric supercapacitors based on Ni₃(PO₄)₂@GO and Fe₂O₃@GO electrodes with high specific capacitance and high energy density, *RSC Adv.* 5 (2015) 41721–41728, <https://doi.org/10.1039/C5RA06050H>.
- [25] X. Peng, H. Chai, Y. Cao, Y. Wang, H. Dong, D. Jia, W. Zhou, Facile synthesis of cost-effective Ni₃(PO₄)₂·8H₂O microstructures as a supercapattery electrode material, *Mater. Today Energy* 7 (2018) 129–135, <https://doi.org/10.1016/j.mtener.2017.12.004>.
- [26] S. Marje, P. Katkar, S. Pujari, S. Khalate, P. Deshmukh, U. Patil, Effect of phosphate (anion) precursor on structural and morphology behavior of nickel phosphate thin films and its supercapacitive performance, *Mater. Sci. Eng.: B* 261 (2020), 114641, <https://doi.org/10.1016/j.mseb.2020.114641>.
- [27] S. Yan, K. Abhilash, L. Tang, M. Yang, Y. Ma, Q. Xia, Q. Guo, H. Xia, Photomechanical organic crystals as smart materials for advanced applications, *Chemistry* 25 (2019) 5611–5622, <https://doi.org/10.1002/smll.201804371>.
- [28] B. Sankapal, R. Mane, C. Lokhande, Successive ionic layer adsorption and reaction (SILAR) method for the deposition of large area (~10 cm²) tin disulfide (SnS₂) thin films, *Mater. Res. Bull.* 35 (2000) 2027–2035, [https://doi.org/10.1016/S0025-5408\(00\)00405-0](https://doi.org/10.1016/S0025-5408(00)00405-0).
- [29] D. Marcano, D. Kosynkin, J. Berlin, A. Sinitskii, Z. Sun, A. Slesarev, L. Alemany, W. Lu, J. Tour, Improved synthesis of graphene oxide, *ACS Nano* 4 (2010) 4806–4814, <https://doi.org/10.1021/nn1006368>.
- [30] D. Malavekar, V. Lokhande, V. Mane, S. Ubale, U. Patil, C. Lokhande, Enhanced energy density of flexible asymmetric solid state supercapacitor device fabricated with amorphous thin film electrode materials, *J. Phys. Chem. Solids* 141 (2020), 109425, <https://doi.org/10.1016/j.jpcs.2020.109425>.
- [31] P. Kulal, D. Dubal, C. Lokhande, V. Fulari, Chemical synthesis of Fe₂O₃ thin films for supercapacitor application, *J. Alloy. Compd.* 509 (2011) 2567–2571, <https://doi.org/10.1016/j.jallcom.2010.11.091>.
- [32] F. Omar, A. Numan, N. Duraisamy, S. Bashir, K. Ramesh, S. Ramesh, Ultrahigh capacitance of amorphous nickel phosphate for asymmetric supercapacitor applications, *RSC Adv.* 6 (2016) 76298–76306, <https://doi.org/10.1039/C6RA15111F>.
- [33] M. Al-Omair, A. Touny, M. Saleh, Reflux-based synthesis and electrocatalytic characteristics of nickel phosphate nanoparticles, *J. Power Sources* 342 (2017) 1032–1039, <https://doi.org/10.1016/j.jpowsour.2016.09.079>.
- [34] J.B. Condon, Surface Area and Porosity Determinations by Physisorption: Measurements and Theory, Elsevier, Amsterdam, 2006, pp. 6–14.
- [35] D. Dubal, G. Gund, C. Lokhande, R. Holze, CuO cauliflower for supercapacitor application: Novel potentiodynamic deposition, *Mater. Res. Bull.* 48 (2013) 923–928, <https://doi.org/10.1016/j.materresbull.2012.11.081>.
- [36] J. Zhao, H. Pang, J. Deng, Y. Ma, B. Yan, X. Li, S. Li, J. Chen, W. Wang, Mesoporous uniform ammonium nickel phosphate hydrate nanostructures as high performance electrode materials for supercapacitors, *CrystEngComm* 15 (2013) 5950–5955, <https://doi.org/10.1039/C3CE40712H>.
- [37] F. Omar, A. Numan, S. Bashir, N. Duraisamy, R. Vikneswaran, Y.-L. Loo, K. Ramesh, S. Ramesh, Enhancing rate capability of amorphous nickel phosphate supercapattery electrode via composition with crystalline silver phosphate, *Electrochim. Acta* 273 (2018) 216–228, <https://doi.org/10.1016/j.electacta.2018.03.136>.
- [38] N. Chodankar, D. Dubal, S. Patil, G. Raju, S. Karekar, Y. Huh, Y.-K. Han, Ni₂P₂O₇ micro-sheets supported ultra-thin MnO₂ nanoflakes: a promising positive electrode for stable solid-state hybrid supercapacitor, *Electrochim. Acta* 319 (2019) 435–443, <https://doi.org/10.1016/j.electacta.2019.06.166>.
- [39] S. Pujari, S. Kadam, Y.-R. Ma, P. Katkar, S. Marje, S. Khalate, A. Lokhande, U. Patil, Facile synthesis of microstrip-like copper phosphate hydroxide thin films for supercapacitor applications, *J. Electron. Mater.* 49 (2020) 3890–3901, <https://doi.org/10.1007/s11664-020-08095-w>.
- [40] P. Katkar, S. Marje, S. Pujari, S. Khalate, A. Lokhande, U. Patil, Enhanced energy density of all-solid-state asymmetric supercapacitors based on morphologically tuned hydrous cobalt phosphate electrode as cathode material, *ACS Sustain. Chem. Eng.* 7 (2019) 11205–11218, <https://doi.org/10.1021/acscuschemeng.9b00504>.
- [41] S. Kulkarni, U. Patil, I. Shackery, J. Sohn, S. Lee, B. Park, S. Jun, High-performance supercapacitor electrode based on a polyaniline nanofibers/3D graphene framework as an efficient charge transporter, *J. Mater. Chem. A* 2 (2014) 4989–4998, <https://doi.org/10.1039/C3TA14959E>.
- [42] W. Xing, S. Qiao, X. Wu, X. Gao, J. Zhou, S. Zhuo, S. Hartono, D. Hulicova-Jurcakova, Exaggerated capacitance using electrochemically active nickel foam as current collector in electrochemical measurement, *J. Power Sources* 196 (2011) 4123–4127, <https://doi.org/10.1016/j.jpowsour.2010.12.003>.
- [43] P. Deshmukh, S. Pusawale, V. Jamadade, U. Patil, C. Lokhande, Microwave assisted chemical bath deposited polyaniline films for supercapacitor application, *J. Alloy. Compd.* 509 (2011) 5064–5069, <https://doi.org/10.1016/j.jallcom.2010.12.009>.
- [44] L. Fan, F. Pan, Q. Tu, Y. Gu, J. Huang, Y. Huang, J. Wu, Synthesis of CuCo₂S₄ nanosheet arrays on Ni foam as binder-free electrode for asymmetric supercapacitor, *Int. J. Hydrog. Energy* 43 (2018) 23372–23381, <https://doi.org/10.1016/j.ijhydene.2018.10.190>.
- [45] Y. Gua, L. Fana, J. Huang, C. Genga, J. Lina, M. Huang, Y. Huang, J. Wua, N-doped reduced graphene oxide decorated NiSe₂ nanoparticles for high-performance asymmetric supercapacitors, *J. Power Sources* 425 (2019) 60–68, <https://doi.org/10.1016/j.jpowsour.2019.03.123>.
- [46] J. Chena, J. Xu, S. Zhou, N. Zhao, C.-P. Wong, Amorphous nanostructured FeOOH and Co-Ni double hydroxides for high-performance aqueous asymmetric supercapacitors, *Nano Energy* 21 (2016) 145–153, <https://doi.org/10.1016/j.nanoen.2015.12.029>.
- [47] N. Zhang, S. Ouyang, T. Kako, J. Ye, Synthesis of hierarchical Ag₂ZnGeO₄ hollow spheres for enhanced photocatalytic property, *Chem. Commun.* 48 (2012) 9894–9896, <https://doi.org/10.1039/C2CC34738E>.
- [48] R. Yi, J. Feng, D. Lv, M. Gordin, S. Chen, D. Choi, D. Wang, Amorphous Zn₂GeO₄ nanoparticles as anodes with high reversible capacity and long cycling life for Li-ion batteries, *Nano Energy* 4 (2013) 498–504, <https://doi.org/10.1016/j.nanoen.2012.12.001>.

Highly sensitive hydrothermally prepared nickel phosphate electrocatalyst as non-enzymatic glucose sensing electrode

Sachin S. Pujari, Sujit A. Kadam, Yuan-Ron Ma, Suraj A. Khalate, Pranav K. Katkar, Supriya J. Marje & Umakant M. Patil

Journal of Porous Materials

ISSN 1380-2224

J Porous Mater

DOI 10.1007/s10934-020-01000-0



Your article is protected by copyright and all rights are held exclusively by Springer Science+Business Media, LLC, part of Springer Nature. This e-offprint is for personal use only and shall not be self-archived in electronic repositories. If you wish to self-archive your article, please use the accepted manuscript version for posting on your own website. You may further deposit the accepted manuscript version in any repository, provided it is only made publicly available 12 months after official publication or later and provided acknowledgement is given to the original source of publication and a link is inserted to the published article on Springer's website. The link must be accompanied by the following text: "The final publication is available at link.springer.com".



Highly sensitive hydrothermally prepared nickel phosphate electrocatalyst as non-enzymatic glucose sensing electrode

Sachin S. Pujari¹ · Sujit A. Kadam² · Yuan-Ron Ma² · Suraj A. Khalate¹ · Pranav K. Katkar¹ · Supriya J. Marje¹ · Umakant M. Patil¹

© Springer Science+Business Media, LLC, part of Springer Nature 2020

Abstract

Present investigation describes a successful preparation of nickel phosphate ($\text{Ni}_3(\text{PO}_4)_2 \cdot 8\text{H}_2\text{O}$) thin film electrodes by facile one pot hydrothermal method. As developed $\text{Ni}_3(\text{PO}_4)_2 \cdot 8\text{H}_2\text{O}$ thin film electrodes with the variation of thickness are examined for morphological change and glucose sensing. The $\text{Ni}_3(\text{PO}_4)_2 \cdot 8\text{H}_2\text{O}$ thin film electrodes exhibit linear response with respect to the variation in glucose concentration from 2.5 to 30 mM and acquire the sensitivity of $8312 \mu\text{A mM}^{-1} \text{cm}^{-2}$ with $437 \mu\text{M}$ LOD. Selectivity performance of $\text{Ni}_3(\text{PO}_4)_2 \cdot 8\text{H}_2\text{O}$ thin film electrode towards glucose in presence of dopamine, fructose and lactose is studied. The results suggest that $\text{Ni}_3(\text{PO}_4)_2 \cdot 8\text{H}_2\text{O}$ thin film electrode is beneficial for glucose sensing application due to enormous active sites with the high specific surface area of the active material.

Keywords Nickel phosphate · Hydrothermal method · Microplates · Non-enzymatic glucose sensor · Thin film electrode

1 Introduction

Nowadays, biosensors are mostly investigated in the area of biomedical analysis, food industry, and clinic diagnosis [1, 2]. Glucose sensors are widely used in clinical diagnostics because of their fast examination and reliability [3]. Therefore, a lot of efforts are underway for the construction of rapid, reliable and reproducible glucose sensing devices [4]. Electrochemical sensors are known as a good scientific device due to their fast and low-cost glucose recognition [5, 6]. Biosensors prepared by various methods have been studied from past few years. Based on the multiple characteristics and phenomena of the techniques as well as detector, applied biosensors would be classified into electrical biosensors, vibrational biosensors, electrochemical

biosensors, optical biosensors and mechanical biosensors. Chronoamperometric or electrochemical glucose sensors are classified into two types an enzymatic and non-enzymatic glucose sensor. In the type first, enzymatic oxidase on the surface of electrode is immobilized and dioxygen quantitatively reduced to the hydrogen peroxide and monitored by chronoamperometric method [7]. The traditional enzymatic glucose sensor offers high selectivity, better time response but some drawbacks are associated such as, limited stability and difference in response with the changing pH as well as temperature [8]. On the other hand, non-enzymatic glucose sensors offer many advantages such as stability, reproducibility and their mechanism for detecting glucose molecules is based on redox reaction of active material [5, 9]. Among different biosensors, electrochemical biosensors involve easy mechanism and fabrication processes, simple operation and quick response time. It is familiar that, transition metal based electrodes are extremely cost-effective, facile to synthesize, highly electroactive and exhibit good glucose sensing [10, 11].

In recent times, there are lots of efforts undergoing for glucose detection using nickel based catalysts. Almost all of them shown improved performance of glucose sensor by developing nickel catalyst on the conductive materials like as carbon nanofiber [12], Mxene [13] and graphene [14]. Yet few works were prepared to simultaneously modify

Electronic supplementary material The online version of this article (<https://doi.org/10.1007/s10934-020-01000-0>) contains supplementary material, which is available to authorized users.

✉ Umakant M. Patil
umakant.physics84@gmail.com

¹ Centre for Interdisciplinary Research, D. Y. Patil Education Society, Kasaba Bawada, Kolhapur 416 006, India

² Department of Physics, National Dong Hwa University, Hualien 97401, Taiwan

components with structure of nickel catalyst to enhance the performance. Numerous metal oxides tested as electrocatalysts, in that nickel oxide has a specific interest because of high chemical stability and thermal stability [15, 16]. Nickel phosphate has many different structures that may increase its ion exchange rate and ionic conductivity [17]. Many methods have been employed for the preparation of nickel phosphate such as hydrothermal [18], sol–gel techniques [19], solvothermal [20], chemical bath deposition [21], wet chemical process [22] and applied for various applications. Some reports are available on the nickel phosphate for non-enzymatic glucose sensor as, Padmanathan et al. [23] hydrothermally prepared $\text{Ni}_3(\text{PO}_4)_2 \cdot 8\text{H}_2\text{O}$ on the substrate of nickel foam (NF) and reported sensitivity of $24,390 \mu\text{A mM}^{-1} \text{cm}^{-2}$. Also, Hassaninejad-Darzi et al. [24] prepared nickel phosphate (VSB 5) nanorods and Al-Omair et al. [25] synthesized nano/micro particles of $\text{Ni}_3(\text{PO}_4)_2 \cdot 8\text{H}_2\text{O}$ by hydrothermal technique for glucose sensing. According to the literature survey, binder free synthesis of $\text{Ni}_3(\text{PO}_4)_2 \cdot 8\text{H}_2\text{O}$ thin films on stainless steel (SS) substrate and their application as non-enzymatic glucose sensor have not been investigated yet.

Herein, we report for first time synthesis of $\text{Ni}_3(\text{PO}_4)_2 \cdot 8\text{H}_2\text{O}$ thin film (thickness variation) using a simple one step hydrothermal technique at 390 K and applied for non-enzymatic glucose sensing application. The structural and morphological studies of as-synthesized electrode were performed by X-ray diffraction (XRD), Fourier transform infrared (FTIR), Brunauer–Emmett–Teller (BET) analysis and scanning electron microscopy (SEM). The $\text{Ni}_3(\text{PO}_4)_2 \cdot 8\text{H}_2\text{O}$ thin film electrode applied as a catalyst and thickness variation for sensing behavior towards the glucose molecule is examined. The obtained $\text{Ni}_3(\text{PO}_4)_2 \cdot 8\text{H}_2\text{O}$ electrode shows glucose sensing in a linear range from 2.5 to 30 mM having the sensitivity of $8312 \mu\text{A mM}^{-1} \text{cm}^{-2}$ with $437 \mu\text{M}$ limit of detection (LOD).

2 Experimental section

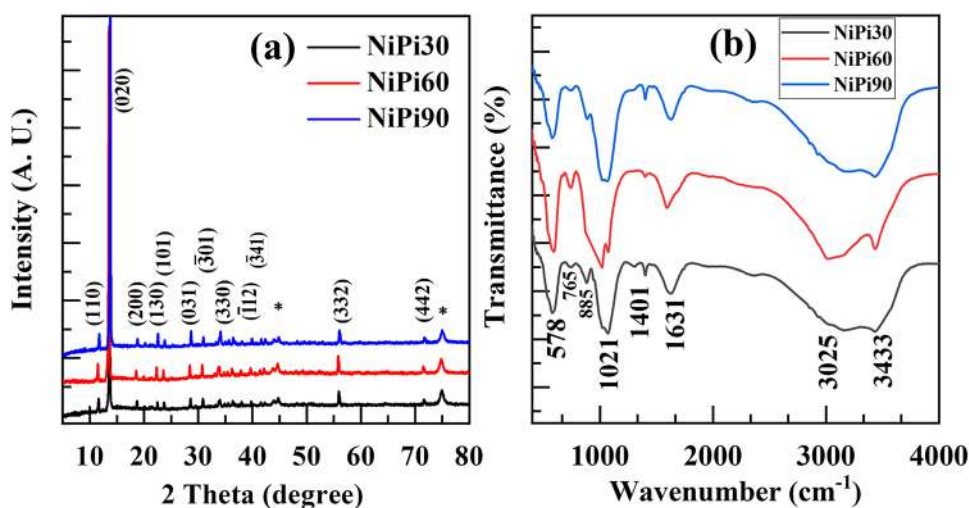
2.1 Synthesis of $\text{Ni}_3(\text{PO}_4)_2 \cdot 8\text{H}_2\text{O}$ thin films

To prepare $\text{Ni}_3(\text{PO}_4)_2 \cdot 8\text{H}_2\text{O}$ thin films by hydrothermal method, analytical grade (AR grade 99.9%), nickel chloride hexahydrate ($\text{NiCl}_2 \cdot 6\text{H}_2\text{O}$), potassium dihydrogen orthophosphate (KH_2PO_4) and urea (NH_2CONH_2) were obtained from Sigma Aldrich and used as received without any purification process. In the typical synthesis process, a chemical bath was arranged with mixing aqueous 0.033 M $\text{NiCl}_2 \cdot 6\text{H}_2\text{O}$ (20 ml), 0.066 M KH_2PO_4 (20 ml) and 0.075 M NH_2CONH_2 (10 ml). The SS (304 grade) substrates with surface area of $1 \text{ cm} \times 5.5 \text{ cm}$ were polished by zero fine grade polish paper. The polished substrates washed with labogent and ultrasonically cleaned for 15 min. Further, the SS substrates were kept vertically in prepared solution bath and a bath was placed in hydrothermal autoclave maintained at 390 K under 15 psi pressure. The reaction time was varied as, 30, 60 and 90 min, and prepared films denoted as NiPi30, NiPi60 and NiPi90, respectively. After reaction, formation of well adherent light green colored $\text{Ni}_3(\text{PO}_4)_2 \cdot 8\text{H}_2\text{O}$ thin films was observed on SS substrate. The thin films were washed with double distilled water (DDW) and dried at ambient condition. As prepared nickel phosphate thin films directly used for further characterizations.

2.2 Material characterizations

The X-ray diffraction pattern (XRD) obtained from Rigaku miniflex-600 with $\text{Cu K}\alpha$ ($\lambda = 0.15406 \text{ nm}$) radiation, operated at 40 kV with scanning rate of 2° min^{-1} for the crystal structure analysis of prepared thin film. The Fourier transform infrared (FTIR) spectra were recorded by an FT-IR 4600 type-A instrument. The surface areas were measured from Brunauer–Emmett–Teller (BET) analysis (Belsorp II mini).

Fig. 1 **a** XRD patterns of prepared $\text{Ni}_3(\text{PO}_4)_2 \cdot 8\text{H}_2\text{O}$ thin film. **b** FT-IR spectra of as-synthesized $\text{Ni}_3(\text{PO}_4)_2 \cdot 8\text{H}_2\text{O}$ thin film for NiPi30, NiPi60 and NiPi90 samples



The field emission-scanning electron microscopy (FE-SEM, JSM-6500F, JEOL) equipped with energy dispersive X-ray spectroscopy (EDS) (Oxford, X-max) was used to observe the surface morphologies of $\text{Ni}_3(\text{PO}_4)_2 \cdot 8\text{H}_2\text{O}$ thin films. All electrochemical sensing was evaluated by using ZIVE MP1 multichannel electrochemical workstation.

2.3 Electrochemical measurements

The electrochemical glucose sensing analysis of $\text{Ni}_3(\text{PO}_4)_2 \cdot 8\text{H}_2\text{O}$ thin film electrode was conducted by three-electrode cell system in 1 M KOH electrolyte. The prepared $\text{Ni}_3(\text{PO}_4)_2 \cdot 8\text{H}_2\text{O}$ thin films, platinum plate and saturated calomel electrode (SCE) were applied as working electrode, counter electrode and reference electrode, respectively. Firstly, the working ($\text{Ni}_3(\text{PO}_4)_2 \cdot 8\text{H}_2\text{O}$) electrode was stabilized for few cyclic voltammogram (CV) cycles in 1 M KOH electrolyte, within 0 to 0.5 V potential window at scan rate of 50 mV s^{-1} , until the steady state of voltammogram was achieved. The electrochemical characteristics of glucose sensing were studied by successively adding different (or same) glucose concentrations in 1 M KOH at a constant (0.43 V vs SCE) potential. To

diminish mass transfer interference, the assistance electrolyte (1 M KOH) was continuously stirred at 230 rpm. The impact of common electroactive species such as dopamine, fructose and lactose was studied in interference test.

3 Result and discussion

3.1 $\text{Ni}_3(\text{PO}_4)_2 \cdot 8\text{H}_2\text{O}$ thin film formation and reaction mechanism

A hydrothermal method was employed for deposition of $\text{Ni}_3(\text{PO}_4)_2 \cdot 8\text{H}_2\text{O}$ thin films at 390 K. In the formation of thin film, basically two steps are involved such as nucleation and particle growth. The nucleation is essential for the growth of particle, thin film deposition occurs successfully when heterogeneous nucleation is promoted over the SS substrate and homogeneous nucleation is inhibited in the solution [26]. In typical process, decomposition of urea (at high temperature 363 K) gradually produces CO_2 and NH_4^+ ions, released NH_4^+ ions react in terms of complexing agent [27, 28]. Afterward Ni^+ ions, form amine

Fig. 2 Nitrogen adsorption/desorption isotherm of sample **a** NiPi30, **b** NiPi60 and **c** NiPi90, and **d** pore size distribution curves of $\text{Ni}_3(\text{PO}_4)_2 \cdot 8\text{H}_2\text{O}$ for sample NiPi30, NiPi60 and NiPi90

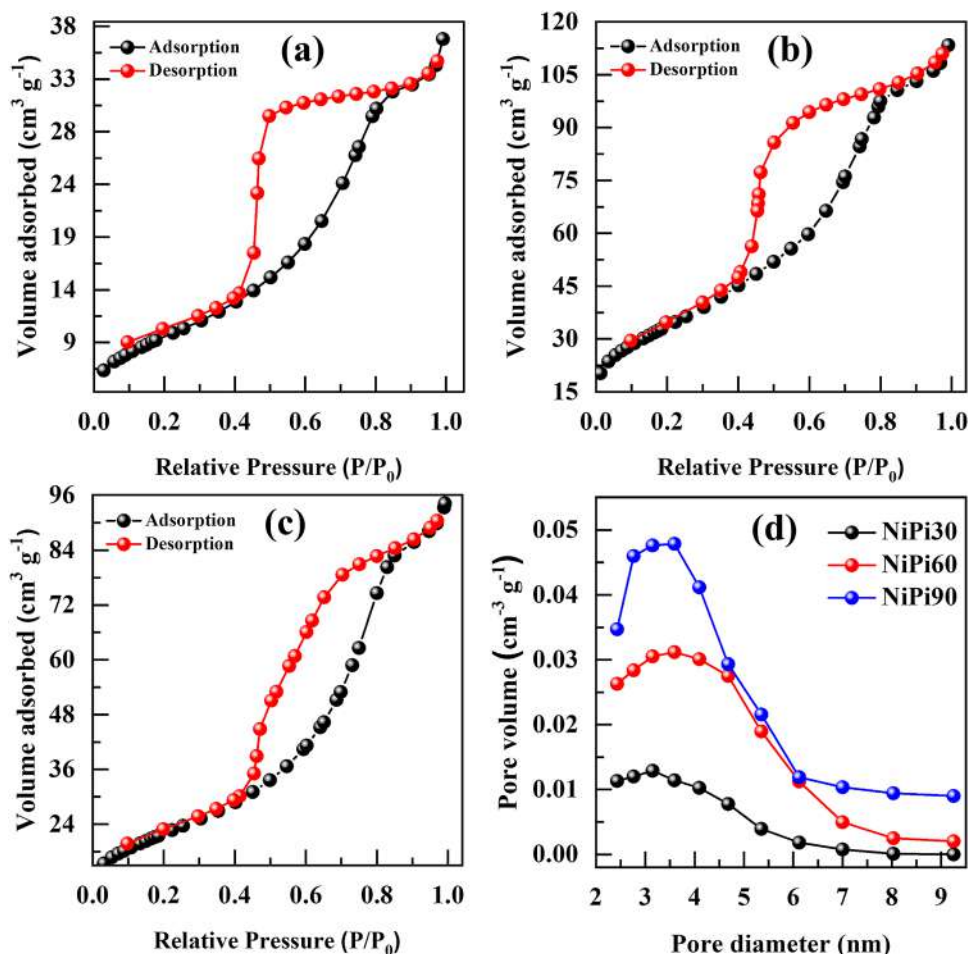
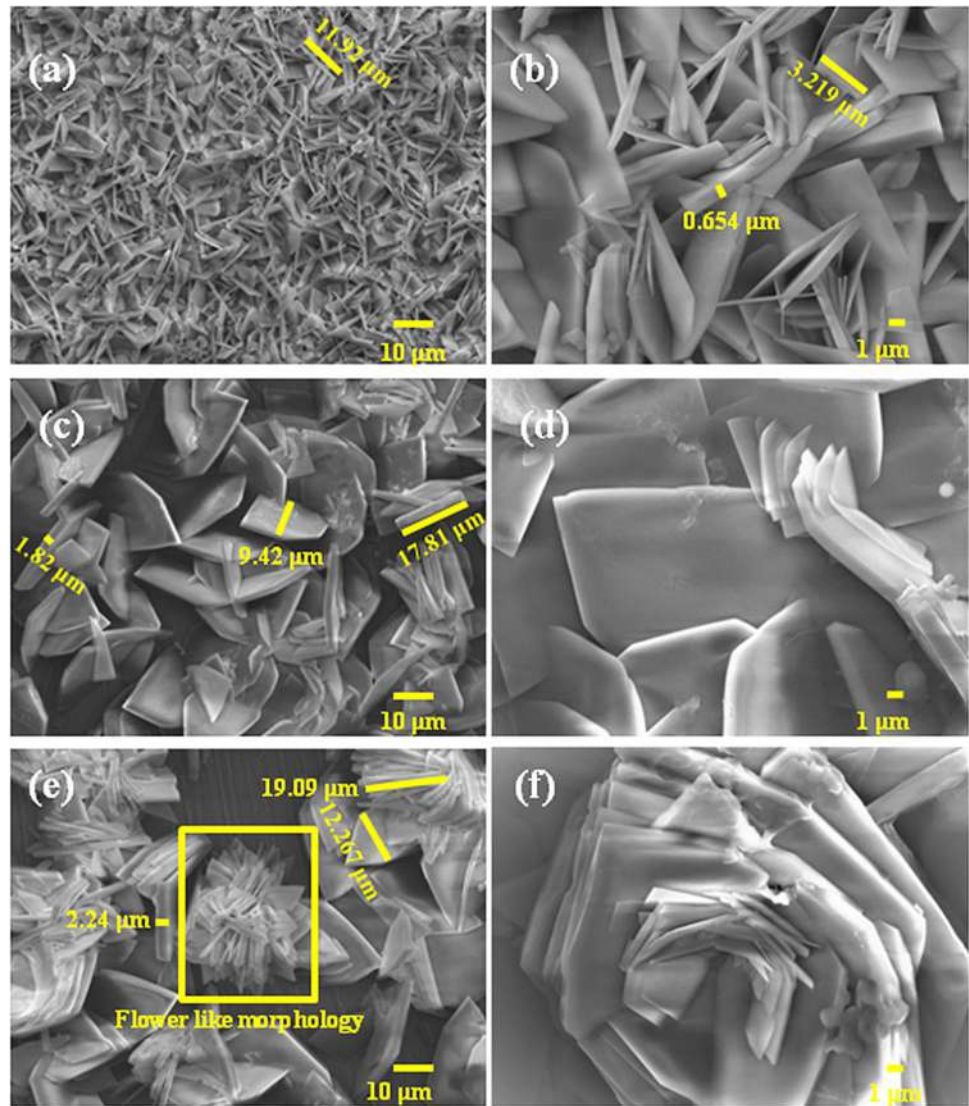
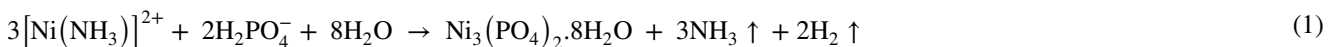


Fig. 3 SEM images of prepared nickel phosphate sample NiPi30 (a, b), NiPi60 (c, d) and NiPi90 (e, f) at different magnification of X1000 and X4000



complex as $[\text{Ni}(\text{NH}_3)]^{2+}$ and this complex acts as source of Ni^{2+} ions and gradually releases Ni^{2+} ions [21]. Also, KH_2PO_4 releases PO_4^- ions and reacts with nickel (Ni^{2+}) ion, which resulted into formation of $\text{Ni}_3(\text{PO}_4)_2 \cdot 8\text{H}_2\text{O}$ thin film as per following reaction:



Formation of uniform thin film was executed by varying reaction time as 30, 60 and 90 min. The deposited mass of thin film material was investigated by gravimetric weight difference method. It was observed that, from the sample NiPi30 to NiPi90 mass of deposited material increases with increasing reaction time. Deposited mass of samples NiPi30, NiPi60 and NiPi90 obtained to be 0.36, 0.44 and 0.47 mg cm^{-2} , respectively.

3.2 XRD analysis

XRD patterns of hydrothermally deposited $\text{Ni}_3(\text{PO}_4)_2 \cdot 8\text{H}_2\text{O}$ thin films on SS substrate (sample NiPi30, NiPi60 and NiPi90) are depicted in Fig. 1a. The peaks marked with

‘*’ correspond to SS substrate in XRD pattern. The major indexed peaks at, 11.72, 13.78, 18.80, 22.59, 23.80, 28.62, 30.96, 34.11, 39.86, 41.61, 56.01 and 71.55° are ascribed to (1 1 0), (0 2 0), (2 0 0), (1 3 0), (1 0 1), (0 3 1), (3 0 1), (3 3 0), (1 1 2), (3 4 1) (3 3 2) and (4 4 2) crystal planes of nickel phosphate hydrate $[\text{Ni}_3(\text{PO}_4)_2 \cdot 8\text{H}_2\text{O}]$, respectively (JCPDS card no. 00–033–0951). Also, the average crystallite size were calculated by Scherrer relation [29],

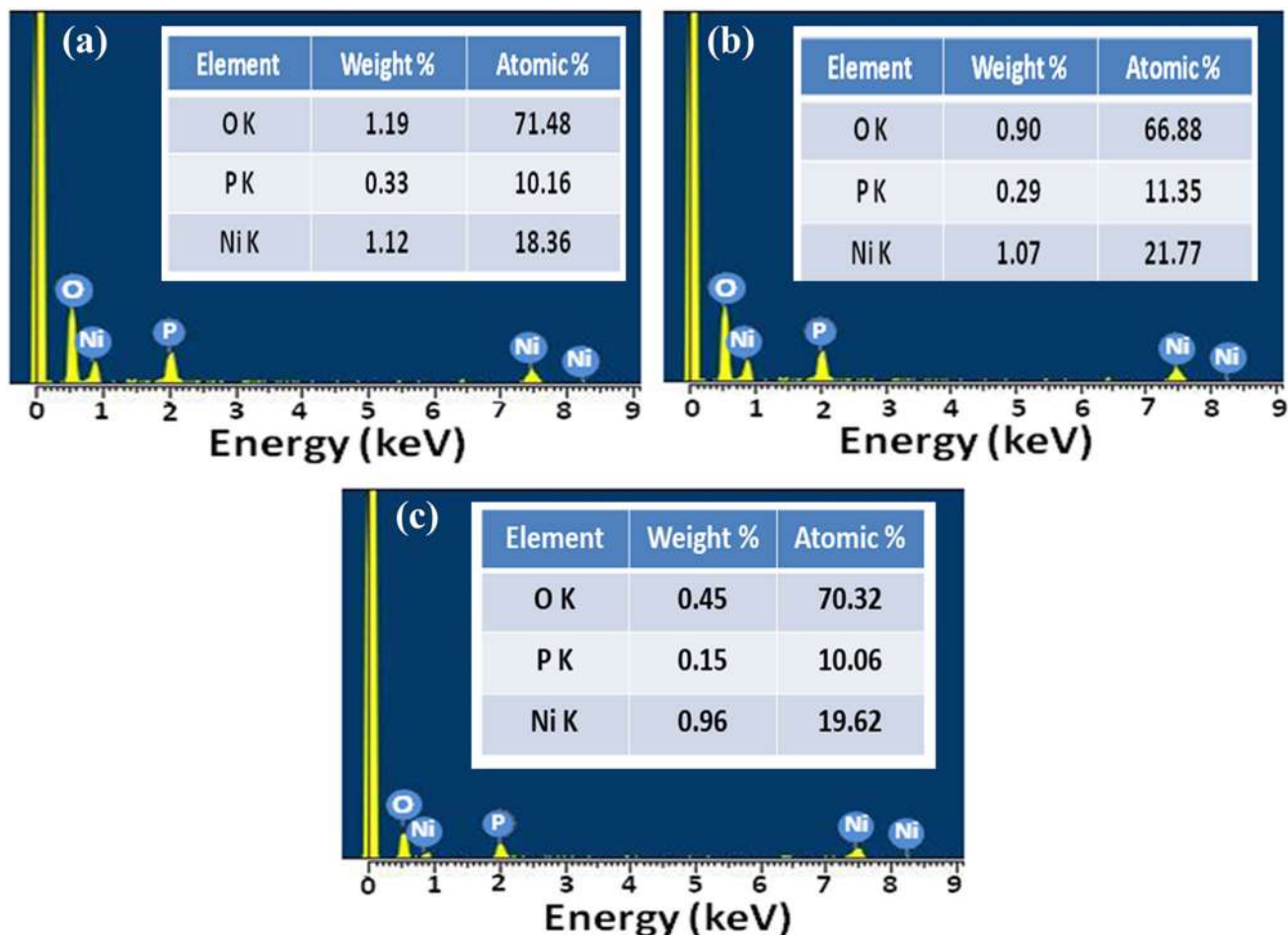


Fig. 4 EDS spectra of as-synthesized $\text{Ni}_3(\text{PO}_4)_2 \cdot 8\text{H}_2\text{O}$ a NiPi30, b NiPi60 and c NiPi90 thin films

$$D = \frac{k\lambda}{\beta \cos \theta} \quad (2)$$

Where, k is the value of shape factor ($k = 0.94$), λ is the wavelength of X-ray ($\lambda = 1.5406 \text{ \AA}$), β is the full width at half maxima (FWHM) of the corresponding (0 2 0) plane and θ is the Bragg's angle. The average crystallite size of $\text{Ni}_3(\text{PO}_4)_2 \cdot 8\text{H}_2\text{O}$ in sample NiPi30, NiPi60 and NiPi90 are 49.51, 55.46 and 54.58 nm, respectively. The maximum average crystallite size of 55.46 nm for (0 2 0) plane is obtained for NiPi60 sample. Increase in crystallite size with film thickness can contribute to improvement in conductivity of electrode and subsequently glucose sensitivity.

3.3 FTIR analysis

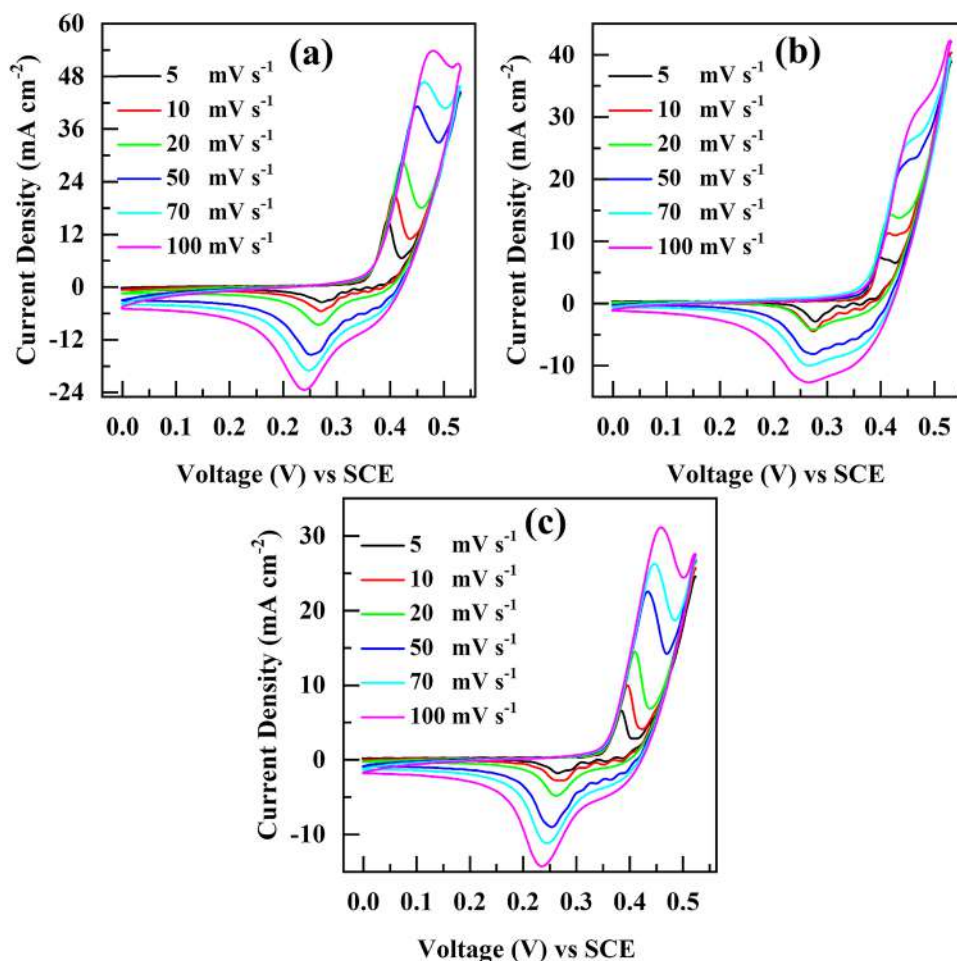
The FTIR spectrum (Fig. 1b) demonstrates that, the band at 578 correspond to the phosphate (PO_4^{3-}) group vibrational modes of the spinal compound [30, 31]. Additionally, the stretching of the P–O–P linkages was attributed to the peak at 765 cm^{-1} and, 885 cm^{-1} shows vibrational mode of

PO_4^{3-} [32, 33]. The strong absorption asymmetric vibration mode of PO_4^{3-} group observed at 1021 cm^{-1} . The characteristics band at 1401 and 1631 cm^{-1} represents bending vibration mode of a water molecule (H–O–H) [34]. Adsorbed water represented by absorption broad band from 3025 to 3433 cm^{-1} and can be assigned to vibrational bond of O–H. These results indicate that, the deposited material contains structural water and formation of hydrous nickel phosphate ($\text{Ni}_3(\text{PO}_4)_2 \cdot 8\text{H}_2\text{O}$) in thin film form.

3.4 BET analysis

To analyze specific surface area, N_2 adsorption/desorption isotherms of prepared $\text{Ni}_3(\text{PO}_4)_2 \cdot 8\text{H}_2\text{O}$ thin films (at 77 K temperature of the liquid nitrogen) were recorded and indicated in Fig. 2a, b, c. The detected isotherms of sample NiPi30 (a), NiPi60 (b) and NiPi90 (c) exhibits a type IV isotherm with H2 type hysteresis loop of physisorption, according to classification of International Union of Pure and Applied Chemistry (IUPAC). The type IV isotherm represents characteristics property of the mesoporous material

Fig. 5 Cyclic voltammetry curves of $\text{Ni}_3(\text{PO}_4)_2 \cdot 8\text{H}_2\text{O}$ thin films at various scan rates from 5–100 mV s^{-1} in 1 M KOH electrolyte for sample **a** NiPi30, **b** NiPi60 and **c** NiPi90



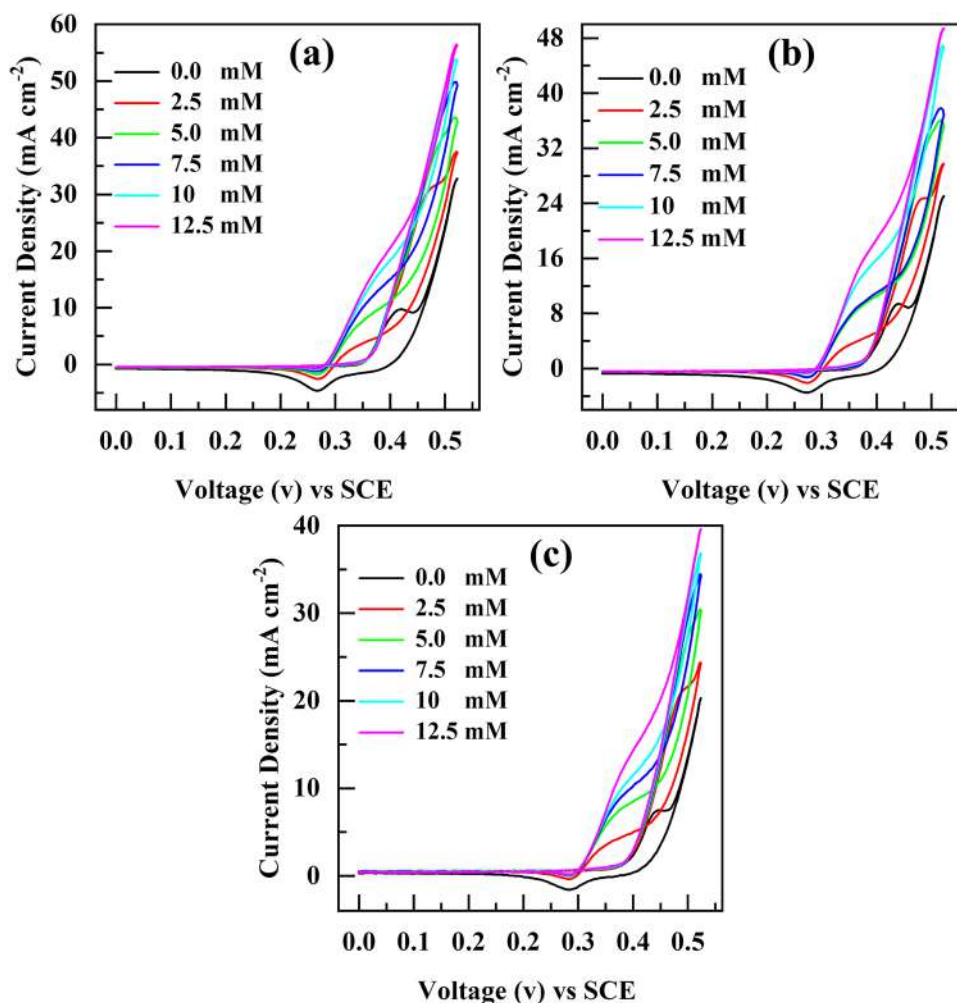
having high energy of adsorption [35]. Such arrangement of type IV isotherm and H2 type hysteresis loop display the existence of well ordered pores with wide and narrow sections and interconnecting channels [36, 37]. According to the analysis of Brunauer–Emmett–Teller (BET) equation, the surface areas were evaluated to be 35.07, 120.34 and 77.04 $\text{m}^2 \text{g}^{-1}$ for sample NiPi30, NiPi60 and NiPi90, respectively. The results reveal that, electrode with optimum thickness shows high surface area. The distribution of pore size of all samples exhibited in Fig. 2d. The mesoporous size distribution graph shows an average pore diameter of 6.41, 5.82 and 7.52 nm for sample NiPi30, NiPi60 and NiPi90, respectively. The BET results confirm formation of well-ordered slit-shaped mesoporous structure of $\text{Ni}_3(\text{PO}_4)_2 \cdot 8\text{H}_2\text{O}$ material [36].

3.5 Morphological analysis

The structural morphology and particle size of $\text{Ni}_3(\text{PO}_4)_2 \cdot 8\text{H}_2\text{O}$ were studied by FE-SEM analysis and revealed in Fig. 3. The microplates like architecture were observed for NiPi30 sample (a and b). The average length,

thickness and width of these microplates are 11.92, 0.65 and 3.21 μm , respectively. The SEM images of NiPi60 sample (c and d) states formation of willow-leaf like microstructure. Here, the microplates are converted into willow-leaf like morphology with the deposition time variation. The average length, thickness and width of willow-leaves are 17.81, 1.82 and 9.42 μm , respectively. The NiPi90 sample exhibits flower like structures as shown in (Fig. 3e and f). At higher thickness, willow-leaf like structure combines and forms flower like architectures. The average length, thickness and width of leaves of micro-flower are 19.09, 2.24 and 12.26 μm , respectively. With increase in reaction time, length, thickness, and width of leaves increased. Also, Peng et al. [38] observed change in the morphology from microsheets to microflower-sheet to microflower of $\text{Ni}_3(\text{PO}_4)_2 \cdot 8\text{H}_2\text{O}$ with varied reaction time in synthesis by using microwave assisted method. Similarly, Wu et al. demonstrated morphology change by adjusting experimental condition in the composition using hydrothermal technique [39]. Moreover, Marje et al. synthesized $\text{Ni}_2\text{P}_2\text{O}_7 \cdot 8\text{H}_2\text{O}$ and observed change in the morphology from willow leaf like petals to microflower

Fig. 6 Cyclic voltammetry curves of $\text{Ni}_3(\text{PO}_4)_2 \cdot 8\text{H}_2\text{O}$ thin films in the existence of various concentrations of glucose (0–12.5 mM) in 1 M KOH at constant scan rate of 20 mV s^{-1} for sample **a** NiPi30, **b** NiPi60 and **c** NiPi90



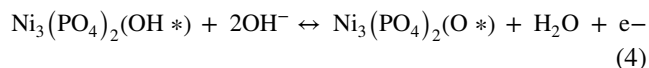
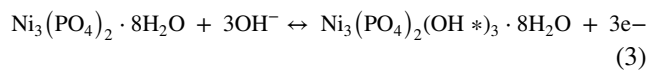
like structure by changing Ni and PO_4^- ratio [21]. In present study, it is observed that morphology changes from microplates to willow-leaf like morphology and flower like architectures with increase in deposition reaction time (30, 60 and 90 min).

The elemental composition of $\text{Ni}_3(\text{PO}_4)_2 \cdot 8\text{H}_2\text{O}$ thin films were studied by energy-dispersive spectroscopy (EDS), and outcomes are demonstrated in Fig. 4. The atomic ratio of nickel and phosphorous (Ni:P) is obtained as, 1.80:1, 1.91:1 and 1.95:1 for the sample NiPi30, NiPi60, and NiPi90, respectively which is near to ratio 1.5:1. The excess oxygen obtained in chemical composition emphasizes that the prepared material is $\text{Ni}_3(\text{PO}_4)_2 \cdot 8\text{H}_2\text{O}$.

4 Determination of glucose oxidation

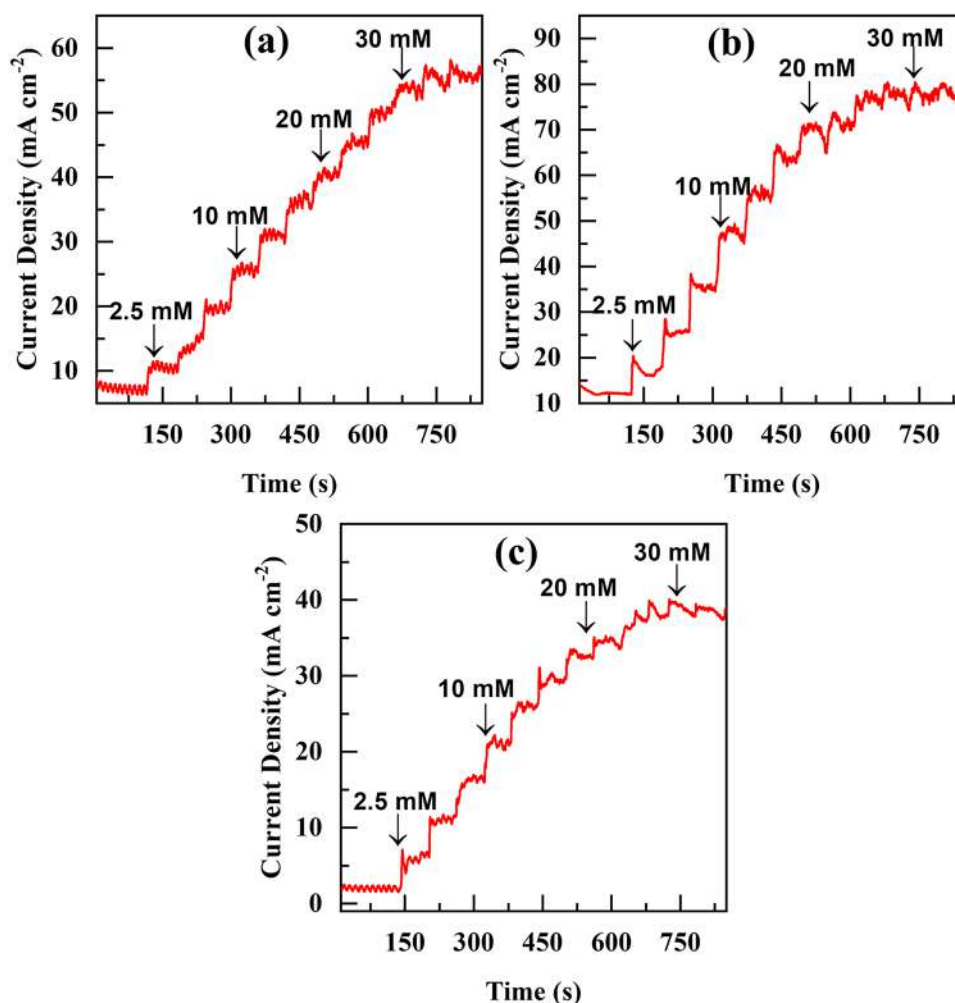
The prepared $\text{Ni}_3(\text{PO}_4)_2 \cdot 8\text{H}_2\text{O}$ thin film electrode was used for non-enzymatic glucose sensor. Figure 5a, b, c exhibits CV curves of $\text{Ni}_3(\text{PO}_4)_2 \cdot 8\text{H}_2\text{O}$ at 5–100 mV s^{-1} scan rates for sample NiPi30, NiPi60 and NiPi90 in 1 M KOH

electrolyte. The peak current of CV curve increases during increasing scan rate which shifts the redox potential from positive region and negative region which highlights the quasi reversible nature of electrode [40]. The redox peaks attributed to the reverse reaction and the oxidation of $\text{Ni}_3(\text{PO}_4)_2 \cdot 8\text{H}_2\text{O}$ as indicated by the following reactions [41],



*denotes the active surface site where can adsorb OH as well as O species. The presence of alkaline condition gives rise to evolution of oxygen during electrochemical reaction due to the adsorption of O and OH groups on the surface of $\text{Ni}_3(\text{PO}_4)_2 \cdot 8\text{H}_2\text{O}$ thin film [41, 42].

Fig. 7 Chronoamperometric response curve of $\text{Ni}_3(\text{PO}_4)_2 \cdot 8\text{H}_2\text{O}$ thin films with successive addition of various concentrations of glucose (2.5 to 30 mM) in 1 M KOH at 0.43 V for sample NiPi30 (a), NiPi60 (b) and NiPi90 (c)

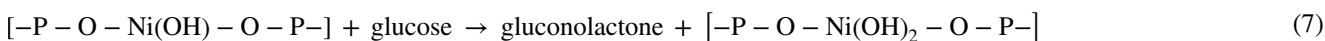
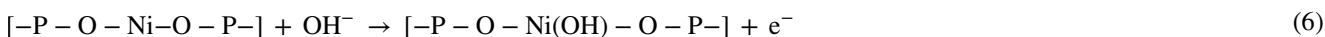
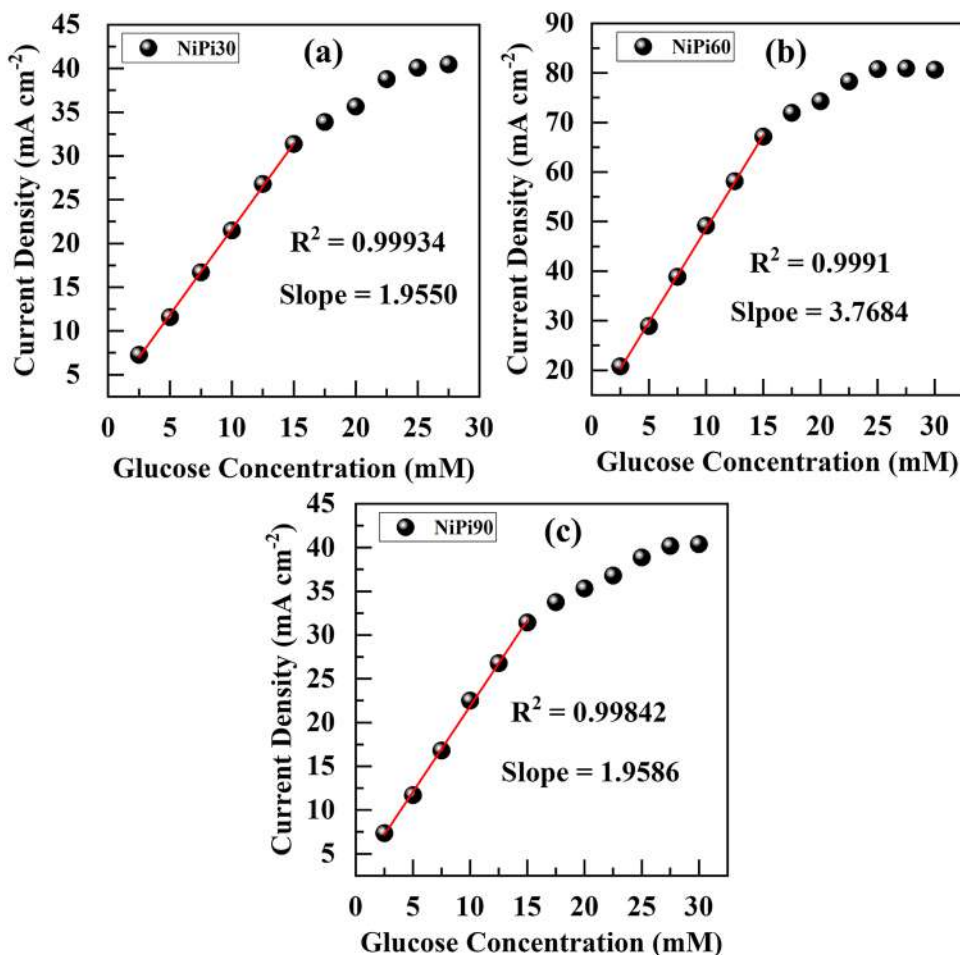


Electrochemical Impedance Spectroscopy (EIS) was conducted for samples NiPi30, NiPi60 and NiPi90 in 1 M KOH electrolyte at 10 mV bias potential with frequency range of 100 kHz to 100 MHz (Fig. S1). The solution resistance (R_s) of samples NiPi30, NiPi60 and NiPi90 are found to be 1.41, 1.18 and 1.34 $\Omega \text{ cm}^{-2}$, respectively. On the other hand electron transfer resistance (R_{ct}) of samples NiPi30, NiPi60 and NiPi90 were observed as 3.06, 2.97 and 3.17 $\Omega \text{ cm}^{-2}$, respectively, confirming a superior electrochemical conductivity of $\text{Ni}_3(\text{PO}_4)_2 \cdot 8\text{H}_2\text{O}$. The equivalent circuit fitted for electrode NiPi60 is displayed in the inset of Fig. (S1). The fitted circuit contains solution resistance (R_s), interface resistance (R_1 and R_2) with a general imperfect capacitor (Q_1 and Q_2) (when $n=1$). The lowest solution resistance (R_s) 1.18 $\Omega \text{ cm}^{-2}$ and electron transfer resistance (R_{ct}) 2.97 $\Omega \text{ cm}^{-2}$ is observed for the NiPi60 electrode. The shorter Warburg impedance ($W = 20 \Omega \text{ cm}^{-2}$) clear the way for higher diffusion of electrolyte inside electrode material and maximum utilization of willow-leaf like structure of

$\text{Ni}_3(\text{PO}_4)_2 \cdot 8\text{H}_2\text{O}$. The EIS results exhibit excellent electrochemical performance of NiPi60 electrode due to its strongly conductive network at optimum thickness of material.

Figure 6 a, b, c demonstrate CV curves of $\text{Ni}_3(\text{PO}_4)_2 \cdot 8\text{H}_2\text{O}$ electrode in a 1 M KOH electrolyte using various glucose concentration ranging from 2.5 to 12.5 mM at 20 mV s^{-1} scan rate for sample NiPi30, NiPi60 and NiPi90. The anodic peaks current increases with the increase in glucose concentration and slightly shift towards the lower positive potential. At another point, little decrement is observed in the cathodic peak current. Electro-oxidation of glucose resulted due to breaking and reconstructing of the bond between nickel and phosphate with an oxygen atom at different kinetic rates [43]. Up to now, not a perfect reaction mechanism is available which can explain the glucose oxidation on nickel based electrodes in the alkaline electrolyte. The accepted glucose oxidation to gluconolactone mechanism, by the familiar of $\text{Ni}^{3+}/\text{Ni}^{2+}$ could be as follows [44],

Fig. 8 The corresponding calibration plot of current response vs glucose concentration in the range from 2.5 mM–30 mM for sample NiPi30 (a), NiPi60 (b) and NiPi90 (c)



The isomerization along with deprotonation process in the glucose is carried out by the oxidative Ni³⁺ species in an electrode.

The sensitivity of the related electrodes is explored through chronoamperometric study. Fig S2 exhibits effect of the applied potential on the current response of Ni₃(PO₄)₂·8H₂O electrode with continuous addition of glucose. It can be noted that, Ni₃(PO₄)₂·8H₂O electrode illustrates the obvious current response of the applied potentials ranging from 0.41 V to 0.43 V. Furthermore, the current response increases with increase in applied potential. The maximum current response is observed when the potential is 0.43 V and an optimal potential (0.43 V) was used in the further chronoamperometric study. The chronoamperometry

analysis of the Ni₃(PO₄)₂·8H₂O was conducted at oxidation potential (0.43 V vs SCE), which is optimized by CV experiment. In 1 M KOH solution different glucose molar concentrations was added at time interval of 60 s (with continuous stirring), which generated a stair-like graph as exhibited in Fig. 7. The proposed sensor exhibited sensitivity of 4700 μA mM⁻¹ cm⁻² for sample (NiPi30), 8312 μA mM⁻¹ cm⁻² (NiPi60) and 2940 μA mM⁻¹ cm⁻² (NiPi90) as displayed in Fig. 7a, b, c, respectively. For each addition of glucose, the current increased stepwise followed by stepwise state current which represent the constant accretion in oxidation current at various glucose concentration [45]. For glucose recognition, the corresponding calibration graphs are plotted and exhibited in Fig. 8a, b, c. The sensor display a linear range from

Table 1 Electrochemical performance comparison of various Ni based materials for non-enzymatic glucose sensing

Electrode material	Linear range (M)	Detection potential (V)	Limit of detection (LOD) (μM)	Sensitivity ($\mu\text{A mM}^{-1} \text{cm}^{-2}$)	Reference
NiO	100–1000 μM	0.5	10	3230	[47]
NiO	0.0002–1 mM	0.5	0.2	2300	[44]
NiO	0–10,000 μM	0.50	0.9	3613	[48]
NiWO ₄	0.006–4122 μM	0.55	0.18	269.83	[49]
HAC/NiO	5–4793 μM	0.5	0.055	1721.5	[50]
NiO/SiC	0.004–7.5 mM	0.5	0.32	2037	[51]
NdNiO ₃	0.0005–4.6 mM	0.54	0.3	1105.1	[52]
NiO-MWCNT/CPE	0.001–14 mM	0.5	19	6527	[53]
Ni foil	10 μM - 10 mM	0.46	1.8	670	[54]
Ni-CCE	0.5–5000 μM	0.45	0.1	0.04	[55]
Ni ₂ P	1.0 μM -3.0 mM	0.5	0.18	7792	[56]
NA/CC					
Ni(OH ₂)-CILE	50 μM - 23 mM	0.55	6	202	[57]
Ni(OH) ₂ HR	0.002–3.8 μM	0.6	0.6	1569	[58]
Ni(OH ₂)-Graphene	2 μM - 3.1 mM	0.54	0.6	11.43	[59]
Ni(OH) ₂ /3D-graphene	0.024–1200 μM	0.45	24 nm	3490	[60]
Ni(OH) ₂ /NF	2–40 μM	0.51	1	1130	[61]
PI/CNT-Ni(OH) ₂	0.001–0.8 mM	0.60	0.36	2071.5	[62]
NiNPs/PEDOT/RGO	1.0 μM - 5.1 mM	0.5	0.8	36.15	[63]
(NiCo)(OH) ₂	25–3700 μM	0.47	–	122.45	[64]
NiCO ₂ O ₄	5–15,000 mM	–	1491	91.34 mV/decade	[65]
Nickel Cobalt Phosphate	2–4470 μM	0.55	0.4	302.99	[66]
Ni ₃ (PO ₄) ₂ ·8H ₂ O/NF	50–1000 μM	0.45	0.097	24,390	[23]
Ni ₃ (PO ₄) ₂ VSB-5	0.1–21 μM 0.5–10.0 mM	0.71	0.04 200	–	[24]
Ni ₃ (PO ₄) ₂ ·8H ₂ O Thin Films	2.5–30 mM	0.43	437	8312	Present work

HAC heteroatom-enriched activated carbon, CPF carbon paste electrode, CC carbon cloth, CCE carbon ceramic electrode, NA/CC nanoarray on conductive carbon cloth, CILE carbon ionic liquid electrode, HR hollow nanorods, NF nickel foam, PI/CNT polyimide/carbon nanotube, PEDOT Poly(3,4-ethylenedioxythiophene), RGO reduced graphene oxide, VSB-5 Versailles Santa Barbara-5

2.5 to 30 mM with correlation coefficient (R^2) of 0.9993 (Fig. 8a), 0.9991 (Fig. 8b) and 0.9984 (Fig. 8c) for sample NiPi30, NiPi60 and NiPi90, respectively. It is observed that, when the glucose concentration increases to 15 mM, it prevents the mass transfer that influences the diffusion of pure glucose molecules closer to the electrode surface. At higher glucose concentrations from 15 to 30 mM the electrochemical response is not linear. The limit of detection (LOD) was calculated using well known following formula [46].

$$LOD = \frac{3 \times SD}{m} \quad (8)$$

where 'SD' is the standard deviation and 'm' is the slope value extracted from calibration graph as shown in Fig. 8a, b, c. The SD of the sensors is 0.2443, 0.5501 and 0.3791 for sample NiPi30, NiPi60 and NiPi90, respectively. Slopes of the NiPi30, NiPi60 and NiPi90 samples are 1.9550, 3.7684 and 1.9586, respectively. The calculated values of LOD using Eq. (8) are 374, 437 and 580 μM for sample NiPi30, NiPi60 and NiPi90, respectively.

Selectivity is the most important analytical factor for the identification of non-enzymatic glucose sensor. The higher sensitivity sample (NiPi60) chosen for selectivity test and sample NiPi60 shows 8312 $\mu\text{A mM}^{-1} \text{cm}^{-2}$ which is higher than all reported data (Table 1) but little lower than Ni₃(PO₄)₂·8H₂O/NF electrode reported by

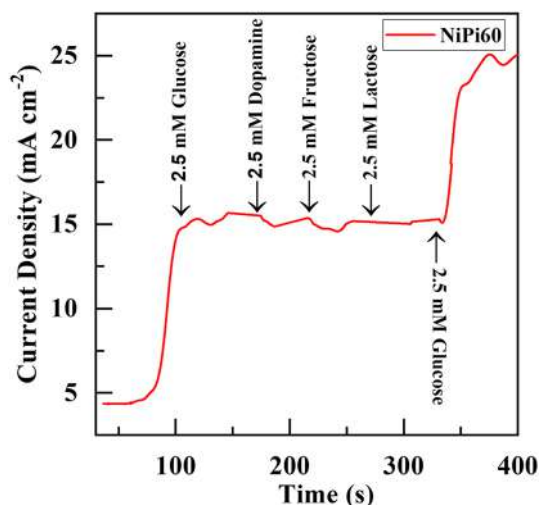


Fig. 9 Chronoamperometric response of the $\text{Ni}_3(\text{PO}_4)_2 \cdot 8\text{H}_2\text{O}$ thin film electrode under the successive additions of 2.5 mM glucose, 2.5 mM dopamine, 2.5 mM fructose and 2.5 mM lactose in 1 M KOH at 0.43 V for sample NiPi60

Padmanathan et al. [23], since they used NF as substrate which may contribute in glucose sensing by self-redox reaction. One of the most essential analytical determinants for a chronoamperometric sensor is the selectivity of the sensor towards goal analytes. The interference test was executed at 0.43 V potential using chronoamperometric technique. The impact of different electroactive species similar to glucose such as, dopamine, fructose and lactose was investigated. Figure 9 shows the chronoamperometric signals of the sensor toward the consecutive addition of glucose (2.5 mM), dopamine (2.5 mM), fructose (2.5 mM) and lactose (2.5 mM) into the 1 M KOH in the 60 s time interval. As expected, $\text{Ni}_3(\text{PO}_4)_2 \cdot 8\text{H}_2\text{O}$ shows extraordinary good feedback for glucose and also negligible feedback for other electroactive species. Subsequently, the current feedback increases sharply for second time glucose addition. This result shows that, the electrode surface was stable as well as sensitive even in the existence of other electroactive species. It concluded that, $\text{Ni}_3(\text{PO}_4)_2 \cdot 8\text{H}_2\text{O}$ has better selectivity toward glucose recognition.

The reproducibility of $\text{Ni}_3(\text{PO}_4)_2 \cdot 8\text{H}_2\text{O}$ sensor is also examined by making at least five electrodes under the similar condition and the chronoamperometric response was noted on injection of 2.5 Mm glucose. The non-enzymatic glucose detection of $\text{Ni}_3(\text{PO}_4)_2 \cdot 8\text{H}_2\text{O}$ sensors with comparative histogram of sensitivity is depicted in Fig. 10.

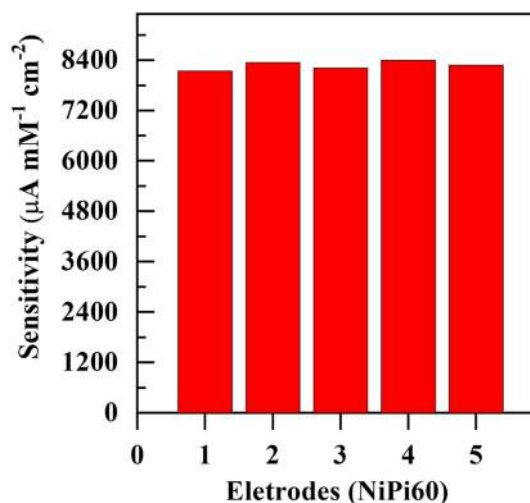
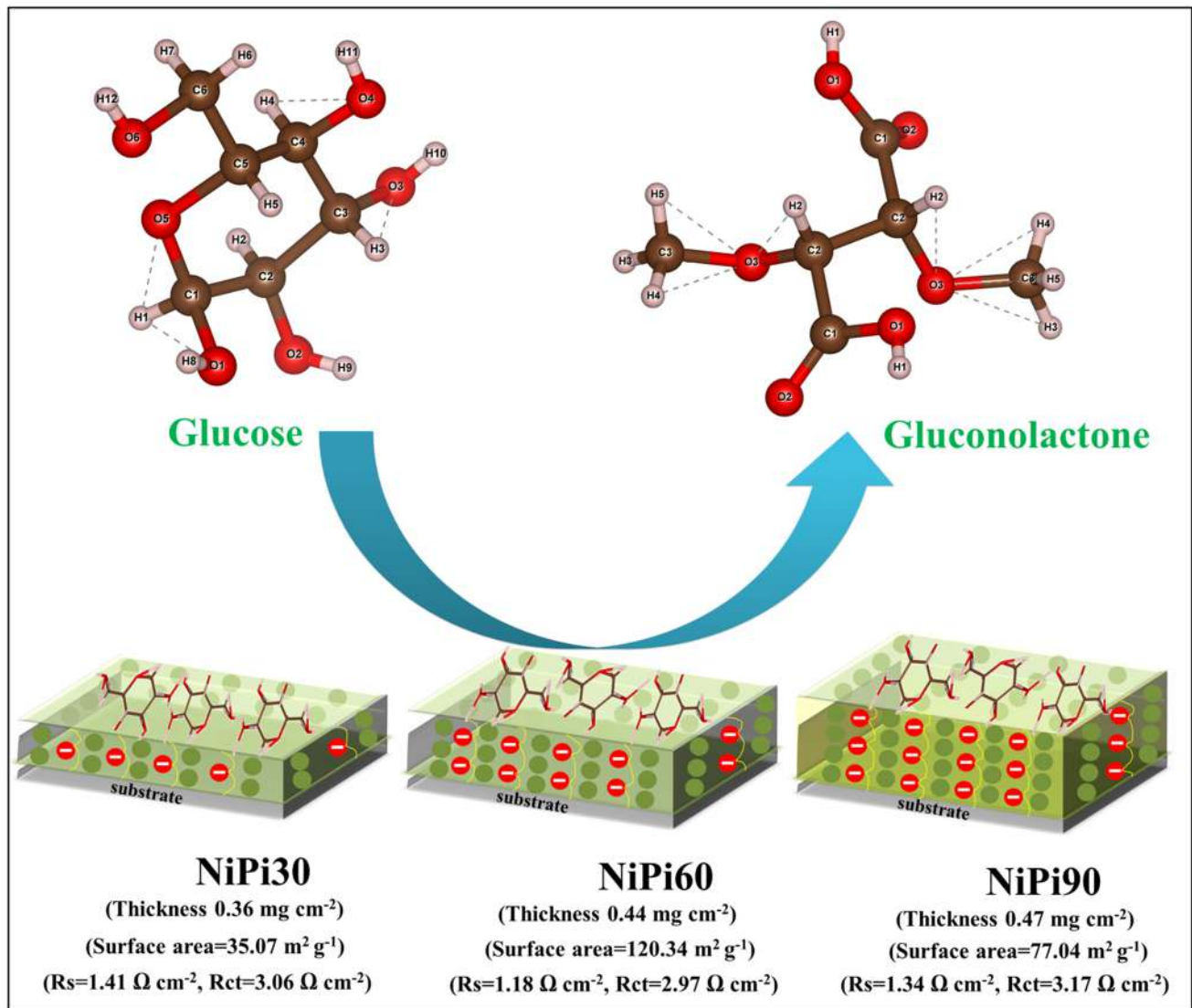


Fig. 10 Reproducibility of five identical $\text{Ni}_3(\text{PO}_4)_2 \cdot 8\text{H}_2\text{O}$ thin films electrode (NiPi60 electrode) for sensitivity of glucose recognition

Low relative standard deviation (RSD) (1.25%) confirms an excellent reproducible sensitivity of $\text{Ni}_3(\text{PO}_4)_2 \cdot 8\text{H}_2\text{O}$ electrodes. The stability of $\text{Ni}_3(\text{PO}_4)_2 \cdot 8\text{H}_2\text{O}$ electrode towards glucose sensing has been determined by executing CV for 1000 cycles in the presence of 1 mM glucose molecules and shown in Fig. S3 (a). It is observed that, $\text{Ni}_3(\text{PO}_4)_2 \cdot 8\text{H}_2\text{O}$ electrode revealed good stability ($\sim 96\%$) in the applied potential window at 100 mV s^{-1} scan rate (Fig. S3 (b)). The good stability of $\text{Ni}_3(\text{PO}_4)_2 \cdot 8\text{H}_2\text{O}$ electrode is mainly because of strong adhesion of willow-leaf like nickel phosphate layers on SS substrate. The above results indicates that, the $\text{Ni}_3(\text{PO}_4)_2 \cdot 8\text{H}_2\text{O}$ sensor has excellent reproducibility as well as long term stability.

Based on the all above results, an exclusive performance of the non-enzymatic glucose sensor is attributed to large surface areas, low resistance pathways possess quickly charge transfer for excellent electrochemical glucose oxidation. Appropriate thickness of the electrode exhibits superior sensing performance due to the presence of multiple electroactive sites of material for adsorption/desorption of glucose molecule and efficient charge transfer as demonstrated in Scheme 1. At the lower thickness, the prepared material gives less active sites for electrochemical glucose sensing. Conversely, film beyond its appropriate thickness, the charge transfer from one site to other up to the charge gathering on the substrate becomes more sluggish and hence resistive.



Scheme 1 Schematic diagram of thickness dependent electrochemical glucose sensing of $\text{Ni}_3(\text{PO}_4)_2 \cdot 8\text{H}_2\text{O}$ thin films electrodes

5 Conclusions

In summary, binder free $\text{Ni}_3(\text{PO}_4)_2 \cdot 8\text{H}_2\text{O}$ thin films with variation in thickness were successfully synthesized by a simple one pot hydrothermal method. As prepared $\text{Ni}_3(\text{PO}_4)_2 \cdot 8\text{H}_2\text{O}$ material shows morphological transformation from micro-plates to willow leaf-like structure with impressively tuned up, by changing the length, thickness and width with varying different reaction time. The glucose sensor of $\text{Ni}_3(\text{PO}_4)_2 \cdot 8\text{H}_2\text{O}$ with optimum thickness (0.44 mg cm^{-2}) revealed maximum sensitivity ($8312 \mu\text{A mM}^{-1} \text{ cm}^{-2}$), a limit of detection ($437 \mu\text{M}$) with favorable linear response range from 2.5 to 30 mM towards glucose. Willow leaf-like structure offers large surface area ($120.34 \text{ m}^2 \text{ g}^{-1}$) with abundant electroactive sites for glucose oxidation. The optimum thickness of $\text{Ni}_3(\text{PO}_4)_2 \cdot 8\text{H}_2\text{O}$ with willow leaf like structure

is favorable for glucose sensor and its better sensitivity suggested usefulness for the practical application.

Acknowledgements Authors are thankful to D. Y. Patil Education Society, Kasaba Bawada, Kolhapur for financial support through research projects sanction No. DYPES/DU/R&D/3109.

Compliance with ethical standards

Conflict of interest The authors declare no competing financial interest.

References

1. E. Crouch, D. Cowell, S. Hoskins, R. Pittson, J. Har, *Biosens. Bioelectron.* **21**, 712–718 (2005)
2. X. Wu, M. Choi, D. Xiao, *Analyst* **125**, 157–162 (2000)

3. Y. Zhang, L. Su, D. Manuzzi, H. Monteros, W. Jia, D. Huo, C. Hou, Y. Lei, *Biosens. Bioelectron.* **31**, 426–432 (2012)
4. Z. Zhu, L. Garcia-Gancedo, A. Flewitt, H. Xie, F. Moussy, W. Milne, *Sensors* **12**, 5996–6022 (2012)
5. S. Park, H. Boo, T. Chung, *Anal. Chim. Acta* **556**, 46–57 (2006)
6. J. Wang, *Chem. Soc. Rev.* **108**, 814–825 (2008)
7. C. Clark, C. Lyons, *Ann. N. Y. Acad. Sci.* **102**, 29–45 (1962)
8. P. Martins, M. Rocha, L. Angnes, H. Toma, K. Araki, *Electroanalysis* **23**, 2541–2548 (2011)
9. R. Mortimer, *Chem. Soc. Rev.* **26**, 147–156 (1997)
10. P. Simon, Y. Gogotsi, *Nat. Mater.* **7**, 845–854 (2008)
11. M. Sivakumar, R. Madhu, S.-M. Chen, V. Veeramani, A. Manikandan, W. Hung, N. Miyamoto, Y.-L. Chueh, *J. Phys. Chem. C* **120**, 17024–17028 (2016)
12. R. Fu, Y. Lu, Y. Ding, L. Li, Z. Ren, X. Si, Q. Wu, *Microchem. J.* **150**, 104106 (2019)
13. M. Li, L. Fang, H. Zhou, F. Wu, Y. Lu, H. Luo, Y. Zhang, B. Hu, *Appl. Surf. Sci.* **495**, 143554 (2019)
14. E. Asadian, S. Shahrokhian, A.-I. Zad, *J. Electroanal. Chem.* **808**, 114–123 (2018)
15. Y. Miao, L. Ouyang, S. Zhou, L. Xu, Z. Yang, M. Xiao, R. Ouyang, *Biosens. Bioelectron.* **53**, 428–439 (2014)
16. B. Li, M. Zheng, H. Xue, H. Pang, *Inorg. Chem. Front.* **3**, 175–202 (2015)
17. X. Li, X. Xiao, Q. Li, J. Wei, H. Xue, H. Pang, *Inorg. Chem. Front.* **5**, 11–28 (2018)
18. S. Jhung, J. Yoon, J. Hwang, A. Cheetham, J. Chang, *Chem. Mater.* **17**, 4455–4460 (2005)
19. J. Yu, A. Wang, J. Tan, X. Li, J. Bokhoven, Y. Hu, *J. Mater. Chem.* **18**, 3601–3607 (2008)
20. X. Wang, Q. Gao, C. Wu, J. Hu, M. Ruan, *Micropor. Mesopor. Mat.* **85**, 355–364 (2005)
21. S. Marje, P. Katkar, S. Kale, A. Lokhande, C. Lokhande, U. Patil, *J. Alloys Compd.* **779**, 49–58 (2019)
22. H. Onoda, T. Ohta, J. Tamaki, K. Kojima, H. Nariai, *Mater. Chem. Phys.* **96**, 163–169 (2006)
23. N. Padmanathan, H. Shao, K. Razeeb, *A.C.S. Appl. Mater. Interfaces* **10**, 8599–8610 (2018)
24. S. Hassaninejad-Darzi, M. Gholami-Esfidvajani, *J. Porous Mater.* **24**, 85–95 (2016)
25. M. Al-Omair, A. Touny, F. Al-Odail, M. Saleh, *Electrocatalysis* **8**, 340–350 (2017)
26. B. Bunker, P. Rieke, B. Tarasevich, A. Campbell, G. Fryxell, G. Graff, L. Song, J. Liu, J. Virden, G. McVay, *Science* **264**, 48–55 (1994)
27. U. Patil, P. Katkar, S. Marje, C. Lokhande, S. Jun, *New J. Chem.* **42**, 20123–20130 (2018)
28. P. Katkar, S. Marje, S. Pujari, S. Khalate, A. Lokhande, U. Patil, *ACS Sustainable Chem. Eng.* **7**, 11205–11218 (2019)
29. S. Khalate, R. Kate, H. Pathan, R. Deokate, *J. Solid State Chem.* **21**, 2737–2746 (2017)
30. F. Omar, A. Numan, S. Bashir, N. Duraisamy, R. Vikneswaran, Y. Loo, K. Ramesh, S. Ramesh, *Electrochim. Acta* **273**, 216–228 (2018)
31. S. Navale, V. Mali, S. Pawar, R. Maneb, M. Naushad, F. Stadler, V. Patil, *RSC Adv.* **5**, 51961–51965 (2015)
32. C. M. Julien, M. Massot (2004) *Proceedings of the International Workshop, (Sofia, Bulgaria)*, pp. 1–1
33. F. Omar, A. Numan, N. Duraisamy, S. Bashir, K. Ramesh, S. Ramesh, *RSC Adv.* **6**, 76298–76306 (2016)
34. N. Prokopchuk, V. Kopilevich, L. Voitenko, *Russ. J. Appl. Chem.* **81**, 386–391 (2008)
35. J.B. Condon, *Surface Area and Porosity Determinations by Physisorption: Measurements and Theory* (Elsevier, Amsterdam, 2006), pp. 6–14
36. U. Patil, R. Ghorpade, M. Nam, A. Nalawade, S. Lee, H. Han, S. Jun, *Sci. Rep.* **6**, 3490 (2016)
37. J. Gunjekar, T. Kim, H. Kim, I. Kim, S. Hwang, *J. Am. Chem. Soc.* **133**, 14998–15007 (2011)
38. X. Peng, H. Chai, Y. Cao, Y. Wang, H. Dong, D. Jia, W. Zhou, *Materials Today Energy* **7**, 129–135 (2018)
39. H. Wu, Y. Gao, H. Li, *CrystEngComm* **12**, 3607–3611 (2010)
40. H. Shao, N. Padmanathan, D. McNulty, C. Dwyer, K. Razeeb, *A.C.S. Appl. Mater. Interfaces* **8**, 28592–28598 (2016)
41. M. Bajdich, M. García-Mota, A. Vojvodic, J. Nørskov, A. Bell, *J. Am. Chem. Soc.* **135**, 13521–13530 (2013)
42. G. Wu, N. Li, D. Zhou, K. Mitsuo, B. Xu, *J. Solid State Chem.* **177**, 3682–3692 (2004)
43. D. Martín-Yerga, J. Carrasco-Rodríguez, J. Fierro, F. Alonso, A. Costa-García, *Electrochim. Acta* **229**, 102–111 (2017)
44. G. Li, X. Wang, L. Liu, R. Liu, F. Shen, Z. Cui, W. Chen, T. Zhang, *Small* **11**, 731–739 (2015)
45. S. Premalatha, P. Sivasakthi, G. Bapu, *RSC Adv.* **5**, 74374–74380 (2015)
46. K. Naik, A. Gangan, B. Chakraborty, S. Nayak, C. Rout, *A.C.S. Appl. Mater. Interfaces* **9**, 23894–23903 (2017)
47. B. Zhao, T. Wang, L. Jiang, K. Zhang, M. Yuen, J. Xu, X. Fu, R. Sun, C. Wong, *Electrochim. Acta* **192**, 205–215 (2016)
48. H. Liu, X. Wu, B. Yang, Z. Li, L. Lei, X. Zhang, *Electrochim. Acta* **174**, 745–752 (2015)
49. S. Mani, V. Vedyappan, S.M. Chen, R. Madhu, V. Pitchaimani, J.Y. Chang, S.B. Liu, *Sci. Rep.* **6**, 24128 (2016)
50. V. Veeramani, R. Madhu, S. Chen, P. Veerakumar, C. Hung, S. Liu, *Sens. Actuator B-Chem.* **221**, 1384–1390 (2015)
51. P. Yang, X. Tong, G. Wang, Z. Gao, X. Guo, Y. Qin, *A.C.S. Appl. Mater. Interfaces* **7**, 4772–4777 (2015)
52. M. Sivakumar, K. Pandi, S.-M. Chen, Y.-H. Cheng, M. Sakthivel, *New J. Chem.* **41**, 11201–11207 (2017)
53. R. Prasad, N. Gorjizadeh, R. Rajarao, V. Sahajwalla, B. Bhat, *RSC Adv.* **5**, 44792–44799 (2015)
54. K. Toghill, L. Xiao, M. Phillips, R. Compton, *Sens. Actuator B-Chem.* **147**, 642–652 (2010)
55. A. Salimi, M. Roushani, *Electrochem. Commun.* **7**, 879–887 (2005)
56. T. Chen, D. Liu, W. Lu, K. Wang, G. Du, A. Asiri, X. Sun, *Anal. Chem.* **88**, 7885–7889 (2016)
57. A. Safavi, N. Maleki, E. Farjami, *Biosens. Bioelectron.* **24**, 1655–1660 (2009)
58. J. Yang, M. Cho, Y. Lee, *Sens. Actuator B-Chem.* **222**, 674–681 (2016)
59. Y. Zhang, F. Xu, Y. Sun, Y. Shi, Z. Wen, Z. Li, *J. Mater. Chem.* **21**, 16949–16954 (2011)
60. I. Shackery, U. Patil, M. Song, J. Sohn, S. Kulkarni, S. Some, S. Lee, M. Nam, W. Lee, S. Jun, *Electroanalysis* **27**, 2363–2370 (2015)
61. Y. Zhao, G. Gu, S. You, R. Ji, H. Suo, C. Zhao, F. Liu, *RSC Adv.* **5**, 53665–53670 (2015)
62. Y. Jiang, S. Yu, J. Li, L. Jia, C. Wang, *Carbon* **63**, 367–375 (2013)
63. N. Hui, S. Wang, H. Xie, S. Xu, S. Niu, X. Luo, *Sens. Actuator B-Chem.* **221**, 606–613 (2015)
64. C. Lien, J. Chen, C. Hu, D. Wong, *J. Taiwan Inst. Chem. Engrs.* **45**, 846–851 (2014)
65. M. Hussain, Z. Ibupoto, M. Abbasi, X. Liu, O. Nur, M. Willander, *Sensors* **14**, 5415–5425 (2014)
66. Y. Shu, B. Li, J. Chen, Q. Xu, H. Pang, X. Hu, *A.C.S. Appl. Mater. Interfaces* **10**, 2360–2367 (2018)

Publisher's Note Springer Nature remains neutral with regard to jurisdictional claims in published maps and institutional affiliations.



Facile Synthesis of Microstrip-Like Copper Phosphate Hydroxide Thin Films for Supercapacitor Applications

SACHIN S. PUJARI,¹ SUJIT A. KADAM,² YUAN-RON MA,²
PRANAV K. KATKAR,¹ SUPRIYA J. MARJE,¹ SURAJ A. KHALATE,¹
ABHISHEK C. LOKHANDE,³ and UMAKANT M. PATIL^{1,4}

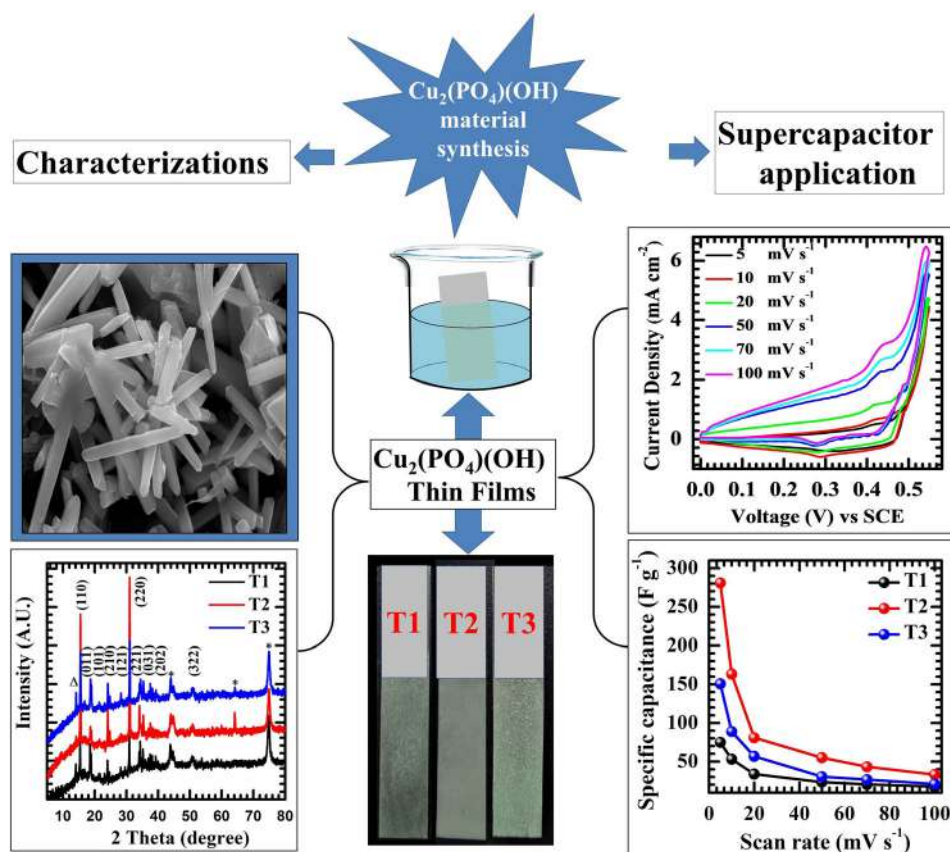
1.—Centre for Interdisciplinary Research, D. Y. Patil Education Society, Kasaba Bawada, Kolhapur 416 006, India. 2.—Department of Physics, National Dong Hwa University, Hualien 97401, Taiwan. 3.—Department of Physics, Khalifa University of Science and Technology (KUST), Abu Dhabi, United Arab Emirates. 4.—e-mail: umakant.physics84@gmail.com

Binder-free copper phosphate hydroxide [Cu₂(PO₄)(OH)] thin films have been prepared on stainless-steel (SS) substrates at 393 K via a facile hydrothermal method. X-ray diffraction analysis confirmed the formation of orthorhombic-structured copper phosphate hydroxide [Cu₂(PO₄)(OH)] thin films with uniform microstrip-like morphology and Brunauer–Emmett–Teller (BET) surface area of 5.26 m² g⁻¹. The electrochemical performance of the films depended on their thickness, with a maximum specific capacitance of 280 F g⁻¹ at a scan rate 5 mV s⁻¹ in 1 M KOH electrolyte. The [Cu₂(PO₄)(OH)] electrode delivered an energy density of 3.85 Wh kg⁻¹ and a power density of 264.70 W kg⁻¹ with excellent (91%) capacitive retention after 2000 cycles. This excellent electrochemical performance shows that such microstrip-like Cu₂(PO₄)(OH) thin films are promising electrodes for high-performance supercapacitors.

(Received October 18, 2019; accepted March 18, 2020)

Published online: 05 April 2020

Graphic Abstract



Key words: Copper phosphate hydroxide, hydrothermal method, microstrip, supercapacitor, thin film

INTRODUCTION

Among current energy storage solutions, supercapacitors are the most practical and effective devices due to their advantages over conventional energy storage devices.^{1,2} All energy storage technologies act as interface between energy generation and conversion, electrochemical energy storage is used as upgraded interface. Supercapacitors have attracted huge attention due to their excellent cycling stability and high power density compared with batteries. The capacitive energy storage effect is based on conduction of electrons and ions, which depends on the electrochemically active sites, surface area, and conductivity of the material.³⁻⁶ Depending on their charge storage mechanism, supercapacitors can generally be divided into two types, viz. electric double-layer capacitors (EDLCs) with carbon-based electrodes^{7,8} and

pseudocapacitors with conducting polymer, metal oxide/sulfide, hydroxide, etc. electrodes.^{9,10}

The class of electrodes comprising metal oxides/hydroxides and sulfides demonstrates good specific capacitance,¹¹⁻¹⁸ but suffers from limitations in terms of poor electrical conductivity and stability.^{19,20} However, many transition-metal phosphates, consisting of an open framework with large solid channels and cavities, have recently been demonstrated to show excellent ion conductivity and been analyzed as pseudocapacitive electrode materials.²¹ Such phosphates contain oxyanions of pentavalent phosphorus, ranging from single PO_4^{3-} to infinite tunnel-type frameworks.²² Metal phosphates exhibit highly preferable electrical conductivity and flexibility in terms of tuning the nanostructure.^{23,24} Depending on the coordination between the metal ions and phosphate anions or molecules, metal phosphates can exhibit distinctive

structures.^{25,26} Only one report on synthesis of copper phosphate material is available in literature. Karaphun et al.²⁷ prepared copper pyrophosphate by a hydrothermal method and reported a maximum specific capacitance of 297.5 F g^{-1} at a current density of 1 A g^{-1} . Various methods have been applied to prepare binder-free copper-based oxide/hydroxide materials for use in supercapacitor applications.^{27–32} To date, copper oxide/hydroxide or mixed phases such as oxyhydroxides have been widely investigated for use in supercapacitor electrodes, since the hydroxide phase with greater interplanar distance can greatly enhance the charge storage performance and improve its stability. Gurav et al.²⁸ synthesized copper hydroxide on nickel foam using a chemical bath deposition (CBD) method and reported a specific capacitance of 120 F g^{-1} at a scan rate of 10 mV s^{-1} . Kang et al.²⁹ prepared uniform copper hydroxide nanotubes using a one-pot solution method and reported a high areal capacitance of 278 mF cm^{-2} at a current density of 1 mA cm^{-2} . Similarly, Patil et al.³⁰ employed the CBD method to deposit $\text{CuO}/(\text{OH})_2$ with different nanostructures over a stainless-steel (SS) surface and achieved a maximum specific capacitance of up to $\sim 340 \text{ F g}^{-1}$ at a current density of 1 mA cm^{-2} . Awale et al.³¹ synthesized copper oxide thin films by using a hydrothermal method and reported a maximum specific capacitance of 133 F g^{-1} . Among the various chemical techniques, the hydrothermal method offers numerous advantages for preparation of nano/micromaterials.³² According to this literature survey, binder-free preparation of copper phosphate hydroxide thin films on SS substrates using a

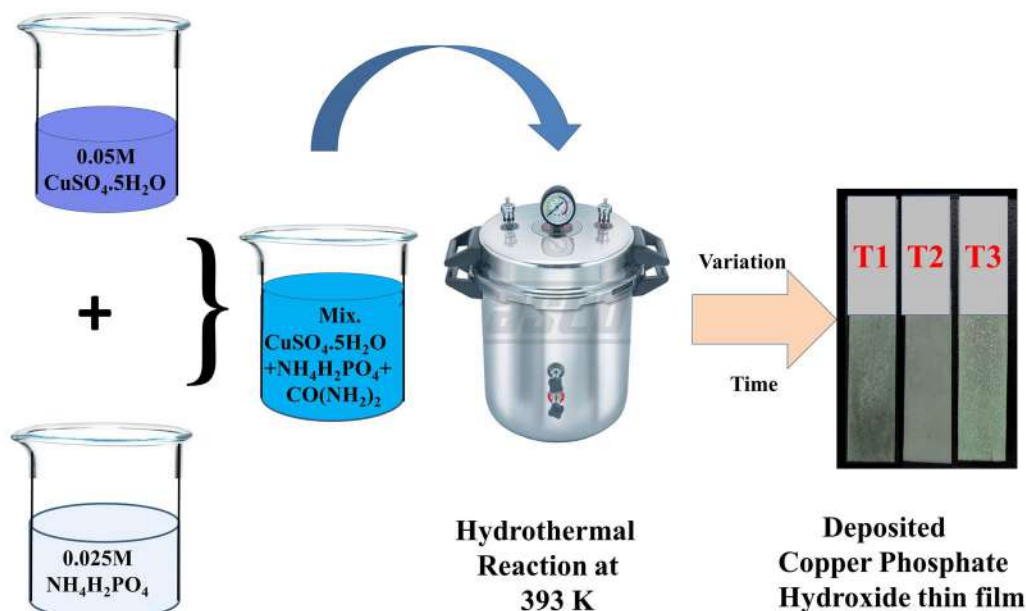
hydrothermal method and their application in supercapacitors have not yet been studied.

We thus report herein for the first time binder-free deposition of copper phosphate hydroxide [$\text{Cu}_2(\text{PO}_4)(\text{OH})$] thin films using a hydrothermal method. The deposition time was varied to 90 min, 120 min, and 150 min and the effect on the structural, compositional, and surface morphological properties investigated. According to surface morphological studies, the $\text{Cu}_2(\text{PO}_4)(\text{OH})$ thin films showed a microstrip-like structure. The surface area of the $\text{Cu}_2(\text{PO}_4)(\text{OH})$ thin films was measured by the Brunauer–Emmett–Teller (BET) technique. The supercapacitive electrochemical performance of the films was studied by cyclic voltammetry (CV), galvanostatic charge/discharge (GCD) measurements, and electrochemical impedance spectroscopy (EIS).

EXPERIMENTAL PROCEDURES

Synthesis of Copper Phosphate Hydroxide Thin Films

All the chemicals used in the hydrothermal preparation of the $\text{Cu}_2(\text{PO}_4)(\text{OH})$ thin films were purchased from Sigma Aldrich with analytical reagent (AR) grade and purity of 99.9%. SS (304 grade) with dimensions of $1 \text{ cm} \times 5 \text{ cm}$ was used as a conducting substrate to deposit the films. The surface of the SS substrates was polished using smooth polishing paper (zero fine grade) then washed with detergent. The substrates were then cleaned ultrasonically in water for 15 min. In a typical synthesis process, a chemical bath was prepared by mixing aqueous 20 mL 0.05 M cupric sulfate ($\text{CuSO}_4 \cdot 5\text{H}_2\text{O}$), 20 mL 0.025 M ammonium



Scheme 1. Schematic of preparation of copper phosphate hydroxide thin film electrode by hydrothermal method.

phosphate monobasic ($\text{NH}_4\text{H}_2\text{PO}_4$), and 10 mL 0.1 M urea (NH_2CONH_2). The SS substrates were held vertically in the solution bath, which was placed in a hydrothermal autoclave maintained at 393 K under pressure of 17 psi. The reaction time was varied to 90 min, 120 min, and 150 min, and the prepared films are denoted as T1, T2, and T3, respectively. A schematic of the $\text{Cu}_2(\text{PO}_4)(\text{OH})$ deposition is shown in Scheme 1. After deposition, the resulting greenish-colored thin films were rinsed in double-distilled water (DDW) and dried at ambient temperature. These films were used for characterization and electrochemical testing.

Materials Characterization

The crystalline phases present in the $\text{Cu}_2(\text{PO}_4)(\text{OH})$ thin films were analyzed by x-ray powder diffractometer (XRD, MiniFlex 600, Cu K_α radiation at $\lambda = 1.5406 \text{ \AA}$; Rigaku). To study the chemical bonding and functional groups present in the prepared samples, Fourier-transform infrared (FTIR) spectroscopy was carried out using an Alpha (II) Bruker unit. The surface area of the films was estimated by Brunauer–Emmett–Teller (BET) analysis (Belsorp II mini). The surface morphology and elemental composition of the films were investigated by field-emission scanning electron microscopy and energy-dispersive x-ray spectroscopy (FESEM, JSM-7001F, JEOL), respectively. The electrochemical supercapacitive properties of the film electrode were tested by using a ZIVE MP1 electrochemical workstation.

Electrochemical Measurements

The electrochemical supercapacitive properties of the $\text{Cu}_2(\text{PO}_4)(\text{OH})$ electrodes were investigated using a half-cell arrangement in 1 M KOH electrolyte with the $\text{Cu}_2(\text{PO}_4)(\text{OH})$ thin film as a working electrode, a platinum plate as a counter-electrode, and a saturated calomel electrode (SCE) as a reference electrode. Cyclic voltammetry (CV), electrochemical impedance spectroscopy (EIS), and galvanostatic charge/discharge (GCD) measurements were performed. CV curves were obtained at different scan rates from 5 mV s^{-1} to 100 mV s^{-1} in the potential window from 0 V to +0.55 V. The GCD performance was studied in the potential window from 0 V to +0.45 V at various current densities from 0.4 mA cm^{-2} to 2 mA cm^{-2} . EIS was carried out in the range from 100 mHz to 1 MHz at an amplitude of 10 mV. The specific capacitance (C_s), energy density (E_d), and power density (P_d) were calculated from the CV and GCD curves using Eqs. 1–4:

$$C_s (\text{F g}^{-1}) = \frac{\int I dv}{m \times v \times \Delta V} \quad (\text{for CV}), \quad (1)$$

$$C_s (\text{F g}^{-1}) = \frac{I \times \Delta t}{m \times \Delta V} \quad (\text{for GCD}), \quad (2)$$

$$E_d (\text{W h kg}^{-1}) = \frac{1}{2} C_s (\Delta V)^2, \quad \text{and} \quad (3)$$

$$P_d (\text{W kg}^{-1}) = \frac{E}{\Delta t}, \quad (4)$$

where $\int I dv$, m , v , I , Δt , and ΔV represent the area under the CV curve, the mass of active substance on the electrode (g), the scan rate (mV s^{-1}), the current density (mA cm^{-2}), the discharge time (s), and the potential window (V), respectively.

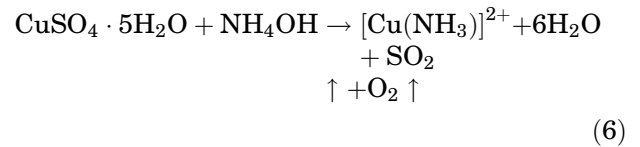
RESULTS AND DISCUSSION

$\text{Cu}_2(\text{PO}_4)(\text{OH})$ Thin Film Formation Mechanism

As shown in the schematic, cupric sulfate ($\text{CuSO}_4 \cdot 5\text{H}_2\text{O}$) and ammonium phosphate monobasic ($\text{NH}_4\text{H}_2\text{PO}_4$) were used as copper and phosphate precursors, respectively, whereas urea was used as hydrolyzing agent. In the film formation reaction, urea decomposes at temperatures above 363 K as per Eq. 5.^{33,34}



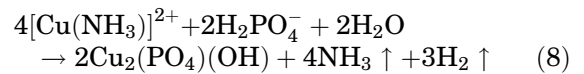
The NH_4^+ released from urea as per this reaction acts as a complexing agent in the bath, and Cu^{2+} ions present in the solution are complexed as $[\text{Cu}(\text{NH}_3)]^{2+}$ (Eq. 6).



This complex acts as a source of Cu^{2+} ions and slowly releases Cu^{2+} ions to prevent fast homogeneous nucleation. Conversely, in aqueous medium, decomposition of $\text{NH}_4\text{H}_2\text{PO}_4$ takes place according to Eq. 7:



The dihydrogen phosphate (H_2PO_4^-) ions react with the $[\text{Cu}(\text{NH}_3)]^{2+}$ complex, resulting in formation of copper phosphate hydroxide $[\text{Cu}_2(\text{PO}_4)(\text{OH})]$ as described in Eq. 8:



$\text{Cu}_2(\text{PO}_4)(\text{OH})$ thin films were thus prepared using different reaction times of 90 min, 120 min, and 150 min and are shown in Scheme 1 as T1, T2, and T3, respectively. It was observed that the films obtained using the different deposition times showed a uniform coating over the SS substrate. The weight of the deposited film material was measured using the gravimetric weight difference method, revealing that the deposited mass increased with increasing deposition time (Supplementary Fig. S1). The deposited mass was 0.21 mg cm^{-2} , 0.34 mg cm^{-2} , and 0.62 mg cm^{-2} for samples T1, T2, and T3, respectively.

XRD, FTIR, and BET Analyses

Figure 1 shows the XRD patterns of the copper phosphate hydroxide thin films hydrothermally deposited on SS substrates (samples T1, T2, and T3). The major peaks observed at 15.52° , 18.69° , 18.96° , 24.16° , 28.27° , 30.93° , 34.33° , 35.41° , 37.52° , and 50.81° can be ascribed to orthorhombic (110), (011), (101), (210), (121), (220), (221), (031), (202), and (322) crystal planes of copper phosphate hydroxide [$\text{Cu}_2(\text{PO}_4)(\text{OH})$] in Joint Committee on Powder Diffraction Standards (JCPDS) card no. 01-083-1557. The peak at 14.17° (Δ) corresponds to the (001) crystal plane of copper hydrogen phosphate ($\text{CuH}_2\text{P}_2\text{O}_7$) in JCPDS card no. 00-034-0605. The peaks marked with an asterisk at 43.90° , 64.21° , and 74.76° can be ascribed to the SS substrate.

Figure 2 shows the FTIR spectrum of the $\text{Cu}_2(\text{PO}_4)(\text{OH})$ thin-film sample T2 in the wavenumber range from 400 cm^{-1} to 4000 cm^{-1} . The absorption band at 446 cm^{-1} is attributed to Cu–O stretching vibrations.³⁵ The peak at 617 cm^{-1} corresponds to the stretching vibration mode of phosphate molecules (P–O–P).³⁶ The vibrational bands of the PO_4^{3-} anion are observed at wavenumbers of around 876 cm^{-1} , 980 cm^{-1} , and 1082 cm^{-1} .^{37,38} The band at 1640 cm^{-1} is caused by the twisting mode of water molecules $\delta(\text{H-OH})$ present in the sample.³⁹ A broad band ranging from 3136 cm^{-1} to 3563 cm^{-1} is assigned to stretching vibrations of adsorbed water molecules and O–H from hydroxide,⁴⁰ and vibration of hydrogen-bonded metal hydroxide.⁴¹ These results confirm that the material contained phosphate and hydroxide groups, attributed to the formation of $\text{Cu}_2(\text{PO}_4)(\text{OH})$ thin film.

To calculate the surface area of the $\text{Cu}_2(\text{PO}_4)(\text{OH})$ thin films, N_2 adsorption–desorption (BET) measurements were applied on sample T1, T2, and T3; the results are presented in Fig. 3a, b, and c. According to the International Union of Pure and Applied Chemistry (IUPAC) classification,⁴² the most physisorption isotherms can be separated into six types. In the present case, all the samples displayed a typical type III isotherm and a type H3 hysteresis loop, indicating plate-like particles producing slit-shaped pores. The prepared materials exhibited a macroporous structure with surface

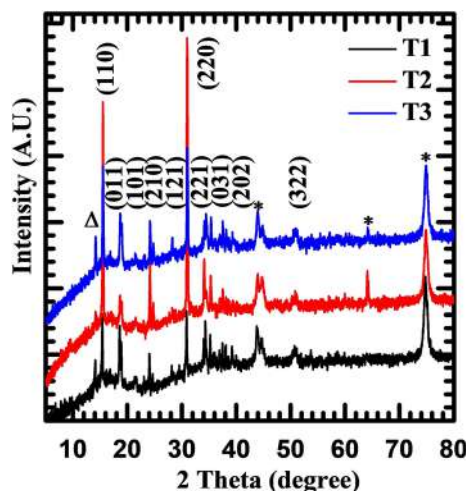


Fig. 1. XRD patterns of copper phosphate hydroxide thin film samples T1, T2, and T3.

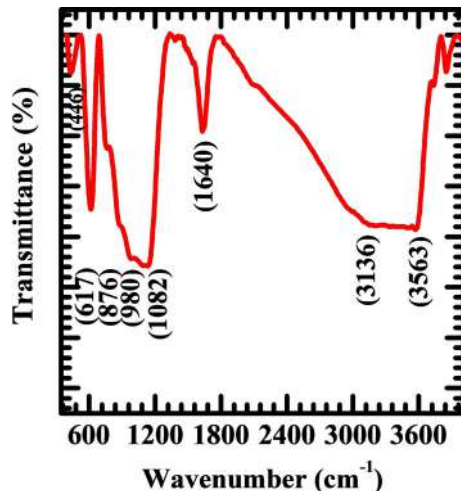


Fig. 2. FTIR spectrum of $\text{Cu}_2(\text{PO}_4)(\text{OH})$ thin-film sample T2.

area of $2.70 \text{ m}^2 \text{ g}^{-1}$, $5.26 \text{ m}^2 \text{ g}^{-1}$, and $3.91 \text{ m}^2 \text{ g}^{-1}$ for sample T1, T2, and T3, respectively. The pore volume versus pore diameter is plotted for all samples in Supplementary Fig. S2, revealing an average pore diameter of 10.65 nm, 24.35 nm, and 21.3 nm for sample T1, T2, and T3, respectively. This high surface area and macroporosity of the electrodes could be favorable for high electrochemical capacitive performance.

FE-SEM Analysis

FE-SEM images of the $\text{Cu}_2(\text{PO}_4)(\text{OH})$ thin-film sample T2 at different magnifications ($\times 2\text{k}$, $\times 4\text{k}$, and $\times 6\text{k}$) are shown in Fig. 4a, b, and c. The substrate surface is well covered with microflowers consisting of bunches of microstrips (Fig. 4a). FE-SEM imaging at higher magnification ($\times 4\text{k}$, Fig. 4b) shows that the microstrips are interconnected with each other. The average length, width, and thickness of the microstrips were $3.96 \mu\text{m}$, $0.37 \mu\text{m}$, and

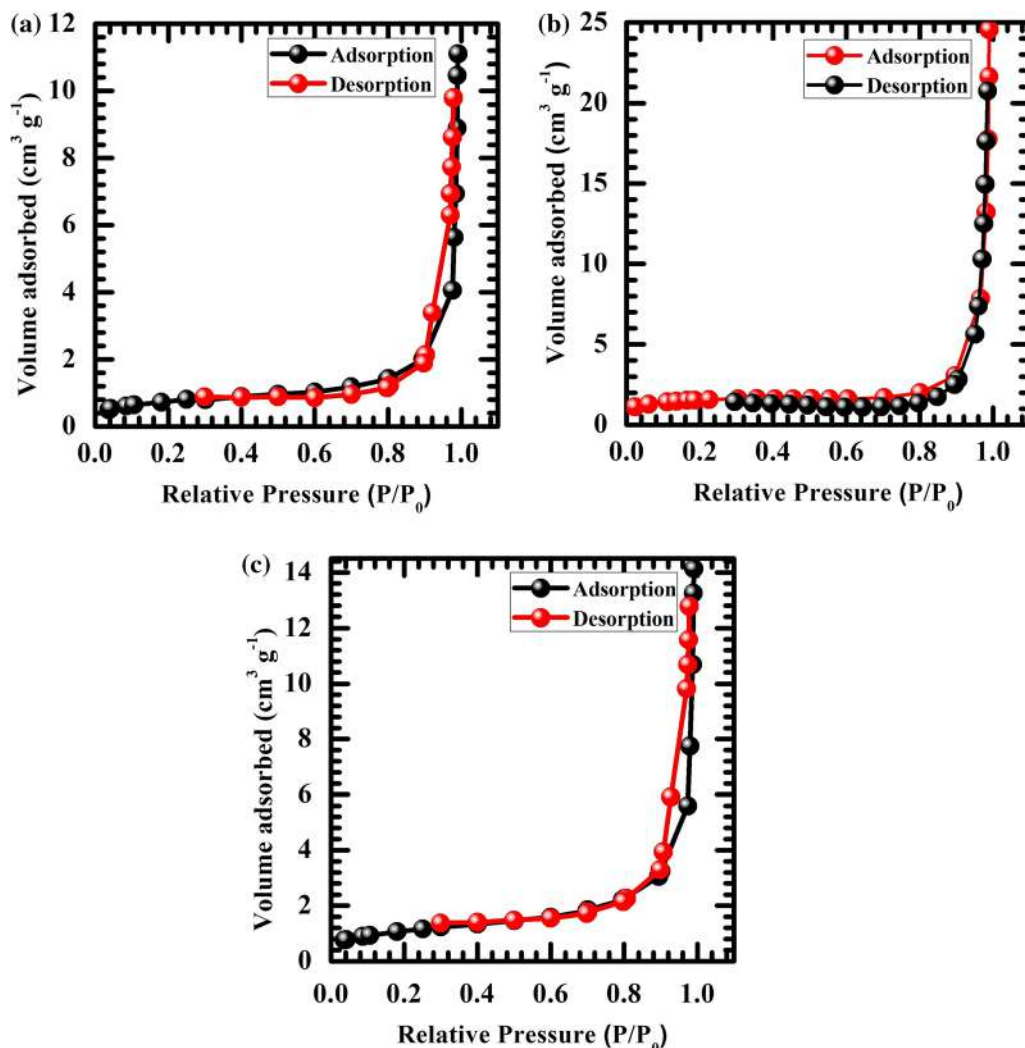


Fig. 3. Nitrogen adsorption–desorption isotherms of $\text{Cu}_2(\text{PO}_4)(\text{OH})$ thin-film samples (a) T1, (b) T2, and (c) T3.

$0.29 \mu\text{m}$, respectively, as revealed in Fig. 4c ($\times 6\text{k}$). The images show a good coverage of identical crack-free bunches of microrods all over the SS substrate. Also, to measure the thickness, cross-sectional FE-SEM images of samples T1, T2, and T3 (at $850\times$ magnification) are provided in Supplementary Fig. S3. The thickness increased from sample T1 ($8.23 \mu\text{m}$) to T3 ($13.03 \mu\text{m}$), analogous to the results obtained by the weight difference method. The energy-dispersive x-ray (EDX) spectrum for sample T2 (Fig. 4d) shows the elemental composition of the $\text{Cu}_2(\text{PO}_4)(\text{OH})$ material. The EDX results for samples T1 and T3 are shown in Supplementary Fig. S4. The EDX results reveal that copper (Cu), oxygen (O), and phosphorus (P) elements were present in the material. The atomic ratio of copper to phosphorus (Cu:P) for samples T1, T2, and T3 was 2:1.04, 2:1.33, and 2:1.03, respectively, being close to the 2:1 as per the chemical composition. The obtained chemical composition and excess oxygen confirm that the material in the thin films was $\text{Cu}_2(\text{PO}_4)(\text{OH})$. These EDX results thus confirm the

formation of copper phosphate hydroxide in thin-film form, consistent with the XRD and FTIR analyses described above.

A schematic of a possible growth model for $\text{Cu}_2(\text{PO}_4)(\text{OH})$ thin film with microstrip-like structure is shown in Fig. 4e. The growth of the particles occurs via various steps, viz. nucleation and coalescence, followed by stacking of the particles to form microstrips.⁴³ The microstrip-like structure may increase the surface area and electrochemically active sites, while the interconnected morphology decreases the resistance and provides feasible paths for charge transfer. Moreover, the microstrip-like structure may support fast ion and electron transport during charging and discharging.⁴⁴

Electrochemical Capacitive Study

Cyclic Voltammetry (CV)

Figure 5a compares the CV curves of the $\text{Cu}_2(\text{PO}_4)(\text{OH})$ thin films within the potential range

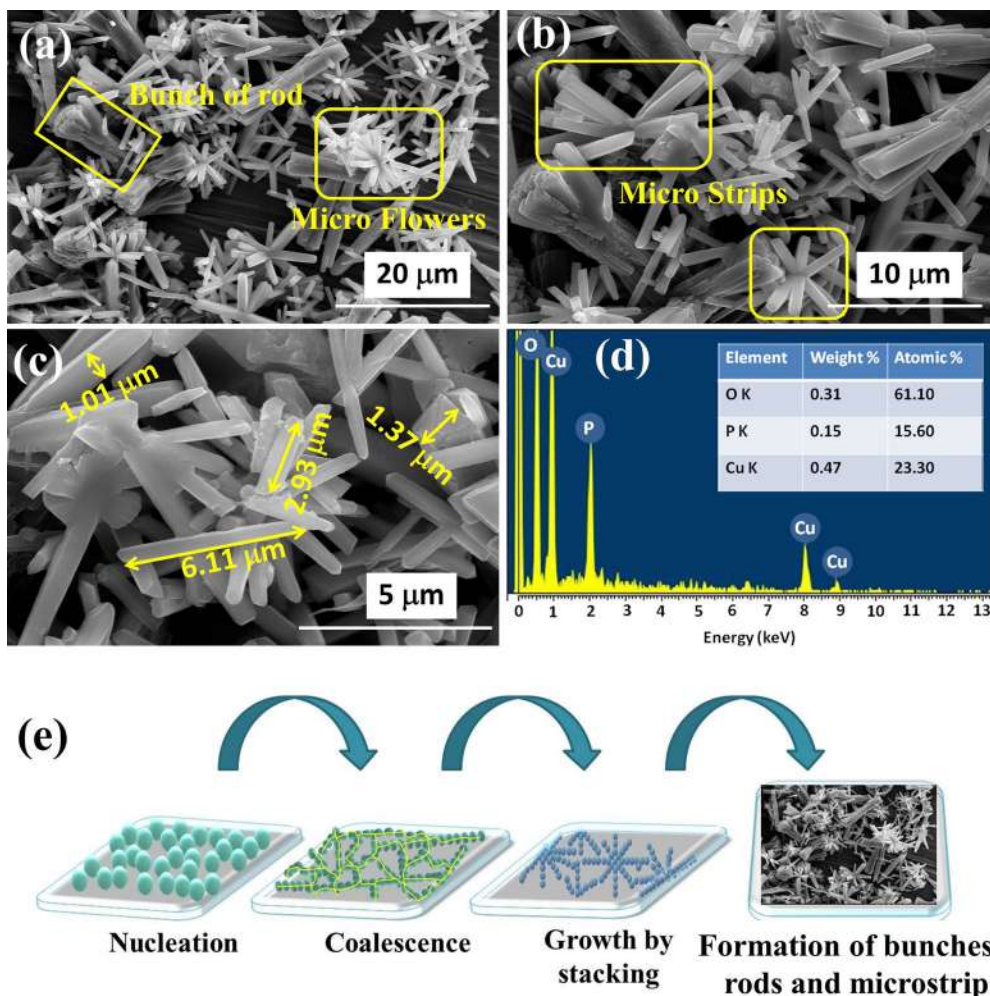
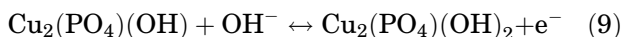


Fig. 4. FE-SEM images of $\text{Cu}_2(\text{PO}_4)(\text{OH})$ sample T2 at (a) $\times 2\text{k}$, (b) $\times 4\text{k}$, and (c) $\times 6\text{k}$, and (d) EDX spectrum of $\text{Cu}_2(\text{PO}_4)(\text{OH})$ sample T2 and, (e) schematic showing growth model for $\text{Cu}_2(\text{PO}_4)(\text{OH})$ thin film.

of 0 V to +0.55 V versus SCE, obtained at a constant scan rate of 50 mV s^{-1} for samples T1, T2, and T3. Note that all three CV curves exhibit strong redox peaks for faradaic reversible reaction in KOH electrolyte. This result indicates that the capacitance is based on a redox mechanism of the $\text{Cu}_2(\text{PO}_4)(\text{OH})$ electrode and confirms the pseudocapacitive nature of the material. Intercalation and deintercalation of OH^- ions by the electrode is a characteristic of the pseudocapacitance, as follows:



It was observed that sample T2 showed the maximum current under the curve compared with the T1 and T3 electrodes. Figure 5b shows the CV curves of sample T2 obtained at various scan rates from 5 mV s^{-1} to 100 mV s^{-1} , showing that the area under the curve increases with increasing scan rate. It can be concluded that the voltammetric current is directly proportional to the CV scan rate, indicating the capacitive behavior of the electrode.⁴⁵ The CV

curves of samples T1 and T3 obtained at scan rates from 5 mV s^{-1} to 100 mV s^{-1} are shown in Supplementary Fig. S5. Figure 5c shows a plot of the specific capacitance versus the scan rate. At high scan rate, the low values of specific capacitance can be attributed to inner active sites where redox transitions cannot proceed completely, possibly because of the diffusion effect in the electrode.^{46,47} The maximum specific capacitances for the T1, T2, and T3 electrodes were 74.8 F g^{-1} , 280.8 F g^{-1} , and 150.5 F g^{-1} , respectively, at a scan rate of 5 mV s^{-1} . These results clearly show that the maximum specific capacitance of the electrode (280.8 F g^{-1}) was based on a redox mechanism with sufficient electroactive material, since the maximum specific capacitance was observed for the optimum thickness ($12.85 \mu\text{m}$).

A power law was used to differentiate the relative contributions of battery- and capacitive-type mechanisms for the $\text{Cu}_2(\text{PO}_4)(\text{OH})$ thin-film electrode. According to this power law, the relation between the peak current and scan rate can be expressed as

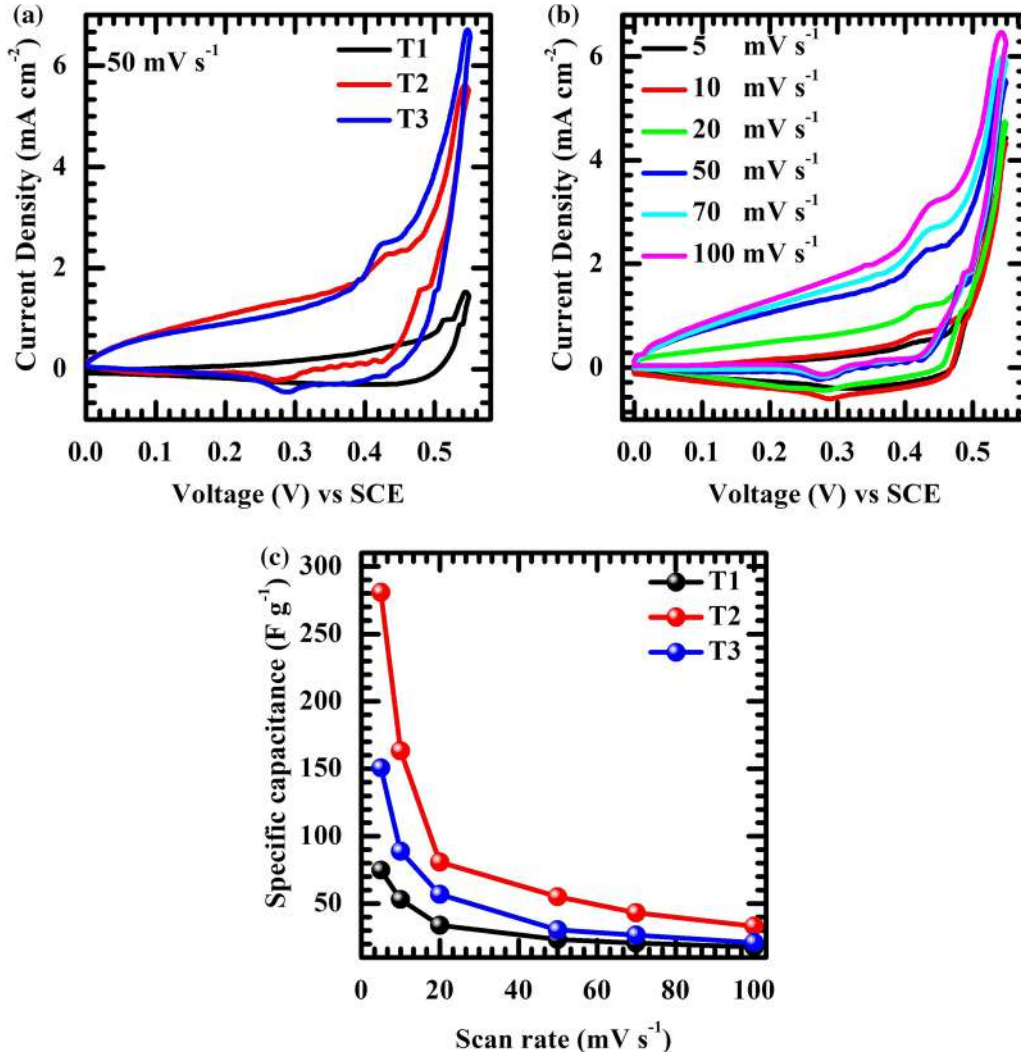


Fig. 5. Electrochemical results for $\text{Cu}_2(\text{PO}_4)(\text{OH})$ electrodes: (a) comparative CV curves of $\text{Cu}_2(\text{PO}_4)(\text{OH})$ electrodes (samples T1, T2, and T3) at scan rate of 50 mV s^{-1} , (b) scan-rate-dependent (5 mV s^{-1} to 100 mV s^{-1}) CV curves of sample T2, and (c) specific capacitance versus scan rate for samples T1, T2, and T3.

$$I(V) = av^b, \quad (10)$$

where $I(V)$ represents the current (A) at potential V , a and b are adjustable parameters, and v is the scan rate (mV s^{-1}). The electrochemical activity is diffusion controlled (battery type) when $b = 0.5$, while for a capacitive process $b = 1$. The b values calculated from the slope (linear fit) of the $\log(I)$ versus $\log(v)$ graph are shown in Fig. 6a. In the present work, the b values of all the $\text{Cu}_2(\text{PO}_4)(\text{OH})$ electrodes lay in the range of 0.5 to 1 (Fig. 6b–d), indicating that the charge storage mechanism can be contributed to battery- and pseudocapacitive-type mechanism. Therefore, using a modified power law, the charge storage mechanism under diffusion control and the capacitive process can be expressed as

$$I_p = C_s v + C_b v^{1/2}, \quad (11)$$

where I_p is the current density at peak, and $C_s v$ and $C_b v^{1/2}$ correspond to the current contributions from the pseudocapacitive (I_{surface}) and bulk process (I_{bulk}), respectively. The current density representing the contributions of the diffusion-controlled battery-type and capacitive processes at scan rates from 5 mV s^{-1} to 100 mV s^{-1} for all three $\text{Cu}_2(\text{PO}_4)(\text{OH})$ thin-film electrodes are shown in Supplementary Fig. S6.

Galvanostatic Charge–Discharge (GCD) Results

Figure 7a compares the GCD plots for the $\text{Cu}_2(\text{PO}_4)(\text{OH})$ electrodes within the potential range from 0 V to +0.45 V versus SCE at a current density of 0.4 mA cm^{-2} for samples T1, T2, and T3. The discharge plateau followed by linear discharge in each curve reveals the pseudocapacitive behavior of the $\text{Cu}_2(\text{PO}_4)(\text{OH})$ samples. Sample T2 showed a long discharge time as compared with samples T1

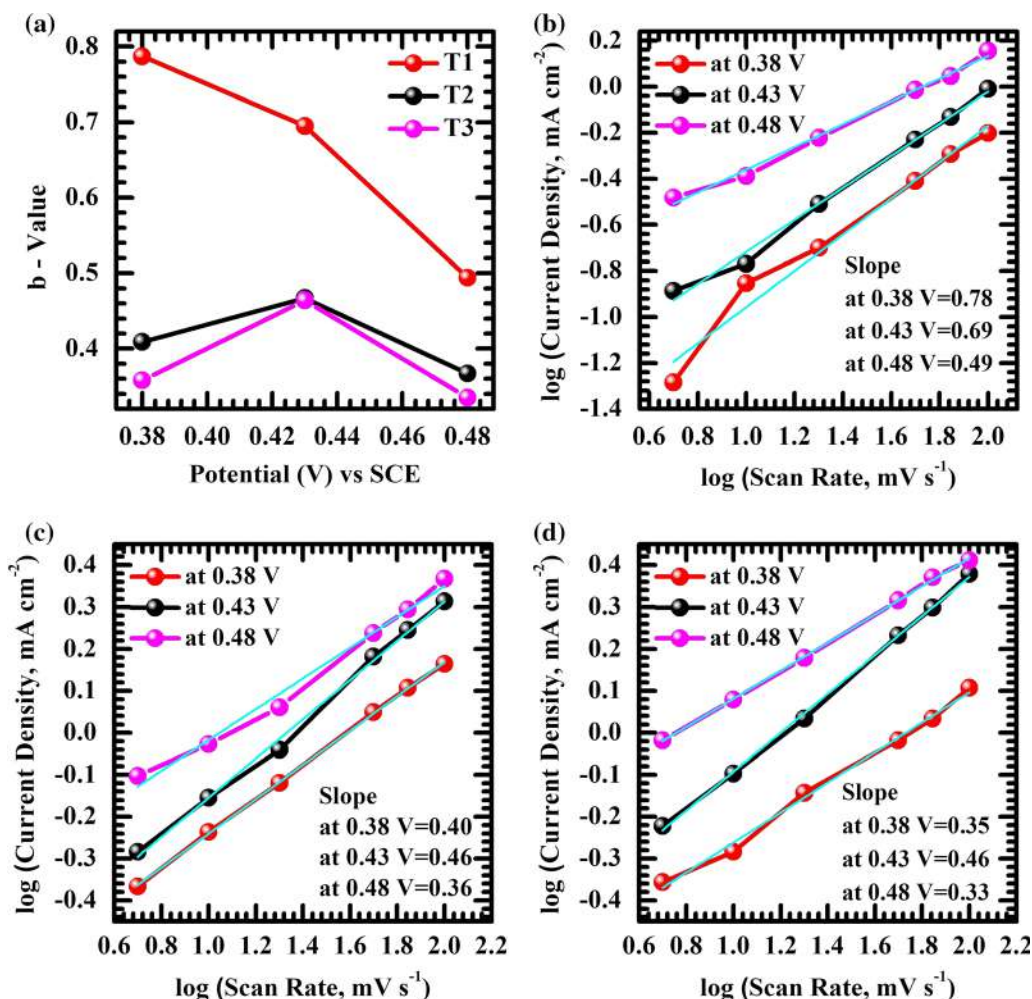


Fig. 6. (a) b -Values at different potentials for samples T1, T2, and T3. (b–d) Log current density versus log scan rate for samples T1, T2, and T3 at different potentials of 0.38 V, 0.43 V, and 0.48 V versus SCE.

and T3. Its maximum discharge time can be attributed to its large specific capacitance. Sample T2 was thus further tested by GCD measurements at current densities from 0.4 mA cm^{-2} to 2 mA cm^{-2} (Fig. 7b). Similarly, the GCD graphs for samples T1 and T3 at current densities from 0.4 mA cm^{-2} to 2 mA cm^{-2} are provided in Supplementary Fig. S7. Figure 7c shows that, as the applied current density was increased, the discharge time decreased, suggesting that the specific capacitance was inversely proportional to the applied current density. Also, the curved and symmetric charge profile suggests pseudocapacitive behavior. It is observed that the time period for discharge and charge were nearly the same, suggesting high reversibility and coulombic efficiency of the electrode. The maximum specific capacitances for samples T1, T2, and T3 were 24.87 F g^{-1} , 137.02 F g^{-1} , and 50.05 F g^{-1} , respectively, at a current density of 0.4 mA cm^{-2} . Sample T2 exhibited the maximum specific capacitance compared with samples T1 and T3. The corresponding energy

and power densities calculated from the GCD results obtained at current densities of 0.4 mA cm^{-2} to 2 mA cm^{-2} are shown in Fig. 8a. Sample T2 exhibited the maximum energy density (3.85 Wh kg^{-1}) with a power density of 264.70 W kg^{-1} . These results are slightly higher than those for a $\text{Cu}(\text{OH})_2$ electrode and comparable to those for copper pyrophosphate reported by Gurav²⁷ and Karaphun et al.,²⁸ respectively.

Electrochemical Impedance Spectroscopy (EIS)

EIS was carried out on samples T1, T2, and T3 at open-circuit potential (OCP) in the frequency range from 100 mHz to 1 MHz (Fig. 8b). The solution resistance (R_s) and charge-transfer resistance (R_{ct}) of samples T1, T2, and T3 were $1.09 \text{ } \Omega \text{ cm}^{-2}$, $1.25 \text{ } \Omega \text{ cm}^{-2}$, and $1.43 \text{ } \Omega \text{ cm}^{-2}$ and $123.92 \text{ } \Omega \text{ cm}^{-2}$, $67.30 \text{ } \Omega \text{ cm}^{-2}$, and $96.62 \text{ } \Omega \text{ cm}^{-2}$, respectively. The fit equivalent circuit for electrode T2 is presented in the inset of Fig. 8b. The fit circuit consists of the solution resistance (R_s), interface resistance (resistances R_1 , R_2 , and R_3 in series) with a capacitor (C)

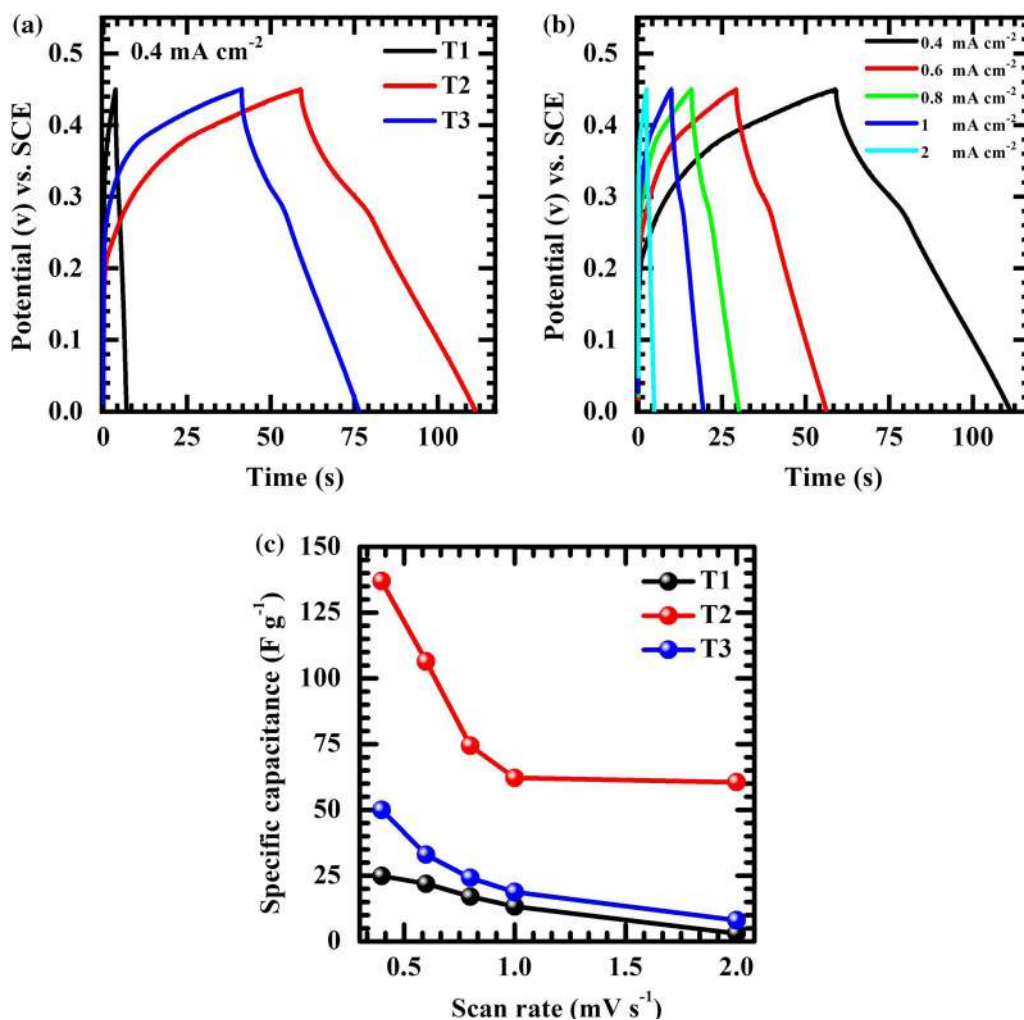


Fig. 7. Electrochemical results for $\text{Cu}_2(\text{PO}_4)(\text{OH})$ thin-film electrodes: (a) comparative galvanostatic charge/discharge (GCD) plots of $\text{Cu}_2(\text{PO}_4)(\text{OH})$ thin-film electrodes (samples T1, T2, and T3) at constant current density of 0.4 mA cm^{-2} , (b) GCD curves of sample T2 at different current densities from 0.4 mA cm^{-2} to 2 mA cm^{-2} , and (c) specific capacitance versus current density for samples T1, T2, and T3.

and general imperfect capacitor (Q) (when $n = 1$).⁴⁸ The charge-transfer resistance and solution resistance were lower for sample T2 than the other samples.

Electrochemical Stability

The cyclic stability of the $\text{Cu}_2(\text{PO}_4)(\text{OH})$ electrode (sample T2) tested over 2000 cycles by GCD measurements at current density of 1.2 mA cm^{-2} is presented in Fig. 9. This stability test revealed 91% retention of the specific capacitance after 2000 GCD cycles. The potential versus time curves of the first and last 10 charge/discharge cycles are displayed in the inset of Fig. 9 as (i) and (ii), both showing symmetric potential–time response behavior. The reduction in the capacitance can be ascribed to slight degradation of the material after many swelling and shrinking cycles. Such a low degradation (9%) of the material suggests good electrochemical stability of the $\text{Cu}_2(\text{PO}_4)(\text{OH})$ thin-film

electrode. This long-term cycling stability is achieved due to the microstrip-like macroporous surface morphology.

Note that the specific capacitance increased up to an optimum thickness of sample T2 ($12.85 \mu\text{m}$) from T1 ($8.23 \mu\text{m}$), then decreased again with further increase in the thickness to sample T3 ($13.03 \mu\text{m}$), as shown in Supplementary Fig. S8. The $\text{Cu}_2(\text{PO}_4)(\text{OH})$ thin film with optimum thickness (sample T2) showed excellent supercapacitive performance of 280 F g^{-1} . The T2 electrode exhibited macroporous structure with high surface area of $5.26 \text{ m}^2 \text{ g}^{-1}$ compared with the T1 and T3 electrodes. Also, the charge-transfer resistance ($R_{\text{ct}} = 67.30 \Omega \text{ cm}^{-2}$) and solution resistance ($R_{\text{s}} = 1.25 \Omega \text{ cm}^{-2}$) of sample T2 were comparatively lower than those of the other samples. This observation may be due to the presence of abundant active sites for a sufficient thickness of material, for intercalation/deintercalation of ions and efficient charge transfer. Below this optimum thickness, the

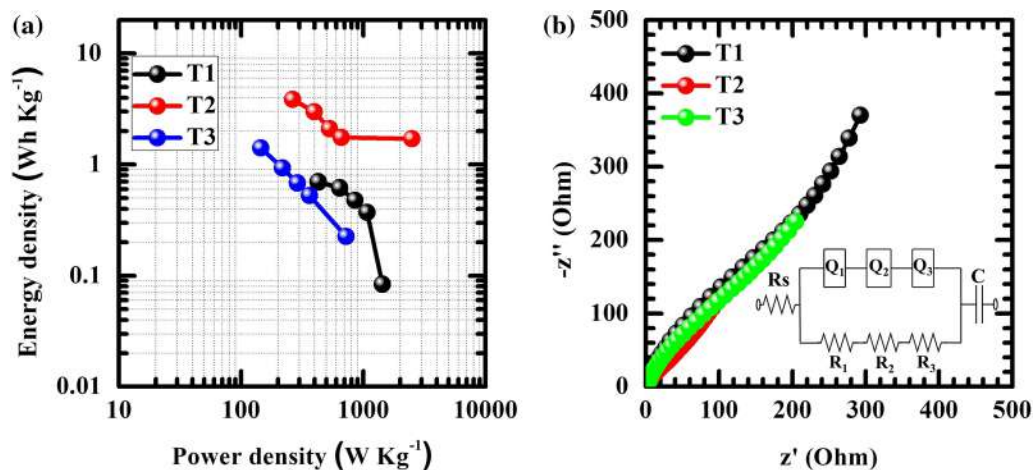


Fig. 8. (a) Ragone plots for $\text{Cu}_2(\text{PO}_4)(\text{OH})$ electrodes and (b) Nyquist plots of samples T1, T2, and T3; inset shows the equivalent circuit model used to fit the electrochemical impedance data of the $\text{Cu}_2(\text{PO}_4)(\text{OH})$ electrode.

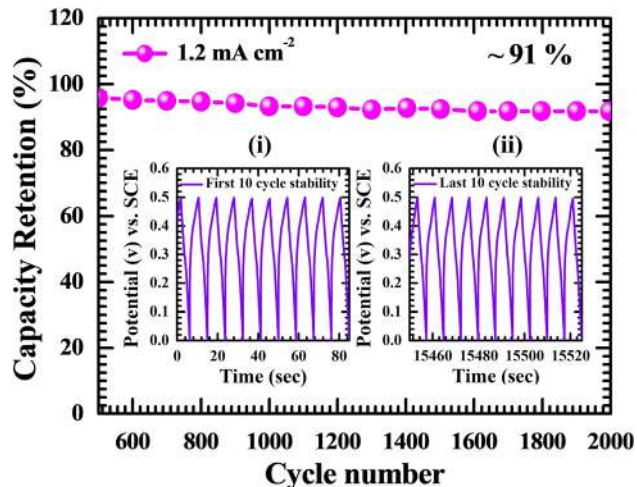


Fig. 9. Stability of $\text{Cu}_2(\text{PO}_4)(\text{OH})$ electrode (sample T2) during 2000 cycles at current density of 1.2 mA cm^{-2} . Inset shows the GCD curves of the first (i) and last (ii) 10 cycles of sample T2.

electrode shows lower capacitance due to the smaller amount of active sites available for charge storage. Conversely, the charge-transfer resistance from one site to another increases when the thickness exceeds its optimum value. Therefore, achieving an optimum thickness of $\text{Cu}_2(\text{PO}_4)(\text{OH})$ is favorable to achieve high capacitive performance.

CONCLUSIONS

A facile one-step hydrothermal method was successfully utilized for deposition of $\text{Cu}_2(\text{PO}_4)(\text{OH})$ thin films on SS substrates. The structural and morphological results confirmed $\text{Cu}_2(\text{PO}_4)(\text{OH})$ thin films with orthorhombic crystal structure and microstrip-like morphology. $\text{Cu}_2(\text{PO}_4)(\text{OH})$ thin-film electrodes exhibited macroporous structure with specific surface area of $5.26 \text{ m}^2 \text{ g}^{-1}$. The microstrip-like $\text{Cu}_2(\text{PO}_4)(\text{OH})$ thin-film electrodes

exhibited a maximum specific capacitance of 280 F g^{-1} for the optimum thickness of $12.85 \mu\text{m}$. The electrode exhibited an energy density of 3.85 Wh kg^{-1} and a power density of 264.70 W kg^{-1} with cycling stability of up to 91% after 2000 GCD cycles. This facile method for preparation of $\text{Cu}_2(\text{PO}_4)(\text{OH})$ thin films could enable scalable chemical synthesis of such material and open up a new class of pseudocapacitive electrode materials for use in asymmetric supercapacitor devices.

ACKNOWLEDGMENTS

The authors thank D. Y. Patil Education Society, Kasaba Bawada, Kolhapur and Department of Science and Technology, India-Innovation in Science Pursuit for Inspired (DST-INSPIRE), for financial support through research projects sanction No. DYPES/DU/R&D/3109 and DST/INSPIRE/04/2016/000260. The authors acknowledge the Analytical Instrumentation Laboratory, Jaysingpur College, Jaysingpur for characterization facilities.

CONFLICT OF INTEREST

There are no conflicts of interest to declare.

ELECTRONIC SUPPLEMENTARY MATERIAL

The online version of this article (<https://doi.org/10.1007/s11664-020-08095-w>) contains supplementary material, which is available to authorized users.

REFERENCES

1. D. He, G. Wang, G. Liu, J. Bai, H. Suo, and C. Zhao, *J. Alloys Compd.* 699, 706 (2017).
2. D. Dubal, O. Ayyad, V. Ruiz, and P. Romero, *Chem. Soc. Rev.* 44, 1777 (2015).

3. P. Simon and Y. Gogotsi, *Nat. Mater.* 7, 845 (2008).
4. C. Zhou, Y. Zhang, Y. Li, and J. Liu, *Nano Lett.* 13, 2078 (2013).
5. D. Dubal, G. Gund, R. Holze, and C. Lokhande, *J. Power Sources* 242, 687 (2013).
6. Y. Zhang, F. Li, and M. Huang, *Mater. Lett.* 112, 203 (2013).
7. L. Dai, W. Dong, J. Baek, and L. Wen, *Small* 8, 1130 (2012).
8. D. Dubal, N. Chodankar, D. Kim, and P. Gomez-Romero, *Chem. Soc. Rev.* 47, 2065 (2018).
9. C. Lee, *J. Ind. Eng. Chem.* 18, 433 (2012).
10. M. Seo, A. Saouab, and S. Park, *Mater. Sci. Eng. B* 167, 65 (2010).
11. H. Zhang, Y. Chen, W. Wang, G. Zhang, M. Zhuo, H. Zhang, T. Yang, Q. Li, and T. Wang, *J. Mater. Chem. A* 1, 8593 (2013).
12. W. Wei, X. Cui, W. Chena, and G. Douglas, *Chem. Soc. Rev.* 40, 1697 (2011).
13. A. Pendashteha, M. Mousavia, and M. Rahmanifar, *Electrochim. Acta* 88, 347 (2013).
14. D. Fang, Z. Chen, B. Wu, Y. Yan, and C. Zheng, *Mater. Chem. Phys.* 128, 311 (2011).
15. H. Wang, Z. Hu, Y. Chang, Y. Chen, H. Wu, Z. Zhang, and Y. Yang, *J. Mater. Chem.* 21, 10504 (2011).
16. G. Zhang and X. Lou, *Adv. Mater.* 25, 976 (2013).
17. K. Karthikeyan, D. Kalpana, and N. Renganathan, *Ionics* 15, 107 (2009).
18. J. Xu, J. Ding, X. Zhou, Y. Zhang, W. Zhu, Z. Liu, S. Ge, N. Yuan, S. Fang, and R. Baughman, *J. Power Sources* 340, 302 (2017).
19. G. Wang, L. Zhang, and J. Zhang, *Chem. Soc. Rev.* 41, 797 (2012).
20. M. Zhi, C. Xiang, J. Li, M. Li, and N. Wu, *Nanoscale* 5, 72 (2013).
21. S. Natarajan and S. Mandal, *Angew. Chem. Int. Ed.* 47, 4798 (2008).
22. R. Murugavel, A. Choudhury, M. Walawalkar, R. Pothiraja, and C. Rao, *Chem. Rev.* 108, 3549 (2008).
23. Y. Shao, Y. Zhao, H. Li, and C. Xu, *ACS Appl. Mater. Interfaces* 8, 35368 (2016).
24. T. Li, S. Kaercher, and P. Roesky, *Chem. Soc. Rev.* 43, 42 (2014).
25. Y. Chang and S. Wang, *J. Am. Chem. Soc.* 138, 9848 (2012).
26. S. Wilson, B. Lok, C. Messina, T. Cannan, and E. Flanigen, *J. Am. Chem. Soc.* 104, 1146 (1982).
27. A. Karaphun, P. Chirawatkul, S. Maensiri, and E. Swatsitang, *J. Sol. Gel. Sci. Technol.* 88, 407 (2018).
28. K. Gurav, U. Patil, S. Shin, G. Agawane, M. Suryawanshi, S. Pawar, P. Patil, C. Lokhande, and J. Kim, *J. Alloys Compd.* 573, 27 (2013).
29. J. Kang, J. Sheng, Y. Ji, H. Wen, X. Fu, G. Du, R. Sun, and C. Wong, *ChemistrySelect* 2, 9570 (2017).
30. U. Patil, M. Nam, S. Lee, S. Liu, S. Kang, B. Park, and S. Jun, *J. Alloys Compd.* 701, 1009 (2017).
31. D. Awale, S. Bhise, S. Patil, M. Vadiyar, P. Jadhav, G. Navathe, J. Kim, P. Patil, and S. Kolekar, *Ceram. Int.* 42, 2699 (2016).
32. K. Wang, X. Dong, C. Zhao, X. Qian, and Y. Xu, *Electrochim. Acta* 152, 433 (2015).
33. U. Patil, J. Sohn, S. Kulkarni, S. Lee, H. Park, K. Gurav, J. Kim, and S. Jun, *ACS Appl. Mater. Interfaces* 6, 2450 (2014).
34. P. Katkar, S. Marje, S. Kale, A. Lokhande, C. Lokhande, and U. Patil, *CrystEngComm* 21, 884 (2019).
35. B. Ameri, S. Davarani, R. Roshani, H. Moazami, and A. Tadjarodi, *J. Alloys Compd.* 695, 114 (2017).
36. N. Prokopchuk, V. Kopilevich, and L. Voitenko, *Russ. J. Appl. Chem.* 81, 386 (2008).
37. S. Kullyakool, C. Danvirutai, K. Siritwong, and P. Noisong, *J. Therm. Anal. Calorim.* 115, 1497 (2014).
38. P. Noisong, C. Danvirutai, T. Srithanratana, and B. Boonchom, *Solid State Sci.* 10, 1598 (2008).
39. S. Chakraborty, I. Sarkar, K. Haldar, S. Pal, and S. Chakraborty, *Appl. Clay Sci.* 107, 98 (2015).
40. R. Silverstein, F. Webster and D. Kiemle, *Spectrometric Identification of Organic Compounds* 7th edn, (Wiley, New York, 2014), pp. 87–95.
41. B. Sahu and G. Pugazhenthii, *J. Appl. Polym. Sci.* 120, 2485 (2011).
42. K. Sing, D. Everett, R. Haul, L. Moscou, R. Pierotti, J. Rouquerol, and T. Siemieniewska, *Pure Appl. Chem.* 57, 603 (1985).
43. U. Patil, S. Kulkarni, P. Deshmukh, R. Salunkhe, and C. Lokhande, *J. Alloys Compd.* 509, 6196 (2011).
44. K. Sankar, Y. Seo, S. Lee, and S. Jun, *ACS Appl. Mater. Interfaces* 10, 8045 (2018).
45. T. Gujar, V. Shinde, C. Lokhande, W. Kim, K. Jung, and O. Joo, *Electrochem. Commun.* 9, 504 (2007).
46. T. Gujar, W. Kim, I. Puspitasari, K. Jung, and O. Joo, *Int. J. Electrochem. Sci.* 2, 666 (2007).
47. S. Kulkarni, U. Patil, I. Shackery, J. Sohn, S. Lee, B. Park, and S. Jun, *J. Mater. Chem. A* 2, 4989 (2014).
48. P. Deshmukh, S. Pusawale, V. Jamadade, U. Patil, and C. Lokhande, *J. Alloys Compd.* 509, 5064 (2011).

Publisher's Note Springer Nature remains neutral with regard to jurisdictional claims in published maps and institutional affiliations.

Growth Dynamics-Dependent Chemical Approach to Accomplish Nanostructured Cobalt Vanadium Oxide Thin Film Electrodes with Controlled Surface Area for High-Performance Solid-State Hybrid Supercapacitor Devices

Sambhaji S. Kumbhar, Shraddha B. Bhosale, Sachin S. Pujari, Vinod V. Patil, Nitish Kumar, Rahul R. Salunkhe, Chandrakant D. Lokhande, and Umakant M. Patil*

Rational designing of electrode materials having high surface area can accomplish the enhanced charge-storing ability of the electrochemical energy storage devices. Therefore, the surface area of cobalt vanadium oxide (CVO) material is controlled by changing growth dynamics in successive ionic layer adsorption and reaction methods. Structural analysis confirms the formation of hydrous cobalt vanadium oxide nanoparticles ($\text{Co}_3\text{V}_2\text{O}_8 \cdot n\text{H}_2\text{O}$) thin film electrodes, and alteration in the surface area with change in growth dynamics is observed in Brunauer–Emmett–Teller analysis. The CVO1:1 thin film electrode prepared at optimal growth dynamics illustrates high specific capacitance (C_s) (capacity) of 793 F g^{-1} (396.7 C g^{-1}) at 0.5 A g^{-1} , respectively. Moreover, aqueous hybrid supercapacitor devices constructed using CVO1:1 as cathode exhibit high C_s of 133.5 F g^{-1} at 1.1 A g^{-1} , specific energy (SE) of 47.7 Wh kg^{-1} with specific power (SP) of 0.90 kW kg^{-1} . The solid-state hybrid supercapacitor devices also offer high C_s of 102.9 F g^{-1} at 0.3 A g^{-1} , SE of 36.6 Wh kg^{-1} at SP of 0.30 kW kg^{-1} . In the SILAR approach, the dipping time plays a critical role in improving the surface area of the material and, consequently, electrochemical performance, as the current work amply indicates.

of researchers has been focused on new energy storage applications like batteries, supercapacitors, etc. Among available electrochemical energy storage devices (EESDs), aqueous electrochemical energy storage devices (AEESDs) systems are considered a promising alternative to batteries owing to their nontoxic nature, low cost, and superior safety.^[3] Furthermore, in AEESDs, the combination of capacitive and battery features in hybrid supercapacitors (HSCs) are promising AEE systems and offer features such as high energy, power, and stability simultaneously.^[4,5] Moreover, an additional highly anticipated tactic to enhance the energy density of HSCs is to refine the storage capacity of electrodes by controlling the physical (e.g., crystallinity, hydrous nature, conductivity) and morphological (e.g., surface area, porosity, particle size) characteristics of storing materials.

Therefore, in HSCs, several metal hydroxides, oxides, phosphates, and sulfides have been assessed as cathode materials. Based on charge storage mechanisms, most ever-used pseudocapacitive materials can be categorized into intrinsic, intercalation, and extrinsic (battery-type) pseudocapacitive.^[6] Moreover, decreasing the size or crystallinity (nanomaterials) of battery-type materials can illustrate pseudocapacitive activities and are referred to as extrinsic pseudocapacitive

1. Introduction

Energy storage devices (ESDs) are an essential component for the daily operation of nearly all technological necessities, such as electric vehicles, mobile phones, and laptops. Hence, ESDs with extensive cycle life, high energy, and power density, with cost-effectiveness, are in high demand.^[1,2] Therefore, the attention

S. S. Kumbhar, S. B. Bhosale, S. S. Pujari, V. V. Patil, C. D. Lokhande, U. M. Patil
Centre for Interdisciplinary Research
D. Y. Patil Education Society
Kasaba Bawada, Kolhapur 416006, India
E-mail: umakant.physics84@gmail.com

S. S. Pujari
Department of Physics
Yashwantrao Chavan Warana Mahavidyalaya
Warananagar, Kolhapur 416113, India

 The ORCID identification number(s) for the author(s) of this article can be found under <https://doi.org/10.1002/ente.202300400>.

V. V. Patil
School of Chemical Sciences
Punyashlok Ahilyadevi Holkar Solapur University
Solapur 413255, India

N. Kumar, R. R. Salunkhe
Department of Physics
Indian Institute of Technology Jammu
Jagti, Jammu, J & K 181221, India

U. M. Patil
Department of Materials Science and Engineering
Yonsei University
Seodaemun-gu, Seoul 03722, Korea

DOI: 10.1002/ente.202300400

materials. However, extrinsic materials endure low power density and poor stability, excluding exceptional energy density. Therefore, developing cost-effective energy storage materials with high specific surface area, maximum specific capacitance (C_s), and promising cycle life is necessary to produce advanced energy values under certain economic constraints. Among several extrinsic pseudocapacitive materials, vanadium oxides have garnered considerable attention due to their distinctive layered structure, ability to exhibit multiple valence states, and cost-effectiveness. These exceptional attributes have generated substantial enthusiasm for their potential utilization in diverse fields, particularly emphasizing energy storage applications.^[7,8] Also, transition metal oxides (TMOs) are the favorite because of their special properties; multivalent states can provide ideal pseudocapacitance, proceeding electrons and ions intercalation into a metallic compound lattice, along with good intrinsic stability.^[9–11] Several single TMOs like IrO_2 , Co_3O_4 , V_2O_5 , MnO_2 , RuO_2 , NiO , etc., and binary TMOs such as NiFe_2O_4 , NiCo_2O_4 , $\text{Co}_3\text{V}_2\text{O}_8$, MnCo_2O_4 , $\text{Ni}_3\text{V}_2\text{O}_8$, etc. have been investigated as cathode material in HSCs. Moreover, the binary TMOs possess high charge-storing performance due to good electric conductivity, various valance states, electrochemical activity, etc., owing to the synergistic effects of different metals compared to single TMOs.^[12]

Therefore, due to rich redox behavior, transition metal vanadium oxide-based materials ($\text{TM}_3\text{V}_2\text{O}_8$, $\text{TM} = \text{Co}, \text{Ni}$) have recently taken special attention in energy-storing applications.^[13,14] Among several TMVOs, cobalt vanadium oxide (CVO) is gaining attention as cathode material in hybrid energy storage devices (HSCs). Some reports exist on the preparation of CVO for supercapacitor application, and the CVO has been prepared by different chemical methods such as hydrothermal,^[15] coprecipitation,^[16] solvothermal,^[17] etc., according to the literature survey. Zang et al. prepared $\text{Co}_3\text{V}_2\text{O}_8$ nanoplates by hydrothermal method and reported the C_s of 739 F g^{-1} at 0.5 A g^{-1} .^[18] Isacfranklin et al. synthesized nanoparticles of cobalt vanadium oxide by hydrothermal method and showed C_s of 285.65 F g^{-1} at 0.5 mA g^{-1} current density.^[15] Using the microwave-assisted hydrothermal method, Teng's group prepared a micron-block of CoV_2O_6 , exhibiting C_s of 114.1 F g^{-1} at 1 mA cm^{-2} .^[19] Wang et al. synthesized quasi-cuboidal CoV_2O_6 by microwave-assisted method and obtained C_s of 233 F g^{-1} at 1 A g^{-1} .^[20] However, in all these reports, cobalt vanadate-based HSC device cathodes were fabricated using a binder-assisted casting approach since the prepared materials were in crystalline powder form with microscale morphologies. Also, rationalizing the microstructure of material can lead to a change in the pseudocapacitive charge-storing mechanism from intercalation to extrinsic pseudocapacitive type. Hence, it is crucial to finely tune the features of electrode materials, such as electrical conductivity, surface area, and porous structure, by preparing binder-free electrodes using a novel synthesis approach to accomplish an advanced capacity of ESDs. To date, there are no reports on the binder-free preparation of CVO thin film electrodes and their usage in HSCs.

Therefore, the binder-free successive ionic layer adsorption and reaction (SILAR) synthesis approach is demonstrated for

the first time to prepare nanostructured cobalt vanadium oxide (CVO) thin film electrodes with controlled growth dynamics. Here, we have studied the dip time (in adsorption, reaction, and rinsing baths) effect for CVO thin films over their structural and morphological properties and reported tuned electrochemical properties for HSCs application. The as-prepared CVO thin film electrodes at optimal (1:1) dip time variation exhibited elevated surface area with mesoporous nature and enhanced intercalation-type pseudocapacitive performance. Moreover, the best-performing cobalt vanadium oxide electrode is used as a cathode, and reduced graphene oxide (rGO) is used as an anode to fabricate HSC devices. The aqueous hybrid supercapacitor devices (AHSD) and solid-state hybrid supercapacitor devices (SHSD) are fabricated, and their supercapacitive performances are tested and exhibited herein.

2. Experimental Section

2.1. Precursors Used and Cleaning of Substrates

$\text{CoCl}_2 \cdot 6\text{H}_2\text{O}$ (cobalt chloride), NH_4VO_3 (ammonium metavanadate), $\text{C}_6\text{H}_{15}\text{NO}_3$ (triethanolamine (TEA)), potassium hydroxide (KOH), polyvinylidene fluoride (PVDF), *N*-methyl-2-pyrrolidone (NMP), sodium nitrate (NaNO_3), graphite flakes, and potassium permanganate (KMnO_4) were bought from Sigma Aldrich (AR grade), and without any process of purification, they were used as reaction precursors. The stainless steel (SS) 304 grade from the market was used as conducting substrates, and a $1 \times 5 \text{ cm}^2$ area was used for deposition. Before using SS substrates, they were cleaned by a standard process; initially, zero-grade polish paper was used to polish the substrate surface and create nucleation centers. Further, the SS substrate was washed with acetone, and then ultrasonicated in double distilled water (DDW) for 15 min.

2.2. Preparation of Cobalt Vanadium Oxide (CVO) Thin Films

The thin films of CVO were prepared by a simple chemical SILAR method. In one beaker, 0.05 M $\text{CoCl}_2 \cdot 6\text{H}_2\text{O}$ precursor was dissolved in DDW, and occurred pink-colored solution was used as a cationic precursor. Also, 0.05 M NH_4VO_3 precursor dissolved in DDW at 60°C temperature at constant stirring, and after cooling, 0.05 M $\text{C}_6\text{H}_{15}\text{NO}_3$ was added dropwise into the NH_4VO_3 solution to maintain pH around 8.5 and used as an anionic precursor. For rinsing purposes, DDW was used. The prepared solution beakers were placed in the sequence of $\text{CoCl}_2 \cdot 6\text{H}_2\text{O}$, DDW, NH_4VO_3 , and again DDW, respectively, as shown in a schematic of the SILAR method in **Figure 1**. The precleaned SS substrates were immersed vertically in each placed beaker for the desired time, called dipping time. In the synthesis process, the dipping time of adsorption/reaction with respect to rinsing was varied in proportion of 1:2, 1:1, and 2:1, as given in Table S1, Supporting Information, for cobalt vanadium oxide deposition on the SS substrate and denoted by CVO1:2, CVO1:1, and CVO2:1, respectively. As a result, the uniform deposition of brownish CVO thin films occurred at room temperature after continuous 150 SILAR cycles. To study the impact of

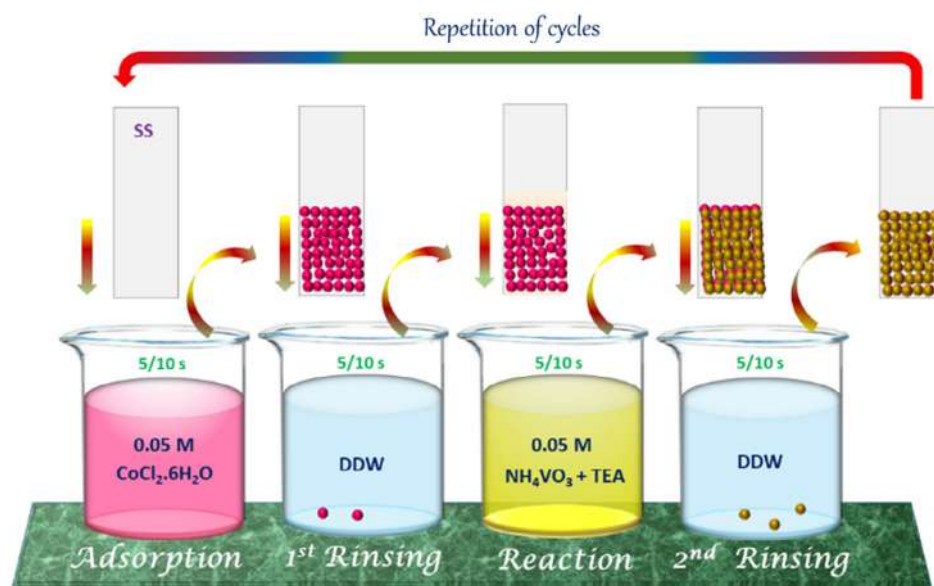


Figure 1. Schematic representation of dip time variation of CVO by SILAR method.

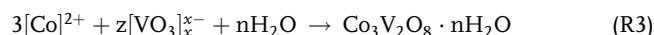
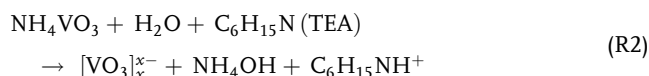
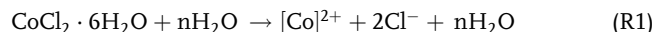
dipping time variation, all other preparative parameters were kept constant such as the concentration of precursors, deposition cycles (150), deposition temperature, etc. These CVO series thin films were exercised for further structural, morphological, and electrochemical characterizations.

2.3. Material Characterizations

The structural investigation of the synthesized CVO thin films was carried out using the X-ray diffractometer (XRD) of the Rigaku miniflex-600 with radiation of Cu $K\alpha$. The accessible, functional groups in produced thin films were investigated using the alpha (II) Bruker instrument for the Fourier transform-infrared spectrometry (FT-IR) technique. Energy dispersive spectroscopy (EDS) and field emission scanning electron microscopy (FESEM) (Hitachi S4800) were used to examine the surface morphology and elemental mapping of the synthesized CVO material. Using the Belsorp II mini equipment, the Brunauer–Emmett–Teller (BET) and Barrett–Joyner–Halenda (BJH) procedures were used to analyze the surface area and pore size, respectively. The ESCALAB 250 (ThermoElectron, Al $K\alpha$) apparatus was used for X-ray photoelectron spectroscopy (XPS) measurement. The electrochemical reactions were recorded using a ZIVE MP1 electrochemical battery cyler. The supercapacitive performances of as-synthesized CVO series thin-film electrodes were examined using cyclic voltammetry (CV), galvanostatic charge-discharge (GCD), and electrochemical impedance spectroscopy (EIS) techniques. The CVO and rGO electrodes as a cathode and anode were used to construct the aqueous and solid-state hybrid supercapacitor devices. The formulas used to evaluate the supercapacitive performance of CVO electrodes in half-cell and full-cell systems are described in Note S1, Supporting Information. Moreover, the rGO and polymer gel electrolyte were prepared as procedures described in Note S2 and S3, Supporting Information, respectively.

3. Results and Discussion

The current study uses the SILAR technique to prepare binder-free CVO thin film electrodes at room temperature. The SILAR method works on the adsorption of cations followed by a reaction with anions on the substrate surface while rinsing in DDW baths. In the cationic bath, Co^{2+} cations are obtained from the dissociation of cobalt chloride in the DDW at RT, as described in reaction (R1). These cations get adsorbed at nucleation centers of the well-cleaned SS substrate. Further adsorbed cations react with anions, where metavanadate $[\text{VO}_3]_x^-$ anions are obtained from dissociating ammonium metavanadate at 60°C in DDW at around 8.5 pH maintained using TEA, as per the reactions given in R2. Thus, the deposition of CVO thin films is occurred in thin film form as per the reaction R3.



After 150 cycles, as-prepared films were dried at ambient temperature; the brown-colored CVO series thin films were obtained, as shown inset of Figure S1, Supporting Information. The thicknesses of CVO series thin films are determined by the gravimetric weight difference process by means of deposited mass per unit area (mg cm^{-2}) over SS substrate after 150 cycles, as depicted in Figure S1, Supporting Information. The graph reveals that the dipping time variation alters the mass loading over the SS substrate. As a result, a maximum thickness is observed for CVO2:1 sample; however, sample CVO1:2 shows less thickness, and it concludes that less rinsing time demonstrates faster growth of the material and effectively increases

thickness. Hence, the growth rate of CVO thin film deposition is strongly influenced by dipping time variation, and such a change in the growth dynamics of the CVO thin films can lead to a change in the physicochemical properties. Consequently, it may influence the pseudocapacitive properties of CVO series electrodes. So, apart from the apparent advantages of quality yield and cost-effectiveness, control overgrowth dynamics and, subsequently the thickness of CVO thin film is the prime advantage of the SILAR method. So, one can efficiently manipulate electrode material properties according to the prerequisites of the electrochemical application.

3.1. Structural and Morphological Studies

The SILAR-synthesized CVO thin films were characterized by different techniques in which the XRD is used for the structural study. **Figure 2a** shows XRD patterns of crystalline CVO thin film electrodes prepared with varying dipping times. Three peaks of CVO are intensely associated with 2θ degrees of 21.5°, 29.7°, and 36.7°, denoted by the 'x' symbol, and are observed in all CVO series samples. The obtained diffraction peaks indicate the formation of an orthorhombic phase of $\text{Co}_3\text{V}_2\text{O}_8$ (JCPDS card no. 01-074-1486), which are attributed to the (200), (002) and (311) of (hkl) planes, respectively. Also, peaks associated with angles 44.9°, 51.5°, and 75.2° showed the SS peaks, which are indicated by the 'Ø' symbol. The effect of growth dynamics is significantly evident from the XRD peak intensity of the materials; the CVO1:1 sample shows a slightly higher intensity than the CVO1:2 sample. The peak intensity of the CVO1:2 sample is more elevated than sample CVO2:1, and such different diffraction peak intensities are attributed to the change in growth kinetics of material with variation in dipping time. The XRD results suggest that a slow CVO thin film growth rate can lead to forming material with improved crystallinity. Moreover, the obtained nanocrystalline nature of CVO thin film electrodes can exhibit exceptional electrochemical capacitive performance.^[21] The FT-IR peaks scrutiny of prepared CVO thin films was accomplished in 400 to 4,000 cm^{-1} region and exhibited in **Figure 2b**.

The peaks are located at a range of 410–435 cm^{-1} (γ_1) correlates to the cobalt-oxygen stretching mode. The well-built and typical peaks (γ_2) about 551, 776, and 1073 cm^{-1} have been attributed to the vanadyl group stretching vibration belonging to the out-of-plane, and in-plane vibrational modes of V–O–V related to the V–O, respectively.^[22] The (γ_3) peak at 1310 cm^{-1} is associated with the C–O stretching from impurities of TEA in the prepared material.^[23] The peak γ_4 of absorption at 1648 cm^{-1} is attributed to the vibration of water molecule bending. The stretching vibrations of the O–H molecules from the structural water are responsible for the broad range at higher wavenumbers between 2640 and 3990 cm^{-1} .^[24] According to the FT-IR and XRD results, the prepared CVO thin films are hydrous and nanocrystalline, which can be beneficial for supercapacitor application.

The growth dynamics variation on the morphology of CVO thin films is probed by FE-SEM analysis. The morphologies of prepared samples at different dipping times are shown in **Figure 3a,c,e** at different magnifications. It is observed that fine spherical particles are deposited over the SS substrates. Also, the morphology contains porous structures with voids and cavities that can help easy access to the electrolyte. At higher magnification, it can be seen that these spherical particles consist of nanoparticles and are interconnected with each other, as shown in **Figure 3b,d,f**. However, even with aggregation of nanoparticles present in morphology, which are acquiescent with high aspect ratio particles, they can physically proceed to enhance the clearness of their electrolytes from surfaces.^[25,26] Furthermore, the average particle size is determined from the magnified image shown in **Figure 3b',d',f'** and found to be ≈ 18 , 22, and 32 nm for CVO1:2, CVO1:1, and CVO2:1, respectively. It is observed that the average particle size increases as rinsing time decreases, owing to faster growth kinetics resulting in the agglomeration of the particles at a less rinsing time. In contrast, double rinsing time than adsorption and reaction time leads to forming a compact thin film with a smaller particle size in the CVO1:2 sample. Furthermore, the elemental composition of CVO was probed using EDS mapping, as shown in **Figure S2**, Supporting Information. The EDS mapping depicts that Co, V, and O elements are present in all the CVO series samples, as illustrated

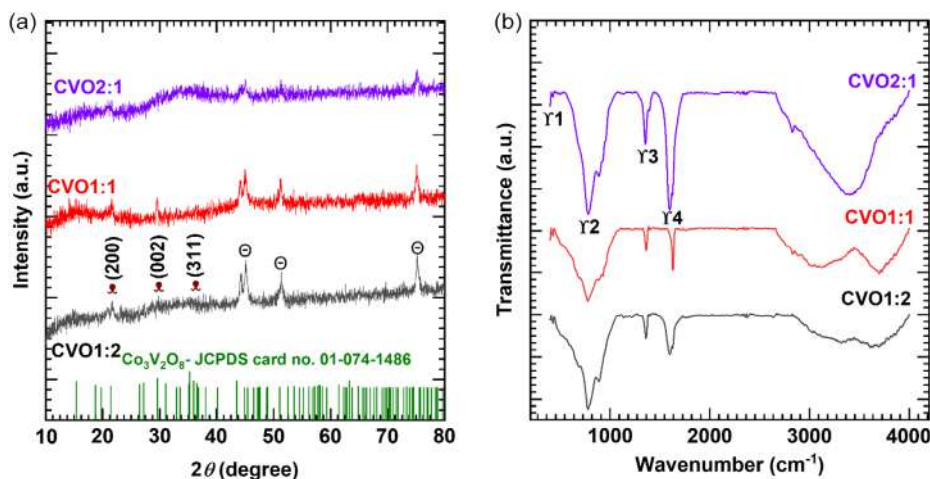


Figure 2. a) XRD patterns of dip time variation CVO thin films (CVO1:2, CVO1:1, and CVO2:1), and b) FT-IR spectra of CVO thin films series (CVO1:2, CVO1:1, and CVO2:1).

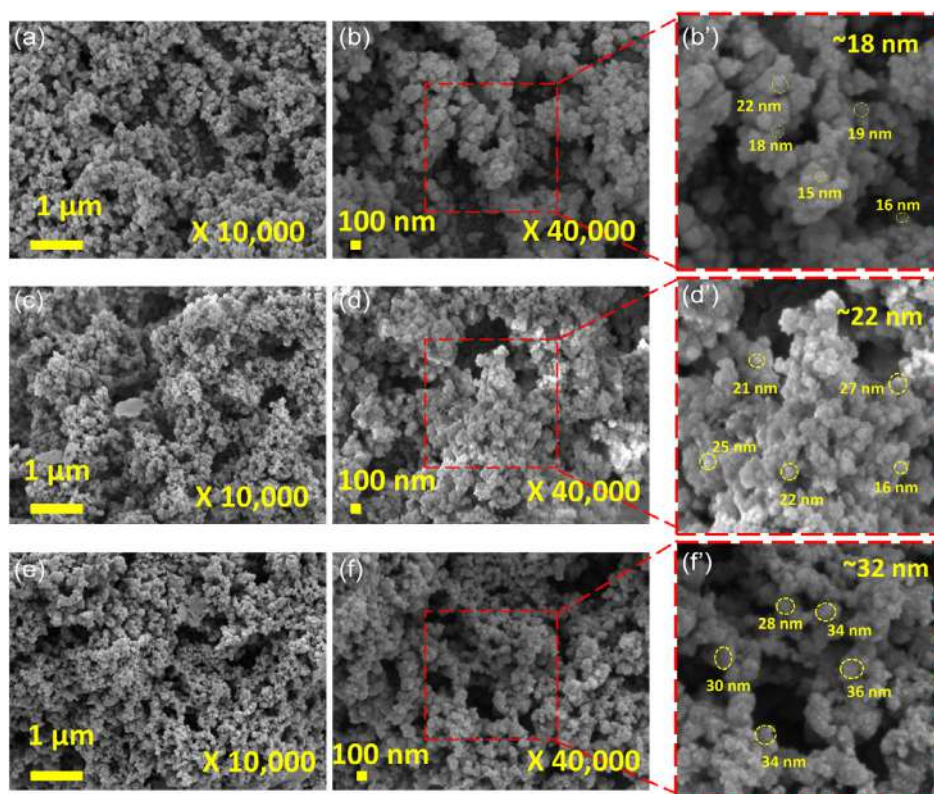


Figure 3. FE-SEM images of CVO electrodes: a,b,b') CVO1:2, c,d,d') CVO1:1, and e,f,f') CVO2:1 at different magnifications.

in orange, blue, and green in Figure S2a–l, Supporting Information. Also, EDS analysis confirms atomic percentages of 36.26, 29.33, and 34.42% of Co, V, and O elements, respectively, in the CVO 1:1 sample. As a result, the FE-SEM and EDS analysis confirms the preparation of nanostructured, porous CVO material in thin film form.

The surface area of the CVO1:2, CVO1:1, and CVO2:1 sample was analyzed by adsorption and desorption of N_2 isotherms and shown in Figure 4a–c. The obtained isotherms showed type-III isotherm with H3 type hysteresis loop in the P/P_0 (relative pressure) range of 0.04–0.9 by the International Union of Pure and Applied Chemistry (IUPAC) classification. Using BET, the calculated surface area is found to be 54.95, 74.32, and 18.67 $m^2 g^{-1}$ for CVO1:2, CVO1:1, and CVO2:1 samples, respectively. The maximum surface area obtained for sample CVO1:1 sample confirms that dipping time influences the surface area of prepared CVO material. Also, the pore diameter is measured by the BJH technique and shown in the inset of Figure 4a–c. The obtained mean pore size diameters of CVO1:2, CVO1:1, and CVO2:1 samples are 9.54, 9.14, and 17.88 nm, respectively, and confirm the mesoporous nature of the CVO series samples. The maximum surface area is obtained for CVO1:1 owing to the optimum average particle size and pore size distribution. However, the CVO1:2 and CVO2:1 exhibited low surface area due to the compact morphology with fine nanoparticles and larger average particle size with wide porous structure, respectively. The results concluded that the different growth kinetics due to changes in dipping time influence the resultant surface area and porous structure.

Thus, obtaining a larger surface area envisioned that the SILAR-deposited CVO nanoparticles could exhibit good supercapacitive performance.^[27] The higher surface area can offer a highly electrochemically active surface by creating an easy path for ion transportation in the material; consequently, the electrochemical capacitive performance of such material is higher since capacitance is proportional to the surface area of electrode materials.^[28]

The XPS study of the CVO sample was conducted to scrutinize the chemical composition with states of elements of prepared CVO thin films. The total survey spectrum of sample CVO1:1 is shown in Figure 5a, which depicts Co 2p, V 2p, O 1s, and C 1s peaks. The spectrum of Co 2p shown in Figure 5b split into two core binding energies, i.e., Co 2p_{1/2} and Co 2p_{3/2} at 796.8 and 780.7 eV, respectively. Also, those energies deconvoluted into two valance states such as Co³⁺ and Co²⁺; Co 2p_{1/2} split at 796.4 and 797.9 eV, and Co 2p_{3/2} split at 780.4 and 782 eV, respectively. In the cobalt spectrum, two satellite peaks are identified at binding energies of 802.9 and 786.4 eV.^[29] Furthermore, the V 2p spectrum is demonstrated in Figure 5c, where the vanadium spectrum is deconvoluted into two primary energies of V 2p_{1/2} and V 2p_{3/2} at 524 and 516.5 eV, respectively. The V 2p_{3/2} split into two valance states are attributed to the V⁴⁺ and V⁵⁺ at energies of 516.5 and 517.6 eV, respectively, and another broad peak at 524 eV corresponds to the V⁵⁺ valance state. Also, the deconvoluted O 1s spectrum is displayed in Figure 5d, and there are three deconvolute peaks: O_I, O_{II}, and O_{III} at 529.9, 531.4, and 532.9 eV binding energies, respectively. The characteristic O_I is

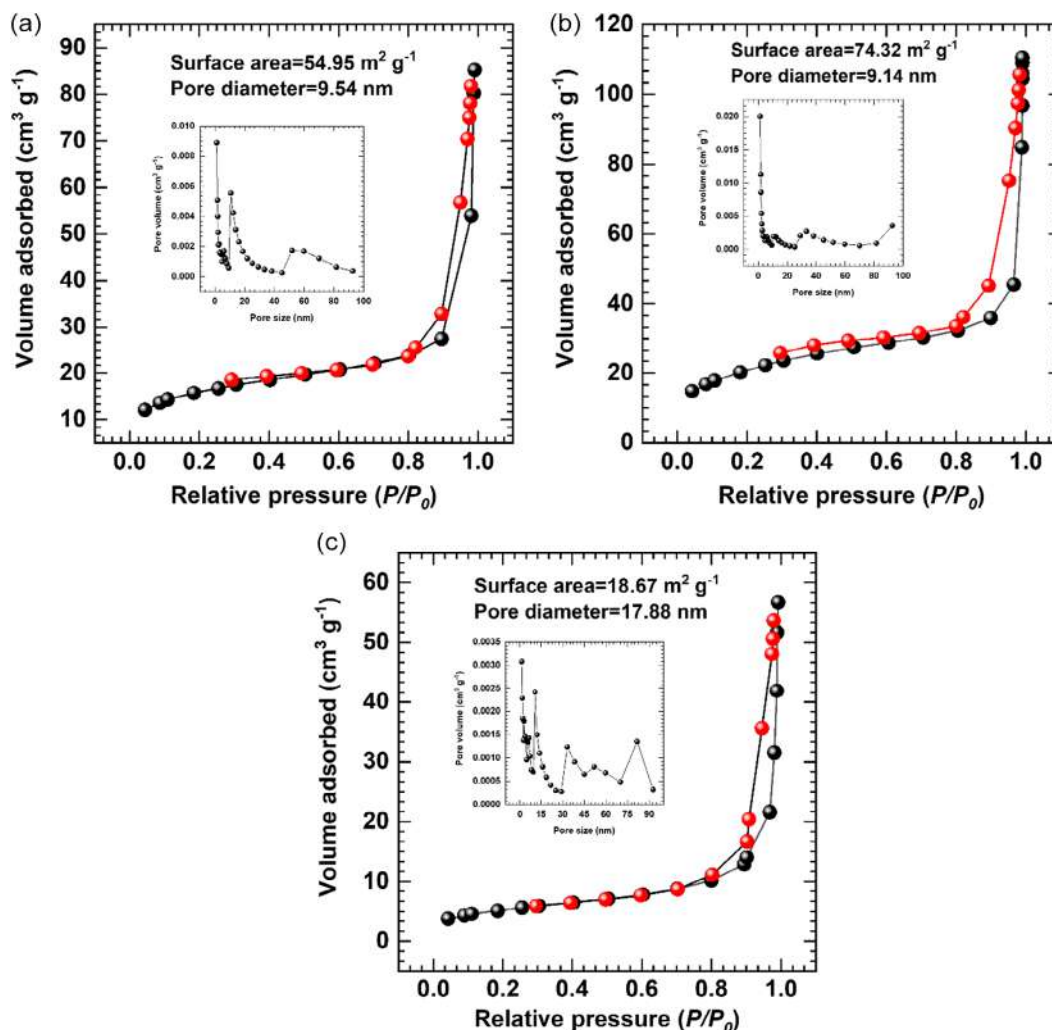


Figure 4. Surface area and inset pore size distribution of samples a) CVO1:2, b) CVO1:1, and c) CVO2:1.

the oxygen related to lattice oxygen, and the second peak of O_{II} is attributed to the oxygen vacancies.^[10,30,31] At 529.9 eV, the O_{III} peak corresponds to the oxygen of water adsorbed by the surface or hydroxyl species. Similarly, XPS spectra of CVO1:2 and CVO2:1 samples are provided in Figure S3, Supporting Information, which reveals similar results to CVO1:1. In conclusion, the dominant states of Co^{2+} and V^{5+} support the formation of hydrous CVO in the polymorph of $Co_3V_2O_8$ in thin films, which agrees with the XRD result. All the structural analysis confirms the growth dynamics variation from CVO1:2, CVO1:1 to CVO2:1, ultimately influencing the morphology, pore size distribution, and surface area of nanostructured CVO ($Co_3V_2O_8 \cdot nH_2O$) thin film electrodes, which are viable to accomplish high supercapacitive performance.

3.2. Electrochemical Capacitive Performance Evaluation of CVO Electrodes

In CVO thin film electrodes, the physicochemical properties are altered by dipping time variation, and its impact on

supercapacitive performance was analyzed through electrochemical characterization by forming a three-electrode system. The three-electrode system comprises of CVO electrode as the working electrode, a platinum plate (Pt) as an auxiliary (counter) electrode, and mercury/mercury oxide (Hg/HgO) as a reference electrode. An electrolyte of KOH (1 M) is used for the ion intercalations to store the charges. The correlative CV curves of samples CVO1:2, CVO1:1, and CVO2:1 at a fixed 20 mV s^{-1} scan rate in the potential range of 0–0.6 V Hg^{-1}/HgO are displayed in Figure 6a.

All CVO series thin film electrodes depict individual redox pairs related to the Faradaic reversible redox responses among $Co_3V_2O_8$ to $Co_3V_2O_8-xOH_x$. The noticeable redox pair in ≈ 0.1 to 0.25 V Hg^{-1}/HgO can be allocated to the reversible redox reactions involving Co^{II} to Co^{III} transformation. Alternatively, the dominant redox pair in the potential range of 0.45 to 0.65 V of $Co_3V_2O_8$ thin films are owing to the redox reaction related to Co^{III} to Co^{IV} transformation.^[32] Thus, redox pairs correspond to the intercalation of OH^- ions into the CVO while the charging phenomenon occurs, and electrolyte ions are deintercalated

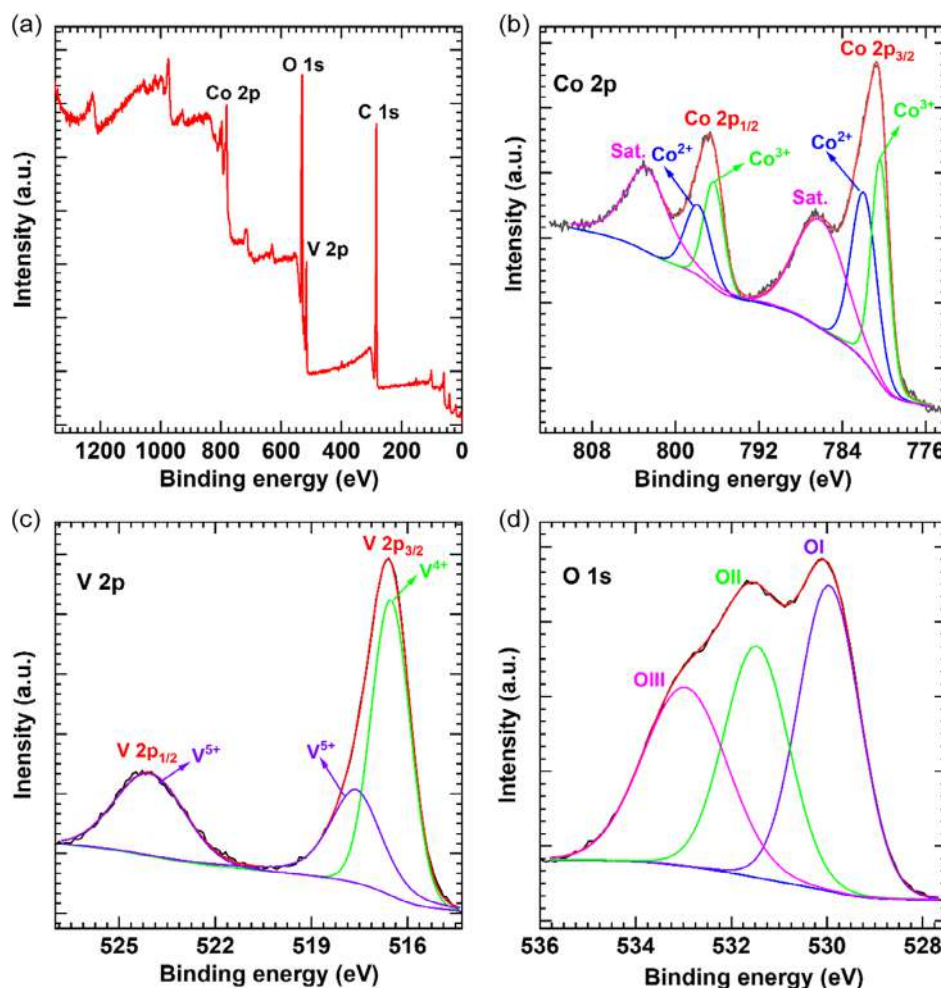
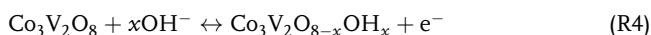


Figure 5. a) XPS full survey spectra and the corresponding b) Co 2p, c) V 2p, and d) O 1s of the sample CVO1:1.

whenever discharging occurs, as given in the following reaction (R4).



Also, the absolute area under the CV curve of the CVO1:1 electrode is larger than the CVO1:2 and CVO2:1 electrode, representing that the CVO1:1 has a maximum capacity for charge storage. Due to the mesoporous structure and high surface area of CVO1:1 electrode, electrolyte ions permeate effortlessly in the interior of an electrode and enable maximum area for charge storage. Thus, it shows an increment in the current under the curve of the CVO1:1 electrode than other electrodes. The CV curves of the CVO1:1 electrode at different scan rates of 2 to 20 mV s^{-1} are displayed in Figure 6b, and for other CVO1:2 and CVO2:1 electrodes provided in Figure S4a,b, Supporting Information. Evidently, when the voltage scan rate increases, the area under the CV curve increases, although the redox pairs shift slightly in the CV loop owing to the polarization effect.^[33,34]

Furthermore, in a direction to evidently divulge the mechanism of charge storage of CVO series electrodes, their electrochemical kinetics are prodigious to study.^[35] The scan rate (ν)

versus peak current (i) in the CV area under the loop satisfied the “Power’s law” as given below in Equation (R5)^[36]

$$i = a\nu^b \quad (\text{R5})$$

Where “ a ” and “ b ” are both adjustable parameters, Equation (R5) determines the value of “ b ” by measuring the slopes of $\log(i)$ and $\log(\nu)$. When the value of “ b ” is near 0.5, the diffusion-controlled electrochemical charge storage process is dominant, and the surface capacitive process is conquered when the value “ b ” is near 1.^[37] The “ b ” values of the CVO1:2, CVO1:1, and CVO2:1 is 0.86, 0.85, and 0.78, respectively, as depicted in Figure S5a–c, Supporting Information, and it deduced that the CVO series material exhibits more surface capacitive charge storage process, i.e., extrinsic pseudocapacitive behavior owing to nanoparticle like morphology. Additionally, using the Trasatti method, the surface capacitive contribution in the charge storage was determined,^[38] and additional insight into the kinetics of charge storage of electrodes is examined, illustrating the battery type (diffusion-controlled) and pseudocapacitive owing to surface extrinsic charge storage. The pseudocapacitive charge on the surface (Q_s) and battery type (Q_d) is measured by the total response

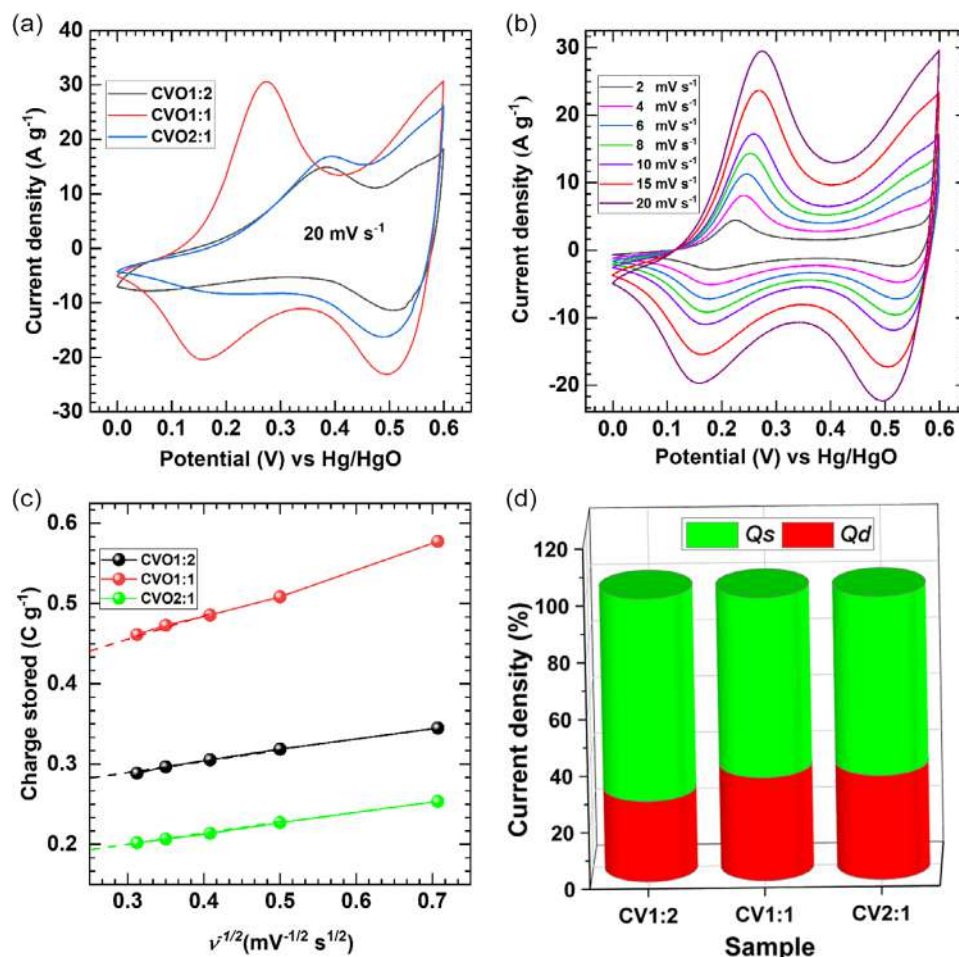


Figure 6. a) At 20 mV s^{-1} scan rate comparative CV curves, b) CV curves of CVO1:1 electrode at different scan rates ($2\text{--}20 \text{ mV s}^{-1}$), c) the plot of \log (peak current) versus the \log (scan rate) for electrode CVO1:1, and d) comparative plot of surface and diffusive charge contribution with respect to scan rate (CVO1:2, CVO1:1, and CVO2:1).

of current from CV. The total charge, i.e., Q_{total} is the combination of battery and diffusive type, as mentioned in Equation (R6),^[39,40]

$$Q_{\text{total}} = Q_s + Q_d \quad (\text{R6})$$

Moreover, the following Equation (R7) examines the charge contributions using CV curves since the Q_d varies with $\nu^{-1/2}$ and Q_s is independent of scan rate (ν).

$$Q_{\text{total}} = Q_s + \text{Const.} \nu^{-1/2} \quad (\text{R7})$$

The plot of Q_{total} versus $\nu^{-1/2}$ is shown in Figure 6c, and the Y-axis intercept represents the capacitive contribution of the CVO electrodes. The slow scan rates are designated for estimating Q_s on the Y-axis and calculating the charge contribution in CVO electrodes. The charge contribution from Q_s is lower in the CVO2:1 electrode and higher in other CVO series electrodes, as shown in Figure 6d. The charge contribution from the Q_s , i.e., surface pseudocapacitive, is attributed to the nanostructured morphology and high surface area of CVO electrodes, and this

result further ensures that the miniaturization of material size is crucial to attain the pseudocapacitance. Also, a contribution from Q_s increases with the scan rate and accomplishes battery type process (diffusive), leading to slow scan rates. Therefore, the CVO material displays a diffusive (battery-type) behavior at the lower scan rate and higher scan rates showing capacitive nature, as shown in Figure S6, Supporting Information.^[41]

The GCD analysis is further used for the electrochemical performance evaluation of CVO thin film electrodes. The comparative GCD curves of CVO1:2, CVO1:1, and CVO2:1 electrodes at 1 A g^{-1} constant current density are displayed in Figure 7a. All-tested CVO electrodes characteristically show bell-shaped, symmetric charging–discharging curves, typically representing intercalation-type pseudocapacitive charge storage mechanisms. In the pseudocapacitive type, charge storage contains two concepts: surface oxidation–reduction and intercalative type.^[42] The GCD/CV curve analysis depicts that CVO electrodes possess a combination of intercalation type and extrinsic pseudocapacitive behavior owing to their nanostructured morphologies and augmented surface area. The Figure 7b displays GCD curves of CVO1:1 electrode at different current densities, respectively,

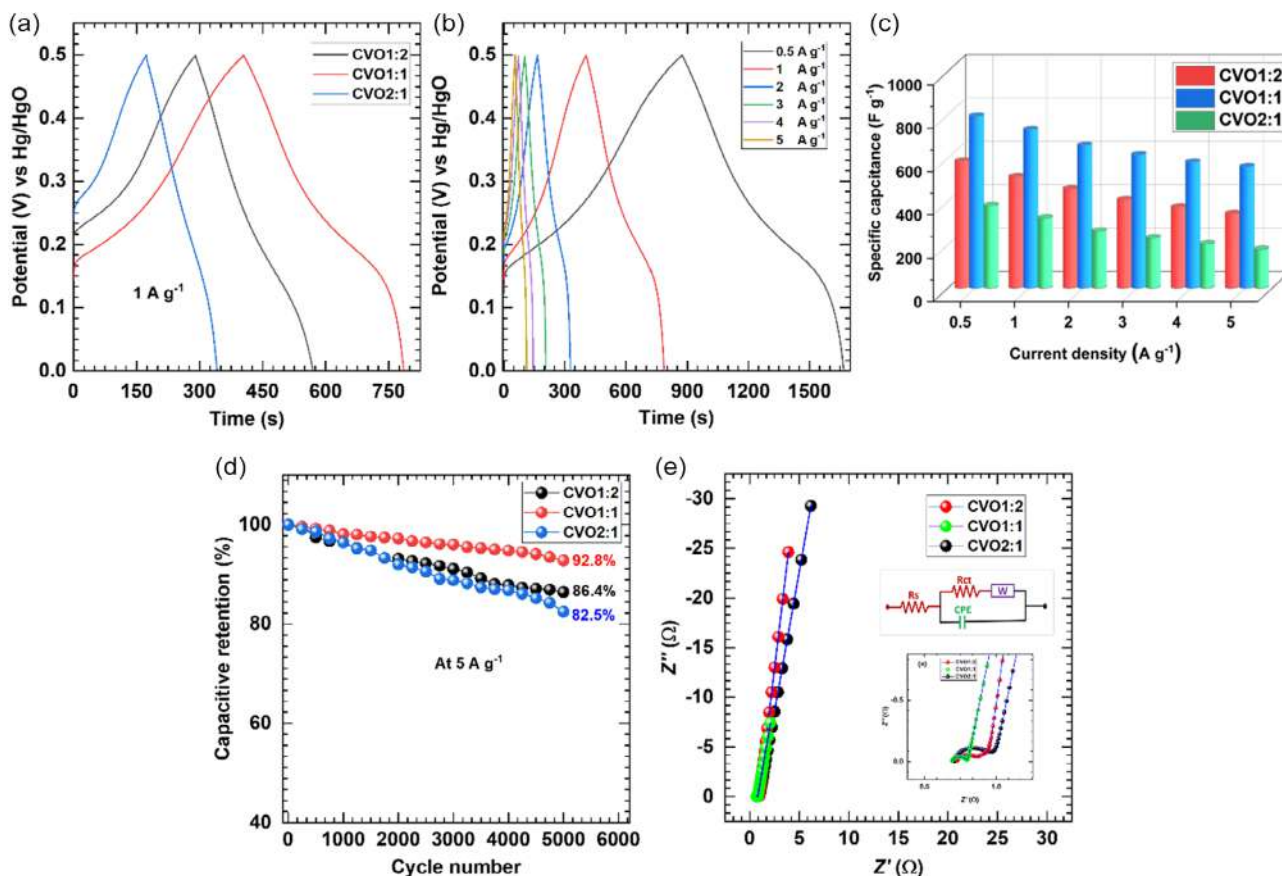


Figure 7. a) Comparative GCD curves of cobalt vanadium oxide electrodes (CVO1:2, CVO1:1, and CVO2:1) at 1 A g^{-1} current density, b) GCD curves at different current densities from 0.5 to 5 A g^{-1} of CVO1:1 electrode, c) the plots of specific capacitance at 0.5 – 5 A g^{-1} current density of CVO1:2, CVO1:1, and CVO2:1 electrodes, d) the plot of capacitive retention of CVO series electrodes at 5 A g^{-1} for 5,000 cycles, and e) the Nyquist plots of cobalt vanadium oxide dip time variation electrodes (CVO1:2, CVO1:1, and CVO2:1).

and GCD curves of CVO1:2, and CVO2:1 is provided in Figure S7a,b, Supporting Information. It can be seen that, as the current density decreases, GCD time increases, representing typical electrochemical reactions step rate by the diffusion of ions. Consequently, at the higher current densities, the ions of electrolyte access the outer surfaces of active material and hardly reach the interior of the material, and hence internal space is not fully used for abundant redox reactions.^[43] The specific capacitance and capacity of dipping time-varied electrodes are calculated by standard formulae mentioned in Note S1, Supporting Information (Equation E(1) and E(2), Supporting Information). The calculated C_s of CVO series electrodes at distinct current densities are shown in Figure 7c. The maximum C_s of 793.5 F g^{-1} (specific capacity (SC) 396.7 C g^{-1}) at 0.5 A g^{-1} is obtained for the CVO1:1 electrode and maintains C_s of 561 F g^{-1} (171.9 C g^{-1}) at 5 A g^{-1} current density, representing excellent capacitance retention even at a high current density. The CVO1:2 and CVO2:1 electrode exhibits maximum C_s of 586.4 F g^{-1} (293.2 C g^{-1}) and 381.1 F g^{-1} (190.5 C g^{-1}) at 0.5 A g^{-1} , respectively, which is relatively less than CVO1:1 electrode. The maximum C_s obtained for the CVO1:1 electrode is attributed to the maximum surface area of the CVO1:1 electrode than the other CVO1:2 and CVO2:1 electrode. The improved

electrochemical performance of the CVO1:1 thin film electrode is mainly ascribed to the mesoporous structure and maximum surface area; moreover, the synergy between cobalt and vanadium implies enhanced electrical conductivity and multifarious valences. Furthermore, the cycling stability performances of the CVO series electrodes over 5,000 charge-discharge cycles at 5 A g^{-1} are tested and presented in Figure 7d. After 5,000 cycles, the CVO1:1 electrode demonstrates 92.8% capacity retention, while the CVO1:2 and CVO2:1 electrode exhibits 86.4 and 82.5% capacity retention, respectively. So, the cyclic stability of the CVO1:1 sample is higher than that of CVO1:2 and CVO2:1, which is attributed facile interface with electrolyte owing to the high surface area and mesoporous nature. Moreover, decreased cyclic stability of CVO series electrodes may be linked to the little degradation of material and/or the formation of undesired intermediate or side products during intercalation and deintercalation.^[44] Moreover, the FE-SEM images of the CVO1:1 thin film electrode after electrochemical measurements (cyclic stability) at different magnifications of X15,000 and X50,000 are investigated and provided in Figure S8a,b, Supporting Information. The particle-like morphology (Figure 3c) of the CVO1:1 electrode remains relatively undisturbed after stability, as observed in the low magnification

FE-SEM images (Figure S8a, Supporting Information). However, upon closer inspection of the FE-SEM image (Figure S8b, Supporting Information), a slight change in morphology is noticeable where particles are made up of nanoflakes after cycling rather than nanoparticles. This change in morphology, i.e., the formation of nanoflakes through the interconnection of nanoparticles, suggests that the cobalt vanadium oxide material undergoes slight surface conversion (undesired intermediates), leading to diminished cyclic stability of the electrode after 5000 cycles.^[44]

The CVO electrodes are further characterized using the EIS technique to understand better physicochemical mechanisms involved in electrochemical charge storage. The Kramers–Kronig transformation analysis was accomplished in the frequency range of 10 mHz to 1 MHz to ensure the precision of the measurements. The ZView-Impedance software was used to match the equivalent electric circuit for impedance data fits, and an appropriate fitting was established as having a lower deviation of the total fit (Chi-square <0.001). The Nyquist plots of CVO samples are shown in Figure 7e, and the assessed minimum solution resistance (R_s) and charge transfer resistance (R_{ct}) values of 0.7 and 0.101 (Ω) are observed for CVO1:1 electrode, and all other fitting parameters are provided in Table S2, Supporting Information. The vertical line has almost a phase angle of -90° in the low-frequency range, indicating the capacitive behavior of the CVO electrodes, and little inclination

suggests a small Warburg impedance caused by ion diffusion in the active material. Also, the R_s and R_{ct} values are associated with electrolyte and faradaic leakage current resistance. All the CVO series electrodes indicate minute R_s and R_{ct} values, which are attributed to the binder-free synthesis of CVO materials on conductive SS substrate by the SILAR method. Among all three CVO electrodes, the CVO1:1 electrode exhibits less R_s and R_{ct} values owing to the elevated surface area with the mesoporous morphology, resulting in an enhanced electrochemical capacitive performance.

3.3. Hybrid Aqueous Supercapacitor Device

The feasibility of CVO electrodes for applied purposes is also revealed by making a hybrid aqueous supercapacitor device (HASD), as shown schematically in Figure 8a. The high-performed electrode CVO1:1 is used as the positive electrode, and the negative electrode is rGO. The rGO electrode is acknowledged as the best-performing negative electrode in an aqueous KOH electrolyte, as described in Note S4, Supporting Information. To attain the utmost supercapacitive performance, balancing charges among cathode and anode are most important in device fabrication by balancing mass among them according to Equation (E3), Supporting Information provided in Note S1, Supporting Information. Based on the evaluation by the

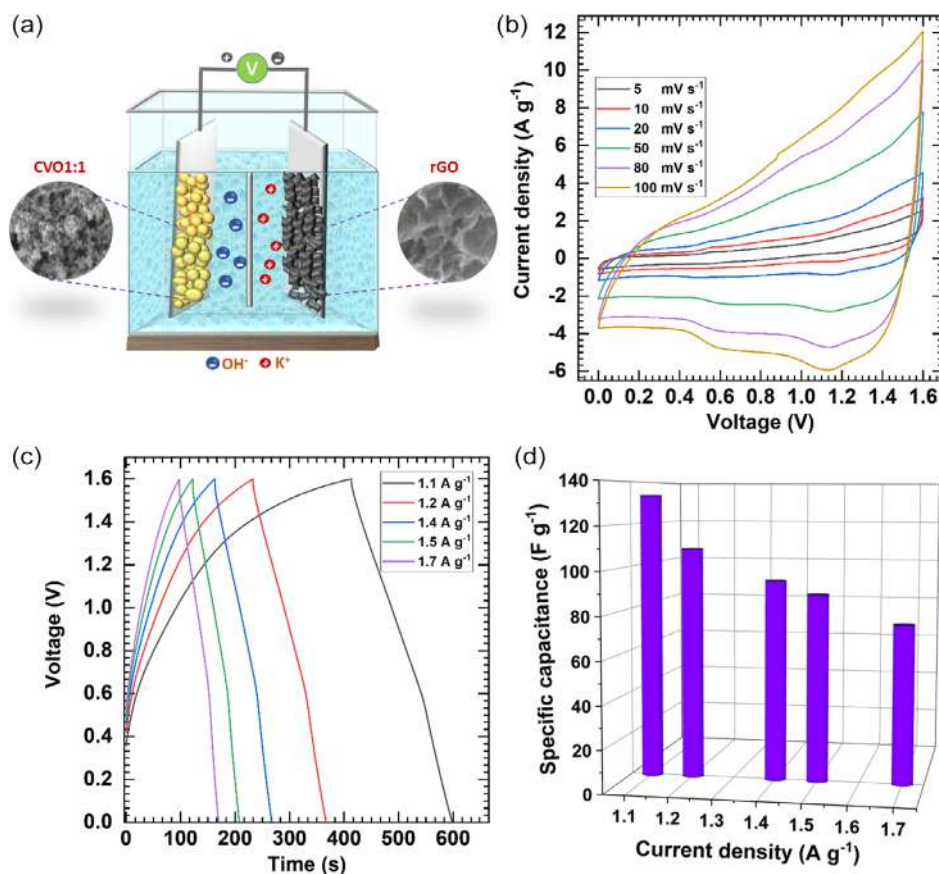


Figure 8. a) Schematic illustration of the process to fabricate the HASD, b) CV curves of CVO1:1 electrode HASD, c) GCD curves at various current densities, and d) plot of specific capacitance versus current density.

three-electrode system, the rGO and CVO1:1 electrodes, as provided in Figure S9, Supporting Information and Figure 6, separate working potential windows benefit the enhancement of the voltage of HASD. The CVO1:1 electrode is functional in 0–0.6 V versus Hg/HgO positive potential window and the potential window of the rGO electrode is between 0 and –1 V versus Hg/HgO, as displayed in Figure S10, Supporting Information. For the HASD, the potential window range of 0 to 1.2, 1.3, 1.4, 1.5, 1.6, and 1.7 V was carried out at 50 mV s⁻¹ scan rate, as shown in Figure S11a, Supporting Information, to conclude the potential window of the device. The result optimizes the 0 to 1.6 V potential window suitable for the CVO1:1//rGO device (HASD) since the water-splitting process can occur after 1.6 V. Therefore, the CV curves carried out at various scan rates from 5 to 100 mV s⁻¹ in the potential window of 0 to 1.6 V and displayed in Figure 8b. The quasi-rectangular nature of CV loops suggests supercapacitive behavior of the HASD device.

Moreover, the GCD curves of HASD were tested in various potential windows of 0 to 1.2/1.7 V, as shown in Figure S11b, Supporting Information, at 1.2 A g⁻¹ current density. The GCD plots in the optimized potential window of 0 to 1.6 V, at current densities of 1.1 to 1.7 A g⁻¹, are displayed in Figure 8c. The charge–discharge curves are not precisely triangular, suggesting the excellent pseudocapacitive performance of the HASD device. The C_s values of the HASD are 133.5 F g⁻¹ at 1.1 A g⁻¹ and maintain C_s of 74.5 F g⁻¹ at 1.7 A g⁻¹, as displayed

in Figure 8d. The CVO1:1//rGO (HASD) achieved a maximum SE of 47.4 Wh kg⁻¹ at 0.9 kW kg⁻¹ SP and a minimum SE of 26.5 Wh kg⁻¹ at 1.3 kW kg⁻¹ SP, as Ragone plot shown in Figure 9a, which are calculated by using Equation (E4) and (E5), Supporting Information, provided in Note S1, Supporting Information. The cycling stability of HASD was checked by continuing given 5000 cycles of GCD at the constant current density of 1.5 A g⁻¹ and maintained 83.6% capacitive retention with 79.7% coulombic efficiency, as shown in Figure 9b. The HASD shows good stability, SE, and SP, which can conclude the CVO (CVO1:1) and rGO electrode materials are applicable in energy storage applications.

The EIS analysis was also done to understand ion migration's kinetics in the HASD, and the Nyquist plot is shown in Figure 9c with an analogous fitted circuit inset. The HASD shows less R_s and R_{ct} of 2.3 and 19.4 Ω before the stability. The small values of R_s and R_{ct} indicate efficient ion transportation and outstanding electrochemical conduction of the constituent electrode. While the HASD maintains less R_s and R_{ct} values of 1.7 and 36.2 Ω after stability, other fitted parameters are provided in Table S3, Supporting Information. Additionally, the vertically inclined lines in the low-frequency region indicate a lesser Warburg impedance for the electrolyte ions diffusion between the respective electrodes in HASD. Furthermore, the HASD shows high electrochemical performance, including the C_s, increased working potential window, and SE, caused by the synergy between the

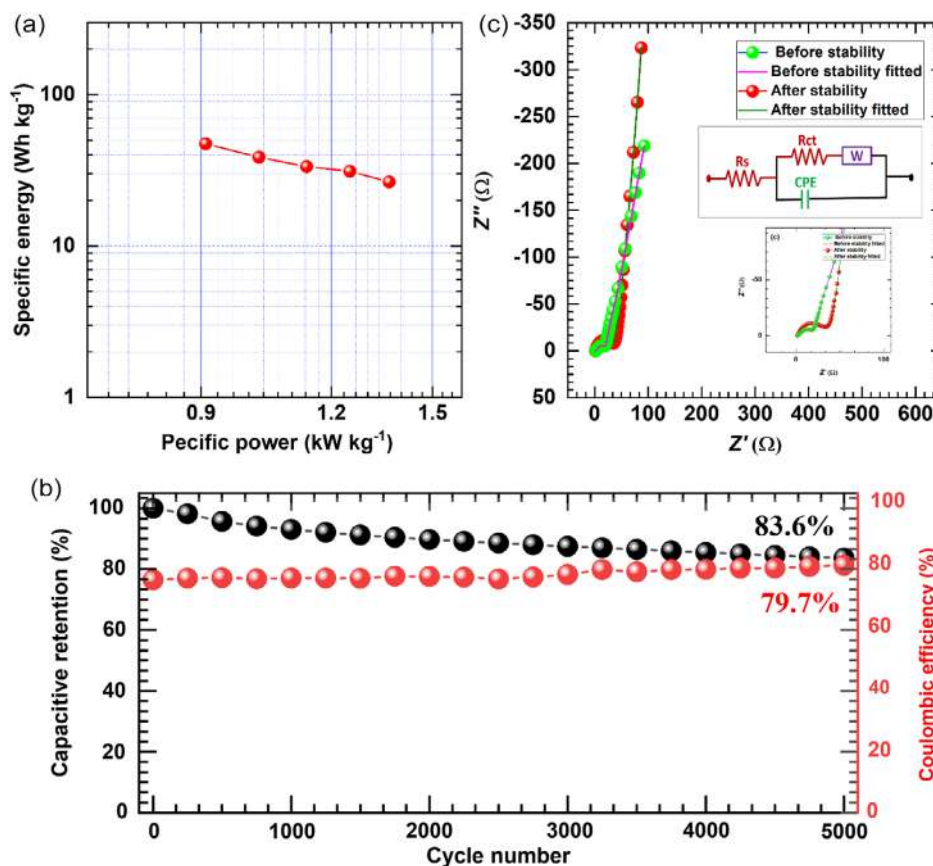


Figure 9. a) Ragone plot of HASD, b) a plot of capacitive retention, coulombic efficiency versus cycle number for HASD, and c) Nyquist plot of before and after stability for HASD.

two electrodes (CVO and rGO). The current findings demonstrate the positive effects of mesoporous CVO1:1 nanoparticle, which can offer maximum surface area; it is beneficial for exposure to more electrochemical active sites and electrolyte diffusion during electrochemical processes.

3.4. Solid-State Hybrid Supercapacitor Device

The solid-state hybrid supercapacitor device (SHSD) has developed as an appealing subject in research because of its applicability in portable and bendable devices. Moreover, it has excellent superiority, like the easy carriage or handling, due to its leak-proof and lower-weight properties and excellent stability.^[45] In addition, SHSD is probable to yield in different sizes and shapes as chosen in the application.^[46] The rGO and CVO1:1 electrodes were prepared on a large area of the SS substrate ($4 \times 4 \text{ cm}^2$), as shown in Figure S12, Supporting Information. Combining the CVO1:1 and rGO electrodes in PVA-KOH gel electrolyte makes an SHSD, as schematically shown in Figure 10a. The potential window variation for the optimization of the voltage of the SHSD, as illustrated in Figure S11c,d, Supporting Information, is varied from 0 to 1.2 and up to 1.7 V in CV

and GCD studies at fixed scan rate (50 mV s^{-1}) and current density (0.7 A g^{-1}), respectively. By concluding this potential window variation analysis, the potential window of 0 to 1.6 V for CV and GCD is perfect for the device study. Figure 10b displays CV graphs at various scan rates, from higher 100 mV s^{-1} to lower 5 mV s^{-1} scan rates, of the SHSD device. The GCD curves at different current densities ($0.3\text{--}1.1 \text{ A g}^{-1}$) are shown in Figure 10c, and the nonlinear GCD graph affirms the combinational pseudocapacitive and EDLC charge-storing ability of both electrodes.^[47,48] The SHSD achieves an excellent $102.9 \text{ F g}^{-1} C_s$ at 0.3 A g^{-1} , as shown in Figure 10d. Furthermore, the SHSD exhibited SE and SP of 36.6 Wh kg^{-1} and 0.30 kW kg^{-1} , as plotted in Figure 11a. By executing 500 consecutive GCD cycles at a fixed current density of 0.9 A g^{-1} , the continuing stability of SHSD is assessed, as illustrated in Figure 11b. After 5000 GCD cycles, the SHSD displays capacitance retention of 85.2% with coulombic efficiency of 71.9%, showing strong cycling stability and a long lifespan. EIS study, as depicted in Figure 11c, further explores the better charge transfer characteristics of SHSD. The less electrical resistivity of the electrodes and improved electrolyte-electrode intimacy without any considerable ohmic loss are responsible for the minor R_s (0.41Ω) and R_{ct}

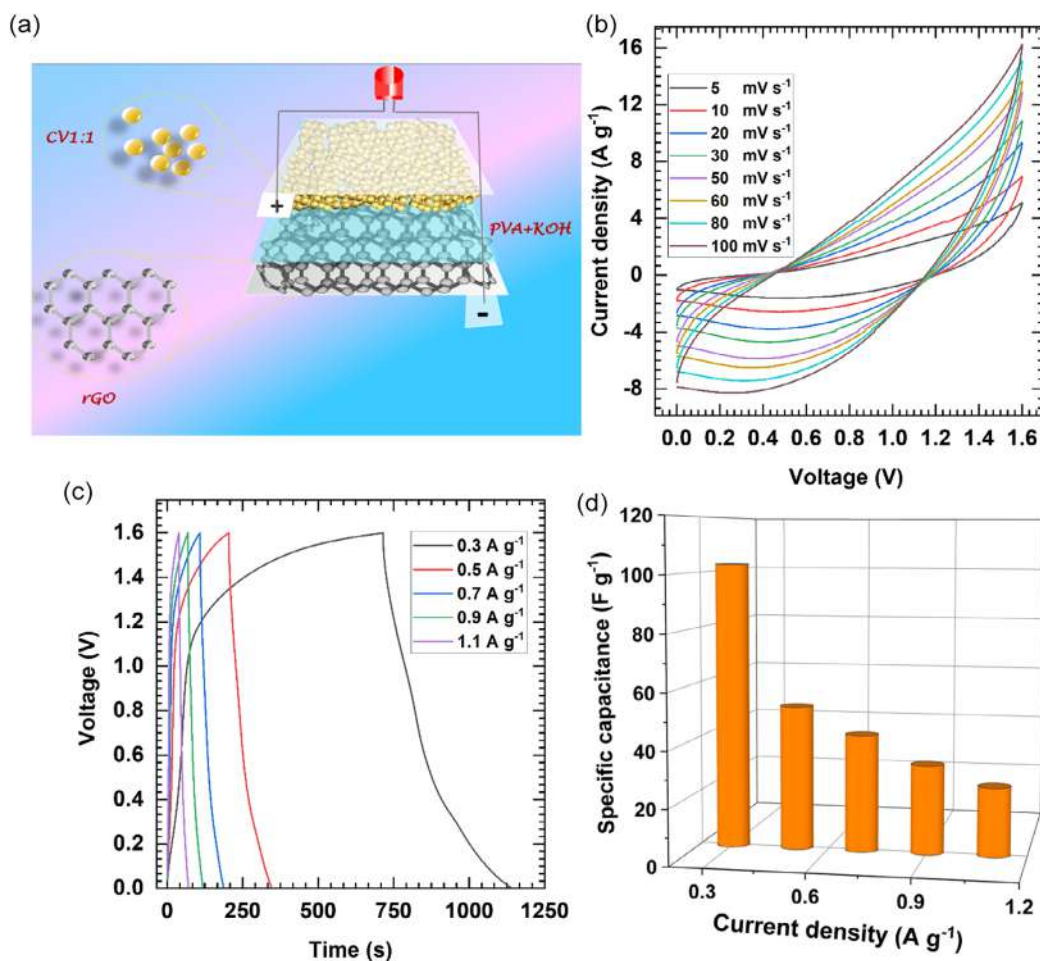


Figure 10. a) Schematic illustration of assembled SHSD, b) the CV at different scan rates, c) GCD curves of SHSD at various current densities, and d) the variation of specific capacitance with current density for SHSD.

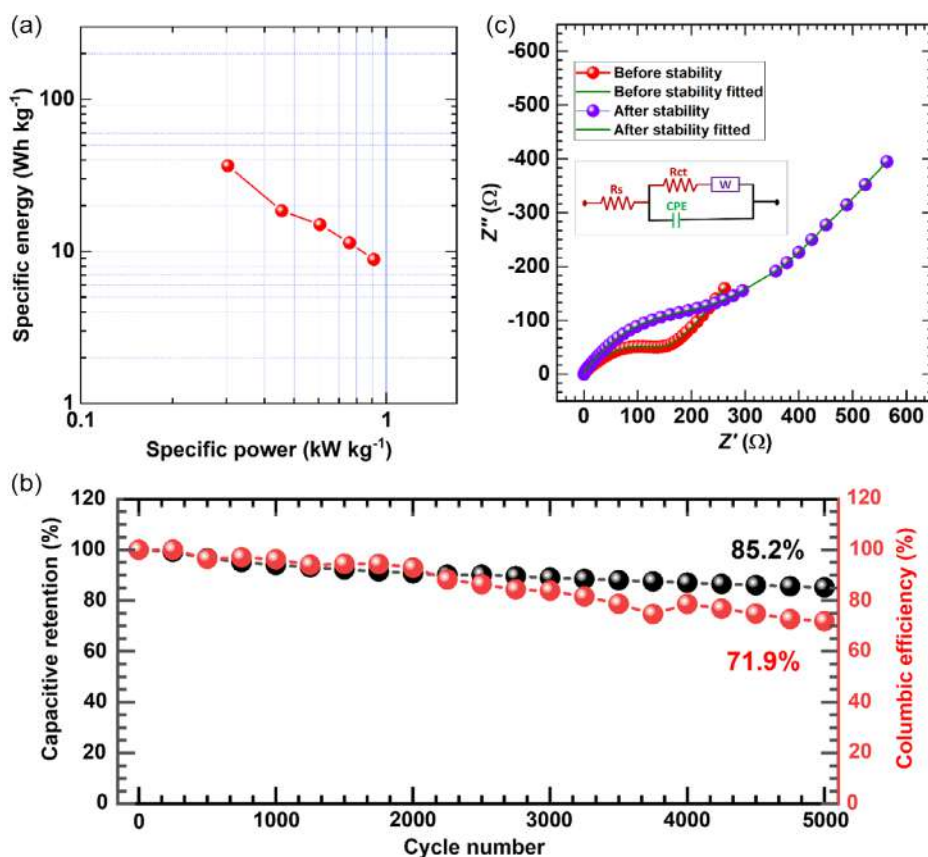


Figure 11. a) Ragone plot of SHSD, b) a plot of capacitive retention, coulombic efficiency versus cycle number for SHSD, and c) Nyquist plot of before and after stability for SHSD.

(165.8 Ω) values of SHSD before the stability. The retention of R_s (0.23 Ω) and R_{ct} (244.6 Ω) after the 5000 cycles suggests good stability of SHSD. Other EIS parameters are provided in Table S3, Supporting Information. Moreover, two devices are connected serially and utilized to light a lamp of 12 white LEDs to evaluate the practicality of SHSD, as shown in Figure 12a–d. The lamp was used to discharge these connected devices after charging for 30 s. The first, intense glow of the lamp after discharge implies that the SHSD produces considerable specific power. Furthermore, the long-lasting LED lamp brilliance implies that SHSD has excellent energy density. A comparative Ragone plot with reported literature on CVO-based hybrid supercapacitor devices is shown in Figure 12e. In CVO-based hybrid energy storage devices, Fahimi et al.^[49] fabricated ($\text{Co}_3\text{V}_2\text{O}_8//\text{AC}$), which exhibits a high SE of 59.2 Wh kg^{-1} at 250 W kg^{-1} SP. Nguyen et al. constructed a $\text{Co}_3\text{V}_2\text{O}_8//\text{AC}$ device and achieved SE of 55.5 Wh kg^{-1} at a higher SP of 800 W kg^{-1} .^[50] Moreover, Sun et al.^[16] developed $\text{Co}_2\text{V}_2\text{O}_7 \cdot 3.3\text{H}_2\text{O}//\text{rGO}$, and Liu et al.^[51] prepared $\text{CoV}_2\text{O}_6 \cdot 2\text{H}_2\text{O}//\text{AC}$ devices reported SE of 19 Wh kg^{-1} at 375.8 W kg^{-1} SP and SE of 19 Wh kg^{-1} at 400 W kg^{-1} SP, respectively. Lv et al.^[52] fabricated $\text{Co}_3\text{O}_4/\text{CoV}_x\text{O}_y//\text{AC}$ asymmetric device and reported SE of 26.1 Wh kg^{-1} at 400 W kg^{-1} . Zhang et al.^[53] assembled $\text{Co}_3\text{O}_4/\text{Co}_3(\text{VO}_4)_2//\text{AC}$ device obtained SE of 38 Wh kg^{-1} at 275 W kg^{-1} SP. Fahimi et al.^[54] constructed a $\text{Co}_3\text{V}_2\text{O}_8/\text{CNT}//\text{AC}$ solid-state

device and reported SE of 37.55 Wh kg^{-1} at 660 W kg^{-1} . Mishra et al.^[55] assembled $\text{Co}_3\text{V}_2\text{O}_8/\text{CN}_x//\text{AC}$ device and obtained SE of 41 Wh kg^{-1} at 385.18 W kg^{-1} . Also, Hosseini et al.^[56] fabricated $\text{Co}_3\text{V}_2\text{O}_8\text{-Ni}_3\text{V}_2\text{O}_8$ TLs@PCNFs//PCNFs reported SE of 59.7 Wh kg^{-1} at 1970 W kg^{-1} . Similar to the present work, the aqueous hybrid supercapacitor device based on $\text{Co}_2\text{V}_2\text{O}_7//\text{rGO}$ was fabricated by Wang et al.,^[11] which attained 35.2 Wh kg^{-1} SE at 101 W kg^{-1} SP. Moreover, the SHSD and ASHD devices manufactured in the present work demonstrated higher performance than the reported only similar device by Wang et al.^[11] in terms of SE and SP. However, the reported energy densities for $\text{Co}_3\text{V}_2\text{O}_8//\text{AC}$,^[49] $\text{Co}_3\text{V}_2\text{O}_8//\text{AC}$,^[50] and $\text{Co}_3\text{V}_2\text{O}_8\text{-Ni}_3\text{V}_2\text{O}_8\text{-PCNFs}//\text{PCNFs}$ ^[56] HASDs are slightly higher than the present work due to the use of Ni-foam (NF) as a conductive substrate since Ni foam can add its self-capacitance in the alkaline device.^[37] This work uses only SS as a conductive substrate, which avoids the redox reaction in the alkaline electrolyte; hence the obtained SE and SP originated from the CVO1:1 and rGO materials. Moreover, the position of the HASD device in the Ragone plot is higher than SHSD and reported hybrid devices in terms of SP, without sacrificing much SE,^[11,16,49–56] suggesting the suitability of CVO1:1 thin film electrode for next-generation hybrid energy storage devices.

The excellent energy storage capabilities of HASD and SHSD devices are credited to the apparent features of CVO1:1

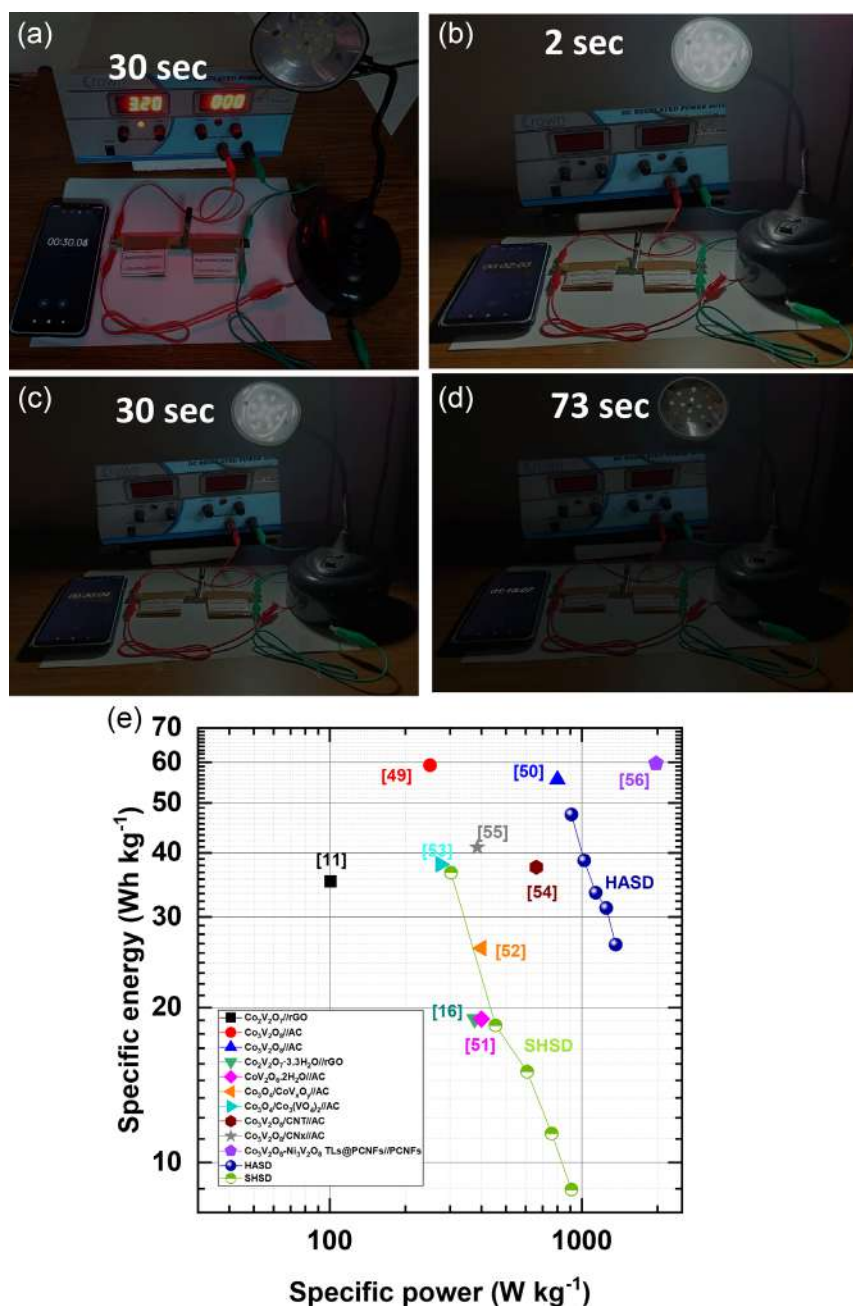


Figure 12. The photographs of SHSD demonstration by glowing LED lamp at a) charging for 30 s, b–d) discharging for 2, 30, and 73 s. e) Comparative Ragone plot of HASD and SHSD with available literature.

electrodes as, a) most notably the intercalative charge storage mechanism offered by mesoporous nanoparticles-like structure with high surface area (74.32 m² g⁻¹), b) synergy among transition metal species (Co and V), and c) binder-free preparation of thin film electrodes tends low impedance and diminishes the dead volume of resistive binders. Overall, SILAR synthetic approach provides an ultimate opportunity to produce CVO thin film electrodes with tuned surface area and nanostructured morphology by simply varying growth dynamics, improving supercapacitive performance. In light of the impressive outcomes, the

present work may reveal a new path for creating unique nanostructured materials for highly competent hybrid supercapacitor devices.

4. Conclusion

In conclusion, the growth dynamics-based SILAR method productively synthesizes CVO (CO₃V₂O₈·nH₂O) thin film electrodes having nanoparticles-like morphology with high surface area and

mesoporous structure. The altered growth dynamics of CVO series thin film electrodes result in a change in morphology, surface area, and porous structure, which ultimately influences the electrochemical performance of the electrodes. The optimized CVO1:1 thin film electrode displayed the highest C_s of 793 F g^{-1} at 0.5 A g^{-1} , owing to the maximum surface area of $74.32 \text{ m}^2 \text{ g}^{-1}$. Additionally, the HASD manifested the maximum C_s of 133.5 F g^{-1} with the SE of 47.7 Wh kg^{-1} with SP of 0.90 kW kg^{-1} . Likewise, the SHSD achieved the maximum C_s of 102.9 F g^{-1} at 0.30 kW kg^{-1} SP and 36.6 Wh kg^{-1} of SE. Moreover, the superior electrochemical capacitive characteristics in terms of C_s , SE, SP, and stability of the SHSD (CVO1:1//PVA-KOH//rGO) and HASD (CVO1:1//KOH//rGO) devices point to their considerable potential use in a variety of portable electronic devices. In conclusion, SILAR is a feasible approach to produce binder-free, mesoporous, cobalt vanadium oxide (CVO) thin film electrodes with tuned surface area as a potential cathode for HSC.

Supporting Information

Supporting Information is available from the Wiley Online Library or from the author.

Acknowledgements

The authors are thankful to the Ministry of Science and Technology India, Department of Science and Technology-Innovation in Science Pursuit for Inspired (DST-INSPIRE), for financial support through research project sanction no. DST/INSPIRE/04/2016/000260. Also, this research is supported through internal university research project sanction no. DYPES/DU/R&D/2022/2353 by D. Y. Patil Education Society, Kasaba Bawada, Kolhapur. The author S.S.K. acknowledges the Mahatma Jyotiba Phule Research Fellowship, Nagpur (Government of Maharashtra) for awarding as MJPRF FELLOW (MJPRF-2021).

Conflict of Interest

The authors declare no conflict of interest.

Data Availability Statement

The data that support the findings of this study are available from the corresponding author upon reasonable request.

Keywords

cobalt vanadium oxide, growth dynamics, hybrid supercapacitor devices, successive ionic layer adsorption and reaction method, surface area

Received: April 13, 2023

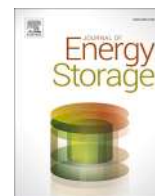
Revised: July 19, 2023

Published online:

- [1] X. Wang, Y. Zhang, J. Zheng, X. Liu, C. Meng, *J. Colloid Interface Sci.* **2019**, *554*, 191.
[2] Y. Zhang, X. Jing, Y. Cheng, T. Hu, C. Meng, *Inorg. Chem. Front.* **2018**, *5*, 2798.

- [3] P. Shinde, S. Jun, *ChemSusChem* **2020**, *13*, 11.
[4] J. Yan, Q. Wang, T. Wei, Z. Fan, *Adv. Energy Mater.* **2014**, *4*, 1300816.
[5] S. Huang, X. Zhu, S. Sarkar, Y. Zhao, *APL Mater.* **2019**, *7*, 100901.
[6] N. Chodankar, H. Pham, A. Nanjundan, J. Fernando, K. Jayaramulu, D. Golberg, Y. Han, D. Dubal, *Small* **2020**, *16*, 2002806.
[7] J. Zheng, Y. Zhang, Q. Wang, H. Jiang, Y. Liu, T. Lv, C. Meng, *Dalton Trans.* **2018**, *47*, 452.
[8] Y. Zhang, M. Chen, T. Hu, C. Meng, *ACS Appl. Nano Mater.* **2019**, *2*, 2934.
[9] W. Low, P. Khiew, S. Lim, C. Siong, E. Ezeigwe, *J. Alloys Compd.* **2019**, *775*, 1324.
[10] S. Marje, P. Deshmukh, J. Gunjekar, C. Lokhande, U. Patil, *Energy Fuels* **2021**, *35*, 14110.
[11] H. Wang, H. Zhang, D. Zhang, J. Chen, S. Zhang, S. Zhang, J. Yu, Q. Wu, Q. Li, *ACS Appl. Mater. Interfaces* **2022**, *14*, 8106.
[12] K. Le, M. Gao, D. Xu, Z. Wang, G. Wang, G. Lu, W. Liu, F. Wang, J. Liu, *Inorg. Chem. Front.* **2020**, *7*, 3646.
[13] P. Devi, M. Srivastava, N. Kim, J. Lee, D. Mishra, *Composites B: Eng.* **2021**, *227*, 109384.
[14] B. Huang, W. Wang, T. Pu, J. Li, C. Zhao, L. Xie, L. Chen, *Chem. Eng. J.* **2019**, *375*, 121969.
[15] M. Isacfranklin, C. Deepika, G. Ravi, R. Yuvakkumara, D. Velauthapillai, B. Saravanakumar, *Ceram. Int.* **2020**, *46*, 28206.
[16] H. Sun, X. Chen, H. Chai, Y. Wang, D. Jia, Y. Cao, A. Liu, *Appl. Surf. Sci.* **2019**, *469*, 118.
[17] W. Low, C. Siong, C. Chia, S. Lim, P. Khiew, *J. Sci.: Adv. Mater. Dev.* **2019**, *4*, 515.
[18] Y. Zhang, Y. Liu, J. Chen, Q. Guo, T. Wang, H. Pang, *Sci. Rep.* **2014**, *4*, 5687.
[19] Y. Teng, Y. Li, D. Yu, Y. Meng, Y. Wu, X. Zhao, X. Liu, *ChemistrySelect* **2019**, *4*, 956.
[20] Y. Wang, H. Chai, H. Dong, J. Xu, D. Jia, W. Zhou, *ACS Appl. Mater. Interfaces* **2016**, *8*, 27291.
[21] W. Lv, C. Yang, G. Meng, R. Zhao, A. Han, R. Wang, J. Liu, *Sci. Rep.* **2019**, *9*, 10831.
[22] G. Barbosa, C. Graeff, H. Oliveira, *Ecl. Quím.* **2005**, *30*, 7.
[23] D. Malavekar, V. Lokhande, V. Mane, S. Kale, R. Bulakhe, U. Patil, I. In, C. Lokhande, *J. Solid State Electrochem.* **2020**, *24*, 2963.
[24] C. Zeinalipour-Yazdi, E. Loizidou, *Chem. Phys.* **2021**, *550*, 111295.
[25] J. Han, L. Zhang, S. Lee, J. Oh, K. Lee, J. Potts, J. Ji, X. Zhao, R. Ruoff, S. Park, *ACS Nano*, **2013**, *7*, 19.
[26] L. Zhang, X. Zhao, *Chem. Soc. Rev.* **2009**, *38*, 2520.
[27] M. Aghazadeh, I. Karimzadeh, M. Ganjali, *J. Mater. Sci. Mater. Electron.* **2017**, *28*, 13532.
[28] X. Dong, Y. Yang, B. Wang, Y. Cao, N. Wang, P. Li, Y. Wang, Y. Xia, *Adv. Sci.* **2020**, *7*, 2000196.
[29] P. Katkar, S. Marje, S. Pujari, S. Khalate, A. Lokhande, U. Patil, *Langmuir* **2021**, *37*, 5260.
[30] D. Chao, X. Xia, J. Liu, Z. Fan, C. Ng, J. Lin, H. Zhang, Z. Shen, H. Fan, *Adv Mater.* **2014**, *26*, 5794.
[31] H. Chen, D. Yang, X. Zhuang, D. Chen, W. Liu, Q. Zhang, H. Hng, X. Rui, Q. Yan, S. Huang, *Nano Res.* **2020**, *13*, 1867.
[32] E. Goda, A. Rehman, B. Pandit, A. Eissa, S. Hong, K. Yoon, *J. Chem. Eng.* **2022**, *428*, 132470.
[33] J. William, I. Babu, G. Muralidharan, *J. Chem. Eng.* **2021**, *422*, 130058.
[34] C. Li, D. Ma, Q. Zhu, *Nanomaterials* **2022**, *12*, 848.
[35] S. Luo, J. Li, J. Lu, F. Tao, J. Wan, B. Zhang, X. Zhou, C. Hu, *Mater. Today Phys.* **2021**, *17*, 100337.
[36] L. Chen, Z. Yang, J. Wu, H. Chen, J. Meng, *Electrochim. Acta* **2020**, *330*, 135347.
[37] S. Pujari, S. Kadam, Y. Ma, Jadhav, S. Kumbhar, S. Bhosale, J. Gunjekar, C. Lokhande, U. Patil, *J. Energy Storage* **2022**, *22*, 52105037.
[38] C. Huang, J. Zhang, N. Young, H. Snaith, P. Grant, *Sci. Rep.* **2016**, *6*, 25684.

- [39] J. Kim, V. Augustyn, B. Dunn, *Adv. Energy Mater.* **2012**, 2, 141.
- [40] G. Muller, J. Cook, H. Kim, S. Tolbert, B. Dunn, *Nano Lett.* **2015**, 15, 1911.
- [41] S. Marje, V. Patil, V. Parale, H. Park, P. Shinde, J. Gunjekar, C. Lokhande, U. Patil, *Chem. Eng. J.* **2022**, 429, 132184.
- [42] V. Augustyn, J. Come, M. Lowe, J. Kim, P. Taberna, S. Tolbert, H. Abruña, P. Simon, B. Dunn, *Nat. Mater* **2013**, 12, 518.
- [43] G. Raju, E. Pavitra, G. Nagaraju, S. Sekhar, S. Ghoreishian, C. Kwak, J. Yu, Y. Huh, Y. Han, *J. Mater. Chem. A* **2018**, 6, 13178.
- [44] Y. Gono, Y. Kimura, K. Yashiro, S. Watanabe, S. I. Hashimoto, T. Kawada, *J. Electrochem. Soc.* **2014**, 161, 11.
- [45] Z. Tang, C. Jia, Z. Wan, Q. Zhou, X. Ye, Y. Zhu, *RSC Adv.* **2016**, 6, 112307.
- [46] S. Patil, N. Chodankar, R. Pujari, Y. Han, D. Lee, *J. Power Sources* **2020**, 46, 6228286.
- [47] P. Simon, Y. Gogotsi, *Nat. Mater.* **2008**, 6, 845.
- [48] B. E. Conway, *Electrochemical Supercapacitors: Scientific Fundamentals and Technological Applications*, Springer, Berlin **1999**.
- [49] Z. Fahimi, O. Moradlou, A. Sabbah, K. Chen, L. Chen, M. Qorbani, *Chem. Eng. J.* **2022**, 436, 135225.
- [50] V. Nguyen, F. Saria, J. Ting, *RSC Adv.* **2022**, 12, 29170.
- [51] S. Liu, S. Sarwar, H. Zhang, Q. Guo, J. Luo, X. Zhang, *Electrochim. Acta* **2020**, 364, 137320.
- [52] X. Lv, W. Huang, J. Tang, L. Tang, Q. Shi, *Electrochim. Acta* **2021**, 380, 138248.
- [53] W. Zhang, L. Kong, X. Ma, Y. Luo, L. Kang, *J. Power Sources* **2014**, 269, 61.
- [54] Z. Fahimi, O. Moradlou, *J. Energy Storage* **2022**, 50, 104697.
- [55] R. Mishra, P. Panda, S. Barman, *New J. Chem.* **2021**, 45, 5897.
- [56] H. Hosseini, S. Shahrokhian, *Chem. Eng. J.* **2018**, 341, 10.



Research papers

Development of binder-free, amorphous nickel vanadate cathodes by SILAR method for hybrid supercapacitors: Exploiting surface area by monitoring growth rate

Shraddha B. Bhosale^a, Sambhaji S. Kumbhar^a, Sachin S. Pujari^a, Vinod V. Patil^{a,b}, Nitish Kumar^c, Rahul R. Salunkhe^c, Chandrakant D. Lokhande^a, Jayavant L. Gunjekar^a, Umakant M. Patil^{a,d,*}

^a Centre for Interdisciplinary Research, D. Y. Patil Education Society, Kasaba Bawada, Kolhapur 416006, India

^b School of Chemical Sciences, Punyashlok Ahilyadevi Holkar Solapur University, Solapur 413255, India

^c Department of Physics, Indian Institute of Technology Jammu, Jagti, Jammu, J & K 181221, India

^d Department of Materials Science and Engineering, Yonsei University, 50 Yonsei-ro, Seodaemun-gu, Seoul 03722, Republic of Korea



ARTICLE INFO

Keywords:

Growth rate variation
Nickel vanadate
SILAR
Surface area
Supercapacitor
Thin film

ABSTRACT

Developing self-supported electrode material in the absence of electro-inert binders considering the effortless transfer of charges and manipulating physicochemical properties of electrodes in energy storage devices is essential. Hence, the present attempt emphasizes the facile synthetic strategy of successive ionic layer adsorption and reaction (SILAR) for controlled nickel vanadate (NV) growth over the conducting plate. In SILAR synthesis, the growth rate is monitored by rinsing and adsorption/reaction time variation to tune the surface area, mesoporous structure, and surface morphology of NV thin films. As a result, the formation of mesoporous, amorphous, hydrous nanoparticles of NV over the stainless-steel substrate is affirmed by structural analysis. Furthermore, alteration in specific surface area with variation in growth rate is observed in BET analysis. As a result, the optimal NV(1:2) thin film electrode exhibited the highest specific capacity (capacitance) of 355C g^{-1} (710 F g^{-1}) at 1 A g^{-1} current density. Moreover, the fabricated aqueous hybrid supercapacitor device (NV(1:2)//rGO) delivered 109 F g^{-1} specific capacitance at 1.3 A g^{-1} current density, and the device exhibited a maximum specific energy (SE) of 44 Wh kg^{-1} at a particular specific power (SP) of 1.14 kW kg^{-1} . Furthermore, the solid-state hybrid supercapacitor (NV(1:2)//PVA-KOH//rGO) device conferred a specific capacitance of 89 F g^{-1} at 0.5 A g^{-1} current density and an SE of 36 Wh kg^{-1} at 0.482 kW kg^{-1} SP. This research paved an avenue to the binder-free, scalable synthesis of NV electrodes and employed them as a cathode in practical applications of hybrid energy storage devices.

1. Introduction

Increasing concern over the depletion of fossil fuels turned the attention of this generation toward environmentally friendly energy generation and conversion systems. On the other hand, the fluctuations, intermittency, and less continuity of conventional energy generation have urged researchers toward sources of electrical energy devices (EEDs) [1,2]. Hence, efforts toward a highly efficient, sustainable, low-cost, and environmentally friendly energy storage system are still in progress. Among the various energy storage systems, electrochemical energy storage devices (EESDs), such as supercapacitors, batteries, fuel

cells, etc., are highly desirable and environmentally friendly [3,4]. Among the consortium of clean energy storage systems, ‘supercapacitors’ are the most common alternative to batteries in many applications and have been extensively studied for many decades because of their high specific power (SP), rapid discharge-recharge rate, and exceptional cyclic stability. But less specific energy (SE) sometimes limits the practical use of supercapacitors compared to battery systems. Hence, it is necessary to contribute more significant potential for developing high-energy supercapacitors without sacrificing the SP. Efforts toward enhancing the SE of supercapacitors by fabricating a hybrid device that emphasizes cathode materials superiority, exhibits high

* Corresponding author at: Centre for Interdisciplinary Research, D. Y. Patil Education Society, Kasaba Bawada, Kolhapur 416006, India.
E-mail address: umakant.physics84@gmail.com (U.M. Patil).

<https://doi.org/10.1016/j.est.2023.108417>

Received 6 April 2023; Received in revised form 27 June 2023; Accepted 16 July 2023

Available online 24 July 2023

2352-152X/© 2023 Elsevier Ltd. All rights reserved.

specific capacitance (C_{sp}), and provides a wide potential window when combined with an electrochemical double layer capacitive (EDLC) type anode material is a well-known method [5–7].

As we know, the electrode material and choice of electrolyte play a crucial role in the performance of applicable technologies; hence, identifying high-performance electrode materials is essential to develop hybrid energy storage devices (HESDs) [8]. A material with a substantial surface area, mesoporous nature, electrochemical stability, and more significant conductivity can achieve high energy-storing performance. The evolution of vanadium compounds with transition metals displays superior redox behavior due to their coordination environment and manifold valencies. With their richer valencies of vanadium and nickel, such as vanadium from 2+ to 5+ and nickel from 2+ to 3+, they can make a diverse atomic ratio. Therefore, nickel vanadate (NV) materials with multiple valencies and unique dielectric and magnetic behavior are more suitable as electrodes in batteries, electrocatalysis, photocatalysis, sensors, and HESDs application [9–15]. Apart from choosing the suitable electrode material, producing a rationally designed structure with an enhanced specific surface area and plenty of diffusion channels is essential for active site exposure and ease of electrolyte transportation. Also, it is well known that most redox activities in pseudocapacitors occur on or near the surface of the material [16]. Thus, preparing nanostructured materials is essential and mainly relies on synthetic approaches and preparative parameters. The hydrothermal method has been mostly employed to develop the different nanostructures of NV for HESD applications. For instance, Li et al. [9] prepared NiV_2O_6 , Singh et al. [17] designed a stone-like morphology of $Ni_3V_2O_8$, Nandi et al. [18] synthesized nanopetals of NiV_2O_6 , $Ni_3V_2O_8$ nanosheets were developed by Merum et al. [19], $Ni_3(VO_4)_2$ prepared by Kumar et al. [20] through the hydrothermal method. Also, the hydrothermal method is used by Chandra Sekhar et al. [21] to prepare $Ni_2V_2O_7$, and the nanorods of $Ni_2V_2O_7$ were prepared by Ezhil Arsi et al. [22] through the co-precipitation method. However, most of these reports have described the preparation of nickel vanadate materials in powder form; additionally, the electrode preparation for supercapacitors in those reports involved conventional binder-assisted coating techniques using PVDF. In contrast, this study explores the direct growth of NV thin film on conductive stainless steel (SS) current collectors, which is considered a more effective approach for enhancing interfacial contact than binder-enriched coating methods. Moreover, the improved electrochemical capacitive performance of the NV electrode can be achieved by controlling parameters such as the size of particles, morphology, and porous structure. Among several deposition methods, the SILAR method is the most efficient way to produce binder-free, amorphous, or nanocrystalline materials thin film electrodes. The SILAR method can control the growth rate and, consequently, the thickness of films across a wide range, ranging from a few layers to microns, through varying preparative parameters. Also, an advantageous feature of SILAR is that it can be performed at low temperatures, making it convenient and energy-efficient. These unique characteristics make SILAR a versatile and influential method for the preparation of binder-free thin film electrodes.

It is crucial to create novel structural designs and optimization strategies to surpass the limits of conventional electrodes. So far, the very first time a facile SILAR approach has been applied for developing binder-free NV electrodes and utilized for EESDs. Apart from the precursor concentrations, immersion cycles, pH of the cationic and anionic precursor solutions, and bath temperature, the present study emphasizes the influence of rinsing, adsorption/reaction time interval on the growth kinetics, and consequent physicochemical properties of NV thin film electrodes. The tuned surface area with the mesoporous structure of the NV(1:2) electrode prepared at optimal growth rate exhibits excellent charge-storing ability. Furthermore, the aqueous and solid-state hybrid devices were fabricated benefiting from a cathode of NV(1:2), and rGO electrode as an anode, and their electrochemical capacitive performances are recorded and demonstrated herein.

2. Experimental section

2.1. Materials

Nickel nitrate ($Ni(NO_3)_2$), sodium orthovanadate (Na_3VO_4), potassium hydroxide (KOH), graphite flakes, sodium nitrate ($NaNO_3$), potassium permanganate ($KMnO_4$), *N*-methyl pyrrolidone (NMP), polyvinylidene fluoride (PVDF), polyvinyl alcohol (PVA), hydrogen peroxide (H_2O_2), sulfuric acid (H_2SO_4) and hydrazine hydrate (N_2H_4) were purchased from Sigma Aldrich. Purchased chemicals are analytical grade, afterward utilized as-received without any purification. In addition, stainless steel (SS) substrates (grade 304) were purchased from the local market of Kolhapur, India, for the NV thin film deposition.

2.2. Synthesis of nickel vanadate

The NV thin films are synthesized via a binder-free SILAR process at ambient temperature. Deposition of NV has been performed upon the SS substrates used as the current collector. The cleaning of the substrate plays a crucial role in the uniform deposition of NV material. First, SS substrates were finely polished with smooth polish paper, followed by acetone and double distilled water (DDW) sonication. Briefly, layer-by-layer formation of the NV thin films comprises nickel cations adsorption over SS substrate from the first bath containing 0.05 M of nickel nitrate solution, followed by rinsing in a second beaker containing DDW, where excessive and loosely adsorbed ionic species of nickel were rinsed away. Then the third beaker contains the 0.05 M solutions of sodium orthovanadate, where the reaction occurs between nickel and vanadium species. Rinsing in DDW is also performed after the formation of the NV thin layer to eliminate loosely bounded NV molecules/particles. This entire process is repeated a hundred times to achieve the desired thickness of the NV thin film, as depicted in Fig. 1(a). Furthermore, obtained lively yellow-colored NV thin films, the photograph shown in Fig. 1(b), were rinsed 2 to 3 times in DDW. Unlike other chemical methods, such as co-precipitation and hydrothermal, the sequential layer-by-layer assembly of the SILAR process avoids precipitate formation and wastage of material. Finally, the prepared NV series samples were dried at ambient conditions. The dried NV series sample was further characterized for structural, morphological, and electrochemical analyses. Also, rGO used as an anode was prepared by modified Hummers method followed by chemical reduction, and detailed synthesis of rGO is discussed in Note S1 (see electronic supporting information (ESI))

2.3. Material characterizations

As prepared material is characterized using various analytical characterization techniques. Structural properties of prepared NV thin films were studied using an X-ray diffractometer (XRD) from Rigaku miniflex-600 with $Cu K\alpha$ ($\lambda = 0.15425$ nm) target radiations between 10° to 80° . Fourier transform infrared spectrometry (FT-IR) was carried out using the Alpha (II) Bruker unit to investigate the functional groups and chemical bonding materials. The surface morphology, cross-section, and elemental composition of NV thin films were studied by using field emission scanning electron microscopy (FE-SEM) (Hitachi S4800) and energy-dispersive electron microscopy (EDS). The surface topographical features were observed using atomic force microscopy (Oxford cipher S). TEM measurements were performed using a JEOL JEM-ARM200F NEOARM at 200 KeV. Surface topographical features were observed using atomic force microscopy (Oxford cipher S). Brunauer-Emmett-Teller (BET) and Barrett-Joyner-Halenda (BJH) techniques were used to examine the specific surface area and pore size distribution using the Belsorp II mini instrument. The X-ray photoelectron spectroscopy (XPS) measurement was done using the ESCALAB 250 (ThermoElectron, Al $K\alpha$) instrument. The electrochemical measurements of the NV series electrode were performed using a VersaStat 4 electrochemical workstation.

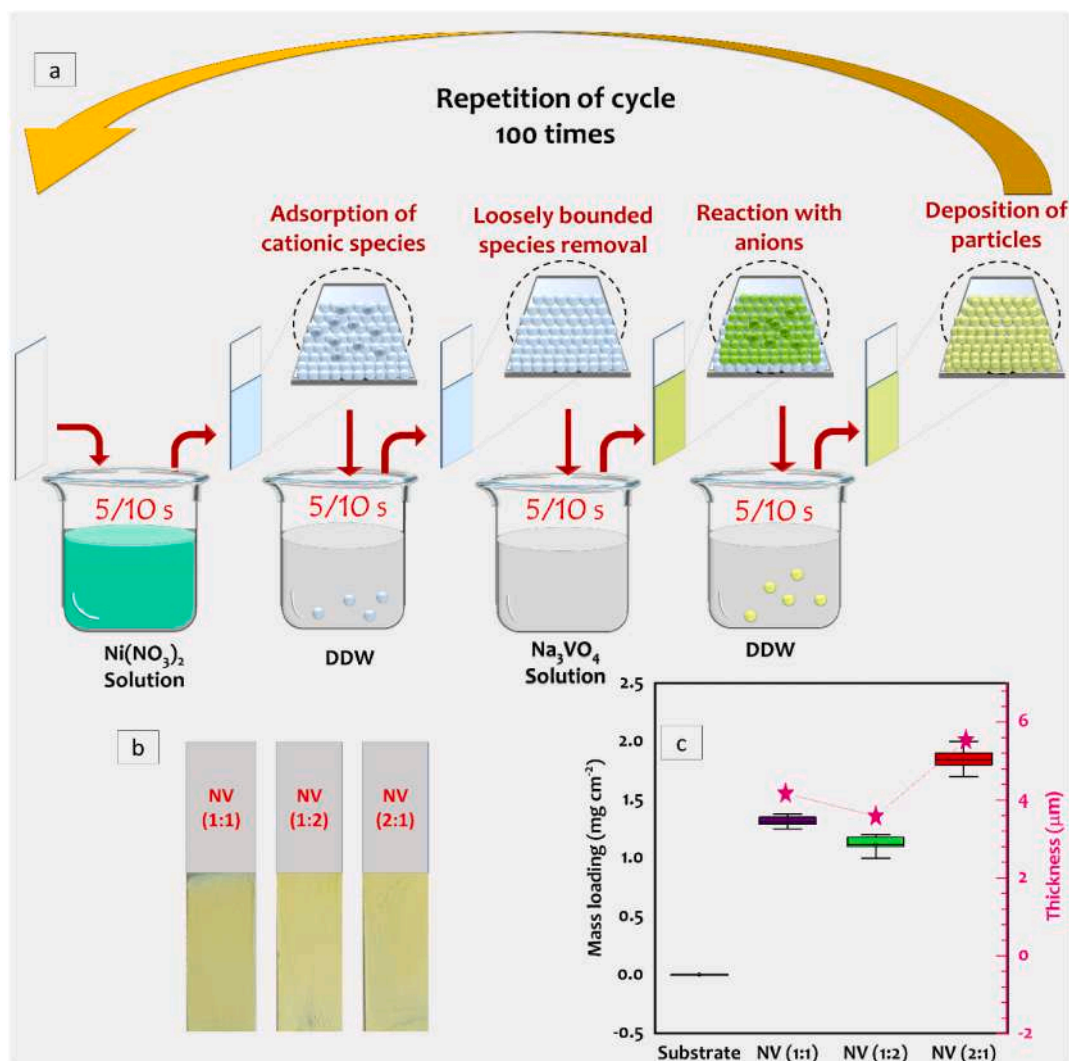


Fig. 1. (a) Schematic illustration of NV thin film preparation by SILAR method, (b) Photographs of deposited NV series thin films, and (c) Plot of mass loading and thickness versus NV series samples.

2.4. Electrochemical measurements

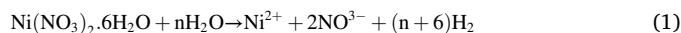
The electrochemical activities of NV series and rGO electrodes were performed individually using a three-electrode system (Half-test cell). Electrochemical analysis was carried out by using cyclic voltammetry (CV), galvanostatic charge-discharge (GCD), electrochemical impedance spectroscopy (EIS), and cycling stability tests in 1 M aqueous KOH electrolyte. As-deposited NV electrodes were used as working electrodes. Platinum plate and Hg/HgO were utilized as counter and reference electrodes, respectively. More details about the preparation of gel electrolytes are discussed in Note S2 (see ESI), and the required formulae for capacitive performance calculation are given in Note S3 (see ESI).

3. Results and discussion

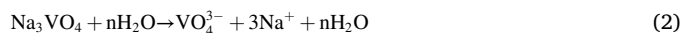
3.1. Formation of nickel vanadate thin film

The SILAR method employs a series of steps, including the adsorption of cations onto the surface of the substrate, followed by rinsing in DDW. The same water rinsing procedure is pursued after the reaction among pre-adsorbed cations and anions in the anionic precursor solution. Then the whole process is repeated to increase the thickness of the thin film, as shown in the schematic synthesis procedure of the NV thin film in Fig. 1a. In SILAR deposition, the layers of cations and anions are

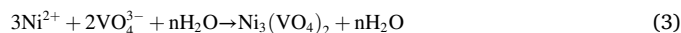
consecutively performed to grow nucleated species; the layer-by-layer deposition procedure takes place to develop thin films. To carefully control the deposition process, layer-by-layer assembly executes the following steps: adsorption of nickel ions produced as per reaction (1) from nickel nitrate precursor over SS substrate and removal of excessive ionic species in a pure solvent of DDW in rinsing.



The exact process of rinsing and removing the excessive ionic species is followed even after the pre-adsorbed nickel ions reacted with vanadium ion species obtained as per reaction (2) from an anionic precursor containing sodium orthovanadate. The dissolution of sodium orthovanadate in water gives,



Additionally, the reaction is carried out by immersing a substrate with a layer of Ni^{2+} ions on it in a precursor solution of sodium orthovanadate, in which a reaction between vanadium and nickel ions results in the deposition of adherent NV on the substrate as per the subsequent reaction (3),



Apart from the noticeable benefits of high yield and energy-

preserving, the leading advantages of the SILAR method are the control over growth rates and the film thickness, which can be accomplished by changing adsorption/reaction and rinsing time and changing deposition cycles. Therefore, to investigate the effect of dipping time in adsorption/reaction and rinsing baths on growth rates of NV films, it varied in the ratio of 1:1, 1:2, and 2:1, and termed as NV(1:1), NV(1:2), and NV(2:1), respectively. The photographs of deposited thin films at different dipping time variations are shown in Fig. 1 (b). Furthermore, the mass loading of NV series thin films, after 100 cycles, was quantified by the gravimetric weight difference method through the mass per unit area (mg cm^{-2}) over SS substrate and shown in Fig. 1 (c). Change in the deposited weight with variation in dipping time suggests that the mass loading of the NV thin films particularly belongs to the alteration in growth rate, which in the SILAR method is associated with adsorption/reaction along with rinsing periods. Also, to ensure the alteration of growth rate, the thickness of NV series samples was measured through cross-sectional FE-SEM images and provided in Fig. S1 (a-c) (see ESI). More specifically, cross-sectional FE-SEM images reveal that the NV(1:1) sample exhibits a thickness of $4.2 \mu\text{m}$, the NV(1:2) sample displays a thickness of $2.5 \mu\text{m}$, and the NV(2:1) sample shows a thickness of $5.6 \mu\text{m}$. The obtained thickness trend with respect to the dipping time variation is analogous to the mass loading trend of NV series samples, as shown in Fig. 1 (c). Mass loading and thickness measurements unanimously reveal that the NV (2:1) achieves a maximum thickness; on the other hand, sample NV (1:2) shows less thickness, which concludes that more rinsing time results in lowering the thickness due to the slow growth rate of the material [23]. Hence, the growing rate of NV material is influenced by the duration of the substrate in cationic/anionic precursor and rinsing solutions, where more rinsing time slows down the growth rate and results in less thickness and vice versa. Therefore, such a change in the growth kinetics of the NV materials can lead to a change in the physicochemical properties of the material over SS substrate, and it can influence the electrochemical properties of NV series electrodes.

3.2. Structural and morphological study of NV series thin films

The structural examination of prepared NV thin films was performed using the XRD technique, as shown in Fig. 2(a). The XRD patterns of all the NV series thin film samples illustrate similar diffraction spectra without any significant peaks from the material, except peaks from the SS substrate. The diffraction peaks highlighted by the emblem (*) in Fig. 2 (a) appeared from the SS substrate. The obtained spectra in the range of 10° to 80° do not contain any significant peak of the material,

which suggests the formation of amorphous NV over the SS substrates. The poor crystallinity of NV samples resulted from the lack of periodic arrangement of atoms due to the atomic shielding between the nucleated species and adsorbed layers of material [15]. Moreover, such an amorphous material structure significantly enhances the electrochemical performance by providing an improved surface area of the material and structural flexibility, allowing deeper diffusion of the electrolyte ions to access the active materials [24].

The presence of various functional groups in the NV series samples was probed by FT-IR analysis, as shown in Fig. 2 (b). It represents the FT-IR spectra of synthesized NV (1:1), NV(1:2), and NV(2:1) samples in the scanning range of 400 to 4000 cm^{-1} . The occurrence of absorption bands within the range of 400 – 900 cm^{-1} is specially related to the stretching vibrations of metal oxides. As-plotted FT-IR spectra show similar features for all samples, and the band ν_1 at 476 cm^{-1} is allocated to Ni–O vibrations (stretching) [25,26]. Moreover, the occurrence of band ν_2 at 693 cm^{-1} corresponds to the V–O–V vibrations (antisymmetric stretching) [27]. The presence of band ν_3 around 909 cm^{-1} is attributed to the symmetric stretching mode of the V=O group. [28]. Also, the absorption band ν_4 related to N–O stretching vibrations is around 1351 cm^{-1} , obtained from trapped nitrate (NO_3^-) ions from the precursor [29]. Furthermore, the bands ν_5 at 1627 cm^{-1} and ν_6 at 3429 cm^{-1} are accredited to the bending and vibrations of the hydroxyl group (H–O–H, stretching), respectively, from structural water entrapped during the rinsing process in synthesis [30]. Obtained characteristic peaks underscore the presence of structural water content in prepared material. Regardless of the growth rate variation, the XRD and FT-IR spectra confirm amorphous and hydrous nickel vanadate material formation in thin films in all NV series samples.

The detailed chemical oxidation states of each element contained in the NV series sample were uncovered by XPS analysis. Observing Ni, V, and O elements in the XPS survey spectrum (Fig. 3 (a)) indicates the presence of the elements, as mentioned earlier, on the surface of the NV samples. As illustrated in Fig. 3 (b), Ni 2p has two leading spectral peaks, which rise from the spin-orbit splitting at a binding energy of 855.58 and 873.28 eV and are termed Ni 2p_{3/2} and Ni 2p_{1/2}, respectively. The two prominent peaks of Ni 2p_{3/2} and Ni 2p_{1/2} are separated by 17.7 eV binding energy difference along with better-christened ‘satellite peaks’ at energy of 861.28 and 879.58 eV . The peaks reveal the presence of Ni²⁺ and Ni³⁺ species [29–31], which confirms the divalent and trivalent states of nickel in bulk and near the surface of NV material, respectively. The fitted spectra of V 2p, as shown in Fig. 3 (c), demonstrated two peaks at a binding energy of 517.88 and 524.28 eV are

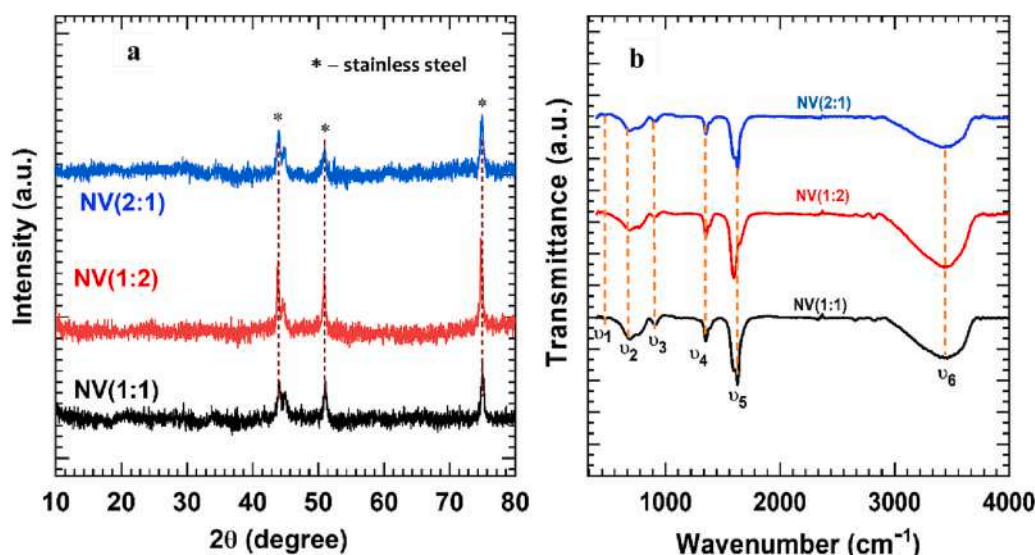


Fig. 2. (a) XRD pattern (b) FT-IR spectra of NV series thin films for NV(1:1), NV(1:2), and NV(2:1) samples.

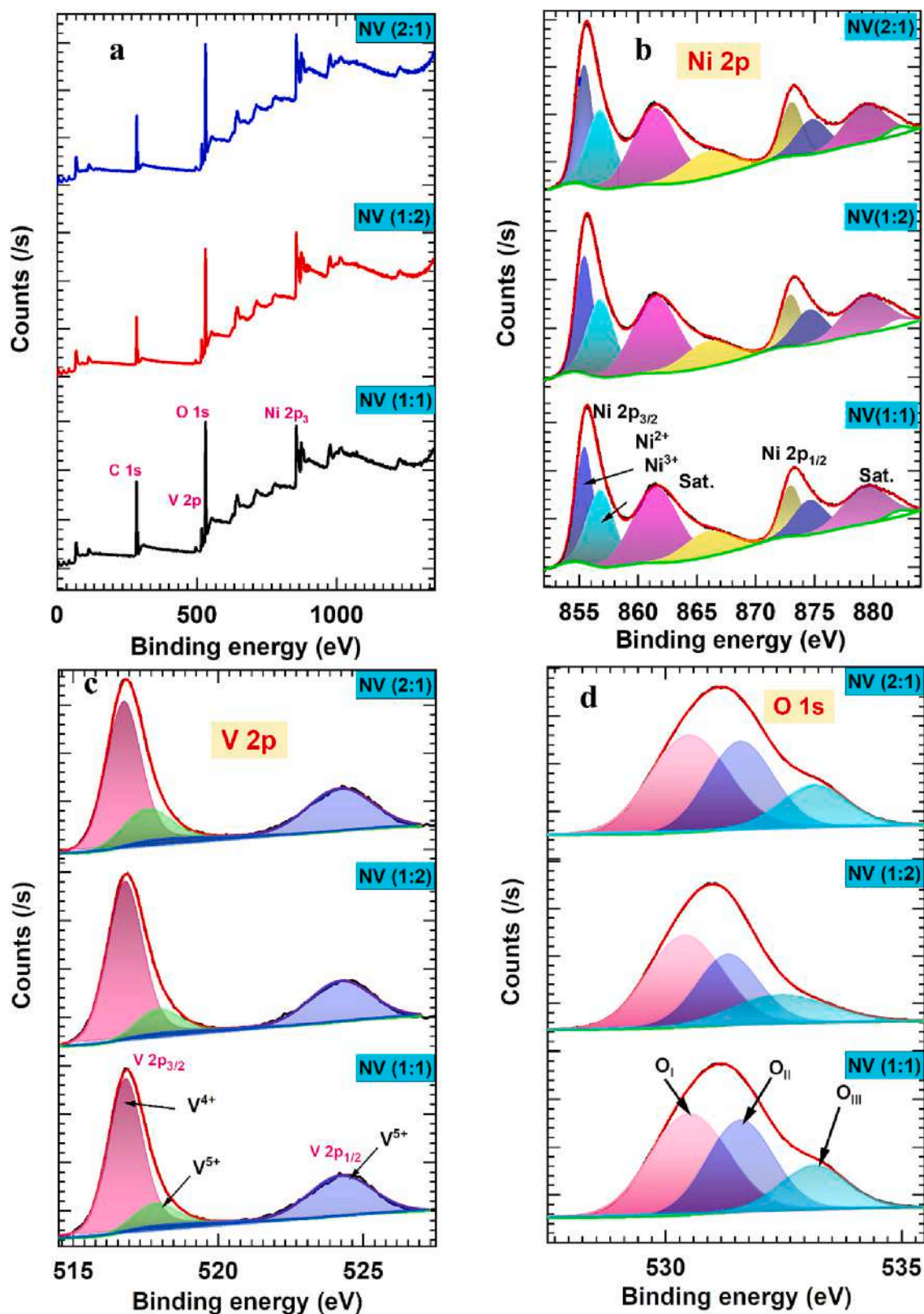


Fig. 3. (a) Full survey spectra, (b) Ni 2p, (c) V 2p, (d) O 1s XPS spectra of sample NV series samples.

designated to V^{5+} state, and the formfitting peak at a binding energy of 516.78 eV represents the V^{4+} state [13,32,33]. The presence of 2+ and 5+ states of nickel and vanadium, respectively, validate the formation of the $Ni_3V_2O_8$ phase in all NV series thin films. The deconvoluted O 1s spectra for all NV series samples are demonstrated in Fig. 3 (d). The

decomposition of O 1s peaks in three parts manifests the different environments of oxygen in the samples. The peak located at a binding energy of 530.48 eV is attributed to the lattice oxygen (O_I), whereas the peak situated at 531.58 eV corresponds to the oxygen vacancies (O_{II}), and at 533.18 eV assigned to the adsorbed water (O_{III}) [34,35]. In

addition to providing electroactive sites for redox processes, oxygen vacancies can significantly increase the conductivity by facilitating the transit of charge carriers [36]. Moreover, the deconvolution of O 1 s spectra affirms the presence of hydrous content in NV samples and confirms the deposition of hydrous Nickel Vanadate ($\text{Ni}_3\text{V}_2\text{O}_8 \cdot n\text{H}_2\text{O}$) in thin films over SS substrate.

The surface morphologies were recorded at different magnifications (x5000 and x40000) of the NV thin films and are shown in Fig. 4(a₁, a₂), (b₁, b₂), (c₁, c₂). The overview of SEM images at lower magnification (Fig. 4 (a₁), (b₁), and (c₁)) demonstrated the congested spherical nanoparticle-like morphology decorated over conducting plate of SS. Besides, randomly decorated particles are entwined, creating large cavities and void space. Obtained voids and cavities in the surface texture are more beneficial by providing a lower diffusion length for the migration of ions [37]. The agglomeration of spherical nanoparticles is

observed in SEM images recorded at higher magnification, as displayed in Fig. 4 (a₂), (b₂), and (c₂). The calculated average particle size is found to be an average diameter of 120, 101.4, and 167.1 nm for samples NV (1:1), NV(1:2), and NV(2:1), respectively, as histograms displayed in Fig. 4 (a₃, b₃, c₃). This difference in the average particle size reveals the impact of alteration in the duration of adsorption/reaction and rinsing time in their respective baths and the subsequent change in growth rate. The slow growth rate of NV particles reduces the size of the particles when rinsing time is twofold than the adsorption and reaction duration. Relatively higher and sufficient time for rinsing of ions in DDW, lowering the particle size by removing most loosely bounded or unreacted species. In contrast, comparatively large particle size is observed while the adsorption/reaction period was twice that of rinsing in DDW owing to the agglomeration of the particles due to increased growth rates of film formation. Thus, SEM analysis confirms that the

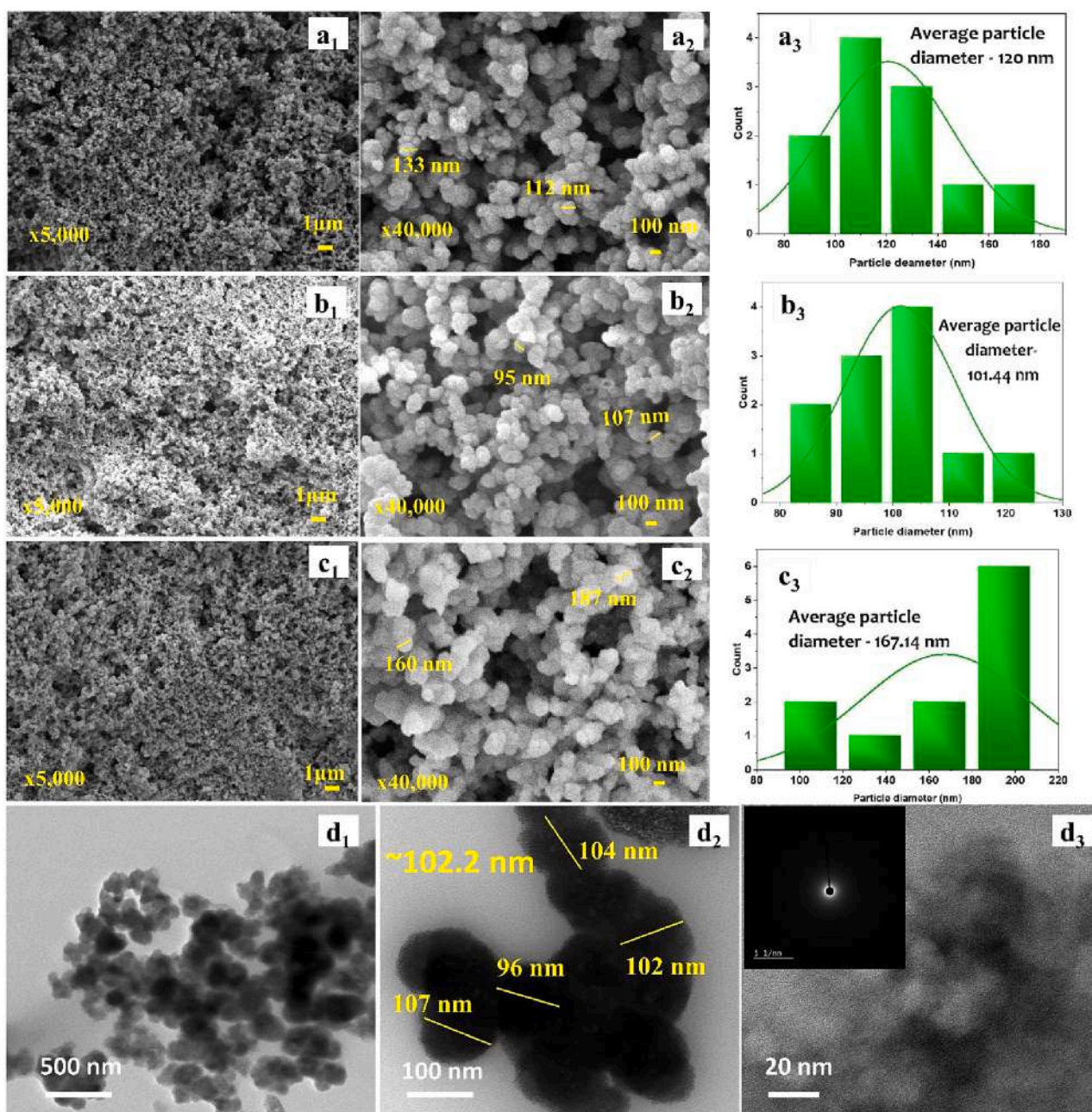


Fig. 4. SEM images of sample (a₁, a₂) NV(1:1), (b₁, b₂) NV(1:2), and (c₁, c₂) NV(2:1) at the magnification of x5000 and x40000, respectively and (a₃, b₃, c₃) histograms of particles size distribution, (d₁-d₃) HR-TEM image and SEAD pattern of NV(1:2) sample.

growth rate variation by dip time adjustment significantly alters the morphology of NV thin film electrodes, which can influence the electrochemical performance. The captured 2D and 3D AFM images of NV (1:2) sample are provided in Fig. S2 (see ESI). The topographical images illustrate the spherical nature of nanoparticles and are well covered over the substrate surface (Fig. S2 (a)), and obtained 3D image coincides well with the SEM morphology of the sample, as shown in Fig. S2 (b). Moreover, the average line (Ra) and surface roughness (Sa) is found to be ~ 10.2 nm, and the maximum height of the surface (Rz) around 12.81 nm was analyzed using Profilm software, as shown in Fig. S2 (c). The AFM profiles and analysis shown in Fig. S2 demonstrate high surface roughness which possesses a larger surface area, and it further helps to enhance the electrochemical properties of the NV (1:2) sample. Moreover, high-resolution transmission electron microscope (HRTEM)

images of the NV (1:2) sample presented in Fig. 4 (d₁-d₃) reveals agglomerated spherical particles of nickel vanadate. Moreover, the HR-TEM image in Fig. 4 (d₂) displays interconnected spherical particles with an average size of ~ 102.2 nm, and Fig. 4 (d₃) demonstrates that the merged spheres are composed of clusters of quantized particles. Also, the SAED pattern shown in Fig. 4 (d₃) inset reveals diffused ring, which affirms the amorphous nature of nickel vanadate and agrees with the obtained XRD results.

Furthermore, in order to scrutinize the presence of elements in the NV sample, an EDS spectrum analysis was carried out and shown in Fig. S3 (see ESI). EDS images demonstrated a peak corresponding to Ni, V, and O elements with atomic percentages of 24.01 %, 12.03 %, and 63.96 %, respectively. Moreover, the elemental mapping images displayed in Fig. S4 demonstrate the uniform distribution of Ni, V, and O

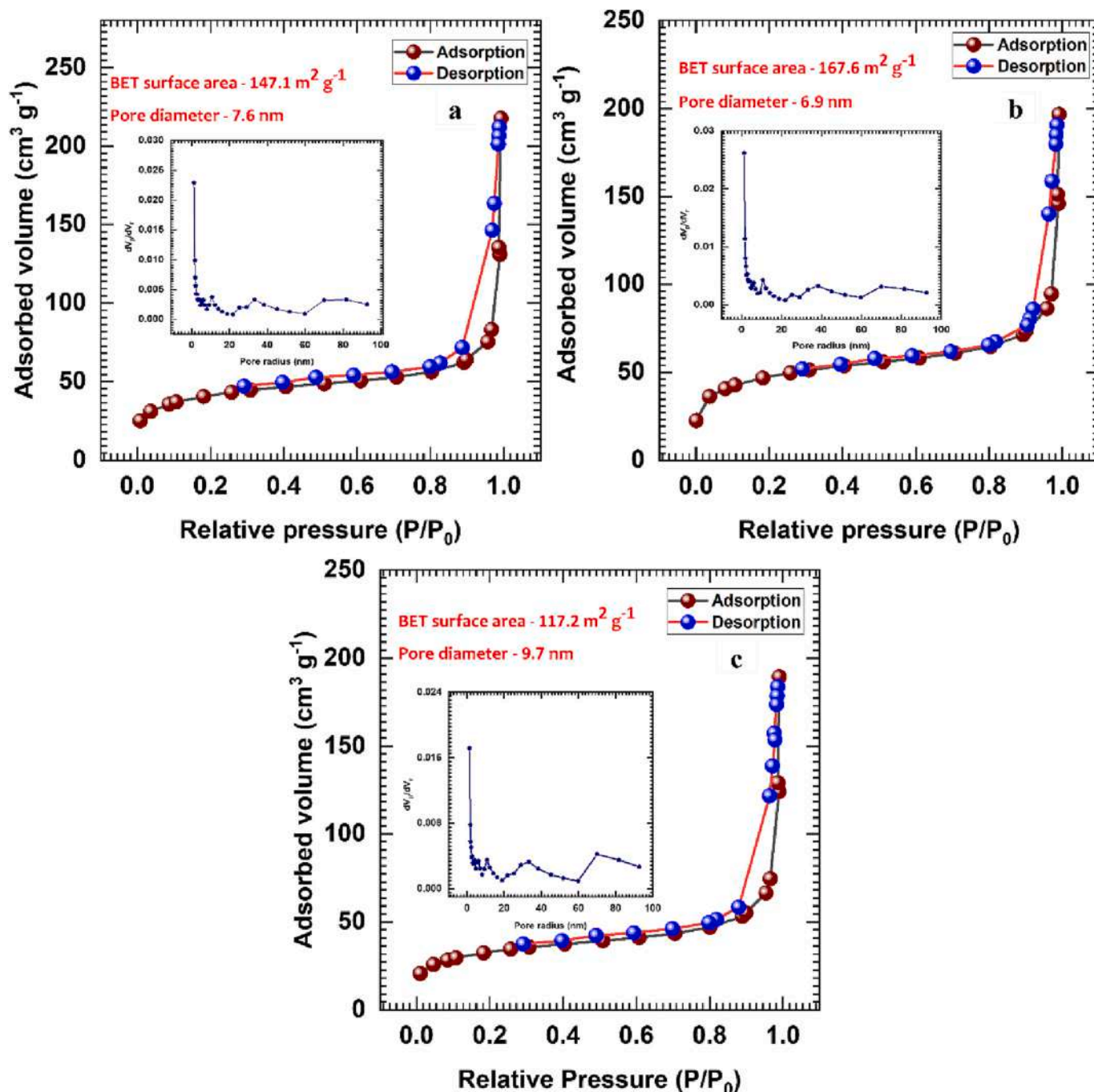


Fig. 5. Nitrogen adsorption/desorption isotherm of (a) NV(1:1), (b) NV(1:2), and (c) NV(2:1), (inset: pore size distribution).

elements (see ESI) of NV thin film over the SS substrate. These EDS mapping results indicate the successful hydrous nickel vanadate series thin film electrode preparation.

To probe the influence of growth rate variation on the porosity and surface area of deposited NV series samples, BET and BJH measurements were performed. The plots of N_2 adsorption-desorption isotherms (at 77 K liquid nitrogen) and BJH pore size distribution are displayed in Fig. 5 (a-c), and according to the International Union of Pure and Applied Chemistry (IUPAC), obtained N_2 adsorption-desorption isotherms of all NV series samples display an H3-type hysteresis loop, endorsing the existence of aggregated particles [38]. The assessment of the specific surface area is found to be 147.1, 167.6, and 117.2 $m^2 g^{-1}$ for NV(1:1), NV(1:2), and NV(2:1) series samples, respectively. The obtained specific surface area of 167.6 $m^2 g^{-1}$ of NV (1:2) sample is higher than ever achieved for NV materials prepared by different synthetic methods, as described in Table S1 (See ESI). Additionally, the mesoporous structure of NV samples is confirmed from the pore size distribution (BJH) analysis, as displayed in the inset of Fig. 5 (a-c). The BJH plots display the average pore size distribution of 7.6, 6.9, and 9.7 nm for NV(1:1), NV (1:2), and NV(2:1) samples, respectively. The deviations in specific surface area and pore size are observed due to fluctuations in growth kinetics of the material. Consequently, obtained change in the surface area agrees with the alteration in the surface morphology of NV samples. The relatively higher surface area is attributed to the smaller particle diameter with a pore size of 6.9 nm owing to the slower growth kinetics of NV(1:2) thin film. Moreover, the high surface area with the mesoporous structure having shortened pore diameter can introduce hierarchical channels to contact the electrolyte and easy ion diffusion in the deep pore of the particles [39,40].

The overall physicochemical analysis concludes that the surface area and porous structure of the NV samples correspond to changes in surface

morphology and average particle size, and it can be tuned by varying growth rates via changing dip time intervals for adsorption/interaction and rinsing in the SILAR method. In this attempt, the dipping interval of the substrate in cationic/anionic precursor and rinsing baths is varied to achieve different growth kinetics as slow (1:2), intermediate (1:1), and fast (2:1) growth rates, as schematically shown in Fig. 6. When the rinsing time is twice, the adsorption and reaction time (NV 1:2) and ion-by-ion growth kinetics are slow, where particle size reduces since a sufficiently excess rinsing time avoids the agglomeration of particles and results in smaller particle size. On the other hand, rapid growth is observed for the larger/equal time to adsorption/reaction than rinsing of NV(1:1) and NV(2:1) samples, resulting in relatively larger particles than NV(1:2) samples. The increasing growth rates of NV material lead to the formation of relatively bigger particles due to the SILAR synthesis approach; the dipping time variation primarily results in the controlled growth and size of the particles, which aids in tuning the surface area of the material and consequently affects electrochemical performance.

3.3. Electrochemical study of NV series electrodes

The influence of dipping time on the structure and morphology and its consequent impact is further scrutinized for electrochemical measurements. The three-electrode electrochemical cell system is applied to examine the electrochemical performance of as-deposited NV thin films electrodes. The comparative CV curves are displayed in Fig. 7 (a) for NV (1:1), NV(1:2), and NV(2:1) electrodes in the optimized potential window of 0 to 0.7 V/Hg/HgO at a 20 $mV s^{-1}$ scan rate. The elevated area of the CV curve for NV(1:2) electrode leads to a higher charge-storing capacity than another two electrodes, implying a good correlation between specific surface area and CV curves. The CV curves of the NV(1:2) thin film electrode at various scan rates from 2 to 50 $mV s^{-1}$ are shown

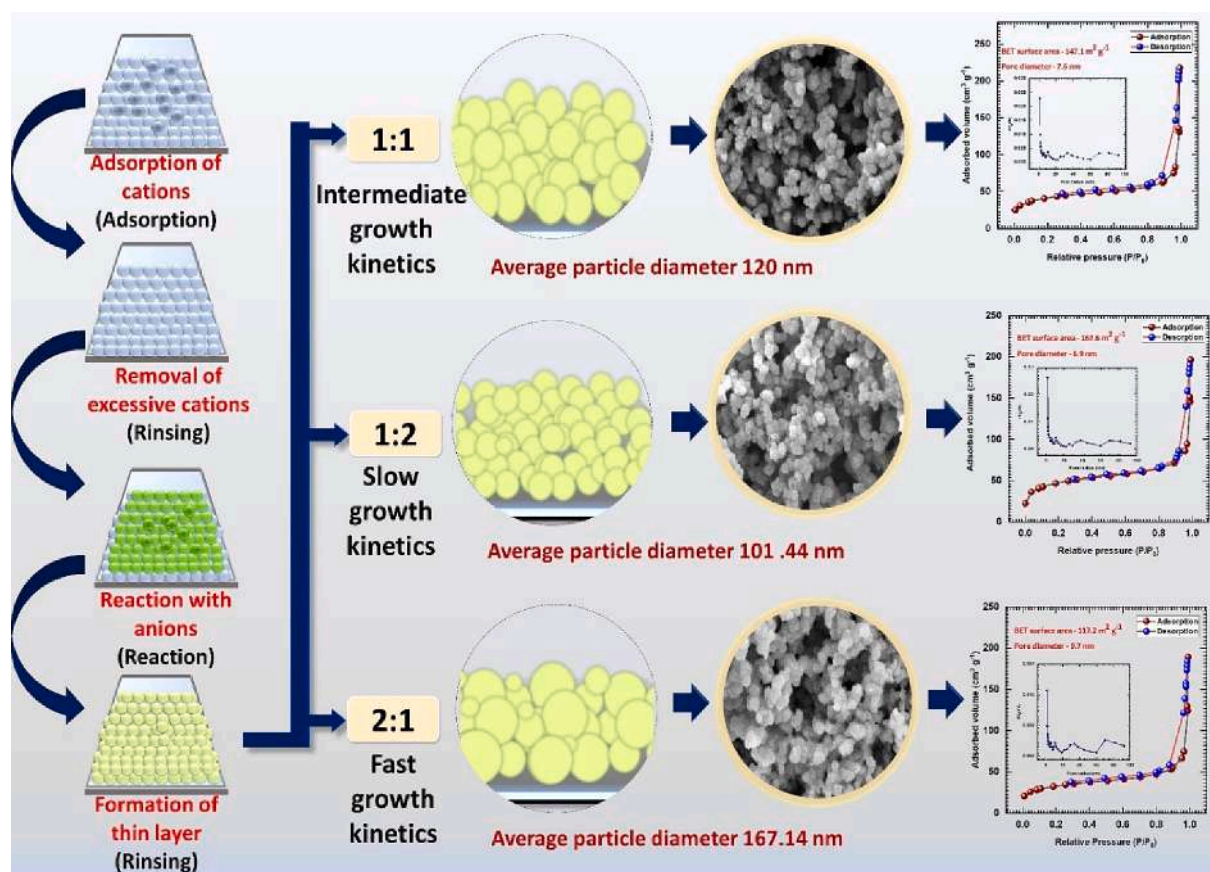


Fig. 6. Schematic representation of the effect of the dipping time variation on growth kinetics, surface morphology, and surface area of NV material over a substrate.

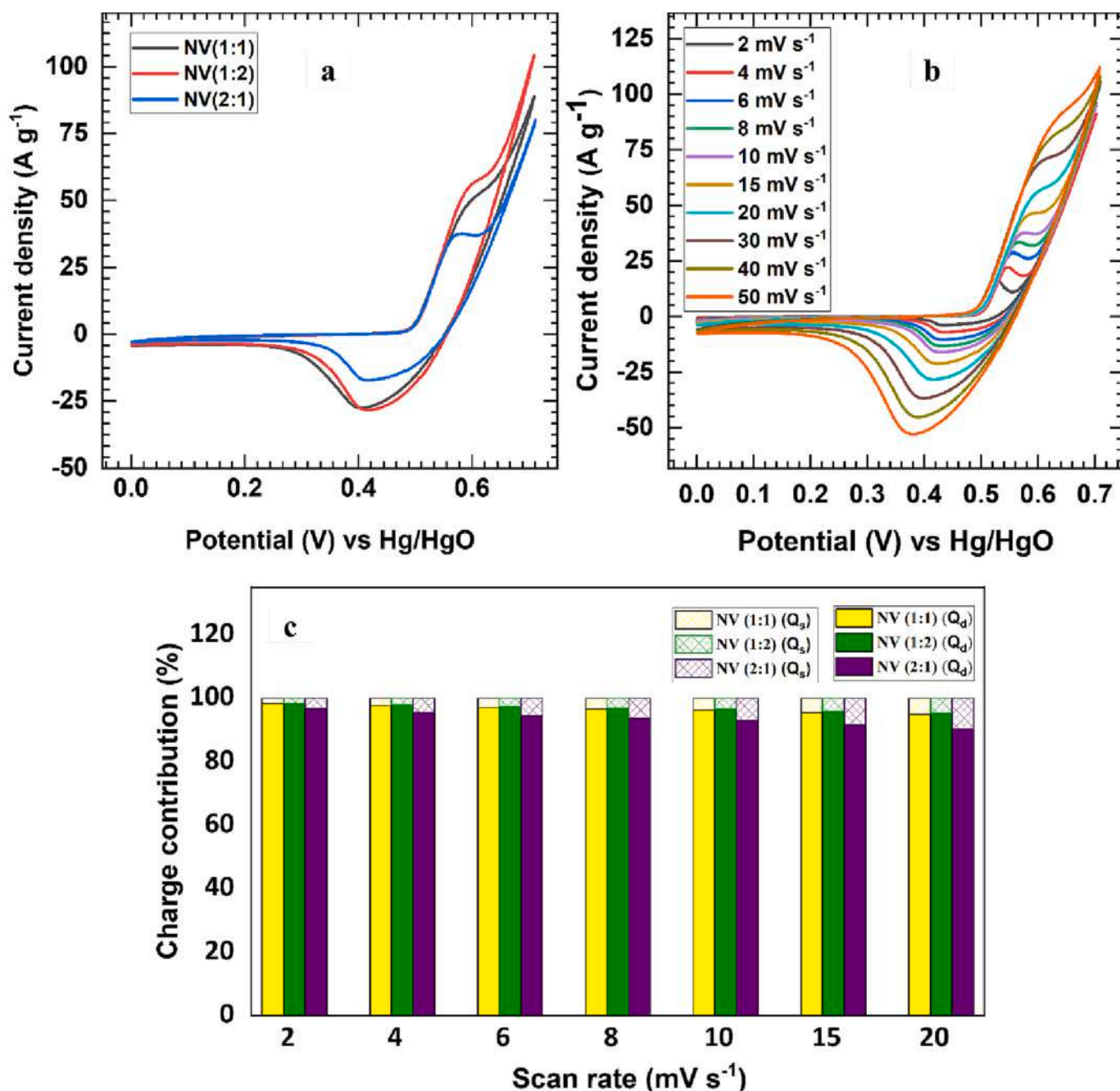
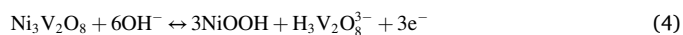


Fig. 7. (a) Comparative CV curves at 20 mV s⁻¹ scan rate of NV series electrodes, (b) CV curves at various scan rates from 2 to 50 mV s⁻¹ of NV(1:2) electrode (c) the plot of surface and diffusive charge contribution with respect to scan rate for NV(1:1), NV(1:2), and NV(2:1) electrodes. (Filled area represents diffusive charge contribution, and the cross-lined area represents surface charge contribution).

in Fig. 7 (b). The increasing trend of the area under CV curves with scan rate infers the battery-type behavior of NV material. In the redox process, a greater scan rate causes ion depletion or saturation in the electrolyte inside the electrode, which mainly raises ionic resistance [41]. The observed CV curves are associated with two different domains; a couple of oxidation-reduction peaks are obtained in the region from 0.35 to 0.7 V, mainly associated with the reversible transition of Ni²⁺ to Ni³⁺ and the remaining part in region 0 to 0.35 V of the CV curve point toward the transfer of double layer charges. Also, the absence of additional redox peaks due to impurity phases of V₂O₅, V₄O₉, V₃O₇, VO₂, etc., confirms that the redox couple originated from Ni₃V₂O₈ [19,42]. During the process of intercalation and de-intercalation, OH⁻ ions get exchanged into the bulk of the material and near the electrode-

electrolyte interface, and the electrochemical reactions of NV electrodes could be presented as follows.



Further, a similar trend of CV curves for NV(1:1) and NV(2:1) electrodes at 2 to 50 mV s⁻¹ is observed, as shown in Fig. S5 (see ESI). The CV curve provides more insights into understanding the charge storage mechanism quantitatively. Fig. 7 (c) provides a graphic illustration of the scan rate-dependent current response, and the following equation summarizes the relationship:

$$i_{\text{peak}}(v) = a v^b \quad (5)$$

where i_{peak} denotes the peak of cathodic current, a and b are adjustable

factors, and v is the sweep rate. The b parameter can be determined from the slope of $\log(i_{\text{peak}})$ vs. $\log(v)$ (Fig. S6, see ESI) graph. Generally, the value of $b = 1$ signifies charge storage mainly due to the surface-controlled (electrical double layer (EDL)) process indicating capacitive nature. In contrast, the diffusion-controlled battery-type nature is considered for $b = 0.5$ [43]. In contrast, NV series electrodes exhibited b values of approximately 0.5, suggesting that the battery type diffusive process contributed to store charges. Further, total volumetric charge (Q_t) differentiates into capacitive (Q_s) and diffusive (Q_d) behaviors and determine by the following equation:

$$Q_t = Q_s + Q_d \quad (6)$$

Q_s is mainly attributed to the rapid kinetics and independent of the scan rate, while Q_d parallels relatively sluggish diffusion, and it is a function of the reciprocal of the square root of the scan rate. The Q_s is derived by plotting the total charge against the inverse reciprocal of the square root of the scan rate (v)^{-1/2}. Using CV curves, the following equation helps to examine the scan rate-dependent charge components and the overall charge contribution,

$$Q_t = Q_s + \text{Const} \cdot v^{-1/2} \quad (7)$$

The charge contribution against the scan rate strikes a similar charge storage mechanism. The overall contribution indicates more diffusive battery-type charge storage; however, increasing the scan rate provides a slight capacitive behavior. Thus, at a scan rate of 2 mV s^{-1} , diffusive contribution accounts for 98 %, whereas it is decreased to 95 % at 20

mV s^{-1} for NV(1:2) electrode. In addition, comparatively more surface contribution charge storage is achieved by NV(2:1) electrode, which decreases from 9 % to 4 % with scan rate lowering from 20 to 2 mV s^{-1} , respectively. Also, it is possible to distinguish between the kinetics of charge transfer at different scan rates, and the diffusion coefficient against scan rate is plotted in Fig. S7 (see ESI) for NV(1:1), NV(1:2), and NV(2:1) samples. The cyclic voltammetric peaks during the positive polarization of the cell are used to calculate the electrolytic diffusion coefficient as described by the Randles-Sevcik equation:

$$I_p = 2.69 \times 10^{-5} n^{3/2} A.C.D^{1/2}.v^{1/2} \quad (8)$$

where, "Ip" represents the peak current, "n" is the number of electrons transferred in the electrochemical reaction, "A" is the active electrode area, "D" is the chemical diffusion coefficient, "C" is the concentration, and " v " is the scan rate. At higher scan rates, a lower diffusion coefficient of ions is observed for all NV series samples, and it increases with decreasing scan rates. Moreover, NV (1:2) electrode exhibits a higher diffusion coefficient, it is attributed to the high surface area and mesoporous structure.

Further, GCD analysis provides more insights to evaluate the C_{sp} of the NV series electrodes. Fig. 8 (a) presented comparative galvanostatic charge-discharge curves measured at a current density of 1 A g^{-1} for NV (1:1), NV(1:2), and NV(2:1) series electrodes. It is observed that the obtained GCD profiles for all samples are similar voltage plateaus and are analogs to CV curves. The battery-type behavior of GCD curves with a minor voltage drop further points out the reversible nature and

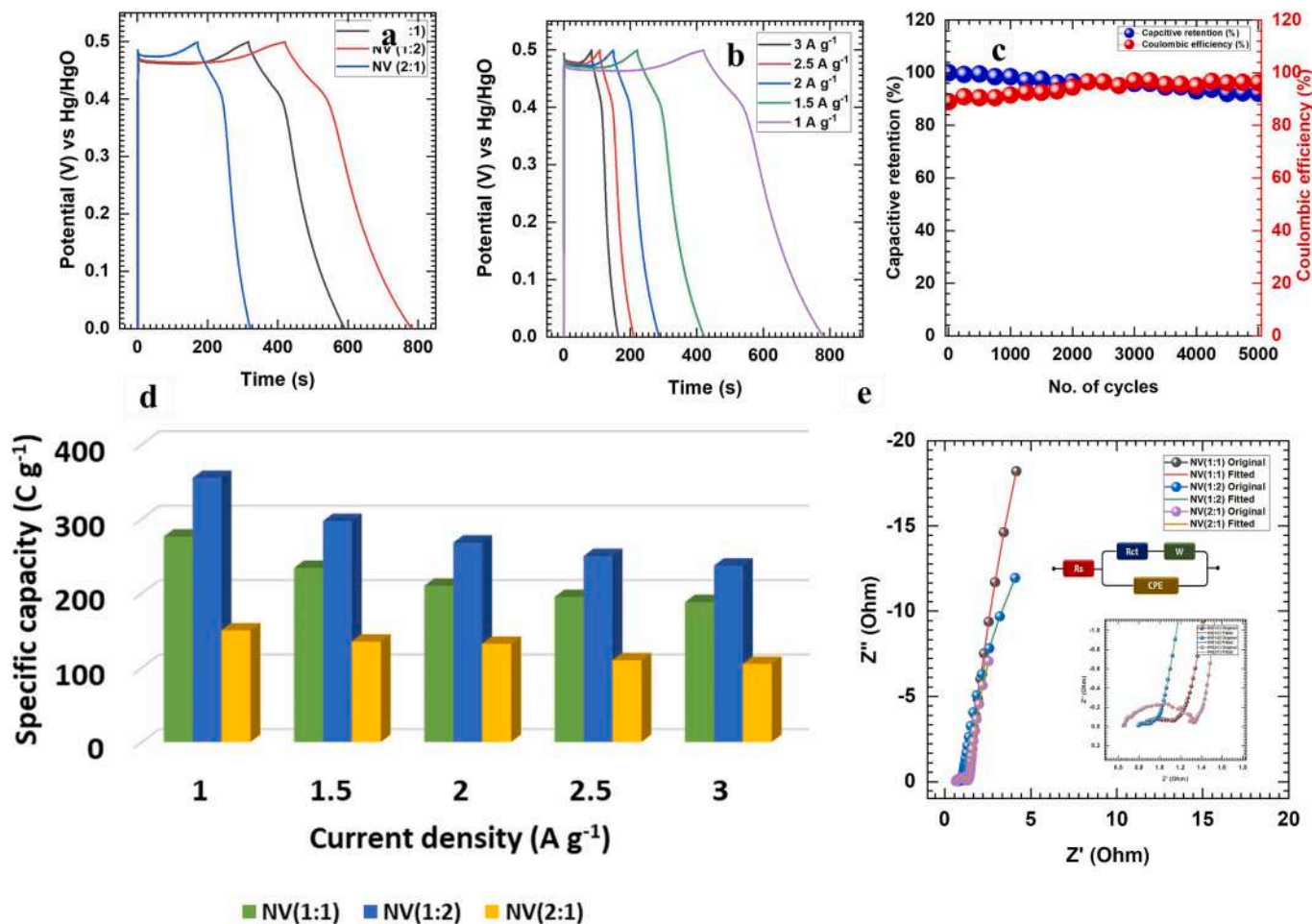


Fig. 8. (a) Comparative GCD curves of NV series electrodes at 1 A g^{-1} current density, (b) GCD curves at various current densities from 1 to 3 A g^{-1} of NV(1:2) electrode, (c) plot of capacitive retention and coulombic efficiency versus number of cycles. (d) The plot of current density as a function of C_s for NV(1:1), NV(1:2), and NV(2:1) electrodes (e) The Nyquist plots of NV(1:1), NV(1:2), and NV(2:1) electrodes and the fitted equivalent circuit for the EIS data is an inset of the figure.

superior conductivity of the CV materials [44]. The C_{sp} , capacity, and C_a of the prepared NV electrodes are calculated using Eqs. S1, S2, and S3 (See ESI Note S3). The GCD profiles at different current densities (1.0–3.0 A g⁻¹) obtained for the NV(1:2) electrode are illustrated graphically in Fig. 8 (b), and GCD plots for NV(1:1) and NV(2:1) electrodes are provided in Fig. S8 (see ESI). The cyclic stability and coulombic efficiency of the nickel vanadate electrode (NV (1:2)) for 5000 cycles were carried out at a current density of 3A g⁻¹ and provided in Fig. 8. (c) The NV (1:2) electrode exhibits ~92 % capacitive retention with 96 % coulombic efficiency over 5000 GCD cycles and increase of coulombic efficiency and stability after initial cycles attributed to the activation of material by means of opening the pores. When using battery-type material, throughout the potential range, average capacitance is not constant [6]; in this account, the maximum C_s along with C_{sp} is calculated and found to be 355C g⁻¹ and 710 F g⁻¹ at 1 A g⁻¹ current density for NV(2:1) electrode. Also, calculated values of C_s (C_{sp}) for NV (1:1) and NV(2:1) electrodes are 276C g⁻¹ (552 F g⁻¹) and 150C g⁻¹ (300 F g⁻¹), respectively, as shown graphically in Fig. 8 (d). Moreover, calculated areal capacitance and specific capacity values (mAh g⁻¹) values are provided in Table S2 (see ESI). The obtained storing capacity of NV electrodes is comparable to the reported performance of NV-based electrodes in earlier literature; for instance, Li et al. [9] prepared NiV₂O₆ by the hydrothermal route and obtained nanosphere with a C_{sp} of 565 F g⁻¹. Singh et al. [17] reported a hydrothermal method to prepare a stone-like morphology of Ni₃V₂O₈, which provided a maximum C_{sp} of 548 F g⁻¹. Nandi et al. [18] synthesized nanopetals of NiV₂O₆ through a similar hydrothermal route, which exhibited a maximum C_{sp} of 1252 F g⁻¹. Also, Ni₃V₂O₈ nanosheets were developed hydrothermally over the nickel foam (NF) by Merum et al. [19], providing a high C_{sp} of 1300 F g⁻¹. Furthermore, Ni₃(VO₄)₂ prepared by Kumar et al. [20] through hydrothermal method provided maximum C_s of 402.8C g⁻¹ at 1 A g⁻¹, and also the hydrothermal method is used by Chandra Sekhar et al. [21] to prepare Ni₂V₂O₇ which provides maximum C_s of 77.1 μAh cm⁻². The nanorods of Ni₂V₂O₇ were prepared by Ezhil Arsi et al. [22] through the co-precipitation method and reported a maximum capacitance of 894 F g⁻¹. The detailed summary of NV-based electrodes performance with surface area and morphology is tabulated and given in Table S1 (see ESI), which demonstrates the obtained C_{sp} in the present study is analogous and exceeds several reports [9,16–21]. Only Nandi et al. [18], Merum et al. [19], and Kumar et al. [20] reported higher C_{sp} than present work. However, in these works, NF and steel mesh were used as conductive mediators, where NF may contribute to the enhanced capacitance of the electrode [45]. Subsequently, the prepared NV thin films over SS substrate thus receive full credit for the obtained exceptional capacitive performance in the current study owing to the high surface area ever achieved for NV materials using any synthetic approach.

EIS is quantitatively analyzed to extract more information related to the electrical and ionic conductivity of the electrode material and electrolyte. The Nyquist plots for NV series samples are shown in Fig. 8 (e). The EIS study was conducted at an amplitude of 10 mV, AC in the frequency range of 10 mHz to 1 MHz at open circuit potential. The experimental data of the Nyquist plot were fitted with a selected equivalent model, and different parameters such as solution resistance (R_s), charge transfer resistance (R_{ct}), and Warburg impedance (W), and fitted parameters are provided in Table S3 (see EIS). The Nyquist plot shows a slight arc that accounts for the charge transfer reactions and double-layer capacitance at the electrode/electrolyte interface since the ions do not have adequate time intervals to penetrate inside the bulk of the electrode. The diameter of the semicircle determines the R_{ct} values, and these are 0.32, 0.09, and 0.72 Ω for NV(1:1), NV(1:2), and NV(2:1) samples, respectively. Also, a slightly vertical line to the imaginary axis at the lower frequency region with a phase angle of close to 90° suggests capacitive behavior and complete diffusion of ions in the results in Warburg diffusion resistance. Also, the low R_{ct} value of the NV (1:2) electrode leads to a high capacitance of the NV electrode owing to the

spontaneous electrochemical reaction among the electrolyte and active electrode material due to its high surface area and mesoporous structure. Furthermore, the smaller R_s and R_{ct} values of NV series electrodes suggest an excellent attachment (binder-free) of active material with a current collector (SS substrate). Thus, the SILAR synthesized binder-free, mesoporous, amorphous NV(1:2) thin film electrode with a high specific surface area (167.8 m² g⁻¹), having a maximum C_s of 355C g⁻¹ owing to low EIS values, is suitable as cathode for fabrication of hybrid supercapacitor devices. Furthermore, the FE-SEM images of the NV(1:2) thin film electrode after electrochemical measurements at different magnifications of ×3000 and ×40,000 are shown in Fig. S9 (a-c) (see ESI). At low magnification (Fig. S9 (a)), it is clearly seen that the particle-like morphology does not disturb and looks similar to before electrochemical measurements (Fig. 4 (b1)). However, at higher magnification of SEM image (Fig. S9 (b)), it is observed that the average particle size slightly reduced after the electrochemical study. The negligible change in surface morphology with a reduction in particle size of ~83.2 nm (Fig. S9 (c)) indicates less damage in the particle-like microstructure of amorphous NV material, which confirms good electrochemical stability.

3.4. Aqueous hybrid supercapacitor (AHSc) device

Recently, hybrid supercapacitor devices have grabbed much attention by providing a large SE without sacrificing SP for practical applications. To address the device-level practical feasibility of prepared electrodes using the two-electrode system, an aqueous hybrid supercapacitor (AHSc) device was constructed, as shown in schematic Fig. 9 (a). For the development of the AHSc device, the best-performed NV (1:2) electrode is used as a positive electrode, and rGO-coated SS substrate is utilized as a negative electrode in 1 M KOH electrolyte. The structural and electrochemical analysis of the capacitive type rGO electrode is carried out and provided in Fig. S10 (see EIS). To achieve the maximum energy-storing capacity of the AHSc device, both electrodes are coupled with an appropriate mass ratio derived using the mass balancing Eq. (S4) (Note S3, see ESI). The comparative CV performances of NV(1:2) and rGO electrodes at 50 mV s⁻¹ in a single frame are shown in Fig. S11. Moreover, the optimum potential window of the AHSc device was determined by measuring CV curves at 50 mV s⁻¹ and GCD curves at 2.2 A g⁻¹ within different upper cutoff voltages in the 1.2 to 1.8 V range, as shown in Fig. S12 (See ESI). The maximum cell voltage is extended up to 1.7 V; afterward, the oxygen evolution mechanism causes a dramatic spike in current. In the AHSc device, the charge storing is based on the intercalation/de-intercalation of OH⁻ ions from the electrolyte at the interface of the NV electrode during the charging/discharging process occurs, and at the same time, adsorption/desorption of K⁺ ions on the interface of the rGO electrode as schematic presented in Fig. S13 (see ESI), which shows the typical arrangement of cations and anions during charging and discharging process. The CV plots for the AHSc device were recorded in a 0–1.7 V voltage window at various scan rates of 5 to 100 mV s⁻¹, as shown in Fig. 9 (b). The similar trend of CV curves at higher scan rates implies that the device can withstand higher scan rates. Also, it can be seen that the current response under CV increases with the increasing scanning rate. Fig. 9 (c) depicts GCD curves for the AHSc device at distinct current densities from 1.3 to 3.1 A g⁻¹. The nearly similar and non-linear trend of GCD curves was observed for the AHSc device, confirming the hybrid charge storage mechanisms of the AHSc device. The AHSc device reaches C_{sp} as high as 109 F g⁻¹ at 1.3 A g⁻¹ current density and retains up to 93 F g⁻¹ for 3.1 A g⁻¹ current density. The calculated C_{sp} values from charge-discharge curves are plotted against the current densities in Fig. 9 (d). Moreover, SE and SP are calculated using Eqs. S6 and S7 (see ESI) in order to find the place of AHSc devices among existing hybrid devices. The AHSc device can achieve a maximum SE of 44 Wh kg⁻¹ at an SP of 1.14 kW kg⁻¹ and retaining SE of 37 Wh kg⁻¹ at an SP of 2.66 kW kg⁻¹, as revealed in Ragone plot (Fig. 9 (e)). Additionally, the AHSc device cycled up to

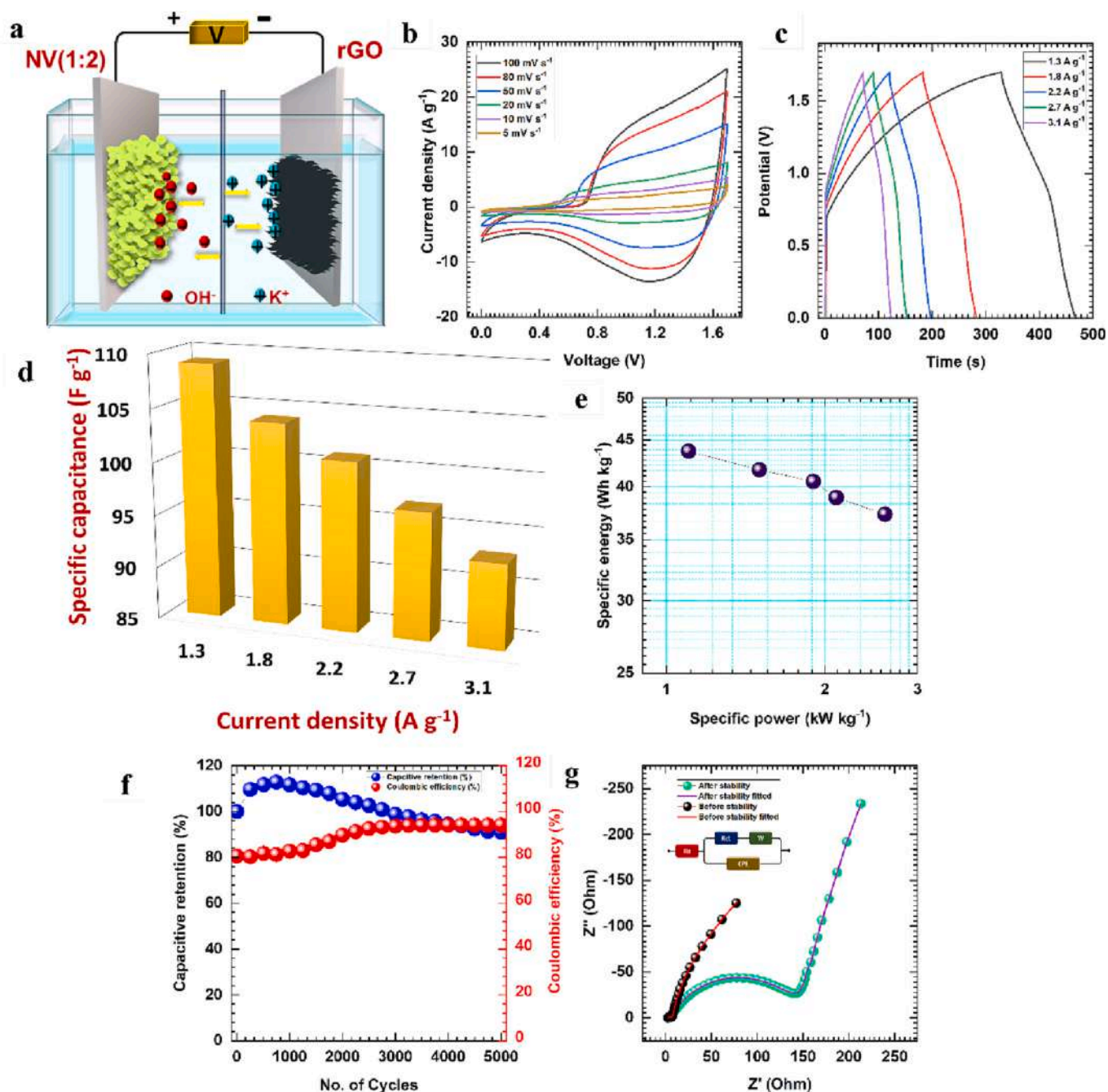


Fig. 9. (a) Schematic illustration of AHSc device, (b) The CV curves at different scan rates from 5 to 100 mV s⁻¹, (c) The GCD curves at different current densities, (d) Plot of C_{sp} as a function of current density, (e) the Ragone plot, (f) Plot of capacitive retention and coulombic efficiency and (g) Nyquist plot of NV(1:2)//rGO AHSc device.

5000 cycles at 4.5 A g⁻¹ to check the cyclic stability, and it was found that the AHSc device sustained 91 % of its initial capacitance (Fig. 9 (f)) along with coulombic efficiency of 94 %. It is observed that capacitive retention of the AHSc device initially increases with increasing charge-discharge cycles, which might be due to the activation of material and opening of the mesoporous structure for facile intercalation of ions, and further slight loss in capacitance implies distortion of material surface [46]. The EIS study further provides more information about the charge transfer kinetics in AHSc devices. For instance, the Nyquist plot for NV (1:2)//rGO AHSc device shown in Fig. 9 (g) demonstrated good electrical/ionic conductivity and interface between material and electrolyte as displayed in terms of lower R_s (2.77 Ω) and R_{ct} (3.69 Ω) values. Also, EIS was recorded after 5000 cycles (Fig. 9 (g)), and fitted parameters are

provided in Table S4 (see ESI), which shows a slight increase in R_s and R_{ct} values owing to the deterioration of active material [47].

3.5. Solid-state hybrid supercapacitor (SHSc) device

The SHSc device was fabricated using NV(1:2) electrode as a positive electrode, rGO as a negative electrode, and a prepared gel of PVA-KOH (Note S2, See ESI) utilized as a quasi-solid electrolyte, as shown in Fig. 10 (a). Similar to the AHSc device, CV profiles in various voltage windows from 0 to 1.2 to 1.8 V for the SHSc device are shown in Fig. S14 (a). Also, charge-discharge curves of the SHSc device (Fig. S14 (b)) (see ESI) in different windows were recorded up to 1.2 to 1.8 V. The equal potential of both electrodes initiates the discharging process, taking into

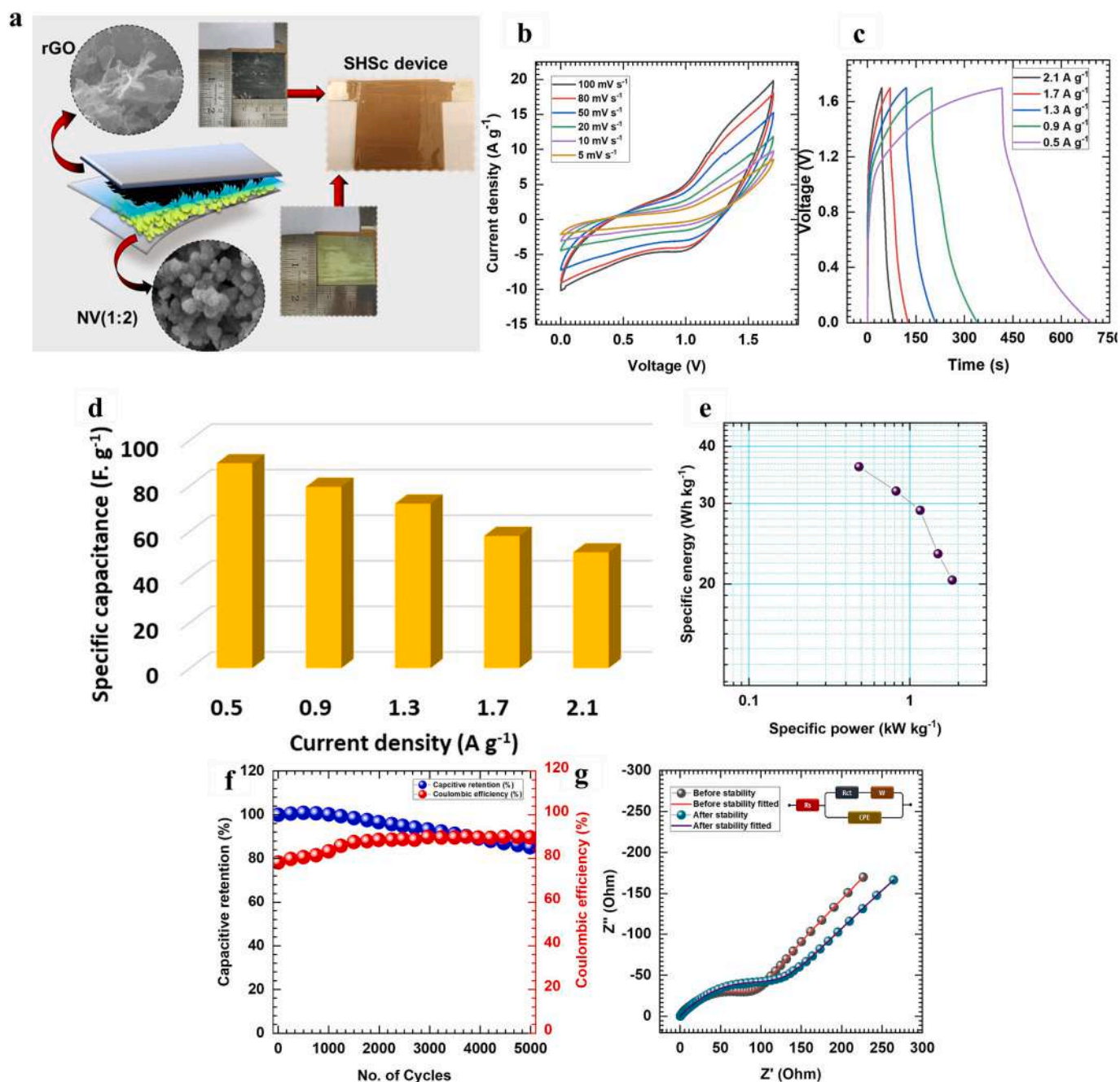


Fig. 10. (a) Schematic illustration of SHSc device, (b) The CV curves at different scan rates from 5 to 100 mV s^{-1} , (c) The GCD curves at different current densities, (d) Plot of C_{sp} as a function of current density, (e) the Ragone plot, (f) Plot of capacitive retention and coulombic efficiency, and (g) Nyquist plot of SHSc device.

account that the oxidation potential of NV reaches up to 0.7 V, and the full reduction potential of rGO requires 1 V; hence it takes 1.7 V to charge the SHSc device completely. So, further electrochemical study of the SHSc device is carried out in the optimized potential window of 0 to 1.7 V. The quasi-rectangular CV curves of the hybrid supercapacitor at various sweep rates within the 0 to 1.7 V window are recorded and depicted in Fig. 10 (b). The GCD curves were plotted in the range of current densities and are shown in Fig. 10 (c). The calculated maximum C_{sp} of the SHSc is found to be 89 F g^{-1} at 0.5 A g^{-1} current density, and it decreases up to 50 F g^{-1} at high current density of 2.1 A g^{-1} as shown in Fig. 10 (d). Furthermore, SE and SP are the most important factors for assessing the practical performance of hybrid supercapacitor devices. In this context, calculated SE and SP at an operating voltage of 1.7 V are plotted in the Ragone plot (Fig. 10 (e)). The estimated maximum SE is

36 Wh kg^{-1} at an SP of 0.482 kW kg^{-1} . Moreover, the SE still sustains up to 20 Wh kg^{-1} and provides a maximum SP of 1.835 kW kg^{-1} . Apart from the SE and SP, the long-term charge-discharge cycling stability of the SHSc device is recorded up to 5000 cycles at 5 A g^{-1} current density and plotted in Fig. 10 (f). After completing 5000 charge-discharge cycles, the device retained its 85 % capacitance with coulombic efficiency of $\sim 90 \%$ over the initial value over 5000 GCD cycles representing a longer life span. The complex plane EIS spectra of before and after cycling of the SHSc are plotted in Fig. 10 (g). The fitted equivalent model for experimental data is provided in Fig. 10 (g) inset, and corresponding values for before and after stability are given in Table S5 (see ESI). The superior SHSc device performance implies lower R_s (0.449Ω) and R_{ct} (85.4Ω) values, and a slight increase in these values (R_s -0.76 and R_{ct} -117.6) after 5000 cycles advocate excellent interaction of electrode/

electrolyte interface. Moreover, the self-discharge behavior of SHSc (NV (1:2)//PVA-KOH//rGO) device is investigated by charging it with a constant current density of 0.7 A g^{-1} and allowing it to discharge freely where the device maintained a voltage of 0.49 V even after 24 h, as depicted in Fig. S15 (a). Initially, the discharge rate was rapid up to 1.1 V but gradually stabilized thereafter. The fast initial discharge rate can be attributed to the easy release of charges stored on the surface of electrodes. However, the charges stored due to the redox reaction at the electrodes require more time to be released, resulting in a slower discharge rate [48,49]. Furthermore, the leakage current of the SHSc (NV(1:2)//PVA-KOH//rGO) device was recorded for constant voltages above 0.8 V up to 1.7 V and presented in Fig. S15 (b). The current decreases rapidly at the initial constant-voltage charging stage due to the charge saturation. After the initial rapid leakage, the current density stabilizes up to $19.2, 11.8, 7.6, 4.6, 2.2,$ and 1.1 mA cm^{-2} at the applied potential of $1.7, 1.6, 1.4, 1.2, 1,$ and 0.8 V , respectively. It has been discovered that the leakage current increased with the applied voltage correspondingly. Also, reasonable leakage current and self-discharge of SHSc (NV(1:2)//PVA-KOH//rGO) device suggest its prospect in practical applications [50,51].

Additionally, the findings of the present work in terms of SE and SP are compared with those reported with NV electrode-based energy storage devices, and more details are provided in Table S5 (see ESI). The obtained SE and SP for AHSc device surpass previously reported for NV

electrode-based energy storage devices, as shown in the Ragone plot (Fig. 11 (a)). Conspicuously, both AHSc and SHSc devices exhibited high SE than the reported work. Li et al. [9] reported 24.3 Wh kg^{-1} and 800 W kg^{-1} energy and power density for the liquid-state (rGO//NiV₂O₆) device and 7.8 Wh kg^{-1} and 850 W kg^{-1} for the solid-state (rGO//NiV₂O₆) device. Furthermore, a relatively high SP of 2400 W kg^{-1} is reported by Merum et al. [19], but the SE of 33.2 Wh kg^{-1} is less than the present work. Kumar et al. [20] fabricated an asymmetric device (Ni₃(VO₄)₂//AC) that achieves 25.3 Wh kg^{-1} and 240 W kg^{-1} SE and SP, respectively. The symmetric device based on Ni₃V₂O₈/Ni foam developed by Haldar et al. [42] exhibited SE of 32.9 Wh kg^{-1} and SP of 189.9 W kg^{-1} . Comparably higher SP reported by Merum [19] and Haldar [42] than the present work may be due to the preparation of electrodes using NF. On the other hand, the outcomes of the present investigation are solely attributable to the active material of SILAR-synthesized NV thin film electrodes. The excellent supercapacitive performance of fabricated NV(1:2)//PVA-KOH//rGO SHSc device leads us to consider its possible commercial prospect by glowing the white LED lamp, and two connected devices lightened white LED lamp up to 80 s after charging for 30 s, as depicted in Fig. 11 (b), and the overall video of glowing lamp is provided in supporting information S16 (see ESI).

Overall, mentioned aspects of binder-free, mesoporous, hydrous, amorphous NV spherical particles prepared through the SILAR method significantly contributed to enhanced electrochemical performance in

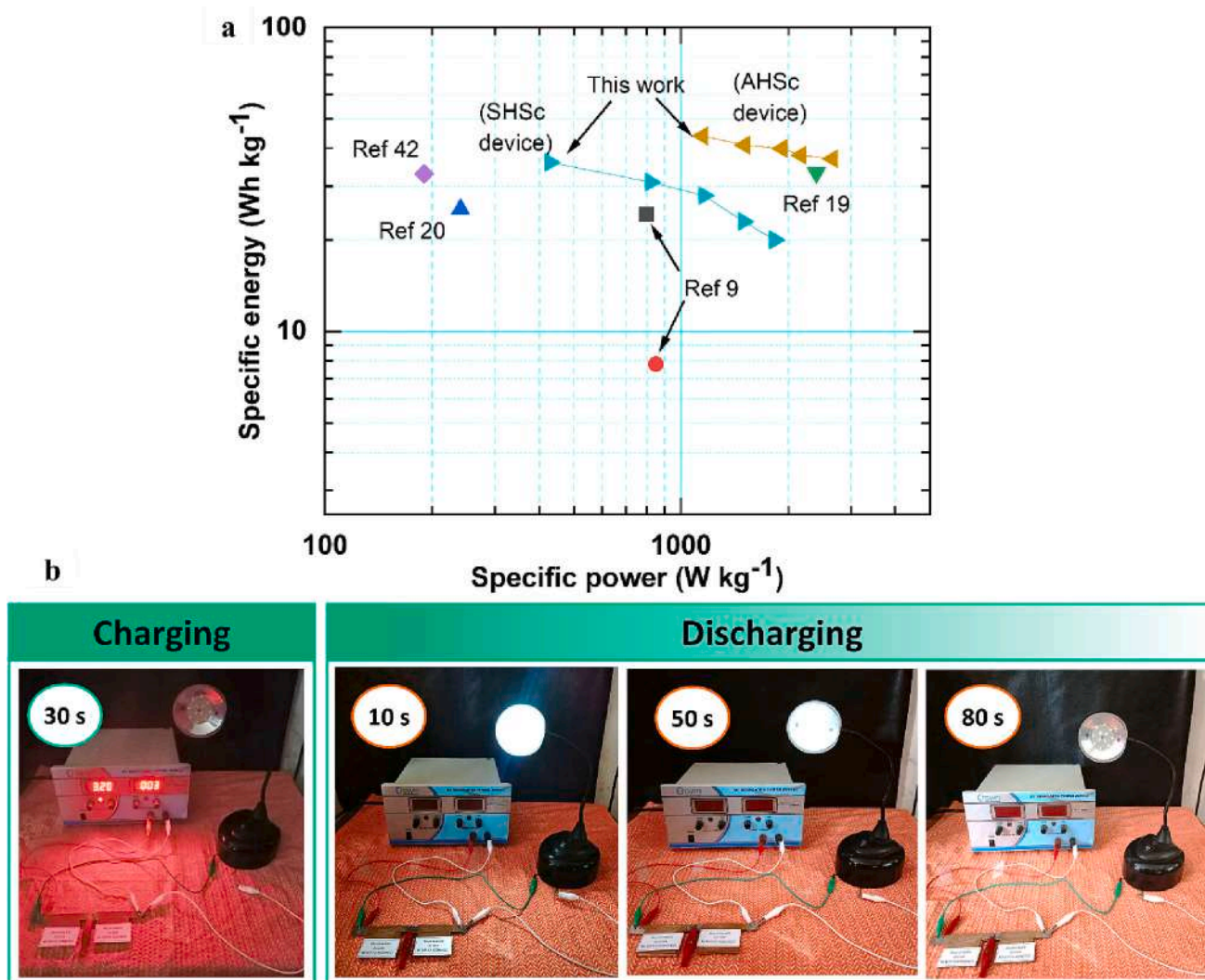


Fig. 11. (a) Ragone plot of SP and SE, including AHSc and SHSc devices with the available literature on NV-based hybrid supercapacitor devices, and (b) demonstration of glowing LED table lamp using serially connected SHSc devices.

hybrid supercapacitor devices. A) In the first place, the thin film electrode engineering strategy by the SILAR method with an optimized growth rate (slow, at 1:2) possesses a higher surface area ($167.2 \text{ m}^2 \text{ g}^{-1}$) and mesoporous structure due to a reduced average particle size (101.4 nm), provides abundant electroactive sites for charge storage. B) Less EIS values in terms of R_s and R_{ct} are attributed to the binder-free synthetic approach and the excellent interface of hydrous NV material with electrolyte. C) Moreover, structurally disordered amorphous NV particles provide more active sites with structural flexibility that increases the electrochemical performance in terms of electrode storage capacity and stability.

4. Conclusions

In a nutshell, amorphous, hydrous, nickel vanadate ($\text{Ni}_3\text{V}_2\text{O}_8 \cdot n\text{H}_2\text{O}$) spherical particles are prepared over SS substrate using the binder-free SILAR method. Alteration in adsorption, reaction, and rinsing time of substrate in respective baths leads to a change in the growth kinetics of the NV thin film electrode; consequently, it alters the physicochemical properties of a material. As a result, a twofold rinsing time than the duration of adsorption and reaction (NV (1:2)) results in a slow growth rate, which a relatively larger specific surface area of $167.6 \text{ m}^2 \text{ g}^{-1}$ with a mesoporous structure due to the restricted average particle size of 101.44 nm. The inherited redox characteristics of nickel and vanadium and their synergies with high surface area of NV (1:2) electrode provide improved electrochemical performance with a maximum C_s (C_{sp}) of 355 C g^{-1} (710 F g^{-1}) at 1 A g^{-1} current density. Additionally, the prepared AHSc device delivers a maximum C_{sp} of 109 F g^{-1} and SE and SP of 44 Wh kg^{-1} and 1.14 kW kg^{-1} , respectively, along with 96 % retention after 5000 cycles. The SHSc device exhibited a C_{sp} of 89 F g^{-1} with an SE of 36 Wh kg^{-1} at an SP of 0.482 kW kg^{-1} . Moreover, the SHSc device possesses outstanding charge-discharge performance with 84 % capacitive retention after 5000 GCD cycles. The obtained results concluded that the binder-free, facile SILAR synthetic approach is feasible to produce hydrous nickel vanadate ($\text{Ni}_3\text{V}_2\text{O}_8 \cdot n\text{H}_2\text{O}$) thin films with a tuned specific surface area and morphologies, and optimized NV(1:2) thin film electrode is a promising candidate as a cathode in hybrid supercapacitor devices.

Supplementary data to this article can be found online at <https://doi.org/10.1016/j.est.2023.108417>.

CRedit authorship contribution statement

Ms. S. B. Bhosale carried out an investigation and formal analysis, data curation, and original draft writing, Mr. S. S. Kumbhar, Mr. S. S. Pujari, Mr. V. V. Patil, Dr. J. L. Gunjekar and Prof. C. D. Lokhande carried out modification, creation, and presentation and visualization of the manuscript. Mr. N. Kumar and Dr. R. R. Salunkhe provided resources and formal analysis. Dr. U. M. Patil carried out funding acquisition, administration, supervision, manuscript editing. All persons made substantial contributions to the work reported in the manuscript.

Declaration of competing interest

The authors declare that they have no known competing financial interests or personal relationships that could have appeared to influence the work reported in this paper.

Data availability

Data will be made available on request.

Acknowledgment

We are thankful to the Ministry of Science and Technology India, Department of Science and Technology-Innovation in Science Pursuit for

Inspired (DST-INSPIRE), for financial support through research project sanction no. DST/INSPIRE/04/2016/000260. Also, this research is supported through internal university research project sanction No. DYPES/DU/R&D/2022/2353 by D. Y. Patil Education Society, Kasaba Bawada, Kolhapur.

References

- [1] I. Dincer, Renewable energy and sustainable development: a crucial review, *Renew. Sust. Energ. Rev.* 4 (2000) 157–175.
- [2] M. Kim, G. Saeed, A. Alam, Y. Choi, L. Zhang, D. Lee, S. Kwon, S. Mathur, K. Kim, Ultrafine nanoparticles of tin-cobalt-sulfide decorated over 2D MXene sheets as a cathode material for high-performance asymmetric supercapacitor, *J. Ind. Eng. Chem.* (2023) 294–303.
- [3] S. Pande, B. Pandit, B. Sankapal, Electrochemical approach of chemically synthesized HgS nanoparticles as supercapacitor electrode, *Mater. Lett.* 209 (2017) 97–101.
- [4] A. Alam, G. Saeed, K. Kim, S. Lim, Sonochemical synthesis of welded titanium dioxide-silver nanocomposite as a 3-dimensional direct ink writing printed cathode electrode material for high-performance supercapacitor, *J. Energy Storage* 45 (2022), 103524.
- [5] S. Marje, V. Patil, V. Parale, H. Park, P. Shinde, J. Gunjekar, C. Lokhande, U. Patil, Microsheets like nickel cobalt phosphate thin films as cathode for hybrid asymmetric solid-state supercapacitor: influence of nickel and cobalt ratio variation, *J. Chem. Eng.* 429 (2022), 132184.
- [6] N. Chodankar, H. Pham, A. Nanjundan, J. Fernando, K. Jayaramulu, D. Golberg, Y. Han, D. Dubal, True meaning of pseudocapacitor and their performance metrics: asymmetric versus hybrid supercapacitors, *Small* 16 (2020) 2002806–2002841.
- [7] E. Baasanjav, P. Bandyopadhyay, G. Saeed, S. Lim, S. Jeong, Dual-ligand modulation approach for improving supercapacitive performance of hierarchical zinc-nickel-iron phosphide nanosheet-based electrode, *J. Ind. Eng. Chem.* 99 (2021) 299–308.
- [8] K. Poonam, A. Sharma, S. Arora, Tripathi, review of supercapacitors: materials and devices, *J. Energy Storage* 21 (2019) 801–825.
- [9] Y. Li, H. Sun, Y. Yang, Y. Cao, W. Zhou, H. Chai, Controllable fabrication of NiV_2O_6 nanospheres as a high-performance flexible all-solid-state electrode material for supercapacitors, *J. Colloid Interface Sci.* 3 (2020) 298–307.
- [10] J. Park, J. Cho, Y. Kang, Nickel vanadate microspheres with numerous nanocavities synthesized by spray drying process as an anode material for Li-ion batteries, *J. Alloys Compd.* 780 (2019) 326–333.
- [11] R. Rathore, R. Ameta, S. Ameta, Role of nickel vanadate in photocatalytic degradation of azure a, *J. Curr. Chem. Pharm. Sci.* 4 (2014) 157–163.
- [12] A. Yan, Gas sensing properties of nickel vanadate and composite of nickel vanadate/polypyrrole, *Sens. Mater.* 6 (2018) 1277–1282.
- [13] R. Biswas, A. Kundu, M. Saha, V. Kaur, B. Banerjee, R. Dhayal, R. Patil, Y. Ma, T. Sen, K. Halder, Rational design of marigold shape composite $\text{Ni}_3\text{V}_2\text{O}_8$ flower: a promising catalyst for oxygen evolution reaction, *New J. Chem.* 44 (2020) 12256–12265.
- [14] R. Kumar, T. Bhuvana, P. Rai, A. Sharma, Highly sensitive non-enzymatic glucose detection using 3-d $\text{Ni}_3\text{V}_2\text{O}_8$ nanosheet arrays directly grown on Ni foam, *J. Electrochem. Soc.* 165 (2018) 1–9.
- [15] K. Dastafkan, Q. Meyer, X. Chen, C. Zhao, Efficient oxygen evolution and gas bubble release achieved by a low gas bubble adhesive iron-nickel vanadate electrocatalyst, *Small* 16 (2020) 2002412–2002424.
- [16] S. Pande, B. Pandit, B. Sankapal, Facile chemical route for multiwalled carbon nanotube/mercury sulfide nanocomposite: high performance supercapacitive electrode, *J. Colloid Interface Sci.* 514 (2018) 740–749.
- [17] J. Singh, J. Kumar, C. Rastogi, B. Mandal, Surfactant assisted synthesis of $\text{Ni}_3\text{V}_2\text{O}_8$ and their application as a supercapacitor, *Mater. Today: Proc.* 79 (2023) 231–234.
- [18] D. Nandi, M. Gnanaseelan, F. Simon, J. Pionteck, Unique nanoplates of nickel vanadate: crystal structure elucidation and supercapacitive performance, *New J. Chem.* 41 (2017) 5620–5627.
- [19] D. Merum, R. Nallapureddy, M. Pallavolu, T. Mandal, R. Gutturu, N. Parvin, A. Banerjee, S. Joo, Pseudocapacitive performance of freestanding $\text{Ni}_3\text{V}_2\text{O}_8$ nanosheets for high energy and SP asymmetric supercapacitors, *ACS Appl. Energy Mater.* 5 (2022) 5561–5578.
- [20] R. Kumar, P. Rai, A. Sharma, 3D urchin-shaped $\text{Ni}_3(\text{VO}_4)_2$ hollow nanospheres for high-performance asymmetric supercapacitor applications, *J. Mater. Chem. A* 4 (2016) 9822–9831.
- [21] S. Chandra Sekhar, G. Nagarjun, R. Bhimanaboina, D. Narsimulu, J.S. Yu, Designing chain-like nickel pyro-vanadate porous spheres as an advanced electrode material for supercapacitors, *Inorg. Chem. Front.* 6 (2019) 1087–1096.
- [22] S. Ezhil Arasi, R. Ranjithkumar, P. Devendran, M. Krishnkumar, A. Arivarasan, Electrochemical evaluation of binary $\text{Ni}_2\text{V}_2\text{O}_7$ nanorods as pseudocapacitor electrode material, *Ceramics* 46 (2020) 22709–22717.
- [23] S. Ratnayake, J. Ren, E. Colusso, M. Guglielmi, A. Martucci, E. Gaspera, SILAR deposition of metal oxide nanostructured films, *Small* 17 (2021) 2101666.
- [24] C. Chen, N. Zhang, Y. He, B. Liang, R. Ma, X. Liu, Controllable fabrication of amorphous co-Ni pyrophosphates for tuning electrochemical performance in supercapacitors, *ACS Appl. Mater. Interfaces* 8 (2016) 23114–23121.
- [25] K. Thiagarajan, J. Theerthagiri, R. Senthil, P. Arunachalam, J. Madhavan, M. Ghanem, Synthesis of $\text{Ni}_3\text{V}_2\text{O}_8$ @graphene oxide nanocomposite as an efficient electrode material for supercapacitor applications, *J. Solid State Electrochem.* 22 (2018) 527–536.

- [26] A. Mohamed Azharudeen, R. Karthiga, M. Rajarajan, A. Suganthi, Fabrication, characterization of polyaniline intercalated NiO nanocomposites and application in the development of non-enzymatic glucose biosensor, *Arab. J. Chem.* 13 (2020) 4053–4064.
- [27] C. O'Dwyer, V. Lavayen, S. Newcomb, M. Santa Ana, E. Benaventa, G. Gomzalez, C. Sptomayor Torres, Vanadate conformation variations in vanadium pentoxide nanostructures, *J. Electrochem. Soc.* 154 (2007) K29–K35.
- [28] J. Gunjaker, A. Inamdar, B. Hou, S. Cha, S. Pawar, A. Tallha, H. Chavan, J. Kim, S. Cho, S. Lee, Y. Jo, H. Kim, H. Im, Direct growth of 2d nickel hydroxide nanosheets intercalated with polyoxovanadate anions as a binder-free supercapacitor electrode, *Nanoscale* 10 (2018) 8953–8961.
- [29] B. Chang, G. Zhao, Y. Shao, L. Zhang, B. Huang, Y. Wu, X. Hao, Photo-enhanced electrocatalysis of sea-urchin shaped $\text{Ni}_3(\text{VO}_4)_2$ for hydrogen evolution reaction, *J. Mater. Chem. A* 5 (2017) 18038–18043.
- [30] X. Liu, J. Wang, G. Yang, In situ growth of the $\text{Ni}_3\text{V}_2\text{O}_8$ @PANI composite electrode for flexible and transparent symmetric supercapacitors, *ACS Appl. Mater. Interfaces* 10 (2018) 20688–20695.
- [31] A. Karmakar, S. Srivastava, In situ fabricated nickel vanadate/N-doped reduced graphene oxide hybrid as an advanced electrocatalyst in alkaline hydrogen evolution reaction, *J. Mater. Chem. A* 7 (2019) 15054–15061.
- [32] G. Silversmit, D. Depla, H. Poelman, G. Marin, R. Gryse, Determination of the V_{2p} XPS binding energies for different vanadium oxidation states (V^{5+} to V^{0+}), *J. Electron Spectrosc. Relat. Phenom.* 135 (2004) 167–175.
- [33] S. Zhao, K. Tao, Y. Gong, Co-incorporated $\text{NiV}_2\text{O}_6/\text{Ni}(\text{HCO}_3)_2$ nanoflake arrays grown on nickel foam as high-performance supercapacitor electrode, *Dalton Trans.* 48 (2019) 5315–5326.
- [34] Y. Teng, Y. Li, D. Yu, Y. Meng, Y. Wu, X. Zhao, X. Liu, The microwave-assisted hydrothermal synthesis of CoV_2O_6 and $\text{Co}_3\text{V}_2\text{O}_8$ with morphology tuning by pH adjustments for supercapacitor applications, *ChemistrySelect* 4 (2019) 956–962.
- [35] M. Can, S. Shah, M. Doty, C. Haughn, T. Firat, Electrical and optical properties of point defects in ZnO thin films, *J. Phys. D: Appl. Phys.* 45 (2012), 195104.
- [36] X. Lv, W. Huang, Q. Shi, L. Tang, J. Tang, Synthesis of amorphous $\text{NiCo}_2\text{V}_x\text{O}_y$ nanosphere as a positive electrode material via a facile route for asymmetric supercapacitors, *J. Power Sources* 492 (2021), 229623.
- [37] V. Patil, S. Pujari, S. Bhosale, S. Kumbhar, V. Parale, J. Gunjaker, H. Park, C. Lokhande, M. Mali, D. Mhamane, U. Patil, Hydrous and amorphous cobalt phosphate thin-film electrodes synthesized by the SILAR method for high-performing flexible hybrid energy storage devices, *Energy Fuel* 36 (2022) 12791–12806.
- [38] D. Dubal, G. Gund, C. Lokhande, R. Holze, CuO cauliflowers for supercapacitor application: novel potentiodynamic deposition, *Mater. Res. Bull.* 48 (2013) 923–928.
- [39] J. Zhao, H. Pang, J. Deng, Y. Ma, B. Yan, X. Li, S. Li, J. Chen, W. Wang, Mesoporous uniform ammonium nickel phosphate hydrate nanostructures as high-performance electrode materials for supercapacitors, *CrystEngComm* 15 (2013) 5950–5955.
- [40] K. Kuratani, T. Kiyobayashi, N. Kuriyama, Influence of the mesoporous structure on capacitance of the RuO_2 electrode, *J. Power Sources* 189 (2009) 1284–1291.
- [41] B. Conway, *Electrochemical Supercapacitors: Scientific Fundamentals and Technological Applications*, Kluwer–Plenum, New York, 1999.
- [42] K. Haldar, R. Biswas, A. Arya, I. Ahmad, S. Tanwar, A. Sharma, Construction of Three-dimensional Marigold Flower-shaped $\text{Ni}_3\text{V}_2\text{O}_8$ for Efficient Solid-state Supercapacitor Applications 4, 2022.
- [43] S. Pujari, S. Kadam, Y. Ma, S. Jadhav, S. Kumbhar, S. Bhosale, J. Gunjaker, C. Lokhande, U. Patil, Hydrothermally synthesized nickel copper phosphate thin film cathodes for high-performance hybrid supercapacitor devices, *J. Energy Storage* 52 (2022), 105037.
- [44] R. Sahoo, T. Lee, D. Pham, T. Luu, Y. Lee, Fast-charging high-energy battery-supercapacitor hybrid: anodic reduced graph oxide–vanadium(iv) oxide sheeton-sheet heterostructure, *ACS Nano* 13 (2019) 10776–10786.
- [45] Q. Sa, Y. Wang, Ni foam as the current collector for high capacity C–Si composite electrode, *J. Power Sources* 208 (2012) 46–51.
- [46] S. Karade, D. Dubal, B. Sankapal, Decoration of ultrathin MoS_2 nanoflakes over MWCNTs: enhanced supercapacitive performance through electrode to symmetric all-solid-state device, *ChemistrySelect* 2 (2017) 10405–10412.
- [47] A. Alam, G. Saeed, K. Kim, S. Lim, Metal-organic framework-derived NiS @cobalt-molybdenum layered double hydroxides shell@core as cathode and CoFe_2O_4 -nanoparticles@MXene shell@core as anode materials for ultra-high energy-density flexible asymmetric supercapacitor, *J. Energy Storage* 25 (2022), 105592.
- [48] R. Mishra, G. Choi, Y. Sohn, S. Lee, J. Gwag, Reduced graphene oxide based supercapacitors: study of self-discharge mechanisms, leakage current and stability via voltage holding tests, *Mater. Lett.* 253 (2019) 250–254.
- [49] I. Ike, I. Sigalas, S. Iyuke, Understanding performance limitation and suppression of leakage current or self-discharge in electrochemical capacitors: a review, *Phys. Chem. Chem. Phys.* 18 (2016) 661–680.
- [50] X. Sun, Y. An, L. Geng, X. Zhang, K. Wang, J. Yin, Q. Huo, T. Wei, X. Zhang, Y. Ma, Leakage current and self-discharge in lithium-ion capacitor, *J. Electroanal. Chem.* 850 (2019), 113386.
- [51] G. Leftheriotis, S. Papaefthimiou, P. Yianoulis, Dependence of the estimated diffusion coefficient of Li_xWO_3 films on the scan rate of cyclic voltammetry experiments, *Solid State Ionics* 178 (2007) 259–263.



Dual functional SILAR deposited NiWO₄ electrocatalyst for non-enzymatic glucose sensing and hydrogen evolution reaction

S. B. Jadhav¹ · D. B. Malavekar¹ · D. J. Patil¹ · S. S. Pujari¹ · U. M. Patil¹ · C. D. Lokhande¹ · P. N. Pawaskar¹

Received: 7 February 2023 / Accepted: 19 June 2023

© The Author(s), under exclusive licence to Springer-Verlag GmbH, DE part of Springer Nature 2023

Abstract

An effective route towards improving the electrocatalytic performance of materials is the synthesis of nanocrystalline, porous, and layer-structured materials. Herein, porous nickel tungstate (NiWO₄) film electrode was prepared on stainless steel (SS) substrate by inexpensive successive ionic layer adsorption and reaction (SILAR) method. This method provides a binder-free, porous, and nanocrystalline thin layer on a SS substrate. The electrocatalytic performance of the nanocrystalline NiWO₄ electrocatalyst was evaluated for enzymeless glucose measurement and water-splitting application. This electrocatalyst exhibited excellent sensitivity of 9731 $\mu\text{A mM}^{-1} \text{cm}^{-2}$ within the linear range of 25–325 μM . Further, the glucose concentrations present in human blood samples were measured using the proposed nanocrystalline NiWO₄ electrocatalyst. Also, hydrogen evolution reaction, the electrocatalyst exhibited 171 mV of overpotential at 10 mA cm^{-2} with a Tafel slope of 70 mV dec^{-1} . Further, chronopotentiometry study was carried out at 100 mA cm^{-2} and it showed 94% retention after 24 h. These findings greatly promote the outstanding electrocatalytic performance of nanocrystalline and porous NiWO₄ electrocatalysts that outline their applicability for electrochemical catalysis purposes.

Keywords Electrocatalyst · Hydrogen evolution reaction · Nickel tungstate · Non-enzymatic glucose sensing · Thin film

1 Introduction

Several catalyst materials for various types of electrocatalytic processes have been invented so far. Research on the synthesis of economical catalyst materials has been persuaded for a long time. Inestimable research in electrochemical catalysis has been performed due to its clean, rapid, and economic nature [1]. Innovative ways have been implemented for the synthesis of electrocatalytic materials, such as the formation of meso/microporous materials, layered structures, synthesis of multi-metallic materials, and composite materials [2]. A reduction in crystallinity results in an enhancement of defect sites in the material, which will create the possibility of improvements in electrochemical activity. However, the surge in defects reduces

the conductivity of the material and causes additional resistance from charge transfer at grain boundaries [3, 4]. So, the appropriate nature of crystallinity is crucial for an excellent electrocatalysis process [5]. The synthesis of porous catalyst materials will overcome the shortcomings caused by their excessive nanocrystalline nature. The porous nature allows the percolation of electrolytes inside the material [6]. Therefore, optimized nanocrystalline and porous nature will be beneficial for excellent electrocatalytic performance.

For non-enzymatic glucose sensing and water splitting, binder-free, nanocrystalline, and porous electrocatalytic materials are required. Binder-free nature reduces resistive parameters and provides more active sites for catalysis, which could not be the case with the binder [7]. The atomic defects generated in nanocrystalline nature provide tremendous amounts of electroactive sites. The homogeneous nature and short-range ordering of these materials favor electrocatalysis. In addition to this, the appropriate porosity of the material would be an advantage. The catalytic material's porosity will assist the electrolyte diffusion inside the electrode, providing additional active sites [8].

Considering the above points, the preparation of novel nanocrystalline materials for catalysis purposes has become

S. B. Jadhav, D. B. Malavekar have authors equally contributed.

✉ P. N. Pawaskar
samgrish@gmail.com

¹ Centre for Interdisciplinary Research, D. Y. Patil Education Society (Institution Deemed to be University), Kolhapur 416 006, India

a challenge [9, 10]. Therefore, various chemical preparation methods have been used to develop highly porous and nanocrystalline materials, for example, successive ionic layer adsorption and reaction (SILAR), co-precipitation, hydrothermal, chemical bath deposition, etc. Among these synthesis methods, the SILAR method has advantages like great control over deposition, low-temperature synthesis, large-area deposition, effective control over film thickness, and the choice of deposition on non-conducting and conducting thin sheets. Thus, a simple SILAR technique is being used for the deposition of a large number of materials on different substrates to synthesize nanocrystalline and mesoporous materials [11].

At present, chronic illness caused by abnormally high or low blood sugar levels can lead to many ailments such as abdominal pain, poor appetite, lethargy, nausea, and weight loss due to glucose deficiency [12]. The higher glucose level in diabetes patients has become a human health fear worldwide. Hence, the simple fabrication of electrode materials and investigation of electrochemical non-enzymatic glucose detection are crucial roles in the current stage with highly sensible and selectivity criteria. Also, severe environmental problems related to fossil fuels have grown. This has diverted conventional energy production to other energy sources, mainly wind turbines, hydrogen, and solar photovoltaics [13, 14]. Therefore, environmentally beneficial hydrogen energy production is favorable towards green energy from an upcoming perspective. Water splitting using an electrocatalytic method means the oxidation of water. The evolution of hydrogen has a high energy potential, which generates electricity [15]. Therefore, the electrochemical production of hydrogen energy at an industry level is essential for its future scope. So, it is necessary to develop low-cost catalytic material for the hydrogen evolution reaction (HER) [16].

Nickel-based composite materials have been developed for catalytic reaction purposes due to their admirable electrocatalytic results and high stability [17]. In addition, the metal tungstate has exhibited higher conductivity than oxides and sulfides. Therefore, few reports are available employing nickel tungstate (NiWO_4) for electrochemical non-enzymatic glucose sensing and HER [18–20]. Still, the nanocrystalline and mesoporous NiWO_4 catalyst material is not reported for glucose sensing and HER applications using the SILAR method.

In the present study, NiWO_4 film electrode is fabricated by the SILAR method on a stainless steel (SS) substrate. The prepared nanocrystalline film electrode is successfully employed for enzymeless glucose detection from human blood samples and hydrogen production. Tungsten ions are supported for the enhancement of electrocatalytic current response. Therefore, the proposed electrode showed remarkable sensitivity with desirable stability and selectivity. The

influential parameters were optimized for the effective detection of glucose molecules in an alkaline medium. Further, reliable electrocatalytic performance during hydrogen production was observed.

2 Experimental details

2.1 Synthesis of nickel tungstate thin film.

The binder-free NiWO_4 electrocatalyst was synthesized by a simple SILAR method. For NiWO_4 film deposition, $\text{Na}_2\text{WO}_4 \cdot 2\text{H}_2\text{O}$ and $\text{NiSO}_4 \cdot 6\text{H}_2\text{O}$ precursors were employed as tungstate ion (WO_4^{2-}) and nickel ion (Ni^{2+}) sources, respectively. A stainless steel (SS) substrate of dimensions of 1×5 cm was used to deposit the films. The surface of the SS substrates was polished using smooth polishing paper (fine grade) and then cleaned ultrasonically in double distilled water (DDW) for 15 min. First, the SS substrate was dipped in the cationic precursor (0.1 M $\text{NiSO}_4 \cdot 6\text{H}_2\text{O}$) for 20 s. During this step, Ni^{2+} ions are adsorbed on the substrate. After that, this substrate was lightly washed in DDW for 20 s due to the unbounded weakly adsorbed Ni^{2+} ions were easily removed. Afterward, the substrate was inserted into an anionic precursor (0.1 M $\text{Na}_2\text{WO}_4 \cdot 2\text{H}_2\text{O}$) containing tungstate (WO_4^{2-}) ions for 20 s. In this step, the pre-adsorbed Ni^{2+} ions react with WO_4^{2-} to form solid NiWO_4 nanoparticles. After that, the substrate was washed with DDW for 20 s to remove loosely bound NiWO_4 nanoparticles. Finally, solid NiWO_4 particles were adsorbed on the SS substrate at 100 SILAR cycles. The synthesis process of NiWO_4 thin films using the SILAR method on the SS sheet is presented in supporting information (Fig. S1).

2.2 Electrochemical measurement

The electrocatalytic properties of the prepared NiWO_4 electrocatalyst were studied by using the VersaSTAT instrument in a traditional three-electrode cell. The three-electrode cell was placed in a 50 mL glass cell with mercury/mercury oxide (Hg/HgO), platinum, and NiWO_4 electrodes as a reference, counter, and working electrode, respectively. For the enzyme-less glucose detection study, cyclic voltammetry (CV) and $i-t$ amperometric techniques were utilized in freshly prepared 0.5 M KOH electrolyte. The CV study was performed at various potential scan rates ($10-100 \text{ mV s}^{-1}$). The $i-t$ amperometric method was used to evaluate the current response during the subsequent addition of 25 μL glucose solution to 40 mL KOH electrolyte.

For water splitting, CV and linear sweep voltammetry (LSV) techniques were used to investigate the oxidation and reduction processes of the prepared NiWO_4 electrode. The LSV polarization curves were performed at different

potential scan rates between 1 and 50 mV s⁻¹. These measured potential responses were altered into one of the standard reversible hydrogen electrode (RHE) scales from the Hg/HgO scale using the Nernst Eq. (1),

$$E_{\text{RHE}} = E_{\text{Hg/HgO}} + 0.059 \times \text{pH} + E_{\text{Hg/HgO}}^0 \quad (1)$$

where $E_{\text{Hg/HgO}}$ denotes the measured potential vs. Hg/HgO electrode, $E_{\text{Hg/HgO}}^0$ is the standard redox potential of Hg/HgO, and E_{RHE} denotes the measured potential vs. RHE. The LSV curves at current density (mA cm⁻²) were used to calculate the electrocatalytic effectiveness of the catalyst in terms of overpotential using Eqs. 2 and 3,

$$\eta_{@j}(\text{V}) = E_{\text{RHE}}(\text{V}) - (-1.23(\text{V})) \quad (2)$$

$$\eta = b \log j + a \quad (3)$$

The Tafel slope from the linear fit of the Tafel plot was calculated using Eq. 3, where 'a' stands for the fitting parameter and 'b' is the Tafel slope. The CV study was performed to evaluate the electrochemical double-layer capacitances

(C_{dl}) within the potential range of 0.15–0.25 V vs. Hg/HgO at different scan rates (20–100 mV s⁻¹). The electrochemical active surface area (ECSA) was determined using C_{dl} values from following relations [21, 22],

$$\text{ECSA} = \frac{C_{\text{dl}}}{0.04} \quad (4)$$

Here, the specific capacitance is 0.04 mF cm⁻² at a typical 1 cm⁻² flat surface. In the range of 100 MHz–100 kHz, the electrochemical impedance spectroscopy (EIS) investigation examined various resistive characteristics and an alternating current waveform with an amplitude of 5 mV.

3 Result and discussion

To determine the crystallinity and phase structure of the prepared NiWO₄ film electrode, XRD analysis was conducted. Figure 1a depicts the XRD pattern of NiWO₄ film electrode. In that the observed diffraction peaks at 2θ values of 23.97 and 30.95° correspond to (011) and (111) crystallographic

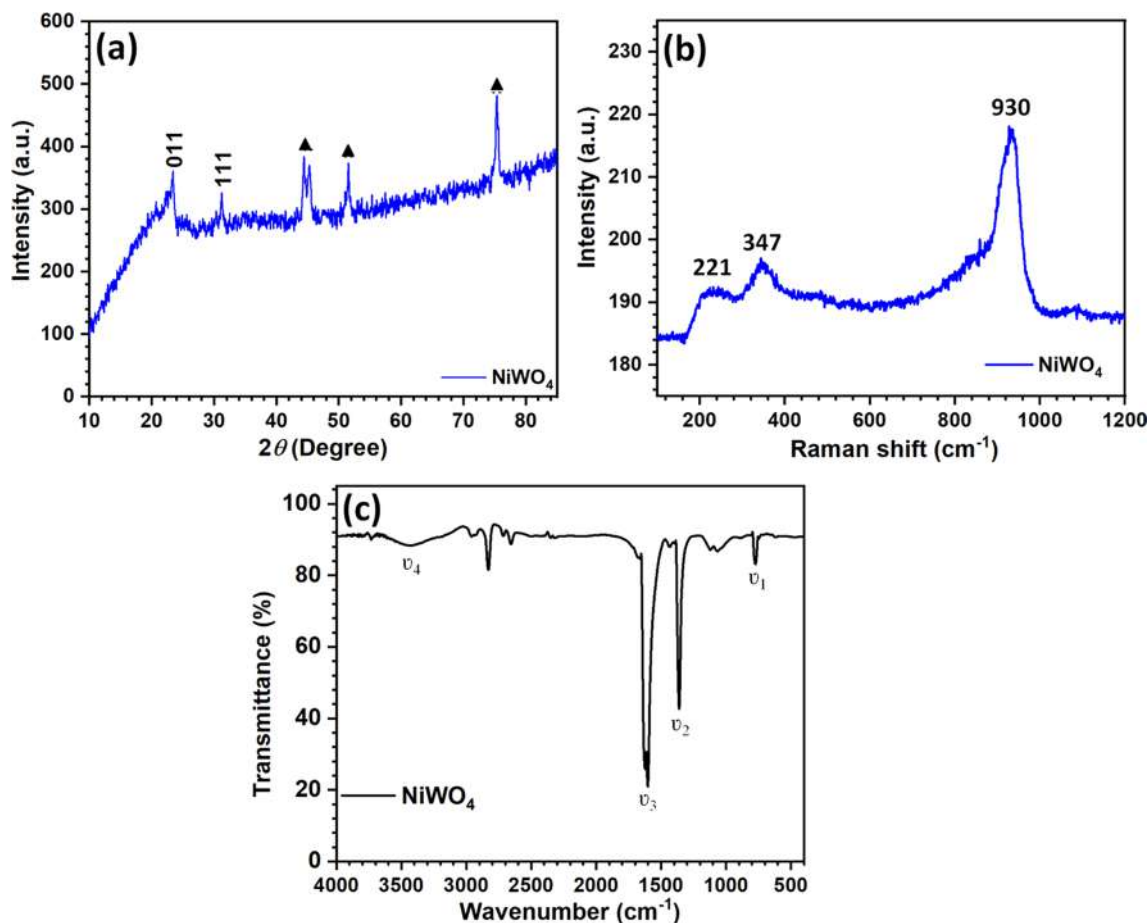


Fig. 1 a The XRD pattern, b Raman spectrum, and c) FT-IR spectrum of NiWO₄

planes of monoclinic NiWO_4 , respectively. These diffraction peaks and hkl planes were matched with the powder diffraction file (PDF) no. 96–591–0278. The axial lengths and angles are $a=4.6000 \text{ \AA}$, $b=5.6650 \text{ \AA}$, $c=4.9120 \text{ \AA}$ and $\alpha=\gamma=90^\circ$, and $\beta=90.5^\circ$, respectively, confirming the crystallographic structure of the prepared material. The peaks denoted by the triangle in the XRD pattern represent the SS substrate. The average crystallite size of the deposited thin film was calculated using the Scherrer formula,

$$D = \frac{0.9\lambda}{\beta \cos \theta} \quad (5)$$

where ' λ ' stands for X-ray radiation wavelength (1.5406 \AA), ' β ' stands for modified band broadening, and ' θ ' stands for Bragg's angle in radians. The calculated average crystal size for (011) plane was 2.25 nm . The bonding of various groups present in NiWO_4 was investigated using Raman and FT-IR spectroscopy. The Raman spectrum of NiWO_4 is shown in Fig. 1b. The three prominent broad peaks in the spectrum indicate the unique nature of nanocrystalline NiWO_4 . The peak at 930 cm^{-1} is assigned to the symmetric stretching modes of the O–W–O bond [23, 24]. Furthermore, the peak at 347 cm^{-1} corresponds to the terminal bond bending vibrations in WO_6 octahedra. Due to the symmetric stretching vibration of O–Ni–O, a less intense peak at 221 cm^{-1} is seen [25]. Thus, the above information about chemical structure and vibrational modes is consistent with Raman spectrum reports [26].

Figure 1c depicts the FT-IR spectrum of NiWO_4 sample. A wolframite-type structure appears in the range $4000\text{--}400 \text{ cm}^{-1}$, which is a significant absorption band. The presence of adsorbed water in the sample is confirmed by the broad absorption ν_4 at a wavenumber of 3460 cm^{-1} , which corresponds to stretching vibrations of –OH. The bending vibrations of –OH group are allocated to the absorption band ν_3 at $1605\text{--}1631 \text{ cm}^{-1}$. The band ν_2 at 1365 cm^{-1} is due to the stretching modes of (W=O) terminal bond present in the octahedron of WO_3 [27]. The band ν_1 at 775 cm^{-1} arises from vibrations of the WO_2 entity present in the W_2O_8 groups. Xing et al. [28] reported similar absorption bands for NiWO_4 . Therefore, the XRD, FT-IR, and Raman characterization studies of NiWO_4 material are consistent.

The surface texture of NiWO_4 film electrode was investigated using FE-SEM (Fig. 2a, b) at magnifications of 3000X and 10,000X. It can be seen that particles are combined to form clusters, resulting in porous structures with large openings and voids in between. The simultaneous processes of nucleation and particle growth are the leading causes behind such porous morphology. The porous nature of the material allows the diffusion of electrolyte ions, providing a substantial active site for catalytic application. Hence, the fast electron transfer rate can be enhanced due to porous active sites

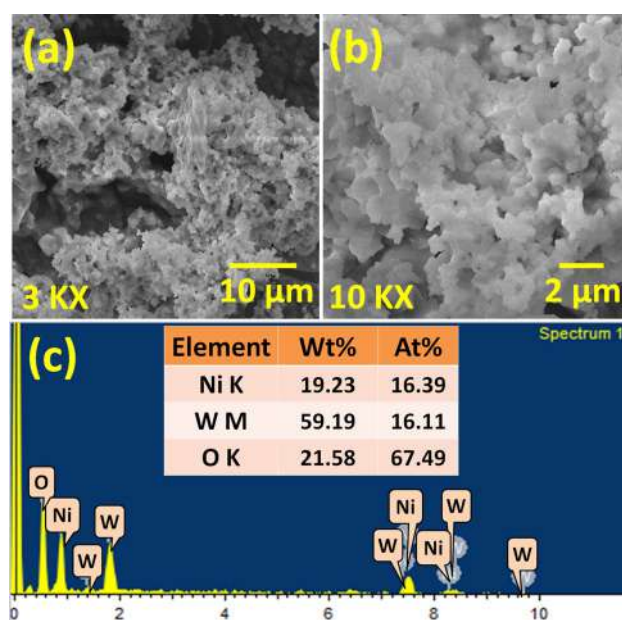


Fig. 2 The FE-SEM images at **a** 3kX and **b** 10kX magnifications and **c** EDX spectrum of NiWO_4 (inset shows elemental composition of NiWO_4)

present on the electrode surface [11]. The specific surface area was calculated using the BET sorption study, and it is observed to be $25 \text{ m}^2 \text{ g}^{-1}$ (supporting information, Fig. S2). The BET study was supported to confirm the porous morphology of NiWO_4 material. The EDS of NiWO_4 is shown in Fig. 2c, and the inset displays the atomic percentage. The atomic ratio of Ni:W is 1:0.98, and that of Ni:O is 1:4.12, confirming the formation of NiWO_4 .

The crystallographic structure of NiWO_4 material is analyzed using HR-TEM, which is presented in Fig. 3a–c. In the HR-TEM images, cluster nanoparticles were observed, which is similar to the FE-SEM images. The crystallographic planes (011) and (100) of NiWO_4 show interplanar distances of 0.37 and 0.46 nm, respectively, as shown in Fig. 3d, e. Also, Fig. 3f shows the selected area electron diffraction (SAED) pattern of NiWO_4 material. The crystallographic planes (030), (200), and (121) of monoclinic NiWO_4 correspond to interplanar distances of 0.29, 0.22, and 0.14 nm, respectively. The predicted interplanar distance from XRD studies is coherent with HR-TEM and SAED patterns, which confirm that the obtained NiWO_4 material has a monoclinic crystal structure.

The XPS analysis was performed to examine the elemental configuration and oxidation states of NiWO_4 film electrode. Figure 4a shows the full-range XPS spectrum, in which Ni, W, and O can be seen clearly. Figure 4b denotes the XPS spectrum of $\text{Ni}2p$, which deconvoluted into $\text{Ni}2p_{3/2}$ and $\text{Ni}2p_{1/2}$ at binding energies of 642.3 and 653.9 eV, respectively. These binding energies indicate Ni is in the +2

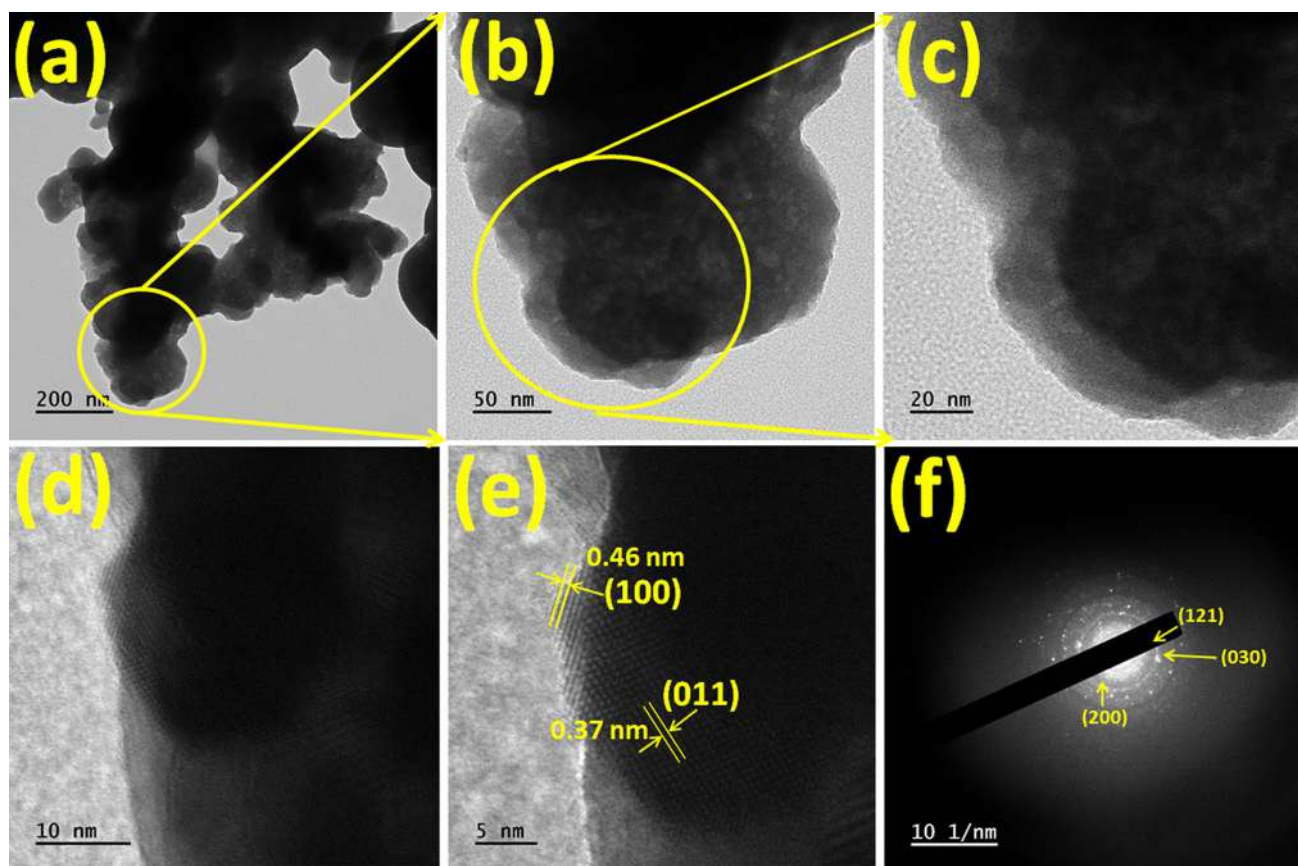


Fig. 3 a–e High-resolution TEM images and **f** SEAD pattern of NiWO₄ material

bound state. The energy separation (17.7 eV) between the two states of Ni2p_{3/2} and Ni2p_{1/2} is well followed in the literature [29]. The two satellite peaks were detected in the XPS spectrum of Ni2p at binding energies of 863.8 and 881.5 eV [30]. The W4f peak deconvoluted into two W4f_{5/2} and W4f_{7/2} peaks at binding energies of 37.42 and 35.27 eV, respectively. Therefore, W is confirmed in the +6 chemical state, as shown in Fig. 4c. The separation energy of 2.15 eV between the two states is described in the literature. Besides, O1s spectrum at 530.73 eV represents metal–oxygen bonding, as shown in Fig. 4d [31]. The XRD and FT-IR analyses supported the XPS result and confirmed that the synthesized material is NiWO₄.

4 Enzymeless glucose detection

The CV study was performed at different scan rates (10–100 mV/s) by varying the applied potential between 0.15 and 0.65 V vs. Hg/HgO, as shown in Fig. 5a. The current response depends on scan rates, and oxidation peak potentials shift towards the positive and reduction peak potentials towards the negative side as scan rates increase.

This result indicates a diffusion-controlled mechanism at the surface of the electrode due to easy electron transfer between the catalytic material and the supporting electrode. This film electrode displays a pair of asymmetric behaviors in the positive potential region at anodic peak current (E_{pa}) = 0.6 mV and cathodic peak current (E_{pc}) = 0.45 mV. The redox peak current density was linearly correlated to the square root of the scan rates (Fig. 5b). The potentials E_{pa} and E_{pc} correspond to interchanges of Ni(II) to Ni(III) and vice-versa are observed. As aforementioned, it confirms the further viability of NiWO₄ nanostructure for enzymeless glucose measurement. Therefore, the CV study was performed in different glucose concentrations from 0.5 to 2.5 mM at a fixed scan rate (20 mV/s). The successive addition of 0.5 mM glucose concentration in the supporting electrolyte significantly increased the anodic peak current response was increased, as depicted in Fig. 5c. The linear rise in current density with successive additions of glucose between the working and counter electrodes. Also, five different CVs with various glucose concentration studies were performed under the same condition, and it is concluded that the current response of five electrodes with glucose concentration studies is evidently the same as shown in supporting

Fig. 4 **a** Survey spectrum, **b** Ni_{2p} spectrum, **c** W4f spectrum, and **d** oxygen (O) spectrum of NiWO₄

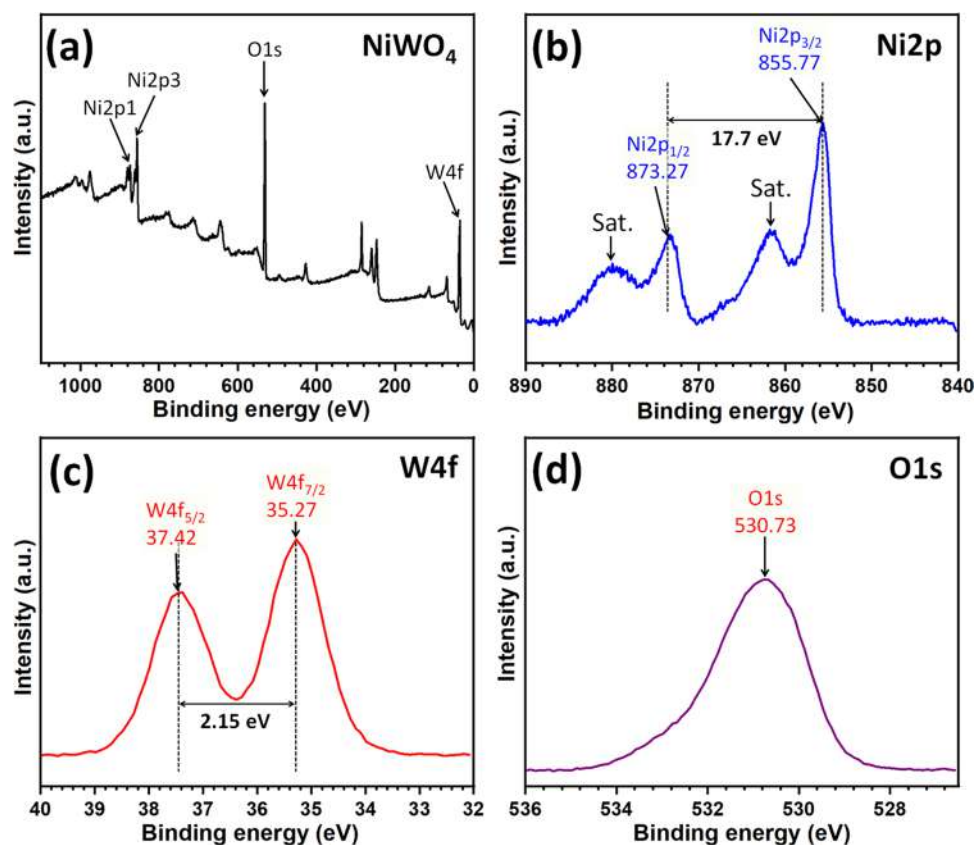
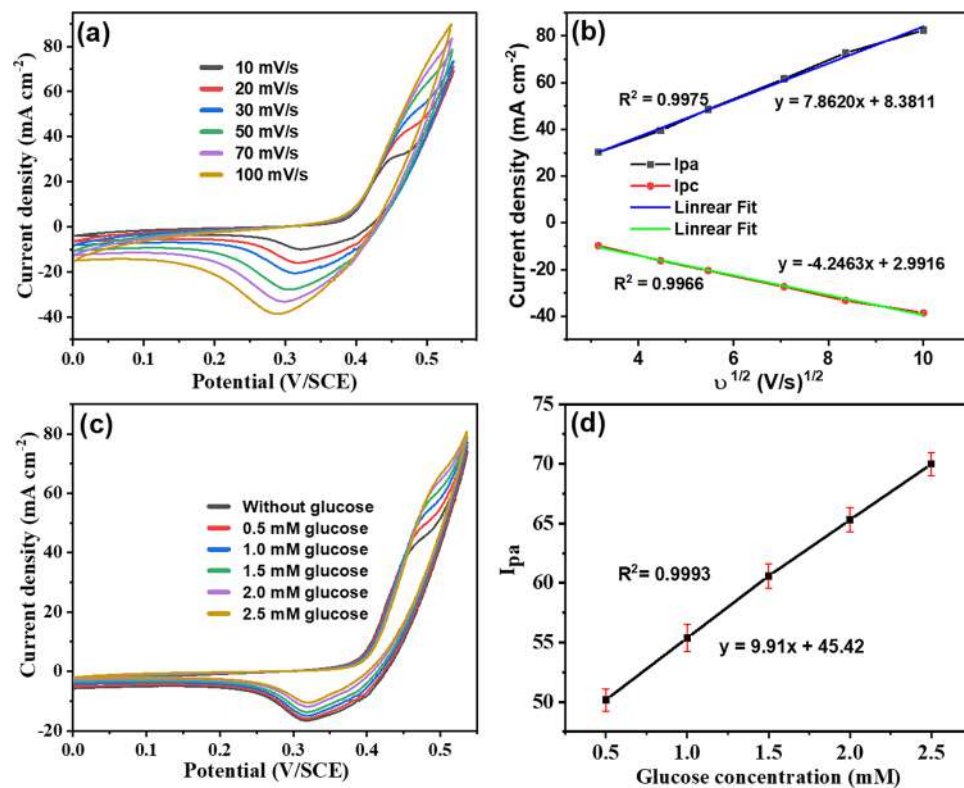
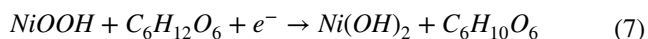
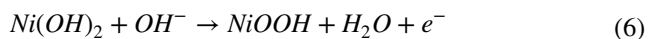


Fig. 5 **a** The CV curves of NiWO₄ electrode at various scan rates from 10 to 100 mV s⁻¹, **b** graph of current density vs. square root of scan rate, **c** the CV curves with and without glucose concentration at the fixed scan rate of 50 mV s⁻¹, and **d** graph of anodic peak current response vs. different glucose concentrations along with error bar



information (Fig. S3). From this study, the excellent non-enzymatic electrocatalytic activity of NiWO₄ catalyst was observed. The correlation coefficient and error bar were calculated at anodic peak current density, and the correlation coefficient was found to be 0.9993, as shown in Fig. 5d. The rise in current response to increasing glucose concentrations involved a pair of redox reactions of nickel species expressed in the form of reactions [18, 19].



The above reaction mechanism represents Ni(II) ions converted into Ni(III) oxidation state in the alkaline medium during the anodic scan. Alteration of redox behavior may improve electrocatalytic non-enzymatic glucose measurement activity. In this context, the existence of WO₄²⁻ poly-anions in the NiWO₄ electrode material helps to promote higher electrical conductivity [19]. Also, NiOOH works as an electron transfer mediator, which leads to the oxidizing glucose molecules to gluconolactone. Further, the gluconolactone molecule is converted into gluconic acid by the hydrolyzing process. Thus, this electrode increases the kinetic behavior of the anodic signal after the addition of

glucose molecules. Then, an additional glucose molecule blocks the active pore sites present in the electrode material, thereby saturating the current response.

The *i-t* amperometric study was performed with NiWO₄ film electrode at an optimized working potential of 0.64 V vs. Hg/HgO in an aqueous 0.5 M KOH electrolyte under constant stirring (300 rpm). The current response observed during the addition of glucose concentration is depicted in Fig. 6a. The five different experiments were performed in the same conditions as shown in supporting information (Fig. S4). The stepwise increase in current response is observed upon increasing the glucose concentrations from 25 to 325 μM. Therefore, a correlation was observed between the successively increased current steps with respect to glucose concentration from 25 to 325 μM.

The analytical performance of NiWO₄ electrocatalyst compared with previous reports (Table 1) indicates that NiWO₄ electrode is better than other electrodes. Moreover, the nanocrystalline nature of NiWO₄ film electrode provided fast electron transfer rates during the oxidation of glucose. Figure 6b displays the calibration curve of step current response and linear concentration range that exhibits kinetic behavior, sensitivity, and detection limit. The sensitivity (S) and limit of detection (LOD) were calculated from S = slope of calibration curve/electrode surface area, and LOD = σ × SD/m, respectively; where 'σ' is the signal-to-noise ratio (S/N = 3), 'SD' is the standard deviation, and 'm' is the slope of the calibration curve. The prepared electrocatalyst

Fig. 6 **a** Response of current density vs. time measurement at the potential of +0.64 V/ Hg/HgO, **b** calibration curve, **c** anti-interference study, and **d** long term stability graph of during 1800s by adding 100 μM glucose concentration

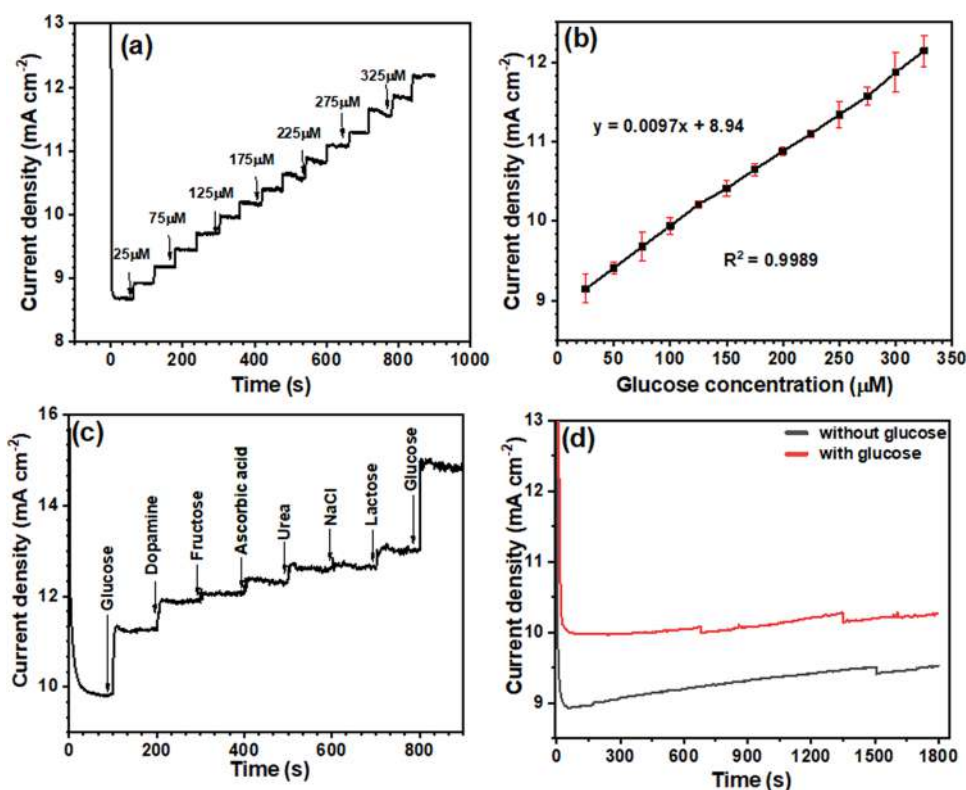


Table 1 Literature survey of NiWO₄ for non-enzymatic electrochemical glucose sensor

Sr. No	Electrode materials	Preparation methods	Sensitivity ($\mu\text{A mM}^{-1} \text{cm}^{-2}$)	Linear range (mM)	LOD (μM)	Working potential (V)	Electrolyte	References
1	NiWO ₄	Electrodeposition	1200	0.0005–0.280	0.15	0.6	0.1 M KOH	[18]
2	NiWO ₄	Hydrothermal	269.6	0.006–0.0041	0.18	0.55	0.1 M NaOH	[19]
3	NiO	Hydrothermal	400.29	Up to 2.2	1	0.6	0.1 M NaOH	[32]
4	NiO	Hydrothermal	724	0.050–3	10	0.6	0.15 M NaOH/ 0.1 M KCl	[33]
5	NiO	Hydrothermal	1618.4	0.25–3.75	2.5	0.37	0.1 M NaOH	[34]
6	NiO	Hydrothermal	2739.5	0.075–3.837	0.75	0.47	0.5 M NaOH	[35]
7	NiO	coordinating etching and precipitating	1323	0.0025–1.10	0.32	0.6	0.1 M NaOH	[36]
8	NiO	Sonoelectrochemistry	206.9	0.1–10	1.16	0.55	0.1 M KCl+0.5 M NaOH	[37]
9	NiO	laser-induced oxidation procedure	5222	0.005–1.1	3.31	0.6	0.1 M NaOH	[38]
10	NiCo ₂ O ₄	Hydrothermal	4120	0.001–0.63	0.5	0.5	0.1 M NaOH	[39]
11	NiCo ₂ O ₄	Hydrothermal	4710	0.001–0.88	0.063	0.4	0.1 M NaOH	[40]
12	NiCo ₂ O ₄	Electrodeposition	387.1	0.01–21	1	0.45	0.1 M NaOH	[41]
13	NiWO ₄	SILAR	9731	0.0025–0.325	0.28	0.5	0.5 M KOH	This work

exhibited remarkable electrocatalytic performance thereof sensitivity ($9731 \mu\text{A mM}^{-1} \text{cm}^{-2}$) and LOD $0.28 \mu\text{M}$. The efficient sensitivity response was attributed to excellent electrocatalytic activity towards glucose molecules.

The two main important characteristics of electrocatalytic enzymeless glucose sensing are determining the glucose concentration at the lowest surface area and enhancing long-term stability. Various analytes are present in human blood samples that can interfere during glucose detection, and they are strong oxidizing agents. The main interfering species fructose, lactose, ascorbic acid, urea, sodium chloride, and dopamine generally present with glucose molecules. Hence, the selectivity study was important for the identification of proper glucose molecules. In this study, successive addition of $250 \mu\text{M}$ interfering species towards glucose molecules under the constant stirring in a freshly prepared 0.5 M KOH electrolyte is carried out, as shown in Fig. 6c. From this result, no significant current appeared except for glucose sensing response. Furthermore, the long-term stability of NiWO₄ film electrodes was investigated towards glucose molecules. Figure 6d shows with and without glucose concentration (0.5 mM) for the time interval of 1800s, indicating that this electrode possesses excellent stability retention of 102.66% after 1800s.

The glucose level present in human samples were measured using NiWO₄ electrocatalyst. For the measurement of current response during the oxidation of glucose molecules, *i-t* amperometric method was used. First, the blood samples

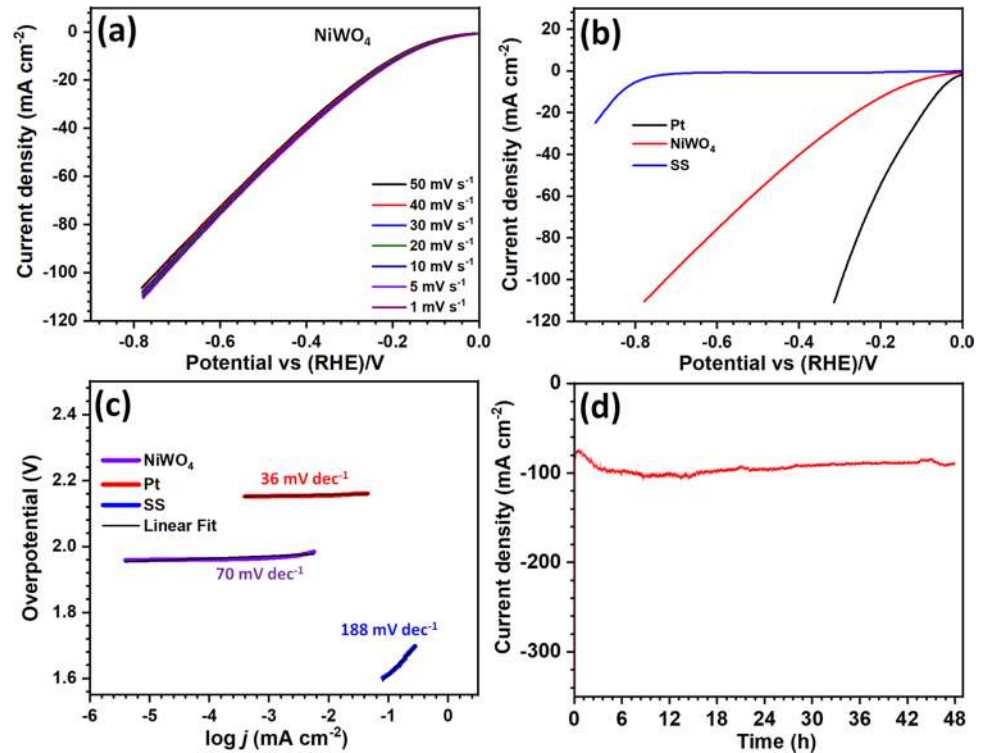
were collected from the blood bank and stored in an ice bath before the experiment. Then, the 5 and $10 \mu\text{M}$ glucose concentrations were added into the human blood samples. The recovery rate was calculated for three blood samples, which were observed to be between 98.02 and 101.4%. The relative standard deviation was in acceptable range through five repetitions. Recovery and the relative standard deviation are mentioned in Table 2. Thus, the prepared electrode catalyst can be reliable and highly sensitive for glucose detection from human blood samples.

5 Electrocatalytic performance analysis

The electrocatalytic performance of NiWO₄ electrode was used for HER application and evaluated through polarization curves at $1, 5, 10, 20, 30, 40,$ and 50 mV s^{-1} (Fig. 7a). All polarization curves are *iR*-corrected. The overpotential was measured at 100 mA cm^{-2} current density, which negligibly changed from the potential of $0.73\text{--}0.74 \text{ V vs. RHE}$ as the scan rate changed from 1 to 50 mV s^{-1} . The overpotential values calculated using a scan rate of 1 mV s^{-1} at a current density of 10 mA cm^{-2} and 100 mA cm^{-2} were 0.17 and 0.73 V vs. RHE/V , respectively. The value of onset potential (0.73 V vs. RHE) is lower than the previously reported Ni-based electrocatalysts summarized in Table 3. For comparison, the polarization curves of Pt and SS at the scan rate of 1 mV s^{-1} are shown in Fig. 7b. The overpotential

Table 2 The glucose level measurement from three different human blood samples using NiWO₄ catalyst

Human blood	Samples	Added (μM)	Founded (μM)	Our method (μM)	Recovery (%)	RSD (%)
a	1	5	13.40	8.31	98.90	1.42
	2	10	18.14	8.19	100.6	2.07
b	1	5	12.18	7.05	98.18	2.65
	2	10	19.56	9.40	98.32	2.29
c	1	5	10.41	5.49	101.4	3.02
	2	10	16.58	6.45	98.02	3.34

Fig. 7 **a** The LSV polarization curves at different scan rates, **b** the LSV polarization curves of SS, NiWO₄, and Pt at a scan rate of 1 mV s⁻¹, **c** Tafel plots, and **d** chronoamperometry test at the potential of 0.93 vs RHE/V of NiWO₄ electrocatalysts**Table 3** Literature survey of NiWO₄ catalyst for hydrogen evolution reaction

Catalysts	Preparation method	Electrolyte	Over potential (mV)@current density (mA cm^{-2})	Tafel slope (mV dec^{-1})	References
Ni ₃ S ₂	Sulfurization method	0.1 M KOH	158@10	83	[41]
Ni _{0.9} Fe _{0.1} /NC	Hydrothermal	1 M KOH	231@10	111	[43]
Ni ₃ S ₂ /NF	Hydrothermal	1 M KOH	170@10	91	[44]
MoS ₂ -Ni ₃ S ₂ HNRs/NF	Hydrothermal	1 M KOH	98@10	61	[45]
Co-Ni ₃ N	Hydrothermal	1 M KOH	194@10	156	[46]
Ni ₃ FeN	Hydrothermal	1 M KOH	238@10	46	[47]
Ni ₃ N/NF	Calcination	1 M KOH	121@10	109	[48]
NiO/Ni-CNT	CBD + annealing	1 M KOH	86@10	82	[49]
NiMo ₃ S ₄	Anion exchange route	0.1 M KOH	98@10	252	[50]
NiFe LDH NiSe/NF	Hydrothermal	1 M KOH	276@100	70	[51]
NiWO ₄	SILAR	0.5 M KOH	171@10	70	This work

value for Pt at 100 mA cm^{-2} is 0.29 V vs. RHE. The LSV curve indicates that the overpotential value for SS is higher. Compared to NiWO_4 , a higher value for overpotential for SS confirms a fast catalytic kinetics response from NiWO_4 . But the overpotential value for Pt is less than that for NiWO_4 . The Tafel plot was used to evaluate the intrinsic catalytic kinetics properties (Fig. 7c). The Tafel slope for NiWO_4 , SS, and Pt are 70 , 188 , and 36 mV dec^{-1} , respectively. The smaller value of the Tafel slope shows fast catalytic kinetics for HER on NiWO_4 electrode. For practical application, electrocatalyst requires long-term stability towards H_2 production. The overpotential of 0.7 E (V vs. RHE) remains the same after 48 h of durability at the current density of 100 mA cm^{-2} (Fig. 7d).

The ECSA was calculated from the CV curves (Fig. 8a) performed in a non-faradaic potential range between 1.11 and 1.21 E (V vs. RHE). The slope of the graph of capacitive current density and scan rate gives the value of the parameter used for the calculation of ECSA, as shown in Fig. 8b. The different five experiments were performed to observe the repeatability of the NiWO_4 electrode. It is evidently concluded that the NiWO_4 electrode showed nearly equal performance as shown in Fig. S5 (supporting information). For NiWO_4 , the average value of 24.9 cm^2 of ECSA reveals the origin of excellent catalytic activity for HER (Fig. 8c). The semicircle-like structure was observed in a middle-frequency range in the Nyquist plot of NiWO_4 (Fig. 8d). The Zview EIS data analysis software was used to investigate

fitted experimental data analysis. The lower values of series resistance R_s of $0.68 \Omega \text{ cm}^{-2}$ and charge transfer resistance R_{ct} of $43.7 \Omega \text{ cm}^{-2}$ are due to the direct growth of material on conducting substrate. The Nyquist plot was fitted with an electrical circuit, shown as the inset of Fig. 8d. This electrical circuit consists of R_s , R_{ct} , W , and C_{dl} .

The overall electrochemical water splitting capabilities of NiWO_4 electrocatalyst were measured using a two-electrode system. Steady-state polarization curves with iR -correction of water breaking at 1 mV s^{-1} scan rate, indicate an onset potential of about 1.82 V to achieve 100 mA cm^{-2} , as shown in Fig. 9a. The stability of NiWO_4 film electrode was studied using chronoamperometric method at 1.82 V for 48 h by a current density of 100 mA cm^{-2} (Fig. 9b). The current density remains at 100 mA cm^{-2} after 48 h, confirming superior stability of NiWO_4 for overall water splitting. The present electrocatalyst can be potentially applicable to hydrogen production. The captured water splitting is provided in the supporting information. From this video, it is concluded that hydrogen production is possible for different uses.

6 Conclusions

The nanocrystalline NiWO_4 electrocatalyst is found to be potentially applicable for dual purposes. The SILAR technique was used to successfully synthesize NiWO_4 electrocatalyst. The nanocrystalline electrocatalyst showed exceptional

Fig. 8 **a** The CV curves in non-faradaic potentials at various scan rates, **b** plot of current density vs. scan rate at the potential of $1.150 \text{ vs. (Hg/HgO)/V}$, **c** the ECSA study of different electrodes, and **d** the Nyquist plot of NiWO_4

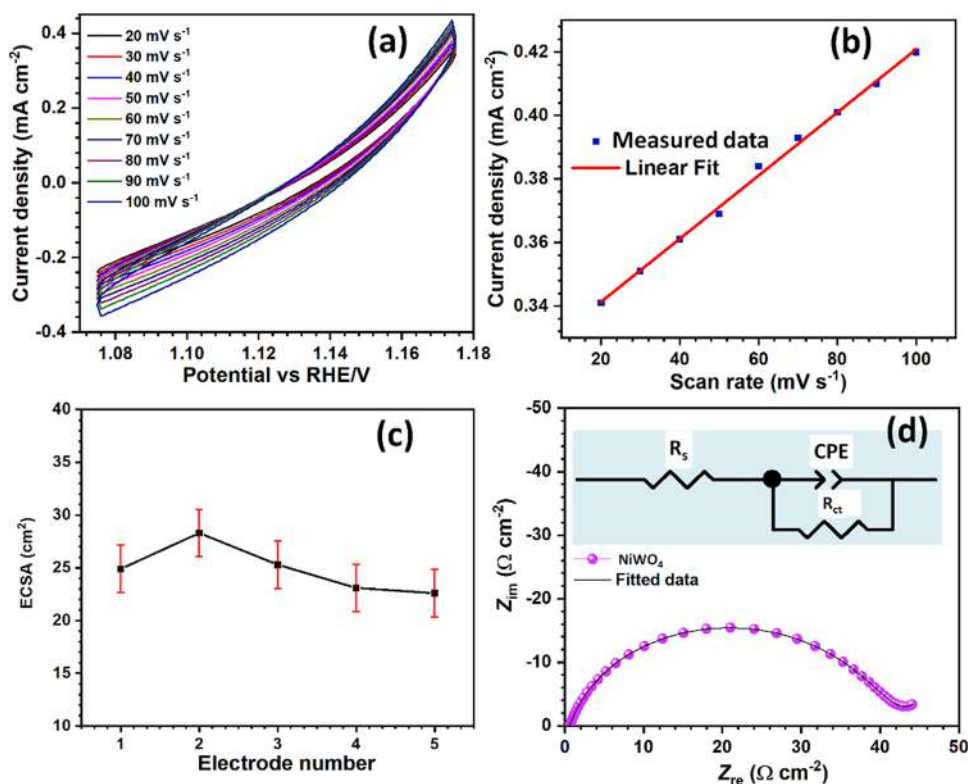
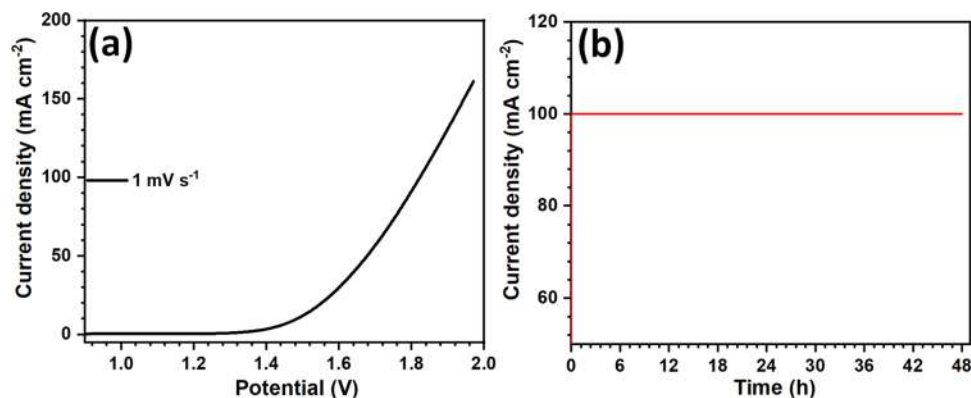


Fig. 9 Overall water splitting test of NiWO₄ **a** the LSV polarization curve, **b** chronoamperometric test at the potential of 1.82 V



sensitivity of 9731 $\mu\text{A mM}^{-1} \text{cm}^{-2}$ within the linear range from 25 to 325 μM . The LOD was found to be 0.28 μM with desirable stability and selectivity performance. The electrocatalyst also demonstrated a 171 mV overpotential at 10 mA cm^{-2} with the lowest Tafel slope of 70 mV dec^{-1} for HER. Furthermore, the chronopotentiometry measurement at 100 mA cm^{-2} over 24 h exhibited 97% retention of HER activity with an ECSA of NiWO₄ film was 25.5 cm^2 . Therefore, NiWO₄ electrode catalyst can be applicable for enzymeless glucose detection and hydrogen production.

Supplementary Information The online version contains supplementary material available at <https://doi.org/10.1007/s00339-023-06798-5>.

Acknowledgements The authors are thankful to D. Y. Patil Education Society, (Institution Deemed to be University) Kolhapur-416006 (India), for giving financial support through research project sanction No. DYPES/DU/R&D/3099. In addition, S. B. Jadhav acknowledges the Chhatrapati Shahu Maharaj Research Training and Human Development (SARTHI), Government of Maharashtra, India for awarding Senior Research Fellow (SRF). Authors are also thankful to DST-FIST analytical Instrumental laboratory Jaysingpur college, Jaysingpur for experimental and characterization facilities.

Author contributions SJ and DM equally contributed for this work.

Data availability Data is available from corresponding author.

Declarations

Conflict of interest The authors declare that they have no known competing financial interests.

References

- W. Yanga, S. Chen, *Chem. Eng. J.* **393**, 124726 (2020). <https://doi.org/10.1016/j.cej.2020.124726>
- W.-C. Lee, K.-B. Kim, N.G. Gurudatt, K.K. Hussain, C.S. Choi, D.-S. Park, Y.-B. Shim, *Biosens. Bioelectron.* **130**, 48–54 (2019). <https://doi.org/10.1016/j.bios.2019.01.028>
- F. Xiea, T. Liu, L. Xie, X. Sun, Y. Luo, *Sens. Actuators B Chem.* **255**, 2794–2799 (2018). <https://doi.org/10.1016/j.snb.2017.09.095>
- K.-N. Kang, S.-I. Kim, J.-C. Yoon, J. Kim, C. Cahoon, J.-H. Jang, *ACS Appl. Mater. Interfaces.* **14**, 33013–33023 (2022). <https://doi.org/10.1021/acsami.2c04471>
- Y.Y. Li, P. Kang, H.Q. Huang, Z.G. Liu, G. Li, Z. Guo, X.J. Huang, *Sens. Actuators B Chem.* **307**, 127639 (2020). <https://doi.org/10.1016/j.snb.2019.127639>
- R. Madhu, V. Veeramani, S.-M. Chen, A. Manikandan, A.-Y. Lo, Y.-L. Chueh, A.C.S. *Appl. Mater. Interfaces.* **7**, 15812–15820 (2015). <https://doi.org/10.1021/acsami.5b04132>
- A. Koyappayil, S. Berchmans, M.H. Lee, *Colloids Surfaces B Biointerfaces* **189**, 110840 (2020). <https://doi.org/10.1016/j.colsurfb.2020.110840>
- S.B. Jadhav, D.B. Malavekar, R.N. Bulakhe, U.M. Patil, I. Insik, C.D. Lokhande, P.N. Pawaskar, *Surf. Interfaces.* **23**, 101018 (2021). <https://doi.org/10.1016/j.surf.2021.101018>
- R. Zahra, E. Pervaiz, M. Yang, O. Rabi, Z. Saleem, M. Ali, S. Farrukh, *Int. J. Hydrog. Energy.* **45**, 24518–24543 (2020). <https://doi.org/10.1016/j.ijhydene.2020.06.236>
- W. Hua, H.-H. Sun, F. Xu, J.-G. Wang, *Rare Met.* **39**, 335–351 (2020). <https://doi.org/10.1007/s12598-020-01384-7>
- D.B. Malavekar, V.C. Lokhande, D.J. Patil, S.B. Kale, U.M. Patil, T. Ji, C.D. Lokhande, *J. Colloid Interface Sci.* **609**, 734–745 (2022). <https://doi.org/10.1016/j.jcis.2021.11.074>
- C. Kung, C. Lin, Y. Lai, R. Vittal, K. Ho, *Biosens Bioelectron* **27**, 125–131 (2011). <https://doi.org/10.1016/j.bios.2011.06.033>
- Q. Shao, Y. Wang, S. Yang, K. Lu, Y. Zhang, C. Tang, J. Song, Y. Feng, L. Xiong, Y. Peng, Y. Li, H.L. Xin, X. Huang, *ACS Nano* **12**, 11625–11631 (2018). <https://doi.org/10.1021/acsnano.8b06896>
- W.L. Kwong, C.C. Lee, J. Messinger, *J. Phys. Chem. C.* **121**, 284–292 (2017). <https://doi.org/10.1021/acs.jpcc.6b09050>
- S. Gao, A. Zavabeti, B. Wang, R. Ren, C. Yang, Z. Liu, Y. Wang, A.C.S. *Appl. Nano Mater.* **4**, 4542–4551 (2021). <https://doi.org/10.1021/acsnm.1c00134>
- J. Chang, K. Li, Z. Wu, J. Ge, C. Liu, W. Xing, A.C.S. *Appl. Mater. Interfaces* **10**, 26303–26311 (2018). <https://doi.org/10.1021/acsami.8b08068>
- S.-S. Lu, X. Shang, L.-M. Zhang, B. Dong, W.-K. Gao, F.N. Dai, B. Liu, Y.-M. Chai, C.-G. Liu, *Appl. Surf. Sci.* **445**, 445–453 (2018). <https://doi.org/10.1016/j.apsusc.2018.03.177>
- F. Mollarasouli, M.R. Majidi, K.A. Zeynali, *J Taiwan Inst Chem Eng.* **118**, 301–308 (2021). <https://doi.org/10.1016/j.jtice.2021.01.003>
- S. Mani, V. VEDIYAPPAN, S.-M. Chen, R. Madhu, V. Pitchaimani, J.-Y. Chang, S.-B. Liu, *Scientific report* **6**, 1–8 (2016). <https://doi.org/10.1038/srep24128>

20. J.M.V. Nsanzimana, Y. Peng, M. Miao, V. Reddu, W. Zhang, H. Wang, B.Y. Xia, X. Wang, A.C.S. Appl. Nano Mater **3**, 1228–1235 (2018). <https://doi.org/10.1021/acsnm.7b00383>
21. C. Wei, S. Sun, D. Mandler, X. Wang, S.Z. Qiao, Z.J. Xu, Chem. Soc. Rev. **48**, 2518–2534 (2019). <https://doi.org/10.1039/C8CS00848E>
22. W. Li, J. Lv, W. Cai, X. Chen, Q. Huang, L. Wang, B. Wang, Chem. Mater. (2023). <https://doi.org/10.1021/acs.chemmater.2c03723>
23. S.M.M. Zawawi, R. Yahya, A. Hassan, H.N.M.E. Mahmud, M.N. Daud, Chem. Cent. J. **7**, 80 (2013). <https://doi.org/10.1186/1752-153X-7-80>
24. P. Sharma, M. Minakshi, J. Whale, A. Jean-Fulcrand, G. Garnweitner, Nanomaterials **11**, 580 (2021). <https://doi.org/10.3390/nano11030580>
25. G. Poirier, Y. Messaddeq, S.J.L. Ribeiro, M. Poulain, J. Solid State Chem **178**, 1533–1538 (2005). <https://doi.org/10.1016/j.jssc.2004.10.032>
26. P.R. Kasturi, S. Shanmugapriya, M. Elizabeth, K. Athira, R.K. Selvan, J Mater Sci: Mater Electron **31**, 2378–2387 (2020). <https://doi.org/10.1007/s10854-019-02773-0>
27. E.S. Babu, B.J. Rani, G. Ravi, R. Yuvakkumar, R.K. Guduru, V. Ganesh, S. Kim, Mater. Lett **220**, 209–212 (2018). <https://doi.org/10.1016/j.matlet.2018.03.018>
28. X. Xing, J. Wang, J. Mater. Sci. Mater. Electron **27**, 11613–11622 (2016). <https://doi.org/10.1007/s10854-016-5293-8>
29. A. Bhardwaj, I.-H. Kim, L. Mathur, J.-Y. Park, S.-J. Song, J. Hazard. Mater **403**, 123797 (2021). <https://doi.org/10.1016/j.jhazmat.2020.123797>
30. Y. Huang, Y. Gao, C. Liu, Z. Cao, Y. Wang, Z. Li, Y. Yan, M. Zhang, G. Cao, J. Phys. Chem. C **123**, 30067–30076 (2019). <https://doi.org/10.1021/acs.jpcc.9b08448>
31. Y. Zhang, Z. Jin, Catal. Sci. Technol. **9**, 1944–1960 (2019). <https://doi.org/10.1039/C8CY02611D>
32. S. Wang, C. Wang, G. Wei, H. Xiao, N. An, Y. Zhoua, C. An, J. Zhang, Colloids Surf. A **509**, 252–258 (2016). <https://doi.org/10.1016/j.colsurfa.2016.08.076>
33. A. Ibrahim, E.M. Sodki, A. Umar, A. Amine, R. Kumar, M. Al-Assiri, A.E. Al-Salami, S. Baskoutas, New J. Chem. **42**, 964–973 (2018). <https://doi.org/10.1039/C7NJ03253F>
34. R. Ahmad, M. Khan, N. Tripathy, M. Iqbal, R. Khan, A. Khosla, J. Electrochem. Soc. **167**, 107504 (2020). <https://doi.org/10.1149/1945-7111/ab9757>
35. Y. Zhang, D. Zhao, W. Zhu, W. Zhang, Z. Yue, J. Wang, R. Wang, D. Zhang, J. Wang, G. Zhang, Sens. Actuators, B **255**, 416–423 (2018). <https://doi.org/10.1016/j.snb.2017.08.078>
36. G. He, L. Tian, Y. Cai, S. Wu, Y. Su, H. Yan, W. Pu, J. Zhang, L. Li, Nanoscale Res. Lett. **13**, 1–10 (2018). <https://doi.org/10.1186/s11671-017-2406-0>
37. C. Heyser, R. Schrebler, P. Grez, J. Electroanal. Chem. **832**, 189–195 (2018). <https://doi.org/10.1016/j.jelechem.2018.10.054>
38. S. Sedaghat, C.R. Piepenburg, A. Zareei, Z. Qi, S. Peana, H. Wang, R. Rahimi, A.C.S. Appl. Nano Mater. **3**, 5260–5270 (2020). <https://doi.org/10.1021/acsnm.0c00659>
39. X. Luo, M. Huang, D. He, M. Wang, Y. Zhang, P. Jiang, Analyst **143**, 2546–2554 (2018). <https://doi.org/10.1039/C8AN00668G>
40. M. Saraf, K. Natarajan, M.M.M. Shaikh, New J. Chem. **41**, 9299–9313 (2017). <https://doi.org/10.1039/C7NJ01519D>
41. W. Li, H. Qi, B. Wang, Q. Wang, S. Wei, X. Zhang, Y. Wang, L. Zhang, X. Cui, Microchim. Acta **185**, 1–9 (2018). <https://doi.org/10.1039/C7NJ01519D>
42. W. Zhu, X. Yue, W. Zhang, S. Yu, Y. Zhang, J. Wang, J. Wang, Chem. Commun. **52**, 1486–1489 (2016). <https://doi.org/10.1039/C5CC08064A>
43. X. Zhang, H. Xu, X. Li, Y. Li, T. Yang, Y. Liang, ACS Catal. **6**, 580–588 (2016). <https://doi.org/10.1039/C7NJ01519D>
44. L. Jinlong, L. Tongxiang, J. Solid State Chem. **243**, 106–110 (2016). <https://doi.org/10.1016/j.jssc.2016.08.017>
45. Y. Yang, K. Zhang, H. Lin, X. Li, H.C. Chan, L. Yang, Q. Gao, ACS Catal. **7**, 2357–2366 (2017). <https://doi.org/10.1021/acscatal.6b03192>
46. C. Zhu, A. Wang, W. Xiao, D. Chao, X. Zhang, N.H. Tiep, S. Chen, J. Kang, X. Wang, J. Ding, J. Wang, H. Zhang, H. Fan, Adv. Mater. **30**, 1–8 (2018). <https://doi.org/10.1002/adma.201705516>
47. Q. Chen, R. Wang, M. Yu, Y. Zeng, F. Lu, X. Kuang, X. Lu, Electrochim. Acta. **247**, 666–673 (2017). <https://doi.org/10.1016/j.electacta.2017.07.025>
48. Z. Xing, Q. Li, D. Wang, X. Yang, X. Sun, Electrochim. Acta. **191**, 841–845 (2016). <https://doi.org/10.1016/j.electacta.2015.12.174>
49. M. Gong, W. Zhou, M.-C. Tsai, J. Zhou, M. Guan, M.-C. Lin, B. Zhang, Y. Hu, D.-Y. Wang, J. Yang, S.J. Pennycook, B.-J. Hwang, H. Dai, Nat. Commun. **5**, 1–6 (2014). <https://doi.org/10.1038/ncomms5695>
50. J. Jiang, M. Gao, W. Sheng, Y. Yan, Angew. Chem. Int. **128**, 15466–15471 (2016). <https://doi.org/10.1002/ange.201607651>
51. S. Dutta, A. Indra, Y. Feng, T. Song, U. Paik, A.C.S. Appl. Mater. Interfaces **9**, 33766–33774 (2017). <https://doi.org/10.1021/acsmi.7b0798>

Publisher's Note Springer Nature remains neutral with regard to jurisdictional claims in published maps and institutional affiliations.

Springer Nature or its licensor (e.g. a society or other partner) holds exclusive rights to this article under a publishing agreement with the author(s) or other rightsholder(s); author self-archiving of the accepted manuscript version of this article is solely governed by the terms of such publishing agreement and applicable law.



Cobalt doped iron phosphate thin film: An effective catalyst for electrochemical water splitting



Suraj A. Khalate^a, Sujit A. Kadam^b, Yuan-Ron Ma^b, Sachin S. Pujari^a, Umakant M. Patil^{a,*}

^a Centre for Interdisciplinary Research (CIR), D.Y. Patil Education Society, Kolhapur 416006, India

^b Department of Physics, National Dong Hwa University, Hualien 97401, Taiwan

ARTICLE INFO

Article history:

Received 26 March 2021

Received in revised form 9 June 2021

Accepted 19 June 2021

Available online 24 June 2021

Keywords:

Catalytic stability

Doping

Electrochemistry

Heterogeneous catalysis

Water splitting

ABSTRACT

For practically feasible water splitting to fulfill the need of energy, the development of efficient, robust and long lasting catalyst is necessary. Transition metal compounds facilitates the good catalytic properties due to facile transition of their oxidation states. We here reported a novel process for the synthesis of novel material as cobalt doped iron phosphate thin films. The pristine iron phosphate thin films have synthesized by regular facile hydrothermal method and to achieve doping of the cobalt into iron phosphate, second step hydrothermal ion-exchange process was used. The as synthesized cobalt doped iron phosphate thin film electrode exhibits excellent electrochemical OER and HER catalytic water splitting performance. The prepared material was demonstrated by two electrodes overall water splitting electrolyzer in alkaline medium at lowest potential of 1.72 V to deliver 10 mA/cm² current density after 4 days' continuous water splitting test. The outstanding catalytic stability proved 0.4 Co:FePi thin film electrodes are robust water splitting electrocatalyst.

© 2021 Elsevier B.V. All rights reserved.

1. Introduction

Upon looking at the present scenario of the energy generation and consumption, an eye capturing fact can be realized that we need greater energy than what we have today. It is the necessity to produce energy from green and sustainable energy resources to maintain our benign environment and future from the energy crisis, global warming and environmental pollution. Hydrogen is one of the best energy sources from clean and green energy sources, and is expected to play a major role in a future sustainable energy sector [1,2]. Hydrogen from energy sources such as solar or wind electricity is the clean production of energy, also the storage of energy in the clean form as a standby during the ups and downs of solar and wind power. Electrochemical water splitting is an effective technique to convert electrical energy into chemical energy in the form of hydrogen by using proper catalyst electrode. Electrochemical water splitting is the combined reaction of two half reactions as oxygen evolution reaction (OER) and complimentary hydrogen evolution reaction (HER). These reactions of water splitting (OER and HER) are constrained by the rate determining sluggish four electron coupled proton transfer process and hence have low conversion efficiency

[3–5]. At present, the best electrocatalysts with high efficiency are the state-of-the-art materials as platinum, ruthenium/iridium based oxides which are widely used. The best electrocatalyst for HER is platinum, which only requires onset overpotential of nearly zero. But the commercial use of these state-of-the-art catalyst materials is limited by their scarcity, high cost, large overpotentials at high current densities and poor stability [6]. Many researchers are interested and engage in the development of alternative cost-effective, non-noble metal and highly stable electrocatalysts for efficient overall water splitting. Variety of new non-noble metal based catalysts are under research and development process. First row (3d) transition metal based materials have good catalytic properties due to facile transition of their oxidation states. Transition metal based materials such as, transition metal-transition metal alloys (TMAs), transition metal oxides (TMOs), transition metal nitrides (TMNs), transition metal dichalcogenides (TMDs), transition metal phosphides (TMPs), transition metal carbides (TMCs), transition metal borides (TMBs), etc. are playing leading role in water splitting [7]. Few reports are available on transition metal phosphate electrode materials for electrochemical water splitting. Transition metal phosphates play an important role by facilitating adsorption and stabilizing active centers, also phosphate ligands give the favorable conditions for electrolyte ion adsorption and oxidation by distorting local atomic geometry and facilitating the oxidation of metal atoms during proton coupled electron transfer [8].

* Corresponding author.

E-mail address: umakant.physics84@gmail.com (U.M. Patil).

Compounds of transition metals such as Ni, Co, and Fe are outstanding electrocatalysts for water splitting. Doping of these metals could appreciably boost the catalytic activity which delivers high current density and lowers the overpotential by improving the electrical conductivity and metal-to-metal partial-charge-transfer activation process and the reduction of adsorption energy on the surface [9]. Due to similar atomic structure of 8/VIII, 9/VIII and 10/VIII subgroup elements, doping of Ni, Co, and/or Fe is advantageous to keep the original morphology and surface of the transition metal compounds. Cobalt based materials have their existence as catalyst for water splitting from long duration [10]. Cobalt-based oxygen evolving catalysts are exceptional since they have various advantages such as they operate safely with high activity under benign conditions, they are tough, self-healing, and can deposited on variety of conducting substrates [11]. The benefit behind the use of cobalt into the catalyst materials is that the involvement of Co^{2+} , Co^{3+} , and likely Co^{4+} oxidation states in the redox cycles of $\text{O}_2/\text{H}_2\text{O}$ at cobalt centers which can enhance the oxygen evolution reaction (OER) efficiency [12].

In the present study, we have investigated the synergistic effect of cobalt doping in iron phosphate thin films on electrochemical water splitting performance. Herein, pristine iron phosphate thin films were prepared on stainless steel (SS) substrates by facile hydrothermal method and then cobalt was doped by the ion-exchange process using second step hydrothermal. SS substrates are highly conducting, inexpensive, easily available and non-reacting than the other substrates like carbon cloth, copper foil, titanium or nickel foam. As compared to the SS substrates, the nickel foam, carbon cloth, copper foil, titanium mesh shows their own response to the electrochemical water splitting and hence the observed performance is due to the synergistic effect between active material and the substrate material [13–19]. Also, SS is very stable in acidic and alkaline media hence, it is used as substrates for present study. The prepared thin film electrodes were characterized by different physico-chemical techniques to identify compositional, structural, morphological, and electrochemical properties. The electrochemical analyses as OER and HER are carried out in 1 M KOH and 1 M H_3PO_4 electrolytes, respectively. Particularly, 0.4 Co:FePi thin film electrode show the lowest overpotential of 266 mV for the current density of 10 mA/cm^2 . After 10 h continuous catalytic OER, Co:FePi thin film electrode show more than 99% catalytic activity. Also, for HER the same material electrode show outstanding performance with 82.3 mV overpotential at 10 mA/cm^2 current density and around 100% catalytic stability after 10 h continuous catalysis. The overall water splitting stability test was performed for 4 days in alkaline medium and achieved lowest potential (1.72 V) at 10 mA/cm^2 current density after test.

2. Experimental section

2.1. Materials used and substrate cleaning

All the required chemicals and materials such as ferric chloride (FeCl_3), sodium nitrate (NaNO_3), potassium dihydrogen orthophosphate (KH_2PO_4) and cobalt chloride (CoCl_2) of analytical reagent grade were purchased from Sigma-Aldrich and used as it was without any further purification. 1 cm × 6 cm sized stainless steel (SS) (304 grade) was purchased from local market and used as a conducting substrates. The SS substrates were cleaned by polishing with zero grade polish paper, rinsed by doubly distilled water (DDW) several times and then ultrasonicated for 10 min in the solution of ethanol and DDW. After 10 min ultrasonication, the cleaned substrates were dried and used for further reactions.

2.2. Synthesis of pristine iron phosphate thin films

The pristine iron phosphate thin films were synthesized by facile hydrothermal method as procedure followed previously [8]. For this synthesis, ferric chloride (FeCl_3) 0.1 M and potassium dihydrogen orthophosphate (KH_2PO_4) 0.15 M were used as precursors of iron and phosphate, respectively and sodium nitrate (NaNO_3) 0.5 M was used as oxidizing agent. 60 ml solution was prepared as continuous stirring with one by one addition of above chemicals in DDW. The prepared solution transferred in 100 ml Teflon liner and thoroughly cleaned SS substrates were kept vertically in the solution. The liner was closed, kept in SS vessel and completely sealed by nut-bolt fitting. The prepared hydrothermal bomb was kept in laboratory oven at 130 °C for 14 h. After 14 h, bomb was cooled naturally, and pristine iron phosphate deposited thin films were removed from Teflon liner and washed severally by DDW and dried naturally at ambient temperature. The as synthesized pristine iron phosphate thin films marked as '0.0 Co:FePi' and were used as it is for further doping process.

2.3. Synthesis of cobalt doped iron phosphate thin films

For the cobalt doping in iron phosphate thin films, iron phosphate thin films were kept into the beakers of cobalt chloride solutions of different concentrations (0.1, 0.2, 0.3, 0.4 and 0.5 M) and denoted as '0.1 Co:FePi', '0.2 Co:FePi', '0.3 Co:FePi', '0.4 Co:FePi', and '0.5 Co:FePi', respectively. These beakers were kept in hydrothermal autoclave and heated at 120 °C for 4 h which allow the cobalt ions to diffuse into the pores and voids of iron phosphate. The doping has done by the ion-exchange process and Fe atoms partially substituted by the Co atoms. After the completion of reaction, samples were removed from autoclave and washed severally by DDW. The prepared thin films were dried naturally in ambient temperature and used for the physico-chemical characterizations and also for electrochemical testing. The photographs of the as deposited thin film catalysts are shown in Fig. S1 (See Electronic Supporting Information (EIS)).

2.4. Characterizations

The X-ray diffraction (XRD) patterns of the samples were collected from the Rigaku Miniflex 600 ($\text{Cu-K}\alpha$, $\lambda = 1.5406 \text{ \AA}$) in the 2θ range 10–70°. Molecular bond vibrational spectra of the prepared samples were analyzed by Fourier Transform Infrared Spectroscopy (FTIR) using alpha (II) Bruker spectroscope in the wavenumber range 400–4000 $/\text{cm}$. N_2 adsorption-desorption isotherms were characterized for surface analysis as surface area and pore size using Belsorp II mini. Chemical composition and surface morphology were observed by Field Emission Scanning Electron Microscope (FESEM, JEOL JSM-6500F). With microfocus monochromatic Al $\text{K}\alpha$ X-ray, electronic structure information probed by X-ray photoelectron spectrometer (XPS, Thermo Scientific Inc. K-alpha).

2.5. Electrochemical characterizations

ZIVE MP1 electrochemical workstation used to analyze electrochemical properties of the prepared materials in standard three electrode electrochemical cell. Prepared materials coated SS substrates were used as working electrode, platinum metal plate and a saturated calomel electrode (SCE) (saturated KCl) were used as a counter and reference electrodes, respectively. 1 M KOH (pH = 13.7) and 1 M H_3PO_4 (pH = 1.5) solutions were used as electrolytes to measure OER and HER activities. All the applied potentials were converted in terms of reversible hydrogen electrode (RHE) potentials

from SCE by the equation: $V_{\text{RHE}} = V_{\text{SCE}} + 0.059 \times \text{pH} + 0.241$. The cyclic voltammetry (CV) was performed in the potential window 1.05–1.6 V vs RHE at 50 mV/s scan rate. The linear sweep voltammetry (LSV) at 1 mV/s scan rate in the potential window 1.05–1.75 V vs RHE (for OER) and 0.33 to –0.85 V vs RHE (for HER) implemented to measure electrochemical catalytic response. The electrochemical impedance spectroscopy (EIS) was made in frequency range of 0.1 MHz–100 MHz with an amplitude of 10 mV. To study the durability of the catalyst material electrodes, the chronoamperometry tests were performed at the overpotentials. The overpotential η (V) calculated by the Eq. (1) as:

$$\eta = V_{\text{RHE}} - 1.23 \quad (1)$$

where V_{RHE} (V) is the potential in terms of reversible hydrogen electrode (RHE).

Overall water splitting was studied using two electrode system, where deposited material electrodes were used as both an anode and cathode in 1 M KOH electrolyte. LSV polarization curves were recorded at 1 mV/s scan rate in the potential window of 0–2.2 V. Long term overall catalytic water splitting stability was performed by chronoamperometry at 1.8 V potential for continuous 4 days in alkaline bath.

3. Results and discussion

3.1. Structural analysis

Fig. 1(A) shows the XRD patterns of pristine iron phosphate (0.0 Co:FePi) thin film deposited by first step hydrothermal method and cobalt doped iron phosphate (Co:FePi) thin films (0.1 Co:FePi, 0.2 Co:FePi, 0.3 Co:FePi, 0.4 Co:FePi and 0.5 Co:FePi) synthesized by second step hydrothermal ion-exchange processing in CoCl_2 bath on SS substrates. XRD patterns matched and indexed with the standard data JCPDS card 96-900-1208 confirms the formation of tetragonal lipscombite iron phosphate ($\text{Fe}_{11.78}\text{P}_8\text{O}_{40}$) (space group P 41 21 2, $a = b = 7.31 \text{ \AA}$, $c = 13.2120 \text{ \AA}$, $\alpha = \beta = \gamma = 90^\circ$). The peak marked with star (*) indicates diffraction from SS substrate. Patterns suggesting that the phase of the synthesized materials does not change due to cobalt doping. The dominant peak (1 1 3) in all samples indicates the major crystal growth along the same plane of lipscombite. It is observed that, there is no any other phase formation rather than lipscombite iron phosphate ($\text{Fe}_{11.78}\text{P}_8\text{O}_{40}$). The intensity of the prominent peak (1 1 3) goes on decreasing and contrarily the broadening with the increase in Co doping concentration as shown in the resolved XRD (Fig. 1(B)). The broadening of the peaks and dislocations within crystals may occur due to the inhomogeneous strain developed by the guest atoms within crystallites. This decrease in peak intensity and increase in peak width reveals that, there is decrease in crystallite size with increase in doping concentration. The shift in the peaks from the peak position of pristine 0.0 Co:FePi material is observable in all diffraction patterns (tabulated in Table S1) for cobalt doping (0.1 Co:FePi, 0.2 Co:FePi, 0.3 Co:FePi, 0.4 Co:FePi and 0.5 Co:FePi) as shown in Fig. 1(B). The microstructural properties as microstrain and dislocation density were calculated and given in ESI (See Supporting Information). The existence of internal microstrain can easily induce the formation of defect centers [20]. It is attributed that, increase in microstrain and dislocation within the crystal (Fig. S2) can induce the crystal compactness and hence the shift in peak position towards higher angle.

3.2. FTIR vibrational analysis

Fourier transform infra-red spectroscopy was performed in the wavenumber range 400–4000 cm^{-1} for the analysis of molecular bonds present and intermolecular vibrations in the prepared materials. Fig. 1(C) shows the FTIR spectra of pristine iron phosphate and

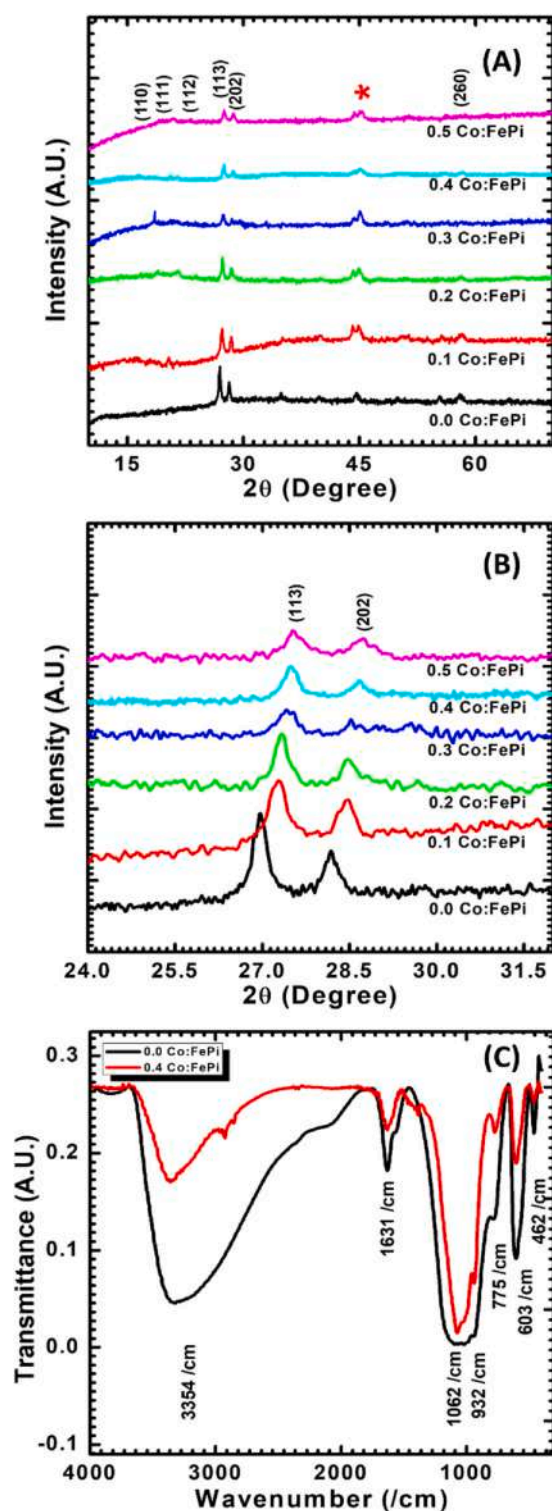


Fig. 1. Structural information of the cobalt doped iron phosphate catalysts: (A, B) X-ray diffraction patterns of hydrothermally synthesized pristine 0.0 Co:FePi and hydrothermally doped 0.1 Co:FePi, 0.2 Co:FePi, 0.3 Co:FePi, 0.4 Co:FePi and 0.5 Co:FePi thin films on SS substrates, (C) FTIR spectra of pristine 0.0 Co:FePi and 0.4 Co:FePi.

0.4 Co:FePi thin films. The absorption band at 462 cm^{-1} in the spectra belongs to the phosphate asymmetric stretching (ν_2) vibrations. The sharp absorption at 603 cm^{-1} reveals the phosphate bending mode (ν_4) vibrations. A small absorbance at 775 cm^{-1} was committed to the stretching of P-O-P linkages [21–23]. The broad band composed with two absorption bands wise 932 cm^{-1} and 1062 cm^{-1} revealed the

symmetric stretching (ν_1) and asymmetric stretching (ν_3) vibrations, respectively of P–O bonds. The shrill band at 1631 /cm and broad band at 3354 /cm are attributed to the absorption due to surface adsorbed water by the material.

3.3. N_2 adsorption-desorption isotherm analysis

Material surface area, pore structure and pore size distribution of pristine (0.0 Co:FePi) and doped (0.4 Co:FePi) samples were analyzed by nitrogen adsorption-desorption isotherm. As plotted in Fig. S3(A), the high hysteresis at $p/p_0 = 0.45$ and minor N_2 adsorption at $p/p_0 = 0.4$, revealed that the most porosity prompted from the mesopores. The isotherms of pristine (0.0 Co:FePi) and doped (0.4 Co:FePi) materials can be categorized as Brunauer–Emmett–Teller (BET) having type-IV isotherm shape which contains mesoporosity and has a high adsorption energy [24]. The hysteresis loop of both the samples corresponds to the type-H2 according to IUPAC taxonomy which designates the existence of regimented pores with narrow and wide sections and integrated channels [25]. With the fitting analysis by BET equations, the surface area of $\sim 53.43 \text{ m}^2/\text{g}$ for the 0.0 Co:FePi sample and $\sim 22.56 \text{ m}^2/\text{g}$ for the 0.4 Co:FePi sample are observed. It is observed that, surface area of the 0.4 Co:FePi is smaller than the 0.0 Co:FePi. The pore size distribution of the prepared materials is calculated using Barrett–Joyner–Halenda (BJH) method. The pore size distribution curves of 0.0 Co:FePi and 0.4 Co:FePi materials are shown in Fig. S3(B), from which it is observed that the narrow distribution of pores with pore diameters $\sim 14.03 \text{ nm}$ (for 0.0 Co:FePi) and $\sim 10.64 \text{ nm}$ (for 0.4 Co:FePi), confirming the formation of mesoporous structure. From the pore volume, it is observed that, after cobalt doping, pore volume reduced from $0.034 \text{ cm}^3/\text{g}$ (0.0 Co:FePi) to $0.028 \text{ cm}^3/\text{g}$ (0.4 Co:FePi). This reveals that, the diffused cobalt atoms through the mesopores may also get deposited at the inner surface of the pores. This cobalt diffusion reduces the pore diameter and pore volume but their synergy may enhance electroactive sites.

3.4. X-ray photoelectron spectroscopy (XPS) analysis

X-ray photoelectron spectroscopy (XPS) measurement was carried out to analyze the valance states of the elements present in the prepared samples. Fig. 2 shows the XPS spectra of pristine iron phosphate thin film. The survey scan spectrum reveals the presence of P, C, O and Fe elements as shown in the Fig. S4(A) in Electronic Supporting Information (ESI). The high resolution spectrum of Fe2p was deconvoluted and observed in four contributing peaks in which, two main peaks at 712.83 eV and 726.34 eV mentioned as $\text{Fe}2p_{3/2}$ and $\text{Fe}2p_{1/2}$, respectively and corresponding two satellite peaks at 714.68 eV and 728.38 eV (Fig. 2(A)). It proves that the presence of Fe in pristine iron phosphate is in the Fe^{2+} electronic state [26,27]. As shown in Fig. S4(B), the photoelectron spectrum for P2p is split into two different peaks at 132.12 eV ($\text{P}2p_{3/2}$) and 134.18 eV ($\text{P}2p_{1/2}$) which can be attributed to the phosphate group (P–O) and metal-oxygen-phosphorous (P–O–M) bond in phosphate series corresponding to P^{5+} oxidation state [28,29]. The prominent peak of O1s observed in Fig. S4(C) present at 532.23 eV was split into two different peaks at 531.37 eV and 532.45 eV which are corresponding to the O and P–O bond in phosphate demonstrating the existence of phosphate group in pristine 0.0 Co:FePi thin films and surface adsorbed water molecules, respectively [30], which is correlated with the results drawn from FTIR.

On the other hand, survey spectrum of 0.4 Co:FePi gives the presence of P, C, O, Fe and Co elements as shown in the Fig. S5(A). In Fig. 2(B), presence of Fe^{2+} electronic state of Fe element is confirmed by the Fe2p main peaks observed at 712.12 eV and 725.58 eV corresponding to $\text{Fe}2p_{3/2}$ and $\text{Fe}2p_{1/2}$ energy levels respectively, and two satellite peaks at 715.87 eV and 734.27 eV. Similarly, spectrum of Co2p at resolved scale is shown in Fig. 2(C), which reveals the

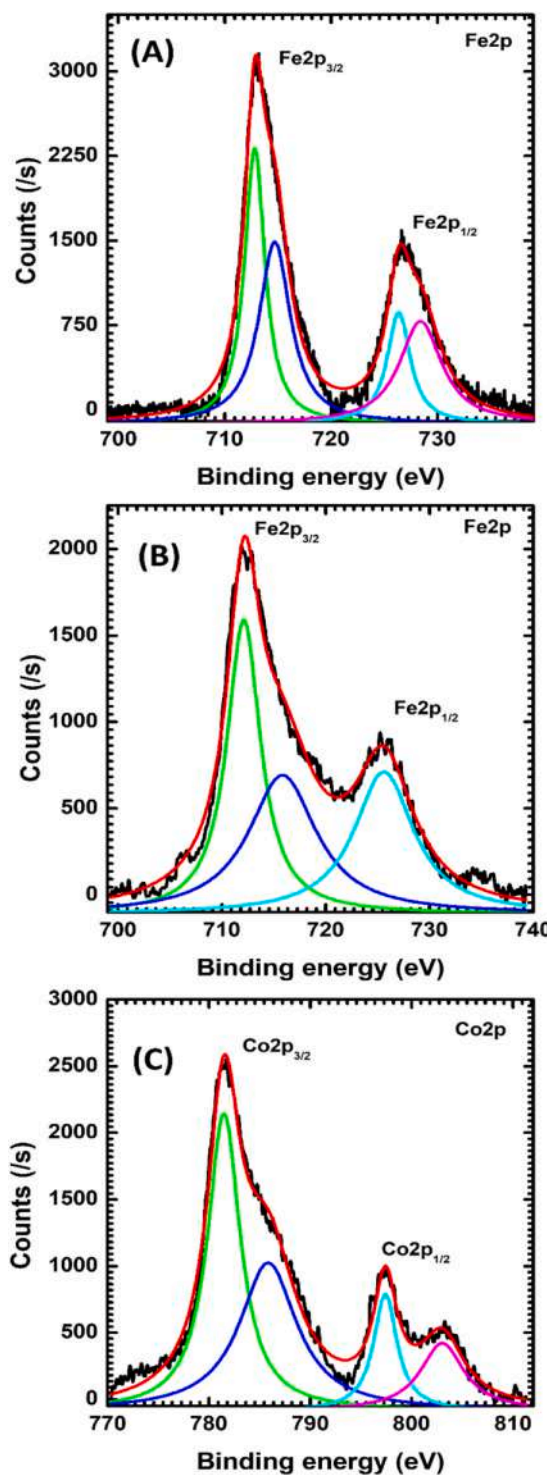


Fig. 2. Electronic state determination of the cobalt doped iron phosphate catalysts: High resolution XPS spectra of (A) Fe2p in the sample 0.0 Co:FePi, (B) Fe2p in the sample 0.4 Co:FePi and (C) Co2p in the sample 0.4 Co:FePi.

presence of main peaks as $\text{Co}2p_{3/2}$ at 781.47 eV and $\text{Co}2p_{1/2}$ at 797.40 eV and their corresponding satellite peaks at 785.79 eV and 803.03 eV, respectively. Position of peaks confirms that the observed Co element is in Co^{2+} electronic state [31]. Sharp peak of P2p present at 133.04 eV (Fig. S5(B)) can be split into two distinct peaks as $\text{P}2p_{3/2}$ at 132.49 eV and $\text{P}2p_{1/2}$ at 133.85 eV corresponding to P^{5+} oxidation state in phosphate group (P–O) and metal-oxygen-phosphorous (P–O–M) bond in phosphate series. The O1s main peak is composed

of three distinct peaks located at 530.05, 531.05 and 532.11 eV as shown in Fig. S5(C). Deconvoluted peaks (530.05 and 531.05 eV) represent the O and P-O bonds in phosphate and the peak at 532.11 eV related to the surface adsorbed water molecules [32].

3.5. Surface morphological and elemental analysis

The surface morphology of the catalyst materials plays an important role in electrochemical behavior. Field emission scanning electron microscopy (FESEM) images at different magnifications of the prepared material electrodes are shown in Fig. 3. As stated earlier, due to similar atomic structure, doping of Co is advantageous to keep the original morphology and surface of the transition metal compound like FePi. Low magnification (1000x) images revealed that all prepared pristine and doped materials are particle like, well covered and uniformly distributed over the SS substrates as shown in Fig. 3(A, D, G, J, M and P). In higher magnification (10000x) images, it is observed that the particles are spherical in nature and having size around 1–3 μm . By the closer view, it is observed that the surface of the spherical particles gets modified slightly. The surface roughness of particles, consisting of numerous indiscriminately packed particles with a sub-micron size, uniformly increases with the increase in doping concentration and it is maximum for the 0.4 Co:FePi and 0.5 Co:FePi samples (Fig. 4(C, F, I, L, O and R)). It is easily observed that, there are few agglomeration sites formed in the 0.5 Co:FePi sample due to higher concentration of CoCl_2 during second step hydrothermal process. It can be predicted that, the present kind of morphology gives easy access of electrolyte to adsorption and electron transfer which is advantageous for electrochemical water splitting. By carrying the energy dispersive X-ray spectra (EDS) of pristine FePi and doped Co:FePi catalyst materials, it confirmed that in pristine FePi (0.0 Co:FePi) sample Fe, O and P elements and in doped Co:FePi (0.1 Co:FePi, 0.2 Co:FePi, 0.3 Co:FePi, 0.4 Co:FePi, and 0.5 Co:FePi) samples Fe, Co, O and P elements are present as shown in Fig. S6(A–F). Additional observed peaks of element (Cr) are found from the surface of SS substrate. Table S2 gives the clear cut idea about the percentage of elements present in the prepared materials. The atomic percentages of the cobalt doping are observed as 0, 0.33, 1.37, 1.75, 2.01 and 3.12. The metal to phosphorous ratio (M:P) is nearly the same (~3:2) for all prepared materials, which is in accordance with the material formula attained from JCPDS by matching XRD. The EDS elemental mapping of 0.4 Co:FePi sample is shown in Fig. S6(G). It is observed that, there is successful doping of Co into the FePi and the homogeneous distribution of Co, Fe, P, and O elements throughout the whole deposited coating without any aggregation at any specific site.

3.6. Electrochemical catalytic performance analysis

The tests of pristine FePi and cobalt doped Co:FePi material electrodes were carried out for the investigation of their electrochemical catalytic activity. The electrochemical water splitting in terms of oxygen evolution reaction (OER) and hydrogen evolution reaction (HER) are performed in 1 M KOH and 1 M H_3PO_4 electrolytes using three electrode system. As shown in Fig. 4(A), polarization curves were plotted by carrying linear sweep voltammetry (LSV) experiments in the potential window range 1.05–1.75 V vs RHE at sweep scan rate of 1 mV/s for all electrode materials deposited on SS substrates. It is observed that, all curves exhibit similar nature and persistent increase in current density with increase in doping concentration up to 0.4 (sample code: 0.4 Co:FePi) and decreases for further. Also, overpotential at 10 mA/cm² current density gives similar trend. The onsetpotentials of all material electrodes have recorded and tabulated in Table S3. Lowest onset potential (227 mV) observed for 0.4 Co:FePi thin film electrode. The lowest overpotential of 266 mV recorded at 10 mA/cm²

current density and delivers maximum current density of 272 mA/cm² with overpotential of 500 mV for the sample having doping concentration of 0.4. To evaluate electrochemical response of the material, cyclic voltammetry examination was performed in the potential range 1.05–1.6 V vs RHE at scan rate of 50 mV/s (Fig. S7). All the observed peaks are due to the electrochemical conversion of Fe^{2+} to Fe^{3+} and vice-versa during oxidation and reduction process. It is observed that, redox peaks are shifted towards lower potential due to the incorporation of cobalt into the iron phosphate and hence conversion of Co^{2+} to Co^{3+} and vice-versa during redox process, this synergy is great evidence for reduction in overpotential by the doping. The trend of overpotential as a function of doping concentration is shown in Fig. 4(B). The overpotential at 10 mA/cm² current density decreases continuously from 281 mV (0.0 Co:FePi) to 266 mV (0.4 Co:FePi) and it again increases to 285 mV at doping concentration of 0.5 (0.5 Co:FePi). Increase in overpotential at doping concentration of 0.5 can be attributed to decrease in catalytic active sites due to agglomeration of particles at higher concentration. The chemical reaction kinetics during OER can be examined by the study of Tafel slope which indicate diverse rate determining steps. Fig. 4(C) gives the Tafel plots achieved from LSV curves. By the smallest Tafel slope of 42.6 mV/dec for 0.4 Co:FePi, it is proved that 0.4 cobalt doping gives the outstanding electrochemical catalytic performance than that of the pristine FePi and other Co:FePi material electrodes. All the Tafel values are given in Table S3. Large Tafel values for pristine FePi and other Co:FePi material electrodes reveals the rate limiting kinetic process of electron transfer during $-\text{OH}$ adsorption [33]. Simultaneously, a small Tafel slope of 0.4 Co:FePi corresponds to the OER mechanism involving a reversible one-electron transfer prior to a chemical turnover-limiting step [34].

To achieve additional perceptions into electrochemical kinetic performance, electrochemical impedance spectroscopy (EIS) was performed at open circuit potential (OCP). The Nyquist plots of pristine FePi and Co:FePi thin film electrodes are shown in Fig. 4(D), inset figures gives the magnified image of Nyquist plots and corresponding equivalent simple Randle circuit. All the plots containing quasi-semicircle as a result of charging of double layer (C_{dl}) which is associated with charge transfer resistance (R_{ct}), the intercept to real axis at higher frequency region known as solution resistance or series resistance (R_s) which is the combination of electrode resistance, interface resistance and electrolyte resistance. Solution resistances (R_s) are 0.652, 0.651, 0.668, 0.665, 0.666 and 0.632 Ω for 0.0 Co:FePi, 0.1 Co:FePi, 0.2 Co:FePi, 0.3 Co:FePi, 0.4 Co:FePi, and 0.5 Co:FePi thin film electrodes, respectively. Smaller values of R_s designated that all the material electrodes have small internal resistances and good conductivity. The charge transfer resistance (R_{ct}), attributed to the interfacial charge transfer resistance and mass transport through the material, values for 0.0 Co:FePi, 0.1 Co:FePi, 0.2 Co:FePi, 0.3 Co:FePi, 0.4 Co:FePi, and 0.5 Co:FePi thin film electrodes are 102.23, 0.878, 0.864, 0.753, 0.734, and 0.908 Ω , respectively. There is drastic decrease in charge transfer resistance observed due to the high conductivity of the cobalt. The smallest R_{ct} value indicates that 0.4 Co:FePi thin film electrode has outstanding conductivity and favors fast charge transport during electrochemical catalytic reaction. Stability of the prepared material is important criteria before tagging it as an excellent electrocatalyst and their application in daily life. Catalytic stability of our best catalyst electrode, i.e., 0.4 Co:FePi was tested by performing chronoamperometric study in 1 M KOH electrolyte at overpotential to deliver 10 mA/cm² and 50 mA/cm² current densities for 10 h as shown in Fig. 4(E). Figure reveals that there is almost stable delivery of current even at higher current density throughout the period and gives more than 99% OER catalytic stability in alkaline conditions. There is small decrease in performance observed after 10 h at higher current density. The overpotential of the reaction increased by only 2 mV in the

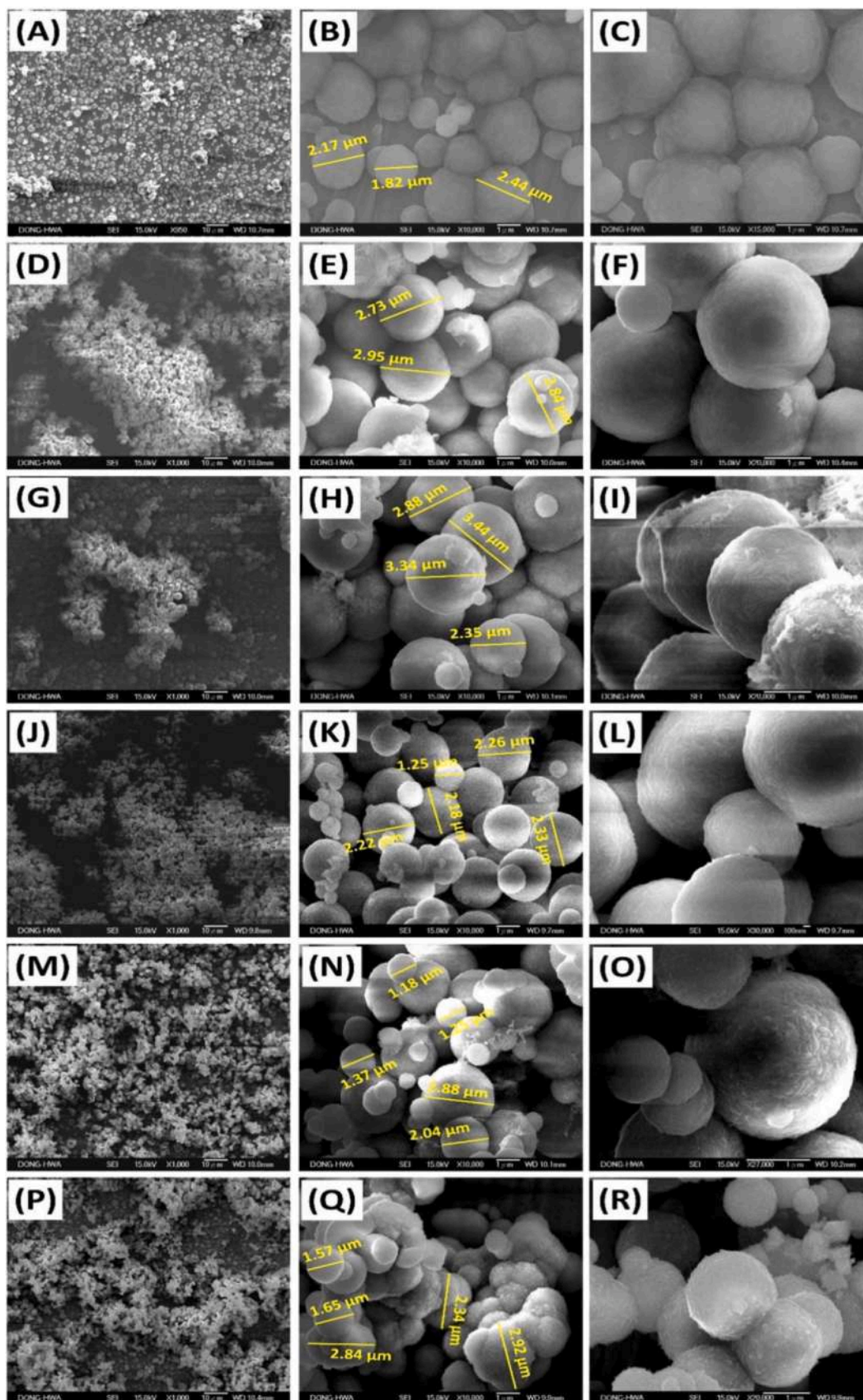


Fig. 3. Surface morphological study of the cobalt doped iron phosphate catalysts: FESEM images at different magnifications of (A–C) 0.0 Co:FePi, (D–F) 0.1 Co:FePi, (G–I) 0.2 Co:FePi, (J–L) 0.3 Co:FePi, (M–O) 0.4 Co:FePi, and (P–R) 0.5 Co:FePi.

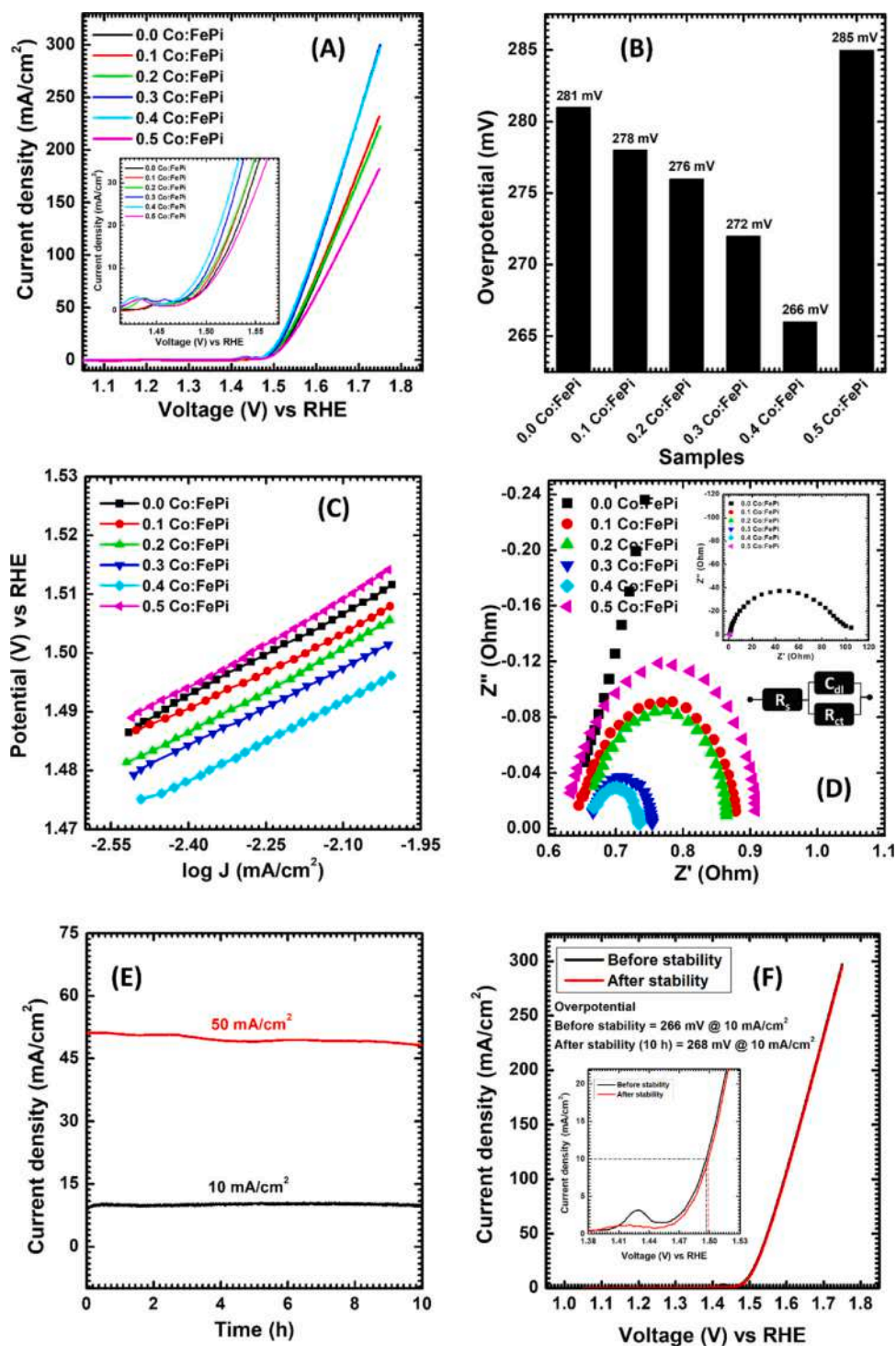


Fig. 4. Electrochemical (OER) analysis of the cobalt doped iron phosphate catalysts: (A) LSV polarization curves recorded with scan rate 1 mV/s in 1 M KOH electrolyte, inset shows magnified view at current shoot point, (B) bar diagram of overpotentials observed at 10 mA/cm² current density, (C) Tafel plots derived from LSV curves, (D) magnified electrochemical impedance spectra (EIS) at higher frequency region recorded at OCP, inset figures gives the whole image of EIS and equivalent circuit, (E) Chronoamperometric (I-t) plot for electrocatalytic stability study in 1 M KOH electrolyte at different current densities, (F) comparative study of LSV before and after 10 h OER catalysis, inset figure gives the magnified image at current shoot point.

entire duration of study which is shown in Fig. 4(F). Collectively the good stability and exceptional OER performance corroborates that 0.4 Co:FePi can job as an outstanding and robust electrocatalyst.

Hydrogen evolution reaction (HER) is another and most important half reaction of water splitting which can be carried out in the negative potential window of the i-v plot. The pristine FePi and Co:FePi thin film electrodes were studied to perform HER in acidic

environment (1 M H₃PO₄) within the potential window of 0.33 to -0.85 mV vs RHE. LSV polarization curves were recorded with scan rate 1 mV/s within the given potential window for all the sample electrodes and plotted in Fig. 5(A). Interestingly, 0.4 Co:FePi thin film electrode exhibits smallest overpotential of 82.3 mV to deliver -10 mA/cm² current density and achieve nearly -255 mA/cm² current density at -0.85 V vs RHE potential. In contrast, pristine FePi and

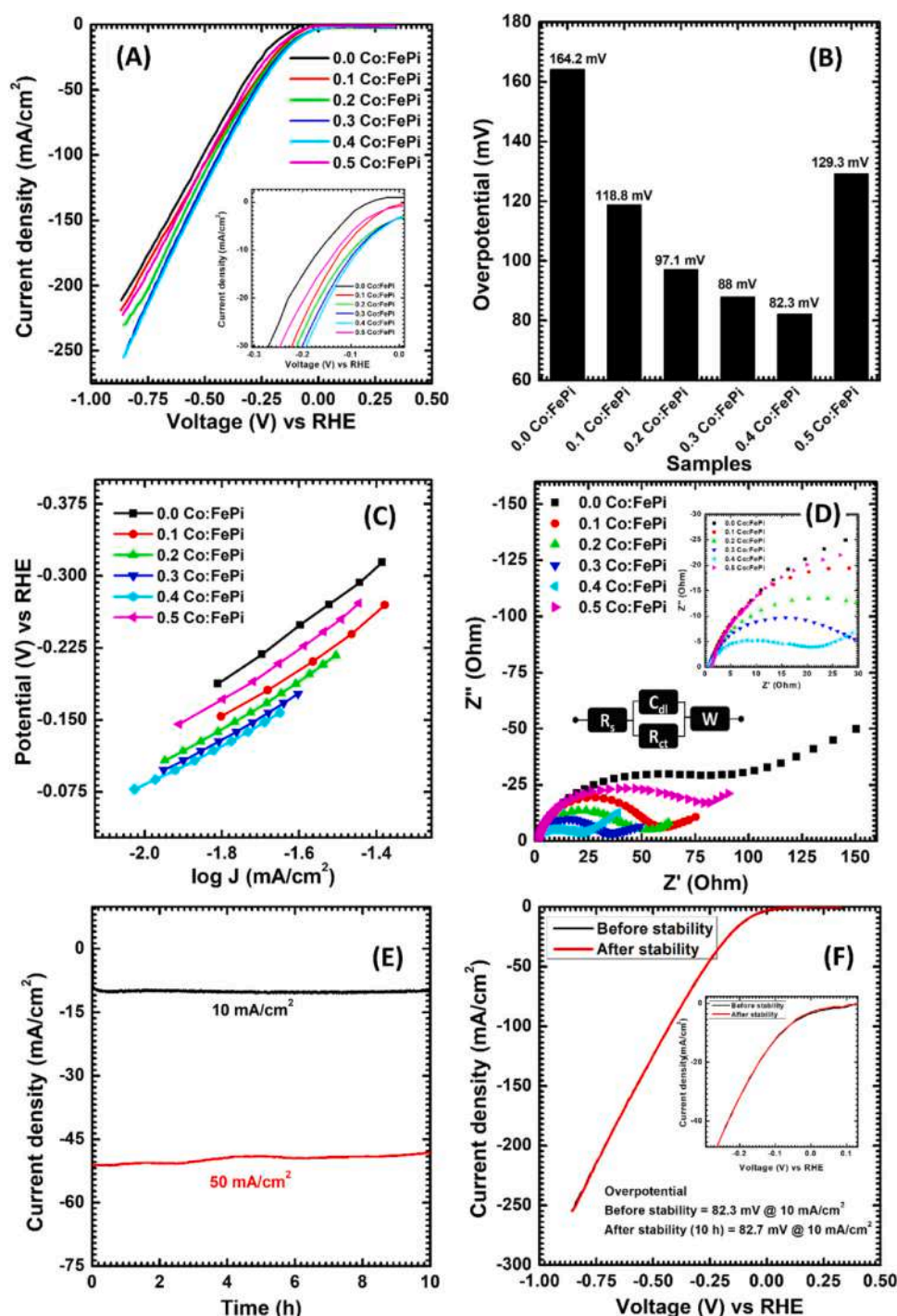


Fig. 5. Electrochemical (HER) analysis of the cobalt doped iron phosphate catalysts: (A) LSV polarization curves recorded with scan rate 1 mV/s in 1 M H₃PO₄ electrolyte, inset shows magnified view at current shoot point, (B) bar diagram of overpotentials observed at 10 mA/cm² current density, (C) Tafel plots derived from LSV curves, (D) electrochemical impedance spectra (EIS) recorded at OCP, inset figures gives the magnified image of EIS at higher frequency region and equivalent circuit, (E) Chronoamperometric (I-t) plot for electrocatalytic stability study in 1 M H₃PO₄ electrolyte at different current densities, (F) comparative study of LSV before and after 10 h HER catalysis, inset figure gives the magnified image at current shoot point.

other Co:FePi electrodes require quite larger overpotentials to achieve same current density. The trend of HER overpotentials with doping concentration given in Fig. 5(B). Tafel slope values were calculated by Tafel plot shown in Fig. 5(C) conquered from polarization curves gives the information about reaction kinetics. The smallest Tafel value was recorded by the 0.4 Co:FePi thin film electrode which is 211 mV/dec. The values of overpotentials, overpotentials and Tafel slopes for all prepared material electrodes are

tabulated in Table S4. Electrochemical impedances of sample electrodes were studied by EIS spectra at OCP, which is composed with R_s, C_{dl}, R_{ct} and Warburg diffusion (W) as shown in Fig. 5(D). The R_s values are 0.79, 1.06, 1.21, 0.95, 0.90, and 1.09 Ω for 0.0 Co:FePi, 0.1 Co:FePi, 0.2 Co:FePi, 0.3 Co:FePi, 0.4 Co:FePi, and 0.5 Co:FePi thin film electrodes which reveals the good conductivity along with exceptional contact between the active material and SS substrate. The smallest R_{ct} of 23.2 Ω for 0.4 Co:FePi thin film electrode confirms

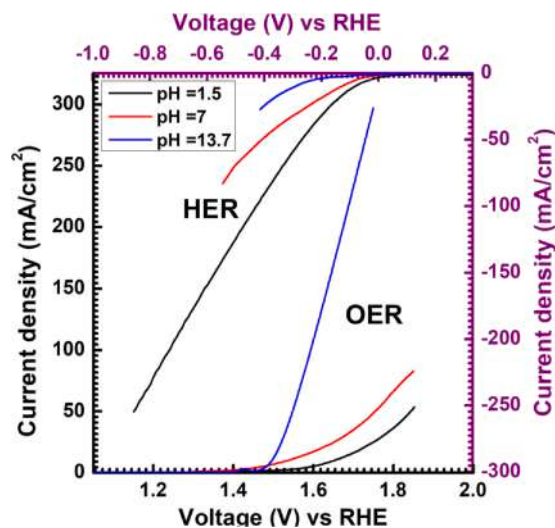


Fig. 6. Effect of electrolyte pH on OER and HER test of the cobalt doped iron phosphate catalyst: LSV polarization plots of 0.4 Co:FePi thin film electrode for OER and HER in different electrolyte media at 1 mV/s scan rate.

easy electron transfer and good conductivity during catalysis. Electrochemical HER stability test of 0.4 Co:FePi thin film electrode was performed to study material robustness for their handy application. Chronoamperometry was performed at constant overpotential to achieve 10 mA/cm² and 50 mA/cm² current densities for 10 h as shown in Fig. 5(E). From the figure, it is observed that, there is practically steady delivery of current even at higher current density during the study. The comparison between LSV curves before and after stability test (Fig. 5(F)) gives almost 100% HER catalytic stability in acidic environment which proves that the 0.4 Co:FePi thin film electrode has outstanding stability and robustness.

The nonprecious metal-based cobalt doped iron phosphate thin films catalyst electrode not only show outstanding performance of OER and HER respectively in alkaline and acidic medium, but also exhibits high catalytic performance over a wide pH range. The effect of the pH of electrolyte in which the OER and HER carried out was studied over here. The pH of electrolyte was varied from highly acidic (pH = 1.5) to highly basic (pH = 13.7) including neutral (pH = 7). The LSV curves were recorded at 1 mV/s scan rate for OER and HER. For OER, polarization curves for 0.4 Co:FePi thin film electrode in acidic, neutral and basic electrolytes were plotted at left lower corner as shown in Fig. 6, which illustrates that, similar trend of electrocatalytic activity in all electrolytes. The required overpotentials to achieve 10 mA/cm² current density are 422 mV, 306 mV, and 266 mV in acidic (pH = 1.5), neutral (pH = 7), and basic (pH = 13.7) electrolytes, respectively. Similarly, the HER performance was studied and plotted in Fig. 6 at the right top corner. It is observed that, the required overpotentials are 82.3 mV, 128 mV, and 290 mV to achieve -10 mA/cm² current density in acidic (pH = 1.5), neutral (pH = 7), and basic (pH = 13.7) electrolytes, respectively. The present investigation reveals that, the synthesized 0.4 Co:FePi thin film electrode exhibit electrochemical catalysis in electrolytes having wide pH range.

The long term catalytic property of the material was studied for overall water splitting in same alkaline bath by constructing a full cell device using the same 0.4 Co:FePi thin film electrodes as anode and cathode. The chronoamperometric test was performed by applying the potential of 1.8 V to the cell for 4 days' continuous water splitting in 1 M KOH as shown in inset of Fig. 7. It is observed that, there is initial increase in current density with time due to the activation of the material and then a small reduction in current every day because of the dehydration of the electrolyte. After adjusting the level by addition of electrolyte, increment in the current also

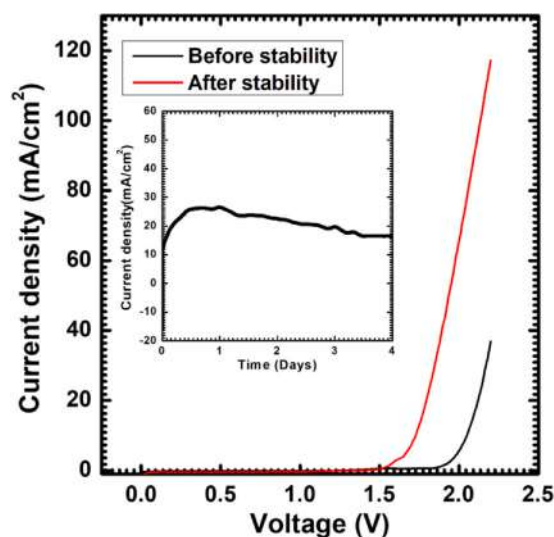


Fig. 7. Overall water splitting test of the cobalt doped iron phosphate catalyst: LSV polarization plots of 0.4 Co:FePi thin film electrode before and after 4 days' catalysis in alkaline medium at 1 mV/s scan rate. Inset figure gives the 4 days' continuous catalytic stability test.

observed. The LSV plots before and after catalytic stability test are shown in Fig. 7 and it revealed that, there is decrease in the potential from 2.04 V to 1.72 V to deliver 10 mA/cm² current density. EIS was measured initially and after 4 days to measure the change in charge transfer resistance and very small decrease is observed after the catalysis as shown in Fig. S8. The present material (0.4 Co:FePi) performance is compared with some previously reported cobalt-iron based phosphate and other materials as tabulated in Table S5. After demonstrating the enhanced catalytic performance in 4 days' stability test, it proves their strongest candidature for forthcoming alkaline electrolysis.

The influences of electrochemical testing on the structural, electronic state and morphology were studied by conducting the post-mortem characterizations of the thin films restored from the electrochemical cell. The collected thin films were kept in DDW to washout the ions of electrolyte. XRD pattern was compared with the pattern of same material before electrolysis as shown in Fig. S9(A). There is no any diffraction peak observed in the sample after long term electrolysis. It reveals that the material become amorphous in nature after electrochemical testing which is beneficial for electrochemical applications. It can provide large surface area and hence large number of active sites and easy ion transfer. X-ray photoelectron spectroscopy (XPS) measurements were carried out to examine the electronic states present in the sample after electrochemical testing (survey spectrum and high resolution spectrum of O1s are shown in ESI Fig. S10(A and B)). Fig. S9(B–D) shows the high resolution spectra of Fe2p, Co2p and P2p states. It is observed that, the prominent peaks Fe2p_{3/2} and Fe2p_{1/2} located at 710.05 and 723.46 eV (Fig. S9(B)) can be divided into two peaks at binding energies 709.62 and 711.34 eV, 723.29 and 725.17 eV corresponding to Fe²⁺ and Fe³⁺ states, respectively. The presence of both Fe²⁺ and Fe³⁺ electronic states of Fe atom can be observed due to the oxidation of the material and conversion from Fe²⁺ to Fe³⁺ during 10 h continuous electrolysis. Similarly, spectrum of Co2p at high resolution (Fig. S9(C)), which reveals the presence of main peaks as Co2p_{3/2} at 779.53 eV and Co2p_{1/2} at 795.26 eV and their corresponding satellite peaks at 785.65 eV and 802.67 eV, respectively. The peak Co2p_{3/2} can be divided into two peaks at 779.39 and 781.55 eV corresponding to Co²⁺ and Co³⁺, respectively. Fig. S9(D) shows the spectrum in the energy range of P2p. It is observed that, there is no any evidential peak present for phosphorus. The presence of higher order oxidation states of Co and Fe and

the absence of P can give the idea about the conversion of iron phosphate into the highly stable and electrochemically active iron oxide. The similar results were also observed by Yin et al. [35]. In the spectrum of O1s, the intense peak at 529.35 eV attributed to the metal–O bond [36]. The decrement in the intensity of phosphate peak observed at 530.55 eV again evident to the conversion of phosphate to oxide. FESEM images of 0.4 Co:FePi thin film electrode after long term (10 h and 4 days') electrocatalysis at overpotentials to deliver 50 and 10 mA/cm² current densities, respectively are studied and shown in Fig. S11 at different magnifications. From figure, it is observed that, the morphology after 10 h continuous catalysis of the material tested at overpotential to deliver 50 mA/cm² current density, is almost the same as the synthesized one (Fig. S11(A–C)). The average size of spherical particles is almost the same. After 96 h electrochemical testing, at overpotential to deliver 10 mA/cm² current density, the surface of the micro spheres become rough slightly without material degradation (Fig. S11(D–F)). Also, no change in average particle size is observable after long term catalysis. This illustrates the robustness of the catalyst material. The roughness of surface observed in high magnification FESEM image (Fig. S11(F)), facilitates the large number of active sites for –OH adsorption and oxidation and hence the enhancement in electrochemical water splitting.

Remarkably, the cobalt doped iron phosphate gives best performance for electrochemical water splitting in terms of OER, HER and overall water splitting. Doping of transition metal (Co) have significantly enhance the catalytic activity by delivering high current density and small overpotentials by improving the electrical conductivity and metal to metal partial-charge-transfer activation process. The mesoporosity and the synergistic effect of both metal atoms results in the improved performance than the pristine iron phosphate. The compounds having higher valence state metal atoms, which results in the formation of high surface adsorbed intermediates. During the long term catalysis process, there is the transition of Co²⁺ and Fe²⁺ states to the higher. Spectroscopic results point to a catalyst active state is composed of Co^{2+/3+} and Fe^{2+/3+} mixed valence clusters. The conversion from crystalline to amorphous, mesoporous structure, synergistic effect of Co and Fe metals, and electronic transition to higher states results in the outstanding and improved performance of overall water splitting.

4. Conclusions

In sum, we hereby synthesized pristine iron phosphate (FePi) and cobalt doped iron phosphate (Co:FePi) thin film catalyst electrodes by facile hydrothermal method. For cobalt doping, hydrothermal ion-exchange process was preferred first time. XRD, FTIR and XPS confirms phase, chemical bonding and electronic states of the prepared materials. The microspherical structure uncovered more active sites, resulting in the superior water splitting performance. The as synthesized pristine FePi and Co:FePi catalyst electrodes showed excellent electrochemical water splitting in terms of OER and HER. Best performing 0.4 Co:FePi thin film electrode exhibited smallest overpotential of 266 mV for OER at 10 mA/cm² current density and more than 99% catalytic OER stability for 10 h in alkaline medium. Also, it can perform HER with 82.3 mV overpotential at 10 mA/cm² current density and almost 100% catalytic HER stability for 10 h in acidic environment. This phenomenon may cause due to the manifestation of Co improves the electrical conductivity and metal to metal partial-charge-transfer activation process. Also, due to the reduction of adsorption energy of the surface by changing the surface electronic states of iron phosphate which enhances the adsorption of OH⁻ ions to the electrode surface. The two electrode electrolyzer using 0.4 Co:FePi thin film electrodes as both an anode and cathode in alkaline medium achieved lowest potential of 1.72 V after 4 days' continuous water splitting test. The excellent electrochemical performance, outstanding

stability and robustness of 0.4 Co:FePi thin film electrode material proved their applicability for overall water splitting.

Electronic supporting information (ESI)

Electronic supporting information contains photograph of the as deposited cobalt doped iron phosphate thin film catalysts; formulae used to study the microstructural properties, table of calculated microstructural parameters; plot of variation of microstrain and dislocation density with respect to the cobalt doping; N₂ adsorption-desorption isotherms and pore diameter distribution curves; XPS survey spectrum, high resolution P2p and O1s spectra of pristine FePi (0.0 Co:FePi) material; XPS survey spectrum, high resolution P2p and O1s spectra of 0.4 Co:FePi material; EDS spectrum of 0.0 Co:FePi, 0.1 Co:FePi, 0.2 Co:FePi, 0.3 Co:FePi, 0.4 Co:FePi, 0.5 Co:FePi, and elemental mapping; table of EDS elemental composition analysis of cobalt doped iron phosphate thin films; table of electrochemical OER performance in alkaline medium; cyclic voltammetry study of different electrode materials at scan rate 50 mV/s in 1 M KOH; and table of electrochemical HER performance in acidic medium; Electrochemical impedance spectra of the cobalt doped iron phosphate catalyst before and after 4 days' overall water splitting test; Comparison between present work and other cobalt-iron based phosphate and related materials for water splitting; x-ray diffraction patterns of 0.4 Co:FePi thin films on SS substrates, before and after electrocatalytic stability tests, high resolution XPS spectra of Fe2p, Co2p and P2p in the sample 0.4 Co:FePi; XPS survey spectrum, high resolution O1s spectrum of 0.4 Co:FePi material after long term electrocatalytic test; FESEM images at different magnifications of 0.4 Co:FePi, after electrocatalytic stability test.

CRediT authorship contribution statement

Suraj A. Khalate: Conceptualization, Methodology, Writing - original draft. **Sujit A. Kadam:** Characterizations. **Yuan-Ron Ma:** Characterizations. **Sachin S. Pujari:** Editing. **Umakant M. Patil:** Conceptualization, Editing, Supervision.

Declaration of Competing Interest

The authors declare that they have no known competing financial interests or personal relationships that could have appeared to influence the work reported in this paper.

Acknowledgment

The author Mr. Suraj A. Khalate acknowledges the Chhatrapati Shahu Maharaj Research Training and Human Development Institute (SARTHI), Pune (Government of Maharashtra) for awarding as SARTHI FELLOW and the financial support under the Chhatrapati Shahu Maharaj National Research Fellowship (CSMNRF-2019).

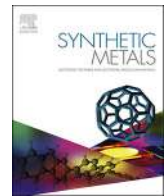
Appendix A. Supporting information

Supplementary data associated with this article can be found in the online version at [doi:10.1016/j.jallcom.2021.160914](https://doi.org/10.1016/j.jallcom.2021.160914).

References

- [1] Y. Shi, B. Zhang, Recent advances in transition metal phosphide nanomaterials: synthesis and applications in hydrogen evolution reaction, *Chem. Soc. Rev.* 45 (2016) 1529–1541, <https://doi.org/10.1039/C5CS00434A>
- [2] D. Kang, T.W. Kim, S.R. Kubota, A.C. Cardiel, H.G. Cha, K.-S. Choi, Electrochemical Synthesis of photoelectrodes and catalysts for use in solar water splitting, *Chem. Rev.* 115 (2015) 12839–12887, <https://doi.org/10.1021/acs.chemrev.5b00498>
- [3] X.F. Lu, L.F. Gu, J.W. Wang, J.X. Wu, P.Q. Liao, G.R. Li, Bimetal-organic framework derived CoFe₂O₄/C porous hybrid nanorod arrays as high-performance

- electrocatalysts for oxygen evolution reaction, *Adv. Mater.* 29 (2017) 1604437, <https://doi.org/10.1002/adma.201604437>
- [4] D. Yan, Y. Li, J. Huo, R. Chen, L. Dai, S. Wang, Defect chemistry of non-precious-metal electrocatalysts for oxygen reactions, *Adv. Mater.* 29 (2017) 1606459, <https://doi.org/10.1002/adma.201606459>
- [5] S. Xu, H. Zhao, T. Li, J. Liang, S. Lu, G. Chen, S. Gao, A.M. Asiri, Q. Wu, X. Sun, Iron-based phosphides as electrocatalysts for the hydrogen evolution reaction: recent advances and future prospects, *J. Mater. Chem. A* 8 (2020) 19729–19745, <https://doi.org/10.1039/D0TA05628F>
- [6] S. Cherevko, S. Geiger, O. Kasian, N. Kulyk, J.P. Grote, A. Savan, B.R. Shrestha, S. Merzlikin, B. Breitbach, A. Ludwig, K.J.J. Mayrhofer, Oxygen and hydrogen evolution reactions on Ru, RuO₂, Ir, and IrO₂ thin film electrodes in acidic and alkaline electrolytes: a comparative study on activity and stability, *Catal. Today* 262 (2016) 170–180, <https://doi.org/10.1016/j.cattod.2015.08.014>
- [7] J. Zhu, L. Hu, P. Zhao, L.Y. Suk Lee, K.-Y. Wong, Recent advances in electrocatalytic hydrogen evolution using nanoparticles, *Chem. Rev.* 120 (2020) 851–918, <https://doi.org/10.1021/acs.chemrev.9b00248>
- [8] S.A. Khalate, S.A. Kadam, Y.-R. Ma, S.S. Pujari, S.J. Marje, P.K. Katkar, A.C. Lokhande, U.M. Patil, Hydrothermally synthesized iron phosphate hydroxide thin film electrocatalyst for electrochemical water splitting, *Electrochim. Acta* 319 (2019) 118–128, <https://doi.org/10.1016/j.electacta.2019.06.162>
- [9] L. Trotochaud, S.L. Young, J.K. Ranney, S.W. Boettcher, Nickel–iron oxyhydroxide oxygen-evolution electrocatalysts: the role of intentional and incidental iron incorporation, *J. Am. Chem. Soc.* 136 (2014) 6744–6753, <https://doi.org/10.1021/ja502379c>
- [10] Y. Surendranath, M.W. Kanan, D.G. Nocera, Mechanistic studies of the oxygen evolution reaction by a cobalt-phosphate catalyst at neutral pH, *J. Am. Chem. Soc.* 132 (2010) 16501–16509, <https://doi.org/10.1021/ja106102b>
- [11] A.J. Esswein, Y. Surendranath, S.Y. Reece, D.G. Nocera, Highly active cobalt phosphate and borate based oxygen evolving catalysts operating in neutral and natural waters, *Energy Environ. Sci.* 4 (2011) 499–504, <https://doi.org/10.1039/C0EE00518E>
- [12] B.S. Brunschwig, M.H. Chou, C. Creutz, P. Ghosh, N. Sutin, Mechanisms of water oxidation to oxygen: cobalt (IV) as an intermediate in the aquacobalt (II)-catalyzed reaction, *J. Am. Chem. Soc.* 105 (1983) 4832–4833, <https://doi.org/10.1021/ja00352a050>
- [13] C. Meng, Y. Cao, Y. Luo, F. Zhang, Q. Kong, A.A. Alshehri, K.A. Alzahrani, T. Li, Q. Liu, X. Sun, A Ni-MOF nanosheet array for efficient oxygen evolution electrocatalysis in alkaline media, *Inorg. Chem. Front.* 8 (2021) 3007–3011, <https://doi.org/10.1039/D1QJ00345C> (Advance Article).
- [14] Y. Cao, T. Wang, X. Li, L. Zhang, Y. Luo, F. Zhang, A.M. Asiri, J. Hu, Q. Liu, X. Sun, A hierarchical CuO@NiCo layered double hydroxide core-shell nanoarray as an efficient electrocatalyst for the oxygen evolution reaction, *Inorg. Chem. Front.* 8 (2021) 3049–3054, <https://doi.org/10.1039/D1QJ00124H> (Advance Article).
- [15] Y. Wang, T. Wang, R. Zhang, Q. Liu, Y. Luo, G. Cui, S. Lu, J. Wang, Y. Ma, X. Sun, CuO@CoFe layered double hydroxide core-shell heterostructure as an efficient water oxidation electrocatalyst under mild alkaline conditions, *Inorg. Chem.* 59 (2020) 9491–9495, <https://doi.org/10.1021/acs.inorgchem.0c01927>
- [16] X. Li, R. Zhang, Y. Luo, Q. Liu, S. Lu, G. Chen, S. Gao, S. Chen, X. Sun, A cobalt-phosphorus nanoparticle decorated N-doped carbon nanosheet array for efficient and durable hydrogen evolution at alkaline pH, *Sustainable, Energy Fuels* 4 (2020) 3884–3887, <https://doi.org/10.1039/D0SE00240B>
- [17] T. Liu, D. Liu, F. Qu, D. Wang, L. Zhang, R. Ge, S. Hao, Y. Ma, G. Du, A.M. Asiri, L. Chen, Enhanced electrocatalysis for energy-efficient hydrogen production over CoP catalyst with nonelectroactive Zn as a promoter, *Adv. Energy Mater.* 7 (2017) 1700020, <https://doi.org/10.1002/aenm.201700020>
- [18] Q. Sun, Y. Tong, P. Chen, L. Chen, F. Xi, J. Liu, X. Dong, Dual anions engineering on nickel cobalt-based catalyst for optimal hydrogen evolution electrocatalysis, *J. Colloid Interface Sci.* 589 (2021) 127–134, <https://doi.org/10.1016/j.jcis.2020.12.098>
- [19] Q. Sun, Y. Tong, P. Chen, B. Zhou, X. Dong, Universal strategy of bimetal heterostructures as superior bifunctional catalysts for electrochemical water splitting, *ACS Sustain. Chem. Eng.* 9 (2021) 4206–4212, <https://doi.org/10.1021/acssuschemeng.1c00037>
- [20] J. He, L. Sun, K. Zhang, W. Wang, J. Jiang, Y. Chen, P. Yang, J. Chu, Effect of post-sulfurization on the composition, structure and optical properties of Cu₂ZnSnS₄ thin films deposited by sputtering from a single quaternary target, *Appl. Surf. Sci.* 264 (2013) 133–138, <https://doi.org/10.1016/j.apsusc.2012.09.140>
- [21] S.J. Marje, P.K. Katkar, S.S. Pujari, S.A. Khalate, A.C. Lokhande, U.M. Patil, Regulated micro-leaf like nickel pyrophosphate as a cathode electrode for asymmetric supercapacitor, *Synth. Met.* 259 (2020) 116224, <https://doi.org/10.1016/j.synthmet.2019.116224>
- [22] S.S. Pujari, S.A. Kadam, Y.-R. Ma, P.K. Katkar, S.J. Marje, S.A. Khalate, A.C. Lokhande, U.M. Patil, Facile synthesis of microstrip-like copper phosphate hydroxide thin films for supercapacitor applications, *J. Electron. Mater.* 49 (2020) 3890–3901, <https://doi.org/10.1007/s11664-020-08095-w>
- [23] F.S. Omar, A. Numan, N. Duraisamy, S. Bashir, K. Ramesh, S. Ramesh, Ultrahigh capacitance of amorphous nickel phosphate for asymmetric supercapacitor applications, *RSC Adv.* 6 (2016) 76298–76306, <https://doi.org/10.1039/C6RA15111F>
- [24] B. James, Condon, Surface Area and Porosity Determinations by Physisorption: Measurements and Theory, first ed., Elsevier, Amsterdam; Boston, 2006.
- [25] S.J. Gregg, K.S.W. Sing, Adsorption, Surface Area, and Porosity, second ed., Academic Press, London; New York, 1982.
- [26] N. Roy, Y. Sohn, K.T. Leung, D. Pradhan, Engineered electronic states of transition metal doped TiO₂ nanocrystals for low overpotential oxygen evolution reaction, *J. Phys. Chem. C* 118 (2014) 29499–29506, <https://doi.org/10.1021/jp508445t>
- [27] Q. Zhang, T. Li, J. Liang, N. Wang, X. Kong, J. Wang, H. Qian, Y. Zhou, F. Liu, C. Wei, Y. Zhao, X. Zhang, Highly wettable and metallic NiFe-phosphate/phosphide catalyst synthesized by plasma for highly efficient oxygen evolution reaction, *J. Mater. Chem. A* 6 (2018) 7509–7516, <https://doi.org/10.1039/C8TA01334A>
- [28] R. Gresch, W. Muller-Warmuth, H. DUTZ, X-ray photoelectron spectroscopy of sodium phosphate glasses, *J. Noncryst. Solid* 34 (1979) 127–136, [https://doi.org/10.1016/0022-3093\(79\)90012-7](https://doi.org/10.1016/0022-3093(79)90012-7)
- [29] B. Li, Y. Shi, K. Huang, M. Zhao, J. Qiu, H. Xue, H. Pang, Cobalt-doped nickel phosphite for high performance of electrochemical energy storage, *Small* 14 (2018) 1703811, <https://doi.org/10.1021/jp508445t>
- [30] P.K. Katkar, S.J. Marje, S.S. Pujari, S.A. Khalate, A.C. Lokhande, U.M. Patil, Enhanced energy density of all-solid-state asymmetric supercapacitors based on morphologically tuned hydrous cobalt phosphate electrode as cathode material, *ACS Sustain. Chem. Eng.* 7 (2019) 11205–11218, <https://doi.org/10.1021/acssuschemeng.9b00504>
- [31] Y. Li, Z. Wang, J. Hu, S. Li, Y. Du, X. Han, P. Xu, Metal-organic frameworks derived interconnected bimetallic metaphosphate nanoarrays for efficient electrocatalytic oxygen evolution, *Adv. Funct. Mater.* 30 (2020) 1910498, <https://doi.org/10.1002/adfm.201910498>
- [32] H. Dan, K. Tao, Q. Zhou, Y. Gong, J. Lin, Ni-doped cobalt phosphite, Co₁₁(HPO₃)₈(OH)₆, with different morphologies grown on Ni foam hydro(solvo)thermally for high-performance supercapacitor, *ACS Appl. Mater. Interfaces* 10 (2018) 31340–31354, <https://doi.org/10.1021/acsami.8b09836>
- [33] M.W. Kanan, J. Yano, Y. Surendranath, M. Dinca, V.K. Yachandra, D.G. Nocera, Structure and valency of a cobalt-phosphate water oxidation catalyst determined by in situ X-ray spectroscopy, *J. Am. Chem. Soc.* 132 (2010) 13692–13701, <https://doi.org/10.1021/ja1023767>
- [34] P.W. Menezes, C. Panda, C. Walter, M. Schwarze, M. Driess, A cobalt-based amorphous bifunctional electrocatalysts for water-splitting evolved from a single-source lazulite cobalt phosphate, *Adv. Funct. Mater.* 29 (2019) 1808632, <https://doi.org/10.1002/adfm.201808632>
- [35] D. Yin, J. Zhaoyu, L. Miaomiao, G. Taotao, Y. Hongyan, X. Dan, Microwave-assisted synthesis of the cobalt-iron phosphates nanosheets as an efficient electrocatalyst for water oxidation, *Electrochim. Acta* 260 (2018) 420–429, <https://doi.org/10.1016/j.electacta.2017.12.007>
- [36] Y. Li, C. Zhao, Iron-doped nickel phosphate as synergistic electrocatalyst for water oxidation, *Chem. Mater.* 28 (2016) 5659–5666, <https://doi.org/10.1021/acs.chemmater.6b01522>



Regulated micro-leaf like nickel pyrophosphate as a cathode electrode for asymmetric supercapacitor

Supriya J. Marje^a, Pranav K. Katkar^a, Sachin S. Pujari^a, Suraj A. Khalate^a, Abhishek C. Lokhande^b, Umakant M. Patil^{a,*}

^a Centre for Interdisciplinary Research, D.Y. Patil Education Society (Deemed to be University), Kasaba Bawada, Kolhapur, 416 006, Maharashtra, India

^b Department of Physics, Khalifa University of Science and Technology (KUST), Abu Dhabi, United Arab Emirates

ARTICLE INFO

Keywords:

Asymmetric supercapacitor
Chemical bath deposition method
Composition variation
Nickel pyrophosphate
Thin film electrode

ABSTRACT

In present work, nickel pyrophosphate ($\text{Ni}_2\text{P}_2\text{O}_7 \cdot 8\text{H}_2\text{O}$) thin film on stainless steel substrate synthesized using facile chemical bath deposition method and used as cathode electrode for asymmetric supercapacitor. Three compositions of nickel phosphate with varying of nickel:phosphate (2:1, 1:1 and 1:2) molar ratio are prepared to study composition effect on microstructure and subsequently on supercapacitive performance. Morphology changes with composition from microflower to leaf like, consequently supercapacitive performance influences with increasing phosphate content in material. The well dispersed leaf like microstructure (nickel:phosphate;1:2) of nickel pyrophosphate offers more active sites and it shows maximum specific capacitance of 482 F g^{-1} at current density of 3 mA cm^{-2} along with 99.73% capacitive retention over 2500 cycles. Moreover, an asymmetric device fabricated using nickel pyrophosphate and reduced graphene oxide as a positive and negative electrode, respectively. Prepared asymmetric supercapacitor offers specific capacitance of 74.81 F g^{-1} at 0.9 mA cm^{-2} current density with 26.6 Wh kg^{-1} energy density at a moderately high power density of 870.6 W kg^{-1} . Also, exhibits 87.35% of capacitive retention over 5500 cycles at 4 mA cm^{-2} current density.

1. Introduction

To reduce global warming, promote green and clean energy, and fight with energy crisis, usage of sustainable energy sources increased [1]. Fulfil increasing demand in global power supply for different application, have to store electricity efficiently produced from sustainable energy sources [2]. So, attention shifted towards cost effective, easy to use and maintenance free energy storage devices with high stability [3]. Supercapacitor come in focus because it offers high energy and power density as compare to conventional capacitors and batteries, respectively [4,5]. These amazing properties of supercapacitor encourage to use it either individually or in combination with batteries/fuel cell for different application [6,7].

Supercapacitors are divided into three categories on the basis of charge storage mechanism such as EDLC, pseudocapacitor and hybrid supercapacitor [8]. There are numerous materials were investigated as an supercapacitor electrode material such as, metal oxides [9,10], hydroxides [11] and sulfides [12] but they suffers from some limitations such as, poor stability, poor conductivity and lower specific capacitance [13,14]. To reach high energy and economical demands, need to

develop electrode material has low-cost, high specific capacitance and favourable cycling ability [15].

Transition metal phosphates widely studies for decades and used in various applications as, catalysis/photocatalysis [16,17], energy storage devices [18] and sensors [19]. Recently, they fascinated for energy storage application owing to their excellent conductivity, abundant active sites, wide structural channels for electrolyte ions percolation and most importantly offer stable structure due to P–O covalent bond [20]. Among metal phosphates, nickel and cobalt aided in energy storage due to excellent redox action and also, they are earth abundant and widely distributed. Various structures of nickel phosphates such as pyrophosphate and orthophosphate, can facilitates different ionic conductivity and consequently rate capability [21].

So, different microstructure and polymorphs of nickel phosphate were prepared using various methods for supercapacitor application and reported in literature. Sankar et al. grown one dimensional nanorods of nickel pyrophosphate on nickel foam by simple hydrothermal method [22]. Similarly, Pang et al. [23] synthesized nickel pyrophosphate microrods by calcination of ammonium nickel phosphate material and Senthilkumar et al. [24] prepared nano grains of nickel

* Corresponding author.

E-mail address: umakant.physics84@gmail.com (U.M. Patil).

pyrophosphate using simple co-precipitation method. Also, nanoparticles like microstructure of nickel phosphate prepared by Li et al. using precipitation method [25]. Nanorods of nickel phosphate synthesized by Mirgani et al. [26] using hydrothermal method and nanosphere by Pramanik et al. [27] using calcination method. Moreover, Peng et al. synthesized microflowers of nickel phosphate by microwave assisted chemical method [28]. Among above reports, only Shankar et al. reported a binder free direct growth of nickel pyrophosphate material on substrate and other all reports are based on preparation of binder assisted electrode by coating powder sample. Literature study inspire us to synthesize binder-free nickel phosphate material on conducting and cost effective stainless steel (SS) substrate as supercapacitive electrode. Till date there is no report available on synthesis of nickel phosphate thin film electrode (binder free) with tuned morphology using chemical bath deposited (CBD) method, for supercapacitor application.

So, for the first time we are reporting binder free synthesis of nickel pyrophosphate thin film electrodes by simple CBD method for supercapacitor application with nickel and phosphate molar ratio variation. The CBD method is facile and cost effective, and any type of complex shape of substrate with large surface area can be deposited. Change in morphology due to composition variation in nickel phosphate is studied and analysed. Moreover, tuned morphology to reach high supercapacitive performance of nickel pyrophosphate thin film electrodes in terms of specific capacitance, energy and power density. Furthermore, nickel pyrophosphate used as cathode material to assemble asymmetric device with reduced graphene oxide as anode material and its performance were studied and reported herein.

2. Experimental section

2.1. Nickel pyrophosphate (cathode) electrode preparation

For synthesis of nickel phosphate, nickel chloride ($\text{NiCl}_2 \cdot 6\text{H}_2\text{O}$) was used as a source of nickel and potassium dihydrogen orthophosphate (KH_2PO_4) as a source of phosphate, and urea (NH_2CONH_2) used as a hydrolyzing agent. All chemicals were purchased from Sigma Aldrich (AR grade) and used without any purification. For binder free synthesis simple chemical bath deposition method was used to deposit nickel phosphate on stainless steel (SS) substrate. In synthesis process, nickel chloride, potassium dihydrogen orthophosphate and urea were dissolved in 50 mL of double distilled water sequentially, with vigorous stirring. To study effect of molar composition of nickel and phosphate, different three solutions were prepared with various molar concentration of nickel chloride and potassium dihydrogen orthophosphate. In this experiment, molar ratio of $\text{NiCl}_2 \cdot 6\text{H}_2\text{O}:\text{KH}_2\text{PO}_4$ varied as, 0.066:0.033, 0.05:0.05 and 0.033:0.066 and indicated as P1, P2 and P3, respectively. The SS is used as a substrate. Since, it offers several advantages such as, low cost, high conductivity and stability in acids and alkaline solution. A well-polished SS substrate placed vertically in prepared three solution baths. All solution bath were placed in water bath and heated at temperature of 363 K, for 2 h. After 2 h, apple green colored nickel pyrophosphate material deposited on SS substrate. Furthermore, prepared films rinsed with double distilled water for 2–3 times to remove residues and dried at room temperature. As prepared thin film electrodes were characterized by different techniques and used as cathode electrode for supercapacitor application.

2.2. Reduced graphene oxide (anode) electrode preparation

In the preparation of reduced graphene oxide (rGO), firstly graphene oxide was synthesized by modified Hummer's method [29] and then it reduced hydrothermally. Negative electrode prepared by combining 75% active material, 20% carbon black, 5% polyvinylidene fluoride (PVDF) with *N*-methyl 2-pyrrolidone (NMP) to make slurry. Prepared slurry coated on $1 \times 1 \text{ cm}^{-2}$ SS substrate, heated for an hour

at a temperature 60°C and used electrode for further fabrication of asymmetric device.

2.3. Characterization

The crystal structure analysis of prepared material was characterized using X-ray diffractometer (XRD) from Rigaku miniflex-600 with $\text{Cu K}\alpha$ ($\lambda = 0.15425 \text{ nm}$) radiation. Alpha (II) Bruker unit was used to record Fourier transform- infrared spectrometry (FT-IR), for detection of functional groups in the prepared material. A ThermoScientific ESCALAB 250 (Thermo Fisher Scientific, UK) instrument was used for X-ray photoelectron spectroscopy (XPS) measurement. Specific surface area for all samples were measured by Brunauer-Emmett-Teller (BET) analysis (Belsorp II mini). Field emission scanning electron microscopy (FE-SEM, JSM-7001 F, JEOL) was used to investigate morphology of material and energy dispersive spectrometer (EDS) for elemental analysis. Electrochemical activities measured using ZIVE MP1 multi-channel electrochemical workstation.

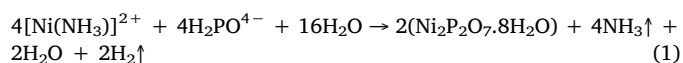
2.4. Electrochemical measurements

All electrochemical analysis of prepared thin film electrodes were measured in three electrode system at ambient conditions. Prepared nickel phosphate thin films with various $\text{Ni}:\text{PO}_4$ molar ratio or rGO electrode used as a working electrodes, platinum plate and saturated calomel electrode (SCE, with saturated KCl solution) as a counter and reference electrode, respectively. Supercapacitive performance of prepared thin film electrodes were tested using cyclic voltammetry (CV), galvanostatic charge-discharge (GCD) and electrochemical impedance spectrometry (EIS).

3. Results and discussion

3.1. Growth mechanism of nickel pyrophosphate thin film

A binder free synthesis is preferred to deposit nickel phosphate thin films on SS substrate by chemical bath deposition method. In CBD method, at supersaturation state of solution firstly ionic species get absorbed on surface of substrate during heterogeneous reaction and further it lead to nucleation with subsequent growth of material. The P1, P2 and P3 thin film electrodes are prepared to study effect of nickel and phosphate composition variation. In the reaction, urea used as a hydrolyzing agent and decomposition of urea took place at 363 K and forms CO_2 along with NH_3 . Simultaneously, Ni^{2+} from $\text{NiCl}_2 \cdot 6\text{H}_2\text{O}$ get mixed with ammonia and form amino complex $[\text{Ni}(\text{NH}_3)]^{2+}$, which act as Ni^{2+} source and control rate of reaction. On the other hand, potassium dihydrogen orthophosphate releases PO_4^{4-} ions which react with Ni^{2+} ion and get the final product of $\text{Ni}_2\text{P}_2\text{O}_7 \cdot 8\text{H}_2\text{O}$ (nickel pyrophosphate) in thin film form over SS substrate. Possible reaction mechanism for formation of nickel pyrophosphate material is as follows,



Reaction time was optimized (2 h), to get apple green colored well adherent thin film of nickel pyrophosphate on SS substrate. Mass of deposited material on SS substrate was calculated by gravimetric weight difference method and it is observed that, the deposited mass of material affected by composition variation. Deposited mass of material get decreased from P1 to P3 as 1.31, 1.23 and 1.11 mg cm^{-2} , respectively. The high phosphate content may favour homogeneous reaction than heterogeneous, which decreases growth of material in the form of thin film on the surface of substrate and increases precipitation of material in the bath. It conclude that, more homogeneous reaction decreases amount of deposited material with increasing phosphate content in the composition.

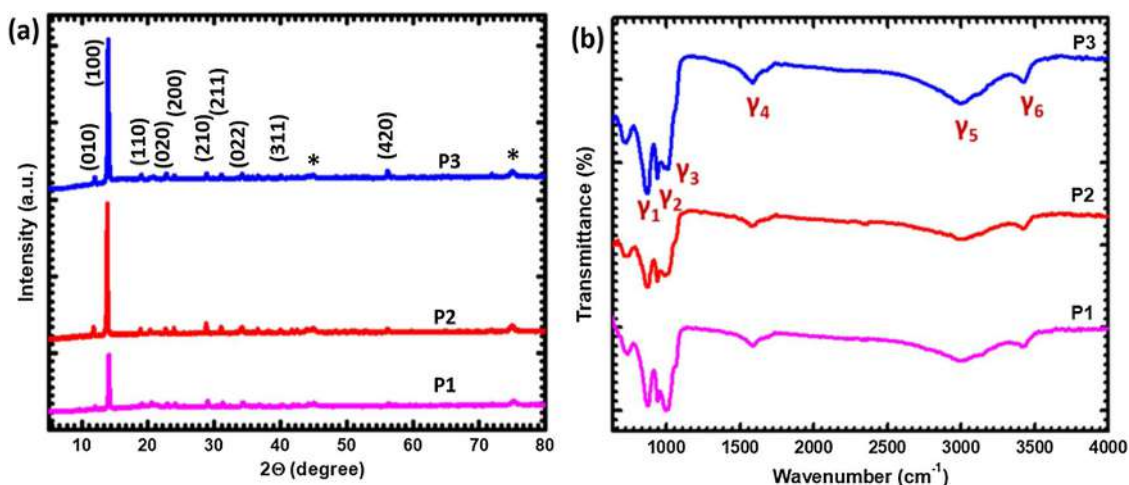


Fig. 1. (a) XRD pattern and (b) FT-IR spectra of P1, P2 and P3 electrode.

3.2. Structural and morphological analysis of nickel pyrophosphate thin film

X-ray diffractometer (XRD) was used to investigate crystal structure of prepared thin films. The XRD patterns of P1, P2 and P3 thin film electrodes are shown in Fig. 1 (a). It shows well defined peaks with d-spacing 7.38, 6.35, 4.7, 3.9, 3.71, 3.1, 2.89, 2.61, 2.26 and 1.64 Å are corresponds to diffraction planes of (010), (100), (110), (020), (200), (210), (211), (022), (311) and (420), respectively. Other peaks in XRD pattern marked with ‘*’ are attributed to SS substrate. The obtained XRD peaks are well matches with JCPDS card no. 49-0672, which confirm formation of hydrous nickel pyrophosphate ($\text{Ni}_2\text{P}_2\text{O}_7 \cdot 8\text{H}_2\text{O}$) material on SS substrate. All prepared electrode shows similar XRD spectra confirms preparation of same material, only intensity of major peak with d-spacing 6.35 Å increases from P1 to P3 electrode (composition variation from 2:1 to 1:2) as increase in phosphate content in the sample. All peaks are narrow and highly intense, which infers good crystallinity of material and oriented growth along (100) plane. Good crystallinity can improve electrochemical performance because of its stable structure may not destroy during charge-discharge cycling and may improve charge transfer [30]. Peaks other than nickel phosphate are not observed in XRD patterns, that confirms formation of $\text{Ni}_2\text{P}_2\text{O}_7 \cdot 8\text{H}_2\text{O}$ material on SS substrate.

FT-IR analysis is used to determine structure and composition of prepared thin film electrode. Fig. 1 (b) shows FT-IR spectra of P1, P2 and P3 electrodes in the range of 600–4000 cm^{-1} . The figure reveals that, stretching vibration mode of P–O–P group at 870 cm^{-1} (γ_1), symmetric stretching vibration mode at 940 cm^{-1} (γ_2) and asymmetric stretching vibration mode at 1010 cm^{-1} (γ_3) of $\text{PO}_4^{3-}/\text{P}_2\text{O}_7^{4-}$ anion [31–33]. Other peaks are corresponds to water molecule: such as peak at 1580–1590 cm^{-1} (γ_4) reveals bending vibration of O–H in crystallization water [32,34]. Also, peaks at 3000 (γ_5) and 3432 cm^{-1} (γ_6) corresponds to stretching vibration mode of O–H in crystallization water [31–35]. Above observations suggest that, structural water is present in the prepared material, in other word can say prepared material is hydrous in nature. FT-IR spectra of prepared P1, P2 and P3 thin film electrodes shows absorption peak in same range that confirms all prepared material exhibits same functional groups. No significant change in absorption spectra in all samples and hydrous content confirms preparation of hydrous nickel pyrophosphate material in thin film form.

XPS analysis was used to investigate chemical environment and valence state of the elements in prepared material. XPS survey spectra of P3 electrode is shown in Fig. 2 (a), which consist all elements such as nickel, phosphorous and oxygen. High resolution XPS spectra of Ni2p (Fig. 2 (b)) shows two intense peak at 857.1 and 874 eV binding

energies assigned to $\text{Ni}2p_{3/2}$ and $\text{Ni}2p_{1/2}$, respectively, and two satellite peak at 863.8 and 881.5 eV attributed to Ni in oxidation state of Ni^{2+} located on the surface [36,37]. Fig. 2 (c) shows XPS spectra of P2p region, only one intense peak at 133.6 eV can be assigned to P–O bonding and pentavalent phosphorous [38]. Moreover, O1s spectrum with three peak shown in Fig. 2 (d), metal oxygen bonding confirms by intense peak at 529 eV. Also, core levels and adsorbed water observed in prepared material confirms by peaks at 531 and 532.9 eV, respectively [39–42]. XPS result supports XRD and FT-IR analysis, and confirms hydrous nature of formed material ($\text{Ni}_2\text{P}_2\text{O}_7 \cdot 8\text{H}_2\text{O}$).

Morphology of prepared thin film electrodes were investigated by FE-SEM at different magnifications and shown in Fig. 3. Inter connected and closely packed bunch of triangular microplates seems microflower like structure is observed for P1 electrode (Fig. 3 (a–d)). Higher magnification SEM image of P1 electrode (b–d) shows microplates have average length, width and thickness of 42.3, 22.1 and 2.1 μm , respectively. After changing molar ratio of nickel and phosphate in P2 electrode, number of inter connected triangular microplates decreases up to half of number in comparison with P1 electrode but still it look like flower with triangular microplates as shown in Fig. 3 (e–h). Interestingly, microplates in P2 electrode has average thickness 1.5 μm , which is less as compare to P1 electrode. However, microplate shows slight increment in length and width of 48.5 and 24.1 μm , respectively, as compare to P1 electrode. Similar decrement in thickness of microplates is observed for P3 electrode up to 1.13 μm . Also, microplates length and width in P3 electrode is decreases up to 31.1 and 15.4 μm as compare to other microplates in P1 and P2 electrodes. Importantly, morphology of P3 electrode alter from microflower with rectangular microplates to well disperse leaf like structure, as shown in Fig. 3 (i–l). Such type of decrement noticed in thickness of microplates and change in morphology from microflower to leaf from P1 to P3 electrode may be the reason of increase in phosphate content in the prepared nickel pyrophosphate material.

Schematic for growth of nickel pyrophosphate material at different nickel:phosphate molar ratio is shown in Fig. 3 (m). In CBD method, conversion of supersaturated solution to saturated solution is resulted to solid phase formation. Liquid to solid phase conversion included various steps such as nucleation, aggregation, coalescence and later growth by stacking of the particles. Basically there are two types of growth mechanism, one is homogeneous growth (in solution) and other is heterogeneous growth (on the surface of foreign body). Nucleation is the first step, in which small number of particles get adsorbed on the surface of substrate which known as heterogeneous growth and act as a foundation for aggregation of particle. Furthermore, in the process of coalescence, aggregated particles merge and form a base for growth of nanostructure. After that stacking of particle grows film on the surface

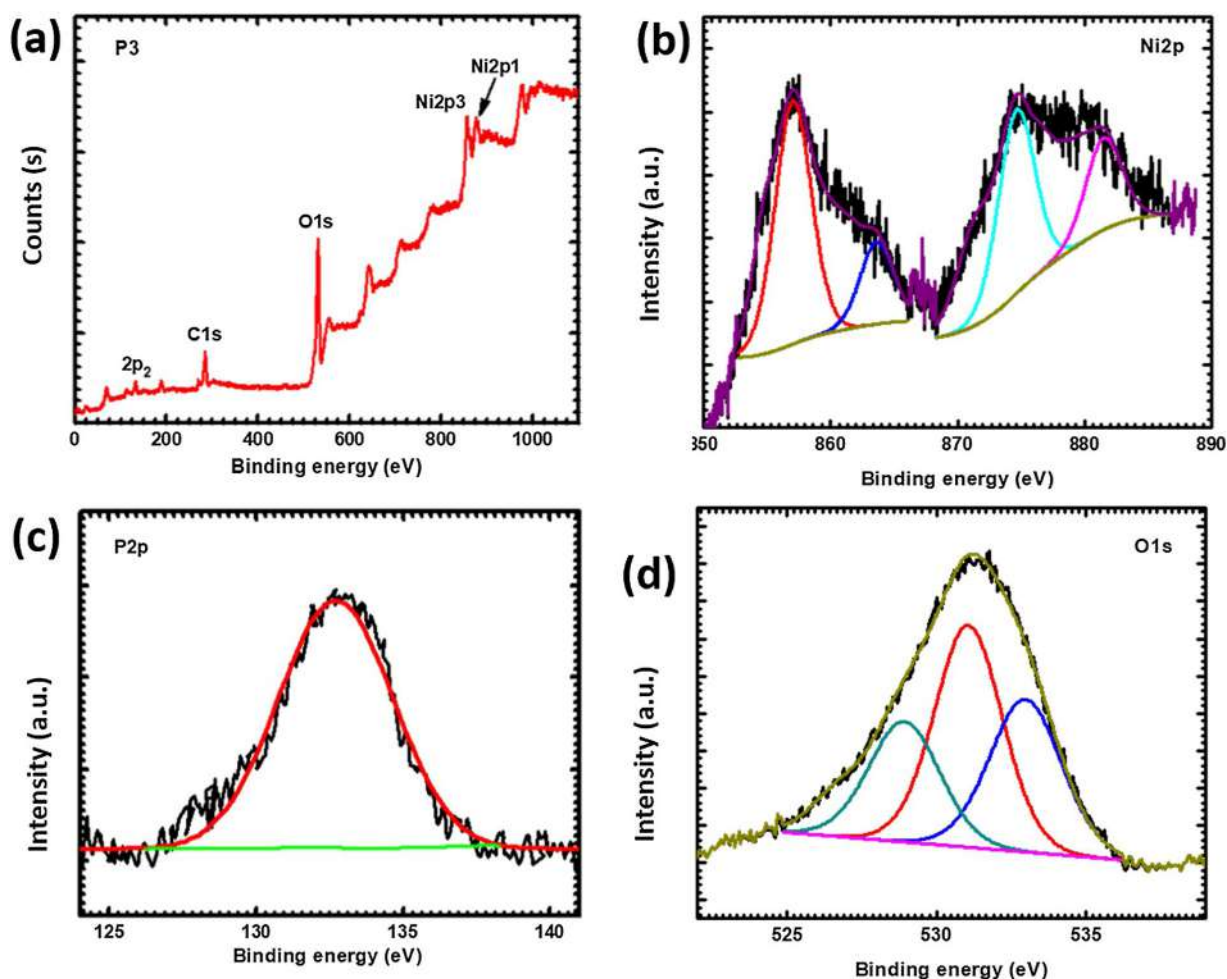


Fig. 2. (a) XPS survey spectra of P3 electrode, (b) Ni 2p spectrum, (c) P 2p spectrum and (d) O 1s spectrum.

of substrate with a certain thickness [43]. Change in morphologies from P1 to P3 electrodes were observed in FE-SEM result, possible formation of that material by stacking of particle as shown in the schematic representation. So, it resulted that, morphology get affected by phosphate content in the material, high phosphate content shows well disperse microstructure (P3 electrode) and less content show compact microflower like structure (P1 and P2 electrode). At higher phosphate content in reaction bath, phosphate ions easily available for nickel bonding, which increase rate of reaction and easy availability forms disperse leaf like structure. But at low phosphate content in reaction bath, less possibility of easy bonding between nickel and phosphate, may be they shares bonding with multiple ions, which decrease rate of reaction and resulted into inter connected complex microflower like structure. Such dispersed leaf like structure may show high electrochemical performance due to high surface area. Specific surface area for all samples were measured by Brunauer-Emmett-Teller (BET) analysis. All samples exhibits a type II isotherm according to classification of International Union of Pure and Applied Chemistry (IUPAC) and displayed in fig. S1 (see ESI). The P3 electrode shows highest specific surface area ($36.09 \text{ m}^2 \text{ g}^{-1}$) as compare to P1 ($31.1 \text{ m}^2 \text{ g}^{-1}$) and P2 ($35.66 \text{ m}^2 \text{ g}^{-1}$) electrodes. The high specific surface area of P3 sample may lead to improve electrochemical performance of the electrode.

Elemental investigation of prepared material is done using energy dispersive spectroscopy (EDS) and displayed in fig. S2 (see ESI). P1, P2 and P3 electrodes shows nickel:phosphorous atomic ratio of 1.1:1, 1:0.9 and 1:1.1, respectively. The EDS result confirm molar ratio variation in nickel and phosphate concentration as 2:1, 1:1 and 1:2 in P1, P2 and P3 electrodes, respectively, and may be reason to change in morphology

from microflower to leaf like structure. Nickel, oxygen and phosphorous elements are present in the prepared material confirms formation of $\text{Ni}_2\text{P}_2\text{O}_7 \cdot 8\text{H}_2\text{O}$ thin film.

3.3. Electrochemical study of nickel pyrophosphate thin film

Effect of nickel:phosphate molar ratio variation in nickel pyrophosphate material on morphology influenced supercapacitive performances were investigated using three electrode system in 1 M KOH electrolyte. Fig. 4 (a) shows CV curve of prepared three P1, P2 and P3 electrodes at 20 mV s^{-1} scan rate in an optimized potential window of 0-0.5 V (vs SCE). P1 electrode shows much smaller current area under curve in comparison with other electrodes. Moreover, P2 electrode shows improve current response than P1 electrode and P3 electrode shows higher current response in CV curve than other electrodes. So, it is observed that, P3 electrode exhibits higher current response because of well disperse leaf like microstructure as compare to P1 and P2 electrode having compact flower like microstructure. The leaf like microstructure may offer high surface area to reaction than the compact structure of P1 and P2 electrode. As increase in phosphate content in the electrode from P1 to P3, current area increases and large area under the CV curve corresponds to high areal capacitance, it is important to increase capacitive performance. The CVs of the P3 electrode at various scan rate from $5\text{--}100 \text{ mV s}^{-1}$ are shown in Fig. 4 (b) and CV curves of the P1 and P2 electrode at different scan rate from $5\text{--}100 \text{ mV s}^{-1}$ are provided in fig. S3 (see ESI). Current area in CV curve increases as increasing scan rate and observed redox peaks corresponds to Ni^{+2} and Ni^{+3} transition, that reveals pseudo-capacitive nature of material [44].

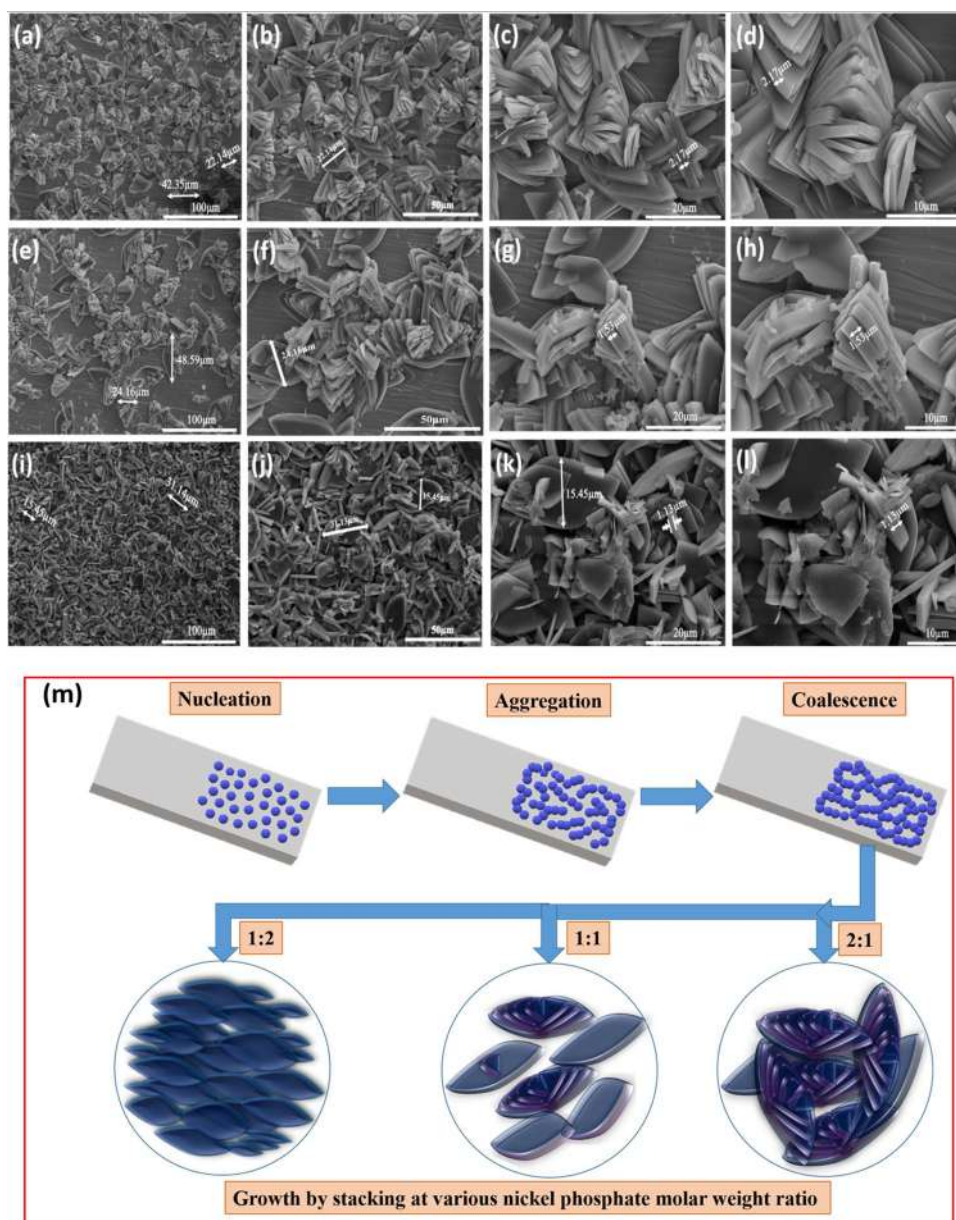
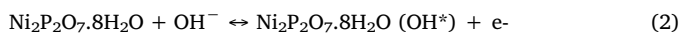


Fig. 3. FE-SEM images of P1 (a–d), P2 (e–h) and P3 electrode (i–l) at different magnifications (X400, X800, X2000 and X3000, respectively). (m) Schematic representation of growth mechanism for nickel pyrophosphate thin film.

Possible redox reaction of material can be expressed as follows,



Specific capacitance of nickel pyrophosphate material was calculated from CV curve using equation as follows,

$$C_s = \frac{\int iV dV}{2v \cdot w \cdot \Delta V} (\text{F g}^{-1}) \quad (3)$$

where, $\int iV dV$, v , w and ΔV are area under the CV curve, scan rate, deposited weight of material and potential window, respectively. Specific capacitance with respect to scan rate plotted and shown in Fig. 4 (c). The P3 electrode shows highest specific capacitance of 416 F g^{-1} at scan rate 5 mV s^{-1} . Higher specific capacitance obtained at slower scan rate and it decreases as increasing scan rate. Higher capacitance obtained at low scan rate because of at a slow scan rate, enough time is available to transfer OH^- from solution to surface of the electrode material and more charges can transfer as compare to high scan rate. It means that, at slow scan rate more charges can be stored than high scan

rate, which offer higher specific capacitance. Other electrodes P1 and P2 shows maximum specific capacitance of 200 and 336 F g^{-1} , respectively at 5 mV s^{-1} scan rate. The result reveals, well disperse leaf like microstructure offers high specific capacitance rather than compact microflower like morphology.

Amount of total charge stored in electrode is due to contribution of capacitive and intercalation process. According to Power's law, CV current dependent on scan rate can be expressed as follows,

$$i = av^b \quad (4)$$

where, i represents current, v is the scan rate, a and b are the adjustable parameters. The value of b is the slope of $\log(i)$ vs $\log(v)$. The graph of $\log(i)$ vs $\log(v)$ for P1, P2 and P3 electrodes are given in fig. S4 (see ESI). It has two conditions when b is 0.5 and 1, then the electrochemical process is diffusive and capacitive, respectively [45]. Using this equation, we can find charge storage mechanism for P1, P2 and P3 electrode. Electrode P1, P2 and P3 demonstrates b values of 0.604, 0.606 and 0.6233, respectively. All electrodes shows b values more than 0.5

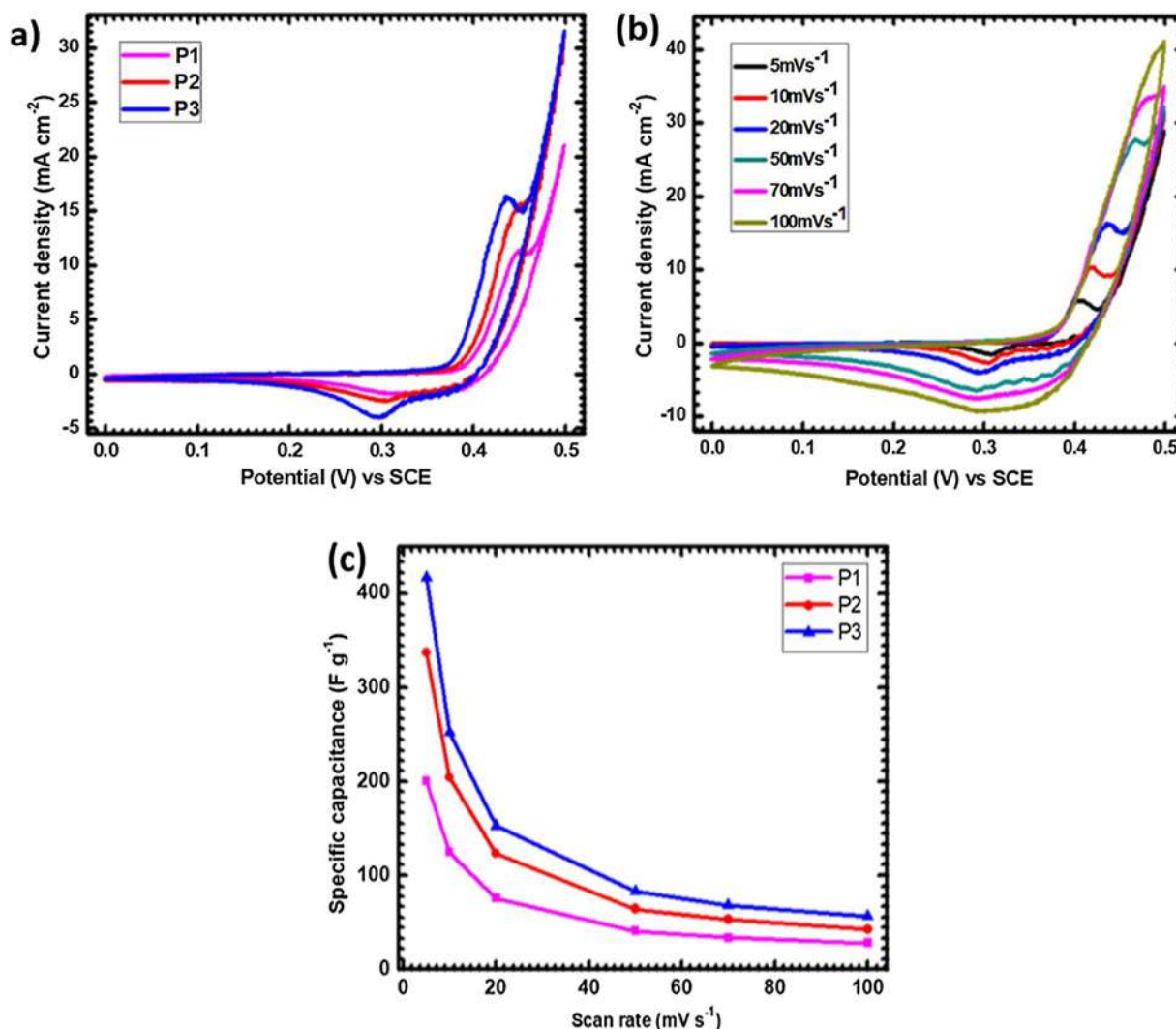


Fig. 4. (a) CV curve of P1, P2 and P3 electrode at scan rate 20 mV s⁻¹, (b) CV curve of P3 electrode at various scan rate from 5–100 mV s⁻¹, and (c) specific capacitance at different scan rate of all electrodes.

and less than 1, indicating charge storage mechanism contributed from both (capacitive and diffusive) type of process.

To determine the respective contribution of current densities from surface pseudocapacitive and battery like bulk process at various scan rates calculated using modified Power's law as given below,

$$I_p = I_{\text{surface}} + I_{\text{bulk}} = C_{\text{surface}} \nu + C_{\text{bulk}} \nu^{1/2} \quad (5)$$

Where, I_p is the peak current density, ν is the scan rate, $C_{\text{surface}} \nu$ represents current contribution from surface pseudocapacitive process (I_{surface}) and $C_{\text{bulk}} \nu^{1/2}$ represents from bulk process (I_{bulk}) [46–48]. Current contribution from pseudocapacitive and bulk process for all three electrode calculated from above equation and plotted in Fig. 5 (a–c). It is observed that, current contribution mainly from battery like bulk process and partially from pseudocapacitive surface process. Contribution in current from pseudocapacitive surface process increases as increasing scan rate, which resulted pseudocapacitive process higher at high scan rate. That conclude active material shows more capacitive nature at high scan rate and battery like nature at low scan rate.

Further, galvanostatic charge discharge (GCD) analysis of material was performed in 1 M KOH electrolyte. The Fig. 6(a) shows GCD graphs of P1, P2 and P3 electrode at 3 mA cm⁻² current density and P3 electrode shows large discharging time at low current density. The charging and discharging curve of P3 electrode at different current densities shown in Fig. 6(b). The P3 electrode shows large discharging time as

compare to P1 and P2, which confirmed capacitance of material depends on composition and morphology of material, and it is important to increase capacitance of material. Discharging time decrease with increasing current density due to inefficient interaction between electrolyte and electrode at high current density. GCD graphs of P1 and P2 electrode at various current densities from 3 to 7 mA cm⁻² plotted and provided in fig. S5 (see ESI). Specific capacitance of nickel pyrophosphate material calculated from GCD graph by following equation,

$$C_s = \frac{I \times \Delta t}{w \times \Delta V} \text{ (F g}^{-1}\text{)} \quad (6)$$

where, I , Δt , w and ΔV are current density, discharging time, mass of active material and potential window, respectively [49]. The maximum capacitance of P1, P2 and P3 electrodes are found to be 225, 292 and 482 F g⁻¹, respectively at 3 mA cm⁻² current density as shown in Fig. 6(c). Furthermore, the specific capacitance decreases up to 147, 162 and 312 F g⁻¹, respectively at higher current density of 7 mA cm⁻². Also, calculated areal capacitance of the electrodes, plotted and provided in the fig. S6 (see ESI). Leaf like well disperse microstructure offer high surface area for electrochemical activity due to high phosphate content which exhibits increment in specific capacitance of nickel pyrophosphate material.

Energy density (E) and power density (P) of nickel pyrophosphate material calculated from GCD by equation (7) and (8), respectively as

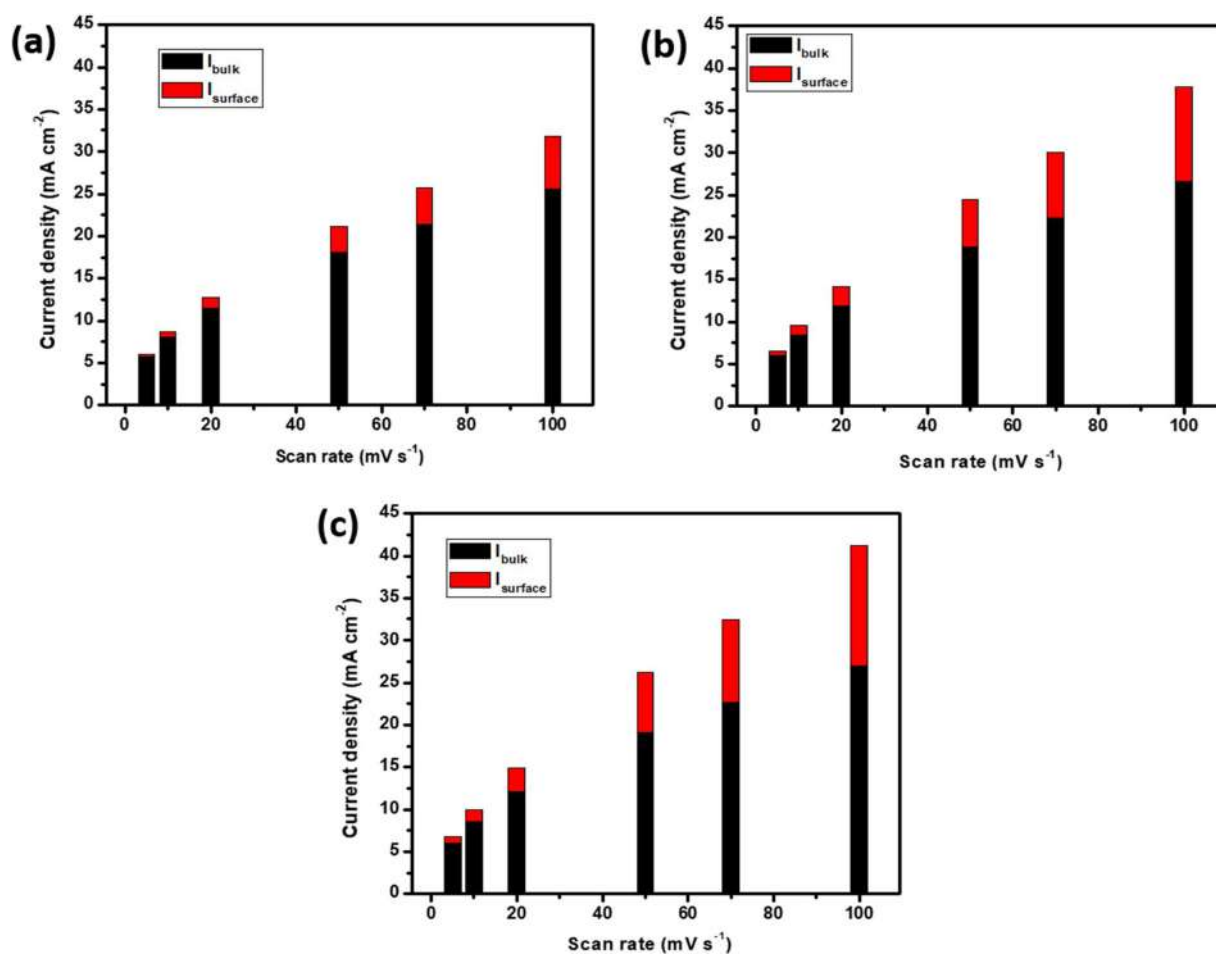


Fig. 5. (a) Graph of calculated contribution of pseudocapacitive (surface current) and battery type (bulk current) current density at various scan rates (5 to 100 mV s^{-1}) of P1, P2 and P3 electrodes, respectively.

follows,

$$E = \frac{0.5 \times C_s \times (\Delta V)^2}{3.6} (\text{Wh kg}^{-1}) \quad (7)$$

And

$$P = \frac{E \times 3.6}{\Delta t} (\text{kW kg}^{-1}) \quad (8)$$

where, C_s , ΔV , and Δt represents specific capacitance, potential window and discharging time, respectively. Calculated energy density and power density is plotted and shown in Fig. 6(d). The P3 electrode shows higher energy density of 10.7 Wh kg^{-1} at 0.5 kW kg^{-1} power density as compare to P1 (5 Wh kg^{-1}) and P2 electrode (6.4 Wh kg^{-1}). The energy density of sample P3 decreases from 10.7 to 6.9 Wh kg^{-1} and power density increases from 0.5 to 1.19 kW kg^{-1} with increase in galvanostatic charge discharge current density from 3 to 7 mA cm^{-2} . Similarly, Shankar et al. [21] reported directly grown 1D nanorods of nickel pyrophosphate on nickel foam substrate using the hydrothermal method, which offers highest areal capacitance of 5272 mF cm^{-2} . However, prepared nickel pyrophosphate thin film on SS substrate exhibits maximum areal capacitance $535.07 \text{ mF cm}^{-2}$, it shows less performance compared with report by Shankar et al. This may be due to use of nickel foam as a substrate, which plays an important role to improve electrochemical performance of electrode material by adding self capacitance by its surface atom conversion to NiO and Ni(OH)_2 during electrochemical testing. So, when nickel foam used as a current collector to test electrochemical properties of small amount active material then nickel foam underestimate the specific capacitance value

of active material [48]. However, in this study, stainless steel substrate is used as a substrate to synthesize nickel pyrophosphate material thin film electrode, which only offers 2D structure and does not take part in electrochemical reaction. So, in this work, obtained capacitance is totally provided only by nickel pyrophosphate material.

Long term stability is important key factor of efficient electrode for supercapacitor application and specific capacitance should be change as little as possible during cycling stability. So, the stability of prepared best electrode (P3) tested at 50 mV s^{-1} for 2500 cycles and respective capacitive retention shown in Fig. 7 (a). Importantly, P3 electrode shows good cycling life and 99.73% capacitive retention after 2500 CV cycles and CV curves of 1st, 500th, 1500th and 2500th cycle shown in inset of Fig. 7 (a). In initial cycles, insertion and extraction of ions increases electrochemical active volume of the electrode material which exhibits initial slight increment in specific capacitance [50] and later little decrement in capacitance is due to minute reduction of material after many charging/discharging cycles. So, well disperse leaf like microstructure exhibits to excellent cyclic stability.

Electrochemical impedance spectroscopy (EIS) was carried out in the range 100 mHz to 1 MHz at open circuit potential (OCP). The Nyquist plot of P1, P2 and P3 electrodes with fitted data, are shown in Fig. 7(b), and inset shows equivalent circuit for P3 electrode. In Nyquist plots, straight line appear in low frequency region and semicircle appear in high frequency region. Semicircle starting point is called as solution resistance (R_s), value of semicircle corresponds to charge transfer resistance (R_{ct}), straight line stands for Warburg diffusion resistance (W) and Q is general imperfect capacitor when $n = 1$, $Q = C$, due to semi-infinite diffusion of charges. Solution resistance, charge

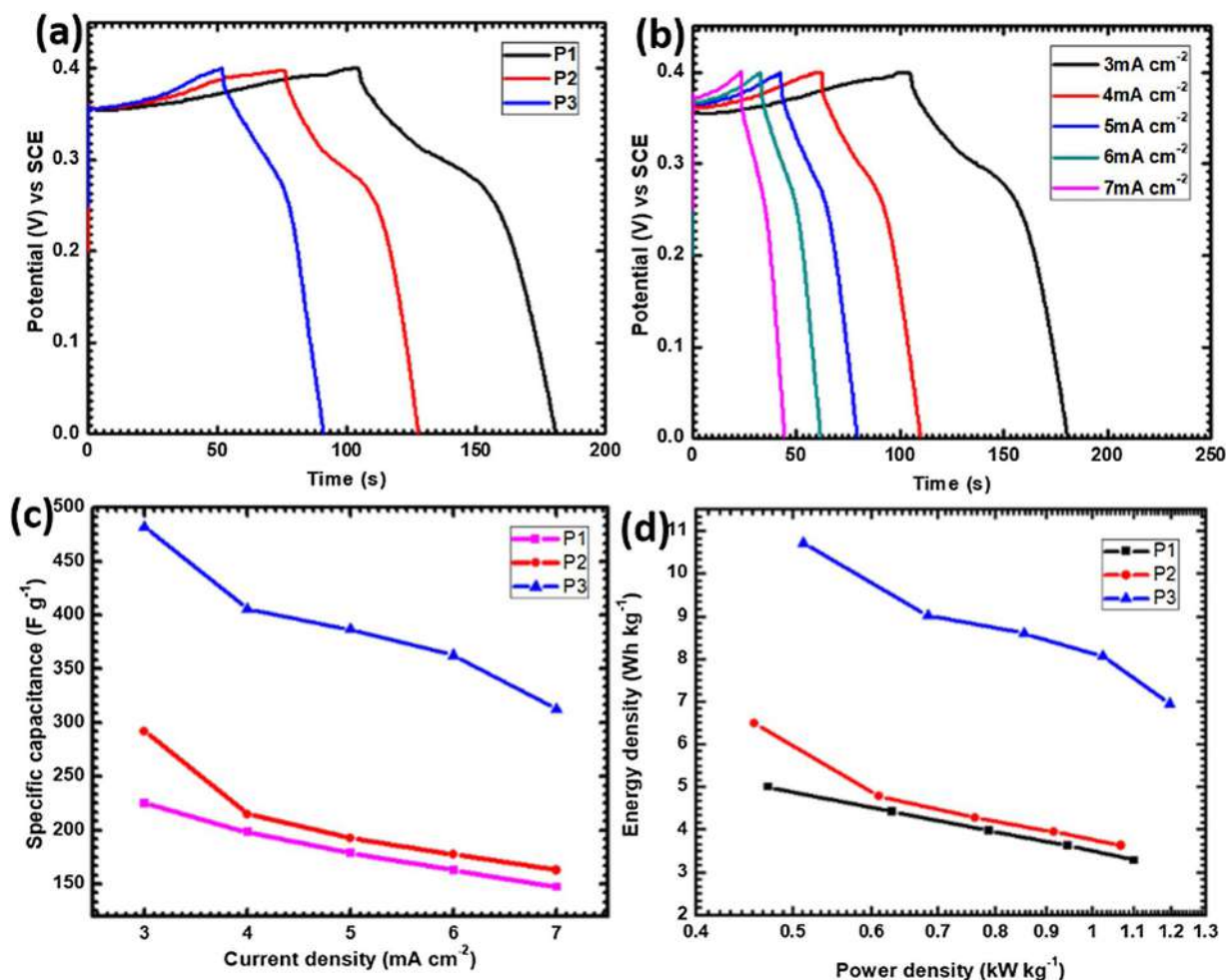


Fig. 6. (a) GCD curve of P1, P2 and P3 electrode at low current density 3 mA cm^{-2} , (b) GCD curve of P3 electrode at various current densities, (c) Specific capacitance at different current densities for P1, P2 and P3 electrode, and (d) Ragone plot of all electrodes.

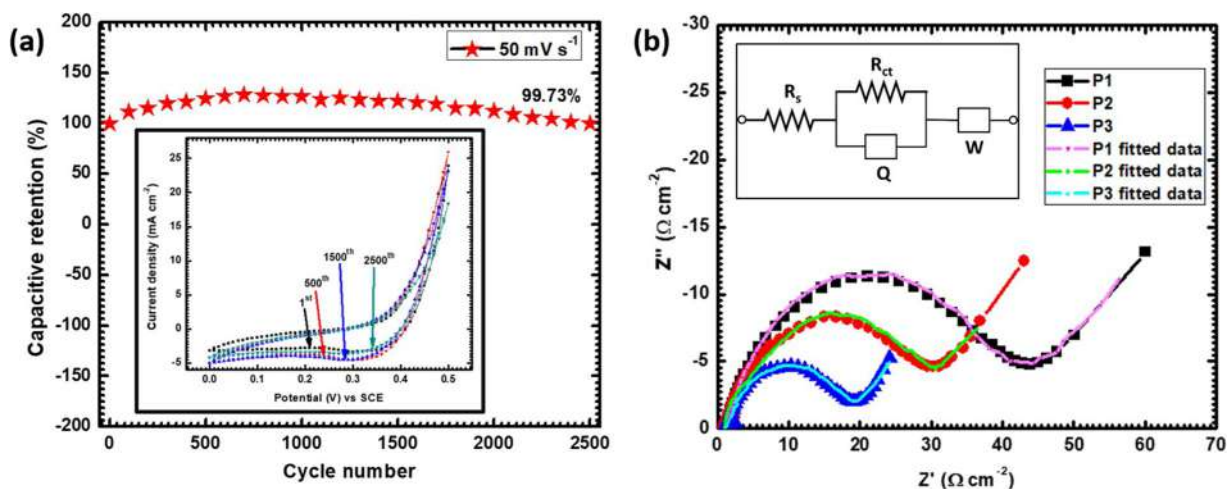


Fig. 7. (a) Stability of $\text{Ni}_2\text{P}_2\text{O}_7 \cdot 8\text{H}_2\text{O}$ electrode (P3) at 50 mV s^{-1} for 2500 cycles (inset: CV curve of 1st, 500th, 1500th and 2500th cycle) and (b) Nyquist plot of prepared P1, P2 and P3 electrodes (inset: equivalent circuit of P3 electrode).

transfer resistance and Warburg resistance of P1, P2 and P3 electrodes are determined by fitting the data with equivalent circuit and given in table S1 (see ESI). Solution resistance of P1, P2 and P3 electrodes are found to be 1.14, 0.97 and 1.19 Ω , respectively and charge transfer resistance are 40.54, 26.88 and 16.52 Ω , respectively. Also, Warburg diffusion resistance measured for the sample P1, P2 and P3 are 0.257,

0.218 and 0.205 Ω , respectively. Charge transfer resistance of electrodes are different due to different morphologies, since, it originates from intercalation of charges between electrode and electrolyte [51]. P3 electrode shows low R_{ct} (16.52 Ω) and total impedance rather than other samples, which confirms low charge transfer and Warburg diffusion resistance contributes for good electrochemical performance

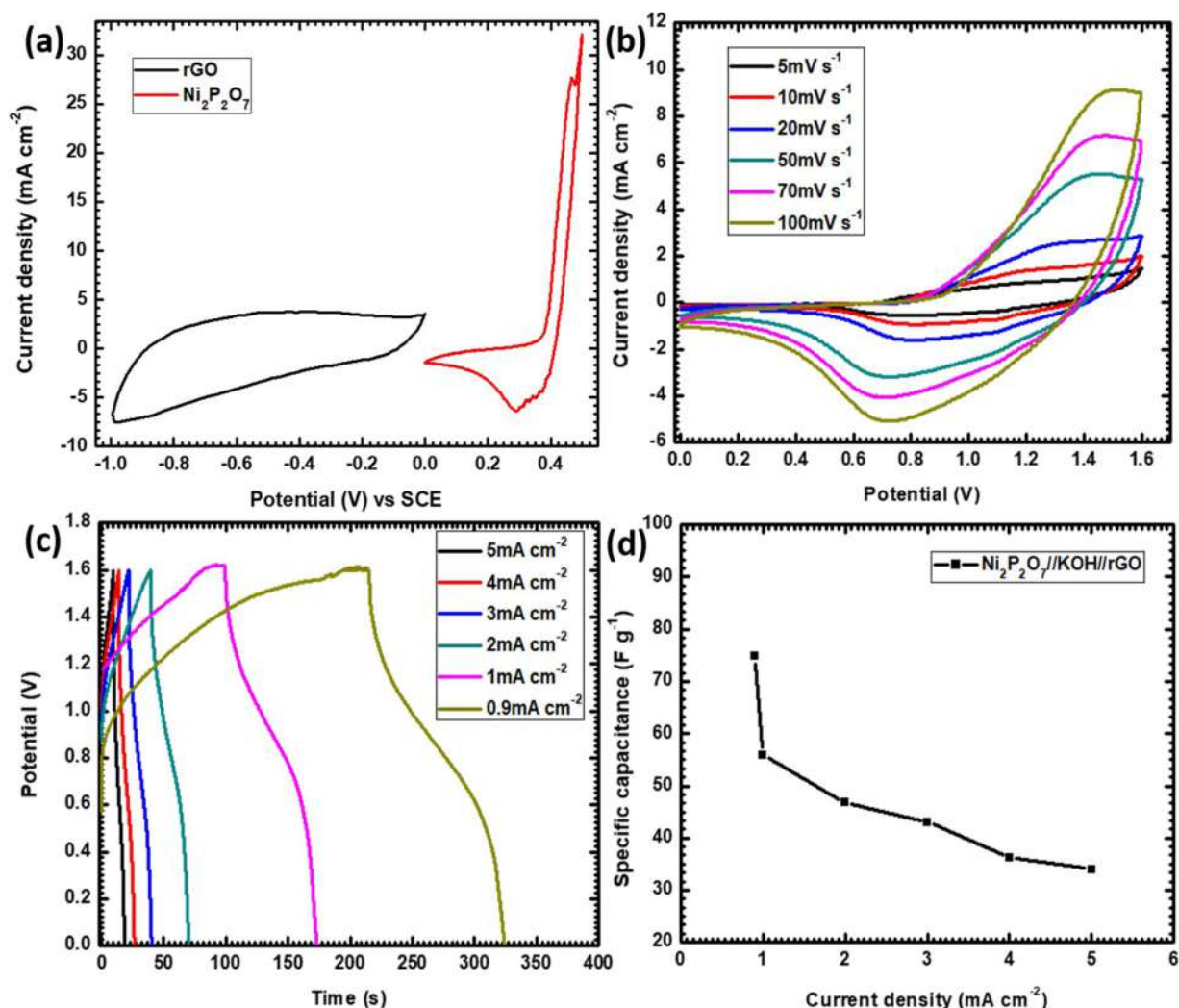


Fig. 8. (a) CV curves of rGO and nickel pyrophosphate electrode, (b) CV curves at various scan rate, (c) GCD curves at various current densities, and (d) specific capacitance at various current densities of $\text{Ni}_2\text{P}_2\text{O}_7//\text{KOH}/\text{rGO}$.

[52].

3.4. Asymmetric supercapacitor (ASC) device

As per obtained results, nickel pyrophosphate as cathode material and rGO as anode material can use to fabricate ASC device. Supercapacitive performance of rGO electrode tested in three electrode system. CV curves of rGO electrode at various scan rate from 5–100 mV s^{-1} in an optimized potential window 0 to -1 V (vs SCE) shown in fig. S7 (a) (see ESI). Absence of redox peak in CV curve and rectangular-like shape confirms electric double layer capacitive nature of rGO, and also confirmed by linear GCD graphs of rGO electrode (display in fig. S7 (b) (see ESI)). The rGO electrode delivers highest specific capacitance of 163.8 F g^{-1} at 1.25 mA cm^{-2} current density calculated using Eq. (6) and given in fig. S7 (c) (see ESI). Electrochemical impedance spectroscopy (EIS) measurement of rGO electrode tested in the range of 100 mHz to 1 MHz (shown in fig. S7 (d) see ESI). A semicircle observed in high frequency region and straight line observed in low frequency region. The obtained graph shows low solution resistance (1.14Ω) and charge transfer resistance (41.4Ω) which is responsible for good electrochemical performance. Equivalent circuit for fitted data display in inset of fig. S7 (d) (see ESI). Best performed P3 electrode of nickel pyrophosphate (with nickel:phosphate molar ratio 1:2) used as positive electrode and rGO (a wider -ve potential window) as negative electrode

with 1 M KOH aqueous electrolyte in ASC device. High energy density and improved operating potential window are main advantages of preparing ASC devices. CV curves of anode electrode rGO and cathode material nickel pyrophosphate at 50 mV s^{-1} scan rate within different potential window are shown in Fig. 8 (a). The theory of charge balance used to obtain best electrochemical performance for ASC device by balancing mass ratio between positive and negative electrode using an equation as follows,

$$\frac{m_+}{m_-} = \frac{C_- \times \Delta V_-}{C_+ \times \Delta V_+} \quad (9)$$

where, $m_{(+or-)}$, $\Delta V_{(+or-)}$, and $C_{(+or-)}$ are the mass of material (g), potential window (V), and specific capacitance of positive and negative electrode, respectively [53,54]. By using above equation, calculated mass ratio of the positive and negative electrode obtained as 0.17:1. To ensure the mass balance ratio in the ASC device tailored the area of electrodes. Applicable potential window of ASC device for CV is optimized in window 1.2–1.7 V and shown in fig. S8 (a). In 1.2 to 1.5 V potential window ASC device does not shows oxidation peak of nickel pyrophosphate electrode and at 1.7 V little straight line observed at the end of CV curve which may indicate oxygen evolution reaction [55–57]. So, 1.6 V is an optimized window for ASC device ($\text{Ni}_2\text{P}_2\text{O}_7//\text{KOH}/\text{rGO}$). Similarly, for GCD operative potential window is optimized and shown in fig. S8 (b). Both graph of CV and GCD curves confirm the operational potential window of the ASC device is 1.6 V.

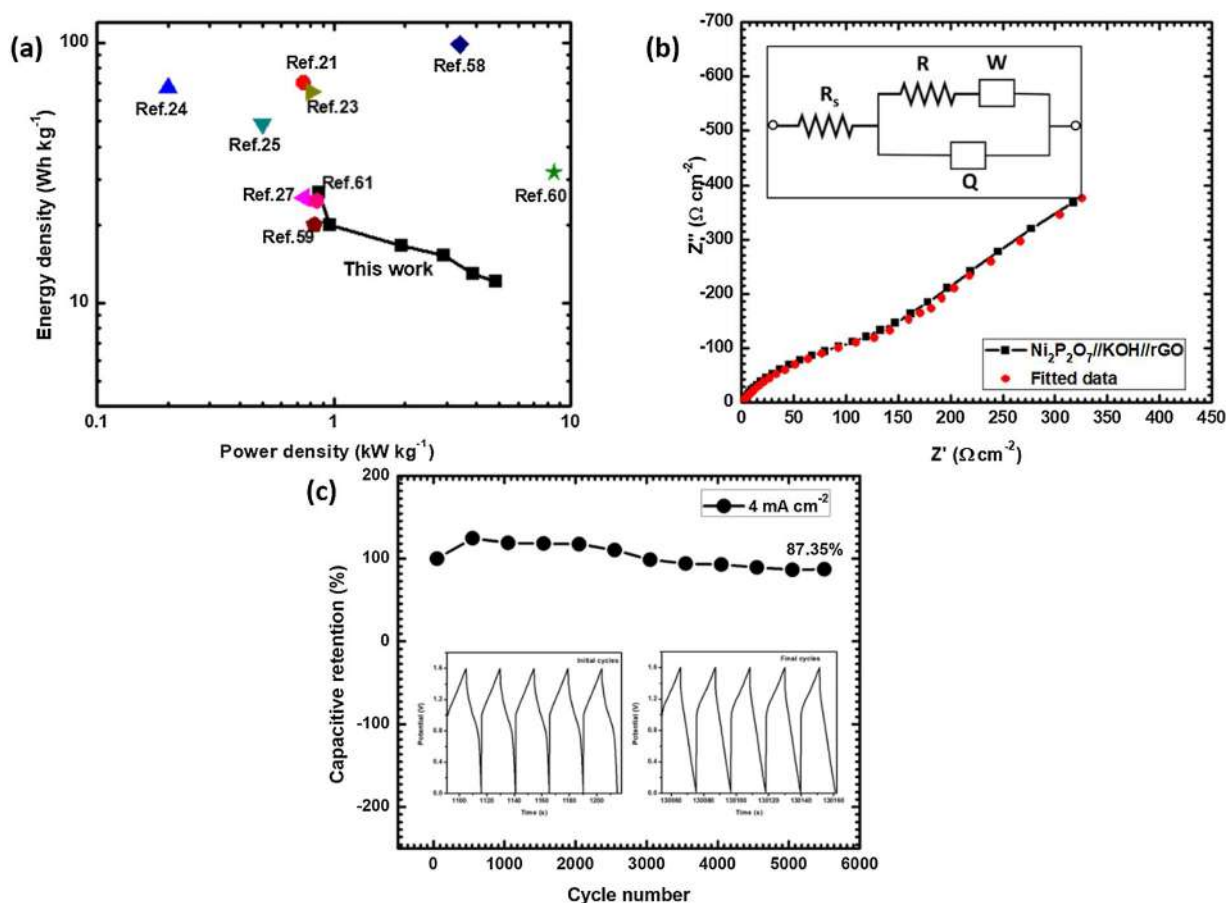


Fig. 9. (a) Ragone plot of Ni₂P₂O₇//KOH//rGO in comparison with reported data, (b) Nyquist plot of Ni₂P₂O₇//KOH//rGO (inset: equivalent circuit of Ni₂P₂O₇//KOH//rGO) and (c) Capacitive retention vs cycle number of Ni₂P₂O₇//KOH//rGO at 4 mA cm⁻² current density over 5500 cycles (inset: (i) initial 5 cycles after 50th cycle and (ii) last 5 cycles after 5000th cycle).

The CV curves of ASC device at various scan rate from 5–100 mV s⁻¹ within potential window of 0–1.6 V are shown in Fig. 8 (b). The CV curves shows only one redox peak due to nickel pyrophosphate electrode. Also, at higher scan rate it reveals good reversibility of device. GCD graph of ASC device shown in Fig. 8 (c), at the beginning of the discharge curve typical IR drop is not observed, that conclude negligible energy of the device used during charge-discharge process. ASC device exhibits maximum specific capacitance 74.81 F g⁻¹ at 0.9 mA cm⁻² current density. As increasing current density, the discharging time of the device decreases, which resulted decrease in specific capacitance of the device due to insufficient electrode-electrolyte interaction (shown in Fig. 8 (d)).

Total mass dependent energy and power density of device calculated and plotted comparatively with reported data in Fig. 9 (a). The device obtained highest energy density of 26.6 Wh kg⁻¹ at power density of 870.6 W kg⁻¹. The prepared ASC device exhibits moderately high power density as compare to reported data (Table S2 (see ESI)) [21,23–25,27,58–61]. But, it shows less energy density as compare to reported data, the main reason to obtain less performance of the ASC device is may be due to, in all reports nickel foam were used as a current collector, which added their capacitance in total capacitance of the device. In this case, SS substrate is used as a current collector for the both positive and negative electrode. So, the obtained results in this study are only due to active material and it further can be improved by using porous nickel foam as a current collector. EIS study of ASC device carried out at open circuit potential in the range 100 mHz to 1 MHz. Nyquist plot of ASC device and fitted data is shown in Fig. 9 (b), solution resistance (R_s) of ASC device is found to be 1.66 Ω and charge transfer resistance (R_{ct}) is 171.54 Ω. In inset of Fig. 9 (b) shows

equivalent circuit for fitted data of ASC device. In this circuit R_s is solution resistance, R_{ct} is charge transfer resistance, W is Warburg diffusion resistance and Q is general imperfect capacitor when n = 1, Q = C, due to semi-infinite diffusion of charges [62]. Stability of the ASC device tested at 4 mA cm⁻² current density for 5500 cycles and displayed in Fig. 9 (c). Initial and final 5 GCD cycles after 50th and 5000th cycle shown in inset of Fig. 9 (c) (i) and (ii), respectively. The ASC device shows 87.35% capacitive retention after 5500 GCD cycles, which is higher than reported data in Table S2 (see ESI). Similar to single electrode (nickel pyrophosphate) ASC device shows increment and little decrement in specific capacitance in initial cycles and after many charge/discharge cycles, respectively.

Overall we observed that, microstructure of prepared material changes with molar ratio variation of Ni:PO₄ (2:1, 1:1 and 1:2) in nickel pyrophosphate. Leaf like microstructure of nickel pyrophosphate thin film electrode offers high capacitance as compare to microflower like microstructure because well disperse leaf like microstructure exhibit high surface area for electrochemical activity. Also, it offers low charge transfer resistance due to well disperse microstructure. The well disperse leaf like microstructure of nickel pyrophosphate electrode offers long term stability. Nickel pyrophosphate with stable microstructure (leaf like microstructure) used as a positive and rGO which has a wide negative potential window (1 V) used as a negative electrode to fabricate asymmetric supercapacitor. So, it is observed that, binder free nickel pyrophosphate (P 3 electrode) material in thin film form electrode is a favorable candidate as cathode for supercapacitor application.

4. Conclusions

In conclusion, nickel pyrophosphate material in thin film form on stainless steel substrate successfully prepared via simple chemical bath deposition method. Morphological conversion from compact microflower to leaf like structure were achieved by varying nickel:phosphate molar ratio. Also, thickness of microplates decreases (2.17 to 1.13 μm) as increasing phosphate content in the electrode. A well disperse leaf like microstructure of nickel pyrophosphate exhibit highest specific capacitance of 482 F g^{-1} at current density 3 mA cm^{-2} with 99.73% stability over 2500 cycles. The asymmetric device fabricated by combining nickel pyrophosphate as cathode and rGO as anode electrodes. The ASC device exhibits highest specific capacitance of 74.81 F g^{-1} with energy density of 26.6 Wh kg^{-1} at a moderately high power density of 870.6 W kg^{-1} . Also, ASC device exhibits 87.35% capacitive retention over 5500 cycles. These results conclude that, nickel pyrophosphate is a promising candidate as cathode in asymmetric supercapacitor devices for practical applications.

Declaration of Competing Interest

The authors declare no competing financial interest.

Acknowledgment

We are thankful to the Ministry of Science and Technology India, Department of Science and Technology-Innovation in Science Pursuit for Inspired (DST-INSPIRE), for financial support through research project sanction no. DST/INSPIRE/04/2016/000260.

Appendix A. Supplementary data

Supplementary material related to this article can be found, in the online version, at doi:<https://doi.org/10.1016/j.synthmet.2019.116224>.

References

- Y. Shao, M. El-Kady, J. Sun, Y. Li, Q. Zhang, M. Zhu, H. Wang, B. Dunn, R. Kaner, *Chem. Rev.* 118 (2018) 9233–9280.
- U. Patil, M. Nam, J. Sohn, S. Kulkarni, R. Shin, S. Kang, S. Lee, J. Kim, S. Jun, *J. Mater. Chem. A* 2 (2014) 19075–19083.
- Y. Huang, J. Tao, W. Meng, M. Zhu, Y. Huang, Y. Fu, Y. Gao, C. Zhi, *Nano Energy* 11 (2015) 518–525.
- S. Tamboli, B. Kim, G. Choi, H. Lee, D. Lee, U. Patil, J. Lim, S. Kulkarni, S. Jun, H. Cho, *J. Mater. Chem. A* 2 (2014) 5077–5086.
- U. Patil, R. Ghorpade, M. Nam, A. Nalawade, S. Lee, H. Han, S. Jun, *Sci. Rep.* 6 (2016) 35490–35501.
- P. Thounthong, S. Rael, B. Davat, *J. Power Sources* 193 (2009) 376–385.
- P. Thounthong, S. Rael, B. Davat, *IEEE Trans. Ind. Electron.* 54 (2007) 3225–3233.
- M. Vangari, Tonya Pryor, L. Jiang, *J. Energy Eng.* 139 (2013) 72–79.
- U. Patil, S. Kulkarni, V. Jamadade, C. Lokhande, *J. Alloy Comp.* 509 (2011) 1677–1682.
- X. Han, K. Tao, Q. Ma, L. Han, *J. Mater. Sci.: Mater. Electron.* 29 (2018) 14697–14704.
- U. Patil, K. Gurav, Kim J, C. Lokhande, S. Jun, *Bull. Mater. Sci.* 37 (2014) 27–33.
- X. Yu, L. Yu, H. Wu, X. Lou, *Angew. Chem. Int. Ed.* 54 (2015) 5331–5335.
- F. Shi, L. Li, X. Wang, C. Gu, J. Tu, *RSC Adv.* 4 (2014) 41910–41921.
- G. Snook, P. Kao, A. Best, *J. Power Sources* 196 (2011) 1–12.
- C. Chen, N. Zhang, Y. He, B. Liang, R. Ma, X. Liu, *ACS Appl. Mater. Interfaces* 8 (2016) 23114–23121.
- S. Marje, P. Katkar, S. Kale, A. Lokhande, C. Lokhande, U. Patil, *J. Alloys Compd.* 779 (2019) 49–58.
- Y. Bi, S. Ouyang, N. Umezawa, J. Cao, J. Ye, *J. Am. Chem. Soc.* 133 (2011) 6490–6492.
- B. Li, P. Gu, Y. Feng, G. Zhang, K. Huang, H. Xue, H. Pang, *Adv. Funct. Mater.* 27 (2017) 1605784–1605795.
- S. Darzi, M. Esfidvajani, *J. Porous Mater.* 24 (2017) 85–95.
- X. Li, A. Elshahawy, C. Guan, *J. Wang, Small* 13 (2017) 1701530–1701554.
- H. Pang, X. Li, X. Xiao, Q. Li, J. Wei, H. Xue, *Inorg. Chem. Front.* 5 (2018) 11–28.
- K. Sankar, Y. Seo, S. Lee, S. Jun, *ACS Appl. Mater. Interfaces* 10 (2018) 8045–8056.
- H. Pang, Y. Zhang, Z. Run, W. Lai, W. Huang, *Nano Energy* 17 (2015) 339–347.
- B. Senthilkumar, Z. Khan, S. Park, K. Kim, H. Ko, Y. Kim, *J. Mater. Chem. A* 3 (2015) 21553–21561.
- J. Li, M. Liu, L. Kong, D. Wang, Y. Hu, W. Han, L. Kang, *RSC Adv.* 5 (2015) 41721–41728.
- A. Mirghni, M. Madito, K. Oyedotun, T. Masikhwa, N. Ndiaye, S. Ray, N. Manyala, *RSC Adv.* 8 (2018) 11608–11621.
- M. Pramanik, R. Salunkhe, M. Imura, Y. Yamauchi, *ACS Appl. Mater. Interfaces* 8 (2016) 9790–9797.
- X. Peng, H. Chai, Y. Cao, Y. Wang, H. Dong, D. Jia, W. Zhou, *Materials Today Energy* 7 (2018) 129–135.
- D. Marcano, D. Kosynkin, J. Berlin, A. Sinitskii, Z. Sun, A. Slesarev, L. Alemany, W. Lu, J. Tour, *ACS Nano* 4 (2010) 4806–4814.
- B. Yan, D. Bin, F. Ren, Z. Xiong, K. Zhang, C. Wang, Y. Du, *Catalysts* 6 (2016) 198–213.
- N. Prokopchuk, V. Kopilevich, L. Voitenko, *Russ. J. Appl. Chem.* 81 (2008) 386–391.
- M. Al-Omair, A. Touny, M. Saleh, *J. Power Sources* 342 (2017) 1032–1039.
- D. Yang, Q. Yu, L. Gao, L. Mao, J. Yang, *Appl. Surf. Sci.* 416 (2017) 503–510.
- H. Wen, M. Cao, G. Sun, W. Xu, D. Wang, X. Zhang, C. Hu, *J. Phys. Chem. C* 112 (2008) 15948–15955.
- P. Noisong, C. Danvirutai, T. Srithanratana, B. Boonchom, *Solid State Sci.* 10 (2008) 1598–1604.
- J. Chang, Q. Lv, G. Li, J. Ge, C. Liu, W. Xing, *Appl. Catal. B* 204 (2017) 486–496.
- W. Bian, Y. Huang, X. Xu, M. Din, G. Xie, X. Wang, *ACS Appl. Mater. Interfaces* 10 (2018) 9407–9414.
- N. Jiang, B. You, M. Sheng, Y. Sun, *ChemCatChem.* 8 (2016) 106–112.
- T. Sun, L. Xu, Y. Yan, A. Zakhidov, R. Baughman, J. Chen, *ACS Catal.* 6 (2016) 1446–1450.
- P. Feng, X. Cheng, J. Li, X. Luo, *ChemistrySelect* 3 (2018) 760–764.
- J. Li, W. Xu, D. Zhou, J. Luo, D. Zhang, P. Xu, L. Wei, D. Yuan, *J. Mater. Sci.* 53 (2018) 2077–2086.
- H. Shao, N. Padmanathan, D. McNulty, C. Dwyer, K. Razeed, *ACS Appl. Mater. Interfaces* 8 (2016) 28592–28598.
- U. Patil, S. Kulkarni, P. Deshmukh, R. Salunkhe, C. Lokhande, *J. Alloys. Compd.* 509 (2011) 6196–6199.
- N. Padmanathan, H. Shao, K. Razeed, *ACS Appl. Mater. Interfaces* 10 (2018) 8599–8610.
- M. Sathiyaa, A. Prakash, K. Ramesha, J. Tarascon, A. Shukla, *J. Am. Chem. Soc.* 133 (2011) 16291–16299.
- P. Katkar, S. Marje, S. Pujari, S. Khalate, A. Lokhande, U. Patil, *ACS Sustainable Chem. Eng.* 7 (2019) 11205–11218.
- B. Senthilkumar, K. Sankar, L. Vasylechko, Y. Lee, R. Selvan, *RSC Adv.* 4 (2014) 53192–53201.
- W. Xing, S. Qiao, X. Wu, X. Gao, J. Zhou, S. Zhuo, S. Hartono, D. Jurcakova, *J. Power Sources* 196 (2011) 4123–4127.
- X. Zheng, X. Han, X. Zhao, Jian Qi, Q. Ma, K. Tao, L. Han 106 (2018) 243–249.
- Y. Jiang, L. Jiang, Z. Wu, P. Yang, H. Zhang, Z. Pan, L. Hu, *J. Mater. Chem. A* 6 (2018) 16308–16315.
- J. Theerthagiri, K. Thiagarajan, B. Senthilkumar, Z. Khan, R. Senthil, P. Arunachalam, J. Madhavan, M. Ashokkumar, *ChemistrySelect.* 2 (2017) 201–210.
- Y. Cheng, R. Li, D. Mu, J. Ren, J. Liu, C. Dai, *J. Electrochem. Soc.* 164 (2017) A1545–A1551.
- K. Sankar, R. Selvan, D. Meyrick, *RSC Adv.* 5 (2015) 99959–99967.
- Z. Yang, Q. Ma, L. Han, K. Tao, *Inorg. Chem. Front.* 6 (2019) 2178–2184.
- L. Fan, G. Liu, C. Zhang, J. Wu, Y. Wei, *Int. J. Hydrog. Energy* 40 (2015) 10150–10157.
- L. Fan, F. Pan, Q. Tu, Y. Gu, J. Huang, Y. Huang, J. Wu, *Int. J. Hydrog. Energy* 43 (2018) 23372–23381.
- Y. Gua, L. Fana, J. Huang, C. Genga, J. Lina, M. Huanga, Y. Huang, J. Wua, *J. Power Sources* 425 (2019) 60–68.
- J. Huang, L. Fan, Y. Gu, C. Geng, H. Luo, Y. Huang, J. Lin, J. Wu, *J. Alloy Comp.* 788 (2019) 1119–1126.
- X. Han, K. Tao, D. Wang, L. Han, *Nanoscale* 10 (2018) 2735–2741.
- K. Tao, X. Han, Q. Cheng, Y. Yang, Z. Yang, Q. Ma, L. Han, *Chem.: Eur. J.* 24 (2018) 12584–12591.
- K. Tao, X. Han, Q. Ma, L. Han, *Dalton Trans.* 47 (2018) 3496–3502.
- P. Deshmukh, S. Pusawale, V. Jamadade, U. Patil, C. Lokhande, *J. Alloy Comp.* 509 (2011) 5064–5069.



Effect of phosphate (anion) precursor on structural and morphology behavior of nickel phosphate thin films and its supercapacitive performance

Supriya J. Marje^a, Pranav K. Katkar^a, Sachin S. Pujari^a, Suraj A. Khalate^a, Prashant R. Deshmukh^b, Umakant M. Patil^{a,*}

^a Centre for Interdisciplinary Research, D. Y. Patil Education Society (Deemed to be University), Kasaba Bawada, Kolhapur 416 006, M.S., India

^b Department of Mechanical Engineering, Chungnam National University, Daejeon, South Korea

ARTICLE INFO

Keywords:

Anion precursor effect
Asymmetric supercapacitor
Binder-free synthesis
Chemical bath deposition method
Nickel phosphate
Thin film electrode

ABSTRACT

In present work, reproducible and economic chemical bath deposition method is used to deposit nickel phosphate thin films on stainless steel substrate for supercapacitor application and effect of anion precursors on structure and morphology of prepared thin film is studied. Change in structure from crystalline to amorphous is observed in prepared thin films due to precursor variation. Also, microplate to microsphere like morphological alteration is observed with the same. The microsphere like morphology of amorphous nickel phosphate thin film electrode exhibits the highest specific capacitance of $\sim 1031 \text{ F g}^{-1}$ (specific capacity 114.6 mAh g^{-1}) at 0.5 mA cm^{-2} current density. Its practical application is tested by preparing asymmetric supercapacitor device comprising amorphous nickel phosphate thin film as positive electrode and reduced graphene oxide as negative electrode. Asymmetric device delivers highest specific capacitance of $\sim 100 \text{ F g}^{-1}$ at 6 mA cm^{-2} current density with energy density of 45.33 Wh kg^{-1} at a high power density of 1.5 kW kg^{-1} and offers 80% capacitance retention over 3000 cycles.

1. Introduction

Today's increasing requirement of energy storage devices for high power applications catches researcher's attention. Main requirements of energy storage device are reversible and fast release of electrical energy and that can be fulfilled by supercapacitor devices [1,2]. Numerous materials has been developed and studied by researcher for supercapacitor application such as, transition metal oxides [3], hydroxides [4], sulfides [5] and phosphides [6]. To develop economical stabled material with high energy and power density for supercapacitor application needs to explore new materials. In the search of inexpensive electrochemically active material, many researchers attracted towards metal phosphate materials for supercapacitor application [7].

Among metal phosphates, nickel and cobalt phosphate were widely studied for different application due to its earth abundancy and high conductivity. Moreover, several chemical methods were used to prepare nickel phosphate materials for supercapacitor application such as hydrothermal [8–12], microwave assisted [13], calcination [14,15], coprecipitation [16,17] and sonochemical [18,19] etc. Different chemical method offers different microstructure of nickel phosphate such as nano-microrod, microflower, nanosphere etc. that ultimately exhibits

different electrochemical capacitive performances.

However, very few reports explored the effect of precursor source on the microstructure and ultimately supercapacitive performance of the material. Li et. al achieved different morphologies of Ag_3PO_4 material using simple way phosphate precursor variation from H_3PO_4 to Na_2HPO_4 in hydrothermal synthesis process. This experiment resulted tremendous change in morphologies in prepared material with respect to precursor variation. Analogous effects are studied in terms of supercapacitive performance, 3D tetrapod like microcrystals of Ag_3PO_4 sample shows 1.6 times higher capacitance than a sample composed with irregular particles and some polyhedrons [20]. Selective shapes/morphology of material can be prepared by changing precursors and these results are observed by Bi. et. al. only changing silver precursor from acetate to nitrate in the preparation of silver phosphate using precipitation process. Without using capping agent selective shapes from rhombic dodecahedrons to perfect cubes of silver phosphate were prepared. Photocatalytic activity of controlled but different morphologies were studied and reported that, the rhombic dodecahedrons are more catalytically active than perfect cubic structured material [21]. Similar type of results obtained by Gunjaker et. al. in the simple chemical bath preparation of silver phosphate thin films. Authors obtained

* Corresponding author.

E-mail address: umakant.physics84@gmail.com (U.M. Patil).

<https://doi.org/10.1016/j.mseb.2020.114641>

Received 30 January 2020; Received in revised form 8 June 2020; Accepted 16 July 2020

0921-5107/ © 2020 Elsevier B.V. All rights reserved.

rhombic dodecahedrons and cubes of silver phosphate material in thin film form by varying phosphate precursor from sodium hydrogen phosphate to ammonium hydrogen phosphate and silver precursor from AgNO_3 to $\text{Ag}(\text{CH}_3\text{COO})$, and their photocatalytic activity were studied [22].

In this work, economic and reproducible chemical bath deposition method was used to synthesize nickel phosphate material in thin film form. Impact of anion precursor studied via only altering phosphate precursor in the synthesis process. Structural and morphological changes observed with respect to precursor variation. The impact of structural and morphological change on electrochemical supercapacitive performance were studied.

2. Experimental section

2.1. Nickel phosphate thin film electrode preparation

In typical synthesis, nickel chloride ($\text{NiCl}_2 \cdot 6\text{H}_2\text{O}$) used as a source of nickel and urea (NH_2CONH_2) as a hydrolyzing agent, and varied source of phosphate precursor potassium dihydrogen orthophosphate (KH_2PO_4) and phosphoric acid (H_3PO_4). All chemicals purchased from Sigma Aldrich and used without any purification (AR grade). For synthesis of nickel phosphate thin film facile chemical bath deposition method was used. Chemical bath for the deposition of nickel phosphate was prepared from an aqueous solution of nickel precursor, phosphate precursor and urea. In this experiment, 0.033 M nickel precursor ($\text{NiCl}_2 \cdot 6\text{H}_2\text{O}$), 0.066 M phosphate precursor and 0.075 M urea were mixed in a double distilled water to prepare a chemical bath. Effect of precursor on synthesized material elaborated by varying precursor of phosphate source. To distinguish effect of precursor two different chemical bath were prepared for synthesis process. First chemical bath prepared using potassium dihydrogen orthophosphate (KH_2PO_4) as a phosphate precursor and synthesized material denoted by P1. Similarly, second chemical bath prepared using phosphoric acid (H_3PO_4) as a source of phosphate and material denoted by P2. A cost effective stainless steel (SS) used as a conducting substrate for synthesis of nickel phosphate. The metallic substrate was cleaned with zero grade polish paper followed by washing with double distilled water and sonication. A well cleaned SS substrate vertically placed in a chemical bath. Both prepared bath heated at a temperature 363 K for 12 h. Finally, an apple green colored films were obtained on SS substrate after 12 h. After that, prepared films removed from chemical bath and rinse with double distilled water for 2–3 times for removal of loosely binded material and residue on it. Deposited films were dried naturally at room temperature and used for further all characterization.

2.2. Preparation of rGO electrode

Modified Hummer's method was used for the synthesis of graphene oxide (GO) [23]. Prepared GO solution reduced hydrothermally and then freeze dried to get porous structure with enhanced surface area. The rGO electrode prepared using slurry which contains 75% rGO powder, 20% carbon black and 5% polyvinylidene fluoride (PVDF) with N-methyl 2-pyrrolidone (NMP). The prepared slurry coated on stainless steel substrate ($1 \times 1 \text{ cm}^{-2}$), heated in an oven at 60 °C for an hour and used as anode in asymmetric device for further study.

2.3. Characterization techniques

The crystal structure of obtained thin films were examined by X-ray diffractometer (XRD) from Rigaku miniflex-600 with $\text{Cu K}\alpha$ ($\lambda = 0.15425 \text{ nm}$) radiation. Fourier transform-infrared spectrometry (FT-IR) of prepared thin films analyzed by Alpha (II) Bruker unit, to study chemical bonding and functional groups. A ThermoScientific ESCALAB 250 (Thermo Fisher Scientific, UK) instrument was used for

X-ray photoelectron spectroscopy (XPS) measurement. Surface morphology and elemental distribution of prepared thin films examined using Field emission scanning electron microscopy (FE-SEM, JSM-7001F, JEOL). Specific surface area of samples were measured by Brunauer-Emmett-Teller (BET) analysis (Belsorp II mini). ZIVE MP1 multichannel electrochemical workstation was used to study electrochemical capacitive properties of prepared thin film electrodes.

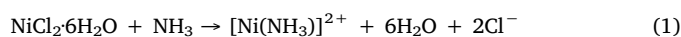
2.4. Electrochemical measurements

Three electrode system used to analyze electrochemical properties of prepared material at room temperature for supercapacitor application. In this system, platinum plate and saturated calomel electrode (SCE, with saturated KCl solution) used as a counter and reference electrode, respectively. Prepared thin films of nickel phosphate used as a working electrode. Cyclic voltammetry (CV), galvanostatic charge-discharge (GCD) and electrochemical impedance spectrometry (EIS) was carried out in three electrode system to study supercapacitive performance of prepared thin films. Asymmetric device was fabricated using prepared best performing nickel phosphate thin film as positive electrode and reduced graphene oxide as negative electrode, and performance studied in two electrode system using 1 M KOH electrolyte.

3. Results and discussion

3.1. Growth mechanism of prepared nickel phosphate thin film

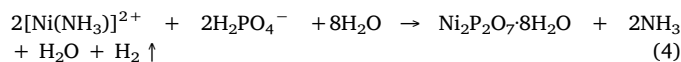
Nickel phosphate material synthesized on SS substrate using chemical bath deposition (CBD) method without using any surfactant and template. CBD method is based on conversion of aqueous solution into solid phase. Important factor in CBD method is direct deposition of material based on heterogeneous nucleation (on the surface of foreign body) and subsequent crystal growth of material on substrate surface. In this work, precursor of phosphate varied to analyze effect of precursor on crystal structure and morphology of product with same composition, reaction time and temperature. Here, precursor exhibit key factor in thin film growth and urea control hydrolysis by slow decomposition in the form of CO_2 and NH_3 . Released ammonia react with Ni^{2+} ions released from $\text{NiCl}_2 \cdot 6\text{H}_2\text{O}$ and form a complex $[\text{Ni}(\text{NH}_3)]^{2+}$ as follows,



Complex of nickel with ammonia act as a Ni^{2+} source and control the rate of reaction. On the other hand decomposition of phosphate carried out as follows,



Complex of $[\text{Ni}(\text{NH}_3)]^{2+}$ get reacted with H_2PO_4^- ions and get form a thin film of hydrous nickel pyrophosphate material as follows,



Decomposition of H_3PO_4 resulted the addition of H^+ ions in bath solution which ultimately decreases pH of solution up to ~1.7 (P2 sample bath) and provide high acidic medium during film formation. On the other hand, in the process of KH_2PO_4 decomposition bath solution has ~4.1 pH (P1 sample bath), which is higher as compare to pH of P2 bath. So, high acidic medium influence the growth rate of material and hence deposited weight of material of sample P2 (0.416 mg cm^{-2}) is very low as compare to sample P1 (3.18 mg cm^{-2}). This difference in weight observed possibly due to variation in pH, which may restrict the growth of material. Adherent apple green color

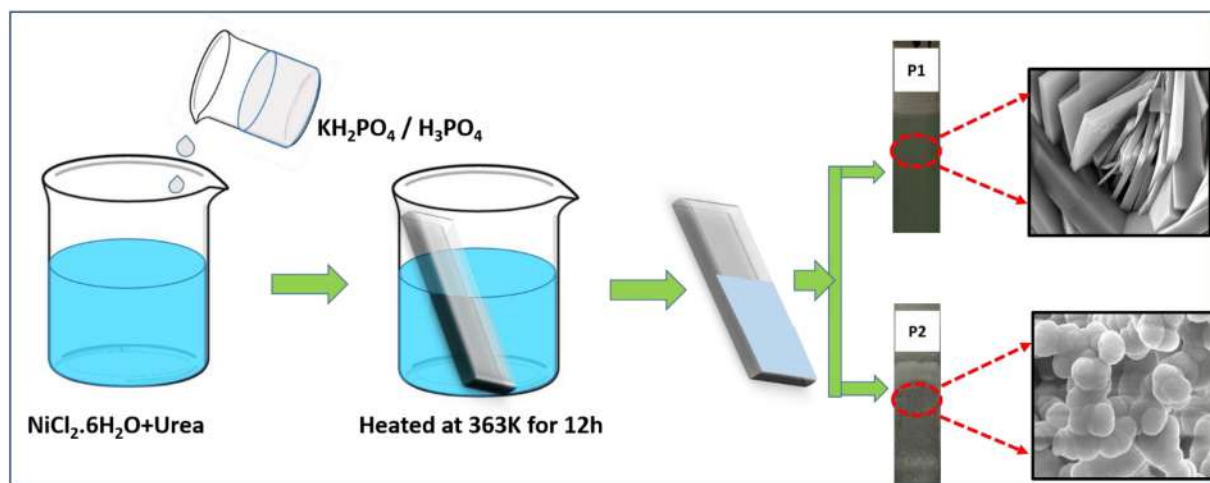


Fig. 1. Schematic representation of synthesis process of nickel phosphate.

film obtained from both phosphate precursor bath using similar reaction time, reaction temperature and composition. Schematic representation of synthesis process of nickel phosphate thin films is shown in Fig. 1.

3.2. Structural and morphological analysis

The Fig. 2 (a) represents XRD patterns of sample P1 and P2 on SS substrate. The P1 sample shows highly intense peak that confirm sample P1 have a crystalline nature. Highly intense peak of sample P1 matches with JCPDS card no. 49–0672 and it confirm prepared material (sample P1) is hydrous nickel pyrophosphate. Interestingly, sample P2 does not shows any peaks in XRD pattern rather than SS substrate peak, which conclude sample P2 has an amorphous nature. Peaks marked with ‘*’ in XRD patterns are corresponding to SS substrate. Only change in phosphate precursor responsible to get crystalline and amorphous phases of nickel phosphate material at the same deposition conditions. Amorphous nature of nickel phosphate may improve electrochemical properties of material by providing high surface area. Moreover, crystalline nature may offers excellent stability due to stable microstructure and good conductivity.

FT-IR spectra of prepared sample in the range of 400–4000 cm^{-1} displayed in Fig. 2 (b). FT-IR analysis used to identify present bonding and chemical composition in the prepared sample. In figure, peak at 590 cm^{-1} reveals a vibrational mode of metal oxygen bonding (Ni-O) [24]. Peaks at the position 753, 881, 942, 994, 1016 and 1073 cm^{-1}

assigned P-O stretching vibrational mode of PO_4^{3-} or $\text{P}_2\text{O}_7^{4-}$ anions [18,25,26]. Bending mode of water molecule observed at the peak position of 1352, 1384 and 1595 cm^{-1} [25,27]. Also, adsorbed water is identified by the peak position of 3025 and 3431 cm^{-1} [25,27]. Above results reveals that, structural water content is present in the prepared material. Both material shows exactly similar peaks that confirm, both prepared sample have similar composition. Similar composition and hydrous content confirm prepared both materials are hydrous nickel phosphate.

Surface chemical composition and valence states in the prepared material investigated by XPS analysis. XPS study of prepared sample P1 and P2 are shown in Fig. 3. XPS survey spectra of sample P1 and P2 are displayed in Fig. 3 (a). Full spectrum of XPS confirms phosphorous, oxygen and nickel species are present in the prepared thin films. Fig. 3 (b) shows the high resolution XPS spectra of Ni2p region. Two intense peak observed in Ni2p region at binding energy of 856.7 and 874.6 eV corresponds to Ni2p_{3/2} and Ni2p_{1/2}, respectively. Also, two satellite peaks at binding energy 861.8 and 881.9 eV represents (Ni²⁺) state of Ni on the surface [28,29]. The XPS spectra of P2p region is shown in Fig. 3 (c), reveals P-O bonding and pentavalent phosphorous availability by one intense peak at the binding energy 132.85 eV [28,30,31]. Moreover, high resolution spectra of O1s region displayed in Fig. 3 (d), peak at 529 eV confirms metal oxygen bonding (Ni-O), peak at 531 and 532.9 eV reveals O in core level of phosphate and adsorbed water, respectively [32–34]. Sample P1 and P2 shows peaks at similar binding energies that confirms prepared material over thin film is hydrous

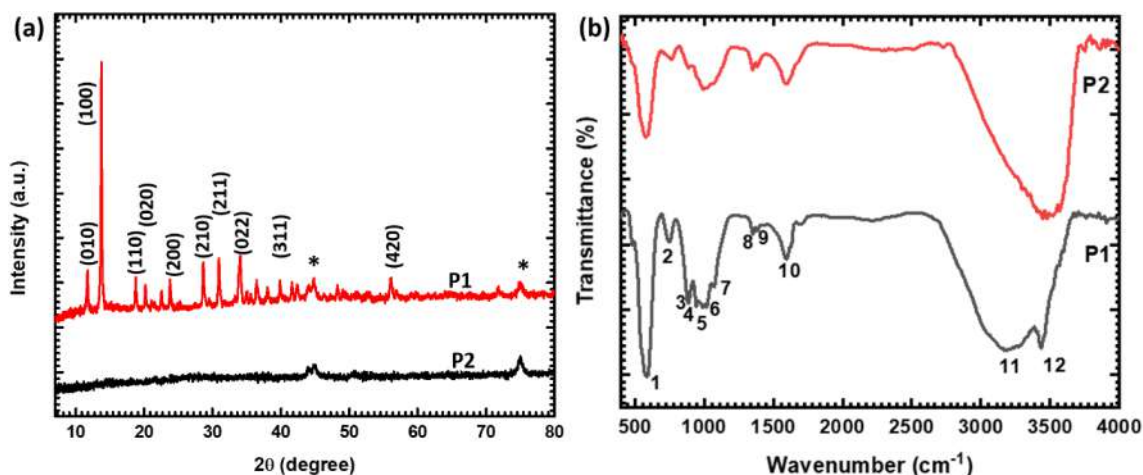


Fig. 2. XRD patterns and FT-IR spectra of P1 and P2 electrode.

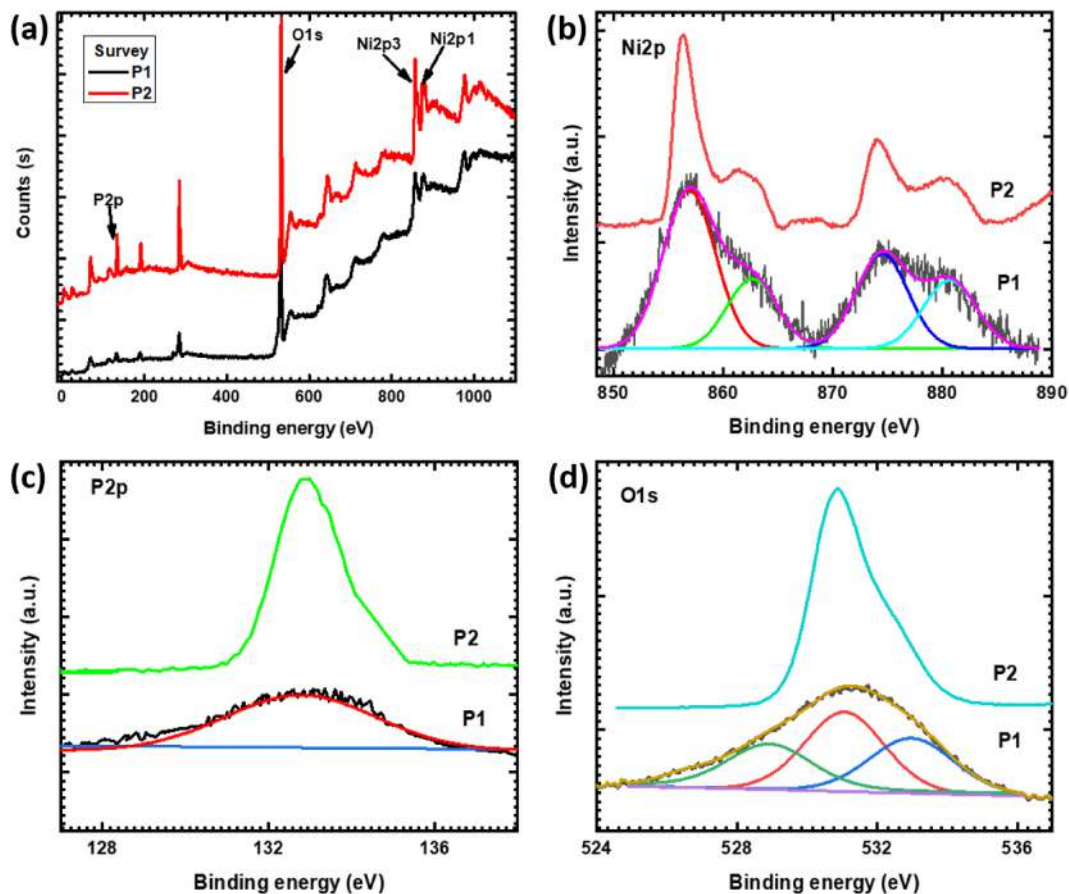


Fig. 3. (a) XPS survey spectra, (b) Ni2p spectrum, (c) P2p spectrum and (d) O1s spectrum of P1 and P2 electrode.

nickel phosphate from both baths.

Fig. 4 displays FE-SEM images of prepared sample P1 and P2. Microflower like structure is observed for sample P1, as shown in Fig. 4(a-c). Large number of microplates get closely packed connected and grown on each other resulted to a flower like morphology. At

higher magnification in Fig. 4(b) dense and interconnected structure of microplates are observed. These microflowers consist microplates has an average thickness of 2.07 μm with sharp edges. Also, smooth surface of microplates for sample P1 is observed in Fig. 4 (c). However, when H₃PO₄ used as a phosphate source in synthesis, prepared material has a

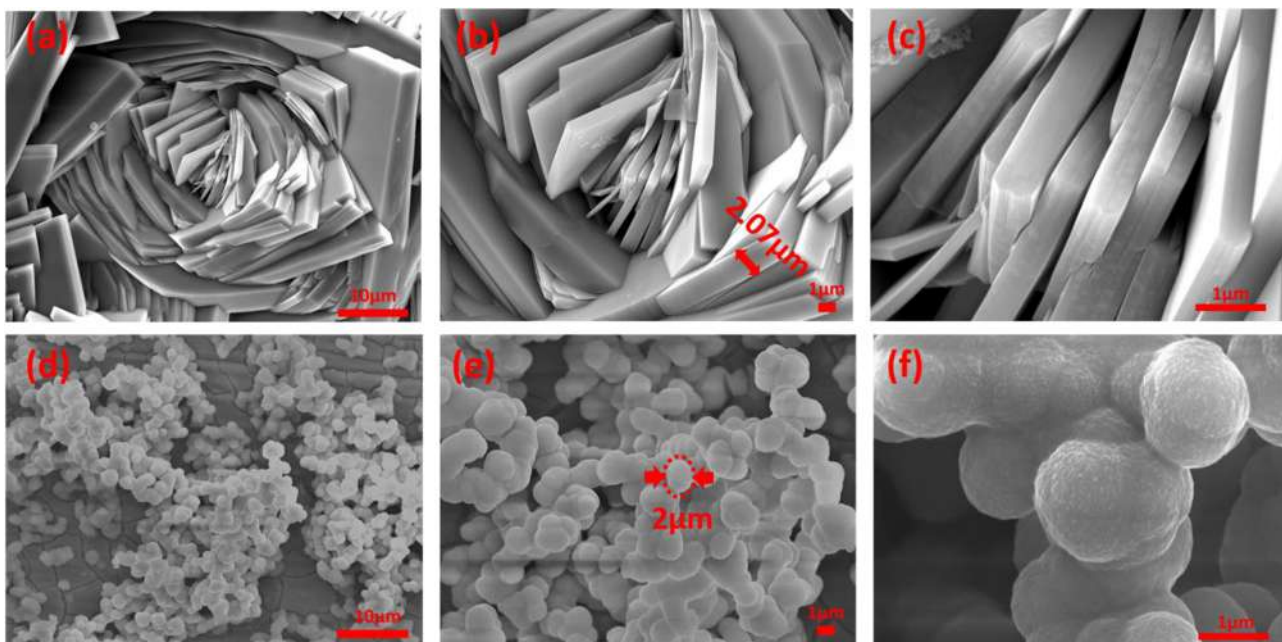


Fig. 4. SEM images of P1 (a-c) and P2 (d-f) electrode at different magnification (X2000, X5000 and X10000, respectively).

particle like morphology as shown in Fig. 4 (d–f). It seems like microspheres in Fig. 4 (d, e). At higher magnification in Fig. 4 (f) seen surface of microsphere fully filled with nanoparticles so may be it amorphous in nature. The microspheres prepared from nanoparticles have a diameter ranging from 1.2 to 2.2 μm , which makes rough surface. Rough surface may offer high surface area and it is important to improve performance of material. Sample P1 prepared using KH_2PO_4 as a precursor of phosphate in synthesis, bath solution shows less acidic medium (~ 4.1 pH) than sample P2 bath solution. Sample P2 prepared using H_3PO_4 as a phosphate source, it makes chemical solution bath highly acidic (~ 1.7 pH). At similar reaction condition two prepared material shows different morphologies it may be resulted due to variation in pH of bath solution. Similar change in morphology due to precursor variation observed by Li et. al., they prepared 3D tetrapod like morphology of Ag_3PO_4 material and this morphology altered to polyhedron due to precursor variation [20]. Also, Bi et al. demonstrated morphology and precursor relation, they prepared rhombic dodecahedral morphology of Ag_3PO_4 and it transformed via precursor variation into smooth surface with sharp edged cubic structure [21]. It resulted that, morphology of material varied by precursor variation which changes the pH of chemical bath.

In CBD method “bottom up” approach was used to deposit material on SS substrate. In this approach nucleation start on SS substrate by self-assembly process then material growth carried out by oriented attachment process. Precursor variation offers pH variation that ultimately influences morphology, schematic of material growth is shown in Fig. 5. Due to high pH of bath solution (P1 sample), after oriented attachment process further growth of material observed and that offers number of microplates which grown on each other and it seems like a microflower like structure. On the other hand, at low pH of bath solution (P2 sample), growth of material is based on disintegration and reconstruction, this may be happens due to less stability of particles at low pH. Further with extending reaction time rearrangement process of material carried out due to coalescence process and Ostwald ripening process tends to form spherical microstructure of the material. In this Ostwald ripening mechanism, a smaller or less stable nucleus get dissolve which is near to large crystal due to ion formation. Eventually smaller nucleus disappears and it results into expense of smaller nucleus or particles.

Fig. S1 (see ESI) display energy dispersive spectroscopy (EDS) of sample P1 and P2, which used to determine elemental composition of prepared material. It helps to identify the prepared material is made up from combining phosphorous with nickel and oxygen. The EDS spectra of sample P1 and P2 resulted that nickel, phosphorous and oxygen elements are existing in prepared samples. The atomic ratio of nickel and phosphorous in sample P1 and P2 are 1:0.56 and 1:0.76, respectively. From EDS result it confirm that prepared material is nickel phosphate in thin film form with different morphologies. Brunauer-Emmett-Teller (BET) analysis used to measure specific surface area of both samples. Both sample shows a type II isotherm according to classification of International Union of Pure and Applied Chemistry (IUPAC) and displayed in fig. S2 (see ESI). Sample P2 shows high specific surface area ($46.51 \text{ m}^2 \text{ g}^{-1}$) as compare to sample P1 ($36.09 \text{ m}^2 \text{ g}^{-1}$). BET confirms that microsphere like microstructure due to amorphous nature shows high surface area. The electrochemical performance of material may be improved due to high specific surface area.

3.3. Electrochemical study of nickel phosphate thin films

Precursor variation impact on supercapacitive performance tested by three electrode system in 1 M KOH electrolyte. CV curves of sample P1 and P2 electrode plotted in Fig. 6 (a), scanned at 5 mV s^{-1} scan rate in window 0–0.5 V (vs SCE). In comparative analysis of CV graph, P2 electrode shows much higher current area at very low scan rate of 5 mV s^{-1} as compare to P1 electrode. Amorphous nature of material offers high surface area which improve electrochemical performance of material in terms of current response in CV curve and it resulted in to high areal capacitance. All CV curves from 1 to 20 mV s^{-1} scan rate of P2 electrode are displayed in Fig. 6 (b). Area of CV curve increases with increasing scan rate and pseudocapacitive nature revealed from redox peak observed in CV graph [19]. Similarly, P1 electrode scanned from 1 to 20 mV s^{-1} scan rate, their CV graph at different scan rate are plotted and given in fig. S3 (a) (see ESI).

GCD analysis of prepared thin film electrodes carried out in potential window of 0–0.4 V (vs SCE) at various current densities. Comparative GCD graphs (at 0.5 mA cm^{-2} current density) of prepared P1 and P2 electrode are given in Fig. 6 (c). In this graph P1 electrode shows higher discharging time as compare to P2 electrode. Specific

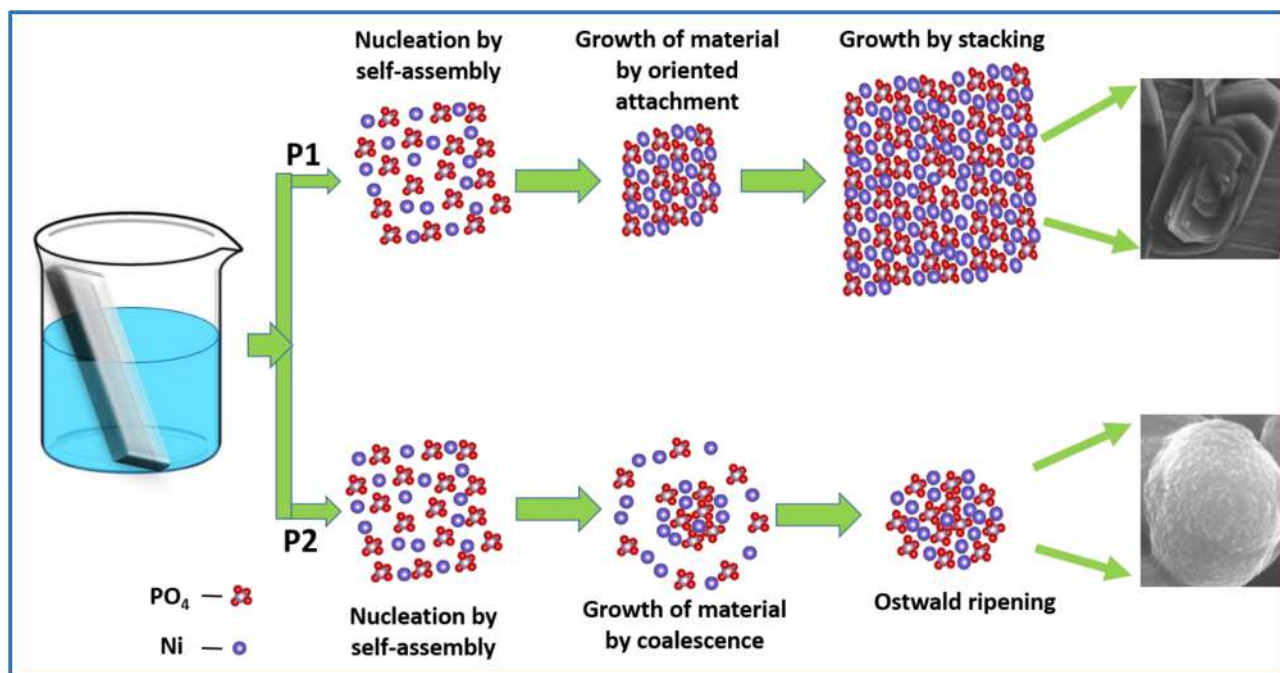


Fig. 5. Schematic representation of growth process of both crystalline and amorphous nickel phosphate material.

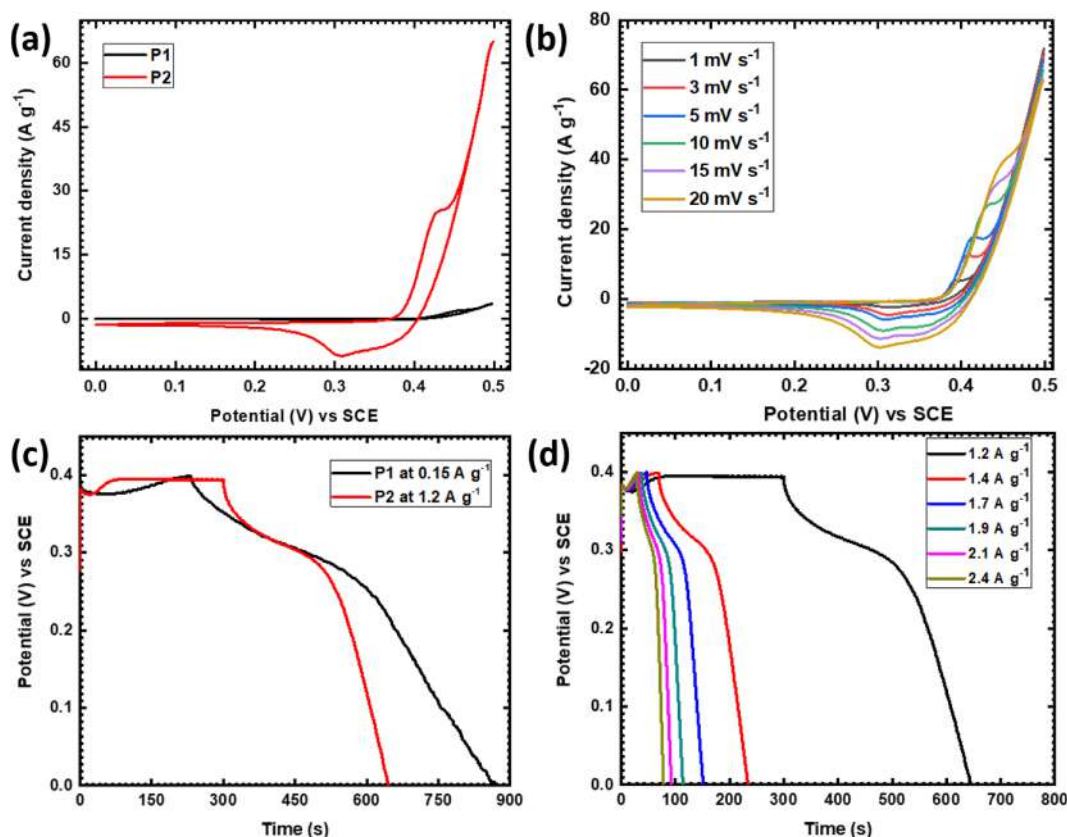


Fig. 6. (a) Comparative CV curves of P1 and P2 electrode at 5 mV s^{-1} scan rate, (b) CV curves of P2 electrode at different scan rate from 1 to 20 mV s^{-1} , (c) Comparative GCD graph of P1 and P2 electrode at gravimetric current density (at constant 0.5 mA cm^{-2} areal current density) and (d) GCD graph of P2 electrode at various gravimetric current density.

capacitance of prepared electrode by GCD graph calculated by following equation,

$$C_s = \frac{I \times \Delta t}{w \times \Delta V} (\text{F g}^{-1}) \quad (5)$$

where, C_s , I , Δt , w and ΔV are specific capacitance (F g^{-1}), current density (A), discharging time (s), weight of active material (g) and potential window (V), respectively. Areal capacitance of prepared electrodes by GCD graph calculated using following equation,

$$C_A = \frac{I \times \Delta t}{A \times \Delta V} (\text{mF cm}^{-2}) \quad (6)$$

where C_A , I , Δt , A and ΔV are specific capacitance (mF cm^{-2}), current density (mA cm^{-2}), discharging time (s), area of active material (cm^{-2}) and potential window (V), respectively. Furthermore, specific capacity calculated by the following equation [10],

$$Q_s = \frac{I \times \Delta t}{3.6 \times w} (\text{mAh g}^{-1}) \quad (7)$$

where, Q_s , I , Δt and w are specific capacity (mAh g^{-1}), current density (A), discharging time (s), weight of active material (g) and potential window (V), respectively.

The GCD curves of P2 electrode at various gravimetric current densities (at areal current densities of $0.5\text{--}1 \text{ mA cm}^{-2}$) are shown in Fig. 6 (d) and GCD graphs of P1 electrode are given in fig. S3 (b) (see ESI). The P2 electrode delivered highest specific capacitance of 1031.6 F g^{-1} (specific capacity 114.6 mAh g^{-1}) at 0.5 mA cm^{-2} areal current density and P1 electrode shows 249.3 F g^{-1} (specific capacity 27.7 mAh g^{-1}) at same current density. Specific capacitance with respect to current density graph for P1 and P2 electrode plotted and shown in Fig. 7 (a), as increase in current density specific capacitance of electrode decreases as decreasing discharging time and at low current

density offers higher specific capacitance. Specific capacitance is low at high current density because of all microstructures are not able to react with the electrolyte at high current density due to less interaction time [35]. Also, areal capacitance with respect to areal current density calculated using Eq. (6) and plotted in Fig. 7 (b). Obtained results are compared with available literature in Table S1 (see ESI) in terms of morphology, capacitance and stability [9,10,12,13,16–18]. Prepared amorphous nickel phosphate electrode exhibits little low capacitance as compare to reported data. This results observed may be due to SS substrate used as a current collector which does not added their capacitance but in all previous work nickel foam used as a current collector which takes part in electrochemical reaction and helps to improve the performance of active material by adding self capacitance [36].

EIS spectrum of nickel phosphate electrodes tested in the range of frequency $1 \text{ MHz}\text{--}10 \text{ mHz}$ at open circuit potential and plotted in Fig. 7 (c) with best fitted data for P2 electrode. Nyquist plot of P1 and P2 electrode reveals both material shows nearly similar solution resistance (R_s) (1.65 and 1.55Ω , respectively) but different charge transfer resistance may be due to different morphology. Low value of charge transfer resistance (R_{ct}) responsible for quick reaction kinetics and resulted into improved electrochemical performance [37]. The P2 electrode (180.2Ω) shows low R_{ct} value in comparison with P1 electrode (394.6Ω). Equivalent circuit for fitted data drawn and shown in inset of Fig. 7 (c). In fitted circuit R_s is solution resistance, R is a combined resistance of nickel phosphate film deposited on substrate, charge transfer and adsorption resistance, W is Warburg resistance and Q is general imperfect capacitor [38].

3.4. Asymmetric supercapacitor (ASC) device

Low crystalline or amorphous nature leads to improve

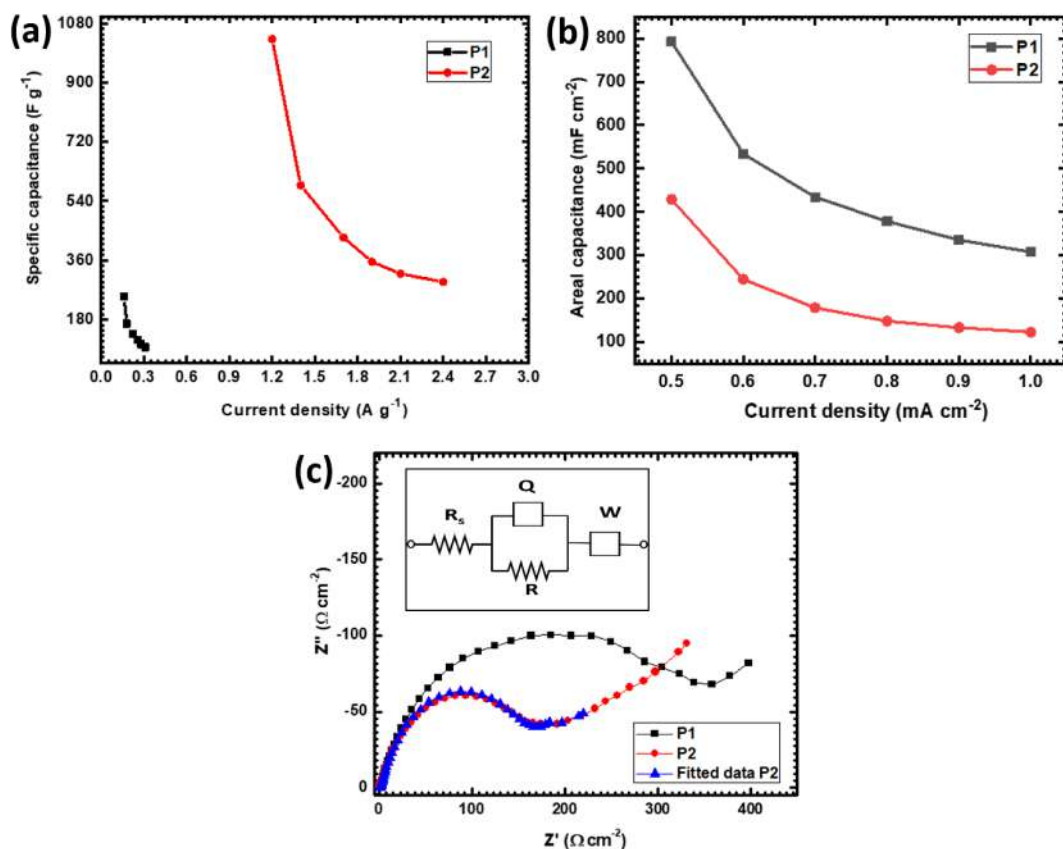


Fig. 7. (a) Graph of gravimetric specific capacitance vs gravimetric current density for P1 and P2 electrodes, (b) Graph of areal capacitance vs areal current density for P1 and P2 electrodes and (c) Nyquist plot of P1 and P2 electrodes (inset: equivalent circuit for P2 electrode).

electrochemical performance of electrode than well crystalline nature. So, practical usefulness of amorphous nickel phosphate electrode studied via preparing an asymmetric device. An asymmetric device fabricated using amorphous nickel phosphate (P2) thin film electrode as positive electrode and reduced graphene oxide (rGO) as negative electrode. Electrochemical study of rGO electrode carried out in 1 M KOH electrolyte in three electrode system. CV and GCD study of rGO electrode tested in negative window of 0 to -1 V (vs SCE) and graphs are given in fig. S4 (a) and (b) (see ESI), respectively. Specific capacitance of the rGO electrode calculated from GCD curve using Eq. (5). Specific capacitance with respect to current density graph plotted and shown in fig. S4 (c) (see ESI). The rGO electrode exhibits maximum specific capacitance of 163 F g^{-1} at 1.25 mA cm^{-2} current density. Nyquist plot of rGO electrode, fitted data and fitted circuit are shown in fig. S4 (d) (see ESI).

CV graph of amorphous nickel phosphate and rGO thin film electrodes at 20 mV s^{-1} scan rate in different potential window is shown in Fig. 8 (a), that is useful to select potential window for asymmetric device. In asymmetric device to obtain better results, theory of mass balance is most important, it was achieved by balancing mass of positive and negative electrode material using following equation,

$$\frac{m_+}{m_-} = \frac{C_- \times \Delta V_-}{C_+ \times \Delta V_+} \quad (8)$$

where, $m_{(+or-)}$, $\Delta V_{(+or-)}$, and $C_{(+or-)}$ are the mass of active material (g), potential window (V), and specific capacitance (F g^{-1}) of positive and negative electrode, respectively [39]. Optimal potential window for asymmetric supercapacitor (ASC) device decided from CV curves of device taking in different potential windows, shown in fig. S5 (a) (see ESI). Fig. S5 (a) suggest that 1.8 V is the best operating potential window for ASC device because above that potential, CV curve shows little straight line which demonstrate water splitting. Similar result

obtained from GCD curves of ASC device in different potential window, displayed in fig. S5 (b) (see ESI). CV curves of ASC device within optimal potential window at different scan rate from 5 to 100 mV s^{-1} tested and shown in Fig. 8 (b). Good reversibility of device revealed from high scan rate CV curve. Fig. 8 (c) demonstrated GCD curves of ASC device at various current densities from 6 to 10 mA cm^{-2} . Specific capacitance of ASC device from GCD graph calculated using Eq. (5) and plotted in Fig. 8 (d). ASC device exhibits highest specific capacitance of 100.7 F g^{-1} at 6 mA cm^{-2} current density and at higher current density it decreases up to 62.4 F g^{-1} . At higher current density less time is available for material and electrolyte interaction, but at lower current density ions can easily interact with material and stores higher charges.

The crucial factors in supercapacitors are energy density (E) and power density (P) calculated using equation as follows,

$$E = \frac{0.5 \times C_s \times (\Delta V)^2}{3.6} (\text{Whkg}^{-1}) \quad (9)$$

And

$$P = \frac{E \times 3.6}{\Delta t} (\text{kWkg}^{-1}) \quad (10)$$

where, C_s , ΔV , and Δt represents specific capacitance (F g^{-1}), potential window (V) and discharging time (s), respectively. Ragone plot of ASC device with the comparative literature data is plotted in Fig. 9 (a) [9,10,13,16–19]. ASC device delivers highest energy density of 45.33 Wh kg^{-1} at power density of 1.5 kW kg^{-1} . Composites of nickel phosphate on nickel foam shows little higher energy density values but only nickel phosphate shows lower values than present study. Nickel foam added their capacitance during charging discharging due to conversion of surface atom of Ni to NiO, it helps to improve total capacitance of electrode and device, and dominates actual active material performance [36]. But in this study, SS substrate used as a backbone to

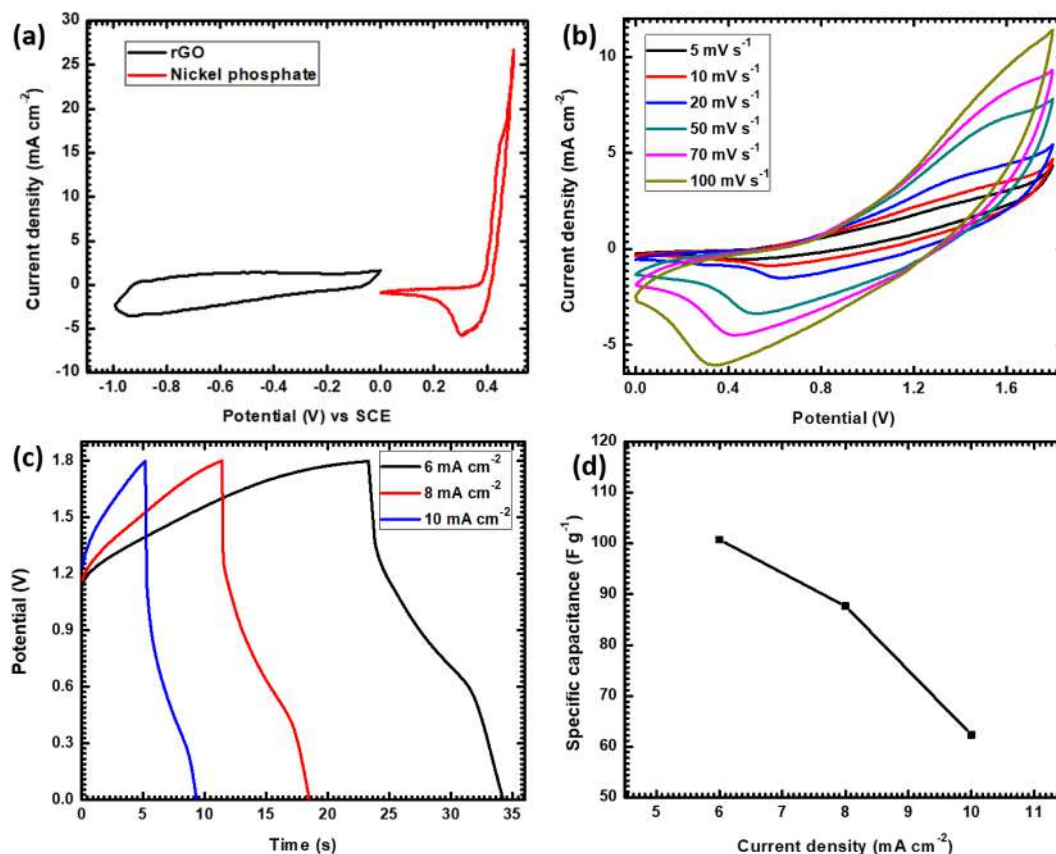


Fig. 8. (a) CV graphs of nickel pyrophosphate and rGO thin film electrodes at 20 mV s^{-1} scan rate, (b) CV graphs of ASC device at various scan rate from 5 to 100 mV s^{-1} , (c) GCD graph of ASC device at different current densities and (d) graph of specific capacitance with respect to current density of ASC device.

deposit material, which does not electrochemically active material to enhance electrochemical performance, it only plays a role of conducting collector. Herein, results reported are only of nickel phosphate and rGO as active materials.

Nyquist plot of ASC device and its fitted data are shown in Fig. 9 (b), EIS study carried out in the frequency range of 1 MHz – 100 MHz at open circuit potential. Semicircle in high frequency region represent charge transfer resistance (R_{ct}) between electrode and electrolyte, starting point of semicircle represents solution resistance (R_s) and straight line in low frequency region stands for Warburg resistance (W). Low R_{ct} value means fast kinetics of electrochemical reaction, which improve electrochemical performance. ASC device shows R_s and R_{ct} values of 1.78 and 237.69Ω , respectively. A low R_s value demonstrated high electrical conductivity of electrode material and electrolyte, it is important for good electrochemical performance [37]. Equivalent circuit of best fitted data shown in inset of Fig. 9 (b), in fitted circuit R_s is solution resistance, combination of R_1 and R_2 is charge transfer resistance, W is Warburg resistance and Q is general imperfect capacitor [40]. The electrochemical stability of ASC device tested in 1 M KOH over 3000 GCD cycles at 10 mA cm^{-2} current density and shown in Fig. 9 (c). Initial and final 10 cycles of GCD are plotted in the inset of Fig. 9 (c). After 3000 GCD cycles ASC device exhibits 80% capacitive retention, during initial steps material shows little improvement in the value of specific capacitance due to increment in active material volume during ions insertion and extraction [41]. Then decrement in mass of active material resulted into further little decrement in capacitance.

Overall in this study, selective morphologies are utilized to achieve high electrochemical performance of material. Crystalline to amorphous structure of nickel phosphate material is achieved by anion precursor variation. Amorphous phase phosphate material shows 4 fold

performance than crystalline. This results obtained due to amorphous material have number of defects in structure that may offers unique physical and chemical properties to it and which offers good electrochemical performance [42]. Electrolytic ions easily diffused in amorphous material due to its defect rich structure, which offers high surface area and useful to access more active material [43]. Also, amorphous material offers long term stability compared to its crystalline structure because amorphous structure does not offers changes in strain during charging/discharging [44]. It is underlined that, amorphous nickel phosphate material is better than the crystalline nickel phosphate.

4. Conclusions

We achieve crystalline and amorphous nature of nickel phosphate thin films using simple chemical bath deposition method by varying anion precursor. Morphological evaluation from microflower to microsphere observed due to precursor variation which is dependence on pH of reaction bath. Amorphous nickel phosphate shows better electrochemical results as compare to crystalline nickel phosphate. Amorphous nickel phosphate electrode delivers highest specific capacitance of 1031.6 F g^{-1} (specific capacity 114.6 mAh g^{-1}) at 0.5 mA cm^{-2} current density. ASC device fabricated using amorphous nickel phosphate as positive and rGO as negative electrode, it offers highest specific capacitance of 100.7 F g^{-1} at 6 mA cm^{-2} current density with energy density of 45.33 Wh kg^{-1} at 1.5 kW kg^{-1} power density, and delivered 80% specific capacitance retention over 3000 GCD cycles. These results reveals that, amorphous nickel phosphate material has a bright future in the field of energy storage devices.

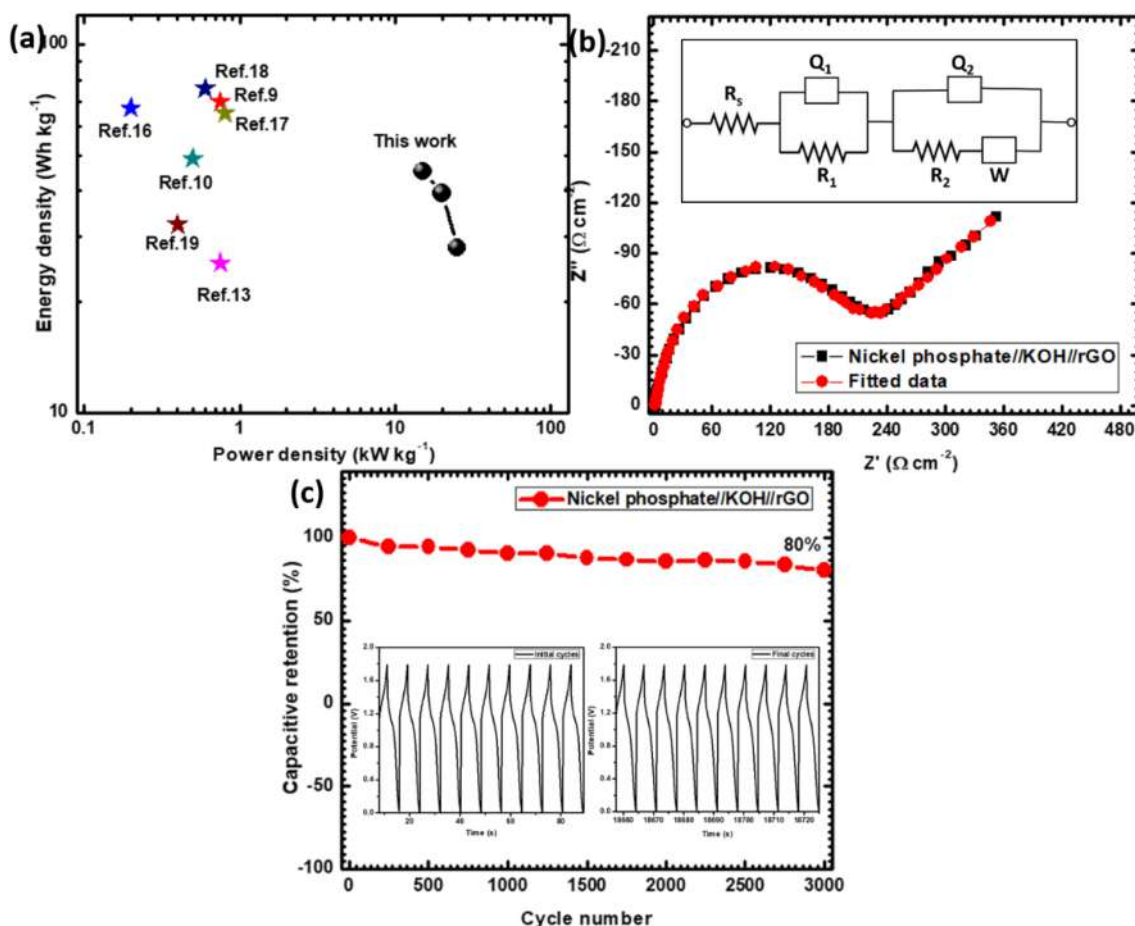


Fig. 9. (a) Ragone plot of ASC device with comparative data, (b) Nyquist plot of ASC device with fitted data (inset: equivalent circuit) and (c) Capacitive retention vs cycle number of ASC device at 10 mA cm⁻² current density (inset: initial (i) and final (ii) 10 cycles of GCD).

Declaration of Competing Interest

The authors declare that they have no known competing financial interests or personal relationships that could have appeared to influence the work reported in this paper.

Acknowledgment

Author UMP is thankful to Department of Science and Technology-Innovation in Science Pursuit for Inspired (DST-INSPIRE) for financial support through research project sanction no. DST/INSPIRE/04/2016/000260.

Appendix A. Supplementary data

Supplementary data to this article can be found online at <https://doi.org/10.1016/j.mseb.2020.114641>.

References

- [1] Y. Shao, M. El-Kady, J. Sun, Y. Li, Q. Zhang, M. Zhu, H. Wang, B. Dunn, R. Kaner, *Chem. Rev.* 118 (2018) 9233–9280.
- [2] U. Patil, M. Nam, J. Sohn, S. Kulkarni, R. Shin, S. Kang, S. Lee, J. Kim, S. Jun, J. Mater. Chem. A 2 (2014) 19075–19083.
- [3] U. Patil, S. Kulkarni, V. Jamadade, C. Lokhande, *J. Alloy Comp.* 509 (2011) 1677–1682.
- [4] U. Patil, K. Gurav, J. Kim, C. Lokhande, S. Jun, *Bull. Mater. Sci.* 37 (2014) 27–33.
- [5] X. Yu, L. Yu, H. Wu, X. Lou, *Angew. Chem. Int. Ed.* 54 (2015) 5331–5335.
- [6] S. Liu, K. Sankar, A. Kundu, M. Ma, J. Kwon, S. Jun, *A.C.S. Appl. Mater. Interfaces* 9 (2017) 21829–21832.
- [7] N. Padman Athan, H. Shao, K. Razeed, *ACS Appl. Mater. Interfaces* 10 (2018) 8599–8610.
- [8] Y. Gao, J. Zhao, Z. Run, G. Zhang, H. Pang, *Dalton Trans.* 43 (2014) 17000–17005.
- [9] K. Sankar, Y. Seo, S. Lee, S. Jun, *A.C.S. Appl. Mater. Interfaces* 10 (2018) 8045–8056.
- [10] A. Mirghni, M. Madito, K. Oyedotun, T. Masikhwa, N. Ndiaye, S. Ray, N. Manyala, *RSC Adv.* 8 (2018) 11608–11621.
- [11] J. Yang, J. Tan, D. Ma, *J. Power Sources* 260 (2014) 169–173.
- [12] J. Zhao, S. Wang, Z. Run, G. Zhang, W. Du, H. Pang, *Part. Part. Syst. Charact.* 32 (2015) 880–885.
- [13] X. Peng, H. Chai, Y. Cao, Y. Wang, H. Dong, D. Jia, W. Zhou, *Mater. Today Energy* 7 (2018) 129–135.
- [14] H. Pang, Y. Zhang, Z. Runa, W. Laib, W. Huang, *Nano Energy* 17 (2015) 339–347.
- [15] M. Pramanik, R. Salunkhe, M. Imura, Y. Yamauchi, *A.C.S. Appl. Mater. Interfaces* 8 (2016) 9790–9797.
- [16] J. Li, M. Liu, L. Kong, D. Wang, Y. Hu, W. Han, L. Kang, *RSC Adv.* 5 (2015) 41721–41728.
- [17] B. Senthilkumar, Z. Khan, S. Park, K. Kim, H. Ko, Y. Kim, *J. Mater. Chem. A* 3 (2015) 21553–21561.
- [18] F. Omar, A. Numan, N. Duraisamy, S. Bashir, K. Ramesh, S. Ramesh, *RSC Adv.* 6 (2016) 76298–76306.
- [19] F. Omar, A. Numan, S. Bashir, N. Duraisamy, R. Vikneswaran, Y. Loo, K. Ramesh, S. Ramesh, *Electrochim. Acta* 273 (2018) 216–228.
- [20] S. Li, F. Teng, M. Chen, N. Li, X. Hua, K. Wang, M. Li, *Chem. Phys. Lett.* 601 (2014) 59–62.
- [21] Y. Bi, S. Ouyang, N. Umezawa, J. Cao, J. Ye, *ACS J. Am. Chem. Soc.* 133 (2011) 6490–6492.
- [22] J. Gunjekar, Y. Jo, I. Kim, J. Lee, S. Patil, J. Pyun, S. Hwang, *J. Solid State Chem.* 240 (2016) 115–121.
- [23] D. Marciano, D. Kosynkin, J. Berlin, A. Sinitskii, Z. Sun, A. Slesarev, L. Alemany, W. Lu, J. Tour, *ACS Nano* 4 (2010) 4806–4814.
- [24] S. Navale, V. Mali, S. Pawar, R. Mane, M. Naushad, F. Stadler, V. Patil, *RSC Adv.* 5 (2015) 51961–51965.
- [25] M. Al-Omair, A. Touny, M. Saleh, *J. Power Sources* 342 (2017) 1032–1039.
- [26] D. Yang, Q. Yu, L. Gao, L. Mao, J. Yang, *Appl. Surf. Sci.* 416 (2017) 503–510.
- [27] P. Noisong, C. Danvirutai, T. Srihanratana, B. Boonchom, *Solid State Sci.* 10 (2008) 1598–1604.
- [28] W. Bian, Y. Huang, X. Xu, M. Din, G. Xie, X. Wang, *A.C.S. Appl. Mater. Interfaces* 10 (2018) 9407–9414.

- [29] T. Sun, L. Xu, Y. Yan, A. Zakhidov, R. Baughman, J. Chen, *ACS Catal.* 6 (2016) 1446–1450.
- [30] K. Kim, J. Jeong, S. Lee, B. Choi, K. Lee, *J. Colloid Interface Sci.* 484 (2016) 44–50.
- [31] P. Katkar, S. Marje, S. Pujari, S. Khalate, A. Lokhande, U. Patil, *A.C.S. Sustain. Chem. Eng.* 7 (2019) 11205–11218.
- [32] P. Feng, X. Cheng, J. Li, X. Luo, *ChemistrySelect* 3 (2018) 760–764.
- [33] J. Li, W. Xu, D. Zhou, J. Luo, D. Zhang, P. Xu, L. Wei, D. Yuan, *J. Mater. Sci.* 53 (2018) 2077–2086.
- [34] J. Theerthagiri, K. Thiagarajan, B. Sethilkumar, Z. Khan, R. Senthil, P. Arunachalam, J. Madhavan, M. Ashokkumar, *ChemistrySelect*, 2 (2107) 201–210.
- [35] F. Butt, M. Tahir, C. Cao, F. Idress, R. Ahmed, W. Khan, Z. Ali, N. Mohmood, M. Tanveer, A. Mohmood, I. Aslam, *A.C.S. Appl. Mater. Interfaces* 16 (2014) 13635–13641.
- [36] W. Xing, S. Qiao, X. Wu, X. Gao, J. Zhou, S. Zhuo, S. Hartono, D. Jurcakova, *J. Power Sources* 196 (2011) 4123–4127.
- [37] Y. Cheng, R. Li, D. Mu, J. Ren, J. Liu, C. Dai, *J. Electrochem. Soc.* 164 (2017) A1545–A1551.
- [38] P. Deshmukh, S. Pusawale, V. Jamadade, U. Patil, C. Lokhande, *J. Alloy Comp.* 509 (2011) 5064–5069.
- [39] K. Sankar, R. Selvan, D. Meyrick, *RSC Adv.* 5 (2015) 99959–99967.
- [40] N. Chodankar, D. Dubal, S. Ji, D. Kim, *Small* 15 (2019) 1901145–1901156.
- [41] Y. Jiang, L. Jiang, Z. Wu, P. Yang, H. Zhang, Z. Pan, L. Hu, *J. Mater. Chem. A* 6 (2018) 16308–16315.
- [42] J. Chen, J. Xu, S. Zhou, N. Zhao, C. Wong, *Nano Energy* 21 (2016) 145–153.
- [43] N. Zhang, S. Ouyang, T. Kako, J. Ye, *Chem. Commun.* 48 (2012) 9894–9896.
- [44] R. Yi, J. Feng, D. Lv, M. Gordin, S. Chen, D. Choi, D. Wang, *Nano Energy* 4 (2013) 498–504.



Hydrothermally synthesized Iron Phosphate Hydroxide thin film electrocatalyst for electrochemical water splitting

Suraj A. Khalate^a, Sujit A. Kadam^b, Yuan-Ron Ma^b, Sachin S. Pujari^a, Supriya J. Marje^a, Pranav K. Katkar^a, Abhishek C. Lokhande^c, Umakant M. Patil^{a,*}

^a Centre for Interdisciplinary Research (CIR), D. Y. Patil Education Society (Deemed to Be University), Kolhapur, 416 006, India

^b Department of Physics, National Dong Hwa University, Hualien, 97401, Taiwan

^c Department of Physics, Khalifa University of Science and Technology (KUST), Abu Dhabi, United Arab Emirates (UAE)

ARTICLE INFO

Article history:

Received 6 March 2019

Received in revised form

31 May 2019

Accepted 27 June 2019

Available online 28 June 2019

Keywords:

Electrochemistry

Hydrothermal synthesis

Heterogeneous catalysis

Ligand effects

Transition metals

Voltammetry

ABSTRACT

Hydrogen production is an immediate need to replace the fossil fuels to keep environmental balance, and water splitting is an effective solution in presence of catalyst through oxygen evolution reaction (OER) and hydrogen evolution reaction (HER). Herein, for the first time, we have synthesized Iron Phosphate Hydroxide ($\text{Fe}_{2.95}(\text{PO}_4)_2(\text{OH})_2$) thin film electrode as a superior electrocatalyst by facile hydrothermal method using binder free approach. The crystallographic properties are studied from X-ray diffraction pattern, and Reitveld refinement analysis shows best fit with the tetragonal Lipscombite structure of Iron Phosphate Hydroxide ($\text{Fe}_{2.95}(\text{PO}_4)_2(\text{OH})_2$). Flower like structure consist of agglomerated nanorods on micro and sub-micrometric spheres of $\text{Fe}_{2.95}(\text{PO}_4)_2(\text{OH})_2$ exhibits lower overpotential of 281 mV at 10 mA/cm² current density towards OER in alkaline (1 M KOH) medium and maintains its activity after 12 h catalytic stability test. Moreover, prepared electrode shows HER with overpotential 165.7 mV at current density 10 mA/cm² in acidic (1 M H_3PO_4) medium and demonstrates enhanced performance (126.4 mV overpotential) after 12 h catalytic stability. The $\text{Fe}_{2.95}(\text{PO}_4)_2(\text{OH})_2$ thin film electrodes show superior performance in OER and HER, compared with its oxide counterpart (Fe_2O_3).

© 2019 Elsevier Ltd. All rights reserved.

1. Introduction

Now days, a very intense work focused on the renewable energy generation by different sources such as wind [1], solar [2], hydrodynamical [3], tidal [4] and geothermal [5], and utilization in terms of electrical energy to control the global energy crisis and reduce environmental issues. Hydrogen is one of the most clean and potential renewable energy sources and the electrolysis of water to generate Oxygen and Hydrogen molecules is the cost-effective and efficient approach to get renewable energy [6–9]. The hydrogen evolution reaction (HER) and oxygen evolution reaction (OER) are the fundamentals of typical water splitting reaction and HER is comparatively easy which takes place at low overpotential. On the other hand, water splitting efficiency is largely constrained by the rate determining sluggish oxygen evolution reaction (OER), which involves four proton-coupled electron transfer causes high overpotential for O_2 assembly. In

electrochemical energy sources, appropriate electrocatalysts are crucial components of an energy efficient hydrogen generation. To minimize the overpotential for OER and energy losses, a good electrocatalyst must have high catalytic activity, superior conductivity and adequate electrocatalytic stability. The state-of-the-art electrocatalysts considered to the noble metal-based valuable materials such as Platinum (Pt), Ruthenium (Ru) and Iridium Oxides (IrO_2) have an identity as best OER catalysts due to low overpotential [10–12]. However, these metals are very rare in the Earth's crust, thus it is difficult to commercialize them. To create the significant development in the field of electrocatalysis and there is need to replace the conventional electrocatalysts. Amongst various non-noble metal catalysts, transition metals are the promising alternative for these rare metal electrocatalysts due to their smaller d orbitals, lower crystal-field activation energies and competent bifunctional catalytic properties for water splitting. The materials of transition metals as Hydroxides, Sulphides, Selenides, Phosphates, Phosphides, Nitrides, have great interest due to their Earth abundance, high-efficiency and stability for large-scale energy production [13–20].

* Corresponding author.

E-mail address: umakant.physics84@gmail.com (U.M. Patil).

Very recently, Fe-based materials are used as electrocatalysts for OER, HER and ORR activity. The intentional and incidental incorporation of Fe in the $\text{Ni}_{0.75}\text{Fe}_{0.25}(\text{OH})_2$ as OER electrocatalyst was studied by Trotochaud et al. and shows that, Fe exerts a partial-charge transfer activation effect on Ni [21]. Off late, there is increasing attention towards the transition metal based Phosphate materials due to its attractive properties such as, unique atomic geometry with open channels and high catalytic performance. The Phosphate groups gives favourable condition for water molecule adsorption and oxidation by distorting local atomic geometry and facilitating the oxidation of metal atoms during proton coupled electron transfer process. The compounds of transition metal Phosphates have been used as potential electrocatalysts, especially Cobalt, Manganese and Nickel based Phosphates [22–25]. Three dimensional Nickel Phosphate was synthesized on Nickel foam (which act as conducting support and Nickel source itself) by autologous hydrothermal and Fe was doped by electrodeposition to study the synergistic effect of doped Iron and Nickel Phosphate on OER action [25]. Wang et al. synthesized FeCo Phosphate composite particles by co-precipitation method and drop casted at room temperature using Nafion solution to bind the particles on the Carbon paper, which exhibits 273 mV overpotential at 10 mA/cm^2 current density [26]. Fe-substituted Nickel Phosphate was synthesized by chemical precipitation using Potassium Phosphate buffer solution (containing K_2HPO_4 and KH_2PO_4) and $\text{NiCl}_2 \cdot 4\text{H}_2\text{O}$ as precursors of Phosphorus and Nickel, respectively. The ink of prepared Fe-substituted Nickel Phosphate catalyst with Carbon black dispersed in Nafion solution, and drop-casted on glassy carbon electrode (GCE), which shows 330 mV overpotential at 10 mA/cm^2 current density [24]. FeP nanoarray derived Iron Phosphate Borate nanoarrays show 434 mV to drive 10 mA/cm^2 current density for OER [27]. Hollow Iron Phosphide–Phosphate composite nanotubes synthesized by template-free hydrothermal coprecipitation method and drop casted on GCE shows 280 mV overpotential [28]. The alkali Iron Phosphates (NaFePO_4 and KFePO_4) synthesized by solution combustion with Carbon coating, exhibits good oxygen reduction reaction (ORR) activity [29]. Only few groups studied the bifunctional water splitting catalytic property of Phosphate based materials. Yoon et al. have synthesized porous and granular Cobalt Iron-Phosphorous ($\text{Co}_x\text{Fe}_{1-x}\text{-P}$) by electrodeposition method and reported 290 mV overpotential at 10 mA/cm^2 for OER and 169 mV overpotential at 10 mA/cm^2 for HER [30]. The microrod like $\text{Ni}_{11}(\text{HPO}_3)_8(\text{OH})_6$ exhibits 232 mV and 121 mV overpotential for OER and HER, respectively [31]. Still there is no single report on OER and HER by using directly grown (binder free) Iron Phosphate thin film electrocatalyst.

For the first time, we report the synthesis of Iron Phosphate thin film electrocatalyst using facile hydrothermal method. Herein, we are demonstrating the electrocatalytic oxygen evolution reaction (OER) and hydrogen evolution reaction (HER) performances of binder free Iron Phosphate and Iron Oxide thin films synthesized by hydrothermal method on the stainless steel (SS) substrates. The structural, morphological, compositional and electrochemical properties of as synthesized Iron Phosphate thin films are explored in detail.

2. Experimental section

2.1. Materials and substrate cleaning

The analytical reagent grade precursors and salts of Ferric Chloride (FeCl_3) (99% pure), Sodium Nitrate (NaNO_3) (99% pure), Potassium Dihydrogen OrthoPhosphate (KH_2PO_4) (98% pure) from Sigma-Aldrich were purchased and used as it was without any further purification process. The doubly distilled water (DDW) was

used as a solvent for all chemicals. The flexible SS-substrates were cut into the pieces ($1 \text{ cm} \times 6 \text{ cm}$) and very fine polished by zero grade polish paper to clean. The polished substrates then thoroughly rubbed in laboratory soap solution and washed several times by DDW. The washed substrates then transferred in the mixture of Ethanol (99.9% pure) and DDW with the ratio 3:7 and ultrasonicated for 10 min.

2.2. Synthesis of Iron Phosphate and Iron Oxide thin films

A single step reaction procedure was followed for the direct growth of Iron Phosphate thin films on SS-substrates by hydrothermal method. A hydrothermal bomb was prepared for the reaction of Iron Phosphate thin films by 50 ml solution of NaNO_3 (1 M) and KH_2PO_4 (0.15 M) keeping for continuous stirring with vigorous addition of 30 ml FeCl_3 (0.15 M) solution. The resulting solution containing cleaned SS-substrates were transferred to the teflon lined hydrothermal bomb. The closed hydrothermal bomb was kept in oven at 130°C constant temperature for 14 h. To study the effect of the thickness of film on the electrochemical performance, Iron Phosphate thin films were deposited for different reaction time (8 h, 10 h, 12 h, 14 h and 16 h). Furthermore, for the comparison, another reaction solution was prepared for Iron Oxide thin films by adding 50 ml solution of NaNO_3 (1 M) and 30 ml FeCl_3 (0.15 M) solution in the teflon lined hydrothermal bomb at same reaction parameters as above for 14 h. The deposited Iron Phosphate and Iron Oxide thin films were removed from the reaction bomb, washed twice in DDW and dried at ambient temperature. As prepared thin films used for the further characterizations and electrochemical water splitting.

2.3. Physical characterizations

The structural and crystallographic characteristics of Iron Phosphate and Iron Oxide thin films were analyzed by X-ray diffractometer D2-Phaser with the radiation source copper K_α ($\lambda = 1.5406 \text{ \AA}$) in the range (2θ) 10° – 90° . The Fourier transform infrared (FTIR) spectra were recorded in the range (400 – 4000 cm^{-1}) with Alpha (II) Bruker spectroscope. The morphological properties and chemical composition were studied by the FE-SEM and EDX spectroscopy (JSM-7001F, JEOL FE-SEM Spectrometer).

2.4. Electrochemical characterizations

All electrochemical performances were studied on ZIVE MP1 electrochemical workstation in standard three electrode configuration cell. Platinum metal plate as a counter electrode and a Saturated Calomel Electrode (SCE) (saturated KCl) was used as a reference electrode. The SS metal plates with directly deposited Iron Phosphate and Iron Oxide catalysts thin films were used as a working electrodes ($\text{Area} = 1 \text{ cm}^2$). To measure OER activity, 1 M KOH solution ($\text{pH} = 14$) was used as electrolyte and for HER measurement, 1 M H_3PO_4 ($\text{pH} = 1.5$) electrolyte was preferred. The electrochemical catalytic response in terms of OER and HER were measured using linear sweep voltammetry (LSV) at scan rate 5 mV/s in the potential window 0 to $+0.6 \text{ V}$ vs SCE (for OER) and 0 to -1.2 V vs SCE (for HER). The cyclic voltammetry (CV) tests were carried out in the potential window 0 to $+0.5 \text{ V}$ vs SCE at 50 mV/s scan rate. The electrochemical impedance spectroscopic (EIS) studies were carried out in frequency range of 0.1 MHz – 100 mHz . The chronoamperometric measurements were followed for the long term stability tests. All the SCE potentials are then converted in terms of Reversible Hydrogen Electrode (RHE) potentials and the overpotential calculated by equations (1) and (2), respectively:

$$V_{\text{RHE}} = V_{\text{SCE}} + 0.059 \times \text{pH} + 0.241 \quad (1)$$

$$\eta = V_{\text{RHE}} - 1.23 \quad (2)$$

where, V_{RHE} (V) is the potential in terms of Reversible Hydrogen Electrode (RHE), V_{SCE} (V) is the potential in terms of Saturated Calomel Electrode (SCE), and η (V) is the overpotential.

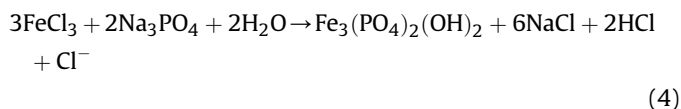
3. Results and discussion

3.1. Reaction mechanism and film formation

Synthesis of Iron Phosphate and Iron Oxide thin films was achieved by the facile hydrothermal method on SS-substrates. Basically, hydrothermal method is “bottom-up” approach, which is based on the formation of solid phase followed by the nucleation, coalescence and particle growth steps from the reaction solution. The particle development process from precursor solution is classified with subsequent crystal growth, as the homogeneous and heterogeneous nucleation. When particle seeds produced on the heterogeneous substrate, the subsequent growth of a uniform thin film is feasible. Sodium Nitrate (NaNO_3) is used as an oxidizing agent in the reaction along with Ferric Chloride (FeCl_3), and Potassium Dihydrogen OrthoPhosphate (KH_2PO_4) as precursors of Iron and Phosphorus, respectively. By the addition of KH_2PO_4 and NaNO_3 solutions, reaction takes place and forms Trisodium Phosphate with HNO_3 and KOH by-products, as given in reaction Eq. (3).



Furthermore, after addition of FeCl_3 in the solution, it reacts with Trisodium Phosphate (Na_3PO_4) and forms a product of Iron Phosphate in the solid form. The reaction equation for the Iron Phosphate solid formation is proposed as given in Eq. (4).



The formation of Iron Phosphate at the molecular level occurs by the heterogeneous nucleation on the SS-substrate. These nuclides grow by coalescing to form a crystalline uniform thin layer of Iron Phosphate. The above reaction mechanism takes place at 130°C and 17 psi hydrothermal pressure. Thickness of the film was measured by weight difference method and it exhibits around 551 nm for 14 h reaction time.

3.2. Structural analysis

The crystallographic properties were studied by X-ray diffraction patterns and shown in Fig. 1. Fig. 1(a) shows the diffraction pattern of Iron Phosphate thin film deposited on SS-substrate. The diffraction pattern matched with standard JCPDS data (Card No.-98-004-5827) and confirms that, the deposited material is tetragonal Lipscombite structured Iron Phosphate Hydroxide ($\text{Fe}_{2.95}(\text{PO}_4)_2(\text{OH})_2$) having space group “p 41 21 2”. The Fig. 1(a) also shows the Reitveld refinement patterns of $\text{Fe}_{2.95}(\text{PO}_4)_2(\text{OH})_2$; where, red dotted pattern represents the observed diffraction data, black line pattern represents calculated data, vertical green ticks represents the possible Bragg diffraction positions and blue line pattern represents the difference between observed and calculated data. The structural parameters of $\text{Fe}_{2.95}(\text{PO}_4)_2(\text{OH})_2$ after refinement were found to be: $a = b = 7.30608 \text{ \AA}$, $c = 13.07000 \text{ \AA}$ and cell volume = 697.660939 \AA^3 . Other specified crystallographic and cell

refinement parameters are given in Table S1 and Table S2 provides its atomic co-ordinates. The 3D structural illustrations of the $\text{Fe}_{2.95}(\text{PO}_4)_2(\text{OH})_2$ crystal are designed in Vesta software from the output files of Reitveld refinement and shown in Fig. 1(b and c). The $\text{Fe}_{2.95}(\text{PO}_4)_2(\text{OH})_2$ framework is built by sharing the edges of three polyhedra of FeO_6 bridging with the four PO_4 tetrahedra, whereas Phosphate ligands are arranged at 8b Wyckoff sites and distort the cell geometry by providing large tunnels throughout the crystal structure. Large tunnels are one of the reason for large cell volume, and favourable to increase the swelling-shrinking capacity during catalysis, which may increase the durability of the catalyst. On the other side, X-ray diffraction pattern with Reitveld refinement patterns of Fe_2O_3 is shown in Fig. 1(d). Diffraction pattern in Fig. 1(d) is in good matching with the standard JCPDS data (Card No.-98-002-3369) and proves hexagonal Hematite structure of Iron(III) Oxide-Alpha (Fe_2O_3) having space group “R-3 c”. The structural parameters of Fe_2O_3 after refinement were found to be: $a = b = 5.06992 \text{ \AA}$, $c = 13.89790 \text{ \AA}$ and cell volume = 309.372728 \AA^3 . The cell refinement and specified crystallographic parameters are given in Table S3 and Table S4 provides its atomic co-ordinates. The 3D structural illustrations of the Fe_2O_3 crystals are shown in Fig. 1(e and f). Fe_2O_3 framework is built by sharing corners of the FeO_3 trihedra interlinked with another FeO_3 trihedra, distinguishing open tunnels along a and b axes. The Fe^{3+} ion species are occupied 12c Wyckoff positions. As compared to Fe_2O_3 , $\text{Fe}_{2.95}(\text{PO}_4)_2(\text{OH})_2$ crystal have wide open channel structure along a, b, and c axes as shown in Fig. S1.

3.3. FTIR vibrational analysis

Fourier Transform Infra-Red (FTIR) spectroscopy was used to analyze the molecular bond formation in the hydrothermally synthesized $\text{Fe}_{2.95}(\text{PO}_4)_2(\text{OH})_2$ and Fe_2O_3 thin films. The FTIR spectra from wavenumber 400 to 2000 cm^{-1} having intermolecular vibrations of metal-oxygen (M-O) bonding and Phosphate anion (PO_4^-) as shown in Fig. 1(g). The absorption bands at 463.29 cm^{-1} can be ascribed for the Fe-O vibrational modes from $\text{Fe}_{2.95}(\text{PO}_4)_2(\text{OH})_2$. The bending vibrational region (from wavenumber 500 to 650 cm^{-1}) shows the absorption peaks of symmetric and asymmetric bending vibrations of PO_4 bonding at 565.36 cm^{-1} and 595.30 cm^{-1} , respectively. The absorption bands of PO_4 symmetric and asymmetric stretching are observed at 945.3 and 1065 cm^{-1} , respectively [29]. The vibrational stretching absorption of water molecule is observed at 1629.14 cm^{-1} wavenumber. For Fe_2O_3 sample, the peaks observed at 436.88 , 461.58 and 619.18 cm^{-1} are the stretching vibrational absorption bands of Fe-O molecule and the peak at 1085.48 cm^{-1} gives the stretching vibrational band of FeOOH molecule [32]. The H-O-H i.e. water molecule vibrational stretching absorption is observed at the wavenumber 1626.82 cm^{-1} [33]. The high wavenumber (2000 – 4000 cm^{-1}) are given in Fig. S2 in ESI. Fig. S2 shows the broad vibrational band of O-H molecules. Broadening of the absorption band for $\text{Fe}_{2.95}(\text{PO}_4)_2(\text{OH})_2$ exhibits that, formation of hydroxide, and is supportive to the XRD results.

3.4. Surface morphological and elemental analysis

Surface morphological properties of $\text{Fe}_{2.95}(\text{PO}_4)_2(\text{OH})_2$ and Fe_2O_3 thin films deposited for 14 h reaction time on SS-substrates were studied and shown in Fig. 2. The Fig. 2(a–d) shows the FE-SEM images of $\text{Fe}_{2.95}(\text{PO}_4)_2(\text{OH})_2$ thin films at different magnifications, and confirms the presence of sub-micrometric grains of the size around $0.261 \mu\text{m}$ and distributed on and around the large particles (average size around $1.291 \mu\text{m}$). The microparticles are formed due to the agglomeration of small particles during growth

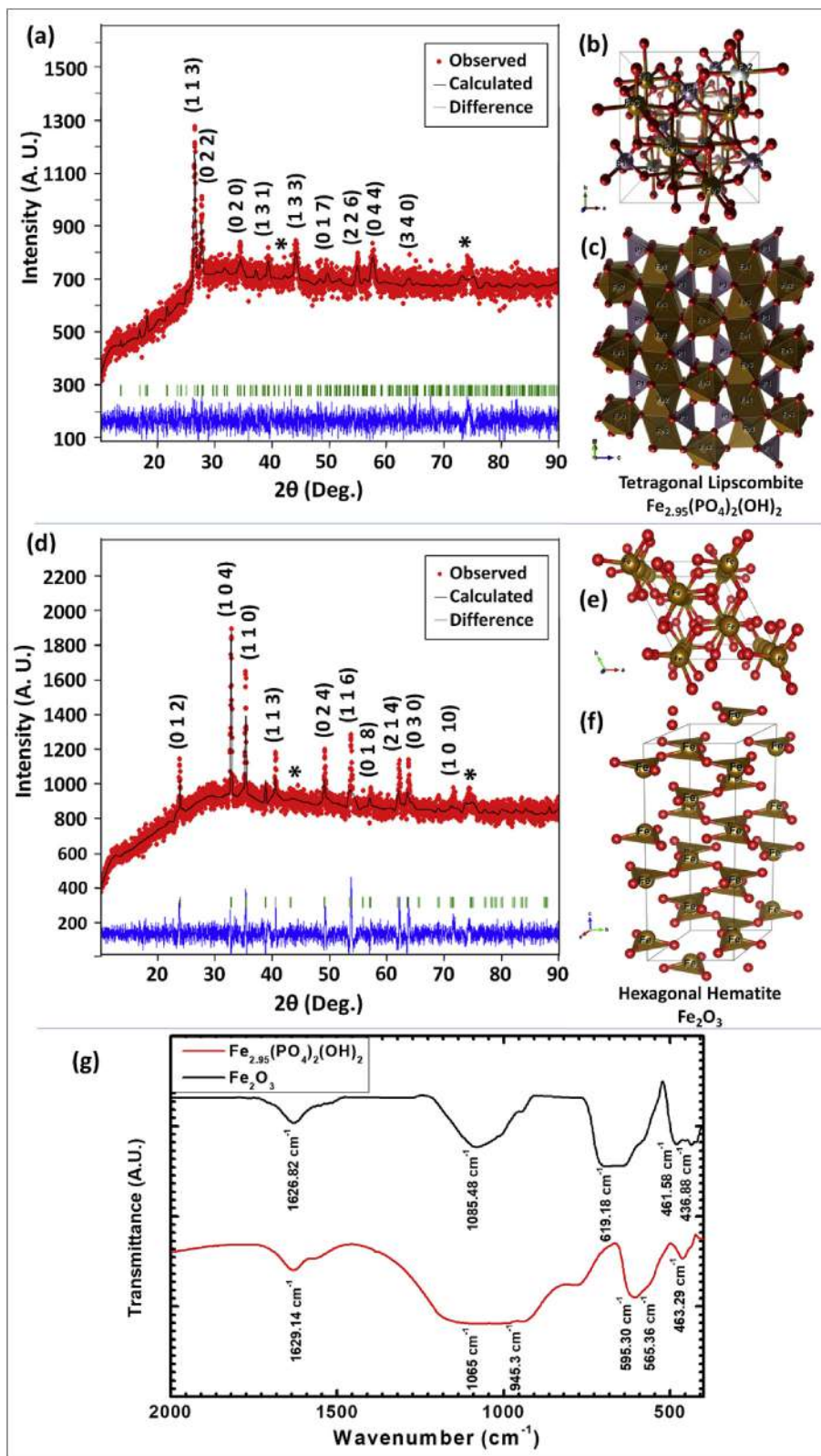


Fig. 1. (a) XRD patterns with Reitveld refinement patterns of $\text{Fe}_{2.95}(\text{PO}_4)_2(\text{OH})_2$, (b, c) 3D-crystal structures of $\text{Fe}_{2.95}(\text{PO}_4)_2(\text{OH})_2$ defined from fitting data and plotted in Vesta software, (d) XRD patterns with Reitveld refinement patterns of Fe_2O_3 thin films deposited at 14 h reaction time, and (e, f) 3D-crystal structures of Fe_2O_3 defined from fitting data and plotted in Vesta software, and (g) FTIR spectroscopic analysis of $\text{Fe}_{2.95}(\text{PO}_4)_2(\text{OH})_2$ and Fe_2O_3 thin films.

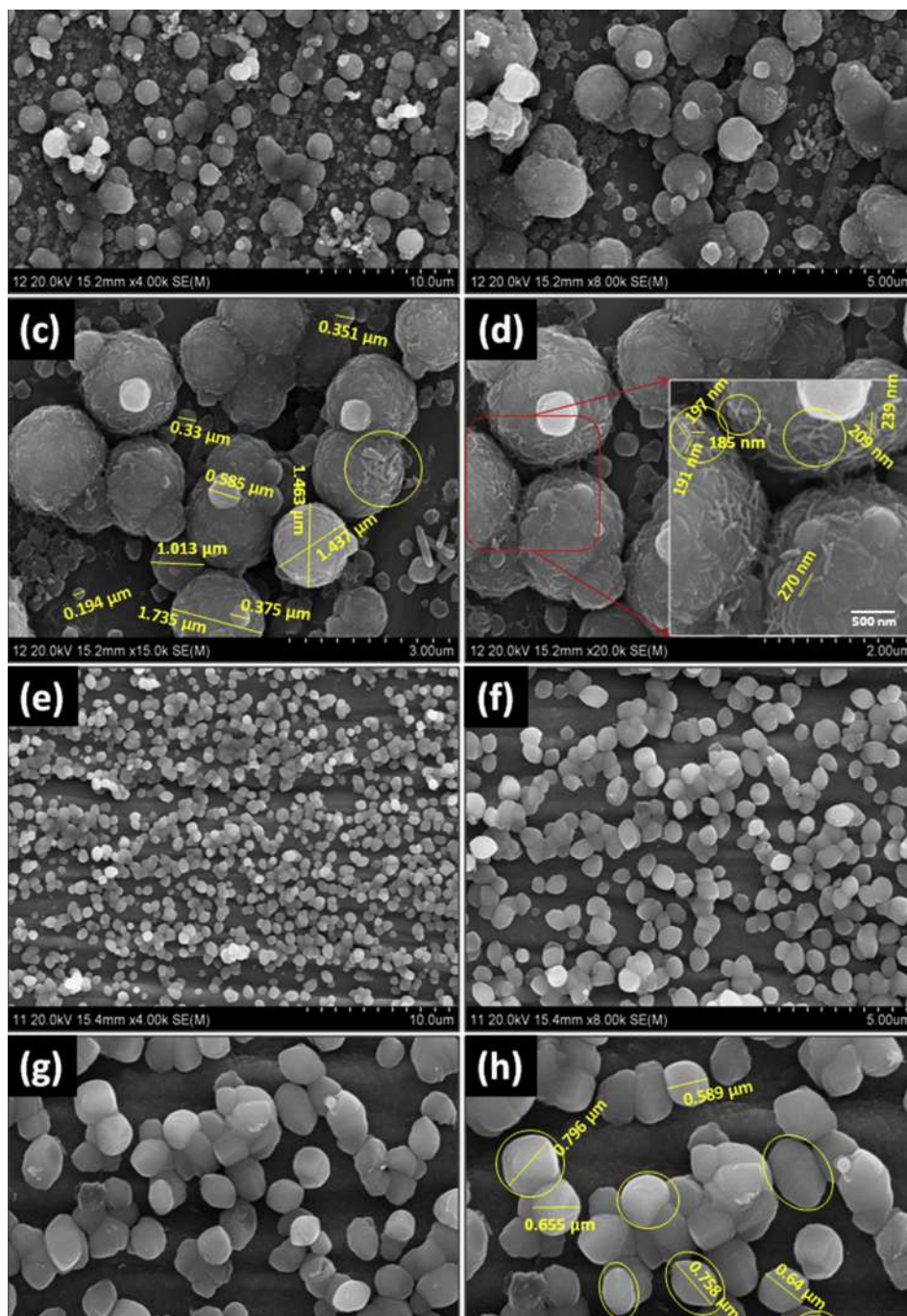


Fig. 2. Surface morphology of $\text{Fe}_{2.95}(\text{PO}_4)_2(\text{OH})_2$ thin film at different magnifications (a) 4 K, (b) 8 K, (c) 15 K and (d) 20 K; surface morphology of Fe_2O_3 thin film at different magnifications (e) 4 K, (f) 8 K, (g) 15 K and (h) 20 K.

of the film. With the closer eye of the FE-SEM, it is observed that the surface of $\text{Fe}_{2.95}(\text{PO}_4)_2(\text{OH})_2$ microspheres is rougher compared with the Fe_2O_3 . The nanorods (~210 nm length) are grown and agglomerated individually on the microspheres and some nanorods look like nanoflakes over microspheres (shown in circles of Fig. 2(d)). From Fig. 2(d), it is observed that the Fe_2O_3 particles are uniformly distributed over the substrate. With the high magnification of FE-SEM, it is observed that the spherical and spheroidal sub-micrometric individual particles of size around 0.733 μm . The spherical and spheroidal shapes of the particles are highlighted by the circles and ellipses in Fig. 2(h). Overall particle size around

1–1.3 μm is observed for all $\text{Fe}_{2.95}(\text{PO}_4)_2(\text{OH})_2$ thin films deposited for 8 h, 10 h and 16 h reaction time (see Fig. S3 in ESI). Interestingly, the surface modification of the spheres is observable for the reaction time 8 h to 16 h, shown in higher magnification FE-SEM images (see ESI Figs. S4(a–e)). For 8 and 10 h reaction time, deposited material show smooth surface of microparticles, moreover the nanorods and nanoflakes are observed over the microspheres for 12–16 h reaction time. Nanosized flake like structures (200–225 nm) is observed over microspheres of $\text{Fe}_{2.95}(\text{PO}_4)_2(\text{OH})_2$ deposited for 12 h reaction time. For 16 h reaction time, there are completely agglomerated flakes can be seen over the microsphere.

Such nanorod like and nanoflake like structure can provide large surface area, which is beneficial for the catalytic activity. To confirm elemental presence and their percentage, EDS analysis is performed. Figs. S5(a and b) shows the graphical representation of elements and inset tables show weight and atomic percentages of the $\text{Fe}_{2.95}(\text{PO}_4)_2(\text{OH})_2$ and Fe_2O_3 samples. It is observed that, the $\text{Fe}_{2.95}(\text{PO}_4)_2(\text{OH})_2$ sample contains Fe/O ratio is 0.98:1 and Fe/P ratio is 4.5:1 and Fe_2O_3 sample contains atomic ratio of Fe/O is 1.31:1. It confirms that, the Iron rich $\text{Fe}_{2.95}(\text{PO}_4)_2(\text{OH})_2$ and Fe_2O_3 is formed.

3.5. Electrochemical catalytic performance analysis

The electrochemical properties of the as prepared thin films of $\text{Fe}_{2.95}(\text{PO}_4)_2(\text{OH})_2$ were tested for the electrochemical water splitting in terms of OER and HER. To evaluate the catalytic activity, the linear sweep voltammetry (LSV) analysis was carried out in 1 M KOH electrolyte for OER and in 1 M H_3PO_4 electrolyte for HER test at 5 mV/s scan rate. The polarization curves for OER activity were plotted in potential range 1.05–1.65 V vs RHE for $\text{Fe}_{2.95}(\text{PO}_4)_2(\text{OH})_2$ thin films deposited at different reaction time and shown in Fig. 3(a). All the LSV curves show similar nature and continuous increase in current density with increasing thickness of the film up to the 14 h deposition time and again decreases for further. It confirms that, the most active thickness was achieved by the deposition for 14 h and it is obtained around 551 nm. The $\text{Fe}_{2.95}(\text{PO}_4)_2(\text{OH})_2$ thin film deposited for 14 h reaction time shows low overpotential 281 mV at 10 mA/cm² current density and very high current density about 125 mA/cm² at 420 mV overpotential. To evaluate electrocatalytic activity, the materials were further

examined by the cyclic voltammetry (CV) tests, performed in the potential window of 0 to +0.55 V vs SCE (1.05–1.55 V vs RHE) at constant scan rate 50 mV/s. All the redox (oxidation/reduction) peaks observed in cyclic voltammogram are due to the conversion of Fe^{2+} to Fe^{3+} and vice versa, during the anodic and cathodic sweeps of voltage [34]. The $\text{Fe}_{2.95}(\text{PO}_4)_2(\text{OH})_2$ thin films deposited at 14 h shows best cyclic performance than the other catalyst, as shown in Fig. 3(b). It is observed that, the optimum thickness of electrode shows excellent performance. Such result observed due to the presence of the abundant active sites at sufficient thickness of material for intercalation/deintercalation of ions and efficient charge transfer. At lower thickness, the deposited material may not offers sufficient active sites to show better electrochemical current-voltage response. On the other hand, when the film thickness exceed from its optimum thickness, the charge transfer from one site to the other up to the charge collecting plate (SS) becomes sluggish and more resistive.

The variation of overpotential as a function of reaction time is plotted as bar diagram in Fig. 3(c). The values of overpotential and onset potential for all samples are tabulated in Table S5. The close proximity into OER mechanism and reaction rate kinetics of the catalytic activity are obtained by Tafel plot and slope which signify different rate determining steps enclosed by a given pathway. If the OER catalyst have higher OH^- ion affinity to adsorb on the surface and form an OH^- intermediate then the electrocatalytic O_2 generation is efficient. If the formation of that intermediate state attain faster, then those steps are the rate determining. Fig. 3(d) shows the Tafel plot of the 8 h, 10 h, 12 h, 14 h and 16 h samples of $\text{Fe}_{2.95}(\text{PO}_4)_2(\text{OH})_2$ and shows the smallest Tafel slope 46.48 mV/dec for sample prepared at 14 h and values for all samples are given in

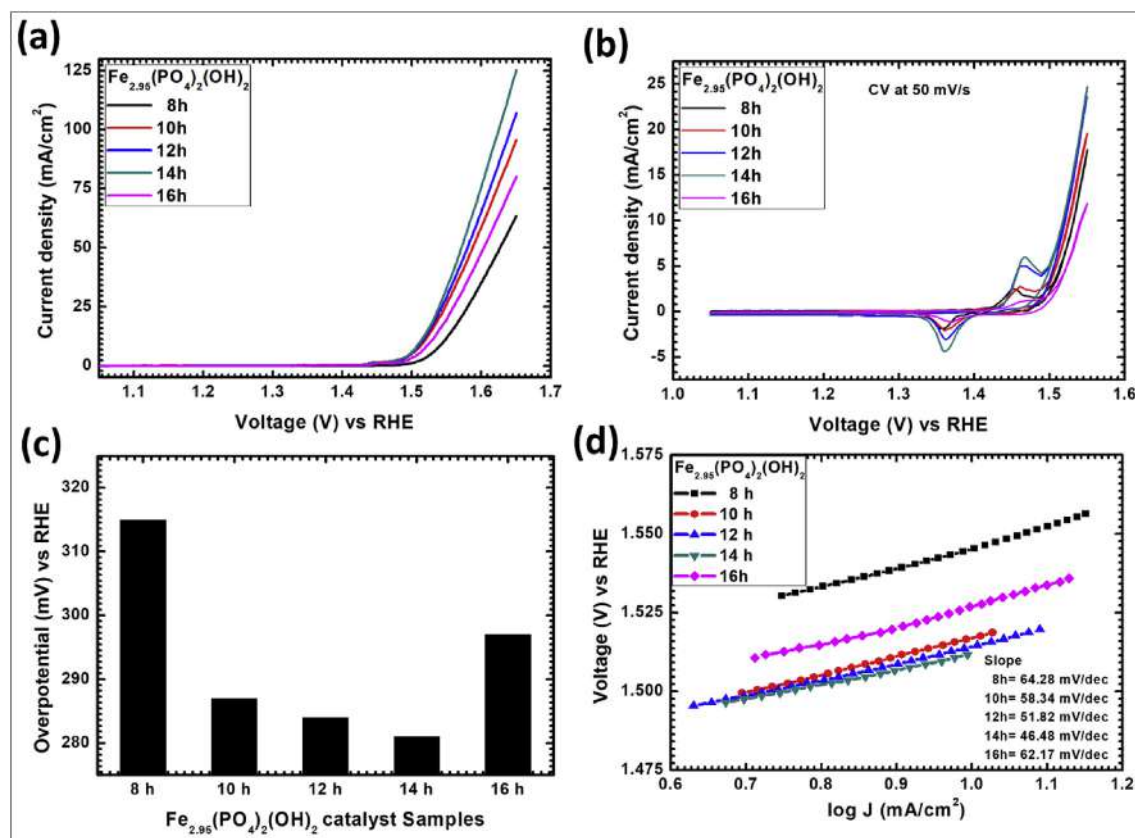


Fig. 3. (a) LSV plots at 5 mV/s scan rate, (b) Cyclic voltammetry at 50 mV/s scan rate, (c) comparative bar diagram of overpotential variation, and (d) Tafel plots of $\text{Fe}_{2.95}(\text{PO}_4)_2(\text{OH})_2$ thin films deposited for different reaction times (8h, 10h, 12h, 14h and 16h).

Table S5. This indicates that, the $\text{Fe}_{2.95}(\text{PO}_4)_2(\text{OH})_2$ thin film deposited for 14 h reaction time shows better electrocatalytic OER performance with high catalytic reaction rate [35].

For comparison, the electrocatalytic performance of bare SS-substrate, best performed $\text{Fe}_{2.95}(\text{PO}_4)_2(\text{OH})_2$ and Fe_2O_3 prepared at same conditions were tested. The LSV plots from Fig. 4(a) show that, the bare SS-substrate cannot show catalytic activity up to 1.56 V overpotential. The sample $\text{Fe}_{2.95}(\text{PO}_4)_2(\text{OH})_2$ thin film deposited for 14 h shows best ever OER catalytic activity than the Fe_2O_3 thin film. To investigate results from LSV, electrochemical active area was studied by CV curves for $\text{Fe}_{2.95}(\text{PO}_4)_2(\text{OH})_2$, Fe_2O_3 and SS. As shown in Fig. 4(b), the cyclic voltammetry curve at a scan rate of 50 mV/s of bare SS cannot show electrochemical performance as compared with $\text{Fe}_{2.95}(\text{PO}_4)_2(\text{OH})_2$ (14h) and Fe_2O_3 (14h) thin films. A very good electrochemical performance with high current density was shown by $\text{Fe}_{2.95}(\text{PO}_4)_2(\text{OH})_2$ and Fe_2O_3 thin films. The CV plot of Fe_2O_3 shows lower current under curve than the $\text{Fe}_{2.95}(\text{PO}_4)_2(\text{OH})_2$ electrode. The comparative Tafel plots of SS-substrate, $\text{Fe}_{2.95}(\text{PO}_4)_2(\text{OH})_2$ and Fe_2O_3 are given in Fig. 4(c) and corresponding values are tabulated in Table S5. This result concludes that, the development of Phosphate can tune the electronic structure around Iron, which is complimentary to accelerate the charge transfer process [21,25,36] and this may predict the smaller charge transfer resistance (as compared to Fe_2O_3) in the catalysis process. Also, comparison of $\text{Fe}_{2.95}(\text{PO}_4)_2(\text{OH})_2$ thin film sample with some previously reported transition metal based and also noble metal based materials synthesized by various methods is shown in Fig. 4(d). From the bar diagram, one can see that the hydrothermally prepared $\text{Fe}_{2.95}(\text{PO}_4)_2(\text{OH})_2$ thin films for 14 h reaction time shows lower overpotential [24,27,37–47].

For handy application, the essential requirement is high stability of catalyst at the time of oxygen evolution. So, the long term oxygen evolution catalytic activity was tested by chronoamperometry in 1 M KOH for $\text{Fe}_{2.95}(\text{PO}_4)_2(\text{OH})_2$ and Fe_2O_3 , and shown in Fig. 5(a). At fixed overpotential 290 mV, the catalyst $\text{Fe}_{2.95}(\text{PO}_4)_2(\text{OH})_2$ thin film was tested for 12 h and compared with the Fe_2O_3 thin film catalyst. It is found that, the hydrothermally synthesized $\text{Fe}_{2.95}(\text{PO}_4)_2(\text{OH})_2$ thin film catalyst demonstrates stable oxygen evolution activity at least for 12 h. After the long term stability test, the electrochemical polarization curves were studied to understand the catalytic retention of the synthesized catalyst and shown in Fig. 5(b). The increase in overpotential observed in LSV curves of the $\text{Fe}_{2.95}(\text{PO}_4)_2(\text{OH})_2$ and Fe_2O_3 thin film catalysts after stability may be due to the material utilization in catalytic activity for long duration, where, some amount of material degrades in the electrolyte [48]. There is slight increase in the overpotential by 12 mV for $\text{Fe}_{2.95}(\text{PO}_4)_2(\text{OH})_2$ and 33 mV for Fe_2O_3 thin film catalysts, since the thickness of the material plays vital role in catalytic performance (overpotential). Corresponding Tafel slopes of $\text{Fe}_{2.95}(\text{PO}_4)_2(\text{OH})_2$ and Fe_2O_3 thin film catalysts after stability were evaluated from LSV curves. From Fig. 5(c) it is observed that, there is increase in the slope for both catalysts (56.37 mV/dec for $\text{Fe}_{2.95}(\text{PO}_4)_2(\text{OH})_2$ and 82.94 mV/dec for Fe_2O_3) than the before stability test. To investigate the kinetics of electrochemical activity, the electrochemical impedance spectroscopy (EIS) was carried out before and after the catalytic stability. The typical Nyquist plots of the catalysts $\text{Fe}_{2.95}(\text{PO}_4)_2(\text{OH})_2$ and Fe_2O_3 , with equivalent circuit fitting are shown in Fig. 5(d), and quite smaller impedance profile than the previous reports [49,50]. As expected, the charge transfer resistance (R_{ct}) of the $\text{Fe}_{2.95}(\text{PO}_4)_2(\text{OH})_2$ thin film catalyst is small

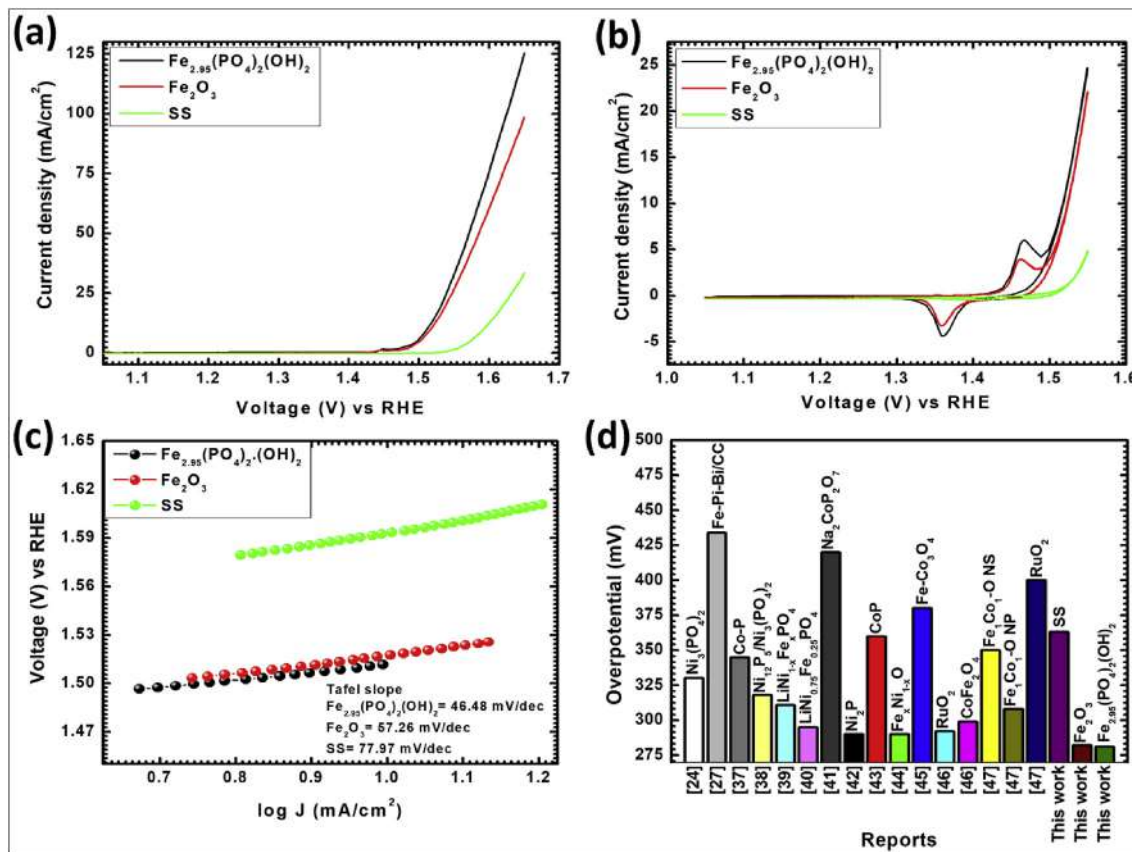


Fig. 4. Comparison of (a) LSV plots at 5 mV/s scan rate, (b) Cyclic voltammetry at 50 mV/s scan rate, (c) Tafel plot of bare SS and thin films of $\text{Fe}_{2.95}(\text{PO}_4)_2(\text{OH})_2$ and Fe_2O_3 deposited for 14h reaction time (d) Comparative diagram of reported literature overpotentials for different transition metal based and noble metal based catalysts, and the present work.

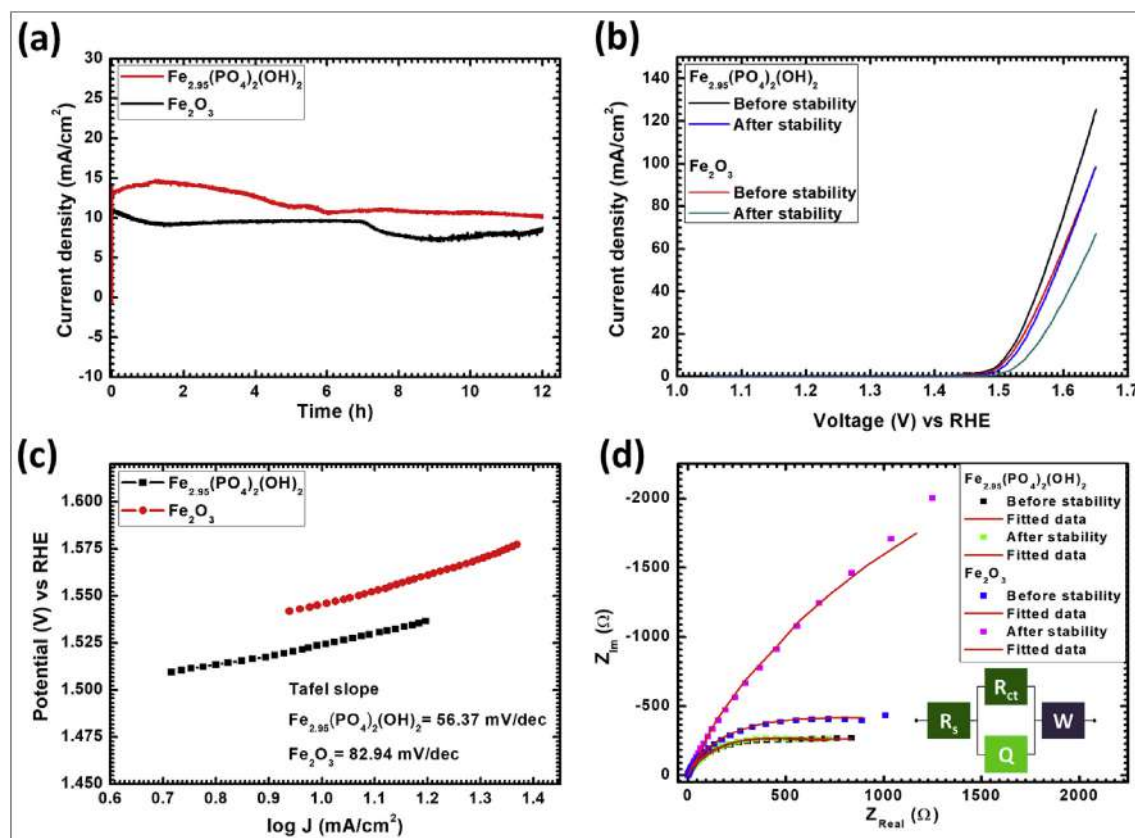


Fig. 5. (a) Long term catalytic stability in chronoamperometric mode, (b) comparison of LSV plots before and after the stability test, (c) Tafel plot after stability, and (d) Nyquist plot with equivalent fitted circuit of $\text{Fe}_{2.95}(\text{PO}_4)_2(\text{OH})_2$ and Fe_2O_3 thin film electrodes before and after stability.

(635.51 Ω) as compared to Fe_2O_3 catalyst (763.44 Ω) before catalytic stability test. After long term (12 h) OER catalytic performance, the R_{ct} of $\text{Fe}_{2.95}(\text{PO}_4)_2(\text{OH})_2$ thin film is increased to 724.66 Ω . Increase in impedance can cause the increase in overpotential after stability test. For Fe_2O_3 , value of R_{ct} dramatically increased from 763.44 Ω to 5882.10 Ω after stability test. General imperfect capacitor (Q) is introduced into the circuit due to the semi-infinite diffusion of charges, and Q is nothing but the constant phase element that takes into account the interfacial irregularities such as porosity, roughness, and geometry [51]. The value of Q is slightly decreased after 12 h stability test for both $\text{Fe}_{2.95}(\text{PO}_4)_2(\text{OH})_2$ and Fe_2O_3 catalyst materials. The values of fitted circuit parameters are tabulated in Table S6 (see ESI).

The hydrogen evolution reaction (HER) was studied for the $\text{Fe}_{2.95}(\text{PO}_4)_2(\text{OH})_2$ and Fe_2O_3 thin film catalyst electrodes by applying potential at the range 0.33 to -0.86 V vs RHE in 1 M H_3PO_4 electrolyte. The polarization curves (LSV) of $\text{Fe}_{2.95}(\text{PO}_4)_2(\text{OH})_2$ and Fe_2O_3 electrodes were carried out as shown in Fig. 6(a), depicts rapid cathodic current rise and steeper curves of both $\text{Fe}_{2.95}(\text{PO}_4)_2(\text{OH})_2$ and Fe_2O_3 catalyst electrodes. At potential -0.86 V vs RHE, the maximum current densities for $\text{Fe}_{2.95}(\text{PO}_4)_2(\text{OH})_2$ and Fe_2O_3 electrodes are 208.7 mA/cm^2 and 176.7 mA/cm^2 , respectively. The overpotential of $\text{Fe}_{2.95}(\text{PO}_4)_2(\text{OH})_2$ electrode is recorded as 165.7 mV and for Fe_2O_3 electrode as 216.1 mV at 10 mA/cm^2 current density. The $\text{Fe}_{2.95}(\text{PO}_4)_2(\text{OH})_2$ thin film electrode catalyst shows best performance than the Fe_2O_3 catalyst. The HER rate determining kinetics (process to convert proton into adsorbed hydrogen) was studied by plotting Tafel slope and it is clear that, smaller the Tafel slope delivers faster hydrogen evolution reaction. The Fig. 6(b) shows high reaction rate and lower

85.54 mV/dec Tafel slope for $\text{Fe}_{2.95}(\text{PO}_4)_2(\text{OH})_2$ catalyst electrode and 97.66 mV/dec for Fe_2O_3 catalyst. The long term HER catalytic stability was studied for 12 h in the chronoamperometric mode. A fixed overpotential 170 mV was applied to $\text{Fe}_{2.95}(\text{PO}_4)_2(\text{OH})_2$ catalyst electrode and 220 mV for Fe_2O_3 catalyst electrode through chronoamperometric stability and shown in Fig. 6(c). Initially, catalytic sites of Fe_2O_3 catalyst become more active and show good performance, but after 6 h Fe_2O_3 catalyst degrade more in the electrolyte and finally peeled off from substrate, and shows poor performance. On the other hand, $\text{Fe}_{2.95}(\text{PO}_4)_2(\text{OH})_2$ catalyst electrode show best ever performance as tested for 12 h. The after stability OER catalytic performance was tested by LSV and compared with the LSV curve before stability, and shown in Fig. 6(d). After stability of 12 h, the overpotential decreases to 126.4 mV at 10 mA/cm^2 current density and the maximum current density rises to 215.4 mA/cm^2 at overpotential -0.86 V vs RHE, and all the hydrogen evolution catalytic performance tabulated in Table S7 (see ESI). The whole region of Nyquist plot (from lower frequency region 100 mHz to higher frequency region 0.1 MHz) with the inset of best fitted equivalent circuit is shown in Fig. 6(e). The Fig. 6(f) shows the magnified view of the Nyquist plot in the higher frequency region. By fitting an equivalent circuit, we have determined that, there is decrement in charge transfer resistance (R_{ct}) by 93.36 Ω from 197.98 Ω to 104.62 Ω for the $\text{Fe}_{2.95}(\text{PO}_4)_2(\text{OH})_2$ catalyst material after 12 h catalytic stability test. On the other hand, for Fe_2O_3 catalyst material, charge transfer resistance (R_{ct}) gets drastically increased from 980.54 Ω to 11320 Ω . The value of Q is slightly increased after 12 h stability test for the $\text{Fe}_{2.95}(\text{PO}_4)_2(\text{OH})_2$ catalyst material. The best fitted circuit parameters are tabulated in Table S8 (see ESI). As expected, $\text{Fe}_{2.95}(\text{PO}_4)_2(\text{OH})_2$ thin film catalyst

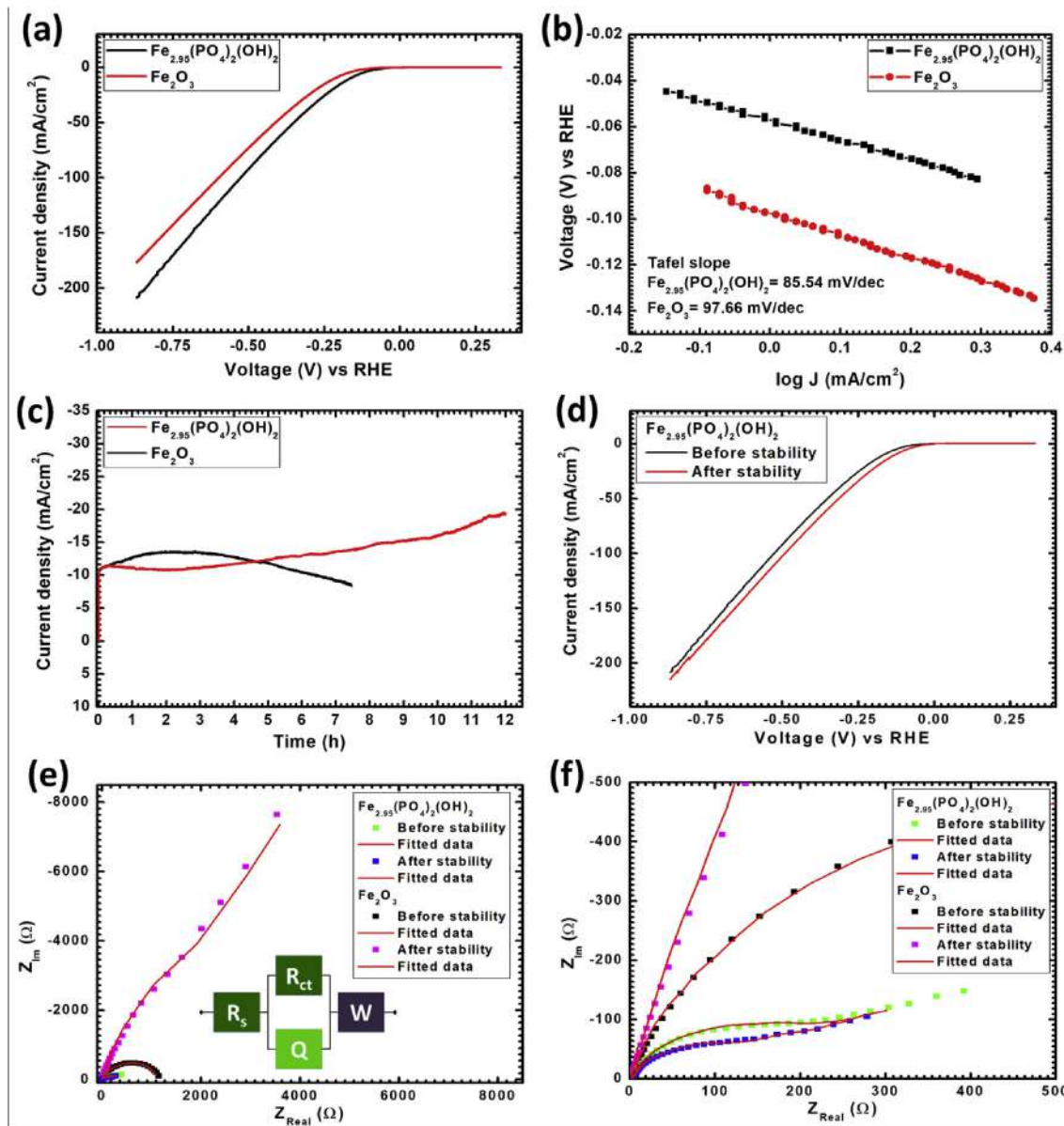


Fig. 6. HER catalytic activity test by (a) LSV plots, (b) Tafel slopes, (c) chronoamperometric mode catalytic stability, (d) comparison of LSV plots before and after stability, (e) Nyquist plots before and after stability of $\text{Fe}_{2.95}(\text{PO}_4)_2(\text{OH})_2$ and Fe_2O_3 thin film electrodes (inset figure shows an equivalent circuit fitted for the Nyquist plots), and (f) magnified view of the Nyquist plot in the higher frequency region.

show small charge transfer resistance and fast reaction rate than Fe_2O_3 thin film catalyst.

On the basis of electrochemical catalytic investigation, hydrothermally synthesized $\text{Fe}_{2.95}(\text{PO}_4)_2(\text{OH})_2$ thin film catalyst electrode show best ever performance for OER and HER in terms of low overpotential, large electrochemical active area and small Tafel slope. The achievement of low overpotential for HER and OER using $\text{Fe}_{2.95}(\text{PO}_4)_2(\text{OH})_2$ thin film catalyst is possible due to the novel structure of sub-micrometric grains and nanoflowers made by nanorods on and around the microspheres which act as an electrocatalytic active centres. The superior water splitting in terms of OER and HER makes $\text{Fe}_{2.95}(\text{PO}_4)_2(\text{OH})_2$ as a competitor bifunctional electrocatalyst to replace conventional noble metal catalysts. The development of Phosphate could introduce (i) distorted local Fe geometry and large open channels (tunnels) to increase swelling-shrinking capacity, (ii) tune the electronic structure around Fe.

These features further facilitates (iii) increase in oxygen adsorbates and (iv) reasonably water splitting with improved stability, which is complimentary to accelerate the charge transfer process.

4. Conclusions

In brief, $\text{Fe}_{2.95}(\text{PO}_4)_2(\text{OH})_2$ thin film electrodes are successfully synthesized using hydrothermal method as a binder free electrocatalyst and compared with its oxide counterpart (Fe_2O_3). The microspherical structure uncovered more active sites, resulting in the superior water splitting performance. The optimized binder free $\text{Fe}_{2.95}(\text{PO}_4)_2(\text{OH})_2$ thin film (14 h sample) catalyst exhibited highest OER activity with an overpotential of 281 mV vs RHE at 10 mA/cm² current density in alkaline electrolyte, and HER activity with an overpotential after stability 126.5 mV vs RHE at 10 mA/cm² current density, in acidic medium. It is mainly due to the large

number of catalytic active sites on the surface of $\text{Fe}_{2.95}(\text{PO}_4)_2(\text{OH})_2$ material offered by flower like structured and agglomerated nano rods on Micro and sub-micrometric spherical novel surface morphology. Due to the structural and compositional merits, the stabilization of Fe^{2+} active centres by the Phosphate framework, the excellent long term catalytic stability proves the $\text{Fe}_{2.95}(\text{PO}_4)_2(\text{OH})_2$ thin film electrode have high structural stability, robustness and best candidature as an electrocatalyst. The present method demonstrates the development of novel architectures of the binder free nano-micro structured Iron Phosphate thin film electrodes for the water splitting, fuel cells, and metal-air batteries applications.

5. Electronic supporting information (ESI)

Electronic supporting information (ESI) contains: Crystallographic and cell refinement fitness parameters of $\text{Fe}_{2.95}(\text{PO}_4)_2(\text{OH})_2$ crystal, Atomic co-ordinates of $\text{Fe}_{2.95}(\text{PO}_4)_2(\text{OH})_2$ crystal, Crystallographic and cell refinement fitness parameters of Fe_2O_3 crystal, Atomic co-ordinates of Fe_2O_3 crystal, Crystal structures of $\text{Fe}_{2.95}(\text{PO}_4)_2(\text{OH})_2$ and Fe_2O_3 extended in a, b, and c directions for the representation of channel structures along the respective directions, FTIR spectra at high wavenumber region of Fe_2O_3 and $\text{Fe}_{2.95}(\text{PO}_4)_2(\text{OH})_2$ thin films, FESEM images of $\text{Fe}_{2.95}(\text{PO}_4)_2(\text{OH})_2$ thin films deposited for 8h, 10 h, 12 h and 16 h reaction time at different magnifications, Higher magnification FE-SEM images of $\text{Fe}_{2.95}(\text{PO}_4)_2(\text{OH})_2$ thin film deposited for 8 h, 10 h, 12 h, 14 h and 16 h, EDS analysis of $\text{Fe}_{2.95}(\text{PO}_4)_2(\text{OH})_2$ thin film, EDS analysis of Fe_2O_3 thin film, Data of Electrochemical Oxygen Evolution Reaction, Electrochemical impedance spectroscopic circuit parameters, Data of Electrochemical Hydrogen Evolution Reaction, Electrochemical impedance spectroscopic circuit parameters.

Acknowledgment

Authors are thankful to The Government of India, Department of Science and Technology (DST) to support financially through the project DST-INSPIRE, sanction No.: DST/INSPIRE/04/2016/000260, and D. Y. Patil Education Society, Kolhapur for funding through internal project, sanction No.: DYPES/DU/R&D/3109.

Appendix A. Supplementary data

Supplementary data to this article can be found online at <https://doi.org/10.1016/j.electacta.2019.06.162>.

References

- [1] J. Bosch, I. Staffell, A.D. Hawkes, Temporally explicit and spatially resolved global offshore wind energy potentials, *Energy* 163 (2018) 766.
- [2] S.A. Khalate, R.S. Kate, R.J. Deokate, A review on energy economics and the recent research and development in energy and the $\text{Cu}_2\text{ZnSnS}_4$ (CZTS) solar cells: a focus towards efficiency, *Sol. Energy* 169 (2018) 616.
- [3] Z. Shen, 1.14 hydro energy, *Comprehensive Energy Systems* 1 (2018) 606.
- [4] V. Khare, C. Khare, S. Nema, P. Baredar, *Tidal Energy Systems Design, Optimization and Control*, Elsevier, 2019.
- [5] S.N. Pandey, V. Vishal, A. Chaudhuri, Geothermal reservoir modeling in a coupled thermo-hydro-mechanical-chemical approach: a review, *Earth Sci. Rev.* 185 (2018) 1157.
- [6] M. Grätzel, Photoelectrochemical cells, *Nature* 414 (2001) 338.
- [7] X. Zou, Y. Zhang, Noble metal-free hydrogen evolution catalysts for water splitting, *Chem. Soc. Rev.* 44 (2015) 5148.
- [8] B. Liu, Y. Zhao, H. Peng, Z. Zhang, C. Sit, M. Yuen, T. Zhang, C. Lee, W. Zhang, Nickel-cobalt diselenide 3D mesoporous nanosheet networks supported on Ni foam: an all-pH highly efficient integrated electrocatalyst for hydrogen evolution, *Adv. Mater.* 29 (2017) 1606521.
- [9] C.C.L. McCrory, S. Jung, J.C. Peters, T.F. Jaramillo, Benchmarking heterogeneous electrocatalysts for the oxygen evolution reaction, *J. Am. Chem. Soc.* 135 (2013) 16977.
- [10] Y. Lee, J. Suntivich, K.J. May, E.E. Perry, Y.S. Horn, Synthesis and activities of rutile IrO_2 and RuO_2 nanoparticles for oxygen evolution in acid and alkaline solutions, *J. Phys. Chem. Lett.* 3 (2012) 399.
- [11] R. Jiang, S. Tung, Z. Tang, L. Li, L. Ding, X. Xi, Y. Liu, L. Zhang, J. Zhang, A review of core-shell nanostructured electrocatalysts for oxygen reduction reaction, *Energy Storage Materials* 12 (2018) 260.
- [12] S. Siracusano, N.V. Dijk, E.P. Johnson, V. Baglio, A.S. Arico, Nanosized IrO_x and IrRuO_x electrocatalysts for the O_2 evolution reaction in PEM water electrolyzers, *Appl. Catal. B Environ.* 164 (2015) 488.
- [13] Y. Wang, Y. Zhang, Z. Liu, C. Xie, S. Feng, D. Liu, M. Shao, S. Wang, Layered double hydroxide nanosheets with multiple vacancies obtained by dry exfoliation as highly efficient oxygen evolution electrocatalysts, *Angew. Chem. Int. Ed.* 56 (2017) 5867.
- [14] Y. Yang, H. Fei, G. Ruan, C. Xiang, J.M. Tour, Efficient electrocatalytic oxygen evolution on amorphous nickel-cobalt binary oxide nanoporous layers, *ACS Nano* 8 (2014) 9518.
- [15] J. Chang, Y. Xiao, M. Xiao, J. Ge, C. Liu, W. Xing, Surface oxidized cobalt-phosphide nanorods as an advanced oxygen evolution catalyst in alkaline solution, *ACS Catal.* 5 (2015) 6874.
- [16] D. Li, H. Baydoun, B. Kulikowski, S.L. Brock, Boosting the catalytic performance of iron phosphide nanorods for the oxygen evolution reaction by incorporation of manganese, *Chem. Mater.* 29 (2017) 3048.
- [17] P. Ganesan, M. Prabu, J. Sanetuntikul, S. Shanmugam, Cobalt sulfide nanoparticles grown on nitrogen and sulfur codoped graphene oxide: an efficient electrocatalyst for oxygen reduction and evolution reactions, *ACS Catal.* 5 (2015) 3625.
- [18] Y. Liu, H. Cheng, M. Lyu, S. Fan, Q. Liu, W. Zhang, Y. Zhi, C. Wang, C. Xiao, S. Wei, B. Ye, Y. Xie, Low overpotential in vacancy-rich ultrathin CoSe_2 nanosheets for water oxidation, *J. Am. Chem. Soc.* 136 (2014) 15670.
- [19] R. Guo, X. Lai, J. Huang, X. Du, Y. Yan, Y. Sun, G. Zou, J. Xiong, Phosphate-based electrocatalysts for water splitting: recent progress, *ChemElectroChem* 5 (2018) 3822.
- [20] P. Chen, K. Xu, Z. Fang, Y. Tong, J. Wu, X. Lu, X. Peng, H. Ding, C. Wu, Y. Xie, Metallic Co_4N porous nanowire arrays activated by surface oxidation as electrocatalysts for the oxygen evolution reaction, *Angew. Chem. Int. Ed.* 54 (2015) 14710.
- [21] L. Trotochaud, S.L. Young, J.K. Ranney, S.W. Boettcher, Nickel-iron oxyhydroxide oxygen-evolution electrocatalysts: the role of intentional and incidental iron incorporation, *J. Am. Chem. Soc.* 136 (2014) 6744.
- [22] F. Song, X. Hu, Ultrathin cobalt-manganese layered double hydroxide is an efficient oxygen evolution catalyst, *J. Am. Chem. Soc.* 136 (2014) 16481.
- [23] M. Huynh, D.K. Bediako, D.G. Nocera, A functionally stable manganese oxide oxygen evolution catalyst in acid, *J. Am. Chem. Soc.* 136 (2014) 6002.
- [24] Y. Zhan, M. Lu, S. Yang, Z. Liu, J.Y. Lee, The origin of catalytic activity of nickel phosphate for oxygen evolution in alkaline solution and its further enhancement by iron substitution, *ChemElectroChem* 3 (2016) 615.
- [25] Y. Li, C. Zhao, Iron-doped nickel phosphate as synergistic electrocatalyst for water oxidation, *Chem. Mater.* 28 (2016) 5659.
- [26] Z. Wang, M. Liu, J. Du, Y. Lin, S. Wei, X. Lu, J. Zhang, A facile co-precipitation synthesis of robust FeCo phosphate electrocatalysts for efficient oxygen evolution, *Electrochim. Acta* 264 (2018) 244.
- [27] W. Wang, D. Liu, S. Hao, F. Qu, Y. Ma, G. Du, A.M. Asiri, Y. Yao, X. Sun, High-efficiency and durable water oxidation under mild pH conditions: an iron phosphate-borate nanosheet array as a non-noble-metal catalyst electrode, *Inorg. Chem.* 56 (2017) 3131.
- [28] J. Xu, D. Xiong, I. Amorim, L. Liu, Template-free synthesis of hollow iron phosphide-phosphate composite nanotubes for use as active and stable oxygen evolution electrocatalysts, *ACS Appl. Nano Mater.* 1 (2018) 617.
- [29] C. Murugesan, S. Lochab, B. Senthilkumar, P. Barpanda, Earth-abundant alkali iron phosphate (AFePO_4) as efficient electrocatalysts for oxygen reduction reaction in alkaline solution, *ChemCatChem* 10 (2018) 1122.
- [30] S. Yoon, J. Kim, J.-H. Lim, B. Yoo, Cobalt iron-phosphorus synthesized by electrodeposition as highly active and stable bifunctional catalyst for full water splitting, *J. Electrochem. Soc.* 165 (2018) H271.
- [31] P.W. Menezes, C. Panda, S. Loos, F.B. Bruns, C. Walter, M. Schwarze, X. Deng, H. Dau, M. Driess, A structurally versatile nickel phosphite acting as a robust bifunctional electrocatalyst for overall water splitting, *Energy Environ. Sci.* 11 (2018) 1287.
- [32] V.S. Jamadade, V.J. Fulari, C.D. Lokhande, Supercapacitive behavior of electro-synthesized marygold-like structured nickel doped iron hydroxide thin film, *J. Alloy. Comp.* 509 (2011) 6257.
- [33] R.A. Nyquist, R.O. Kagel, *Infrared Spectra of Inorganic Compounds*, Academic Press Inc., New York, 1971.
- [34] D. Sarkar, M. Mandal, K. Mandal, Design and synthesis of high performance multifunctional ultrathin hematite nanoribbons, *ACS Appl. Mater. Interfaces* 5 (2013) 11995.
- [35] D.K. Bediako, Y. Surendranath, D.G. Nocera, Mechanistic studies of the oxygen evolution reaction mediated by a nickel-borate thin film electrocatalyst, *J. Am. Chem. Soc.* 135 (2013) 3662.
- [36] M. Görlin, J.F. Araújo, H. Schmies, D. Bernsmeier, S. Dresch, M. Glicke, Z. Jusys, P. Cherev, R. Kraehnert, H. Dau, P. Strasser, Tracking catalyst redox states and reaction dynamics in Ni-Fe oxyhydroxide oxygen evolution reaction electrocatalysts: the role of catalyst support and electrolyte pH, *J. Am. Chem. Soc.* 139 (2017) 2070.
- [37] N. Jiang, B. You, M. Sheng, Y. Sun, Electrodeposited cobalt-phosphorous-derived films as competent bifunctional catalysts for overall water splitting,

- Angew. Chem. Int. Ed. 54 (2015) 6251.
- [38] J. Chang, Q. Lv, G. Li, J. Ge, C. Liu, W. Xing, Core-shell structured $\text{Ni}_{12}\text{P}_5/\text{Ni}_3(\text{PO}_4)_2$ hollow spheres as difunctional and efficient electrocatalysts for overall water electrolysis, *Appl. Catal. B Environ.* 204 (2017) 486.
- [39] S. Ma, Q. Zhu, Z. Zheng, W. Wang, D. Chen, Nanosized $\text{LiNi}_{1-x}\text{Fe}_x\text{PO}_4$ embedded in a mesoporous carbon matrix for high-performance electrochemical water splitting, *Chem. Commun.* 51 (2015) 15815.
- [40] S. Ma, Q. Zhu, L. Chen, W. Wang, D. Chen, Large-scale synthesis of $\text{LiNi}_{0.75}\text{Fe}_{0.25}\text{PO}_4$ covalently anchored on graphene nanosheets for remarkable electrochemical water oxidation, *J. Mater. Chem.* 4 (2016) 8149.
- [41] H. Kim, J. Park, I. Park, K. Jin, S.E. Jerng, S.H. Kim, K.T. Nam, K. Kang, Coordination tuning of cobalt phosphates towards efficient water oxidation catalyst, *Nat. Commun.* 6 (2015) 8253.
- [42] L.-A. Stern, L. Feng, F. Song, X. Hu, Ni_2P as a janus catalyst for water splitting: the oxygen evolution activity of Ni_2P nanoparticles, *Energy Environ. Sci.* 8 (2015) 2347.
- [43] J. Ryu, N. Jung, J.H. Jang, H.-J. Kim, S.J. Yoo, In situ transformation of hydrogen-evolving CoP nanoparticles: toward efficient oxygen evolution catalysts bearing dispersed morphologies with Co-oxo/hydroxo molecular units, *ACS Catal.* 5 (2015) 4066.
- [44] K. Fominykh, P. Chernev, I. Zaharieva, J. Sicklinger, G. Stefanic, M. Döblinger, A. Müller, A. Pokharel, S. Böcklein, C. Scheu, T. Bein, D.F. Rohlfiing, Iron-doped nickel oxide nanocrystals as highly efficient electrocatalysts for alkaline water splitting, *ACS Nano* 9 (2015) 5180.
- [45] C. Xiao, X. Lu, C. Zhao, Unusual synergistic effects upon incorporation of Fe and/or Ni into mesoporous Co_3O_4 for enhanced oxygen evolution, *Chem. Commun.* 50 (2014) 10122.
- [46] L. Wu, L. Shi, S. Zhou, J. Zhao, X. Miao, J. Guo, Direct growth of CoFe_2 alloy strongly coupling and oxygen-vacancy-rich CoFe_2O_4 porous hollow nanofibers: an efficient electrocatalyst for oxygen evolution reaction, *Energy Technol.* 6 (2018) 2350.
- [47] L. Zhuang, L. Ge, Y. Yang, M. Li, Y. Jia, X. Yao, Z. Zhu, Ultrathin iron-cobalt oxide nanosheets with abundant oxygen vacancies for the oxygen evolution reaction, *Adv. Mater.* 29 (2017) 1606793.
- [48] S. Zou, M. Burke, M. Kast, J. Fan, N. Danilovic, S. Boettcher, Fe (oxy)hydroxide oxygen evolution reaction electrocatalysis: intrinsic activity and the roles of electrical conductivity, substrate, and dissolution, *Chem. Mater.* 27 (2015) 8011.
- [49] Y. Hou, F. Zuo, A. Dagg, P. Feng, A three-dimensional branched cobalt-doped $\alpha\text{-Fe}_2\text{O}_3$ nanorod/ MgFe_2O_4 heterojunction array as a flexible photoanode for efficient photoelectrochemical water oxidation, *Angew. Chem.* 125 (2013) 1286.
- [50] D. Cao, W. Luo, J. Feng, X. Zhao, Z. Li, Z. Zou, Cathodic shift of onset potential for water oxidation on a Ti^{4+} doped Fe_2O_3 photoanode by suppressing the back reaction, *Energy Environ. Sci.* 7 (2014) 752.
- [51] P.R. Deshmukh, S.N. Pusawale, V.S. Jamadade, U.M. Patil, C.D. Lokhande, Microwave assisted chemical bath deposited polyaniline films for supercapacitor application, *J. Alloy. Comp.* 509 (2011) 5064.

Enhanced Energy Density of All-Solid-State Asymmetric Supercapacitors Based on Morphologically Tuned Hydrous Cobalt Phosphate Electrode as Cathode Material

Pranav K. Katkar,[†] Supriya J. Marje,[†] Sachin S. Pujari,[†] Suraj A. Khalate,[†] Abhishek C. Lokhande,[‡] and Umakant M. Patil^{*,†}

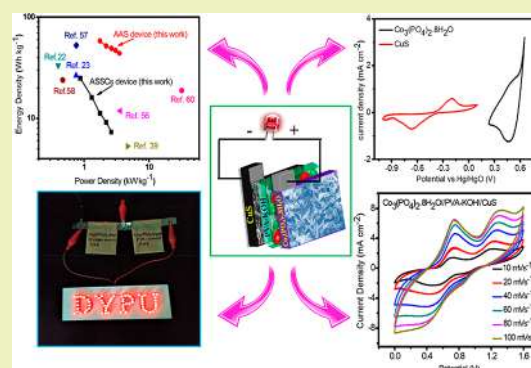
[†]Centre for Interdisciplinary Research, D. Y. Patil Education Society (Deemed to be University), Kasaba Bawada, Kolhapur, 416 006 Maharashtra, India

[‡]Department of Material Science and Engineering, Chonnam National University, Yongbong-dong, Puk-Gu, Gwangju 500 757, Republic of Korea

Supporting Information

ABSTRACT: In the present investigation, microflowers-like hydrous cobalt phosphate is prepared via a facile single-step hydrothermal method on stainless steel substrate. The microflowers-like morphology of hydrous cobalt phosphate thin film consists of microplates and further microplates converted to flakes by means of a change in length, width, and thickness with urea variation. Hydrous cobalt phosphate thin film electrode demonstrates a high specific capacitance of 800 F g^{-1} at 2 mA cm^{-2} with 33.62 Wh kg^{-1} energy density and 3.12 kW kg^{-1} power density. By taking advantage of hydrous cobalt phosphate thin film (as a cathode electrode) and copper sulfide thin film (as an anode electrode), the asymmetric devices (aqueous/all-solid-state) are fabricated. Aqueous asymmetric device shows a high specific capacitance of 163 F g^{-1} at 2 mA cm^{-2} with an energy density of 58.12 Wh kg^{-1} and power density of 3.52 kW kg^{-1} . Moreover, the all-solid-state asymmetric supercapacitor device delivers a high specific capacitance of 70 F g^{-1} at 2 mA cm^{-2} with 24.91 Wh kg^{-1} energy density and 2.63 kW kg^{-1} power density in PVA–KOH gel electrolyte. The long-term cyclic stability (94% after 3000 cycles) and actual practical demonstration (lightning 65 red LEDs) suggest an industrial application of the all-solid-state asymmetric device.

KEYWORDS: Cobalt phosphate, Hydrothermal method, Microflowers, Solid-state asymmetric supercapacitor, Thin film



INTRODUCTION

Increasing demand for portable electronics (like mobile phones, e-papers, laptops, etc.) has significantly encouraged the research community to fabricate high-performing electric energy storage devices.^{1–3} Among the various types of energy storage devices, a supercapacitor (SC) is the supreme choice for clean and green energy, which offers excellent characteristics such as good cycle stability, high power density, and environmental benignity and is presently employed in hybrid vehicles, consumer electronics, and renewable energy storage devices,^{2–5} though the major challenges of a supercapacitor are less stability at high-rate conditions and low energy density (as compared to batteries), which significantly constrains its application.⁵ As per the energy density equation (0.5 CV^2), to increase the energy density development of new electrode materials with a high capacitance (C) is one way and another is to build a supercapacitor device with a wide operating potential window (V). Thus, new superior electrode materials having high specific capacitances, long cycling lives, and rational assemblies of anode and cathode materials in a supercapacitor device are required to be investigated. Therefore, extensive

research has been devoted to fabricating asymmetric supercapacitor devices using different cost-effective electrode materials with high specific capacitance.^{6,7}

Generally, carbon-based materials, e.g., carbon nanotubes (CNTs), graphene and activated carbon (AC), conducting polymers (e.g., polythiophene, polypyrrole, and polyanilines), transition metal oxides/hydroxides/sulfides, and their composites, are employed as active materials for supercapacitors. The transition-metal oxides, metal hydroxides, and metal sulfides such as Co_3O_4 ,⁸ MnCoO ,⁹ RuO_x ,¹⁰ $\beta\text{-Co}(\text{OH})_2$,¹¹ CoS ,¹² CoS_2 ,¹³ etc., have attracted significant attention as pseudocapacitive electrode material, but they suffer from low specific capacitance and energy density due to poor conductivity.^{14,15} Thus, there is a need to develop low-cost alternative electrode materials to improve the performance of supercapacitors. Recently, for supercapacitor as well as catalysis application, various transition-metal phosphates have been studied and

Received: January 25, 2019

Revised: June 7, 2019

Published: June 7, 2019

shown to exhibit exceptional performance.^{3,16–18} In particular, cobalt phosphate is considered to be the best candidate as a positive electrode material in energy storage devices, because of outstanding redox activity, relatively low cost, earth abundance, sustainability, and its eco-friendly nature.¹⁹ Various morphologies of cobalt phosphate have been synthesized by different methods and reported for supercapacitor applications. Li et al.²⁰ prepared a flower-like morphology of $\text{Co}_3(\text{PO}_4)_2 \cdot 8\text{H}_2\text{O}$ using a green precipitate process and reported a high specific capacitance of 350 F g^{-1} at 1 A g^{-1} current density with 102% stability retention over 1000 cycles. Pang et al.²¹ synthesized layered $\text{CoHPO}_4 \cdot 3\text{H}_2\text{O}$ by a hydrothermal method, which exhibits a specific capacitance of 413 F g^{-1} at a current density of 1.5 A g^{-1} with an energy density and power density of 8.7 Wh kg^{-1} and 3225 W kg^{-1} , respectively. The flakes of $\text{Co}_3\text{P}_2\text{O}_8 \cdot 8\text{H}_2\text{O}$ were synthesized by Liu et al.²² using a chemical precipitation method and reported a maximum specific capacitance of 205 F g^{-1} at 1 A g^{-1} current density with 106% stability for 1000 cycles. Sankar et al.²³ successfully synthesized nanograsses like $\text{Co}_3(\text{PO}_4)_2$ using a hydrothermal method, and nanograsses exhibit a specific capacitance of $12\,285 \text{ mF cm}^{-2}$ at a scan rate of 5 mV s^{-1} with an energy density of $0.405 \text{ mWh cm}^{-2}$ at a power density of 1.065 mW cm^{-2} . In the available literature, only a few articles have reported the synthesis of cobalt phosphate electrodes for supercapacitor application but possessing a low specific capacitance and energy as well as power density. Still, there is scope to enhance the capacitive performance of cobalt phosphate through morphology tuning and preparing an electrode using binder-free approaches.

Besides an increase in specific capacitance, widening the operating voltage is an effective approach to improve the energy density of devices. To enhance the electrochemical capacitive performance of SCs, numerous positive and negative electrode materials have been investigated. In several previous works, various carbon-based negative electrodes have been used in asymmetric devices (ASC) like carbon aerogel, graphene, AC, graphite, CNT's, etc. However, limitations to choosing carbonaceous negative electrode materials are their lower specific capacitance and high resistivity, which restrict achieving high energy density.²⁴ To enhance the specific capacitance and energy density of asymmetric devices, an emergent need is to find new alternative anode (negative) electrode materials which combine the properties of a high capacitance without sacrificing the operational potential window. Recently, few pseudocapacitive materials such as CuS ,²⁵ Fe_2O_3 ,²⁶ SnS ,²⁷ etc., have been investigated as a negative electrode in an asymmetric device having a wide negative potential window. Among them, copper sulfide (CuS) is a fascinating negative electrode material for electrochemical capacitors because of its high specific capacitance and wide operating potential window, lower resistance, and abundant availability in nature.²⁵ The combination of cobalt phosphate as a positive and copper sulfide as a negative thin film electrode in aqueous or solid-state asymmetric supercapacitors has not been investigated.

Encouraged by the above discussion, we fabricated an asymmetric devices (all-solid-state and aqueous) with high electrochemical performance by adopting $\text{Co}_3(\text{PO}_4)_2 \cdot 8\text{H}_2\text{O}$ and CuS thin films as a cathode and anode, respectively. Taking advantage of the binder-free approach, hydrous cobalt phosphate thin film electrodes [$\text{Co}_3(\text{PO}_4)_2 \cdot n\text{H}_2\text{O}$] are successfully synthesized with different morphologies by a

single-step hydrothermal method. The effect of urea concentration on the morphological, structural, and consequently electrochemical capacitive behavior of $\text{Co}_3(\text{PO}_4)_2 \cdot n\text{H}_2\text{O}$ electrodes is studied. Furthermore, the aqueous asymmetric supercapacitor (AAS) and all-solid-state asymmetric supercapacitor (ASSC) device are assembled in 1 M KOH and PVA-KOH gel electrolytes, respectively. The capacitive performance of $\text{Co}_3(\text{PO}_4)_2 \cdot 8\text{H}_2\text{O} // \text{CuS}$ -based devices has been studied by means of specific capacitance, energy, as well as power density and cyclic stability.

■ EXPERIMENTAL SECTION

Synthesis of Cobalt Phosphate Thin Films (as a Cathode Electrode). Cobalt phosphate thin films are synthesized by a single-step hydrothermal method, and all chemicals were purchased from Sigma-Aldrich (purity $\approx 99.0\%$). In a typical synthesis, aqueous solutions of 0.05 M cobalt chloride ($\text{CoCl}_2 \cdot 6\text{H}_2\text{O}$) and 0.05 M potassium dihydrogen orthophosphate (KH_2PO_4) were prepared in double-distilled water (DDW). A stock solution of 36 mL (0.05 M) of cobalt chloride and 24 mL (0.05 M) of potassium dihydrogen orthophosphate was mixed, and four similar separate baths were prepared. Then the different concentrations of urea [$\text{CO}(\text{NH}_2)_2$] 0.01 , 0.025 , 0.050 , and 0.10 M were dissolved in the above-mentioned four baths and named as CoPOU-1, CoPOU-2, CoPOU-3, and CoPOU-4, respectively. The above solutions were stirred for 5 min until the salts were completely dissolved. Then well-washed stainless steel (SS) substrate was immersed vertically in the chemical baths, and these baths were put in a hydrothermal autoclave for 90 min , at 393 K , under 18 psi pressure. The violet-colored cobalt phosphate films were deposited over SS substrates after 90 min , which were further rinsed 2–3 times in DDW and dried at ambient conditions. As-prepared cobalt phosphate thin films were directly used as a cathode electrode in asymmetric supercapacitor devices.

Synthesis of Copper Sulfide Thin Film (as an Anode Electrode). To prepare copper sulfide (CuS) thin film over SS substrate a facile chemical bath deposition (CBD) method was used. In bath synthesis, copper sulfate ($\text{CuSO}_4 \cdot 5\text{H}_2\text{O}$) and sodium thiosulfate ($\text{Na}_2\text{S}_2\text{O}_3 \cdot 5\text{H}_2\text{O}$) were taken as copper and sulfur precursor, respectively, and tartaric acid ($\text{C}_4\text{H}_6\text{O}_6$) was used as complexing agent. Initially, 25 mL of a solution of 0.1 M $\text{CuSO}_4 \cdot 5\text{H}_2\text{O}$ was added dropwise in 0.1 M $\text{C}_4\text{H}_6\text{O}_6$ solution (25 mL) with constant stirring. Furthermore, the pH (~ 10) of the bath solution was maintained by dropwise addition of liquid ammonia (NH_3). Further, separately prepared 0.1 M $\text{Na}_2\text{S}_2\text{O}_3 \cdot 5\text{H}_2\text{O}$ solution in 50 mL of DDW was added to the above solution. Then 100 mL of the bath of the above-prepared solution containing vertically immersed SS substrates was kept at a constant temperature of 368 K for 240 min . After 240 min , well-adherent black-colored CuS in thin film form was covered over SS substrate, and it was dried at room temperature. As-prepared CuS thin films were exploited as anode electrode in the ASC devices.

Preparation of PVA-KOH Gel Electrolyte. Selection of the proper gel electrolyte is essential for ASSC device construction because it offers lower leakage, less water content, and most importantly flexibility. The prepared PVA-KOH gel has various advantages like good flexibility and high ionic conductivity, and it can make good contact with the electrodes.²⁵ The PVA-KOH gel was prepared in the subsequent manner: first, 3 g of poly(vinyl alcohol) (PVA) was dissolved in DDW (20 mL) by heating at 353 K with constant stirring. Then 10 mL of a solution of 1 M KOH in DDW was separately prepared and added in PVA solution. Later, the solution was constantly stirred at room temperature to form a clear viscous appearance. This viscous and transparent gel solution was applied as an electrolyte and a separator in ASSC device fabrication.

Fabrication of Asymmetric Device (AAS and ASSC). In the fabrication of an asymmetric supercapacitor device, as-prepared $\text{Co}_3(\text{PO}_4)_2 \cdot 8\text{H}_2\text{O}$ and CuS thin films over a large area ($5 \times 5 \text{ cm}^2$) SS substrate were directly used as cathode and anode electrodes, respectively. In AAS device fabrication, 1 M KOH is used as an electrolyte. On the other hand, anode and cathode electrodes were

soaked in PVA–KOH gel electrolyte and stacked on each other to fabricate the ASSC device. The stack of electrode//gel//electrode was pressed under a hydraulic pressure of 0.5 ton and assembled into the sandwich-like ASSC device.

Materials Characterization. The crystal structures of the obtained cobalt phosphate and copper sulfide electrodes were analyzed using an X-ray diffractometer (Rigaku miniflex-600 with Cu K α ($\lambda = 0.15406$ nm)), functioned at 40 kV and 15 mA, at a scan rate of 2°/min in the scanning range of 5° < θ < 80°. To observe chemical bonding, the FT-IR spectra of samples were measured by an Alpha (II) Bruker instrument. The field emission-scanning electron microscopy (FE-SEM, JSM-7001F, JEOL) equipped with energy-dispersive X-ray spectroscopy (EDS) (Oxford, X-max) technique was used to observe the surface morphologies of cobalt phosphate and copper sulfide thin films. The transmission electron microscopy (TEM) image was recorded using a JEM-2100 instrument. A ThermoScientific ESCALAB 250 (Thermo Fisher Scientific, UK) instrument was used for X-ray photoelectron spectroscopy (XPS) measurement. The ZIVE MP1 multichannel electrochemical workstation equipment was used to measure the electrochemical properties of thin film electrodes.

Electrochemical Capacitive Measurements. Study of the electrochemical behavior of the electrodes was carried out using a conventional three-electrode cell system in 1.0 M KOH electrolyte at ambient conditions. The cobalt phosphate and copper sulfide thin films (an exposed area ≈ 1 cm 2) as working electrodes, a platinum mesh (~ 2 cm 2) as a counter electrode, and mercury/mercury oxide (Hg/HgO) as a reference electrode were used in the three-electrode system. The electrochemical capacitive performance of the electroactive materials was evaluated by cyclic voltammetry (CV), galvanostatic charge–discharge (GCD), and electrochemical impedance spectroscopy (EIS). The specific capacitance was derived from the GCD curve using eq 1

$$C_s = \frac{I \times \Delta t}{m \times \Delta V} \quad (1)$$

where I , ΔV , m , and Δt are the current density (mA cm $^{-2}$), potential window (V), mass of active materials (g), and discharge time (s), respectively. The energy density (E , Wh kg $^{-1}$) as well as power density (P , W kg $^{-1}$) of the supercapacitor were calculated from the GCD curve using eqs 2 and 3, respectively

$$E = \frac{0.5 \times C_s \times (\Delta V)^2}{3.6} \quad (2)$$

$$P = \frac{E \times 3.6}{\Delta t} \quad (3)$$

where ΔV , Δt , and C_s are voltage (V), discharge time (s), and specific capacitance (F g $^{-1}$), respectively. Electrochemical impedance spectroscopy (EIS) was conducted for all samples and measured at open-circuit potential (OCP) with an amplitude of 10 mV in the frequency range from 100 kHz to 100 mHz. The electrochemical properties of the asymmetric device were evaluated by fabricating a two-electrode system composed of cobalt phosphate thin film as positive electrode (cathode) and copper sulfide thin film as negative electrode (anode). To obtain the best electrochemical capacitive performance of the asymmetric device, the mass ratio between the negative and the positive electrode was evaluated by the theory of charge balance ($Q^+ = Q^-$), and accordingly the mass balance is obtained using eq 4²⁸

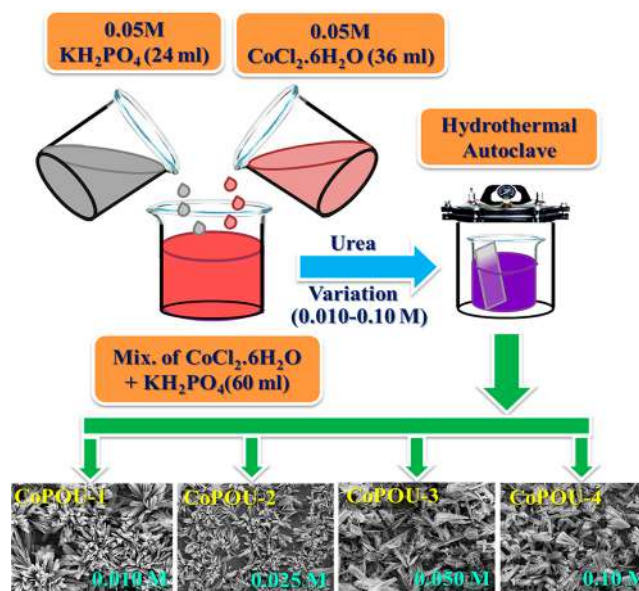
$$\frac{m_+}{m_-} = \frac{C_- \times \Delta V_-}{C_+ \times \Delta V_+} \quad (4)$$

where $m_{(+or-)}$, $\Delta V_{(+or-)}$, and $C_{(+or-)}$ are the mass (g), potential window (V), and specific capacitances (F g $^{-1}$) of the positive and negative electrode, respectively.

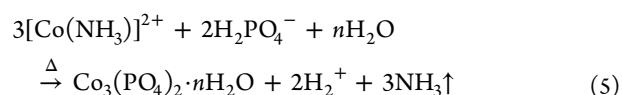
RESULTS AND DISCUSSIONS

Formation and Growth Mechanism of Cobalt Phosphate Thin Film. The formation and growth process of cobalt phosphate thin films on SS substrate using different urea concentrations by a facile hydrothermal method at 393 K is illustrated in Scheme 1. Formation of the solid thin film from

Scheme 1. Schematic Diagram for the Preparation of Hydrous Cobalt Phosphate Thin Films Using Different Urea Concentrations



a supersaturated solution bath involves two steps, nucleation and particle growth. Nucleation is necessary for particle growth, thin solid film occurs when heterogeneous nucleation is promoted on the SS substrate, and homogeneous nucleation is suppressed in the bulk solution.²⁹ Further, growth of cobalt phosphate thin films can take place by adsorption of colloidal particles from the solution at the nucleation centers on the SS substrate. Typically, at high temperature (at 365 K), decomposition of urea gradually forms CO $_2$ and NH $_4^+$ ions in solution, and released NH $_4^+$ acts as a complexing agent in the reaction bath.^{30,31} After decomposition of urea, NH $_4^+$ and Co $^{2+}$ ions get complexed as [Co(NH $_3$)] $^{2+}$. The amine complex avoids rapid nucleation and controls the reaction rate by gradually releasing Co $^{2+}$ ions. At the same time, potassium dihydrogen orthophosphate releases PO $_4^{3-}$ ions; finally, cobalt (Co $^{2+}$) and phosphate (PO $_4^{3-}$) ions react to get a final product of Co $_3$ (PO $_4$) $_2 \cdot n$ H $_2$ O (where, $n = 4, 8, \dots$) material on SS substrate in thin film form. The possible reaction mechanism is given in eq 5.



The deposited mass of cobalt phosphate in thin film form was determined gravimetrically using the weight difference method. Interestingly, from sample CoPOU-1 to CoPOU-3 the deposited weight of material is increased (0.57, 0.71, and 0.87 mg cm $^{-2}$), which may be due to an increase in growth rate with increasing urea concentration. However, a deposited mass in CoPOU-4 sample (0.62 mg cm $^{-2}$) is decreased with further increase in urea concentration, which may be due to pilling off

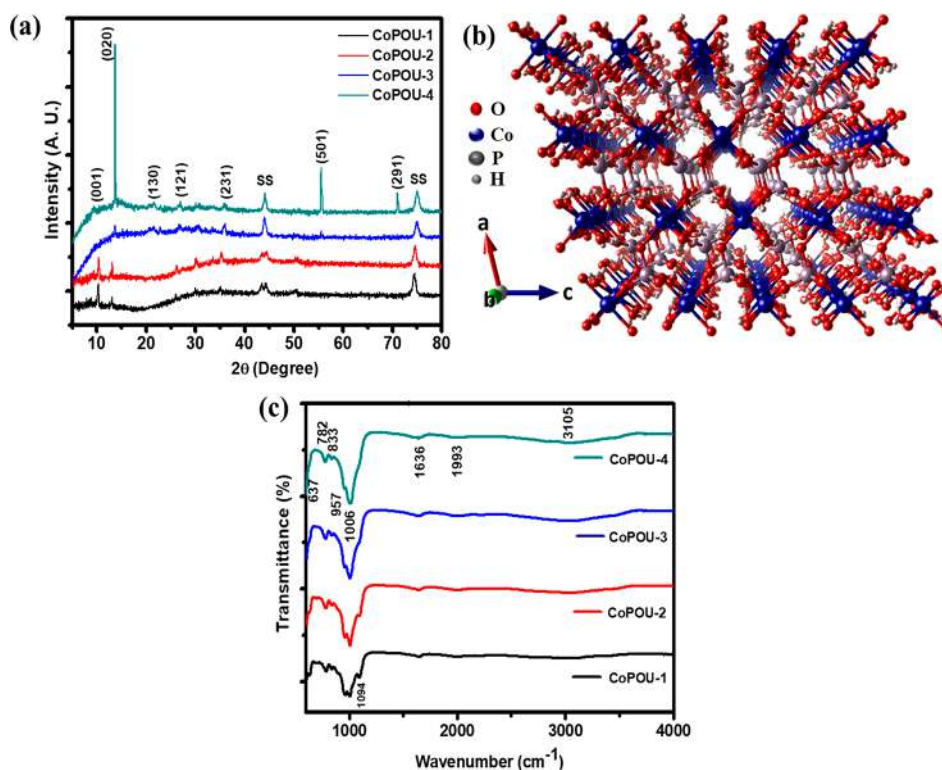


Figure 1. (a) XRD patterns. (b) Crystal structure of hydrous cobalt phosphate $[\text{Co}_3(\text{PO}_4)_2 \cdot 8\text{H}_2\text{O}]$. (c) FTIR spectra of hydrous cobalt phosphate $[\text{Co}_3(\text{PO}_4)_2 \cdot n\text{H}_2\text{O}; n = 4, 8]$ thin films.

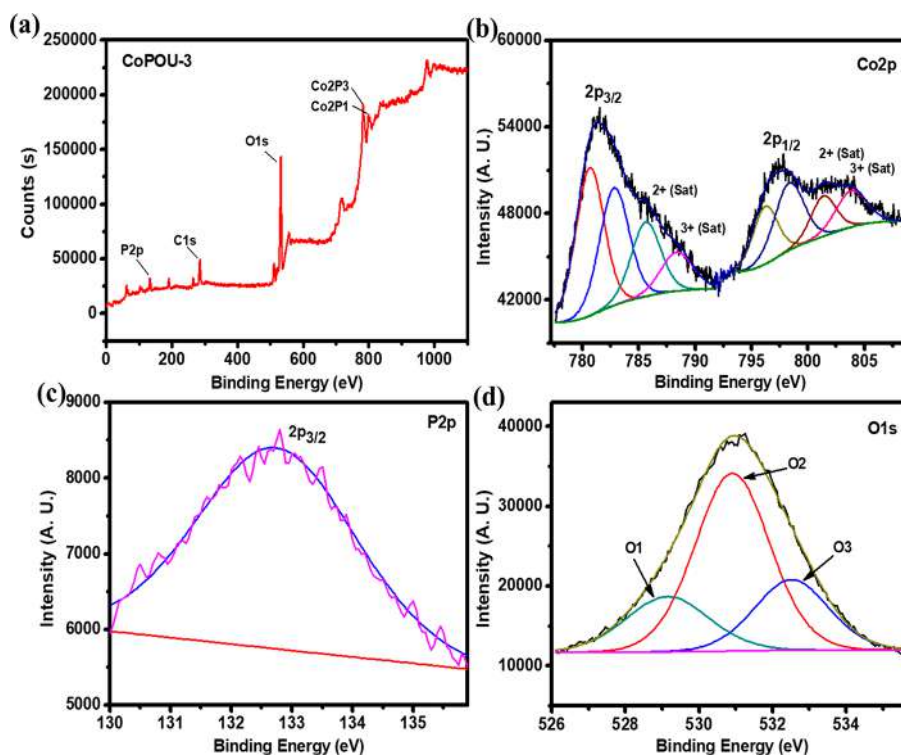


Figure 2. XPS spectra of CoPOU-3 sample: (a) survey spectrum of hydrous cobalt phosphate, (b) Co 2p spectrum, (c) P 2p spectrum, and (d) O 1s spectrum.

the outer layer because of overgrowth of material. In the present case, the concentration of hydrolyzing agent plays an important role which affects the reaction rate and consequently growth of thin films, which show variation in the weight of thin

films.³² According to the above growth mechanism, the violet-colored cobalt phosphate grew on the SS substrate.

X-ray Diffraction, FTIR, and XPS Study. Figure 1a shows the XRD patterns of hydrothermally prepared CoPOU series

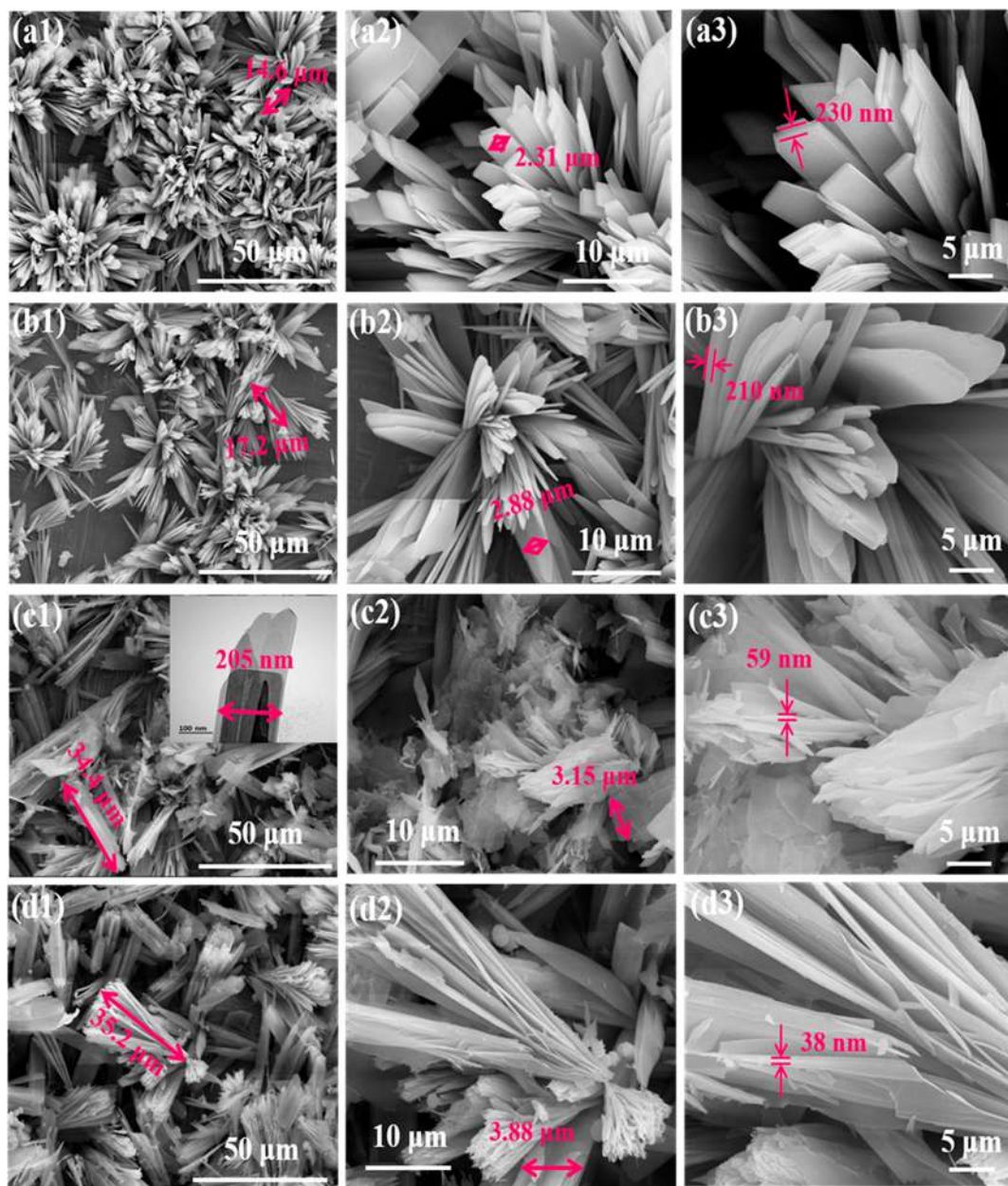


Figure 3. FE-SEM images (1000 \times , 5000 \times , and 9000 \times) of hydrous cobalt phosphate (a1–a3) for CoPOU-1, (b1–b3) CoPOU-2, (c1–c3) CoPOU-3 (inset c1: TEM image for CoPOU-3 thin film), and (d1–d3) CoPOU-4.

of cobalt phosphate thin film electrodes. The peak marked as “SS” corresponds to the stainless steel substrate. The diffraction peaks (2θ) at 10.31° , 13.26° , 21.97° , 26.83° , 35.91° , 55.16° , and 71.19° can be indexed to (0 0 1), (0 2 0), (1 3 0), (1 2 1), (2 3 1), (5 0 1), and (2 9 1) planes, respectively. It is observed that when increasing the concentration of urea, the diffraction peak (2θ) at 10.31° (0 0 1) in CoPOU-1 and CoPOU-2 sample suddenly disappeared from the XRD patterns of CoPOU-3 and CoPOU-4 sample, whereas the intensity of peaks (2θ) at 13.26° (0 2 0) and 55.16° (5 0 1) diffraction plane get gradually stronger and confirms the phase conversion of cobalt phosphate from $\text{Co}_3(\text{PO}_4)_2 \cdot 4\text{H}_2\text{O}$ (JCPDS card no. 34-0844) to $\text{Co}_3(\text{PO}_4)_2 \cdot 8\text{H}_2\text{O}$ (JCPDS No. 33-0432). The peak intensity ratio (with respect to major peak (0 2 0)) decreases from sample CoPOU-1 to CoPOU-4, which is attributed to oriented growth of the material toward the (0 2 0) plane with an increase in the urea

concentration. Figure 1b shows the crystal structure of $\text{Co}_3(\text{PO}_4)_2 \cdot 8\text{H}_2\text{O}$ material, simulated by Rietveld refinement analysis. The structural water ($n\text{H}_2\text{O}$) exists in the cobalt phosphate structure since in $I2/m$ space symmetry R_p values and the positioning vector do not trail the standard Wyckoff positions. The diffraction peaks of all samples are attributed to the monoclinic phase of the crystal structure, changes with increases in urea concentration from $\text{Co}_3(\text{PO}_4)_2 \cdot 4\text{H}_2\text{O}$ to $\text{Co}_3(\text{PO}_4)_2 \cdot 8\text{H}_2\text{O}$, and confirms formation of hydrous cobalt phosphate thin film.

The FTIR spectra of cobalt phosphate thin films (CoPOU-1–CoPOU-4) were recorded in range from 600 to 4000 cm^{-1} and are displayed in Figure 1c. It is observed that the stretching vibration mode at 637 cm^{-1} can be specified to a Co–O bond.³³ The lattice vibration modes of Co–O are assigned at 782 and 833 cm^{-1} wavenumbers. The absorption band near 957 cm^{-1} arises due to the symmetric stretching vibration of

Scheme 2. Schematic Representation for Morphological Evolution of Cobalt Phosphate Microstructure



P–O.³⁴ The sharp absorption bands at 1006 and 1094 cm^{-1} are ascribed to the asymmetric and symmetric stretching vibrations of the PO_4 group and P–O, respectively. The characteristic band around 1636 cm^{-1} presents the water molecules (H–O–H) bending vibration mode,^{34,35} and the intensity of the band progressively increases from CoPOU-1 to CoPOU-4 sample, indicating increasing structural water in cobalt phosphate thin films. Furthermore, the absorption small band at 1993 cm^{-1} and wide band at 3105 cm^{-1} are attributed to the stretching vibration mode of O–H from the water molecule.³⁴ These results revealed that deposited thin films contain structural water and indicate formation of hydrous cobalt phosphate thin films.

The XPS survey scan of CoPOU-3 thin film (Figure 2a) shows the existence of cobalt, phosphorus, and oxygen elements in thin film. The XPS peaks at 781.3 and 797.6 eV binding energies can be ascribed to Co $2p_{3/2}$ and Co $2p_{1/2}$ of cobalt ions, including two pairs of spin–orbit doublets, indicating the coexistence of Co^{2+} and Co^{3+} and their four shakeup satellites denoted as “sat” (Figure 2b).³⁶ The P 2p region of the CoPOU-3 sample exhibits a peak at 133.01 eV binding energy (Figure 2c), which corresponds to the $2p_{3/2}$ core level characteristic peak of the phosphate PO_4 group.^{37,38} The O 1s signal is deconvoluted into three peaks at binding energies of 529.1, 530.9, and 532.5 eV as O1, O2, and O3 (Figure 2d) and can be designated to the core levels in typical metal–oxygen bonds, phosphate species, and hydrated oxide species, respectively.³⁹ XPS, FT-IR, and XRD analysis indicate that hydrous cobalt phosphate thin films are successfully synthesized using a single-step hydrothermal method.

FE-SEM, TEM, and EDS Study. The surface morphological evolution of hydrous cobalt phosphate thin films was investigated through field emission scanning electron microscopy (FE-SEM). The FE-SEM images of hydrous cobalt phosphate samples at three different magnifications (1000 \times , 5000 \times , 9000 \times) are shown in Figure 3. A change in the amount of urea can alter the basic growth and directly affected the morphology of the material.⁴⁰ The FE-SEM images of CoPOU-1 are shown in Figure 3a1–a3, indicating that the sample consists of a microflowers-like structure with uniform microplates that are 14.6 μm , 2.31 μm , and 230 nm in length, width, and thickness, respectively. The SEM images for CoPOU-2 sample are shown in Figure 3b1–b3 and reveal a similar microflowers-like structure as CoPOU-1 sample. However, SEM images show the change in microplates dimensions with a length of 17.2 μm , a width of 2.88 μm , and a thickness of 210 nm. The sample CoPOU-3 (Figure 3c1–c3) shows microflowers-like structure, and interestingly

microplates are converted into microflakes with an increase in length and width and decreases in thickness as 34.4 μm , 3.15 μm , and 59 nm, respectively. Such flakes-like morphology may offer an improved electrochemically active surface area (ECSA), so the electrolyte ions can make better contact with the active sites and effortless diffusion of electrolyte ions.⁴¹ The transmission electron microscopy (TEM) image of hydrous cobalt phosphate (CoPOU-3) (inset Figure 3c1) displays overlaid microflakes with a width of ~ 205 nm nearby tip. Similarly, the sample CoPOU-4 (Figure 3d1–d3) shows microflowers with a microflakes-like structure having 35.2 μm length, 3.88 μm width, and thickness of 38 nm. Fascinatingly, it is observed that the length and width of microplates increase from sample CoPOU-1 to CoPOU-4 with an increase in urea concentration. However, the thickness of the microplates decreases from sample CoPOU-1 to CoPOU-4 sample, as shown in Scheme 2. Such increase in length, width, and decrease in thickness are attributed to conversion of microplates into microflakes, and this morphological evolution is associated with the XRD result, since oriented growth [along (0 2 0) plane] of material suggests an increase in flake size with urea variation. The reaction rate of material is controlled by the hydrolyzing agent concentration and consequently affected the morphology. The growth rate of a particle increases with an increase in urea concentration, since the urea concentration stimulates the hydrolysis rate, and therefore, microplates are converted into microflakes with a continuous reduction in thickness. Likewise, Ibupoto et al.⁴⁰ prepared Co_3O_4 using a hydrothermal method and witnessed morphology conversion from nanoflowers- to nanowires-like structure by varying the hydrolyzing agent (urea). It is expected that this 3D microflower with microflakes-like morphology having large and open interconnected stable structure may facilitate easy electrolyte diffusion and sustain the strain induced during the electrochemical reaction.⁴²

Elemental analysis of hydrous cobalt phosphate was determined by energy-dispersive spectroscopy (EDS), and the results are presented in Supporting Information Figure S1a–d. The EDS spectra evidenced that the hydrous cobalt phosphate consisted of cobalt, phosphorus, and oxygen elements without any other impurity. Cobalt and phosphorus atomic ratios in CoPOU-1, CoPOU-2, CoPOU-3, and CoPOU-4 samples are 3:1.58, 3:1.75, 3:1.80, and 3:1.88, respectively, and excess oxygen confirms that the existing materials are hydrous cobalt phosphate [$\text{Co}_3(\text{PO}_4)_2 \cdot n\text{H}_2\text{O}$].

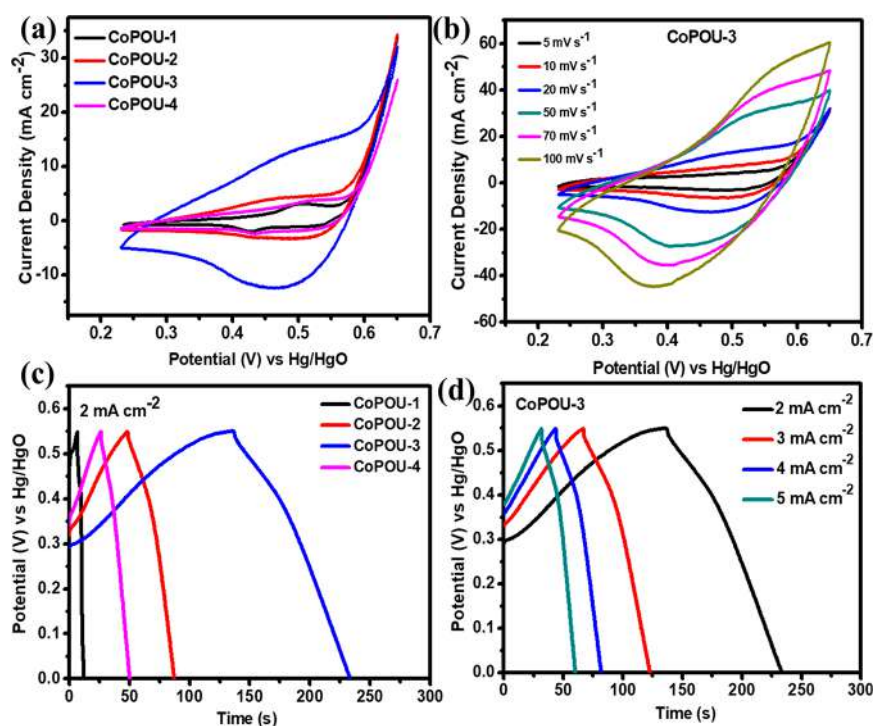


Figure 4. (a) CV curves of CoPOU-1–CoPOU-4 samples at 20 mV s^{-1} scan rate. (b) CV curves of CoPOU-3 sample at a various scan rates (5 – 100 mV s^{-1}). (c) GCD curves of CoPOU-1–CoPOU-4 samples of hydrous cobalt phosphate at 2 mA cm^{-2} current density. (d) GCD curves of CoPOU-3 sample at various current densities (2 – 5 mA cm^{-2}).

ELECTROCHEMICAL CAPACITIVE STUDIES

Hydrous Cobalt Phosphate Electrode Performance.

To tune the impact of morphology and examine the best electrode, the electrochemical capacitive performance of all four hydrous cobalt phosphate (CoPOU-1 to CoPOU-4) thin film electrodes was evaluated using a three-electrode configuration in aqueous electrolyte (1.0 M KOH). The cyclic voltammetry curves of CoPOU-1–CoPOU-4 thin film electrodes were tested in a potential range of 0.23 – 0.65 V (vs Hg/HgO) at a scan rate of 20 mV s^{-1} and are presented in Figure 4a. It clearly shows that the pseudocapacitive properties of all microarchitecture thin film samples are attributed to the reversible surface redox reaction of Co^{2+} to Co^{3+} . All CV curves exhibit a redox couple, and sample CoPOU-3 thin film shows the highest current area under the curve as compared to other samples. The obtained large current area under the curve for CoPOU-3 thin film electrode validates that it can accumulate a maximum amount of energy. Figure 4b shows the $\text{Co}_3(\text{PO}_4)_2 \cdot 8\text{H}_2\text{O}$ (CoPOU-3) thin film electrode delivers good electrochemical capacitance (current area) with increasing scan rate (from 5 to 100 mV s^{-1}) [CV curves of other samples are given in Figure S2a–c (see ESI)].

The correlative contributions from the battery type and/or electrochemical pseudocapacitive type for cobalt phosphate thin film electrodes are investigated using the power law ($i = av^b$). In the power law, b value of 1 indicates surface-controlled current (pseudocapacitive type) and semi-infinite linear diffusion current (battery type) when the b value is 0.5 .⁴³ Graphs of a log of current density vs log of scan rate for all four $\text{Co}_3(\text{PO}_4)_2 \cdot n\text{H}_2\text{O}$ thin film electrodes are shown in Figure S3 (see ESI), and b values of 0.62 , 0.64 , 0.68 , and 0.60 are obtained for samples CoPOU-1, CoPOU-2, CoPOU-3, and CoPOU-4, respectively. In the present case, for scan rates from 5 to 100 mV s^{-1} , the b value of all cobalt phosphate-based

electrodes is more than 0.5 and less than 1 , which indicates charge storage is contributed by both battery- and pseudocapacitive-type mechanisms.

Furthermore, the modified Power's law (given below in eq 6) was used to quantify the amount of charge stored by the surface pseudocapacitive- and battery-type mechanism

$$I_p = C_s \nu + C_b \nu^{1/2} \quad (6)$$

where ν is the scan rate, I_p is the peak current density, and $C_b \nu^{1/2}$ and $C_s \nu$ are consistent with the current originated from the surface pseudocapacitive (I_{surface}) and bulk process (I_{bulk}) mechanism, respectively.^{44,45} The distribution of obtained current density from the battery-like (bulk) and pseudocapacitive (surface) process for all four $\text{Co}_3(\text{PO}_4)_2 \cdot n\text{H}_2\text{O}$ thin film electrodes, at different scan rates, are shown in Figure S4 (see ESI). It is observed that the obtained capacitance is contributed by the battery-like bulk and partially by the surface pseudocapacitive process.

In addition, the galvanostatic charge–discharge (GCD) curves (Figure 4c) show almost linear potential–time profiles of all thin film samples (CoPOU-1–CoPOU-4) at constant current density (2 mA cm^{-2}). The obvious potential platform in the GCD curves mainly results from the typical pseudocapacitive behavior introduced by the electrochemical adsorption/desorption and redox procedure of the transition-metal compound.⁴⁶ The sample $\text{Co}_3(\text{PO}_4)_2 \cdot 8\text{H}_2\text{O}$ (CoPOU-3) shows a long charging–discharging time, which indicates excellent electrochemical capability. The GCD curves of the CoPOU-3 sample in a potential range of 0 – 0.55 V (vs Hg/HgO), at different current densities (2 – 5 mA cm^{-2}), are shown in Figure 4d, and GCD curves of the remaining samples are provided in Figure S5a–c (see ESI).

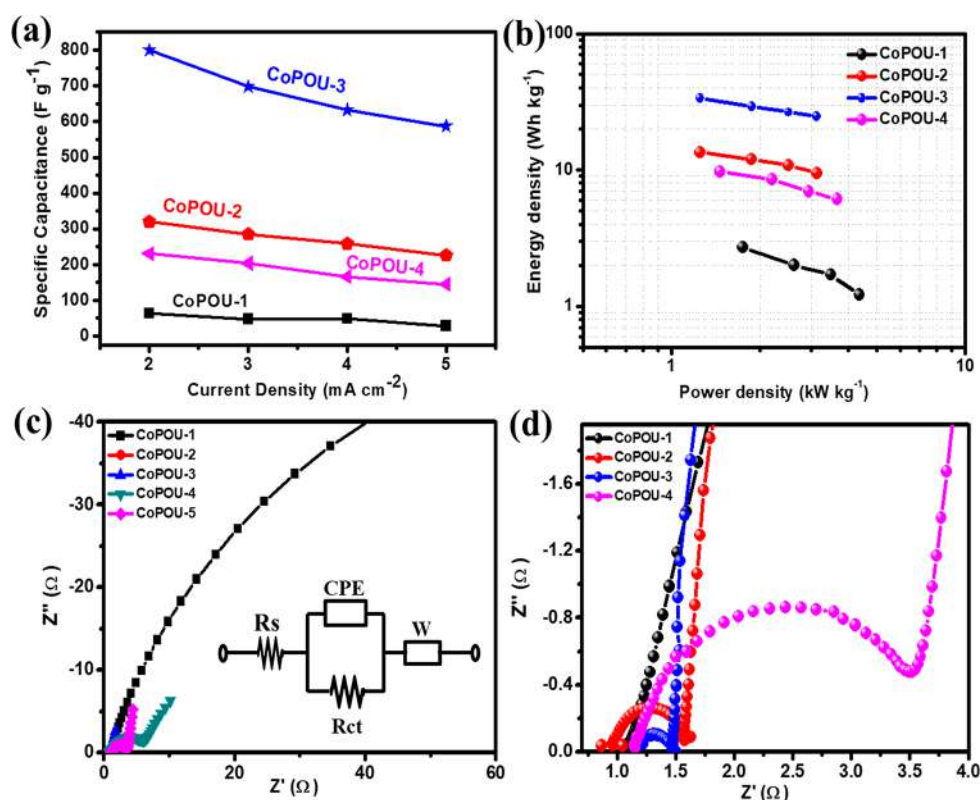


Figure 5. (a) Specific capacitance of hydrous cobalt phosphate electrodes at different current densities from GCD curve. (b) Ragone plot of hydrous cobalt phosphate thin films. (c) Nyquist plot of hydrous cobalt phosphate thin film electrodes (Inset: fitted circuit). (d) Magnified image of EIS graph.

The specific capacitances of all four hydrous cobalt phosphate (CoPOU-1–CoPOU-4) thin films are calculated from GCD curves and plotted with respect to current density (shown in Figure 5a). Hydrous cobalt phosphate micro-architected thin film electrodes (CoPOU-1–CoPOU-4) show good specific capacitance and reach maximum capacitances of 64, 320, 800, and 230 F g^{-1} at 2 mA cm^{-2} current density (Figure 5a). The CoPOU-3 thin film electrode exhibits an excellent specific capacitance of 800 F g^{-1} at low current density (2 mA cm^{-2}) and typically less capacitance at high current density, while the specific capacitances of all samples at a high current density (5 mA cm^{-2}) are 28, 226, 586, and 145 F g^{-1} for CoPOU-1, CoPOU-2, CoPOU-3, and CoPOU-4 samples, respectively, and attributed to less utilization proficiency of the active electrode material by electrolytic ions at a high charge–discharge rate.⁴⁷ Direct growth of active material on conducting substrate is an excellent way for good contact of an electrode and the active material and greater electron diffusion with fast charge transfer.⁴⁸ The unique microflowers-like morphology consisting of radially aligned and close-packed microflakes provides a large surface area and exposed active sites as well as fast ion diffusion. Thus, the cobalt phosphate thin film electrode exhibits excellent performance due to in situ preparation of the electrode and unique microflakes-like morphology. The obtained value of specific capacitance in the present work is comparable to the available literature except for a few reports (Table S1, see ESI). Shao et al.³⁹ prepared cobalt phosphate hydrate ($\text{Co}_3(\text{PO}_4)_2 \cdot 8\text{H}_2\text{O}$) nanoflakes by the hydrothermal method and obtained specific capacitance of 1578.7 F g^{-1} , in 1 M NaOH electrolyte, with an energy density of 1.17 mWh

cm^{-2} and 18.75 mW cm^{-2} power density. Also, Xi et al.⁴⁹ achieved a high specific capacitance of 1174 F g^{-1} at a constant current density of 2 A g^{-1} in 3 M KOH electrolyte for $\text{Co}_3(\text{PO}_4)_2$ (nanowires) prepared by the hydrothermal method. Jiang et al.⁵⁰ prepared Ni–Fe LDH@rGO ultrafine nanosheets by the reflux method and obtained a specific capacitance of 2715 F g^{-1} at a 3 A g^{-1} current density in 1 M KOH electrolyte. Also, $\text{CoSeO}_3 \cdot \text{H}_2\text{O}$ /HWCNTs nanoribbons hybrid paper prepared by Jiang et al.⁵¹ using the refluxing process and achieved a specific capacitance of 2461 F g^{-1} at current density of 5 A g^{-1} in 1 M KOH electrolyte. Pan et al.⁵² achieved a high specific capacitance of 3946.5 F g^{-1} at a 3 A g^{-1} current density in 1 M KOH electrolyte for $\text{ZnCo}_{1.5}(\text{OH})_{4.5}\text{Cl}_{0.5} \cdot 0.45\text{H}_2\text{O}$ nanosheets, prepared by the homogeneous precipitation method. Similarly, Yang et al.⁴⁵ synthesized $(\text{Ni}_x\text{Co}_{1-x})_9\text{Se}_8$ nanodendrite arrays by a solvothermal method, and it exhibits a high specific capacitance of 3762 F g^{-1} at a 5 A g^{-1} current density in 1 M KOH electrolyte. Only in these few reported works, specific capacitance is higher than the present work possibly due to the use of nickel foam as a substrate, which plays a vital role in improving the electrochemical capacity of the electrode material by adding self-capacitance due to its surface atom conversion during electrochemical testing to NiO and $\text{Ni}(\text{OH})_2$. Thus, when nickel foam is used as a current collector to test the electrochemical properties of a small amount active material then nickel foam underestimates the specific capacitance value of the active material. However, in the present study stainless steel substrate is used as a substrate to synthesize hydrous cobalt phosphate material thin film electrode, which offers only a 2D thin film electrode structure

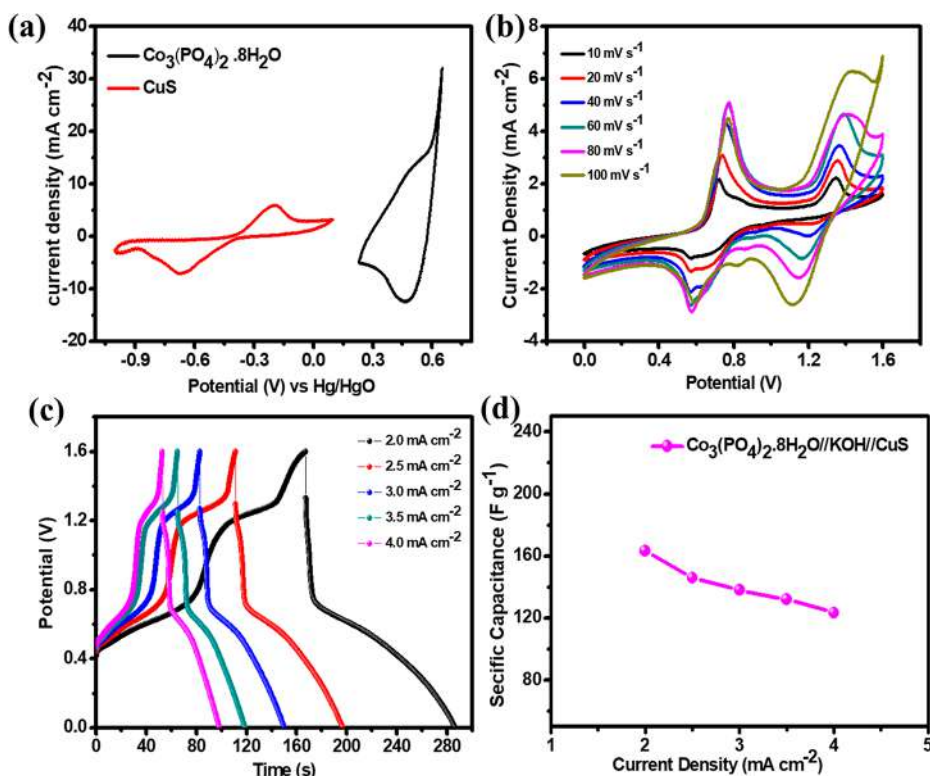


Figure 6. (a) CV curves of $\text{Co}_3(\text{PO}_4)_2 \cdot 8\text{H}_2\text{O}$ and CuS electrode at 20 mV s^{-1} scan rate. (b) CV curve of AAS device at different scan rates ($10\text{--}100 \text{ mV s}^{-1}$). (c) GCD curve of AAS device at various current densities ($2.0\text{--}4.0 \text{ mA cm}^{-2}$). (d) Specific capacitance of AAS device at different current densities.

and does not take part in an electrochemical reaction. Thus, in this work, obtained capacitance is totally provided only by hydrous cobalt phosphate material. As compared with the excellent supercapacitor performance in the available literature of cobalt phosphate-based materials, the CoPOU-3 thin film electrode exhibits competitive performance. For the supercapacitor application of any electrode material, its specific energy and power density plays a very vital role and is expected to provide a high energy density at low GCD current density.⁵³ Figure 5b shows the Ragone plot of hydrous cobalt phosphate (CoPOU-1–CoPOU-4) thin film electrodes, where energy and power density are calculated by eqs 2 and 3, respectively. The CoPOU-3 electrode exhibits good energy density along with power density than other electrodes. The specific power density of CoPOU-3 increases from 1.25 to 3.12 kW kg^{-1} , while the specific energy density decreases from 33.62 to 24.66 Wh kg^{-1} as the GCD current increases from 2 to 5 mA cm^{-2} .

For evaluation of electrolyte diffusion and charge transfer resistance at the electrode–electrolyte interface, electrochemical impedance spectroscopy (EIS) measurements were tested (shown in Figure 5c), and Figure 5d shows its magnified image in the higher frequency region. A very obvious straight line at the low-frequency region accompanied by semicircles at the high-frequency region in Nyquist plot is observed for all CoPOU-1–CoPOU-4 thin film electrodes. The obtained EIS data for hydrous cobalt phosphate electrode (CoPOU-3) can be fitted by an equivalent circuit consisting of R_s (solution resistance), R_{ct} (charge-transfer resistance) from the redox process, and CPE (constant phase element) to account for the capacitance and W (Warburg impedance) as diffusion resistance.⁴⁷ The lowest solution resistance (R_s) 0.95Ω and charge-transfer resistance (R_{ct}) 1.47Ω is obtained for the

CoPOU-3 electrode. At the low-frequency region, the CoPOU-3 electrode displays lower diffusive resistance (W) in conformity with the high slope of the straight line as compared to other thin film electrodes. The less Warburg impedance facilitates high diffusion of electrolyte ions into electrode material and authorizes maximum utilization of the microflakes-like structure of hydrous cobalt phosphate.^{54,55} Therefore, a good electrochemical property with low electrochemical impedance is credited to the microflakes-like structure of the CoPOU-3 electrode. The plot of cyclic stability (CV cycles) is shown in Figure S6 (see ESI), and the inset of the figure shows CV curves of the CoPOU-3 electrode of the 1000th, 2000th, and 3000th cycles. The cyclic stability of the $\text{Co}_3(\text{PO}_4)_2 \cdot 8\text{H}_2\text{O}$ (CoPOU-3) electrode has 83% of the capacity retention after 3000 CV cycles, at 20 mV s^{-1} scan rate, in 1.0 M KOH electrolyte. After stability, a negligible change in the surface of the microflakes without damaging microflowers-like structure indicates stable morphology and better interaction between electrolyte ions (shown in Figure S7a–f (see ESI)). Less damage in a microstructure of microflakes in microflowers confirms the excellent electrochemical stability of the $\text{Co}_3(\text{PO}_4)_2 \cdot 8\text{H}_2\text{O}$ (CoPOU-3) microflakes thin film electrode. Ultimately, this result suggests that the microflakes-like morphology leads to easy access for the electrolytic ions and much longer lifetime.

Aqueous Asymmetric Device (AAS). Additionally, to explore the device application of the hydrous cobalt phosphate electrode, the aqueous asymmetric supercapacitor (AAS) device was fabricated based on CoPOU-3 ($\text{Co}_3(\text{PO}_4)_2 \cdot 8\text{H}_2\text{O}$) thin film as a positive electrode (cathode) and CuS thin film as negative electrode (anode) using 1.0 M KOH aqueous electrolyte. The CuS thin film, used as anode material,

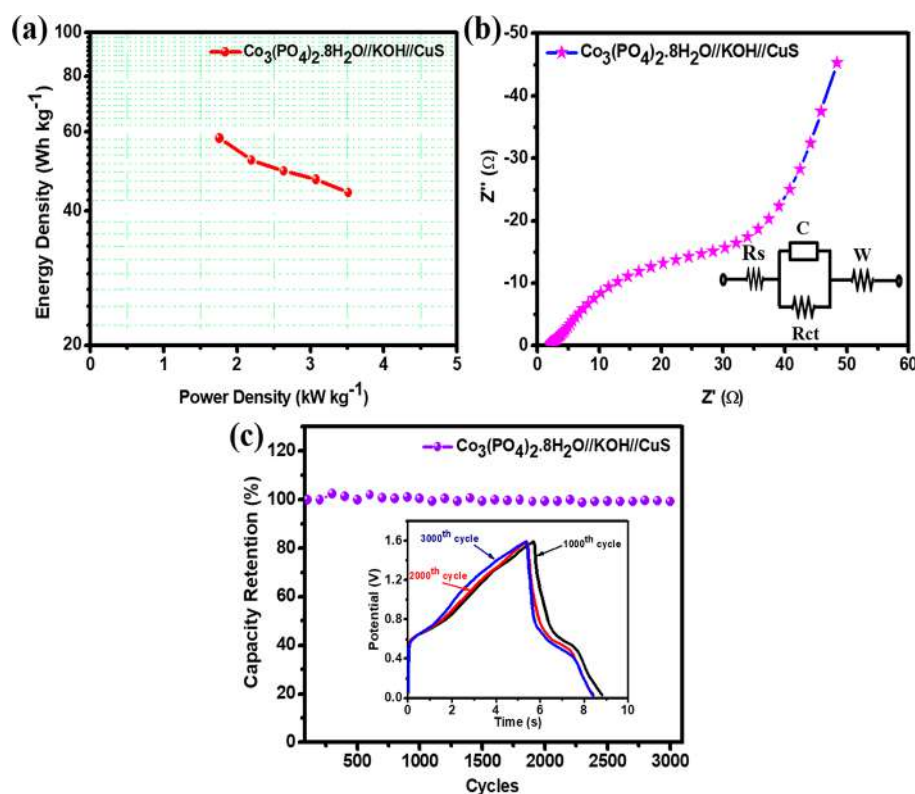


Figure 7. (a) Ragone plot. (b) Nyquist plot (Inset: fitted circuit). (c) Capacity retention vs cycle number plot of AAS device (Inset: GCD cycles at the 1000th, 2000th, and 3000th cycle).

has a hexagonal crystal structure and consists of microparticles with flake-like morphology (XRD pattern and SEM images are provided in ESI Figure S8). The electrochemical capacitive performance of CuS thin film as a negative electrode has been carried out in a three-electrode cell system by CV, GCD, and EIS tests (see ESI Figure S9a–d), and the anode electrode exhibits a maximum specific capacitance of 673 F g^{-1} at a current density of 2 mA cm^{-2} (see ESI Figure S9c). The cyclic stability of the CuS electrode is tested for 2000 cycles at a scan rate of 20 mV s^{-1} , and it exhibits excellent (95%) capacity retention after 2000 cycles as shown in Figure S10 (see ESI).

For equilibrium of the positive and negative charges in an aqueous asymmetric device, the weight ratio of $\text{Co}_3(\text{PO}_4)_2 \cdot 8\text{H}_2\text{O}$ (CoPOU-3) and CuS electrode is calculated by eq 4. By using eq 4, the calculated mass ratio of the cathode and anode is obtained as 1:1.37. Figure 6a shows CV curves of $\text{Co}_3(\text{PO}_4)_2 \cdot 8\text{H}_2\text{O}$ and CuS electrode within different potential windows (at 20 mV s^{-1} scan rate) in 1.0 M KOH . Figure 6a denotes that the two distinctive pseudocapacitive electrodes with rational combination can achieve a wide potential window (voltage) in an aqueous asymmetric device. Figure 6b shows CV curves of the $\text{Co}_3(\text{PO}_4)_2 \cdot 8\text{H}_2\text{O}$ (CoPOU-3)//KOH//CuS AAS device at different scan rates from 10 to 100 mV s^{-1} . The CV curves show an obvious four redox peaks from $\text{Co}_3(\text{PO}_4)_2 \cdot 8\text{H}_2\text{O}$ and CuS thin films. Meanwhile, the GCD curves of the AAS device at different current densities from 2.0 to 4.0 mA cm^{-2} are measured and shown in Figure 6c. The GCD curves show the nonlinear behavior of the discharge curve and confirm pseudocapacitive behavior, which is analogous with CV results. It demonstrates redox reaction kinetics for the AAS device, since both used electrode materials are pseudocapacitive type. The calculated specific capacitances for the aqueous

device (shown in Figure 6d) are found to be 163, 145, 138, 132, and 123 F g^{-1} at 2.0, 2.5, 3.0, 3.5, and 4.0 mA cm^{-2} current densities, respectively. As obvious, the specific capacitance of the AAS device at 2.0 mA cm^{-2} is higher than the 4.0 mA cm^{-2} current density. Furthermore, to study the performance of fabricated aqueous asymmetric SC's device, energy as well as power density are calculated, and the relative Ragone plot of the AAS device is shown in Figure 7a. The AAS device achieved an energy density of 58.12 Wh kg^{-1} at 1.759 kW kg^{-1} power density, and the energy density still remains 43.96 Wh kg^{-1} at 3.517 kW kg^{-1} power density, which demonstrates excellent performance of the AAS device.

The performance of the AAS device is compared with some previously reported works from the literature (see ESI Table S2). Several AAS devices based on cobalt phosphate (as cathode) were fabricated and reported, such as $\text{Co}_3\text{P}_2\text{O}_8 \cdot 8\text{H}_2\text{O}/\text{AC}$ (33.4 Wh kg^{-1} , 399 W kg^{-1}),²² $\text{Co}_3(\text{PO}_4)_2/\text{AC}$ (26.66 Wh kg^{-1} , 750 W kg^{-1}),²³ $\text{Co}_3(\text{PO}_4)_2 \cdot 8\text{H}_2\text{O}/\text{AC}$ (5.33 Wh kg^{-1} , 4687 W kg^{-1}),³⁹ $\text{Co}_3\text{P}_2\text{O}_8 \cdot 8\text{H}_2\text{O}/\text{AC}$ (11.9 Wh kg^{-1} , 3.59 kW kg^{-1}),⁵⁶ $\text{Co}_3(\text{PO}_4)_2 \cdot 4\text{H}_2\text{O}/\text{GF}/\text{C-FP}$ (24 Wh kg^{-1} , 468 W kg^{-1}),⁵⁷ and $\text{Co}_3(\text{PO}_4)_2/\text{Co}_3(\text{PO}_4)_2$ symmetric supercapacitor (52.8 Wh kg^{-1} , 756 W kg^{-1}).⁵⁸ However, in all reported works, cobalt phosphate as cathode and mostly activated carbon as a negative electrode were used for fabrication of an asymmetric device, and they exhibit low energy density as compared to the $\text{Co}_3(\text{PO}_4)_2 \cdot 8\text{H}_2\text{O}/\text{CuS}$ electrodes-based asymmetric (AAS) supercapacitor device. The EIS plot (Figure 7b) of the AAS device consists of a semicircle loop at initial (high-frequency region) and later sloped line (at a low-frequency region). The initial point of the semicircle loop is ascribed to the solution resistance (R_s) and end point to charge-transfer resistance ($R_{ct} = 37.2 \Omega$), and the

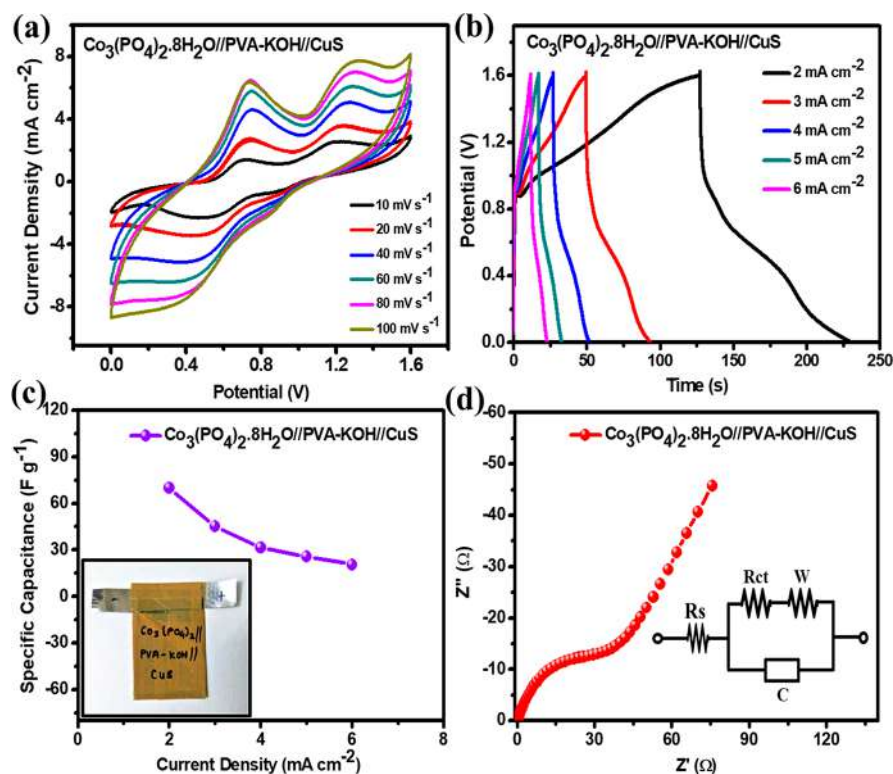


Figure 8. Electrochemical capacitive studies of the $\text{Co}_3(\text{PO}_4)_2 \cdot 8\text{H}_2\text{O} // \text{PVA-KOH} // \text{CuS}$ ASSC device. (a) CV curves at different scan rates (10–100 mV s^{-1}). (b) GCD curves at different current densities (2–6 mA cm^{-2}). (c) Specific capacitance calculated from the GCD curve (Inset: photograph of the ASSC device). (d) Nyquist plot (Inset: fitted circuit).

slope of the line at low frequency is attributed to the Warburg diffusion resistance (W).⁵⁹ The cyclic stability of the $\text{Co}_3(\text{PO}_4)_2 \cdot 8\text{H}_2\text{O} // \text{KOH} // \text{CuS}$ AAS device at 5 mA cm^{-2} for 3000 cycles is displayed in Figure 7c. It shows that the capacity retention of the $\text{Co}_3(\text{PO}_4)_2 \cdot 8\text{H}_2\text{O} // \text{KOH} // \text{CuS}$ AAS device after 3000 cycles is about 94%. The 1000th, 2000th, and 3000th GCD cycle shows little decrease in storing capacity with the GCD cycles (inset of Figure 7c). Ten cycles after the 100th cycle and the last 10 cycles of the GCD test are provided in ESI Figure S11a and S11b, indicating an almost steady redox process at the electrode surface. Thus, it confirms the long-term stability of the AAS device with negligible degradation of electroactive material. Finally, the device consisting of both pseudocapacitive electrodes is beneficial for increasing the specific capacitance without sacrificing operating potential window (unlike symmetric devices) to enhance the electrochemical energy storage performance.

All-Solid-State Asymmetric Device (ASSC). To avoid the leakage problem in the AAS device, we fabricated an all-solid-state asymmetric supercapacitor (ASSC) device and denoted it as $\text{Co}_3(\text{PO}_4)_2 \cdot 8\text{H}_2\text{O} // \text{PVA-KOH} // \text{CuS}$. The ASSC device was assembled with $\text{Co}_3(\text{PO}_4)_2 \cdot 8\text{H}_2\text{O}$ (CoPOU-3) as a cathode (positive electrode) and CuS as an anode (negative electrode) using highly viscous PVA-KOH (gel) as solid electrolyte and separator. Figure 8a exhibits the CV curve of the ASSC device tested at different scan rates (10–100 mV s^{-1}) in a potential window from 0.0 to 1.6 V. The CV curves of the ASSC device show redox peaks similar to the AAS device and confirm capacitance is originated from pseudocapacitance. Figure 8b displays GCD curves of the $\text{Co}_3(\text{PO}_4)_2 \cdot 8\text{H}_2\text{O} // \text{PVA-KOH} // \text{CuS}$ ASSC device at different current densities from 2 to 6 mA cm^{-2} . All GCD curves

display an asymmetrical shape which is attributed to the pseudocapacitive behavior. The specific capacitance of the $\text{Co}_3(\text{PO}_4)_2 \cdot 8\text{H}_2\text{O} // \text{PVA-KOH} // \text{CuS}$ device calculated from the GCD curves at 2, 3, 4, 5, and 6 mA cm^{-2} was found to be 70, 45, 32, 26, and 21 F g^{-1} , respectively (Figure 8c). The actual photograph of the $\text{Co}_3(\text{PO}_4)_2 \cdot 8\text{H}_2\text{O} // \text{PVA-KOH} // \text{CuS}$ device is shown in the inset of Figure 8c. Like in other typical EIS analyses, the $\text{Co}_3(\text{PO}_4)_2 \cdot 8\text{H}_2\text{O} // \text{PVA-KOH} // \text{CuS}$ ASSC device shows a semicircle at the high-frequency range and a straight line at the lower frequency range (Figure 8d). The charge transfer ($R_{ct} = 42.12 \Omega$) resistance is slightly higher than that of the AAS device, which is attributed to restriction of the ion mobility through the PVA matrix. The energy density as well as the power density of the $\text{Co}_3(\text{PO}_4)_2 \cdot 8\text{H}_2\text{O} // \text{PVA-KOH} // \text{CuS}$ ASSC device was calculated at current densities from 2 to 6 mA cm^{-2} and is provided in Figure S12 (see ESI). The energy densities of ASSC are found to be 24.90, 16.11, 11.23, 9.15, and 7.32 Wh kg^{-1} with power densities of 0.879, 1.318, 1.758, 2.197, and 2.637 kW kg^{-1} , respectively.

The comparative Ragone plot for AAS and ASSC devices with previous literature is shown in Figure 9a.^{22,23,39,56–58,60} The maximum energy and power density delivered by AAS and ASSC devices are 58.12 Wh kg^{-1} , 3.517 kW kg^{-1} and 24.90 Wh kg^{-1} , 2.637 kW kg^{-1} , respectively. Table S2 (see ESI) gives a comprehensive comparison of cobalt phosphate material-based ASC device with their deposition methods, capacitance values, energy and power densities, and number of cycles performed for stability and the percentage retention from the previously reported literature. As compared with previous works, it is found that the AAS device surpasses the reported energy and power density for other cobalt phosphates

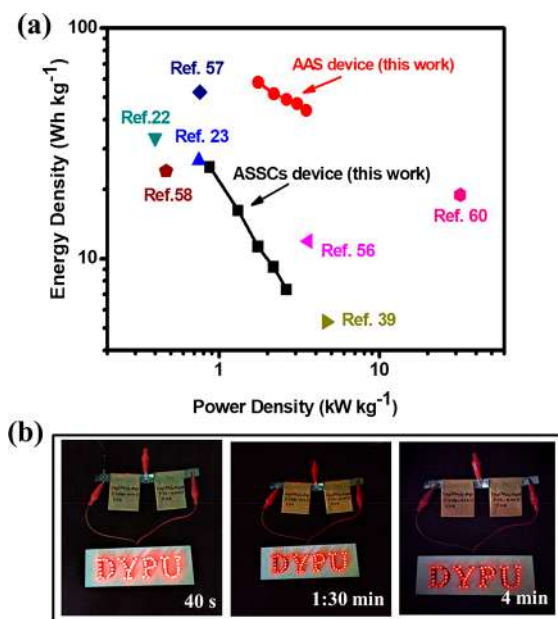


Figure 9. (a) Comparative Ragone plot of $\text{Co}_3(\text{PO}_4)_2 \cdot 8\text{H}_2\text{O} // \text{KOH} // \text{CuS}$ (AAS) and $\text{Co}_3(\text{PO}_4)_2 \cdot 8\text{H}_2\text{O} // \text{PVA-KOH} // \text{CuS}$ (ASSC) device with available literature. (b) Demonstration of the ASSC device by glowing 65 red LED's panel.

(cathode)-based AAS devices. However, ASSC shows moderate energy and power densities as compared with AAS devices and exhibits much higher performance compared with the ASSC device based on $\text{K}_2\text{CO}_3(\text{P}_2\text{O}_7)_2 \cdot 2\text{H}_2\text{O} // \text{Graphene}$ (0.96 mWh cm^{-3} , 54.5 mW cm^{-3}) fabricated by Pang et al.⁶¹ and $\text{MnO}_2 // \text{CuS}$ (18.9 Wh kg^{-1} , 32 kW kg^{-1}) and $\text{CuO} // \text{CuS}$ (22.8 Wh kg^{-1} , 2.5 W kg^{-1}) constructed by Patil et al.^{60,62} The high energy density of the $\text{Co}_3(\text{PO}_4)_2 \cdot 8\text{H}_2\text{O} // \text{CuS}$ is due to the wide operating potential window and maximum specific capacitance offered by both pseudocapacitive electrodes. Figure 9b shows a photograph of the ASSC device, as demonstrated for a series of two ASSC devices to glow a 65 red light-emitting diodes panel (1.8 V, LEDs), called “DYPU”, and it was powered for 4 min after 30 s charging. The image of glowing LEDs for time periods of 40 s, 1:30 min, and 4 min are captured, and it shows the intensity of LEDs decreases with time (shown in Figure 9b). Therefore, the significant initial glowing intensity of LEDs attributed to the high power density of the $\text{Co}_3(\text{PO}_4)_2 \cdot 8\text{H}_2\text{O} // \text{PVA-KOH} // \text{CuS}$ ASSC device as well as the higher energy density of the energy storage device is confirmed by prolonged glowing time. The obtained result suggests potential applicability of AAS and ASSC devices in apparatuses which require a high energy density and leakproof energy storage devices, respectively.

CONCLUSIONS

In this work, a binder-free hydrous cobalt phosphate [$\text{Co}_3(\text{PO}_4)_2 \cdot n\text{H}_2\text{O}$; $n = 4, 8$] microflower has been successfully synthesized by a facile single-step hydrothermal method with different urea concentrations. The microflower with microflakes-like morphology of hydrous cobalt phosphate is effectively tuned by changing the width, length, and thickness of microplates by variation of the urea concentration. The $\text{Co}_3(\text{PO}_4)_2 \cdot 8\text{H}_2\text{O}$ electrode (CoPOU-3 sample) exhibits the highest specific capacitance of 800 F g^{-1} at 2 mA cm^{-2} . The AAS and ASSC devices are successfully assembled with the

morphologically tuned $\text{Co}_3(\text{PO}_4)_2 \cdot 8\text{H}_2\text{O}$ (CoPOU-3) cathode and CuS anode electrodes. The maximum specific capacitances of the AAS and ASSC devices are found to be 163 and 70 F g^{-1} (at 2 mA cm^{-2}), respectively. The cyclic stability with 94% after 3000 GCD cycles denotes the excellent durability of the AAS device for long cycles. The leakproof $\text{Co}_3(\text{PO}_4)_2 \cdot 8\text{H}_2\text{O} // \text{PVA-KOH} // \text{CuS}$ ASSC device drives high energy density of 24.90 Wh kg^{-1} at 0.879 kW kg^{-1} power density. Moreover, a series combination of two ASSC devices glows a 65 red LED panel up to 4 min. These superior results suggest that the high performance of the asymmetric devices (AAS and ASSC) based on $\text{Co}_3(\text{PO}_4)_2 \cdot 8\text{H}_2\text{O} // \text{CuS}$ are a promising energy storage devices for potential application at the industry level and opens a new class of materials as compared to the traditional asymmetric device based on pseudocapacitor and EDLC materials.

ASSOCIATED CONTENT

Supporting Information

The Supporting Information is available free of charge on the ACS Publications website at DOI: 10.1021/acssuschemeng.9b00504.

EDS spectra of CoPOU-1–CoPOU-4 electrode, cyclic voltammetry and charge–discharge plots of hydrous cobalt phosphate electrodes (CoPOU-1, CoPOU-2, and CoPOU-4), plots of $\log(\text{current density})$ against $\log(\text{scan rate})$ for CoPOU-1–CoPOU-4 samples, plots of calculated contribution of pseudocapacitive and battery-type current density of CoPOU-1–CoPOU-4 electrodes, cyclic stability of CoPOU-3 electrode, FE-SEM images of CoPOU-3 before and after cyclic stability, XRD pattern and SEM images of CuS electrode, CV, GCD curves, impedance spectra and cyclic stability of CuS electrode, charge–discharge profile of 10 cycles after the 100th cycle and the last 10 cycles of the GCD test for the AAS device, Ragone plot of the ASSC device, tables of a literature study (PDF)

AUTHOR INFORMATION

Corresponding Author

*E-mail: umakant.physics84@gmail.com.

ORCID

Pranav K. Katkar: 0000-0001-7012-4314

Notes

The authors declare no competing financial interest.

ACKNOWLEDGMENTS

We are thankful to the Department of Science and Technology, India-Innovation in Science Pursuit for Inspired (DST-INSPIRE), for financial support through research project sanction no. DST/INSPIRE/04/2016/000260.

REFERENCES

- Chen, H.; Hu, L.; Chen, M.; Yan, Y.; Wu, L. Nickel-cobalt layered double hydroxide nanosheets for high-performance supercapacitor electrode materials. *Adv. Funct. Mater.* **2014**, *24*, 934–942.
- Wang, Y.; Song, Y.; Xia, Y. Electrochemical capacitors: mechanism, materials, systems, characterization and applications. *Chem. Soc. Rev.* **2016**, *45*, 5925–5950.
- Theerthagiri, J.; Thiagarajan, K.; Senthilkumar, B.; Khan, Z.; Senthil, R.; Arunachalam, P.; Madhavan, J.; Ashokkumar, M. Synthesis of hierarchical cobalt phosphate nanoflakes and their

enhanced electrochemical performances for supercapacitor applications. *ChemistrySelect* **2017**, *2*, 201–210.

(4) Pendashteh, A.; Moosavifard, S. E.; Rahmanifar, M. S.; Wang, Y.; El-Kady, M. F.; Kaner, R. B.; Mousavi, M. F. Highly ordered mesoporous CuCo_2O_4 nanowires, a promising solution for high-performance supercapacitors. *Chem. Mater.* **2015**, *27*, 3919–3926.

(5) Augustyn, V.; Simon, P.; Dunn, B. Pseudocapacitive oxide materials for high-rate electrochemical energy storage. *Energy Environ. Sci.* **2014**, *7*, 1597–1614.

(6) Chen, H. C.; Jiang, J. J.; Zhao, Y. D.; Zhang, L.; Guo, D. Q.; Xia, D. One-pot synthesis of porous nickel cobalt sulphides: tuning the composition for superior pseudocapacitance. *J. Mater. Chem. A* **2015**, *3*, 428–437.

(7) Li, J. J.; Liu, M. C.; Kong, L. B.; Wang, D.; Hu, Y. M.; Han, W.; Kang, L. Advanced symmetric supercapacitors based on $\text{Ni}_3(\text{PO}_4)_2@ \text{GO}$ and $\text{Fe}_2\text{O}_3@ \text{GO}$ electrodes with high specific capacitance and high energy density. *RSC Adv.* **2015**, *5*, 41721–41728.

(8) Hosono, E.; Fujihara, S.; Honma, I.; Zhou, H. Fabrication of morphology and crystal structure controlled nanorod and nanosheet cobalt hydroxide based on the difference of oxygen-solubility between water and methanol, and conversion into Co_3O_4 . *J. Mater. Chem.* **2005**, *15*, 1938–1945.

(9) Chang, J. K.; Lee, M. T.; Huang, C. H.; Tsai, W. T. Physicochemical properties and electrochemical behavior of binary manganese-cobalt oxide electrodes for supercapacitor applications. *Mater. Chem. Phys.* **2008**, *108*, 124–131.

(10) Hu, C. C.; Chen, W. C. Effects of substrates on the capacitive performance of $\text{RuO}_x \cdot n\text{H}_2\text{O}$ and activated carbon- RuO_x electrodes for supercapacitors. *Electrochim. Acta* **2004**, *49*, 3469–3477.

(11) Nethravathi, C.; Rajamathi, C. R.; Rajamathi, M.; Wang, X.; Gautam, U. K.; Golberg, D.; Bando, Y. Cobalt hydroxide/oxide hexagonal ring-graphene hybrids through chemical etching of metal hydroxide platelets by graphene oxide: energy storage applications. *ACS Nano* **2014**, *8*, 2755–2765.

(12) Kubendhiran, S.; Thirumalraj, B.; Chen, S. M.; Karuppiah, C. Electrochemical co-preparation of cobalt sulfide/reduced graphene oxide composite for electrocatalytic activity and determination of H_2O_2 in biological Samples. *J. Colloid Interface Sci.* **2018**, *509*, 153–162.

(13) Venkateshalu, S.; Rangappa, D.; Grace, A. N. Hydrothermal synthesis and electrochemical properties of CoS_2 -reduced graphene oxide nanocomposite for supercapacitor application. *Int. J. Nanosci.* **2018**, *17*, 1760020.

(14) Pang, H.; Yan, Z.; Wang, W.; Chen, J.; Zhang, J.; Zheng, H. Facile fabrication of $\text{NH}_4\text{CoPO}_4 \cdot \text{H}_2\text{O}$ nano/microstructures and their primarily application as electrochemical supercapacitor. *Nanoscale* **2012**, *4*, 5946–5953.

(15) Dai, Y. H.; Kong, L. B.; Yan, K.; Shi, M.; Luo, Y. C.; Kang, L. Facile fabrication of manganese phosphate nanosheets for supercapacitor applications. *Ionics* **2016**, *22*, 1461–1469.

(16) Pang, H.; Liu, Y.; Li, J.; Ma, Y.; Li, G.; Ai, Y.; Chen, J.; Zhang, J.; Zheng, H. Cobalt phosphite microarchitectures assembled by ultralong nanoribbons and their application as effective electrochemical capacitor electrode materials. *Nanoscale* **2013**, *5*, 503–507.

(17) Chen, C.; Chen, W.; Lu, J.; Chu, D.; Huo, Z.; Peng, Q.; Li, Y. Transition-metal phosphate colloidal spheres. *Angew. Chem., Int. Ed.* **2009**, *48*, 4816–4913.

(18) Cho, I. S.; Kim, D. W.; Lee, S.; Kwak, C. H.; Bae, S. T.; Noh, J. H.; Yoon, S. H.; Jung, H. S.; Kim, D. W.; Hong, K. S. Synthesis of $\text{Cu}_2\text{PO}_4\text{OH}$ Hierarchical Superstructures with Photocatalytic Activity in Visible Light. *Adv. Funct. Mater.* **2008**, *18*, 2154–2162.

(19) Li, X.; Elshahawy, A. M.; Guan, C.; Wang, J. Metal phosphides and phosphates-based electrodes for electrochemical supercapacitors. *Small* **2017**, *13*, 1701530.

(20) Li, H.; Yu, H.; Zhai, J.; Sun, L.; Yang, H.; Xie, S. Self-assembled 3D cobalt phosphate octahydrate architecture for supercapacitor electrodes. *Mater. Lett.* **2015**, *152*, 25–28.

(21) Pang, H.; Wang, S.; Shao, W.; Zhao, S.; Yan, B.; Li, X.; Li, S.; Chen, J.; Du, W. Few-layered $\text{CoHPO}_4 \cdot 3\text{H}_2\text{O}$ ultrathin nanosheets for

high performance of electrode materials for Supercapacitors. *Nanoscale* **2013**, *5*, 5752–5757.

(22) Liu, M. C.; Li, J. J.; Hu, Y. X.; Yang, Q. Q.; Kang, L. Design and fabrication of $\text{Ni}_3\text{P}_2\text{O}_8 \cdot \text{Co}_3\text{P}_2\text{O}_8 \cdot 8\text{H}_2\text{O}$ as advanced positive electrodes for asymmetric supercapacitors. *Electrochim. Acta* **2016**, *201*, 142–150.

(23) Sankar, K. V.; Lee, S. C.; Seo, Y.; Ray, C.; Liu, S.; Kundu, A.; Jun, S. C. Binder-free cobalt phosphate one-dimensional nanograsses as ultrahigh-performance cathode material for hybrid supercapacitor applications. *J. Power Sources* **2018**, *373*, 211–219.

(24) Wang, G.; Zhang, L.; Zhang, J. A review of electrode materials for electrochemical supercapacitors. *Chem. Soc. Rev.* **2012**, *41*, 797–828.

(25) Patil, A. M.; Lokhande, A. C.; Chodankar, N. R.; Shinde, P. A.; Kim, J. H.; Lokhande, C. D. Interior design engineering of CuS architecture alteration with rise in reaction bath temperature for high performance symmetric flexible solid state supercapacitor. *J. Ind. Eng. Chem.* **2017**, *46*, 91–102.

(26) Li, Y.; Xu, J.; Feng, T.; Yao, Q.; Xie, J.; Xia, H. Fe_2O_3 nanoneedles on ultrafine nickel nanotube arrays as efficient anode for high-performance asymmetric supercapacitors. *Adv. Funct. Mater.* **2017**, *27*, 1606728.

(27) Patil, A. M.; Lokhande, V. C.; Patil, U. M.; Shinde, P. A.; Lokhande, C. D. High performance all-solid-state asymmetric supercapacitor device based on 3D nanospheres of $\beta\text{-MnO}_2$ and nanoflowers of O-SnS. *ACS Sustainable Chem. Eng.* **2018**, *6*, 787–802.

(28) Jiang, W.; Yu, D.; Zhang, Q.; Goh, K.; Wei, L.; Yong, Y.; Jiang, R.; Wei, J.; Chen, Y. Ternary hybrids of amorphous nickel hydroxide-carbon nanotube-conducting polymer for supercapacitors with high energy density, excellent rate capability, and long cycle life. *Adv. Funct. Mater.* **2015**, *25*, 1063–1073.

(29) Bunker, B. C.; Rieke, P. C.; Tarasevich, B. J.; Campbell, A. A.; Fryxell, G. E.; Graff, G. L.; Song, L.; Liu, J.; Virden, W.; McVay, G. L. Ceramic thin-film formation on functionalized interfaces through biomimetic processing. *Science* **1994**, *264*, 48–55.

(30) Patil, U. M.; Katkar, P. K.; Marje, S. J.; Lokhande, C. D.; Jun, S. C. Hydrous nickel sulphide nanoparticle decorated 3D graphene foam electrodes for enhanced supercapacitive performance of an asymmetric device. *New J. Chem.* **2018**, *42*, 20123–20130.

(31) Marje, S. J.; Katkar, P. K.; Kale, S. B.; Lokhande, A. C.; Lokhande, C. D.; Patil, U. M. Effect of phosphate variation on morphology and electrocatalytic activity (OER) of hydrous nickel pyrophosphate thin films. *J. Alloys Compd.* **2019**, *779*, 49–58.

(32) Patil, U. M.; Nam, M. S.; Lee, S. C.; Liu, S.; Kang, S.; Park, B. H.; Jun, S. C. Temperature influenced chemical growth of hydrous copper oxide/hydroxide thin film electrodes for high performance supercapacitors. *J. Alloys Compd.* **2017**, *701*, 1009–1018.

(33) Nguyen, T. T.; Nguyen, V. H.; Deivasigamani, R. K.; Kharismadewi, D.; Iwai, Y.; Shim, J. J. Facile synthesis of cobalt oxide/reduced graphene oxide composites for electrochemical capacitor and sensor applications. *Solid State Sci.* **2016**, *53*, 71–77.

(34) Wen, H.; Cao, M.; Sun, G.; Xu, W.; Wang, D.; Zhang, X.; Hu, C. Hierarchical three-dimensional cobalt phosphate microarchitectures: Large-scale solvothermal synthesis, characterization, and magnetic and microwave absorption properties. *J. Phys. Chem. C* **2008**, *112*, 15948–15955.

(35) Prokopchuk, N. N.; Kopilevich, V. A.; Voitenko, L. V. Preparation of double nickel(II) cobalt(II) phosphates with controlled cationic composition. *Russ. J. Appl. Chem.* **2008**, *81*, 386–391.

(36) Ma, T. Y.; Dai, S.; Jaroniec, M.; Qiao, S. Z. Metal-organic framework derived hybrid Co_3O_4 -carbon porous nanowire arrays as reversible oxygen evolution electrodes. *J. Am. Chem. Soc.* **2014**, *136*, 13925–13931.

(37) Hu, G. R.; Deng, X. R.; Peng, Z. D.; Du, K. Comparison of AlPO_4^- and $\text{Co}_3(\text{PO}_4)_2$ -coated $\text{LiNi}_{0.8}\text{Co}_{0.2}\text{O}_2$ cathode materials for Li-ion battery. *Electrochim. Acta* **2008**, *53*, 2567–2573.

- (38) Kim, K. H.; Jeong, J. M.; Lee, S. J.; Choi, B. G.; Lee, K. G. Protein-directed assembly of cobalt phosphate hybrid nanoflowers. *J. Colloid Interface Sci.* **2016**, *484*, 44–50.
- (39) Shao, H.; Padmanathan, N.; McNulty, D.; O'Dwyer, C.; Razeed, K. M. Supercapattery based on binder-free $\text{Co}_3(\text{PO}_4)_2 \cdot 8\text{H}_2\text{O}$ multilayer nano/microflakes on nickel foam. *ACS Appl. Mater. Interfaces* **2016**, *8*, 28592–28598.
- (40) Ibupoto, Z. H.; Elhag, S.; AlSalhi, M. S.; Nur, O.; Willander, M. Effect of urea on the morphology of Co_3O_4 nanostructures and their application for potentiometric glucose biosensor. *Electroanalysis* **2014**, *26*, 1773–1781.
- (41) Ma, X. J.; Zhang, W. B.; Kong, L. B.; Luo, Y. C.; Kang, L. Electrochemical performance in alkaline and neutral electrolytes of a manganese phosphate material possessing a broad potential window. *RSC Adv.* **2016**, *6*, 40077–40085.
- (42) Yunyun, F.; Xu, L.; Wankun, Z.; Yuxuan, X.; Yunhan, Y.; Honglin, Q.; Xuatang, X.; Fan, W. Spinel CoMn_2O_4 nanosheet arrays grown on nickel foam for high-performance supercapacitor electrode. *Appl. Surf. Sci.* **2015**, *357*, 2013–2021.
- (43) Simon, P.; Gogotsi, Y.; Dunn, B. Where do batteries end and supercapacitors begin? *Science* **2014**, *343*, 1210–1211.
- (44) Gogotsi, Y.; Penner, R. M. Energy storage in nanomaterials-capacitive, pseudocapacitive, or battery-like? *ACS Nano* **2018**, *12*, 2081–2083.
- (45) Yang, P.; Wu, Z.; Jiang, Y.; Pan, Z.; Tian, W.; Jiang, L.; Hu, L. Fractal $(\text{Ni}_x\text{Co}_{1-x})_9\text{Se}_8$ nanodendrite arrays with highly exposed (0 1 1) surface for wearable, all-solid-state supercapacitor. *Adv. Energy Mater.* **2018**, *8*, 1801392.
- (46) Sugimoto, W.; Iwata, H.; Yasunaga, Y.; Murakami, Y.; Takasu, Y. Preparation of ruthenic acid nanosheets and utilization of its interlayer surface for electrochemical energy storage. *Angew. Chem., Int. Ed.* **2003**, *42*, 4092–4096.
- (47) Chodankar, N. R.; Dubal, D. P.; Lokhande, A. C.; Patil, A. M.; Kim, J. H.; Lokhande, C. D. An innovative concept of use of redox-active electrolyte in asymmetric capacitor based on MWCNTs/ MnO_2 and Fe_2O_3 thin films. *Sci. Rep.* **2016**, *6*, 1–14.
- (48) Jiang, Y.; Jiang, L.; Wu, Z.; Yang, P.; Zhang, H.; Pan, Z.; Hu, L. In situ growth of $(\text{NH}_4)_2\text{V}_{10}\text{O}_{25} \cdot 8\text{H}_2\text{O}$ urchin-like hierarchical arrays as superior electrodes for all-solid-state supercapacitors. *J. Mater. Chem. A* **2018**, *6*, 16308–16315.
- (49) Xi, Y.; Dong, B.; Dong, Y.; Mao, N.; Ding, L.; Shi, L.; Gao, R.; Liu, W.; Su, G.; Cao, L. Well-defined, nanostructured, amorphous metal phosphate as electrochemical pseudocapacitor materials with high capacitance. *Chem. Mater.* **2016**, *28*, 1355–1362.
- (50) Jiang, Y.; Song, Y.; Li, Y.; Tian, W.; Pan, Z.; Yang, P.; Li, Y.; Gu, Q.; Hu, L. Charge transfer in ultrafine LDH nanosheets/graphene interface with superior capacitive energy storage performance. *ACS Appl. Mater. Interfaces* **2017**, *9*, 37645–37654.
- (51) Jiang, Y.; Wu, Z.; Jiang, L.; Pan, Z.; Yang, P.; Tian, W.; Hu, L. Freestanding $\text{CoSeO}_3 \cdot \text{H}_2\text{O}$ nanoribbon/carbon nanotube composite paper for 2.4V high-voltage, flexible, solid-state supercapacitors. *Nanoscale* **2018**, *10*, 12003–12010.
- (52) Pan, Z.; Jiang, Y.; Yang, P.; Wu, Z.; Tian, W.; Liu, L.; Song, Y.; Gu, Q.; Sun, D.; Hu, L. In situ growth of layered bimetallic ZnCo hydroxide nanosheets for high-performance all-solid-state pseudocapacitor. *ACS Nano* **2018**, *12*, 2968–2979.
- (53) Yan, J. A.; Khoo, E.; Sumboja, A.; Lee, P. S. Facile coating of manganese oxide on tin oxide nanowires with high performance capacitive behavior. *ACS Nano* **2010**, *4*, 4247–4255.
- (54) Sennu, P.; Aravindan, V.; Lee, Y. S. High energy asymmetric supercapacitor with 1D@2D structured NiCo_2O_4 @ Co_3O_4 and jackfruit derived high surface area porous carbon. *J. Power Sources* **2016**, *306*, 248–257.
- (55) Zhang, D.; Kong, X.; Zhao, Y.; Jiang, M.; Lei, X. CoOOH ultrathin nanoflake arrays aligned on nickel foam: fabrication and use in high-performance supercapacitor devices. *J. Mater. Chem. A* **2016**, *4*, 12833–12840.
- (56) Li, J. J.; Liu, M. C.; Kong, L. B.; Shi, M.; Han, W.; Kang, L. Facile synthesis of $\text{Co}_3\text{P}_2\text{O}_8 \cdot 8\text{H}_2\text{O}$ for high-performance electrochemical energy storage. *Mater. Lett.* **2015**, *161*, 404–407.
- (57) Mirghni, A. A.; Momodu, D.; Oyedotun, K. O.; Dangbegnon, J. K.; Manyala, N. Electrochemical analysis of $\text{Co}_3(\text{PO}_4)_2 \cdot 4\text{H}_2\text{O}$ /graphene foam composite for enhanced capacity and long cycle life hybrid asymmetric capacitors. *Electrochim. Acta* **2018**, *283*, 374–384.
- (58) Mao, H.; Zhang, F.; Liu, X.; Qiu, J.; Li, B.; Jin, Z. Synthesis of cobalt phosphate nanoflakes for high-performance flexible symmetric supercapacitors. *J. Mater. Sci.: Mater. Electron.* **2018**, *29*, 16721–16729.
- (59) Zhang, G. Q.; Zhao, Y. Q.; Tao, F.; Li, H. L. Electrochemical characteristics and impedance spectroscopy studies of nano-cobalt silicate hydroxide for supercapacitor. *J. Power Sources* **2006**, *161*, 723–729.
- (60) Patil, A. M.; Lokhande, A. C.; Shinde, P. A.; Lokhande, C. D. Flexible asymmetric solid state supercapacitor by highly efficient 3D nanostructured $\alpha\text{-MnO}_2$ and h-CuS electrodes. *ACS Appl. Mater. Interfaces* **2018**, *10*, 16636–16649.
- (61) Pang, H.; Zhang, Y.; Lai, W. Y.; Hu, Z.; Huang, W. Lamellar $\text{K}_2\text{Co}_3(\text{P}_2\text{O}_7)_2 \cdot 2\text{H}_2\text{O}$ nanocrystal whiskers: high-performance flexible all-solid-state asymmetric micro-supercapacitors via inkjet printing. *Nano Energy* **2015**, *15*, 303–312.
- (62) Patil, A. M.; Lokhande, V. C.; Ji, T.; Lokhande, C. D. New design of all-solid state asymmetric flexible supercapacitor with high energy storage and long term cycling stability using m-CuO/FSS and h-CuS/FSS electrodes. *Electrochim. Acta* **2019**, *307*, 30–42.



Single-pot hydrothermal synthesis of manganese phosphate microrods as a cathode material for highly stable flexible solid-state symmetric supercapacitors

Pranav K. Katkar^a, Supriya J. Marje^a, Sachin S. Pujari^a, Suraj A. Khalate^a, Prashant R. Deshmukh^b, Umakant M. Patil^{a,*}

^a Centre for Interdisciplinary Research, D. Y. Patil Education Society (Deemed to Be University), Kasaba Bawada, Kolhapur, 416 006, M.S, India

^b Department of Mechanical Engineering, Chungnam National University (CNU), Daejeon, 34137, Republic of Korea

ARTICLE INFO

Keywords:

Hydrothermal method
Manganese phosphate
Microrods
Flexible symmetric solid-state device
Supercapacitor
Thin film

ABSTRACT

Here, we report a binder-free synthesis of microrods-like manganese phosphate thin film over stainless steel substrate by a facile, single-pot hydrothermal method. The XRD analysis reveals that, the formation of manganese phosphate [Mn₃(PO₄)₂] material of a monoclinic crystal structure. From SEM images observed microrods like morphology of manganese phosphate with an average width of ~25 μm. The manganese phosphate electrode shows a better electrochemical performance with a specific capacitance of 145 F g⁻¹ at 0.2 mA cm⁻² current density in 1.0 M Na₂SO₄ electrolyte. Moreover, the flexible solid-state symmetric electrochemical energy storage device was assembled with PVA-Na₂SO₄ solid gel-electrolyte consists of manganese phosphate as anode and cathode electrode. The corresponding symmetric supercapacitor achieves a high energy density of 11.7 Wh kg⁻¹ at a high power density of 1.41 kW kg⁻¹ with an excellent specific capacitance of 37 F g⁻¹ at 0.1 mA cm⁻² current density. Manganese phosphate shows long-term electrochemical cyclic stability at a current density of 0.8 mA cm⁻² for 9000 galvanostatic charge-discharge cycles with excellent capacitance retention (99 %). This excellent capacitive performance confirms that the manganese phosphate is promising material and fabricated flexible solid-state symmetric supercapacitor has high potential in the field of portable and bendable energy storage devices.

1. Introduction

Global extensions have stimulated the rate of energy consumption to very high levels, and the utilization of highly efficient, clean and sustainable energy conversion technologies and renewable energy resources are getting much attention. Among the existing energy generation and storage devices, supercapacitors (SCs) are considerably well attractive to solve the increasing concern about the energy crisis. [1]. Supercapacitor provides high power density, moderate energy density, longer durability and fast charging capability than batteries or fuel cells. Remarkably, flexible device with long cycle life has attracted significant attention in the field of power-source applications such as portable electronics, rollup/wearable displays, energy back-up device, sensor networks, electric vehicles, and mobile phones [2–4]. On the basis of energy storage mechanism, electrochemical capacitors are categorized into mainly two types, pseudocapacitors and electric double-layer capacitors (EDLCs). The EDLCs based materials with large specific

surface area, like carbonaceous materials, are storing the energies through electrical double layers. However, pseudocapacitor materials display quite a lot of oxidation states and store energy in electric double layers, as well as redox reaction at the electrode surfaces as like the transition metal oxides/hydroxides, sulfides, and conductive polymers [5–7]. Therefore, comparing pseudocapacitors with the EDLCs, pseudocapacitor shows good capacitive behavior with excellent specific capacitance [8].

Significantly more effort for fabricating high-performance supercapacitors has been done using various materials, such as Co(OH)₂ [9], MnCo₂O₄ [10], rGO-MnO₂ [11], α-MnO₂ [12], and Mn(OH)₂ [13]. Mn-based oxide/hydroxides are hard to reach the theoretical capacitance, power and energy density values because of poor electrical conductivity and the less specific capacitance due to the lower ion transfer rate [10,14]. The cobalt-based materials are more concentrated because of their attractive capacitance values, but they shows less cyclic stability compared to manganese based materials [15].

* Corresponding author.

E-mail address: umakant.physics84@gmail.com (U.M. Patil).



Scheme 1. The schematic diagram for preparation of manganese phosphate thin film using one-pot hydrothermal method.

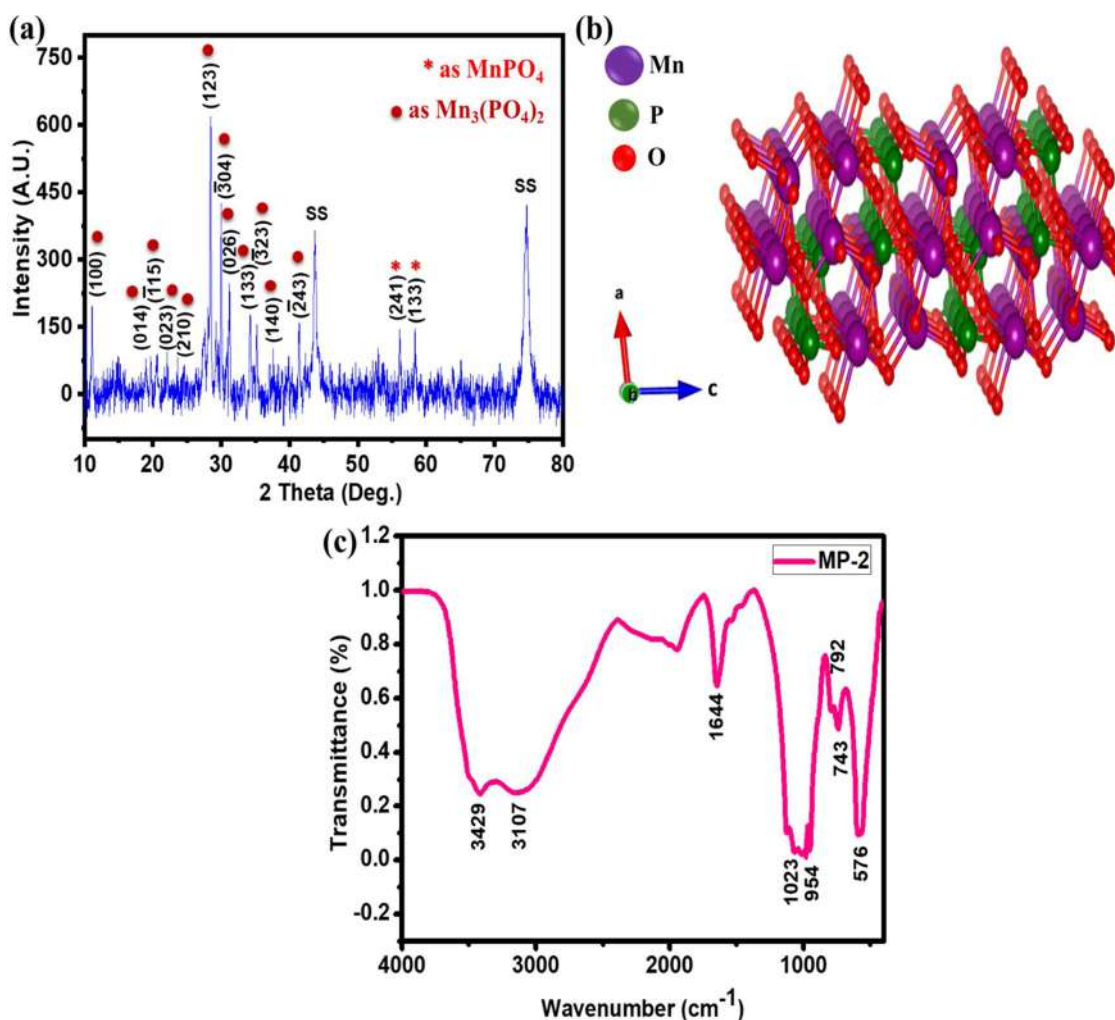


Fig. 1. (a) XRD pattern, (b) Monoclinic crystal structure and (c) FT-IR spectra of manganese phosphate (MP-2) thin film electrode.

Metal phosphates are widely investigated with high performance in lithium-ion batteries [16], solar cells [17] and rarely studied in SCs. In general, non-metal PO_4^{3-} anions are more advantageous than oxides/hydroxides, sulfides, and phosphides, because of their high electrochemical activities, non-toxicity, and chemical stability. The strong P–O covalent bonds to rise up redox potential and which makes the structure of manganese phosphate chemically more stable [18]. The chemically stable structure and a short diffusion path length of charge carriers electrode are the very important aspects for supercapacitor application. However, Mn-based phosphate is considered to be the most

potential pseudocapacitive electrode material due to its natural abundance, low cost, eco-friendly nature and its broad potential (voltage) window in neutral aqueous electrolytes. At ones, neutral electrolytes for supercapacitor have numerous benefits including high ionic conductivity, non-flammability, and good safety. In addition, the energy storage efficiency and supercapacitor application of manganese phosphate thin film electrode material have not been extensively studied. So, there is an opportunity to improve the performance of manganese phosphate thin-film electrodes, and an emerging concept is to direct growth of micro-structures on conducting substrates using the binder-

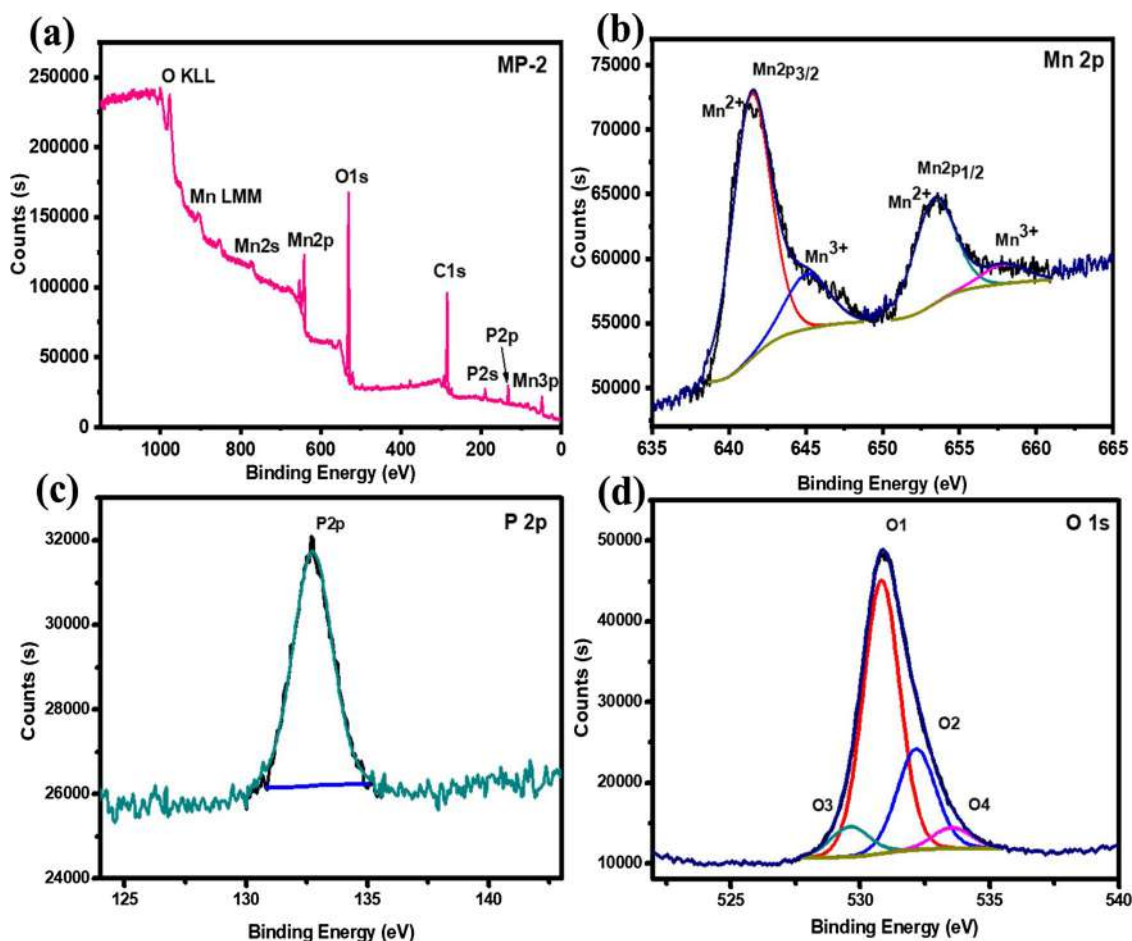


Fig. 2. XPS spectra of MP-2 thin film electrode (a) the whole pattern of MP-2 [$\text{Mn}_3(\text{PO}_4)_2$], (b) Mn 2p, (c) P 2p and (d) O 1s spectrum.

free synthesis method (hydrothermal) for supercapacitor or energy storage applications [3,15].

Recently, the flexible solid-state supercapacitors device gained excessive demand because of their lucrative combination with various modern flexible electronics [19,20]. Manufacturing of symmetric solid-state devices is an advantageous strategy to enhance the energy and power density of supercapacitors. Flexible symmetric solid-state supercapacitors have two identical electrodes material designed as cathode and anode [15]. To fabricate the flexible solid-state devices, appropriate electrode material with improved electrical conductivity, high mechanical strength, and excellent electrochemical stability is essential. Moreover, the good cyclic stability of electrode confirms potential of device in practical application. Therefore, we choose a manganese phosphate thin film electrode for the fabrication of a flexible symmetric device [21].

In this article, $\text{Mn}_3(\text{PO}_4)_2$ microrods were productively synthesized by facile, single-step hydrothermal route. Furthermore, supercapacitive performance of $\text{Mn}_3(\text{PO}_4)_2$ microrods were tested in 1 M Na_2SO_4 neutral electrolyte. It is found that, electrocapacitive performance of $\text{Mn}_3(\text{PO}_4)_2$ microrods has displayed a high specific capacitance with excellent cycling stability. The symmetric device is fabricated using the same material as a cathode and anode, and exhibited a high specific capacitance, superior energy density, and longer cyclic life. For a demonstration of the device, serially connected two devices are charged and it has glowed three red LEDs.

2. Experimental section

2.1. Materials

In this investigation, analytical grade reagents were used as precursors including, manganese chloride ($\text{MnCl}_2 \cdot 4\text{H}_2\text{O}$) and potassium dihydrogen orthophosphate (KH_2PO_4) and purchased from Sigma Aldrich. Polyvinyl alcohol ($\text{C}_2\text{H}_4\text{O}$)_x, urea [$\text{CO}(\text{NH}_2)_2$] and sodium sulphate (Na_2SO_4) were purchased from Alfa Aesar. Stainless steel (SS) (304 grade) of ~ 0.25 mm thickness was purchased from a local market of Kolhapur, India. All chemicals directly used without further purification.

2.2. Synthesis of manganese phosphate thin film

Typically, to prepare manganese phosphate, 0.05 M $\text{MnCl}_2 \cdot 4\text{H}_2\text{O}$ and 0.05 M KH_2PO_4 , were dissolved in 36 mL and 24 mL double distilled water (DDW), respectively. Then, both solutions were mixed with each other and 0.1 M concentration of $\text{Co}(\text{NH}_2)_2$ was dissolved in that bath named MP-1 and stirred for 5 min at 300 rpm. Similarly, the other two baths prepared using the same concentration of $\text{MnCl}_2 \cdot 4\text{H}_2\text{O}$ and KH_2PO_4 but the concentration of urea is increased in baths (0.15 and 0.20 M) and named as MP-2 and MP-3. The stainless steel (SS) substrate which was well cleaned in DDW using sonication and dipped vertically in above 60 mL baths and those baths were placed in a hydrothermal autoclave and heated at 120 °C for 1 h. Then, autoclave was cooled down to room temperature in the ambient environment. Finally, the manganese phosphate loaded milky-white colored films were obtained over SS substrate, which was rinsed several times in DDW and air-dried

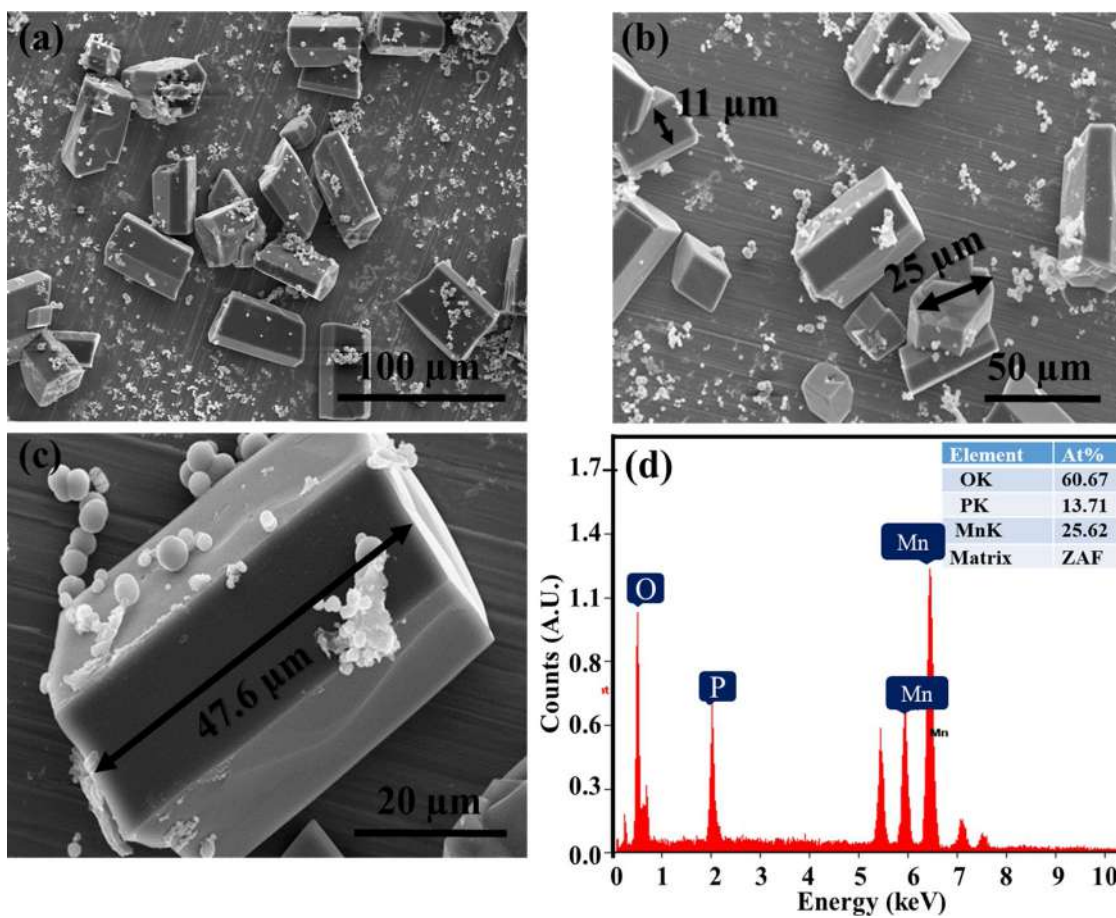


Fig. 3. (a-c) FE-SEM images at various magnifications (4000X, 8000X, 20000X) and (d) EDS spectrum of manganese phosphate (MP-2) thin film sample.

at ambient environment and used as it is for further characterization and electrochemical capacitive performance testing.

2.3. Fabrication of all-solid-State symmetric supercapacitor

For fabrication of a flexible solid-state symmetric supercapacitor device (FSS-SC), two identical manganese phosphate (MP-2) electrodes were assembled in a planar configuration with a PVA- Na_2SO_4 gel electrolyte. While choosing the gel electrolyte for a flexible device, the most important criterion was that the electrolyte must be ionically conducting and should not damage during bending and aqueous gel electrolyte of PVA- Na_2SO_4 perfectly fits the need. The gel electrolyte was obtained as follows: In 60 mL of DDW, 6 g of PVA was dissolved by heating at 80 °C. When, solution appeared clear and transparent, then separately prepared (in 40 mL double distilled water) 1 M Na_2SO_4 solution was mixed slowly in the above solution. Later, the entire solution was vigorously mixed so it became clear and transparent. Then, the prepared gel electrolyte (PVA- Na_2SO_4) was coated over the active material as an electrolyte and another two layers of gel electrolyte were applied after 15–30 min. Eventually, the pieces of two manganese phosphate (MP-2) thin-film electrodes pressed with each other including gel electrolyte and lastly, solid-state flexible symmetric supercapacitor device was developed.

2.4. Materials characterization

The structural characterization of the manganese phosphate was performed using X-ray diffraction, (XRD, Rigaku miniflex-600) equipped with monochromatized $\text{Cu K}\alpha$ (1.5406 Å) radiation. Fourier transform infrared (FTIR) spectra were collected on an Alpha (II)

Bruker unit ranged from 400 to 4000 cm^{-1} . Elemental analysis investigated using X-ray photoelectron spectroscopy (XPS) ES-CALAB 250 spectrometer (Thermo Fisher Scientific, UK). The morphology and elemental composition were observed using scanning electron microscopy (SEM) conducted by JSM-7001 F, JEOL microscope provided with energy-dispersive X-ray spectroscopy (EDS) Oxford, X-max analyzer. The electrochemical characterizations of the materials were performed with a ZIVE MP1 multichannel electrochemical workstation equipment.

2.5. Electrochemical measurements

The electrochemical capacitive performance was characterized by cyclic voltammetry (CV), galvanostatic charge-discharge (GCD), and electrochemical impedance spectroscopy (EIS) techniques at ambient conditions. All electrochemical measurements were conducted in a conventional three-electrode cell system with 1.0 M Na_2SO_4 neutral electrolyte. A saturated calomel electrode (SCE) and platinum (Pt) plate were used as a reference and counter electrode, respectively along with manganese phosphate thin film as a working electrode. The CV and GCD tests were performed within 0.0 and 0.9 V at different scanning rates and current densities, respectively in the three-electrode system. The EIS was measured within frequency range of 100 mHz to 100 kHz with a 10 mV amplitude. Also, the two-electrode system was fabricated using a manganese phosphate thin film as positive and negative electrode with PVA- Na_2SO_4 as a solid gel electrolyte. The specific capacitance, energy density, and power density were calculated using the following equations,

$$C_s = \frac{I \times \Delta t}{m \times \Delta V} \quad (\text{F g}^{-1}) \quad (1)$$

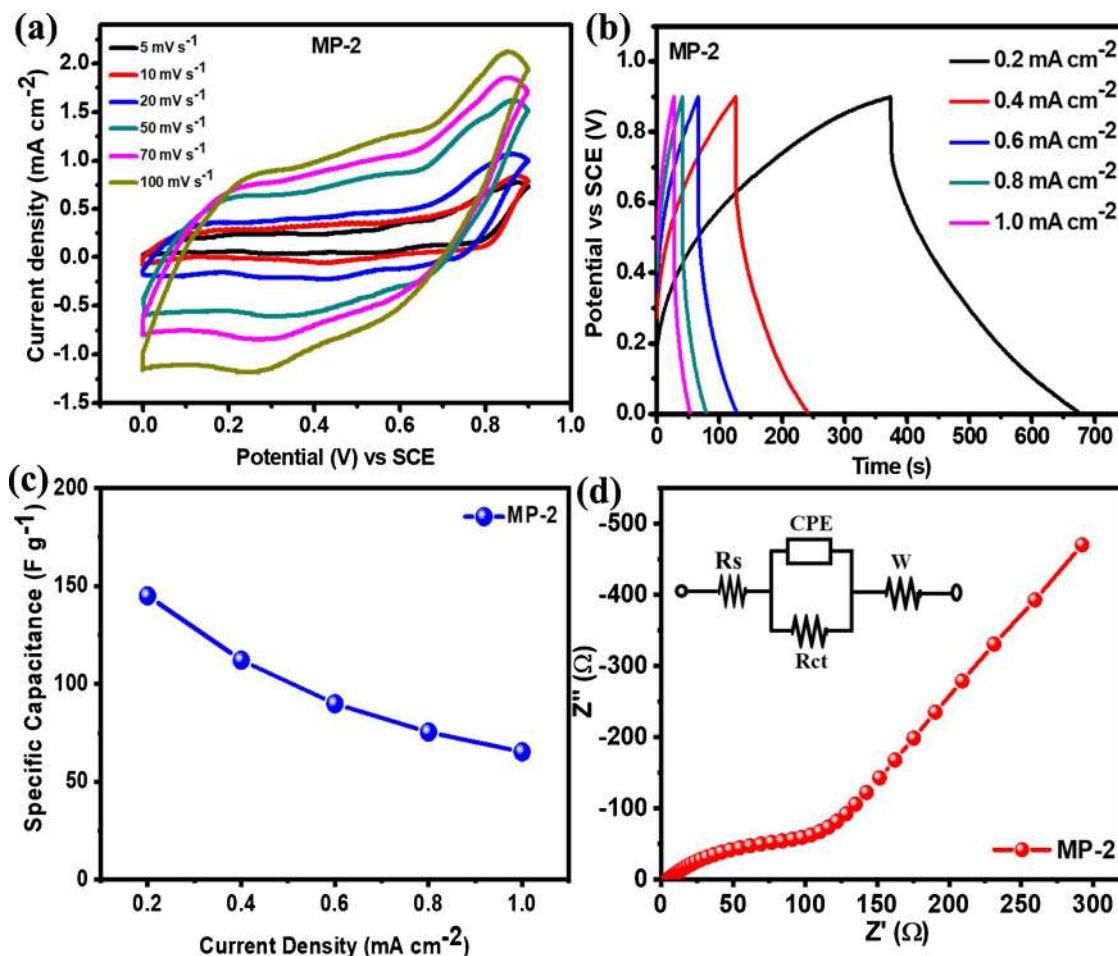


Fig. 4. (a) CV curve recorded at various scan rates from 5–100 mV s^{-1} , (b) GCD curves at various current densities (0.2–1.0 mA cm^{-2}) of MP-2 electrode. (c) Specific capacitance and (d) Nyquist plot of MP-2 thin film electrode (inset: fitted circuit).

Table 1

Comparative literature survey for capacitive performance of manganese phosphate based pseudocapacitive electrodes.

Sr. No.	Material and structure	Method of deposition	Electrolyte	Capacitance at a current density	stability	cycles	Ref.
1.	$\text{Mn}_3(\text{PO}_4)_2/\text{GF}$ (Hexagonal Micro-rods)	Hydrothermal	6 M KOH	270 Fg^{-1} at 0.5 Ag^{-1}	99 %	1000	[14]
2.	$\text{Mn}_3(\text{PO}_4)_2/\text{PANI}$ (Nanoparticle)	Sonochemical	1 M KOH	347 Cg^{-1} at 1 Ag^{-1}	60%	3000	[28]
3.	$\text{KMnPO}_4 \cdot \text{H}_2\text{O}$ (Submicron sized particles)	Sol-Gel	1 M KOH	516 Fg^{-1} at 2 mV s^{-1}	82%	1000	[29]
4.	$\text{NH}_4\text{MnPO}_4 \cdot \text{H}_2\text{O}$ (Micro-Nano Structure)	Heat Treatment	1 mol/L Na_2SO_4	35 Fg^{-1} at 10 mV s^{-1}	–	–	[41]
5.	$\text{MnPO}_4 \cdot \text{H}_2\text{O}/\text{GO}$ (Nanowires)	Hydrothermal	3 M KOH	287.9 Fg^{-1} at 0.625 Ag^{-1}	–	–	[42]
6.	$\text{Mn}_3(\text{PO}_4)_2$ (Nanosheets)	Hydrothermal	1 mol/L Na_2SO_4	203 Fg^{-1} at 0.5 Ag^{-1}	91.1%	10,000	[43]
7.	$\text{Mn}_3(\text{PO}_4)_2 \cdot 3\text{H}_2\text{O}/\text{Graphene}$ (Nanosheets)	Exfoliation Precipitation	6 M KOH	152 Fg^{-1} at 0.5 Ag^{-1}	–	–	[44]
8.	PMn (Nanosheets array)	Electro-deposition	0.1 M Na_2SO_4	6.7 m F cm^{-2} at 5 mV s^{-1}	87.6%	5000	[51]
9.	$\text{Mn}_3(\text{PO}_4)_2$ (Microrods)	Hydrothermal	1 M Na_2SO_4	145 Fg^{-1} at 0.2 mA cm^{-2}	99.5 %	7000	This work

$$E = \frac{0.5 \times C_s \times (\Delta V)^2}{3.6} \quad (\text{Wh kg}^{-1}) \quad (2)$$

$$P = \frac{E \times 3.6}{\Delta t} \quad (\text{W kg}^{-1}) \quad (3)$$

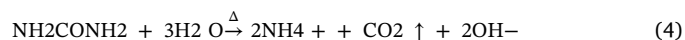
Where, C_s (F g^{-1}) is the specific capacitance, I (mA cm^{-2}) represents current density, ΔV (V/SCE) is a potential window, m (g) is mass of active materials, Δt (s) is discharging time, E (Wh kg^{-1}) is energy density and P (W kg^{-1}) represents power density.

3. Result and discussion

3.1. Film formation and reaction mechanism

The formation of manganese phosphate microrods like structure

was achieved by a facile hydrothermal method. The crystal formation of the manganese phosphate material on SS substrate surface in thin film form can be categorized as heterogeneous nucleation and subsequent particle growth. If crystals are directly grown on the conducting SS substrate in thin film form, it will be feasible for supercapacitor applications since it is a binder-free electrode synthesis approach. In the formation of manganese phosphate, when the solution bath temperature increases to 120 °C, then decomposition of the urea starts at 90 °C and forms NH_4^+ and CO_2 , according to the following reaction equation: [22,23]



Homogeneous precipitation by using hydrolyzing agent (urea) offers the opportunity to produce uniform particles. The NH_4^+ released from

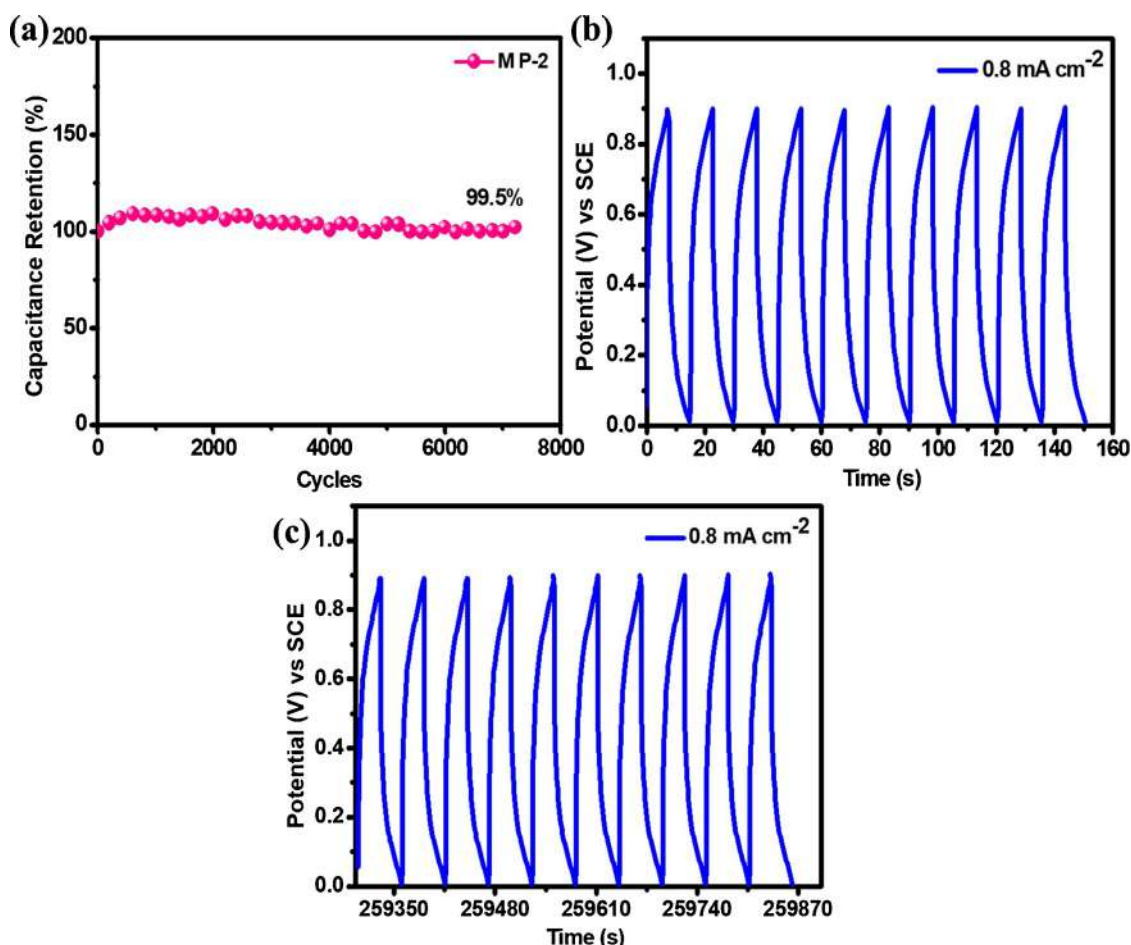
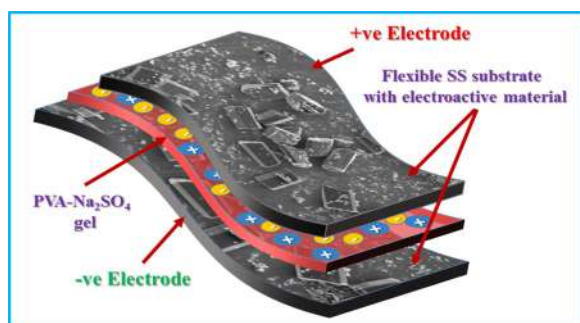
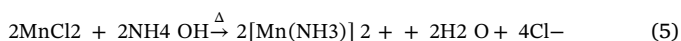


Fig. 5. (a) cyclic stability at 7000 cycles of MP-2 electrode and (b-c) the charge-discharge profile of MP-2 sample for first and last ten cycles of GCD test at 0.8 mA cm^{-2} .



Scheme 2. A Schematic diagram of the flexible symmetric solid-state supercapacitor based on manganese phosphate electroactive material.

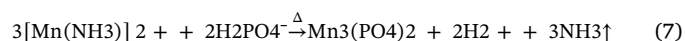
urea in the bath complexed with Mn^{2+} ions present in the solution and form complex as $[\text{Mn}(\text{NH}_3)_2]^{2+}$ which controls the releasing rate of Mn^{2+} ions during the deposition of the manganese phosphate thin films. The expected reaction mechanism can be presented as in eq. (5):



On the other side, potassium phosphate dissociates [24] as per Eq. (6),



Lastly, complexed manganese ions (Mn^{2+}) and phosphate (PO_4^-) precursor ions react and produces $\text{Mn}_3(\text{PO}_4)_2$ material thin films on SS substrate, according to reaction presented below [eq. (7)],



In conformity with the above reaction mechanism, the milky white-colored manganese phosphate grew over the SS substrate (see the photograph of a thin film shown in Scheme 1). The manganese phosphate material on SS substrates was weighed by gravitational weight difference method. It is observed that, with an increasing concentration of urea in the reaction bath, the accumulated mass of the manganese phosphate material decreases from MP-1 to MP-3 (deposited mass 4.62, 3.98, 3.71 mg, respectively). This is may be due to an increase in urea concentration, which increases the rate of hydrolysis. Thus, various concentrations of hydrolyzing agent promote reaction rates and control the film thickness.

3.2. XRD, FTIR and XPS results

The crystal phase of a prepared samples are characterized by X-ray diffraction (XRD) technique and the pattern is shown in Fig. 1 (a) and S1 (a) (see ESI). It is observed that, the diffraction peaks (2θ deg.) at 11.02, 18.96, 20.64, 21.98, 24.51, 28.49, 29.83, 31.23, 34.30, 35.32, 37.60 and 41.59° are indexed to (1 0 0), (0 1 4), ($\bar{1}$ 1 5), (0 2 3), (2 1 0), (1 2 3), ($\bar{3}$ 0 4), (0 2 6), (1 3 3), ($\bar{3}$ 2 3), (1 4 0) and ($\bar{2}$ 4 3) plane of the monoclinic phase of manganese phosphate $[\text{Mn}_3(\text{PO}_4)_2]$ (JCPDS Card no. 01-073-1088) indicated as “**cirf**,” and the diffraction peaks 56.04 and 58.43° are indexed to (2 4 1) and (1 3 3) plane of the orthorhombic phase of manganese phosphate $[\text{MnPO}_4]$ (JCPDS Card no. 01-077-0180) indicated as “*” with a deviation of $\pm 0.001 \text{ \AA}$. Moreover, the peak intensity (with respect to major peak (1 2 3)) increases from sample MP-1 to MP-3, which attributed to oriented growth of material

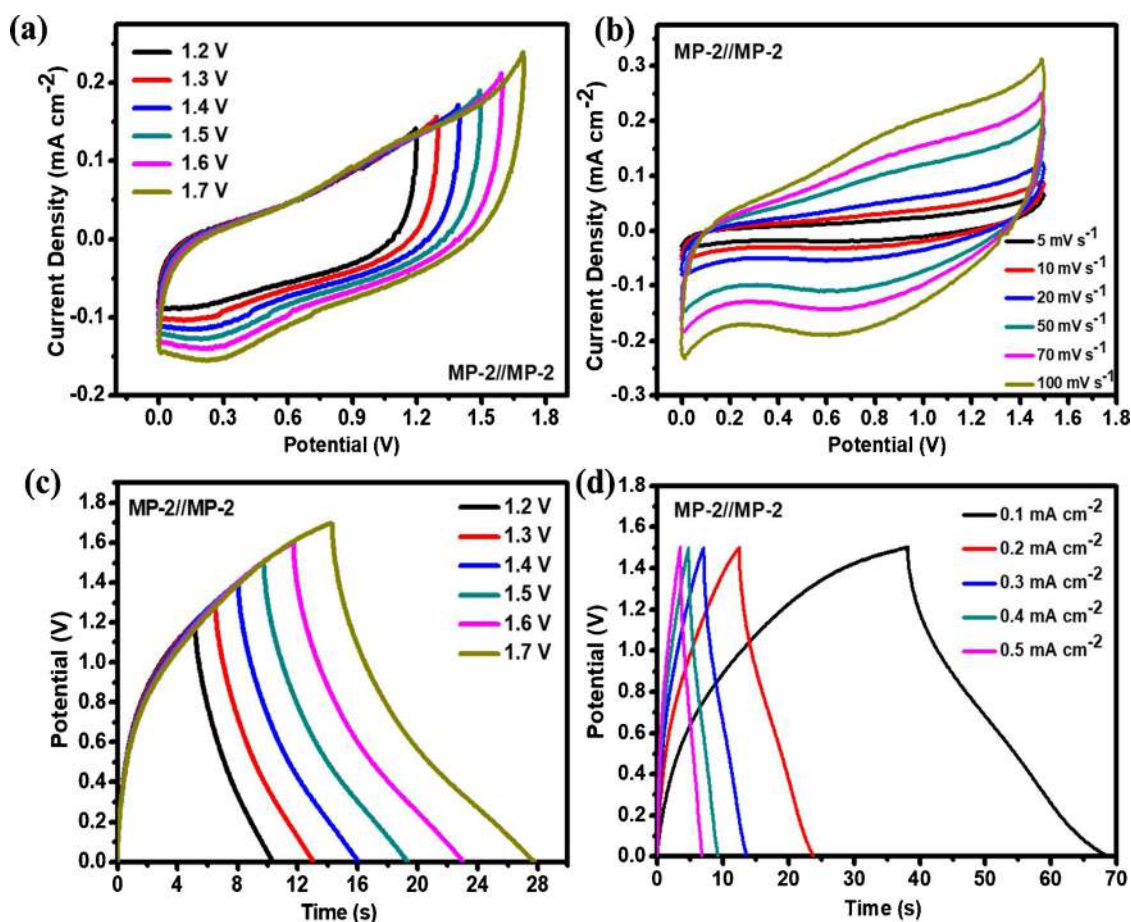


Fig. 6. (a) The CV plots at constant scan rate of 50 mV s^{-1} for different potential ranging from + 1.2 to + 1.7 V, (b) CV curves at different scan rates (5–100 mV s^{-1}), (c) The GCD curves at 0.4 mA cm^{-2} for potentials of +1.2 to +1.7 V and (d) GCD curves from 0.1–0.5 mA cm^{-2} current densities of MP-2//MP-2 FSS-SC device.

towards (1 2 3) and (0 2 6) plane, with an increase in length and a little decrease in the width of microrods, respectively. The monoclinic crystal structure of manganese phosphate is shown in Fig. 1(b). Narrow shaped peak suggests that the MP sample occupies more excellent crystallinity. In general, materials with good crystallinity can improve electrochemical efficiency, as a stable crystal structure cannot be simply damaged between the charge/discharge processes [25].

FTIR analysis was employed to identify the phase and the presence of functional groups in the sample MP-2. The Fig. 1(c) and S1 (b) shows, distinct absorption bands at 576, 743, 792, 954, 1023, 1644, 3107 and 3429 cm^{-1} . The characteristic peak at 576 cm^{-1} of stretching vibrations of the Mn–O bond and the absorption peak at 743 cm^{-1} is observed due to the P–O–P bending modes [26]. The peak intensity of wavenumber 576 cm^{-1} is progressively increased from MP-1 to MP-3 thin film samples. 792 cm^{-1} band is assigned to asymmetric stretching mode of the P–OP– [27]. The symmetric stretching modes of the PO_4^{3-} ion observed at 954 cm^{-1} [28]. The peak at 1023 cm^{-1} attributed to asymmetric P–O stretching [29]. Further, bending vibrations of H–OH– is observed around 1644 cm^{-1} and it indicates moisture adsorbed on the surface of thin film sample [30]. The peak intensity of wavenumber 1644 cm^{-1} is decreased from MP-1 to MP-3 thin film samples, indicates decreasing adsorbed moisture on the surface of manganese phosphate material. The absorption band around 3107 cm^{-1} is attributed to hydrogen phosphate due to P–OH stretching, respectively [31]. The –O–H stretching vibrations of water molecules is observed at 3429 cm^{-1} [29]. The results of the FTIR analysis are synchronized with the XRD results and confirm that the deposited thin film contains structural water. The XRD and FTIR result suggests successful formation of the hydrous manganese phosphate thin film.

The investigation chemical composition of $\text{Mn}_3(\text{PO}_4)_2$ by XPS spectra is shown in Fig. 2. The survey spectrum [Fig. 2 (a)] identifies the characteristic peaks for Mn LMM, O KLL, Mn 2p, Mn 3p, Mn 2s, P 2p, P 2s, C 1s, and O 1s, confirming the presence of respective elements in the thin films but a signal of C element may arise from surface oxidation of the product [32]. Also, O KLL and Mn LMM peaks are some of the most commonly identified transitions during the surface analysis [33]. The Mn 2p XPS spectrum [Fig. 2 (b)] shows two main and their satellite peaks at higher binding energies. The Mn $2p_{3/2}$ main peak is at 641.6 eV with its satellite peak at 645.1 eV and Mn $2p_{1/2}$ main peak is at 653.5 eV with its satellite peak at 657.8 eV . The values are in accordance with that of Mn^{2+} and Mn^{3+} oxidation states, respectively [34]. The XPS spectra of P 2p [Fig. 2(c)] shows peak at 132.7 eV assigned to P 2p spectra from the PO_4^{3-} group ion [35]. The XPS peak of O 1s [Fig. 2 (d)] deconvoluted into four peaks, the 529.5 eV peaks correspond to oxide species (O–Mn–O) between manganese and oxygen [36]. The peaks at binding energy of 530.8 , 532.2 , 533.6 eV are originally obtained from the phosphate (P–O), oxygen and moisture or absorbed water bonding, respectively in $\text{Mn}_3(\text{PO}_4)_2$, which are very well matched with the summarized outcomes [37]. The XRD, FTIR and XPS results show that the hydrous manganese phosphate thin film is successfully synthesized by a one-pot hydrothermal method.

3.3. Morphology of manganese phosphate

The surface morphology of as-synthesized manganese phosphate (MP-1 to MP-3) microrods examined by the SEM and shown in Fig. 3 and S2 (See ESI). Fig. 3 presents low and high resolution (4000X, 8000X, 20000X) SEM images of MP-2 sample. The morphology of MP

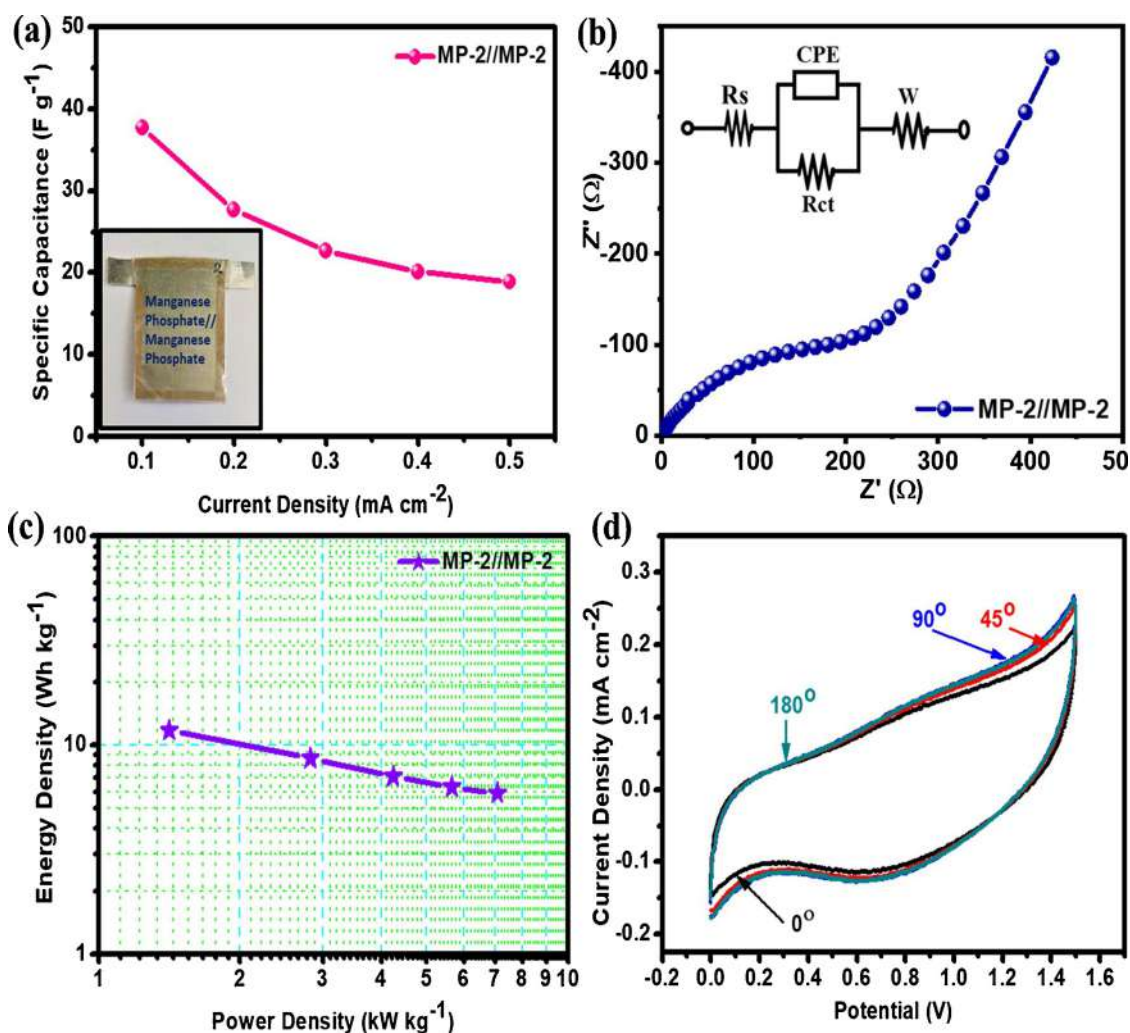


Fig. 7. (a) Specific capacitance at various current densities, (b) EIS plot (Inset: fitted circuit), (c) Ragone plot and (d) CV curve of bending angles at different bending angles from 0-180° of MP-2//MP-2 FSS-SC device.

series thin film electrodes shows hexagonal microrods like structure which are distributed all over the substrate. The Fig. 3 (a–c) shows hexagonal microrods like structure having uniform shapes but different sizes with an average length of $\sim 47.6\ \mu m$ and width of $\sim 25\ \mu m$ for MP-2 sample. Similar, microstructure is observed for other MP-1 and MP-3 samples and shown in figure S2 (see ESI). SEM morphology is consistent with the XRD pattern result, the hexagonal microrods are almost parallel to the substrate, indicating that manganese phosphate microrods preferentially grew along with the (1 2 3) direction and it is much stronger than the other peaks. It suggesting a preferential orientation of the crystals along the c-axis of the manganese phosphate micro-structure. It is expected that the microrods like morphology may possess a stable structure and may facilitate quite and easy electrolyte diffusion [38]. This morphology is considered to perform an important part in improving the stability of a thin film electrode in electrochemical capacitor applications.

The energy-dispersive X-ray (EDX) spectra [Fig. 3 (d) and S3 (See ESI)] of manganese phosphate thin film samples reveal that the as-obtained microrods contains Mn, P and O elements. The Mn:P atomic ratio in MP-1 to MP-3 is 3:1.90, 3:1.60 and 3:1.73, respectively. Furthermore, the extensive EDX analysis confirms that the molar ratios of manganese phosphate are very close to those of their precursors as 3:2.

3.4. Electrochemical capacitive studies

3.4.1. Manganese phosphate electrode performance

The electrochemical performance of manganese phosphate (MP series) samples was assessed in a three-electrode system with conventional electrochemical techniques of cyclic voltammetry (CV), galvanostatic charge-discharge (GCD), and electrochemical impedance spectroscopy (EIS) using 1 M Na_2SO_4 electrolyte. Fig. 4(a) demonstrates a typical CV curve of MP-2 electrode measured in a voltage window ranging from 0.0 to 0.9 V at various scan rates of 5 to 100 $mV\ s^{-1}$. Also, the CV curves of another thin film samples (MP-1 and MP-3) at various scan rates are shown in figure S4 (See ESI). It is found that, the CV curve shows a rectangular shape that represents the quasi-ideal capacitive response of the electrode. Increasing specific capacitance with the decreasing current under area of the curve was further confirmed by determining the area occupied by Na^+ (hydrated) ions over surface of the electrodes with respect to the scan rate. It has been found that ions coming from the electrolyte at a low scan rate allow plenty of time to adsorb/desorb on inner and outer surfaces of the active material. On the other hand, at higher scan rate, movement in the electrolytic ion causes difficulty in accessing all possible sites on the surface of electrode material. So, the specific capacitance is lower with a higher scan rate and vice versa [4,5,39,40].

To further investigate the electrochemical performance of manganese phosphate (MP-series), the GCD study of MP-2 sample is shown in

Table 2
Comparative literature survey of similar or close systems of $\text{Mn}_3(\text{PO}_4)_2$ Symmetric/Asymmetric with FSS-SC device.

Sr. No.	Material and structure	Method of deposition	Capacitance at a current density	Energy density	Power density	stability	cycles	Ref.
1.	$\text{Mn}_3(\text{PO}_4)_2/\text{GF}/\text{AC}$ (Hexagonal Micro-rods)	Hydrothermal	28 Fg^{-1} at 0.5 Ag^{-1}	7.6 Wh kg^{-1}	3528 W kg^{-1}	96%	10,000	[14]
2.	$\text{Mn}_3(\text{PO}_4)_2/\text{PANI}/\text{AC}$ (Nanoparticle)	Sonochemical	73 Cg^{-1} at 0.5 Ag^{-1}	14.7 Wh kg^{-1}	2988 W kg^{-1}	80%	3000	[28]
3.	$\text{MnPO}_4/\text{H}_2\text{O}/\text{GO}/\text{MnPO}_4/\text{H}_2\text{O}/\text{GO}$ (Nanowires)	Hydrothermal	115.63 Fg^{-1} at 0.625 Ag^{-1}	5.78 Wh kg^{-1}	$1.5 \times 10^4 \text{ W kg}^{-1}$	85.3%	1000	[42]
4.	$\text{Mn}_3(\text{PO}_4)_2/\text{AC}$ (Nanosheets)	Hydrothermal	46.8 Fg^{-1} at 0.5 Ag^{-1}	16.64 Wh kg^{-1}	7984.48 W kg^{-1}	90%	10,000	[43]
5.	$\text{Mn}_3(\text{PO}_4)_2/\text{Mn}_3(\text{PO}_4)_2$	Exfoliation Precipitation	53.7 Fg^{-1} at 0.5 Ag^{-1}	19.09 Wh kg^{-1}	8033 W kg^{-1}	90%	10,000	[44]
6.	$\text{Mn}_3(\text{PO}_4)_2/3\text{H}_2\text{O}/\text{Graphene}/\text{Mn}_3(\text{PO}_4)_2/3\text{H}_2\text{O}/\text{Graphene}$ (Nanosheets)	Exfoliation Precipitation	152 Fg^{-1} at 0.5 Ag^{-1}	35.5 Wh kg^{-1}	365 W kg^{-1}	100%	2000	[44]
7.	$\text{Mn}_3(\text{PO}_4)_2/3\text{H}_2\text{O}/\text{AC}$ (Nanosheets)	Chemical precipitation	–	32.32 Wh kg^{-1}	4250 W kg^{-1}	65.22%	2000	[50]
8.	$\text{MoS}_2/\text{Ni}(\text{OH})_2/\text{MoS}_2/\text{Ni}(\text{OH})_2$ (Flowerlike nanoplates/sheets)	Microwave hydrothermal	14.07 m F cm^{-2} in area, 37.53 F cm^{-3} in volume at 1 mV s^{-1}	5.2 mWh cm^{-3}	11 W cm^{-3}	94.2%	9000	[52]
9.	$\text{CeO}_2/\text{MWCNTs}/\text{CeO}_2/\text{MWCNTs}$ (Nanoparticle)	Chemical bath deposition (CBD)	486.5 F g^{-1} at 2 mV s^{-1}	85.7 Wh kg^{-1}	2.6 kW kg^{-1}	92.1%	10,000	[53]
10.	$\text{CeO}_2/\text{SS}/\text{CeO}_2/\text{SS}$ (Nanoparticle)	Refluxing process	321.3 F g^{-1} at 2 mV s^{-1}	61.4 Wh kg^{-1}	3.5 kW kg^{-1}	90.1%	5000	[54]
11.	$\text{VS}_2/\text{SS}/\text{VS}_2/\text{SS}$ (Nanoparticle)	Successive ionic layer adsorption and reaction (SILAR)	118 F g^{-1} at 2 mV s^{-1}	25.9 Wh kg^{-1}	1.5 kW kg^{-1}	89%	6000	[55]
12.	$\text{Mn}_3(\text{PO}_4)_2/\text{Mn}_3(\text{PO}_4)_2$ (Microrods)	Hydrothermal	37 F g^{-1} at 0.1 mA cm^{-2}	11.7 Wh kg^{-1}	7.071 kW kg^{-1}	99 %	9000	This work

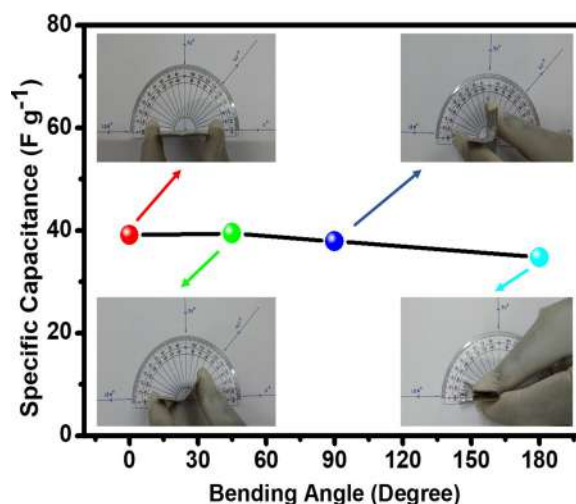


Fig. 8. Specific capacitance at different bending angles of MP-2//MP-2 FSS-SC device from 0-180°.

Fig. 4(b) and MP-1 and MP-3 samples are shown in ESI figure S5 in Supporting Information. It is carried out at different current densities of 0.2, 0.4, 0.6, 0.8, 1.0 mA cm^{-2} in a voltage range of 0.0 to 0.9 V. As illustrated in Fig. 4 (b), there is good symmetry in the GCD curves, which shows their excellent reversal Faradic reactions of $\text{Mn}^{2+}/\text{Mn}^{3+}$ and suggests superior electrochemical stability of manganese phosphate material. The specific capacitance [shown in Fig. 4(c)] of the MP-2 electrode, calculated from GCD graph according to Eq. (1) are 145, 112, 90, 75, 65 F g^{-1} at 0.2–1.0 mA cm^{-2} current densities in neutral (Na_2SO_4) electrolyte. This capacitive behavior is extremely competitive compared to earlier published manganese phosphate-based electrode materials (Table 1). Pang et al. [41] synthesized Micro-Nano like structure of $\text{NH}_4\text{MnPO}_4 \cdot \text{H}_2\text{O}$ using heat treatment and obtained specific capacitance of 35 F g^{-1} at 10 mV s^{-1} scan rate. Yan et al. [42] prepared nanowires like $\text{MnPO}_4 \cdot \text{H}_2\text{O}/\text{GO}$ using a hydrothermal method and obtained specific capacitance of 287.9 F g^{-1} at 0.625 A g^{-1} current density. Ma et al. [43] have prepared Nanosheets-like morphology of $\text{Mn}_3(\text{PO}_4)_2$ using hydrothermal method and reported a high specific capacitance of 203 F g^{-1} at 0.5 A g^{-1} current density. Mirghni et al. [14] prepared hexagonal micro-rods manganese phosphate/graphene foam ($\text{Mn}_3(\text{PO}_4)_2/\text{GF}$) via a facile hydrothermal method and obtained specific capacitance of 270 F g^{-1} at 0.5 A g^{-1} current density in 6 M KOH electrolyte. Lee et al. [28] prepared $\text{Mn}_3(\text{PO}_4)_2/\text{PANI}$ nanoparticles by a sonochemical method and obtained specific capacitance of 347 F g^{-1} at a current density of 1 A g^{-1} in 1 M KOH electrolyte. Also, Yang et al. [44] prepared $\text{Mn}_3(\text{PO}_4)_2 \cdot 3\text{H}_2\text{O}/\text{graphene}$ nanosheets using the exfoliation precipitation process and achieved a specific capacitance of 152 Fg^{-1} at 0.5 Ag^{-1} current density in 6 M KOH electrolyte. The specific capacitance is higher in most current published works, it may be due to the use of graphene or polyaniline supplemental materials, to enhance the conductivity and electrochemical efficiency of the active material. Moreover, the Ni-foam was used as conducting substrate and during electrochemical testing, it plays an important role to increase the electrochemical efficiency of electroactive material by adding self-capacitance by transforming its surface atom into NiO and $\text{Ni}(\text{OH})_2$. However, in the current study, stainless steel is used as the substrate to synthesize manganese phosphate thin film electrode, which provides only 2D structure and does not participate in the electrochemical reaction. Therefore, in this study achieved specific capacitance is completely given by only manganese phosphate material.

The Fig. 4(d) and figure S7 (See ESI) shows the Nyquist plots of MP-2, and MP-1 and MP-3 electrodes, respectively in the frequency range of 100 mHz to 100 kHz with 10 mV amplitude. The equivalent circuit for the fitted data of the impedance curve is presented in the inset of Fig. 5

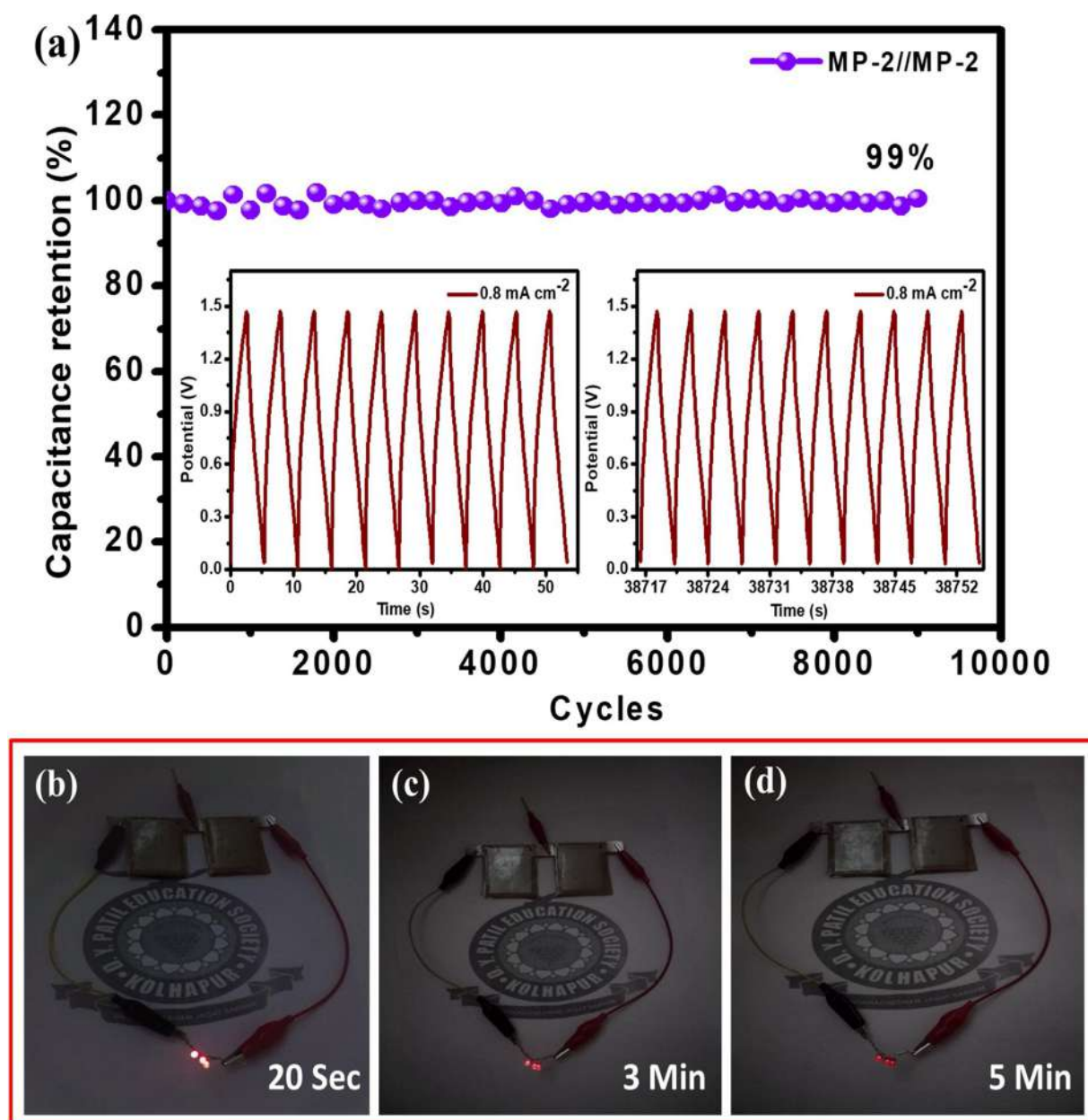


Fig. 9. (a) Cyclic stability of MP-2 FSS-SC device at 9000 cycles (Inset: GCD cycles first and last ten cycles at 0.8 mA cm^{-2}) and (b-d) Demonstration photographs of MP-2//MP-2 FSS-SC device by glowing three red LEDs at initial 20 s, 3 min and after 5 min. (For interpretation of the references to colour in this figure legend, the reader is referred to the web version of this article).

(b). The fitted circuit shows solution resistance (R_s), a charge transfer resistance (R_{ct}) of the electrolyte ions in the MP-2 thin film samples. A constant phase element (CPE) to account for the double-layer capacitance and Warburg diffusion element (W) is an equivalent electrical circuit component in fitted circuit. The curve is made up of a semi-arc in the high-frequency region followed by a linear region in the low-frequency region. The micro-structured sample of MP-2 electrode displayed a very less solution resistance (ESR) (R_s , 4.92Ω and R_{ct} , 138.9Ω) in the electrochemical impedance study. The EIS study explicated that low impedance results in higher electrochemical performance of MP-2 electrodes. The EIS curve shows good electronic conductivity and small values of resistance indicate better charge transfer rate of manganese phosphate, which is beneficial for charging the storage process [45].

Higher cyclic stability is one more important part of the electrode materials in the supercapacitor application. The cyclic stability was

measured by performing charge-discharge tests of the MP-2 electrode at a current density of 0.8 mA cm^{-2} and shown in Fig. 5 (b). The MP-2 sample displays excellent cycling efficiencies of 99.5 % after 7000 cycles in neutral electrolyte. The hexagonal microrods like morphology possess a stable structure and easy electrolyte diffusion for improving cyclic stability of manganese phosphate electrode [38]. In Fig. 5 (c-d) displays the charge-discharge curves of the initial ten and the last ten cycles of 7000 cycles. It is clearly seen that, the curves of the last ten cycles have a minimal difference compared with the initial ten cycles with symmetric shape, highly little internal resistance (iR) drop, which exhibits long-term cycling stability (99.5 %) of MP-2 electrode.

3.4.2. Manganese phosphate symmetric supercapacitor

A flexible symmetric solid-state supercapacitor (FSS-SC) was assembled by employing highly stable manganese phosphate (MP-2) thin film electrodes using PVA- Na_2SO_4 gel electrolyte. Two MP-2

symmetrical electrodes are covered and sandwiched with polymer gel electrolyte which performs as separate as well as an electrolyte, and demonstrated in Scheme 2. The practical applicability of this device is evaluated using a CV, GCD, EIS and electrochemical stability analysis. Fig. 6 (a) presents the potential window variation of FSS-SC MP-2//MP-2 device at a constant scan rate of 50 mV s^{-1} . This analysis decides the suitable potential window for SCs device. The area under CV curve for FSS-SC MP-2//MP-2 devices is symmetric up to 1.5 V. Fig. 6 (b) describes CV curves of symmetric FSS-SC MP-2//MP-2 device for various scan rates ranging from 5 to 100 mV s^{-1} . The area under the CV curve and the high current in the PVA- Na_2SO_4 electrolyte show high capacitance, which is probably due to the high charge transfer capability of the organic polymer solid-state gel electrolyte [46]. It is clearly seen that, better performance of symmetric FSS-SC MP-2//MP-2 supercapacitor device at every scan rates. At a low scan rate, limited restriction on the movement of electrolyte ions, entire electroactive material contribution and extra time possess maximum capacitance [47,48]. Similarly, the potential window selection for FSS-SC MP-2//MP-2 device by GCD is carried out at a constant current density of 0.4 mA cm^{-2} [shown in Fig. 6 (c)]. It is seen that the potential window 0–1.5 V is appropriate for FSS-SC MP-2//MP-2 device. In order to study the performance of symmetric FSS-SC MP-2//MP-2 device, GCD curves at various current densities of 0.1–0.5 mA cm^{-2} were tested and shown in Fig. 6 (d). On the basis of total mass of both electrodes, the calculated capacitance from GCD curve is 37.7, 27.6, 22.6, 20.1 and 18.8 F g^{-1} at current densities of 0.1, 0.2, 0.3, 0.4 and 0.5 mA cm^{-2} , respectively [shown in Fig. 7 (a)]. It is found that, the as-fabricated symmetric supercapacitor reveals excellent rate capability.

EIS is a better way to learn the properties of charge transfer kinetics and its electrode-electrolyte interface [49]. The Nyquist plot of the flexible symmetric solid-state supercapacitor is presented in Fig. 7 (b). The semi-arc at high frequencies correlate with the Faradic charge-transfer resistance (R_{ct}). Intercept (Z) on real impedance axis is the solution resistance (R_s , 0.96Ω). From the EIS, there is a low charge transfer resistance (R_{ct}) of 282.6Ω manifesting the reaction of fast ion diffusion, a CPE to account for the double-layer capacitance and the Warburg (W) impedance specified as a linear part at low frequency resembles the diffusion process of the charges. Moreover, to illustrate the electrochemical efficiency of the device, the Ragone curve is plotted in Fig. 7 (c). A high energy density of 11.7 Wh kg^{-1} is obtained at a power density of 1.414 kW kg^{-1} and device still retains 5.8 Wh kg^{-1} energy density even at 7.071 kW kg^{-1} power density. The performance of the FSS-SC device is compared to some of the earlier published research works (see Table 2). Some symmetric and asymmetric devices based on manganese phosphate were manufactured and reported, such as $\text{Mn}_3(\text{PO}_4)_2/\text{GF}/\text{AC}$ (7.6 Wh kg^{-1} , 3.528 kW kg^{-1}) [14], $\text{Mn}_3(\text{PO}_4)_2/\text{PANI}/\text{AC}$ (14.7 Wh kg^{-1} , 2.988 kW kg^{-1}) [28], $\text{MnPO}_4 \cdot \text{H}_2\text{O}/\text{GO}/\text{MnPO}_4 \cdot \text{H}_2\text{O}/\text{GO}$ (5.78 Wh kg^{-1} , $1.5 \times 10^5 \text{ W kg}^{-1}$) [42], $\text{Mn}_3(\text{PO}_4)_2/\text{AC}$ (16.64 Wh kg^{-1} , 7.984 kW kg^{-1}) [43], $\text{Mn}_3(\text{PO}_4)_2/\text{Mn}_3(\text{PO}_4)_2$ (19.09 Wh kg^{-1} , 8.033 kW kg^{-1}) [43], $\text{Mn}_3(\text{PO}_4)_2 \cdot 3\text{H}_2\text{O}/\text{Graphene}/\text{Mn}_3(\text{PO}_4)_2 \cdot 3\text{H}_2\text{O}/\text{Graphene}$ (35.5 Wh kg^{-1} , 3.65 kW kg^{-1}) [44], $\text{Mn}_3(\text{PO}_4)_2 \cdot 3\text{H}_2\text{O}/\text{AC}$ (32.32 Wh kg^{-1} , 4.250 kW kg^{-1}) [50], $\text{MoS}_2/\text{Ni}(\text{OH})_2/\text{MoS}_2/\text{Ni}(\text{OH})_2$ (5.2 mW h cm^{-3} , 11 W cm^{-3}) [52], $\text{CeO}_2/\text{MWCNTs}/\text{CeO}_2/\text{MWCNTs}$ (85.7 Wh kg^{-1} , 2.6 kW kg^{-1}) [53], $\text{CeO}_2/\text{SS}/\text{CeO}_2/\text{SS}$ (61.4 Wh kg^{-1} , 3.5 kW kg^{-1}) [54], $\text{VS}_2/\text{SS}/\text{VS}_2/\text{SS}$ (25.9 Wh kg^{-1} , 1.5 kW kg^{-1}) [55]. Nevertheless, in several published reports it states that the manganese phosphate was used as a positive and frequently active carbon used as negative electrode to fabricate asymmetric supercapacitors. The manganese phosphate based asymmetric devices present lower energy densities than $\text{Mn}_3(\text{PO}_4)_2$ electrode-based symmetric (FSS-SC) supercapacitors device and only one report is available on manganese phosphate material based symmetric solid-state device [44]. In these few reported works, the obtained specific capacitance is higher than the present work, which may be due to the use of Ni-foam as a substrate and addition of graphene and MWCNTs, which play a vital role to improve the

capacitive performance by adding self-capacitance during electrochemical testing to the electrode material and providing good porosity, electrical conductivity, and more active sites, respectively. Moreover, graphene provides a possibility to maximize surface areas of the electrochemically active material, which contributes to shortening ion diffusion lengths. However, MWCNTs are difficult for maintaining high quality and minimal impurities. Also, different electroactive materials (like vanadium disulfide, cerium dioxide, molybdenum disulfide, and nickel hydroxide) provided different charge storage mechanisms to improving electrochemical performance. Moreover, different methods of fabrication can usually lead to electrode materials with different porous structures which can also affect the diffusion path of the electrolyte ion. In these above mentioned reported works, mostly PVA- LiClO_4 was used as a gel electrolyte because of the relatively easy intercalation/deintercalation of the Li^+ ion due to its smaller ionic radius compared to that of the Na^+ ion. Also, strongly alkaline electrolytes such as KOH have high ionic conductivity, but the operating potential window is very low and it is less stable and shows lower efficiency. In contrast, of the different neutral electrolytes, Na_2SO_4 is the most commonly used neutral electrolyte and has been shown to be a promising electrolyte for manganese phosphate material. This is due to their benefits such as greater working potential windows, less corrosion, and higher safety than that of the alkaline electrolytes [56]. However, in present work we opted Na_2SO_4 as an electrolyte because excellent stability and further performance of manganese phosphate can be improved by composing with carbon derivatives such as CNTs, Graphene/Graphene oxide, etc. Therefore there is scope to further increase the capacitance of manganese phosphate electrode by making composite and using different electrolytes.

The CV curves of symmetric devices at different bending angles (0, 45, 90 and 180°) at constant scan rate 50 mV s^{-1} in the potential window of 0.0–1.5 V are presented in Fig. 7 (d). Fig. 7 (d) reveals that the conjunction of CV curves on each other reflects consistent electrochemical performance with changing bending positions of the device. It recommends that, the FSS-SC device can be utilized as a flexible supercapacitor for moderate energy device purposes [57]. The corresponding specific capacitance was calculated by CV curves (shown in Fig. 8, the corresponding measurement images), with the increasing bending angle from 0 to 180° . The values of specific capacitance show slight decrement (39, 39.4, 37, 34 F g^{-1} at a constant scan rate of 50 mV s^{-1}) with the increasing bending angle.

In a supercapacitor device application, its cyclic stability is an important factor. To study the cyclic stability of the symmetric device, the GCD cycling test was completed over 9000 cycles at 0.8 mA cm^{-2} current density within the voltage window 0.0–1.5 V [shown in Fig. 9 (a)]. Capacitance retention of the symmetric device is 99 % after 9000 cycles imply the stable nature of the device and it indicates outstanding cycling durability. Inset of Fig. 9 (a) shows the GCD curve of the initial and final ten cycles of 9000 cycles. It is evident that the last ten cycles curves moderately changes as compared with the initial ten cycles and still shows the symmetric shape, and exhibited no distinct change after long-term cyclic stability. The stability test of the FSS-SC device is compared to some previously published reports (see Table (2)) [14,28,43]. However, in all reported literature, $\text{Mn}_3(\text{PO}_4)_2$ symmetric (FSS-SC) device exhibits high cyclic stability as compared to manganese phosphate electrode-based asymmetric supercapacitor device. The commercial viability of an FSS-SC device can be tested by exhibiting the device to a practical purpose. The series-connected two FSS-SC devices was charged for 30 s and discharged through three red LEDs connected in parallel sequence. The devices amazingly have lightened up the LEDs for 5 min [Fig. 9 (b–d)]. Correspondingly, the images of lowering the light intensity of three red LEDs while discharging up to 5 min, which obviously demonstrates the glorious potentiality of the developed flexible symmetric device.

4. Conclusions

In summary, $\text{Mn}_3(\text{PO}_4)_2$ microrods were successfully synthesized through a single pot hydrothermal method at 120 °C temperature using different urea concentrations over flexible stainless steel substrate. The electrochemical studies of $\text{Mn}_3(\text{PO}_4)_2$ thin film electrode revealed maximum specific capacitance of 145 F g^{-1} at a current density of 0.2 mA cm^{-2} in $1 \text{ M Na}_2\text{SO}_4$ with 99.5 % capacity retention over 7000 cycles. Additionally, The MP-2//MP-2 FSS-SC device exhibits an operating voltage window of 1.5 V in PVA- Na_2SO_4 gel electrolyte and achieving a high specific capacitance of 37 F g^{-1} at 0.1 mA cm^{-2} current density. The FSS-SC device delivers a high energy density of 11.7 Wh kg^{-1} at 1.41 kW kg^{-1} power density with better cycling stability (99 %) over 9000 cycles. Overall, $\text{Mn}_3(\text{PO}_4)_2$ microrods based thin film electrodes can be a promising candidate in an electrochemically stable supercapacitor device for the purpose of flexible energy storage devices.

Author statement

Authors are very much thankful to the reviewer for valuable suggestions and comments. We have corrected and modified the manuscript as per the reviewer's suggestions.

Declaration of Competing Interest

The authors declare no competing financial interest.

Acknowledgments

Pranav K. Katkar acknowledges the *Chhatrapati Shahu Maharaj Research Training and Human Development Institute (SARTHI), Government of Maharashtra, India* for awarding the Senior Research Fellowship (SRF). Also, we gratefully thank the Ministry of Science and Technology India, DST-INSPIRE for financial support through research project sanction No.: DST/INSPIRE/04/2016/000260.

Appendix A. Supplementary data

Supplementary material related to this article can be found, in the online version, at doi:<https://doi.org/10.1016/j.synthmet.2020.116446>.

References

- G. Gao, H.B. Wu, S. Ding, L.M. Liu, X.W.D. Lou, Hierarchical NiCo_2O_4 nanosheets grown on Ni nanofoam as high-performance electrodes for supercapacitors, *Small* 11 (2015) 804–808, <https://doi.org/10.1002/sml.201402539>.
- S.S. Pujari, S.A. Kadam, Y.R. Ma, P.K. Katkar, S.J. Marje, S.A. Khalate, A.C. Lokhande, U.M. Patil, Facile synthesis of microstrip-like copper phosphate hydroxide thin films for supercapacitor applications, *J. Electron. Mater.* 49 (2020) 3890–3901, <https://doi.org/10.1007/s11664-020-08095-w>.
- L. Yu, G. Zhang, C. Yuan, X.W.D. Lou, Hierarchical $\text{NiCo}_2\text{O}_4/\text{MnO}_2$ core-shell heterostructured nanowire arrays on Ni foam as high-performance supercapacitor electrodes, *Chem. Commun.* 49 (2013) 137–139, <https://doi.org/10.1039/c2cc37117k>.
- U.M. Patil, R.V. Ghorpade, M.S. Nam, A.C. Nalawade, S. Lee, H. Han, S.C. Jun, PolyHIPE derived freestanding 3D carbon foam for cobalt hydroxide nanorods based high performance supercapacitor, *Sci. Rep.* 6 (2016) 1–11, <https://doi.org/10.1038/srep35490>.
- P. Simon, Y. Gogotsi, Materials for electrochemical capacitors, *Nat. Mater.* 7 (2008) 845–854, https://doi.org/10.1142/9789814287005_0033.
- Y. Yang, S. Lee, D.E. Brown, H. Zhao, X. Li, D. Jiang, et al., Fabrication of ultrafine manganese oxide-decorated carbon nanofibers for high-performance electrochemical capacitors, *Electrochim. Acta* 211 (2016) 524–532, <https://doi.org/10.1016/j.electacta.2016.06.012>.
- V. Subramanian, H. Zhu, R. Vajtai, P.M. Ajayan, B. Wei, Hydrothermal synthesis and pseudocapacitance properties of MnO_2 nanostructures, *J. Phys. Chem. B* 109 (2005) 20207–20214, <https://doi.org/10.1021/jp0543330>.
- M. Liu, L. Gan, W. Xiong, Z. Xu, D. Zhu, L. Chen, Development of MnO_2 /porous carbon microspheres with a partially graphitic structure for high performance supercapacitor electrodes, *J. Mater. Chem. A* 2 (2014) 2555–2562, <https://doi.org/10.1039/c3ta14445c>.
- U.M. Patil, M.S. Nam, J.S. Sohn, S.B. Kulkarni, R. Shin, S. Kang, S. Lee, J.H. Kim, S.C. Jun, Controlled electrochemical growth of $\text{Co}(\text{OH})_2$ flakes on 3D multi-layered graphene foam for high performance supercapacitors, *J. Mater. Chem. A* 2 (2014) 19075–19083, <https://doi.org/10.1039/c4ta03953j>.
- L.B. Kong, C. Lu, M.C. Liu, Y.C. Luo, L. Kang, X.H. Li, F.C. Walsh, The specific capacitance of sol-gel synthesized spinel MnCo_2O_4 in an alkaline electrolyte, *Electrochim. Acta* 115 (2014) 22–27, <https://doi.org/10.1016/j.electacta.2013.10.089>.
- D. Shanbhag, K. Bindu, A.R. Aarathy, M. Ramesh, M. Sreejesh, H.S. Nagaraja, Hydrothermally synthesized reduced graphene oxide and Sn doped manganese dioxide nanocomposites for supercapacitors and dopamine sensors, *Mater. Today* 4 (2017) 66–74, <https://doi.org/10.1016/j.mtener.2017.03.006>.
- U.M. Patil, J.S. Sohn, S.B. Kulkarni, H.G. Park, Y. Jung, K.V. Gurav, J.H. Kim, S.C. Jun, A facile synthesis of hierarchical $\alpha\text{-MnO}_2$ nanofibers on 3D-graphene foam for supercapacitor application, *Mater. Lett.* 119 (2014) 135–139, <https://doi.org/10.1016/j.matlet.2013.12.105>.
- G. rong, C.P. Xie, Y. Wen, A.P. Tang, H.S. Song, $\text{Mn}(\text{OH})_2$ electrodeposited on secondary porous Ni nano-architecture foam as high-performance electrode for supercapacitors, *Ionics* 25 (2019) 3287–3298, <https://doi.org/10.1007/s11581-018-2824-8>.
- A.A. Mirghni, M.J. Madito, T.M. Masikhwa, K.O. Oyedotun, A. Bello, N. Manyala, Hydrothermal synthesis of manganese phosphate/graphene foam composite for electrochemical supercapacitor applications, *J. Colloid Interface Sci.* 494 (2017) 325–337, <https://doi.org/10.1016/j.jcis.2017.01.098>.
- P.K. Katkar, S.J. Marje, S.S. Pujari, S.A. Khalate, A.C. Lokhande, U.M. Patil, Enhanced energy density of all-solid-state asymmetric supercapacitors based on morphologically tuned hydrous cobalt phosphate electrode as cathode material, *ACS Sustain. Chem. Eng.* 7 (2019) 11205–11218, <https://doi.org/10.1021/acssuschemeng.9b00504>.
- S. Nishimura, M. Nakamura, R. Natsui, A. Yamada, New lithium iron pyrophosphate as 3.5 V class cathode material for lithium ion battery, *J. Am. Chem. Soc.* 132 (2010) 13596–13597, <https://doi.org/10.1021/ja106297a>.
- Y. Tang, C. Zhou, W. Wang, Y. Zhao, S. Zhou, J. Fei, H. Cao, N^+ emitters realized using ammonium dihydrogen phosphate for silicon solar cells, *Sol. Energy* 95 (2013) 265–270, <https://doi.org/10.1016/j.solener.2013.04.024>.
- X. Hu, R. Li, S. Zhao, Y. Xing, Microwave-assisted preparation of flower-like cobalt phosphate and its application as a new heterogeneous fenton-like catalyst, *Appl. Surf. Sci.* 396 (2017) 1393–1402, <https://doi.org/10.1016/j.apsusc.2016.11.172>.
- J. Cherusseri, K.K. Kar, Hierarchically mesoporous carbon nonopetal based electrodes for flexible supercapacitors with super-long cyclic stability, *J. Mater. Chem. A* 3 (2015) 21586–21598, <https://doi.org/10.1039/c5ta05603a>.
- X. Lu, M. Yu, G. Wang, Y. Tong, Y. Li, Flexible solid-state supercapacitors: design, fabrication and applications, *Energy Environ. Sci.* 7 (2014) 2160–2181, <https://doi.org/10.1039/c4ee00960f>.
- A.D. Jagadale, V.S. Kumbhar, D.S. Dhawale, C.D. Lokhande, Performance evaluation of symmetric supercapacitor based on cobalt hydroxide $[\text{Co}(\text{OH})_2]$ thin film electrodes, *Electrochim. Acta* 98 (2013) 32–38, <https://doi.org/10.1016/j.electacta.2013.02.094>.
- P.K. Katkar, S.J. Marje, S.B. Kale, A.C. Lokhande, C.D. Lokhande, U.M. Patil, Synthesis of hydrous cobalt phosphate electrocatalysts by a facile hydrothermal method for enhanced oxygen evolution reaction: effect of urea variation, *CrystEngComm* 21 (2019) 884–893, <https://doi.org/10.1039/c8ce01653d>.
- G. Briganti, S. Puvvada, D. Blankschtein, Effect of urea on micellar properties of aqueous solutions of nonionic surfactants, *J. Phys. Chem.* 95 (1991) 8989–8995, <https://doi.org/10.1021/j100175a103>.
- S.J. Marje, P.K. Katkar, S.B. Kale, A.C. Lokhande, C.D. Lokhande, U.M. Patil, Effect of phosphate variation on morphology and electrocatalytic activity (OER) of hydrous nickel pyrophosphate thin films, *J. Alloys. Compd.* 779 (2019) 49–58, <https://doi.org/10.1016/j.jallcom.2018.11.213>.
- H. Pang, Y. Liu, J. Li, Y. Ma, G. Li, Y. Ai, J. Chen, J. Zhang, H. Zheng, Cobalt phosphite microarchitectures assembled by ultralong nanoribbons and their application as effective electrochemical capacitor electrode materials, *Nanoscale* 5 (2013) 503–507, <https://doi.org/10.1039/c2nr32597g>.
- Y.P. Zhu, Y.L. Liu, T.Z. Ren, Z.Y. Yuan, Hollow manganese phosphonate microspheres with hierarchical porosity for efficient adsorption and separation, *Nanoscale* 6 (2014) 6627–6636, <https://doi.org/10.1039/c4nr00629a>.
- H.S. Liu, T.S. Chin, S.W. Yung, FTIR and XPS studies of low-melting $\text{PbO-ZnO-P}_2\text{O}_5$ glasses, *Mater. Chem. Phys.* 50 (1997) 1–10, [https://doi.org/10.1016/S0254-0584\(97\)80175-7](https://doi.org/10.1016/S0254-0584(97)80175-7).
- C.C. Lee, F.S. Omar, A. Numan, N. Duraisamy, K. Ramesh, S. Ramesh, An enhanced performance of hybrid supercapacitor based on polyaniline-manganese phosphate binary composite, *J. Solid State Electrochem.* 21 (2017) 3205–3213, <https://doi.org/10.1007/s10008-017-3624-1>.
- N. Priyadharsini, A. Shanmugavani, L. Vasylechko, R.K. Selvan, Sol-gel synthesis, structural refinement, and electrochemical properties of potassium manganese phosphate for supercapacitors, *Ionics* 24 (2018) 2073–2082, <https://doi.org/10.1007/s11581-018-2449-y>.
- M. Aghazadeh, M. Asadi, M.R. Ganjali, P. Norouzi, B. Sabour, M. Emamalizadeh, Template-free preparation of vertically-aligned Mn_3O_4 nanorods as high supercapacitive performance electrode material, *Thin Solid Films* 634 (2017) 24–32, <https://doi.org/10.1016/j.tsf.2017.05.008>.
- B. Boonchom, S. Youngme, S. Maensiri, C. Danvirutai, Nanocrystalline serranacite ($\text{MnPO}_4 \cdot \text{H}_2\text{O}$) prepared by a simple precipitation route at low temperature, *J. Alloys. Compd.* 454 (2008) 78–82, <https://doi.org/10.1016/j.jallcom.2006.12.064>.
- T. Liu, X. Ma, D. Liu, S. Hao, G. Du, Y. Ma, A.M. Asiri, X. Sun, L. Chen, Mn doping of

- CoP nanosheets array: an efficient electrocatalyst for hydrogen evolution reaction with enhanced activity at all pH values, *ACS Catal.* 7 (2017) 98–102, <https://doi.org/10.1021/acscatal.6b02849>.
- [33] http://www.casaxps.com/help_manual/casaxps2316_manual/xps_spectra.pdf.
- [34] G. Neher, T.T. Salguero, δ -Polymorph of manganese phosphate, *Cryst. Growth Des.* 17 (2017) 4864–4872, <https://doi.org/10.1021/acs.cgd.7b00816>.
- [35] R. Yuan, J. Yuan, Y. Wu, P. Ju, L. Ji, H. Li, L. Chen, H. Zhou, J. Chen, Graphene oxide-mono-hydrated manganese phosphate composites: preparation via modified Hummers method, *Colloids Surf. A Physicochem. Eng. Asp.* 547 (2018) 56–63, <https://doi.org/10.1016/j.colsurfa.2018.03.023>.
- [36] W. Wei, X. Cui, X. Mao, W. Chen, D.G. Ivey, Morphology evolution in anodically electrodeposited manganese oxide nanostructures for electrochemical supercapacitor applications-effect of supersaturation ratio, *Electrochim. Acta* 56 (2011) 1619–1628, <https://doi.org/10.1016/j.electacta.2010.10.044>.
- [37] H. Shao, N. Padmanathan, D. McNulty, C. O'Dwyer, K.M. Razeed, Supercapattery based on binder-free $\text{Co}_3(\text{PO}_4)_2 \cdot 8\text{H}_2\text{O}$ multilayer nano/microflakes on nickel foam, *ACS Appl. Mater. Interfaces* 8 (2016) 28592–28598, <https://doi.org/10.1021/acsami.6b08354>.
- [38] F. Yunyun, L. Xu, Z. Wankun, X. Yuxuan, Y. Yunhan, Q. Honglin, X. Xuetao, W. Fan, Spinel CoMn_2O_4 nanosheet arrays grown on nickel foam for high-performance supercapacitor electrode, *Appl. Surf. Sci.* 357 (2015) 2013–2021, <https://doi.org/10.1016/j.apsusc.2015.09.176>.
- [39] K.V. Sankar, D. Kalpana, R.K. Selvan, Electrochemical properties of microwave-assisted reflux-synthesized Mn_3O_4 nanoparticles in different electrolytes for supercapacitor applications, *J. Appl. Electrochem.* 42 (2012) 463–470, <https://doi.org/10.1007/s10800-012-0424-2>.
- [40] M. Rajesh, K.V. Sankar, S.M. Chen, R.K. Selvan, Eco-friendly synthesis of activated carbon from dead mango leaves for the ultrahigh sensitive detection of toxic heavy metal ions and energy storage applications, *RSC Adv.* 4 (2014) 1225–1233, <https://doi.org/10.1039/c3ra45089a>.
- [41] H. Pang, Z. Yan, W. Wang, Y. Wei, X. Li, J. Li, J. Chen, J. Zhang, H. Zheng, Template-free controlled fabrication of $\text{NH}_4\text{MnPO}_4 \cdot \text{H}_2\text{O}$ and $\text{Mn}_2\text{P}_2\text{O}_7$ micro-nanostructures and study of their electrochemical properties, *Int. J. Electrochem. Sci.* 7 (2012) 12340–12353.
- [42] B. Yan, D. Bin, F. Ren, Z. Xiong, K. Zhang, C. Wang, Y. Du, Facile synthesis of $\text{MnPO}_4 \cdot \text{H}_2\text{O}$ nanowire/graphene oxide composite material and its application as electrode material for high performance supercapacitors, *Catalysts* 6 (2016) 1–15, <https://doi.org/10.3390/catal6120198>.
- [43] X.J. Ma, W.B. Zhang, L.B. Kong, Y.C. Luo, L. Kang, Electrochemical performance in alkaline and neutral electrolytes of a manganese phosphate material possessing a broad potential window, *RSC Adv.* 6 (2016) 40077–40085, <https://doi.org/10.1039/c6ra02217k>.
- [44] C. Yang, L. Dong, Z. Chen, H. Lu, High-Performance All-solid-state supercapacitor based on the assembly of graphene and manganese (II) phosphate nanosheets, *J. Phys. Chem. C* 118 (2014) 18884–18891, <https://doi.org/10.1021/jp504741u>.
- [45] X.J. Ma, L.B. Kong, W.B. Zhang, M.C. Liu, Y.C. Luo, L. Kang, Design and synthesis of $3\text{D Co}_3\text{O}_4 @ \text{MMoO}_4$ (M = Ni, Co) nanocomposites as high-performance supercapacitor electrodes, *Electrochim. Acta* 130 (2014) 660–669, <https://doi.org/10.1016/j.electacta.2014.03.080>.
- [46] T. Gu, B. Wei, High-performance all-solid-state asymmetric stretchable supercapacitors based on wrinkled MnO_2/CNT and $\text{Fe}_2\text{O}_3/\text{CNT}$ macrofilms, *J. Mater. Chem. A* 4 (2016) 12289–12295, <https://doi.org/10.1039/c6ta04712b>.
- [47] K. Krishnamoorthy, P. Pazhamalai, G.K. Veerasubramani, S.J. Kim, Mechanically delaminated few layered MoS_2 nanosheets based high performance wire type solid-state symmetric supercapacitors, *J. Power Sources* 321 (2016) 112–119, <https://doi.org/10.1016/j.jpowsour.2016.04.116>.
- [48] H.C. Tao, S.C. Zhu, X.L. Yang, L.L. Zhang, S.B. Ni, Systematic investigation of reduced graphene oxide foams for high-performance supercapacitors, *Electrochim. Acta* 190 (2016) 168–177, <https://doi.org/10.1016/j.electacta.2015.12.179>.
- [49] S.A. Melchior, K. Raju, I.S. Ike, R.M. Erasmus, G. Kabongo, I. Sigalas, S.E. Iyuke, K.I. Ozoemena, High-voltage symmetric supercapacitor based on 2D titanium carbide (MXene , Ti_3CT_x)/carbon nanosphere composites in a neutral aqueous electrolyte, *J. Electrochem. Soc.* 165 (2018) A501–A511, <https://doi.org/10.1149/2.0401803jes>.
- [50] Y.H. Dai, L.B. Kong, K. Yan, M. Shi, Y.C. Luo, L. Kang, Facile fabrication of manganese phosphate nanosheets for supercapacitor applications, *Ionics* 22 (2016) 1461–1469, <https://doi.org/10.1007/s11581-016-1652-y>.
- [51] J. Hao, W. Li, X. Zuo, D. Zheng, X. Liang, Y. Qiang, B. Tan, B. Xiang, X. Zou, Facile electrochemical phosphatization of Mn_3O_4 nanosheet arrays for supercapacitor with enhanced performance, *J. Mater. Sci.* 54 (2018) 625–637, <https://doi.org/10.1007/s10853-018-2842-y>.
- [52] C. Hao, F. Wen, J. Xiang, L. Wang, H. Hou, Z. Su, W. Hu, Z. Liu, Controlled incorporation of $\text{Ni}(\text{OH})_2$ nanoplates into flowerlike MoS_2 nanosheets for flexible all-solid-state supercapacitors, *Adv. Funct. Mater.* 24 (2014) 6700–6707, <https://doi.org/10.1002/adfm.201401268>.
- [53] B. Pandit, B.R. Sankapal, P.M. Koinkar, Novel chemical route for $\text{CeO}_2/\text{MWCNTs}$ composite towards highly bendable solid-state supercapacitor device, *Sci. Rep.* 9 (2019) 5892, <https://doi.org/10.1038/s41598-019-42301-y>.
- [54] B. Pandit, N. Kumar, P.M. Koinkar, B.R. Sankapal, Solution processed nanostructured cerium oxide electrode: electrochemical engineering towards solid-state symmetric supercapacitor device, *J. Electroanal. Chem.* 839 (2019) 96–107, <https://doi.org/10.1016/j.jelechem.2019.02.047>.
- [55] B. Pandit, L.K. Bommineedi, B.R. Sankapal, Electrochemical engineering approach of high performance solid-state flexible supercapacitor device based on chemically synthesized VS₂ nanoregime structure, *J. Energy Chem.* 31 (2019) 79–88, <https://doi.org/10.1016/j.jechem.2018.05.011>.
- [56] C. Zhong, Y. Deng, W. Hu, J. Qiao, L. Zhang, J. Zhang, A review of electrolyte materials and compositions for electrochemical supercapacitors, *Chem. Soc. Rev.* 44 (2015) 7484–7539, <https://doi.org/10.1039/C5CS00303B>.
- [57] B. Pandit, D.P. Dubal, B.R. Sankapal, Large scale flexible solid state symmetric supercapacitor through inexpensive solution processed V_2O_5 complex surface architecture, *Electrochim. Acta* 242 (2017) 382–389, <https://doi.org/10.1016/j.electacta.2017.05.010>.

Journal of Materials Chemistry A

Materials for energy and sustainability

Accepted Manuscript

This article can be cited before page numbers have been issued, to do this please use: S. J. Marje, S. S. Pujari, S. A. Khalate, V. V. Patil, V. Parale, T. Kim, H. Park, J. L. Gunjekar, C. D. Lokhande and U. M. Patil, *J. Mater. Chem. A*, 2022, DOI: 10.1039/D2TA00761D.



This is an Accepted Manuscript, which has been through the Royal Society of Chemistry peer review process and has been accepted for publication.

Accepted Manuscripts are published online shortly after acceptance, before technical editing, formatting and proof reading. Using this free service, authors can make their results available to the community, in citable form, before we publish the edited article. We will replace this Accepted Manuscript with the edited and formatted Advance Article as soon as it is available.

You can find more information about Accepted Manuscripts in the [Information for Authors](#).

Please note that technical editing may introduce minor changes to the text and/or graphics, which may alter content. The journal's standard [Terms & Conditions](#) and the [Ethical guidelines](#) still apply. In no event shall the Royal Society of Chemistry be held responsible for any errors or omissions in this Accepted Manuscript or any consequences arising from the use of any information it contains.

ARTICLE

Intercalation type pseudocapacitive clustered nanoparticles of nickel-cobalt phosphate thin films synthesized via electrodeposition as a cathode for high performing hybrid supercapacitor devicesReceived 00th January 20xx,
Accepted 00th January 20xx

DOI: 10.1039/x0xx00000x

Supriya J. Marje,^a Sachin S. Pujari,^a Suraj A. Khalate,^a Vinod V. Patil,^a Vinayak G. Parale,^b Taehee kim,^b Hyung-Ho Park,^b Jayavant L. Gunjekar,^a Chandrakant D. Lokhande,^a Umakant M. Patil^{a*}**Abstract**

The binder-free synthesis of nickel-cobalt phosphate electrodes grabs tremendous attention in hybrid energy storage devices due to significant electrochemical activity based on a synergy between Ni and Co cations. So, the present work describes a facile scalable synthetic approach of potentiostatic electrodeposition (PED) for binder-free nickel-cobalt phosphate electrodes with Ni:Co variation. Alteration in Ni:Co composition leads into amorphous to crystalline structural conversion and microspheres to nanosheets like morphological evolution of nickel-cobalt phosphate electrodes. The optimal ~1:1 (Ni:Co) composition of nickel-cobalt phosphate electrode with clustered nanoparticle-like morphology exhibits intercalation pseudocapacitive behavior and demonstrates maximum specific capacitance (capacity) of 2228 F g⁻¹ (891 C g⁻¹) at 1.5 A g⁻¹ current density. Moreover, a fabricated aqueous hybrid asymmetric supercapacitor (AHAS) device delivers a high specific capacitance of 185 F g⁻¹, having an energy density of 65.7 Wh kg⁻¹ at 2.2 kW kg⁻¹ power density with 97 % retention. Furthermore, the solid-state hybrid asymmetric supercapacitor (SHAS) device displays a maximum specific capacitance of 90 F g⁻¹ with 32 Wh kg⁻¹ energy density at 0.32 kW kg⁻¹ power density and upholds 89 % capacitive retention. The present study establishes a scalable synthesis of binder-free nickel-cobalt phosphate electrodes as a cathode in hybrid energy storage devices for practical application.

1. Introduction

Recently, the research has primarily been devoted to developing sustainable, ecological, and

renewable energy storage systems due to the deterioration of the environment and fossil fuel depletion.¹⁻³ So, electrochemical energy storage systems such as fuel cells, batteries, and supercapacitors (SCs) stand vital for storing non-renewable energy in the present scenario.⁴ Nevertheless, SCs attract more attention due to their impressive properties like safe to operate, high charging-discharging rate, and significant power density with a larger life span than batteries and fuel cells.^{5,6} So, with these exceptional properties, SCs are gaining significant attention in various small to large-scale electronic appliances, from portable electronic devices to hybrid electric vehicles. However, relatively

^aCentre for Interdisciplinary Research, D. Y. Patil Education Society (Deemed to be University), Kasaba Bawada, Kolhapur-416 006, M.S., India. Email: umakant.physics84@gmail.com

^bDepartment of Materials Science and Engineering, Yonsei University, Seoul 03722, South Korea.

Electronic Supplementary Information (ESI) available: [Synthesis of large area nickel-cobalt phosphate thin film, Synthesis of rGO electrode, PVA-KOH gel electrolyte, Fabrication process of SHAS device, Formulae for calculation, Film thickness graph, XRD patterns of E-NCP series powder samples, EDS spectra of E-NCP series samples, Nitrogen adsorption/desorption isotherm of E-NCP series samples, The CV graphs of E-NCP1, E-NCP2, E-NCP3, E-NCP5, E-NCP6 and E-NCP7 electrodes, Log (current density, A g⁻¹) versus log (scan rate, mV s⁻¹) plot for E-NCP series electrode, Pseudocapacitive (surface current) and battery type (bulk current) current density contribution graph at various scan rates for E-NCP series electrodes, The GCD curves of E-NCP1, E-NCP4 and E-NCP7 electrodes at 1.5 A g⁻¹ current density, ex-situ XPS study, The GCD curves of E-NCP1, E-NCP2, E-NCP3, E-NCP5, E-NCP6 and E-NCP7 electrodes, The specific capacitance (capacity) of E-NCP series electrodes at various current densities, Nyquist plot before and after stability of E-NCP4 electrode, The structural and electrochemical study of rGO electrode, The CV graphs of E-NCP4 and rGO electrodes, The CV and GCD curves of AHAS device in different potential windows, Charted atomic percentage of existing elements in E-NCP series samples, Comparison of electrochemical energy storage performance of nickel-cobalt phosphate based electrodes, EIS fitted circuit parameters of E-NCP series electrodes and E-NCP4 electrode before and after stability, Comparison of electrochemical energy storage performance of nickel-cobalt phosphate based devices]

less energy density than batteries of SCs hinders their application in different electronic devices.^{7,8} Therefore, the improved energy density without negotiating its power density is a prerequisite of SCs for practical application. Moreover, it can be accomplished in two ways: by increasing capacitance (C) of energy storage materials or extending potential window (V), or by enhancing both, since the stored energy is proportional to capacitance and potential window of the SC device ($0.5CV^2$).⁹

Fabrication of hybrid SC devices is a competent way to achieve improved energy and power density since it comprises pseudocapacitive type cathode (energy source) and capacitive type anode (power source),^{10,11} and the expanded cell voltage of hybrid SCs due to well-separated potential windows of electrodes.¹² Nevertheless, another highly desirable way to boost energy density is refining electrode material's capacitance via manipulating the structural and morphological properties of energy storage materials. In this perspective, numerous materials, including metal oxides, hydroxides, sulfides, and phosphates, have been tested as cathode materials in hybrid energy storage devices. Most of the ever-utilized cathode materials can be classified into three categories: extrinsic (battery-type), intercalation, and intrinsic pseudocapacitive based on their charge storage mechanisms.¹³ Generally, intrinsic pseudocapacitive materials store charges via a redox mechanism and/or by forming a double layer on the material surface (e.g., RuO_2 , MnO_2). However, in intercalation type, charges are stored in the tunnels or interplanar space of material through electrolytic ion intercalation (e.g., Layer double hydroxides (LDH)). While the reduction in size or crystallinity (nanomaterials) of battery-type materials can demonstrate pseudocapacitive behavior and refer to extrinsic pseudocapacitive materials.⁷ The extrinsic materials struggle with less power density and poor stability, except for excellent energy density.¹⁴ On the other hand, intrinsic materials have very low energy density. Therefore, to stick out higher energy values and economic demands, low-cost energy storage materials, having maximum specific capacitance and favorable life span, needed to be developed.

Among existing pseudocapacitive materials, open and wide channel structured metal phosphate materials are catching attention as a new emerging

energy storage material as a cathode in hybrid devices due to their excellent properties like large active sites, and excellent conductive nature, and higher stability owing to P-O covalent bond.¹⁵⁻¹⁷ Therefore, different morphologies and polymorphs of cobalt and nickel phosphates were synthesized via various synthesis processes such as $\text{Ni}_3(\text{PO}_4)_2$,¹⁷ $\text{Ni}_2\text{P}_2\text{O}_7$,¹⁸ $\text{Ni}_{11}(\text{HPO}_3)_8(\text{OH})_6$,¹⁹ $\text{Co}_3(\text{PO}_4)_2 \cdot 8\text{H}_2\text{O}$,²⁰ $\text{CoHPO}_4 \cdot 3\text{H}_2\text{O}$,²¹ $\text{Co}_3\text{P}_2\text{O}_8 \cdot 8\text{H}_2\text{O}$,²² $\text{Co}_2\text{P}_2\text{O}_7$,²³ $\text{Co}_2\text{P}_4\text{O}_{12}$,²⁴ etc. and investigated for supercapacitor application. Moreover, some researchers proved that the synergetic effect between two metal species in binary metal compounds exhibits higher capacitive performance than single metal compounds.²⁵⁻²⁹ However, in most reports, nickel-cobalt phosphate materials were prepared in powder form with highly crystalline structures, and microstructure and fabricated cathode using a binder supplemented casting method for energy storage devices.³⁰⁻⁴¹ Also, a considerably higher ratio of surface to the volume of material is the most significant factor in fulfilling demands for energy-efficient application, since downscaling the microstructure of material can regulate different types of pseudocapacitive behaviors from intercalation to extrinsic pseudocapacitive type. So, to achieve a higher capacity of energy storage devices, it is crucial to binder-free fabrication of electrodes and fine-tuning of characteristics of electrode material (surface area, electrical conductivity) in synthesis. Until now, only a few reports are available on binder-free synthesis,⁴²⁻⁴⁵ and only in two reports electrodeposition method was implemented for the synthesis of nickel-cobalt phosphate electrodes.^{42,44}

Therefore, in the present investigation, a binder-free and single-step potentiostatic mode of electrodeposition (PED) method is employed to synthesize nickel-cobalt phosphate thin film electrodes with a variation of Ni:Co composition. The structural and morphological evolution of nickel-cobalt phosphate thin films with molar ratio variation of nickel and cobalt is investigated by XRD, FT-IR, XPS, FE-SEM, and EDS analyses. Also, the influence of structural and morphological evolution on the pseudocapacitive performance of nickel-cobalt phosphate electrodes is studied. Furthermore, the aqueous hybrid asymmetric (AHAS) and solid-state hybrid asymmetric supercapacitor (SHAS) devices are fabricated by combining the best performing nickel-cobalt phosphate

electrode (cathode) and rGO electrode (anode). The supercapacitive performances of hybrid energy storage devices are recorded and demonstrated herein.

2. Experimental section

2.1 Synthesis of nickel-cobalt phosphate thin films

Nickel chloride ($\text{NiCl}_2 \cdot 6\text{H}_2\text{O}$), cobalt chloride ($\text{CoCl}_2 \cdot 6\text{H}_2\text{O}$), and potassium dihydrogen orthophosphate (KH_2PO_4) were purchased (Sigma Aldrich) (AR grade) and used without any further purification. The synthesis of nickel-cobalt phosphate thin films was carried out in an aqueous solution of nickel chloride ($\text{NiCl}_2 \cdot 6\text{H}_2\text{O}$), cobalt chloride ($\text{CoCl}_2 \cdot 6\text{H}_2\text{O}$), and potassium dihydrogen orthophosphate (KH_2PO_4) precursors by the PED method. The schematic presentation and the actual photograph of the specially developed electrodeposition assembly consisting of graphite pot as a counter electrode, large area stainless steel (SS) as a working electrode, and saturated calomel electrode (SCE) (saturated KCl solution) as a reference electrode for the preparation of large area thin film electrodes is shown in Fig. S1 (a) and (b) (see in the electronic supplementary information, ESI). The nickel chloride and cobalt chloride precursor concentrations varied from 0.045-0 M and 0-0.025 M, respectively, while phosphate precursor (potassium dihydrogen orthophosphate) concentration was kept constant (0.125 M) in the deposition solution. To avoid the formation of metal hydroxide or oxide phase, a decisively higher concentration of phosphate precursor was used in the deposition, and the concentration of Ni and Co precursor were varied depending on the growth rate of nickel and cobalt phosphate. The deposition potential of nickel-cobalt phosphate was varied and optimized between -0.85 to -1.1 V/SCE at room temperature. A well-adherent and uniform thin films of nickel-cobalt phosphate were obtained at -0.85 V/SCE potential, as a photograph of large area deposited thin film shown in Fig. S1 (c). The composition of precursors ($\text{NiCl}_2 \cdot 6\text{H}_2\text{O}:\text{CoCl}_2 \cdot 6\text{H}_2\text{O}$) was varied as 1:0, 0.85:0.15, 0.75:0.25, 0.5:0.5, 0.25:0.75, 0.15:0.85 and 0:1 for nickel-cobalt phosphate thin film deposition on SS substrate and denoted by E-NCP1, E-NCP2, E-NCP3, E-NCP4, E-NCP5, E-NCP6, and E-NCP7, respectively.

2.2 Materials characterization

The Rigaku miniflex-600 X-ray diffractometer (with $\text{Cu K}\alpha$ ($\lambda=0.15425$ nm) radiation) was used for structural analysis of synthesized nickel-cobalt phosphate thin films. The Fourier transform-infrared spectrometry (FT-IR) (Alpha (II) Bruker) was employed to study available functional groups in prepared thin films. The X-ray photoelectron spectroscopy (XPS) was measured via ThermoScientific ESCALAB 250 (Thermo Fisher Scientific, UK). The morphological analysis was probed via field emission scanning electron microscopy (FE-SEM, JSM-7001 F, JEOL) and elemental investigation via energy dispersive spectrometer (EDS) analysis. The ZIVE MP1 multichannel electrochemical workstation was used to record the electrochemical capacitive reactions. The cyclic voltammetry (CV), galvanostatic charge-discharge (GCD), and electrochemical impedance spectroscopy (EIS) techniques were employed to probe the supercapacitive performance of prepared thin film electrodes. The aqueous and solid-state asymmetric hybrid supercapacitor devices are fabricated using nickel-cobalt phosphate electrode (cathode) and rGO (anode) electrodes (Fig. S2 (a-e) (see ESI)). The formulae used for supercapacitive performance evaluation in half and full-cell (device) systems are provided in the supplementary information (see ESI).

3. Results and discussion

3.1 Nickel-cobalt phosphate thin film formation

A large scale (5×5 cm²), binder free nickel-cobalt phosphate thin film electrodes with a variation of Ni:Co composition are prepared by facile PED method (synthesis details provided in Experimental section), using the specifically designed electrochemical cell as shown in the schematic presentation (Fig. S1) (see in the electronic supplementary information, ESI). For PED of nickel-cobalt phosphate material, formal reduction potential was examined by linear sweep voltammetry (LSV) curves (as shown in Fig. 1 (a)) of $\text{NiCl}_2 \cdot 6\text{H}_2\text{O}$, $\text{CoCl}_2 \cdot 6\text{H}_2\text{O}$, and $\text{NiCl}_2 \cdot 6\text{H}_2\text{O} + \text{CoCl}_2 \cdot 6\text{H}_2\text{O}$ with KH_2PO_4 aqueous precursor solutions at composition ($\text{NiCl}_2 \cdot 6\text{H}_2\text{O}:\text{CoCl}_2 \cdot 6\text{H}_2\text{O}$) as 1:0, 0:1 and 0.5:0.5, respectively. The LSV curves scanned from 0 to -1.2 V/SCE at 20 mV s⁻¹ scan rate depict tentative deposition potential (onset potential) to encourage potentiostatic deposition of nickel, cobalt, and nickel-cobalt phosphate thin films. The reduction potentials of cobalt and nickel

with potassium dihydrogen orthophosphate precursors are found to be -0.7 and -0.85 V/SCE, respectively. However, the reduction potential (-0.75 V/SCE) of nickel-cobalt precursor solution is in between the reduction potential of individual precursors. It suggests that the advanced deposition of cobalt phosphate is possible, so to achieve the expected composition of Ni:Co the concentration of cobalt precursor was kept a little low.

The nickel-cobalt phosphate thin films deposition was performed at room temperature using PED mode at a constant potential of -0.85 V/SCE for 5400 s, as presented in Fig. 1 (b). The observed chronoamperometric deposition curves show two distinct regions. The first region (I) shows an initial surge in the current response, dependent on the available cation species at the interface of an electrode that discharges immediately after the electrode polarization and then decrease in current elucidates nuclei formation. In the second region (II), current increases slowly up to optimum and then establishes a steady nature corresponding to aggregation and accompanied material growth, respectively. A steady-state current density after the nucleation attributes to the consistent growth of material and a slow growth process in the second region may be responsible for the formation of clusters owed to processes like adsorption and coalescence. Maximum current response observed for E-NCP7 than other samples suggests well crystallization with excellent cobalt phosphate material growth kinetics, and lower current response for E-NCP1 advocates deprived crystallization of nickel phosphate material. An increase in deposited mass of the nickel-cobalt phosphate thin films is observed with different bath compositions of $\text{NiCl}_2 \cdot 6\text{H}_2\text{O}:\text{CoCl}_2 \cdot 6\text{H}_2\text{O}$, and it varies from 1.5 to 1.98 mg cm^{-2} as shown in Fig. S3 (see ESI). A change in whitish-green to purple color of nickel-cobalt phosphate thin films over SS substrate is observed upon Ni:Co composition variation as a photograph shown in Fig. 1 (b) inset.

3.2 Structural and morphological analysis

The XRD analysis employed to investigate the structural properties of prepared E-NCP series thin films is presented in Fig. 1 (c). The XRD result of the E-NCP1 sample shows only stainless-steel peaks (marked as *) and confirms the amorphous structure of the

electrodeposited nickel phosphate material. However, the XRD pattern of the E-NCP7 sample depicts diffraction peaks corresponding to (110), (020), (130), (101), (031), (211), ($\bar{3}21$), (231), (301), (051), and (132) crystal planes which match with the JCPDS card no. 33-0432, and confirms $\text{Co}_3(\text{PO}_4)_2 \cdot 8\text{H}_2\text{O}$ thin film formation. Also, the other E-NCP series sample does not show any diffraction peaks than SS substrate in the XRD pattern and confirms the amorphous nature of nickel-cobalt phosphate thin film samples. For further confirmation of material phase and to avoid dominance of substrate peaks, XRD studies of E-NCP series powder samples (scratched from the SS substrate) are investigated and presented in Fig. S4 (see ESI). The powder XRD pattern of E-NCP7 sample shows a similar diffraction pattern like thin films; nonetheless, few extra peaks are observed, which were suppressed due to intense SS substrate peaks. With the addition of nickel content, peak intensities of E-NCP6 sample in powder XRD are decreased. Furthermore, it is confirmed that increase in nickel content, the structure of nickel-cobalt phosphate material changes from crystalline to amorphous and vice versa. The overall XRD study suggests a synthesis of crystalline hydrous cobalt phosphate ($\text{Co}_3(\text{PO}_4)_2 \cdot 8\text{H}_2\text{O}$) and transformation into amorphous nickel-cobalt phosphate thin films with an increment of nickel.

The existence of functional material groups in E-NCP series electrodes was analyzed via FT-IR analysis in the 400-4000 cm^{-1} region and displayed in Fig. 1 (d). The metal-oxygen bonding in samples is confirmed via peak (γ_1) present in a range of 568-595 cm^{-1} . The peak at 595 cm^{-1} observed in E-NCP1 sample can be ascribed to Ni-O bonding,⁴⁶ and the peak at 571 cm^{-1} is associated with Co-O bonding in E-NCP7 sample.^{47,48} The symmetric stretching of P-O-P linkage is detected at the absorption peak (γ_2) in the region of 708-741 cm^{-1} .⁴⁹ The peaks (γ_3 - γ_5) are noted in the region of 857-1076 cm^{-1} confirm the symmetric and asymmetric P-O stretching vibrational mode of PO_4^{3-} anions.^{50,51} The absorption peaks (γ_6, γ_7) in the region of 1400-1644 cm^{-1} correspond to the bending mode of a water molecule (H-O-H).^{51,52} Moreover, the peaks (γ_8, γ_9) in the range of 3000-3464 cm^{-1} are belonged to O-H stretching vibration mode of adsorbed water content in the material.^{51,52} Moreover, the slight shifting in peaks (γ_1 - γ_6) from sample E-NCP1 to E-NCP7 confirms the cordial interaction between cobalt and nickel elements in nickel-cobalt phosphate.⁵³ Thus,

the FT-IR results demonstrate the successful preparation of hydrous nickel-cobalt phosphate material thin films via the PED method.

The nickel, cobalt, phosphorous, and oxygen elements are observed in the XPS survey spectrum of sample E-NCP4 (Fig. 2 (a)). The intense peaks at binding energies of 854.8 and 872.5 eV in the high-resolution Ni2p XPS spectrum confirm the Ni2p_{3/2} and Ni2p_{1/2} state, respectively, indicating Ni²⁺ oxidation state and satellite peaks at 860.8 and 878.5 eV binding energies (Fig. 2 (b)).⁵⁴⁻⁵⁶ The high-resolution Co2p XPS spectrum shown in Fig. 2 (c) reveals a peak at 781.5 eV binding energy and a satellite peak (785.5 eV) corresponding to Co2p_{3/2} orbits and demonstrates +2 valence state of cobalt near the surface.

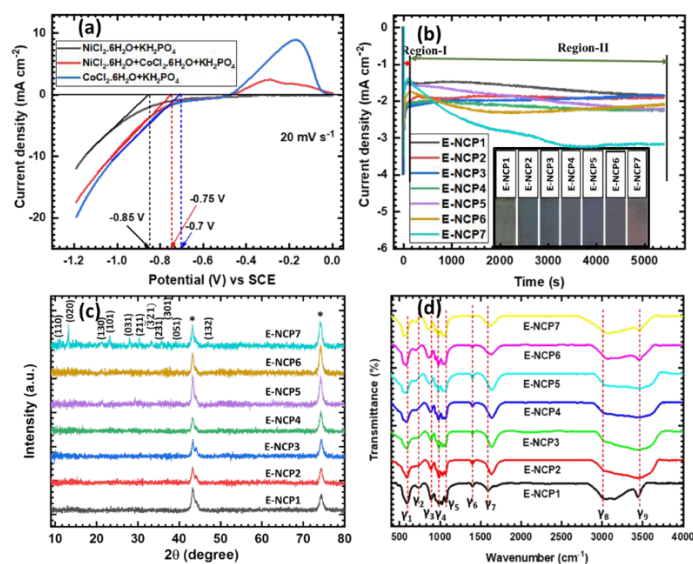


Fig. 1 (a) LSV curves for precursor solution of NiCl₂.6H₂O, CoCl₂.6H₂O and NiCl₂.6H₂O+CoCl₂.6H₂O (with KH₂PO₄) with composition 1:0, 0:1 and 0.5:0.5 (NiCl₂.6H₂O:CoCl₂.6H₂O), respectively at the scan rate of 20 mV s⁻¹, (b) chronoamperometric curves of nickel-cobalt phosphate (E-NCP1 to E-NCP7) at the potential of -0.85 V/SCE on SS substrate (inset: photograph of prepared thin film electrodes), (c) XRD patterns and (d) FT-IR spectra of nickel-cobalt phosphate thin films (E-NCP1 to E-NCP7).

Similarly, the intense peak at 797.8 eV binding energy signifies Co2p_{1/2} orbits, and the satellite peak at 802.9 eV further proves a similar assumption.^{57,58} Fig. 2 (d) shows the high-resolution P2p region XPS spectrum; a single intense peak noted at a binding energy of 132.7 eV demonstrates a pentavalent state of phosphorous in P-O

bonding.⁵⁹ Moreover, one broad peak is observed in the O1s region of the XPS spectrum, as shown in Fig. 2 (e). The broad peak of O1s is deconvoluted into two peaks at 530.6 eV and 531.5 eV binding energies, which corresponds to the core level of oxygen in phosphate species and structural water in the material respectively.⁶⁰⁻⁶² Thus, the XPS results endorse the presence of the divalent state of Ni and Co in nickel-cobalt phosphate thin film. Overall, XPS analysis proves successful preparation of the hydrous nickel-cobalt phosphate material by PED method over SS substrate.

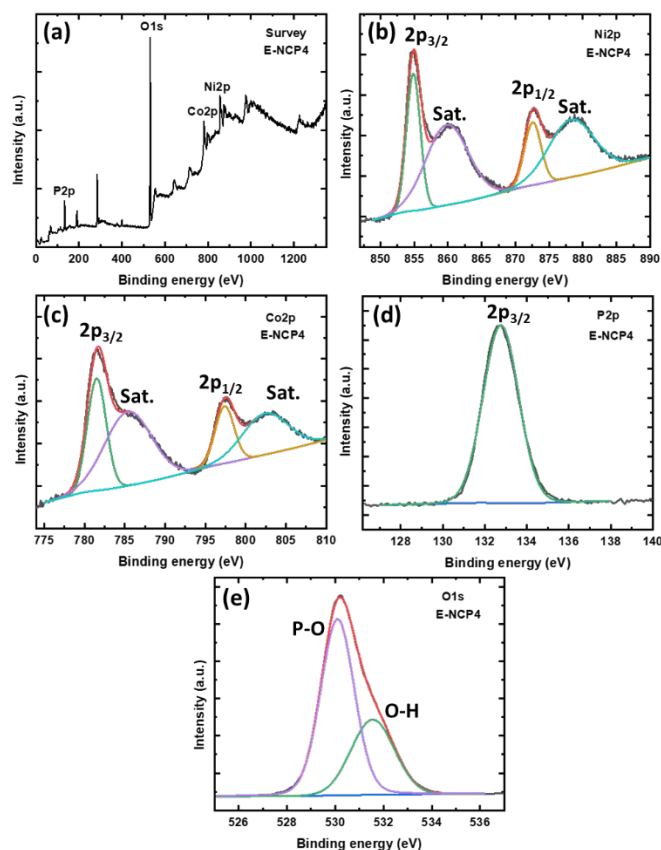


Fig. 2 (a) Survey spectrum, (b) Ni2p spectrum, (c) Co2p spectrum, (d) P2p spectrum and (e) O1s XPS spectrum of sample E-NCP4.

The surface morphological evolution of the electrodeposited E-NCP thin film series was probed via FE-SEM. Fig. 3 shows the morphologies of electrodeposited nickel-cobalt phosphate thin films at different magnifications (20,000X and 50,000X). Interestingly, morphological evolution from microspheres to nanosheets is observed with nickel and cobalt composition variation in E-NCP1 to E-NCP7 samples. The E-NCP1 to E-NCP4 sample (Fig. 3 (a-d)) shows an amalgamated microspheres-like morphology

with an average diameter of $\sim 2\text{-}4\ \mu\text{m}$, which attributed to the growth of material through coalescence and aggregation. The surface of the microsphere probed at higher magnification (Fig. 3 (a'-d')) reveals microspheres are composed of clusters of nanoparticles with uneven pores. Interestingly, a transformation of small pores to nano cracks on the surface of microspheres (inset Fig. 3 (d')) is noticed with increased cobalt content from E-NCP1 to E-NCP4 sample. Furthermore, with an increase of cobalt content in the E-NCP5 sample (Fig. 3 (e, e')), immature nanosheets can be observed with thicknesses of $\sim 257\text{-}299\ \text{nm}$ originating from the mud-like structure of merged microspheres. Microsphere-like architecture completely vanishes and converts into extremely close-packed nanosheets-like architecture (Fig. 3 (f, f')) with a further increase in cobalt content in sample E-NCP6. Moreover, at the higher cobalt content (zero content of nickel), sample E-NCP7 shows well-grown nanosheets-

like structures with curved edges (Fig. 3 (g, g')). Higher cobalt content (more than $\sim 1:1$) is accountable for the development of nano cracks on the surface of microspheres and further evolution into a nanosheets-like structure from the sample E-NCP5 to E-NCP7. Moreover, TEM images of E-NCP4 sample are presented in Fig. 3 (h, h') and affirm the merged microspheres are composed of clusters of nanoparticles. The high-resolution transmission electron microscope (HRTEM) image displays several sorted sets of lattice fringes with d-spacing of $0.78, 0.66, 0.4,$ and $0.38\ \text{nm}$ corresponding to (110), (020), (130), and (101) planes of hydrous nickel-cobalt phosphate, respectively (Fig. 3 (h')), and confirms the clusters of nanocrystals.⁴³ The HRTEM analysis indicates a growth of microspheres with clusters of quantized particles of hydrous nickel-cobalt phosphate.

The EDS elemental analysis (Fig. S5) (see ESI)

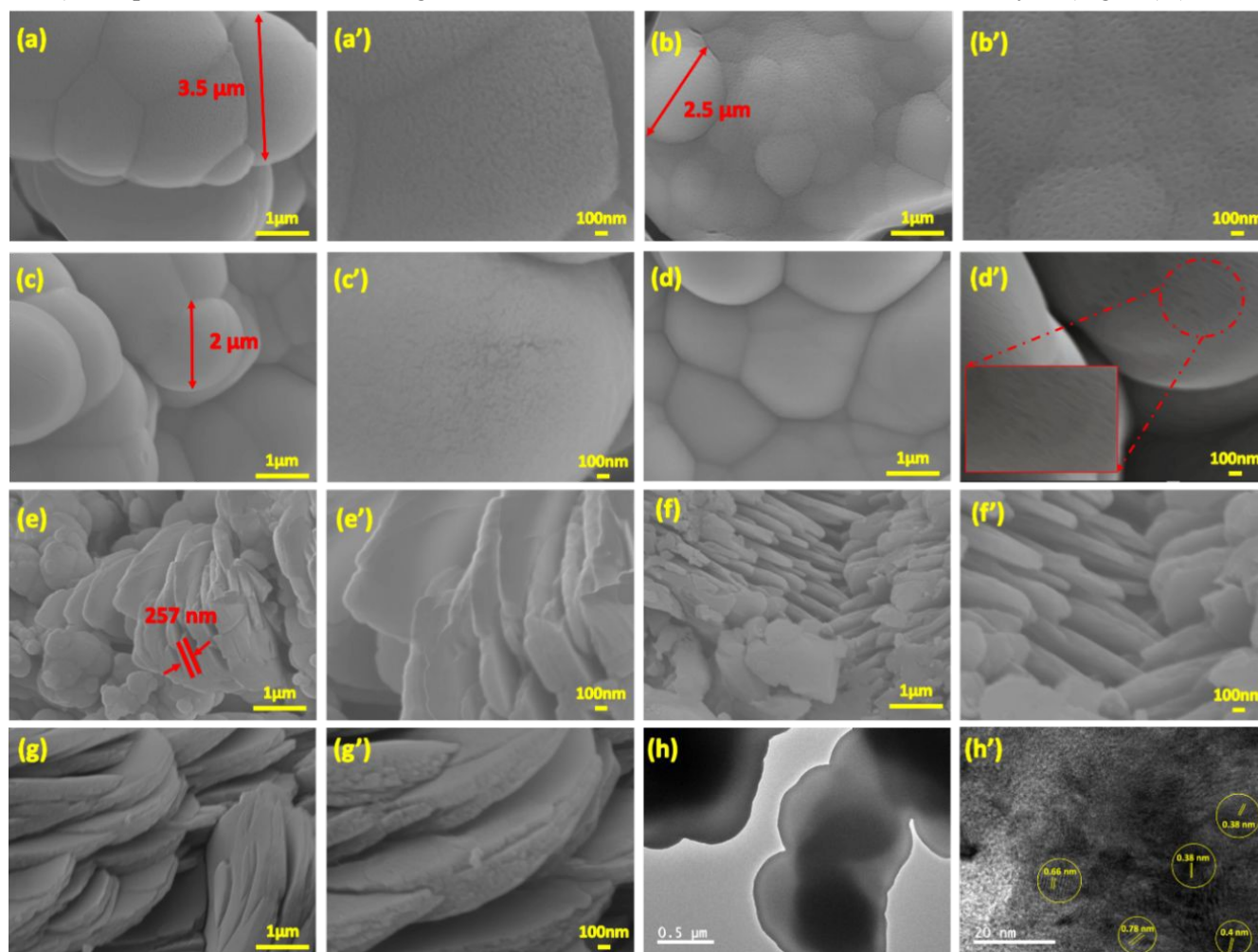


Fig. 3 FE-SEM images of E-NCP1 (a, a'), E-NCP2 (b, b'), E-NCP3 (c, c'), E-NCP4 (d, d'), E-NCP5 (e, e'), E-NCP6 (f, f') and E-NCP7 (g, g') sample at the magnification of 20,000X and 50,000X. (h, h') TEM images of E-NCP4 sample.

of electrodeposited E-NCP series thin films exhibits cobalt and nickel elements with phosphorous and oxygen in the sample E-NCP2 to E-NCP6. It confirms the successful deposition of nickel-cobalt phosphate on SS substrate. As summarized in Table S1 (see ESI), experimental and observed nickel and cobalt ratios for E-NCP series samples are found to be nearly similar. Thus, the EDS and FE-SEM results confirm the composition varied in the sample from E-NCP1 to E-NCP7, ultimately influencing the morphology of thin film samples from microspheres consisting of nanoparticles to nanosheets.

The nitrogen adsorption/desorption isotherms (Fig. S6 (a-f) (see ESI)) of nickel phosphate (E-NCP1), cobalt phosphate (E-NCP7), and nickel-cobalt phosphate (E-NCP4) samples are probed to determine the surface area and pore size distribution. Type III isotherm with H3 type hysteresis loop of physisorption confirmed for all samples according to International Union of Pure and Applied Chemistry (IUPAC) classification. The type III isotherm is attributed to the important feature of mesoporous material, consuming low adsorption energy for particle or plate-like structures. The specific surface area is measured from the Brunauer–Emmett–Teller (BET) equation analysis and found to be 8.5, 17.2, and 5.3 m² g⁻¹ for E-NCP1, E-NCP4, and E-NCP7 sample, respectively. The cracked microspheres-like morphology shows the highest surface area than porous microspheres and nanosheets structure. Further, the Barrett-Joyner–Halenda (BJH) method was used to measure pore size distributions of E-NCP1, E-NCP4, E-NCP7 samples, and observed pore size distribution in the range of ~12–24 nm, which affirms mesoporous nature of samples. The mesoporous architecture and high specific surface area of electrodeposited E-NCP series samples are feasible to perform high electrochemical capacitive performance.

3.3 Electrochemical pseudocapacitive performance of nickel-cobalt phosphate thin films

The electrochemical activity of E-NCP series electrodes (in 1 M KOH) was investigated by CV analysis. Typical CV graphs of E-NCP series electrodes measured at a scan rate of 20 mV s⁻¹ within 0 to 0.5 V/SCE potential window are shown in Fig. 4 (a). Fig. 4 (a) displays that the current response in CV graphs increases with increasing cobalt content in the electrode up to the E-NCP4 sample; furthermore, the current response in the CV graph decreases with increasing

cobalt content. Therefore, the higher charge storage capability is observed for E-NCP4 (~1:1, Ni:Co) electrode by means of a higher current response in the CV graph than other electrodes. The plotted CV graphs of the E-NCP4 electrode at 1–20 mV s⁻¹ scan rates in Fig. 4 (b) show that the current response in the CV graph increases with increasing scan rate. The CV graphs of other electrodes (E-NCP1 to E-NCP7) at scan rates of 1–20 mV s⁻¹ are provided in Fig. S7 (a-f) (see ESI). The distinctive CV natures can be observed for nickel (E-NCP1) and cobalt (E-NCP7) phosphate electrodes. Perfect redox couple to quasi-rectangular CV shapes are obtained from E-NCP1 to E-NCP7 sample and it discloses battery type, intercalation type to intrinsic pseudocapacitive behavior of the nickel-cobalt phosphate electrodes with increasing cobalt content.⁶³ Thus, the nickel and cobalt ratio variation influences the morphology, which ultimately affects the electrochemical pseudocapacitive behaviors and the performance of E-NCP series electrodes. Equal composition (~1:1) of nickel and cobalt in E-NCP4 sample having microspheres composed with clusters of nanoparticles like morphology exhibits higher areal capacitance than the other electrodes (microspheres or nanosheets like architectures).

Furthermore, the charge storage mechanisms (diffusion-controlled and pseudocapacitive type) of the electrodes are investigated by Power's law using scan rate dependent CV curves. The *b* value of E-NCP series electrodes is calculated from the slope of graph log (*i*) vs. log (*v*)⁶⁴ as depicted in Fig. S8 (see ESI). Graphs representing *b* values for E-NCP series electrodes are between 0.55 to 0.90, as plotted in Fig. 4 (c). The obtained values are higher than 0.5 and less than 1, which affirms that total current is contributed from a combination of diffusion-controlled and pseudocapacitive type charge storage mechanisms. The *b* values of electrodes are increased from E-NCP1 to E-NCP7, which means that the electrodes show more pseudocapacitive contribution in nickel-cobalt phosphate thin films as an increase of cobalt content.

Moreover, modified Power's law was used to evaluate the tentative contribution of battery and pseudocapacitive type in total specific current density^{65–67} from CV graphs measured at a scan rate of 20 mV s⁻¹ and shown in Fig. 4 (d). Fig. 4 (d) reveals that the current contribution from the surface pseudocapacitive process

increases as increasing cobalt content in the sample. Also, the contribution of pseudocapacitance (surface) increases with an increase in scan rate, and battery type (bulk) is high at low scan rates (Fig. S9) (see ESI). The E-NCP4 electrode exhibits ~32 % pseudocapacitive current contribution at a 20 mV s⁻¹ scan rate, and it is higher than nickel phosphate (E-NCP1) (~20%) and lower than cobalt phosphate (E-NCP7) (~87%) electrode. Thus, the transformation from battery type (bulk diffusion-controlled) to surface pseudocapacitive charge storage mechanism from E-NCP1 to E-NCP7 electrode is evident with increased cobalt content in E-NCP samples.

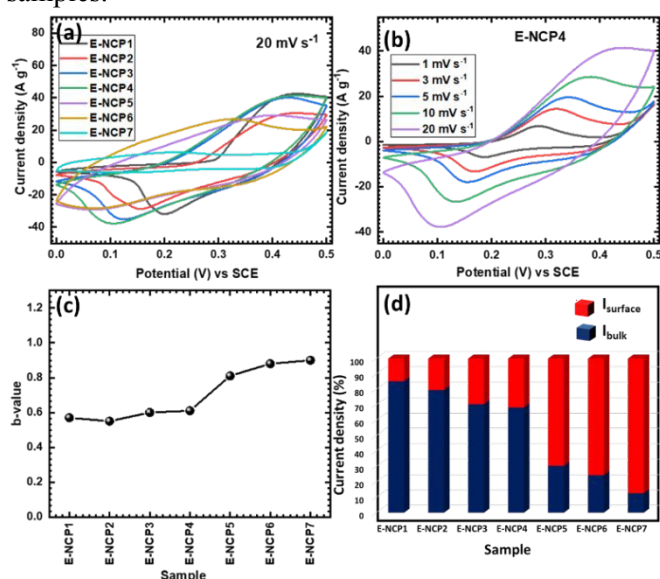


Fig. 4 (a) The comparative CV curves of E-NCP series electrodes at 20 mV s⁻¹ scan rate and (b) the CV curves at various scan rates from 1-20 mV s⁻¹ for E-NCP4 electrode. (c) b-values of different compositions of NiCl₂·6H₂O:CoCl₂·6H₂O and (d) Graph of the calculated contribution of pseudocapacitive (surface current) and battery type (bulk current) current density at 20 mV s⁻¹ scan rate for E-NCP series electrodes.

Furthermore, the optimized potential window of 0 to 0.4 V (vs SCE) is used to investigate GCD analysis of E-NCP series electrodes at 1.5 A g⁻¹ fixed current density and is displayed in Fig. 5 (a). Likewise, the CV curves nature, the nickel phosphate (E-NCP1), nickel-cobalt phosphate (E-NCP4), and cobalt phosphate (E-NCP7) electrode shows different shapes of GCD curves and demonstrates plateau (battery type), bell-shaped (intercalation pseudocapacitive), and quasi-triangular (intrinsic pseudocapacitive) type shape, respectively

(Fig. S10 (a-c)) (see ESI). Thus, the GCD curve of E-NCP series electrodes exhibits transformation from battery-intercalation-intrinsic pseudocapacitive type charge storage mechanism of E-NCP1 to E-NCP7 electrodes. A bell-shaped discharging curve of the E-NCP4 electrode demonstrates intercalation type pseudocapacitive behavior of the material where the charge storage mechanism is based on deep electrolytic ion intercalation and surface redox reactions.⁶⁸⁻⁷⁰

Moreover, to investigate the intercalative charge storage mechanism of nickel-cobalt phosphate electrodes, an ex-situ XPS analysis of pristine, charged (0.4 V/SCE), and discharged (0 V/SCE) nickel-cobalt phosphate (E-NCP4) electrodes were carried out (Fig. S11). In the intercalative charge storage mechanism of E-NCP4 electrode, it is observed that the Ni and Co sites are oxidized after charging and show a change in valence +2 and +3 states. In Ni2p spectra, the Ni²⁺ oxidation state is slightly suppressed after charging and shows an additional Ni³⁺ state (856.5 and 874.5 eV), which is evident in the transition from Ni²⁺ to Ni³⁺ after the electrode is fully charged. Also, after the electrode is fully discharged, a reduction in Ni³⁺ state is observed, and it is an evident transition of Ni states from Ni³⁺ to Ni²⁺ (Fig. S11 (a)).⁷¹ Similar oxidation and reduction in valence states of Co cation are observed in Co2p region, which is evident that oxidation from Co²⁺ to Co³⁺ (780.8 and 796.9 eV) and reduction from Co³⁺ to Co²⁺ (781.4 and 797.9 eV) as presented in Fig. S11 (b).^{58,72} Also, a slight change in Co2p and Ni2p binding energies for fully charged and discharged material confirms a similar transformation of valence states. The slight intensity decrement of P2p (phosphorous) spectra is observed for charged and discharged samples, which shows the pentavalent state of phosphorous (Fig. S11 (c)). However, an extra metal-oxygen bond (M-O) is observed in O1s spectra, as shown in Fig. S11 (d), after the electrode is charged and discharged. Moreover, the intensity of appearing metal-oxygen (M-O) peak is decreased, and O-H peak is increased after discharging. These transformations of valence states of cations and the appearance of M-O bonding confirms the insertion and extraction of OH⁻ ions in the material during the charge-discharge process.

Moreover, the concentrations of cations with different valence states are quantified from the XPS data; after fully charged, 32 % of Ni²⁺ ions and 68 % of Co²⁺

ions are oxidized to Ni^{3+} and Co^{3+} , respectively. In addition, 17 % of Ni^{3+} and Co^{3+} ions are reduced to Ni^{2+} and Co^{2+} after discharge, respectively. A 17 % decrease in P-O peak with raise of M-O (19 %) peak is observed after charging the sample, and after discharge, P-O peak regains 14 % intensity, and a 70 % decrement in M-O peak is observed. Also, only a 9 % decrement in O-H peak intensity is observed for a fully charged sample and regains its original value in the discharged sample. The overall observed changes in ex-situ XPS study states that, the vacancy sites of $(\text{PO}_4)_3$ are occupied by the intercalated hydroxyl ions during charge and deintercalated from their accommodated positions upon undergoing the discharge process.

A comparative study observed that the E-NCP4 electrode shows a longer charging and discharging time than other electrodes, suggesting a high electrode material storage capacity. The GCD analysis at various current densities for the E-NCP4 electrode is presented in Fig. 5 (b), and the GCD curves of other E-NCP series electrodes at different current densities from 1.5-3.5 A g^{-1} are provided in Fig. S12 (a-f) (see ESI).

The GCD study concludes that the E-NCP4 electrode offers a higher charge-discharge response due to the high surface area of specific microstructure (nano cracked microspheres composed of clusters of nanoparticles) and intercalative charge storage mechanism. The specific capacitances (capacities) are calculated from the GCD plots of E-NCP series electrodes at 1.5 A g^{-1} current density and presented in Fig. 5 (c). Also, the specific capacitances (capacities) calculated at various current densities for E-NCP series electrodes are provided in Fig. S13 (see ESI). As a result, the E-NCP4 electrode displays a high specific capacitance (capacity) of 2228 F g^{-1} (891 C g^{-1}) at a current density of 1.5 A g^{-1} than other E-NCP series electrodes, and it retains up to 1750 F g^{-1} (700 C g^{-1}) even at higher 3.5 A g^{-1} current density. Also, as shown in Fig. 5 (d), the microspheres like nickel-cobalt phosphate (E-NCP4) electrode exhibit maximum specific capacitance compared with available literature (detailed comparison given in Table S2 (see ESI)).^{30-44,73-76} The prepared nickel-cobalt phosphate (E-NCP4) electrode in present work delivered the highest capacitance than other reported work, except Huang et al.,⁴² where Cu/p-CuO nanowires used as a conductive current collector, and it improve the conductivity of the electrode and also offers

large specific surface area along with self pseudocapacitance, which ultimately improves the electrochemical performance of the cathode. On the other hand, the exclusive performance of active material is demonstrated herein since the bare SS substrate is utilized as a conducting backbone, which does not influence the capacitive performance of active material. In previous report⁴³ of the binder-free microflowers consisting of microstrips of nickel-cobalt phosphate electrode exhibited maximum specific capacitance of 1116 F g^{-1} , and only by rationalizing the microstructure into spheres of clustered nanoparticles of nickel-cobalt phosphate thin films by PED method, almost 2-fold of electrochemical capacitive performance (2228 F g^{-1}) is achieved in present work.

The electrochemical impedance spectroscopy (EIS) technique is used to probe electrochemical conductivity and ion transfer progression at the electrode/electrolyte interface.⁷⁷ The fitted equivalent circuit of EIS data for E-NCP series electrodes is shown inset Fig. 5 (e) and R_s (solution resistance), R_{ct} (charge transfer resistance), W (Warburg impedance), and Q (constant phase element) elements are fitted using Zview. The fitted circuit parameter values are charted in Table S3 (see ESI). The constant phase element is related to diffusion due to inhomogeneities available at the electrode/electrolyte interface owing to the disorder and porosity of the material and represents a pure capacitor, resistor, and Warburg diffusion impedance, when $n=1$, 0, and 0.5, respectively, where 'n' is the correction factor due to the roughness. In the present study, the n values are between 0.5 to 1, therefore, the Q presents pseudocapacitive behavior of E-NCP series electrodes (Table S3, see ESI).⁷⁸⁻⁸⁰ Moreover, the E-NCP4 electrode shows low charge transfer resistance (0.2 Ω) compared to other electrodes. Such less charge transfer resistance describes good contact of active material with the substrate and easy ion percolation in the morphology of cracked microspheres with clustered nanoparticles. The EIS results demonstrate binder-free synthesis and unique morphology of E-NCP4 electrode contributed to the high pseudocapacitive performance of the material.

Moreover, the long-term applicability of the electrode tested by stability test since it is an essential parameter for the suitable electrode for device fabrication. The cyclic stability by means of capacitive retention of the best-performing electrode (E-NCP4) is

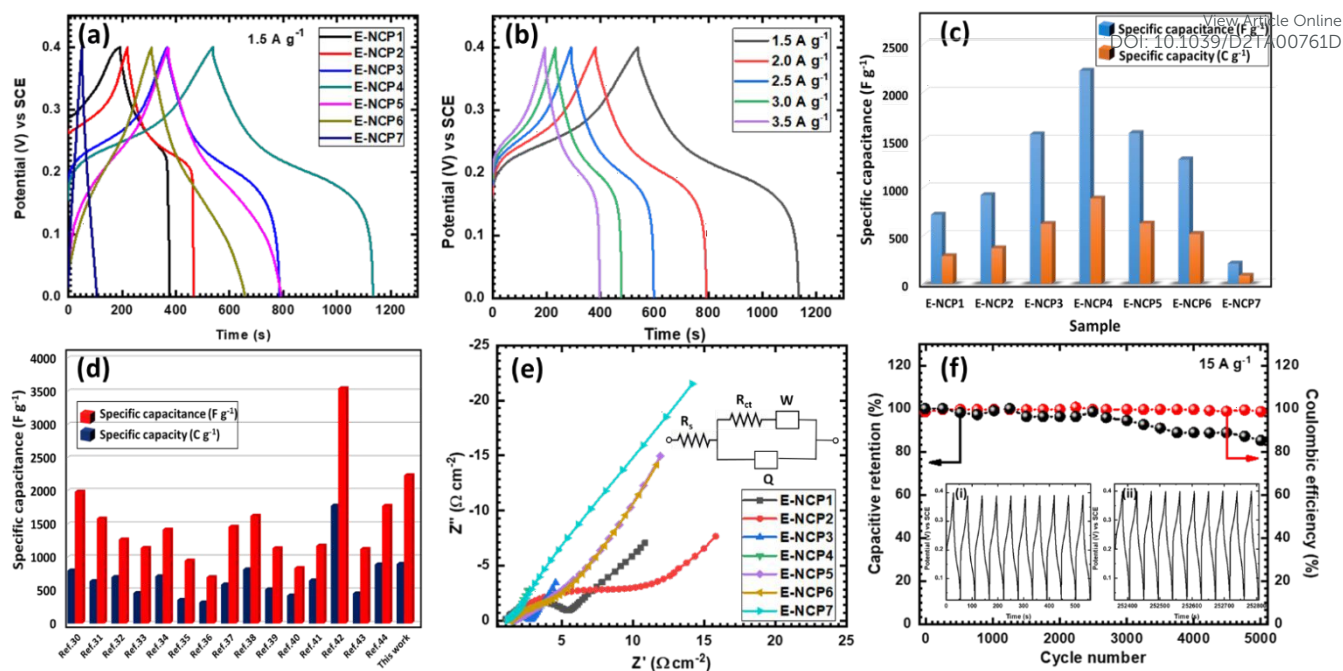


Fig. 5 (a) The GCD curves at a constant current density of 1.5 A g^{-1} for E-NCP series electrodes, (b) GCD curves from $1.5\text{--}3.5 \text{ A g}^{-1}$ current densities for E-NCP4 electrode, (c) The specific capacitance at a constant current density of 1.5 A g^{-1} for E-NCP series electrodes (E-NCP1 to E-NCP7), (d) Comparison of capacitance (capacity) obtained in present work with reported work, (e) The Nyquist plots of E-NCP series electrodes (E-NCP1 to E-NCP7) (inset: equivalent circuit), (f) The cyclic stability of E-NCP4 electrode for 5000 cycles at 15 A g^{-1} current density (inset: (i) initial and (ii) final 10 GCD curves of cyclic stability).

carried out for 5000 GCD cycles at a high current density of 15 A g^{-1} and presented in Fig. 5 (f). The E-NCP4 electrode exhibits $\sim 85\%$ capacitive retention with 98.6% coulombic efficiency over 5000 GCD cycles, as initial and last ten GCD cycles of stability curves are shown in the inset of Fig. 5 (f). The slight depletion of electrode material is accountable for the reduction in specific capacitance after several charge-discharge cycles because of material volume expansion during the insertion of ions.^{81,82} It concludes that the microspheres of the E-NCP4 electrode with clustered nanoparticles and nano-cracks over the surface offer good cyclic life at high charge-discharge current density. The Nyquist plot of E-NCP4 electrode before and after cyclic stability with fitted equivalent circuit is given in Fig. S14 (see ESI), and the fitted equivalent circuit parameters are tabulated in Table S4 (see ESI). It is observed that the solution resistance is quite similar, and only charge transfer resistance slightly changes from 0.2 to $0.48 \Omega \text{ cm}^{-2}$ after 5000 GCD cycles, which suggests well-maintained charge transfer kinetics of electrode during cyclic stability.

The following factors are majorly contributed to achieving an exceptional electrochemical capacitive performance of electrodeposited nickel-cobalt phosphate (E-NCP4) thin film electrode: (i) The microspheres with clustered nanoparticle like morphology and disordered structure (amorphous) offer unique physical and chemical properties with abundant electroactive sites, (ii) The microspheres with nano cracks demonstrates a high surface area with mesoporous structure, which provides facile access of active material for the diffusion of electrolytic ions, (iii) the self-grown (binder-free) active material offers not only structural continuity but also better connectivity between the active material and current collector and eliminate the awful impact of resistive binders.

3.4 Aqueous hybrid asymmetric supercapacitor (AHAS) device

The application of electrodeposited nickel-cobalt phosphate electrode (E-NCP4) as a cathode in a hybrid asymmetric supercapacitor device is tested by fabricating an aqueous hybrid asymmetric supercapacitor (AHAS, E-NCP4//rGO) device with rGO as an anode in aqueous

(1 M KOH) electrolyte. The structural characterizations and electrochemical study of the rGO anode are provided in the supplementary information (Fig. S15, see ESI). The CV graphs of E-NCP4 and rGO electrodes in the distinct potential windows are depicted in Fig. S16 (see ESI). The working potential window (0 to 0.5 and -1 to 0 V/SCE) and capacitances (2228 and 200 F g⁻¹) of positive (E-NCP4) and negative (rGO) electrodes are distinct, so to reach the highest electrochemical performance of AHAS device, the charge balance was maintained by varying mass of active materials as ~0.17:1. The operational potential window of the AHAS device (E-NCP4//rGO) is determined by measuring CV in the range of 0 to 1.2-1.7 V at a fixed scan rate of 50 mV s⁻¹, as shown in Fig. S17 (a) (see ESI). A good quasi-rectangular shape of CV graphs can be observed in potential window of 0 to 1.6 V and after 1.7 V, a sharp increment in CV current is observed due to splitting of aqueous electrolyte and reveals an irreversible reaction. So, the optimum potential window for the AHAS device from the CV analysis is found to be 0 to 1.6 V. The scan rate (5-100 mV s⁻¹) dependent CV graphs of AHAS device are shown in Fig. 6 (a) and unaltered CV shape even at high scan rates indicating the excellent rate capability of AHAS device (E-NCP4//rGO).⁸³

Similarly, to find out the operational potential window of the AHAS device (E-NCP4//rGO), the GCD curves are measured in different potential windows (0 to 1.2-1.7) at 6.7 A g⁻¹ current density and provided in Fig. S17 (b) (see ESI). The observed symmetric GCD curve in the potential window of 0 to 1.6 V demonstrates the suitable potential window for the AHAS device. Moreover, the GCD study of AHAS device in 0 to 1.6 V potential window at different current densities (2.7-6.7 A g⁻¹) are presented in Fig. 6 (b). The discharging time of the AHAS device decreases with an increase in current density, demonstrating insufficient utilization of active material at higher current densities. The specific capacitance of the AHAS device depicted in Fig. 6 (c) shows that the specific capacitance of the device is maximum at a lower current density owing to more interaction of active material and electrolyte. The maximum specific capacitance of 185 F g⁻¹ at 2.7 A g⁻¹ current density is achieved for the AHAS device (E-NCP4//rGO), and upholds up to 159 F g⁻¹ at 6.7 A g⁻¹ current density. The AHAS device sustains almost 86 % of capacitance even at a high current density, suggesting

that the device can be useful even at high charging-discharging rates. DOI: 10.1039/D2TA00761D

Moreover, the energy density and power density of the AHAS device are derived from GCD study and plotted as Ragone plot in Fig. 6 (d). The AHAS device delivers the highest energy density of 65.7 Wh kg⁻¹ at a power density of 2.2 kW kg⁻¹, and it decreases up to 56.4 Wh kg⁻¹ at a power density of 5.4 kW kg⁻¹. The AHAS device (E-NCP4//rGO) shows higher energy and power density as compared to available aqueous supercapacitor devices based on nickel-cobalt phosphate electrodes (Table S5 (see ESI)).^{30-34,37-44,74-76} However, the E-NCP4//rGO device demonstrates less energy density than the reported KCo_{0.33}Ni_{0.67}PO₄//AC device by Liang et al.⁴¹ and for Cu/p-CuO/NiCo-P//3DPG device by Huang et al.⁴² The key reason to obtain improved performance by Liang et al. and Huang et al. is that the nickel foam and Cu/p-CuO nanowires were used as a current collector, which may add a self-capacitive contribution to the overall capacitance of the device. However, in the present work, the SS substrate is used as a current collector for both positive and negative electrodes, and it doesn't interfere with the capacitive performance of the device. The high energy and power values of the AHAS device (E-NCP4//rGO) demonstrate its applicability as per the requirement of high power or energy appliances.

In EIS analysis, the Nyquist plot of the AHAS device shown in Fig. 6 (e) represents lower values of R_s (2 Ω) and R_{ct} (72 Ω), which suggest easy interaction between electrode-electrolyte and excellent contact of active material with the current collector. Also, Warburg impedance (W) and general imperfect capacitor (Q, n=correction factor) are 0.02 Ω and 0.56 mF (n=0.9), respectively, in the fitted circuit. The GCD cycling of the AHAS device (E-NCP4//rGO) was measured at a current density of 15 A g⁻¹ for 4000 GCD cycles, as shown Fig. 6 (f), and the GCD curves of the initial and last 10 cycles are displayed as an inset of figure. For initial cycles, the AHAS device shows a decrement in the specific capacitance, then an increment in specific capacitance due to the expansion of the electrochemical active volume of material after several GCD cycles. The AHAS device withstands 97 % capacitive retention after 4000 GCD cycles and such stable nature of AHAS device with an excellent capacitance encourages further usage of electrodeposited nickel-cobalt phosphate thin films and rGO electrodes in the hybrid energy storage devices.

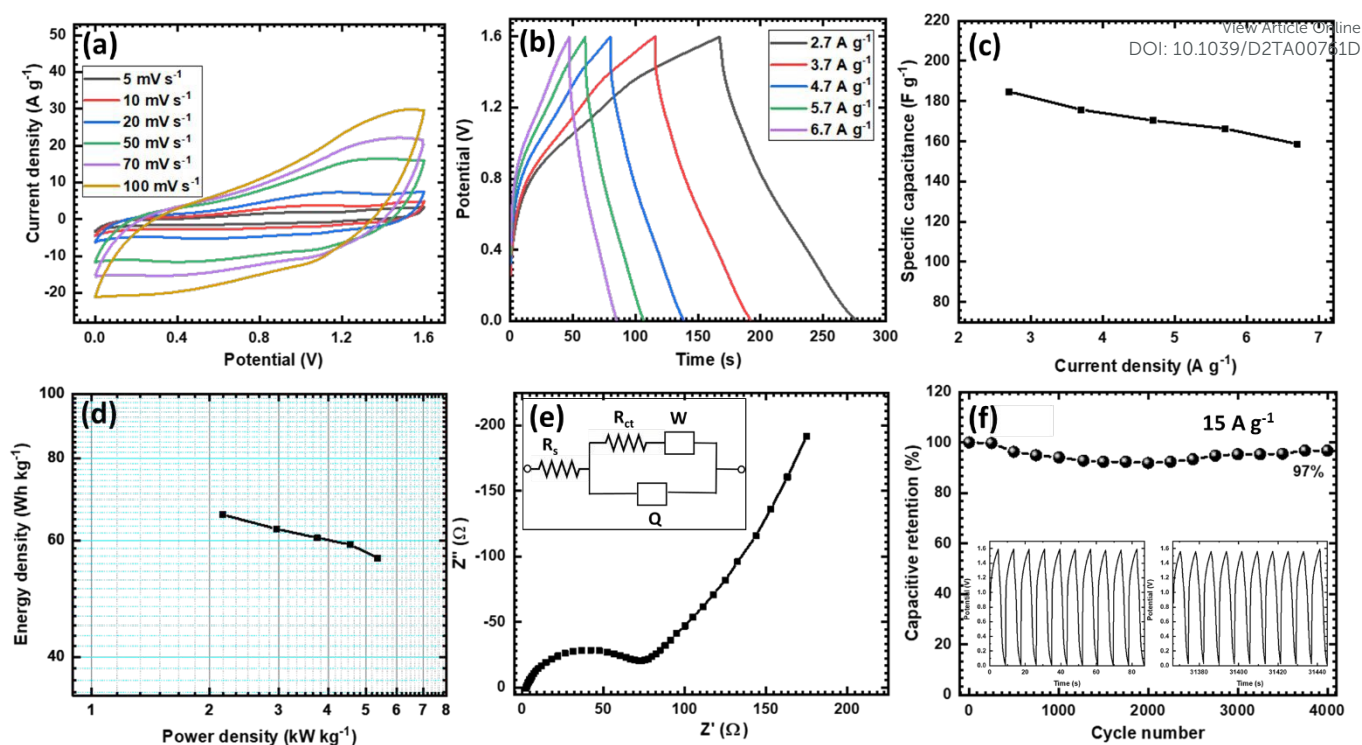


Fig. 6 (a) The CV graphs of the device at 5–100 mV s^{-1} scan rates, (b) The GCD curves at different current densities, (c) Plot of specific capacitance as a function of current density, (d) the Ragone plot, (e) Nyquist plot and (f) Cyclic stability at 15 A g^{-1} current density (inset: (i) initial and (ii) last 10 GCD cycles) of E-NCP4//rGO AHAS device.

3.5 Solid-state hybrid asymmetric supercapacitor (SHAS) device

The solid-state energy storage device has become a prominent topic in the research field because of its application in portable electronic devices. The solid-state energy storage devices offer numerous advantages like the ease in handling owing to being lightweight. Also, they can be fabricated in different designs and sizes due to their leakage-free property as desired for the application.^{84,85} Therefore, the SHAS device is fabricated by integrating E-NCP4 and rGO electrodes as cathode and anode, respectively, with gel electrolyte (PVA-KOH) (Fig. S2 (a-e), see ESI). As per the AHAS device study, the 0 to 1.6 V potential window is also selected for the SHAS device (E-NCP4//PVA-KOH//rGO) and used for further electrochemical analysis. The CV curves of the SHAS device (E-NCP4//PVA-KOH//rGO) are recorded at 5–100 mV s^{-1} scan rates, as displayed in Fig. 7 (a), and well-maintained CV shapes suggest good rate capability of the device. The non-linear GCD curves observed for the SHAS device (E-NCP4//PVA-KOH//rGO) at various current densities

in 0 to 1.6 V potential window as displayed in Fig. 7 (b). The SHAS device (E-NCP4//PVA-KOH//rGO) achieves an optimum 0 to 1.6 V potential window with a prolonged charging-discharging time, demonstrating maximum capacitance with energy density. The specific capacitance of the SHAS device is calculated from GCD analysis at various current densities, as presented in Fig. 7 (c). The SHAS device exhibits maximum specific capacitance of 90 F g^{-1} at a current density of 0.4 A g^{-1} , and decreases up to 65 F g^{-1} at 2 A g^{-1} current density with 72 % capacitive retention at a high current density. The position of SHAS device in Ragone plot (Fig. 7 (d)) shows that the device achieves a maximum energy density of 32 Wh kg^{-1} at a power density of 0.32 kW kg^{-1} and retains 23.1 Wh kg^{-1} energy density at a power density of 1.6 kW kg^{-1} , which suggest good rate capability of SHAS device (E-NCP4//PVA-KOH//rGO).

The Nyquist plot with an equivalent circuit of SHAS device shown in Fig. 7 (e) validates low values of R_s (0.25 Ω) and R_{ct} (15.13 Ω), demonstrating good ionic conductivity of gel electrolyte and its compatibility with

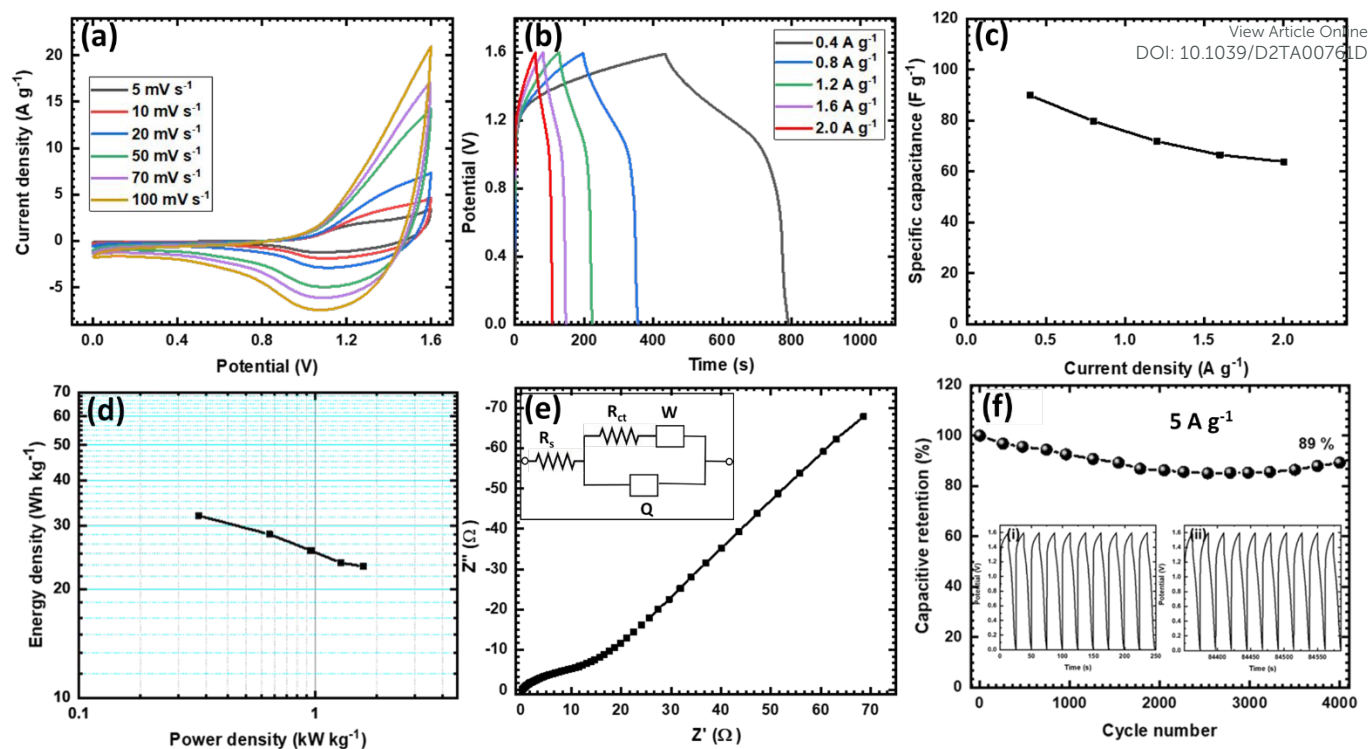


Fig. 7 (a) The CV curves at 5–100 mV s^{-1} scan rates, (b) The GCD curves at different current densities, (c) Plot of specific capacitance as a function of current density, (d) the Ragone plot, (e) Nyquist plot and (f) Cyclic stability at 5 A g^{-1} current density (inset: initial (i) and last (ii) 10 GCD cycles) of E-NCP4/PVA-KOH/rGO SHAS device.

active materials. Warburg impedance (W) and general imperfect capacitor (Q) are found to be 0.037Ω and 1.87 mF (correction factor $n=0.74$), respectively, in an equivalent circuit. Electrochemical stability of the SHAS device (E-NCP4/PVA-KOH/rGO) is tested for 4000 GCD cycles at a current density of 5 A g^{-1} ; the device retains 89 % of initial capacitance after 4000 cycles, as presented in Fig. 7 (f) with the initial and last GCD cycles as an inset. The good cyclic performance for a large number of cycles at high current density suggests the SHAS device can efficiently work at a very high rate for a long time and can be used in various portable devices.

The practical applicability of the SHAS device (E-NCP4/PVA-KOH/rGO) is inspected by charging two serially connected devices at $+3.2 \text{ V}$ for 30 s and then discharged through parallelly connected 201 red light-emitting diodes (LEDs), where they glowed LED panel for 180 s as represented in Fig. 8 (a–c). The demonstration of practical usage of SHAS device (E-NCP4/PVA-KOH/rGO) suggests its potential for application in various electronic appliances. The Ragone plots of AHAS and SHAS device with reported data in the

literature is plotted in Fig. 8 (d) (Table S5 (see ESI)).^{30–34,37–44,74,75}

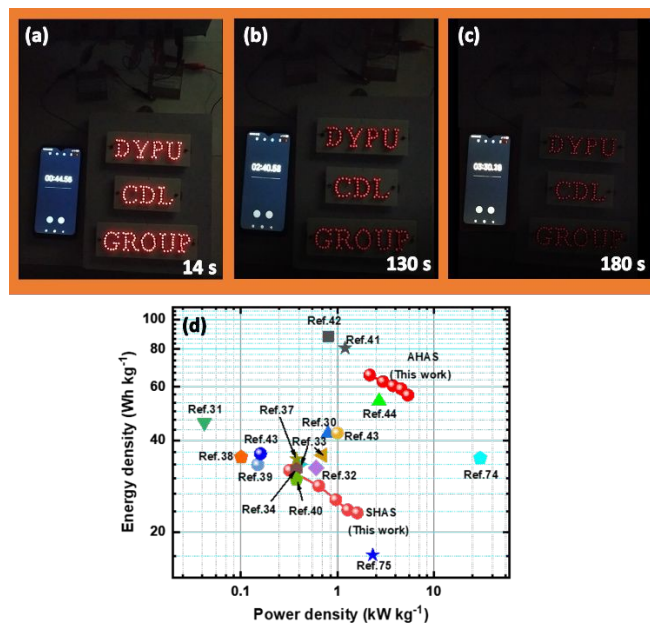


Fig. 8 (a–c) Photographs of two serially connected SHAS devices light up 201 LEDs panel at various time and (d) Comparative Ragone plots of AHAS and SHAS devices with available data.

The prepared SHAS device (E-NCP4//PVA-KOH//rGO) demonstrates comparable energy and power density results with previous reports on hybrid devices. Moreover, the AHAS device (E-NCP4//rGO) exhibits higher energy density than previously reported works due to the high ionic conductivity of the aqueous electrolyte. However, the additional leakage-free characteristic of the SHAS device makes it more advantageous for portable applications. Therefore, both kinds of hybrid devices can be used in the desired application e.g., AHAS device can be used in stationary devices where high energy is required, and SHAS device can be used in portable electronic devices.

Moreover, the achieved excellent capacitive performance of nickel-cobalt phosphate active material in the present work is attributed to the intercalative pseudocapacitive charge storage mechanism, and further, the performance can be enhanced by doping or compositing with other materials or by using the high surface area current collector. The synergy between metal ions (nickel and cobalt) at optimal composition (~1:1) with microspheres of clustered nanoparticles like morphology of E-NCP4 electrode possesses intercalative pseudocapacitance and EDLC capacitance of rGO leads to the high supercapacitive performance of AHAS and SHAS devices.

4. Conclusions

In conclusion, the PED method is an efficient synthetic approach for successful binder-free, large-scale preparation of nickel-cobalt phosphate thin films with a rational combination of cations (nickel and cobalt). Variation in cations (Ni:Co) composition significantly influences the structure and morphology of nickel-cobalt phosphate thin films from amorphous microspheres to crystalline nanosheets. The microspheres with clustered nanoparticles of E-NCP4 electrode with ~1:1 Ni:Co composition delivers enhanced specific capacitance (capacity) of 2228 F g⁻¹ (891 C g⁻¹) at 1.5 A g⁻¹ than other electrodes, which accredited to high specific surface area (17.2 m² g⁻¹) and low electrochemical impedance owing to binder-free synthesis. In addition, the fabricated hybrid devices based on E-NCP4 and rGO electrodes demonstrated excellent energy storage performance as the AHAS device exhibited the highest specific capacitance of 185 F g⁻¹ with an energy density of 65.7 Wh kg⁻¹ at a power density of 2.2 kW kg⁻¹. Likewise, the

SHAS device achieves the highest specific capacitance of 90 F g⁻¹ with 32 Wh kg⁻¹ energy density at 0.32 kW kg⁻¹ power density. Moreover, the SHAS (E-NCP4//PVA-KOH//rGO) and AHAS (E-NCP4//rGO) devices with excellent electrochemical capacitive features suggest their significant potential for application in various electronic devices. Conclusively, the binder-free microspheres of clustered nanoparticles of nickel-cobalt phosphate thin film electrode, with (~1:1) optimum nickel and cobalt composition prepared by PED method, is the prospective cathode for hybrid supercapacitor devices (aqueous and solid-state).

Conflict of interest

There are no conflicts to declare.

Acknowledgments

Authors are thankful to the Ministry of Science and Technology India, Department of Science and Technology-Innovation in Science Pursuit for Inspired (DST-INSPIRE), for financial support through research project sanction no. DST/INSPIRE/04/2016/000260. Also, the authors are thankful to the Science and Engineering Research Board (DST-SERB), New Delhi, India, for financial support through research project sanction no. CRG/2019/005730. HHP, TK and VGP announce that this work was supported by the National Research Foundation of Korea (NRF) grant funded by the Korean government (MSIT) (No.2020R1A5A1019131).

References

- 1 E. Aboelazm, G. Ali, H. Algarni, H. Yin, Y. Zhong and K. Chong, *J. Phys. Chem. C*, 2018, **122**, 12200-12206.
- 2 X. Zhao, W. Cai, Y. Yang, X. Song, Z. Neale, H. Wang, J. Sui and G. Cao, *Nano Energy*, 2018, **47**, 224-234.
- 3 J. Sun, C. Wu, X. Sun, H. Hu, C. Zhi, L. Hou and C. Yuan, *J. Mater. Chem. A*, 2017, **5**, 9443-9464.
- 4 L. Ghadimi, N. Arsalani, I. Ahadzadeh, A. Hajalilou and E. Abouzari-Lotf, *Appl. Surf. Sci.*, 2019, **494**, 440-451.
- 5 D. Jiang, C. Li, W. Yang, J. Zhang and J. Liu, *J. Mater. Chem. A*, 2017, **5**, 18684-18690.
- 6 J. Zhao, Y. Li, G. Wang, T. Wei, Z. Liu, K. Cheng, K. Ye, K. Zhu, D. Cao and Z. Fan, *J. Mater. Chem. A*, 2017, **5**, 23085-23093.

- 7 F. Yu, T. Huang, P. Zhang, Y. Tao, F. Cui, Q. Xie, S. Yao and F. Wang, *Energy Storage Mater.*, 2019, **22**, 235-255.
- 8 H. Jia, Z. Wang, C. Li, X. Si, X. Zheng, Y. Cai, J. Lin, H. Liang, J. Qi, J. Cao, J. Feng and W. Fei, *J. Mater. Chem. A*, 2019, **7**, 6686-6694.
- 9 Y. Gogotsi and P. Simon, *Sci. Mag.*, 2011, **334**, 917-918.
- 10 J. Yan, Z. Fan, W. Sun, G. Ning, T. Wei, Q. Zhang, R. Zhang, L. Zhi and F. Wei, *Adv. Funct. Mater.*, 2012, **22**, 2632-2641.
- 11 X. Lu, X. Chen, W. Zhou, Y. Tong and G. Li, *ACS Appl. Mater. Interface*, 2015, **7**, 14843-14850.
- 12 H. Xia, C. Hong, B. Li, B. Zhao, Z. Lin, M. Zheng, S. Savilov and S. Aldoshin, *Adv. Funct. Mater.*, 2015, **25**, 627-635.
- 13 N. Chodankar, H. Pham, A. Nanjundan, J. Fernando, K. Jayaramulu, D. Golberg, Y. Han and D. Dubal, *Small*, 2020, **16**, 2002806.
- 14 F. Shi, L. Li, X. Wang, C. Gu and J. Tu, *RSC Adv.*, 2014, **4**, 41910-41921.
- 15 X. Li, A. Elshahawy, C. Guan and J. Wang, *Small*, 2017, **13**, 1701530-1701554.
- 16 B. Senthilkumar, Z. Khan, S. Park, K. Kim, H. Ko and Y. Kim, *J. Mater. Chem. A*, 2015, **3**, 21553-21561.
- 17 X. Peng, H. Chai, Y. Cao, Y. Wang, H. Dong, D. Jia and W. Zhou, *Mater. Today Energy*, 2018, **7**, 129-135.
- 18 F. Omar, A. Numan, N. Duraisamy, S. Bashir, K. Ramesh and S. Ramesh, *RSC Adv.*, 2016, **6**, 76298-76306.
- 19 Y. Gao, J. Zhao, Z. Run, G. Zhang and H. Pang, *Dalton Trans.*, 2014, **43**, 17000-17005.
- 20 H. Li, H. Yu, J. Zhai, L. Sun, H. Yang and S. Xie, *Mater. Lett.*, 2015, **152**, 25-28.
- 21 H. Pang, S. Wang, W. Shao, S. Zhao, B. Yan, X. Li, S. Li, J. Chen and W. Du, *Nanoscale*, 2013, **5**, 5752-5757.
- 22 J. Li, M. Liu, L. Kong, M. Shi, W. Han and L. Kang, *Mater. Lett.*, 2015, **161**, 404-407.
- 23 Z. Khan, B. Senthilkumar, S. Lim, R. Shanker, Y. Kim and H. Ko, *Adv. Mater. Interfaces*, 2017, **4**, 1700059.
- 24 D. Patil, B. Koteswararao, K. Begari, A. Yogi, M. Moussa and D. Dubal, *ACS Appl. Energy Mater.*, 2019, **2**, 2972-2981.
- 25 C. Yuan, H. Wu, Y. Xie and X. Lou, *Angew. Chem. Int. Ed.*, 2014, **53**, 1488-1504.
- 26 M. Liu, L. Kong, C. Lu, X. Ma, X. Li, Y. Luo and L. Kang, *J. Mater. Chem. A*, 2013, **1**, 1380-1387.
- 27 H. Chen, J. Jiang, L. Zhang, T. Qi, D. Xia and H. Wan, *J. Power Sources*, 2014, **248**, 28136-28136. View Article Online
DOI: 10.1039/C4TA00761D
- 28 F. Yang, J. Yao, F. Liu, H. He, M. Zhou, P. Xiao and Y. Zhang, *J. Mater. Chem. A*, 2013, **1**, 594-601.
- 29 U. Patil, J. Sohn, S. Kulkarni, S. Lee, H. Park, K. Gurav and S. Jun, *ACS Appl. Mater. Interfaces*, 2014, **6**, 2450-2458.
- 30 M. Liu, J. Li, Y. Hu, Q. Yang and L. Kang, *Electrochim. Acta*, 2016, **201**, 142-150.
- 31 L. Tao, J. Li, Q. Zhou, H. Zhu, G. Hu and J. Huang, *J. Alloys Compd.*, 2018, **767**, 789-796.
- 32 C. Chen, N. Zhang, Y. He, B. Liang, R. Ma and X. Liu, *ACS Appl. Mater. Interfaces*, 2016, **8**, 23114-23121.
- 33 B. Li, P. Gu, Y. Feng, G. Zhang, K. Huang, H. Xue and H. Pang, *Adv. Funct. Mater.*, 2017, **27**, 1605784.
- 34 Y. Tang, Z. Liu, W. Guo, T. Chen, Y. Qiao, S. Mu, Y. Zhao and F. Gao, *Electrochim. Acta*, 2016, **190**, 118-125.
- 35 J. Zhang, Y. Yang, Z. Zhang, X. Xu and X. Wang, *J. Mater. Chem. A*, 2014, **2**, 20182-20188.
- 36 A. Mirghni, K. Oyedotun, B. Mahmoud, A. Bello, S. Ray and N. Manyala, *Compos. B Eng.*, 2019, **174**, 106953.
- 37 S. Zhang, H. Gao and J. Zhou, *J. Alloys Compd.*, 2018, **746**, 549-556.
- 38 Z. Xiao, Y. Bao, Z. Li, X. Huai, M. Wang, P. Liu and L. Wang, *ACS Appl. Energy Mater.*, 2019, **2**, 1086-1092.
- 39 Y. Zhao, Z. Chen, D. Xiong, Y. Qiao, Y. Tang and F. Gao, *Sci. Rep.*, 2016, **6**, 17613.
- 40 M. Liu, N. Shang, X. Zhang, S. Gao, C. Wang and Z. Wang, *J. Alloys Compd.*, 2019, **791**, 929-935.
- 41 B. Liang, Y. Chen, J. He, C. Chen, W. Liu, Y. He, X. Liu, N. Zhang and V. Roy, *ACS Appl. Mater. Interfaces*, 2018, **10**, 3506-3514.
- 42 J. Huang, Y. Xiong, Z. Peng, L. Chen, L. Wang, Y. Xu, L. Tan, K. Yuan, Y. Chen, *ACS Nano*, 2020, **14**, 14201-14211.
- 43 S. Marje, V. Patil, V. Parale, H. Park, P. Shinde, J. Gunjekar, C. Lokhande and U. Patil, *Chem. Eng. J.*, 2022, **429**, 132184.
- 44 M. Li, Y. Luo, C. Jia, Q. Zhang, G. Luo, L. Zhao, R. Boukherroub and Z. Jiang, *J. Alloys Compd.*, 2022, **893**, 162340.
- 45 S. Patil, N. Chodankar, R. Pujari, Y. Han and D. Lee, *J. Power Sources*, 2020, **466**, 228286.
- 46 S. Navale, V. Mali, S. Pawar, R. Mane, M. Naushad, F. Stadler and V. Patil, *RSC Adv.*, 2015, **5**, 51961-51965.

- 47 H. Wen, M. Cao, G. Sun, W. Xu, D. Wang, X. Zhang and C. Hu, *J. Phys. Chem. C*, 2008, **112**, 15948-15955.
- 48 T. Nguyen, V. Nguyen, R. Deivasigamani, D. Kharismadewi, Y. Iwai and J. Shim, *Solid State Sci.*, 2016, **53**, 71-77.
- 49 H. Liu, T. Chin and S. Yung, *Mater. Chem. Phys.*, 1997, **50**, 1-10.
- 50 N. Prokopchuk, V. Kopilevich and L. Voitenko, *Russ. J. Appl. Chem.*, 2008, **81**, 386-391.
- 51 N. Priyadharsini, A. Shanmugavani, L. Vasylechko and R. Selvan, *Ionics*, 2018, **24**, 2073-2082.
- 52 P. Noisong, C. Danvirutai, T. Srithanratana and B. Boonchom, *Solid State Sci.*, 2008, **10**, 1598-1604.
- 53 Y. Zhu, Y. Liu, T. Ren and Z. Yuan, *Nanoscale*, 2014, **6**, 6627-6636.
- 54 J. Chang, Q. Lv, G. Li, J. Ge, C. Liu and W. Xing, *Appl. Catal. B*, 2017, **204**, 486-496.
- 55 W. Bian, Y. Huang, X. Xu, M. Din, G. Xie and X. Wang, *ACS Appl. Mater. Interfaces*, 2018, **10**, 9407-9414.
- 56 J. Zhang, Y. Wang, Y. Zhang, F. Zaman, L. Hou and C. Yuan, *Electrochem. commun.*, 2021, **125**, 107006.
- 57 H. Shao, N. Padmanathan, D. McNulty, C. O'Dwyer and K. Razeeb, *ACS Appl. Mater. Interfaces*, 2016, **8**, 28592-28598.
- 58 Y. Li, Z. Wang, J. Hu, S. Li, Y. Du, X. Han, and P. Xu, *Adv. Funct. Mater.*, 2020, **30**, 1910498.
- 59 N. Jiang, B. You, M. Sheng and Y. Sun, *ChemCatChem*, 2016, **8**, 106-112.
- 60 T. Sun, L. Xu, Y. Yan, A. Zakhidov, R. Baughman and J. Chen, *ACS Catal.*, 2016, **6**, 1446-1450.
- 61 P. Feng, X. Cheng, J. Li and X. Luo, *ChemistrySelect*, 2018, **3**, 760-764.
- 62 J. Li, W. Xu, D. Zhou, J. Luo, D. Zhang, P. Xu, L. Wei and D. Yuan, *J. Mater. Sci.*, 2018, **53**, 2077-2086.
- 63 X. Bai, Q. Liu, Z. Lu, J. Liu, R. Chen, R. Li, D. Song, X. Jing, P. Liu and J. Wang, *ACS Sustain. Chem. Eng.*, 2017, **5**, 9923-9934.
- 64 M. Sathiya, A. Prakash, K. Ramesha, J. Tarascon and A. Shukla, *J. Am. Chem. Soc.*, 2011, **133**, 16291-16299.
- 65 H. Kim, J. Cook, H. Lin, J. Ko, S. Tolbert, V. Ozolins and B. Dunn, *Nat. Mater.*, 2017, **16**, 454-460.
- 66 P. Yang, Z. Wu, Y. Jiang, Z. Pan, W. Tian, L. Jiang and L. Hu, *Adv. Energy Mater.*, 2018, **8**, 1801392.
- 67 J. Duay, S. Sherrill, Z. Gui, E. Gillette and S. Lee, *ACS Nano*, 2013, **7**, 1200-1214.
- 68 S. Kandalkar, H. Lee, S. Seo, K. Lee and C. Kim, *J. Mater. Sci.*, 2011, **46**, 2977-2981. DOI: 10.1039/D2TA00761D
- 69 F. Omar, A. Numan, S. Bashir, N. Duraisamy, R. Vikneswaran, Y. Loo, K. Ramesh and S. Ramesh, *Electrochim. Acta*, 2018, **273**, 216-228.
- 70 K. Sankar, Y. Seo, S. Lee and S. Jun, *ACS Appl. Mater. Interfaces*, 2018, **10**, 8045-8056.
- 71 D. Koushik, M. Jost, A. Ducinkas, C. Burgess, V. Zardetto, C. Weijtens, M. Verheijen, W. Kessels, S. Albrechtbe and M. Creatore, *J. Mater. Chem. C*, 2019, **7**, 12532.
- 72 Z. Tian, Z. Sun, Y. Shao, L. Gao, R. Huang, Y. Shao, R. Kaner and J. Sun, *Energy Environ. Sci.*, 2021, **14**, 1602.
- 73 X. Sun, J. Sun, C. Wu, L. Guo, L. Hou and C. Yuan, *Mater. Today Energy*, 2021, **19**, 100592.
- 74 C. Su, S. Xu, L. Zhang, X. Chen, G. Guan, N. Hu, Y. Su, Z. Zhou, H. Wei, Z. Yang and Y. Qin, *Electrochim. Acta*, 2019, **305**, 81-89.
- 75 S. Xu, C. Su, T. Wang, Y. Ma, J. Hu, J. Hu, N. Hu, Y. Su, Y. Zhang and Z. Yang, *Electrochim. Acta*, 2018, **259**, 617-625.
- 76 S. Xu, T. Wang, Y. Ma, W. Jiang, S. Wang, M. Hong, N. Hu, Y. Su, Y. Zhang and Z. Yang, *ChemSusChem*, 2017, **10**, 4056-4065.
- 77 Z. Huang, G. Natu, Z. Ji, P. Hasin and Y. Wu, *J. Phys. Chem. C*, 2011, **115**, 25109-25114.
- 78 P. Deshmukh, S. Pusawale, V. Jamadade, U. Patil and C. Lokhande, *J. Alloys Compd.*, 2011, **509**, 5064-5069.
- 79 D. Dubal, D. Dhawale, R. Salunkhe and C. Lokhande, *J. Electrochem. Soc.*, 2010, **157**, A812-A817.
- 80 M. Singh, S. Semwal, A. Kumar and S. Singh, *Turk. J. Elec. Eng. & Comp. Sci.*, 2015, **23**, 2208-2214.
- 81 F. Butt, M. Tahir, C. Cao, F. Idress, R. Ahmed, W. Khan, Z. Ali, N. Mohmood, M. Tanveer, A. Mohmood and I. Aslam, *ACS Appl. Mater. Interfaces*, 2014, **16**, 13635-13641.
- 82 J. Cherusseria and K. Kar, *J. Mater. Chem. A*, 2016, **4**, 9910-9922.
- 83 L. Hou, Z. Chen, Z. Zhao, X. Sun, J. Zhang and C. Yuan, *ACS Appl. Energy Mater.*, 2019, **2**, 548-557.
- 84 Z. Tang, C. Jia, Z. Wan, Q. Zhou, X. Ye and Y. Zhu, *RSC Adv.*, 2016, **6**, 112307-112316.
- 85 C. Zhong, Y. Deng, W. Hu, J. Qiao, L. Zhang and J. Zhang, *Chem. Soc. Rev.*, 2015, **44**, 7484-7539.

Hydrous and Amorphous Cobalt Phosphate Thin-Film Electrodes Synthesized by the SILAR Method for High-Performing Flexible Hybrid Energy Storage Devices

Vinod V. Patil, Sachin S. Pujari, Shraddha B. Bhosale, Sambhaji S. Kumbhar, Vinayak G. Parale, Jayavant L. Gunjekar, Hyung-Ho Park, Chandrakant D. Lokhande, Mukund G. Mali, Dattakumar S. Mhamane,* and Umakant M. Patil*

Cite This: <https://doi.org/10.1021/acs.energyfuels.2c02202>

Read Online

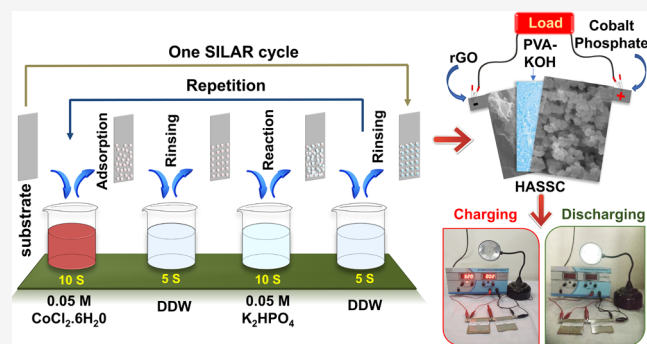
ACCESS |

Metrics & More

Article Recommendations

Supporting Information

ABSTRACT: Recently, excellent electrochemical performance and good conductivity of transition metal phosphates (TMPs) have been obtained, assuring their potential as a cathode in hybrid supercapacitors. Also, amorphous, hydrous materials are supposed to be exemplary active materials for high-performing supercapacitors because of their unique porous structure, structural flexibility, and rich defects. Therefore, the present investigation describes a simple synthesis method for hydrous and amorphous cobalt phosphate thin-film preparation by the simple successive ionic layer adsorption and reaction (SILAR) method on flexible stainless steel (SS) substrate for supercapacitor application. The structural and morphological analyses reveal mesoporous, agglomerated nanoparticle-like, hydrous, and amorphous cobalt phosphate over the SS substrate. The mesoporous nanoparticles of cobalt phosphate material possess the uppermost specific capacitance of 1147 F g^{-1} and 630.7 C g^{-1} specific capacity at a 1 mA cm^{-2} current density. To demonstrate practical relevance, hybrid supercapacitor devices were assembled with cobalt phosphate and rGO (reduced graphene oxide) as cathode and anode electrodes, respectively. Furthermore, the assembled hybrid aqueous supercapacitor device (S-CP4//KOH//rGO) delivers 44.8 Wh kg^{-1} specific energy (SE) at a specific power (SP) of 4.8 kW kg^{-1} with 126 F g^{-1} specific capacitance. The accumulated all-solid-state hybrid supercapacitor device (S-CP4//PVA-KOH//rGO) achieved the uppermost 77 F g^{-1} specific capacitance and SE of 27.37 Wh kg^{-1} at SP of 1.5 kW kg^{-1} with an outstanding 94% capacitive retention over 5000 cycles. Such remarkable supercapacitive performance results demonstrate that the SILAR method is an easy synthesis process for the binder-free preparation of cathode based on hydrous, amorphous cobalt phosphate thin films for hybrid supercapacitor devices.



1. INTRODUCTION

There has been a recent surge in energy demand for escalating electronic appliances and limitations of existing energy storage systems as the traditional energy storage system does not meet the development trend, which instantly demands efficient and clean energy.^{1–3} Therefore, supercapacitor devices are in high demand and are considered an upcoming generation of energy storage devices based on benefits such as excellent energy storage capability and long cycle life.^{4–6} Nevertheless, their low specific energy confines supercapacitor application in devices that require high energy.^{7,8} Therefore, to improve specific energy and power, hybrid asymmetric capacitor devices have been developed, which consist of two dissimilar electrodes: one as an energy source (cathode), where battery-type or pseudocapacitive material is used, and another as a power source (anode), which consists of capacitor-type or electro-

chemical double-layer capacitor (EDLC) electrode materials.^{9–12}

In general, existing pseudocapacitive materials are categorized into intrinsic, intercalation, and extrinsic types, and they exhibit higher specific energy than EDLC materials. Interestingly, battery-type materials can exhibit pseudocapacitive behavior upon changing their crystallite size or morphology (nanocrystalline) and are referred to as extrinsic pseudocapacitive materials.^{13–16} Therefore, recent research interest has been growing in developing and miniaturizing battery-type

Received: July 1, 2022

Revised: September 18, 2022

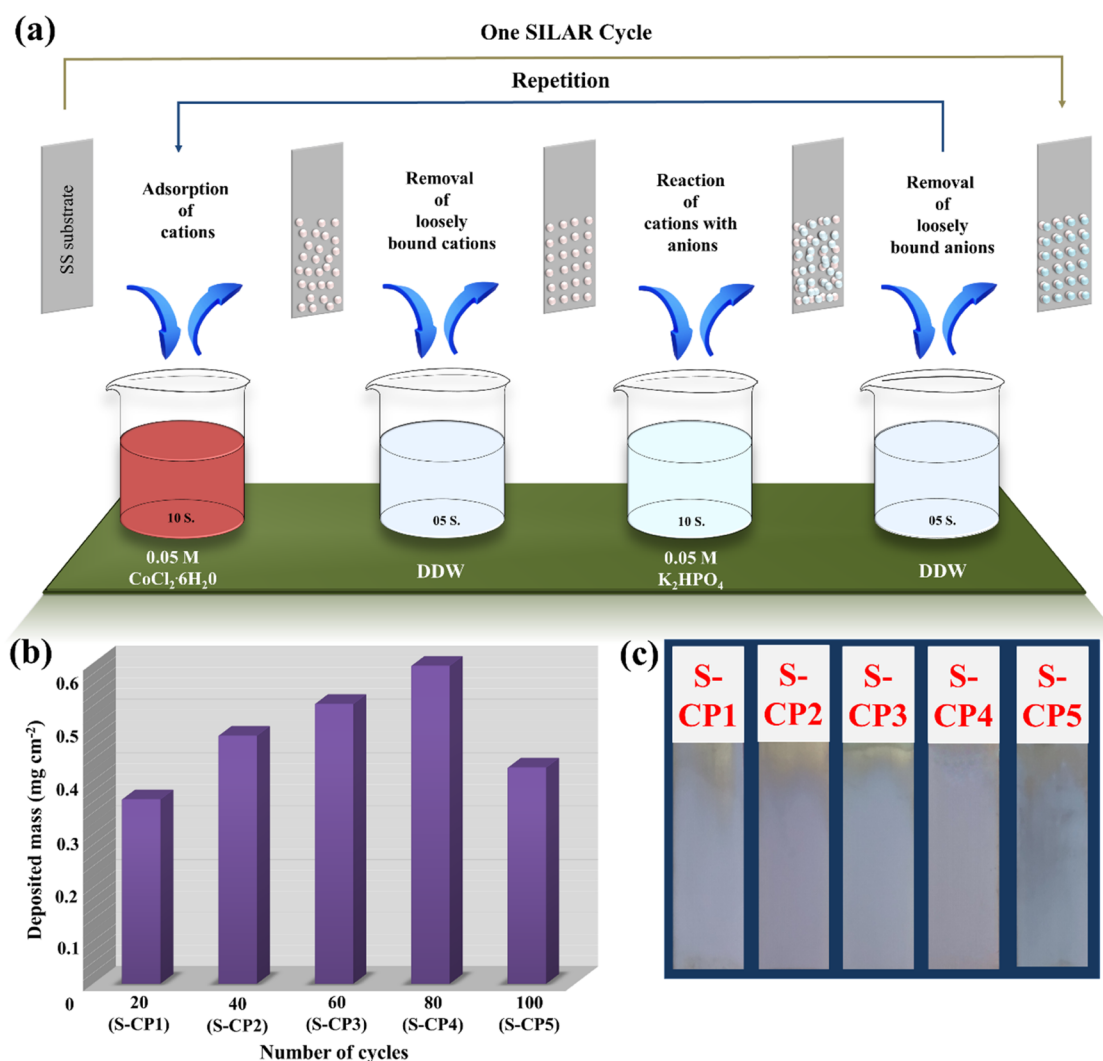


Figure 1. (a) Schematic preparation of cobalt phosphate thin-film deposition using the SILAR method, (b) thickness variation plot, and (c) photographs of S-CP series electrodes.

materials (nanocrystalline) to explore their pseudocapacitive performance in hybrid asymmetric supercapacitor devices as a cathode. Also, amorphous pseudocapacitive materials are gaining more attention than their crystalline counterparts due to their chemical homogeneity, atomic-scale structural flexibility, high surface area, and abundant defects.^{17–19} Owing to these unique features, the amorphous phase affects the charge storage properties of the material in diverse ways as amorphous materials can provide full access to electrolyte ions, and their structural flexibility facilitates the in situ transformation from originally inert species to active phases/species, while the charging–discharging process efficiently improves the intrinsic activity and electrochemical stability.^{17,20–23}

Therefore, several pseudocapacitive materials, including metal phosphates/oxides/hydroxides/sulfides, have been enormously examined as the positive electrode in energy storage devices due to their electrochemical activity and abundant resources.^{24–26} The excellent electrical conductivity and electrochemical stability due to phosphate's covalent bond (P–O) make them extraordinary contenders over the remaining pseudocapacitive materials for supercapacitors. Among several transition metal phosphates (TMPs), cobalt phosphate has been gaining increasing attention since it

portrays several applications as a potential anode for rechargeable batteries, heterogeneous catalysts, magnetism materials, sorbents, and ion exchangers,²⁷ due to its excellent electrochemical redox activity. Therefore, in the last decade or more, many research articles have described the preparation of different polymorphs of crystalline cobalt phosphate material with various sizes and shapes by different chemical synthesis methods,^{28–45} such as green precipitation,²⁸ hydrothermal,²⁹ co-precipitation,³⁰ and solvothermal,³¹ and also investigated them as energy storage devices. Also, different morphologies of well-crystalline cobalt phosphate, such as flowerlike,²⁸ nano-sheets,²⁹ nanoflakes,³⁰ nanowires,³¹ leaflike,³⁴ etc., were synthesized using different synthesis approaches, which eventually provide distinct electrochemical capacitive performances.

Amorphization of materials is a facile and efficient strategy that aims to obtain short-range ordering and achieve the extrinsic pseudocapacitive behavior of battery-type materials. Several synthesis approaches have been reported for the preparation of well-ordered crystalline cobalt phosphate materials; however, the amorphous phase of cobalt phosphate has not yet been prepared and utilized for supercapacitor application. Among several chemical methods, SILAR is a

productive method for synthesizing binder-free, amorphous/nanocrystalline material thin-film electrodes. Also, thin films were prepared by dipping a substrate into placed cationic precursor and anionic precursor solutions one by one in the SILAR process, which prevents crystalline growth of the material since material growth is interrupted during deposition and results in the formation of amorphous/nanocrystalline materials on the substrate. Moreover, the SILAR method is scalable and can be used for large-area deposition on any kind of substrates (flexible/rigid).^{46,47} Moreover, this proficient SILAR method has not yet been explored for synthesizing binder-free cobalt phosphate thin-film electrodes.

Therefore, for the first time, a facile SILAR process is utilized to prepare amorphous cobalt phosphate fine spherical particles on a flexible SS substrate and used for supercapacitor application. The impact of cobalt phosphate electrode thicknesses on electrochemical capacitive performances is studied using specific capacitance and distribution of battery type and extrinsic pseudocapacitive behavior. Furthermore, hybrid asymmetric supercapacitor devices, such as aqueous and all-solid-state devices, were assembled with cobalt phosphate and rGO^{48,49} with aqueous 1 M KOH and PVA-KOH gel electrolyte, respectively. Supercapacitive performances of assembled hybrid supercapacitor devices are evaluated in terms of specific capacitance, SE, SP, and electrochemical durability through capacitive retention and described herein.

2. EXPERIMENTAL SECTION

2.1. Amorphous Cobalt Phosphate Synthesis. For the cobalt phosphate preparation, precursors such as cobalt chloride hexahydrate ($\text{CoCl}_2 \cdot 6\text{H}_2\text{O}$) and dipotassium hydrogen orthophosphate (K_2HPO_4) (AR grade, Sigma-Aldrich) were utilized without any purification. The research-grade flexible SS substrate ($5 \times 1 \text{ cm}^2$) was used for thin-film deposition and to clean the substrate surface and create nucleation centers; it was polished using polish paper (zero-grade) and further cleaned using double-distilled water (DDW) via ultrasonication. The equimolar (0.05 M) $\text{CoCl}_2 \cdot 6\text{H}_2\text{O}$ and K_2HPO_4 dissolved in 50 mL of DDW are used as a cationic precursor and anionic precursor, respectively. The amorphous cobalt phosphate thin films are obtained by the SILAR method, as schematically shown in Figure 1a, which consists of four steps. In the initial step, the finely cleaned SS substrate is immersed for 10 s into a beaker containing a cationic precursor (0.05 M $\text{CoCl}_2 \cdot 6\text{H}_2\text{O}$) to allow for adsorption of cations on the substrate surface. Next, the SS substrate was rinsed in DDW (5 s) in the second step to remove the inadequately adsorbed and excess cations from the substrate surface. In the third step, the cation-adsorbed substrate is sequentially immersed for 10 s in the beaker containing the anionic precursor (0.05 M K_2HPO_4), where anions react with preadsorbed cations to form a cobalt phosphate layer on the SS substrate. Finally, to ensure the removal of unreacted and nonadherent molecules, the deposited substrate was rinsed with DDW (5 s) in the fourth step. The whole four-step process is one SILAR cycle, and similar 20, 40, 60, 80, and 100 SILAR cycles are varied to accomplish thickness variation of cobalt phosphate thin films and designated as S-CP1, S-CP2, S-CP3, S-CP4, and S-CP5, respectively. The optimized preparative parameters are summarized in Table S1 (Electronic Supporting Information, ESI). Moreover, as-prepared thin films are characterized by various physicochemical techniques and used to probe electrochemical capacitive performance.

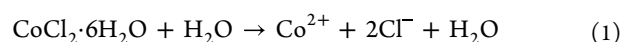
2.2. Material Characterizations. The structural properties of prepared cobalt phosphate electrodes were examined with a Rigaku Miniflex-600 X-ray diffractometer (XRD) using $\text{Cu K}\alpha$ radiation ($\lambda = 0.15425 \text{ nm}$) and functioned at 15 mA and 40 kV in the $5\text{--}80^\circ 2\theta$ range at a 2° min^{-1} scanning rate. Fourier transform-infrared (FT-IR) spectrometry spectra within the region of $4000\text{--}400 \text{ cm}^{-1}$ were recorded using an α (II) Bruker unit to determine functional groups in the prepared samples. The Raman spectrum of the sample was

recorded using a Renishaw Raman microscope at a 532 nm excitation wavelength to analyze the chemical bonding. The Brunauer–Emmett–Teller (BET) method and Barrett–Joyner–Halenda (BJH) method were used to calculate the specific surface areas and pore size distribution, respectively, of samples by adsorption measurement using a Belsorp II mini surface analyzer (77 K). An X-ray photoelectron spectroscopy (XPS) study was carried out on a ThermoScientific ESCALAB 250 (U.K.) instrument. The morphology study and elemental analysis of samples were carried out by employing field emission scanning electron microscopy (FE-SEM, Model-JSM-7001F) and energy-dispersive spectroscopy (EDS, Model-X-max), respectively. Supercapacitive measurements of cobalt phosphate electrodes are studied using the electrochemical workstation instrument (ZIVE MPI).

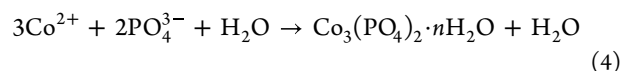
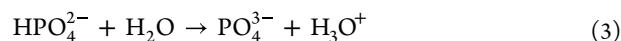
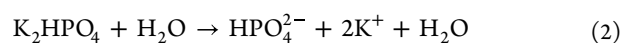
2.3. Electrochemical Capacitive Measurements of Cobalt Phosphate Electrodes. The electrochemical capacitive study of the cobalt phosphate electrodes is performed using a half test cell that includes SS-supported cobalt phosphate, a platinum plate, and mercury/mercury oxide (Hg/HgO) as the working, counter, and reference electrodes in a 1 M KOH electrolyte, respectively. Moreover, the applicability of amorphous cobalt phosphate as a positive (cathode) electrode in a hybrid supercapacitor was probed by assembling a full test cell as described in Note S2 (see ESI). The cyclic voltammetry (CV) measurements, galvanostatic charge–discharge (GCD) measurements are carried out, and electrochemical impedance spectroscopy (EIS) were assessed at the open circuit potential (OCP) over the frequency range of 10 mHz to 1 MHz. Furthermore, the performance of cobalt phosphate thin-film electrodes in terms of specific capacitance, charge contributions, SE, and SP of devices was evaluated using formulae provided in ESI Note S3.

3. RESULTS AND DISCUSSION

3.1. Reaction Mechanism and Film Formation. In the present study, the preparation of cobalt phosphate electrodes is performed using the simple SILAR route. SILAR is established on successive adsorption and reaction on the SS substrate surface by sequentially dipping into separately located cationic and anionic precursors, respectively. The thin film of cobalt phosphate formed by the SILAR process, a layer of Co^{2+} ions adsorbs at nucleation centers that exist on the SS substrate from the cationic precursor (at ambient conditions as per eq 1).



Further reaction was continued in an anionic precursor, where PO_4^{3-} anions are available by dissociation of K_2HPO_4 in DDW as per eqs 2 and 3. When the Co^{2+} ions consisting of the SS substrate are immersed in an anionic precursor solution, the chemical reaction among preadsorbed Co^{2+} and PO_4^{3-} ions expedites the adherent layer formation of cobalt phosphate over a SS substrate as described in eq 4.



Therefore, by way of the ion-by-ion growth mechanism, the thin film is deposited, and it is followed by the ions assembling at nucleation sites on the immersed substrate's surface. Moreover, material growth on the surface of the substrate is attained through coalescence and particle stacking. Therefore, the preparation of cobalt phosphate electrodes employing the SILAR process has several striking features: the ambient deposition temperature, which eludes high-temperature effects

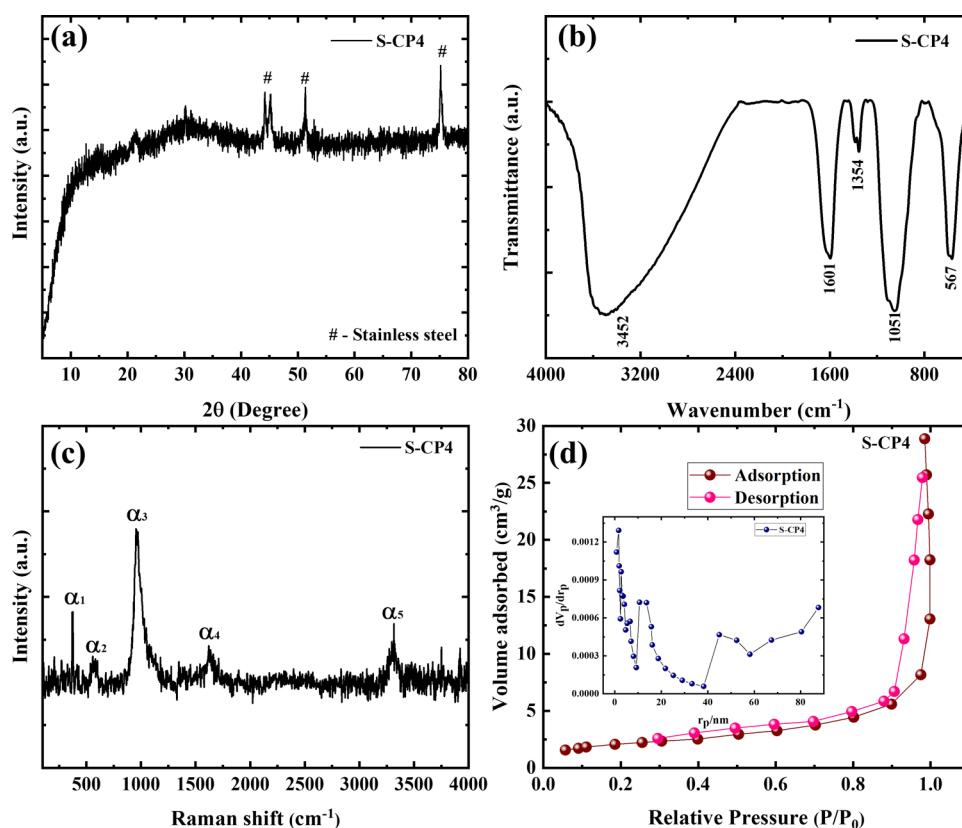


Figure 2. (a) X-ray diffraction pattern, (b) FT-IR spectrum, (c) Raman spectrum, and (d) N_2 adsorption/desorption isotherm of the S-CP4 sample.

such as contamination, interdiffusion, dopant redistribution, and more importantly, it can lead to the formation of amorphous material in thin-film form due to lattice mismatching owing to abruptness in growth mechanism.

Besides the apparent benefits of energy-saving, the prime advantage is the controlled growth rate and the film thickness, which can be simply attained by changing adsorption time and reaction time and varying deposition cycles. Therefore, the thickness of cobalt phosphate on the SS substrate is varied and quantified using the gravimetric weight difference route in terms of the deposited mass of material on the unit area of the SS substrate (mg cm^{-2}). The graph of cobalt phosphate thin-films deposited mass with respect to deposition cycles and photographs of electrodes are shown in Figure 1b,c. The deposited mass of cobalt phosphate material was found to be 0.345, 0.464, 0.523, 0.595, and 0.404 mg cm^{-2} for S-CP1, S-CP2, S-CP3, S-CP4, and S-CP5 samples, respectively. In addition, it is observed that the thickness decreases after 100 SILAR deposition cycles, which may be due to the outer layer peeling off from the film because of the poor adhesiveness of the overgrown material.

3.2. Structural and Morphological Study. X-ray diffraction was carried out to study the structural properties of cobalt phosphate electrodes. Figure 2a shows the X-ray diffraction pattern of the S-CP4 sample. In the pattern, no diffraction peak is observed, and instead, only SS substrate peaks are observed, confirming the amorphous nature of the prepared sample. The SS peak is identified with the “#” symbol. Amorphous materials offer unique features compared to crystalline materials, such as the disordered structure helping to improve structural flexibility with high specific

surface area, which can lead to enhanced specific capacity, rate performance, and good cycle life with the chemical stability of the material.^{50–52}

The molecular bonding present in the S-CP4 sample was investigated using FT-IR analysis. The FT-IR spectrum for the S-CP4 sample in the region of $4000\text{--}400\text{ cm}^{-1}$ is demonstrated in Figure 2b. The peak at 567 cm^{-1} is ascribed to the phosphate group (PO_4^{3-}), and absorption below the 800 cm^{-1} region is related to the Co–O stretching mode.^{37,43} Moreover, two absorption bands (1051 and 1354 cm^{-1}) were attributed to the P=O asymmetric and symmetric stretching vibration of the PO_4^{3-} group, respectively.^{32,53} On the other hand, the wide band at around 3452 cm^{-1} is allocated to the O–H molecular stretching vibration mode, and the vibration band at 1601 cm^{-1} is ascribed to the H–O–H bending mode.^{54,55} The Raman spectrum of the S-CP4 sample is displayed in Figure 2c. A sharp and strong peak at around 971 cm^{-1} (α_3) is observed in the Raman spectrum, denoting a stretching mode of cobalt phosphate. In addition, the shoulder of the observed peak can be assigned to a vibrational symmetric stretching mode of tetrahedron [PO_4], where oxygen coordinated with phosphorus vibrates away.⁴⁴ Along with the sharp peak, four different peaks at 370 (α_1), 571 (α_2), 1620 (α_4), and 3316 cm^{-1} (α_5) are observed and correspond to O–Co–O (bending), H_2PO_4 (bending), H–O–H (bending), and O–H (bending) modes of vibration, respectively.⁴⁶ All bonds present in FT-IR and Raman spectroscopic analyses confirm that the S-CP4 sample contains structural water and hydrous cobalt phosphate formation.

The specific surface area and pore size distribution of the SILAR-synthesized S-CP4 sample were investigated by BET

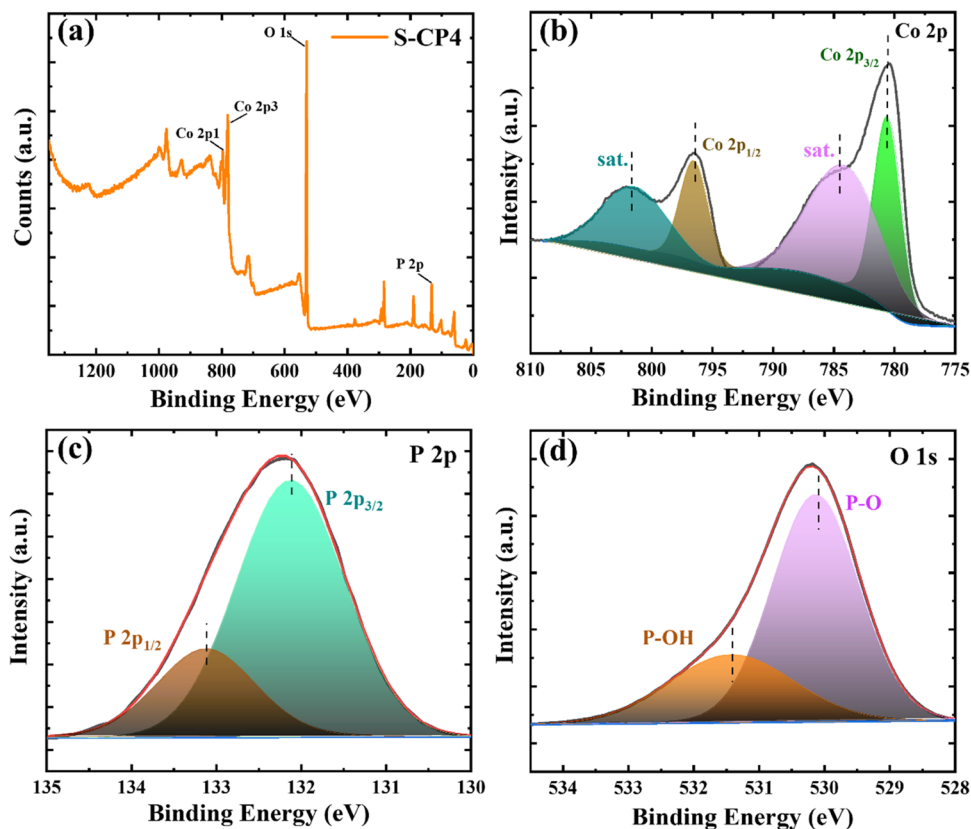


Figure 3. (a) XPS survey spectra of the S-CP4 sample: (b) Co 2p, (c) P 2p, and (d) O 1s spectra.

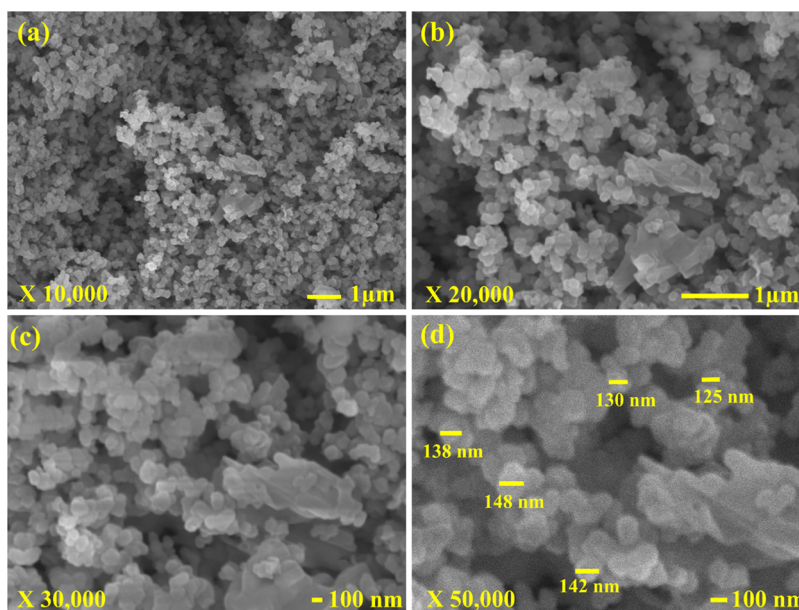


Figure 4. (a–d) FE-SEM images of the S-CP4 sample at different magnifications.

and BJH models, respectively.⁸ The N_2 sorption isotherm of the S-CP4 sample at a relative pressure (P/P_0) range is shown in Figure 2d. In accordance with the International Union of Pure and Applied Chemistry (IUPAC), the graph exhibits an H3-type hysteresis loop and a type IV sorption isotherm, demonstrating $7.47 \text{ m}^2 \text{ g}^{-1}$ specific surface area. Also, in Figure 2d inset, the pore size distribution graph is illustrated, which represents the average pore volume of 22.6 nm. The BET results show that the larger pore size can deliver more charge

transport pathways and active sites for quick transportation of ions in the electrochemical capacitive performance.

Moreover, an XPS study was conducted to understand the chemical environment and electronic valance states of elements in the S-CP4 sample (Figure 3). The XPS survey scan of the S-CP4 sample shown in Figure 3a demonstrates that the sample contains cobalt (Co), phosphorus (P), and oxygen (O) elements. The spectrum of Co 2p is ascribed to Co 2p_{3/2} and Co 2p_{1/2} at 796.4 eV and 780.4, respectively, with

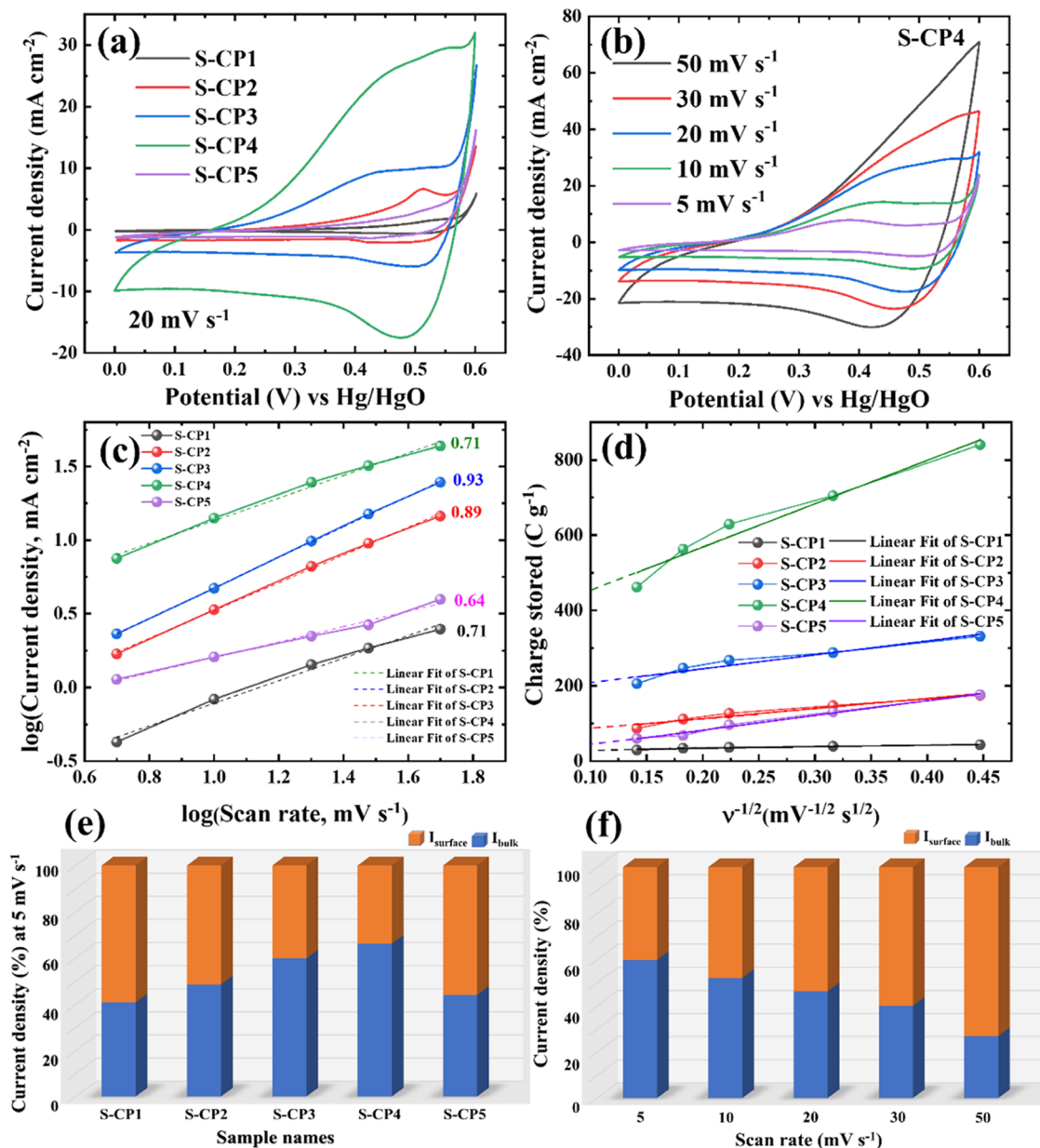


Figure 5. (a) Comparative CV curves of S-CP series at a 20 mV s^{-1} scan rate, (b) CV curves of the S-CP4 electrode at various scan rates from 5 to 50 mV s^{-1} , (c) plot of the log of current density vs log of scan rate for S-CP1 to S-CP5 electrodes to calculate the “ b ” value in the CV curves for 5– 50 mV s^{-1} , (d) plot of the total charge against the reciprocal of the square root of potential scan rate for S-CP series electrodes, (e) proportion of I_{surface} and I_{bulk} contributions for the S-CP series electrodes measured at a 5 mV s^{-1} scan rate, and (f) I_{surface} and I_{bulk} contributions for the S-CP4 series electrode at different scan rates.

two oscillating satellite peaks (784.1 and 801.6 eV). According to the spectrum, cobalt having a divalent state (Co^{2+}) is shown by the energy separation between prominent peaks ($\sim 16 \text{ eV}$) (Figure 3b).³⁵ Furthermore, the presence of P is confirmed by the XPS spectrum of P 2p (Figure 3c), and it is deconvoluted into two core-level characteristic peaks corresponding to P $2p_{3/2}$ (132.12 eV) and P $2p_{1/2}$ (133.13 eV), which correspond to pentavalent phosphate in the PO_4^{3-} group.³⁴ Also, the O 1s signal is deconvoluted into two peaks at 530.1 and 531.4 eV binding energies, which is ascribed to the metal–oxygen (P–O/M–O) bond and hydrated oxide species in cobalt phosphate, respectively (Figure 3d).^{34,35,41} Thus, the chemical composition confirmed that hydrous cobalt phosphate is successfully prepared in thin-film form.

The morphological study of cobalt phosphate thin film (S-CP4 sample) was carried out using a field emission scanning electron microscope at different magnifications (10, 20, 30, and 50 kX) and is exhibited in Figure 4a–d. The FE-SEM images at lower magnifications (Figure 4a–c) show that the binder-free SILAR-synthesized cobalt phosphate material comprises randomly distributed fine spherical particles all over the surface with few large overgrown agglomerated particles. Moreover, the FE-SEM image at a high (50 kX) magnification demonstrated in Figure 4d shows spherical particles accumulated with distinct particle sizes having an average diameter of 100–150 nm. Such fine spherical particles develop multiple large cavities and voids that offer minimum diffusion length for easy electrolytic ion access. Thus, it provides a maximum

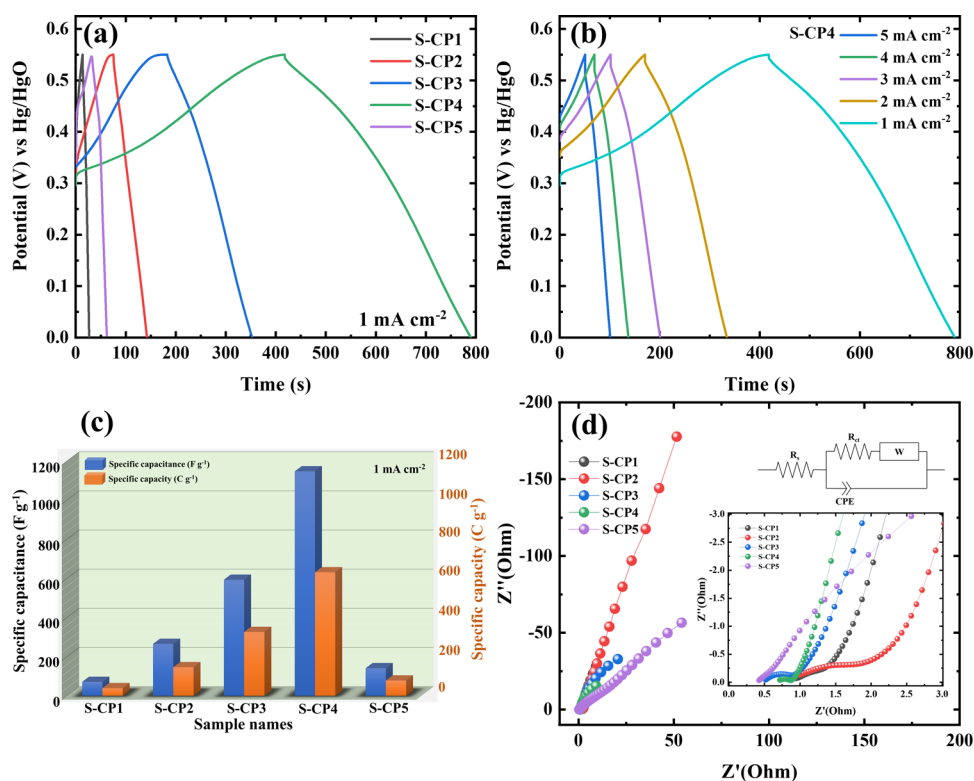
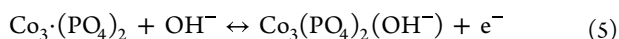


Figure 6. (a) Comparative GCD curves of S-CP series at a 1 mA cm^{-2} current density; (b) GCD curves of best-performing S-CP4 electrode at various current densities from 1 to 5 mA cm^{-2} ; (c) specific capacitance and capacity of S-CP1, S-CP2, S-CP3, S-CP4, and S-CP5 electrodes at a 1 mA cm^{-2} current density; and (d) Nyquist plot of S-CP1, S-CP2, S-CP3, S-CP4, and S-CP5 electrodes at OCP.

electroactive surface area, which may help achieve higher specific capacitance since the capacitance is proportional to an electroactive surface area.⁸ Furthermore, EDS was investigated in FE-SEM mode to examine the elemental composition of the prepared material. The FE-SEM-EDS spectrum of the S-CP4 sample is illustrated in Figure S1a,b, where the atomic percentages of 29.24, 27.49, and 43.27% are observed for cobalt (Co), phosphorous (P), and oxygen (O), respectively. The existence of elements in the EDS spectra confirms the hydrous cobalt phosphate thin-film formation.

3.3. Electrochemical Evaluation of Cobalt Phosphate Electrodes. The supercapacitive behavior of the SILAR-synthesized S-CP series (S-CP1, S-CP2, S-CP3, S-CP4, and S-CP5) electrodes was studied in a 1 M KOH electrolyte using a half test cell. The electrochemical redox behavior of S-CP series electrodes was probed using CV measurements in a potential range of 0–0.6 V vs Hg/HgO. Figure 5a illustrates CV curves at a fixed scan rate of 20 mV s^{-1} of S-CP series electrodes. All samples show quasi-rectangular shapes along with a redox couple due to the electrochemical reaction, confirming the pseudocapacitive behavior of thin-film electrodes. The feasible charge storage is based on a reversible electrochemical reaction of cobalt phosphate $[\text{Co}_3(\text{PO}_4)_2 \cdot n\text{H}_2\text{O}]$ in an aqueous KOH electrolyte, according to eq 5.



Based on the above possible reversible redox reaction, OH^- ions are intercalated and deintercalated into the electrode from the electrolyte in the course of charging–discharging.⁵⁶ The CV analysis illustrates that the current under the curve increases with SILAR cycles and is maximum for the S-CP4 sample. Furthermore, the CV of the S-CP4 electrode at distinct

$5\text{--}50 \text{ mV s}^{-1}$ scan rates indicates that the current area increases with the scan rates (Figure 5b), and other series samples exhibit similar CV trends with respect to scan rate (see Figure S2a–d).

Moreover, to investigate the storage mechanism of the prepared thin films, the diffusion control (battery type) and surface capacitive control processes of electrodes are probed by using power law (eq 6),

$$I_p = av^b \quad (6)$$

where I_p represents the current density (peak) of an electrode, v represents the scan rate, and a and b are denoted for variable factors. The b values are derived from the slope (linear fit) of the log of scan rate versus the log of the current density graph, as illustrated in Figure 5c. The derived b values for samples S-CP1, S-CP2, S-CP3, S-CP4, and S-CP5 are found to be 0.71, 0.89, 0.93, 0.71, and 0.64, respectively. In general, the b value denotes different storage processes as the electrochemical process is diffusive-controlled when b is 0.5, and it is a capacitive type for 1. The b values of S-CP series electrodes are more significant and lie between 0.5 and 1, confirming the diffusion and surface capacitive mechanisms involved in the charge storage process.^{57,58}

Moreover, to further understand the quantitative analysis of the charge storage mechanism of the S-CP series electrodes, surface capacitive charge and diffusion-controlled charge ($Q_s - I_{\text{surface}}$ and $Q_d - I_{\text{bulk}}$) in overall volumetric charge response (Q_t) are calculated using the modified power law as given in eq 7. In the modified power law, Q_s and Q_d govern the overall volumetric charge (Q_t) according to the following equation⁵⁹

$$Q_t = Q_s + Q_d \quad (7)$$

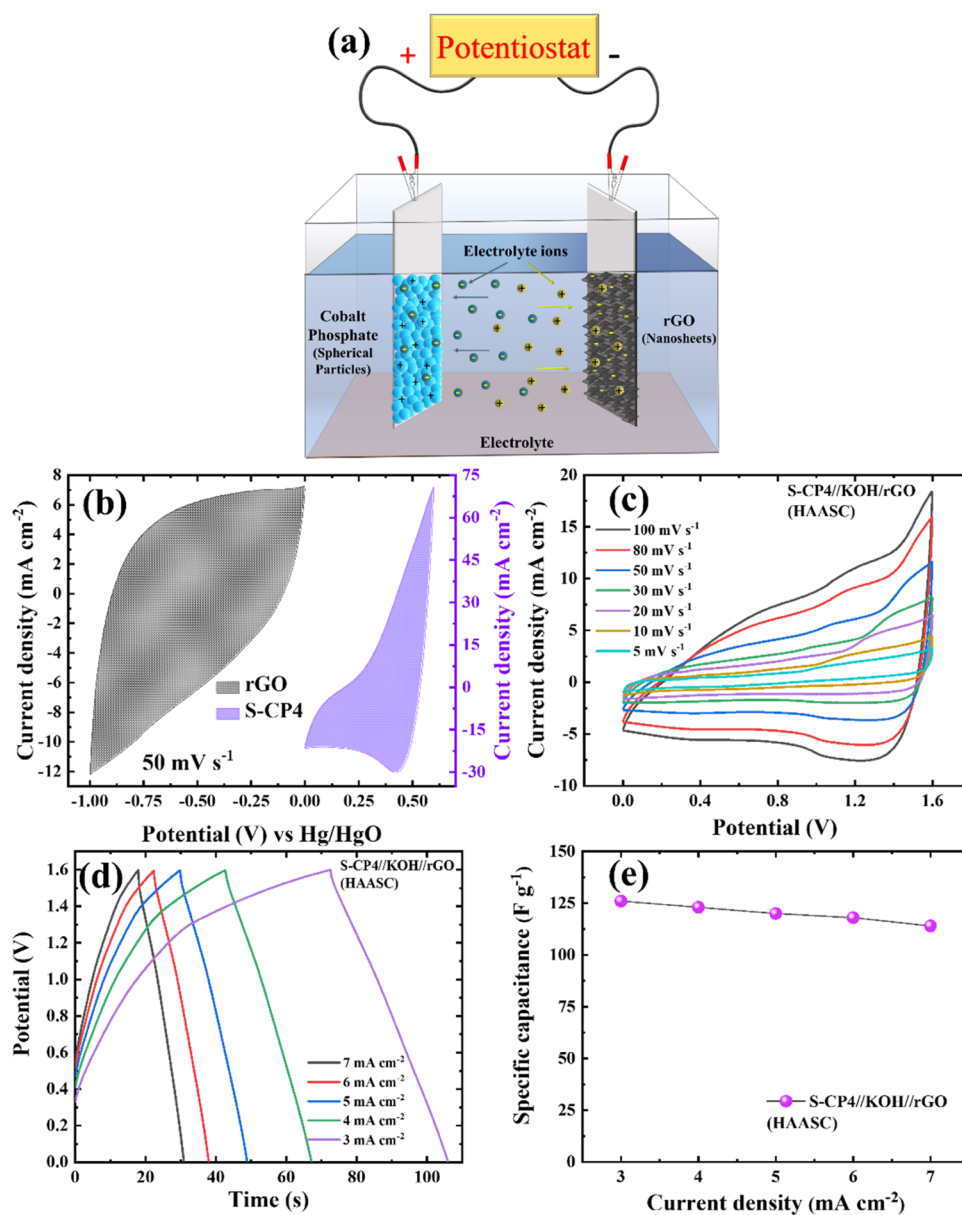


Figure 7. (a) Schematic of the aqueous device, (b) CV curves of S-CP4 and rGO electrodes at a scan rate of 50 mV s^{-1} , (c) CV curves of the HAASC device at different scan rates from 5 to 100 mV s^{-1} , (d) GCD curves of the HAASC device at different current densities from 3 to 7 mA cm^{-2} , and (e) specific capacitance of the HAASC device at different current densities from 3 to 7 mA cm^{-2} .

In total stored charge (Q_t), Q_s is mainly obtained from charge stored at the material's surface and is related to the electric double-layer capacitance. While Q_d arises explicitly from the reduction–oxidation reactions that take place in the bulk of the material and is produced from a slower diffusion process, a semi-infinite linear propagation is supposed for the diffusion process. Moreover, Q_s is linearly dependent on the scan rate, while Q_d depends on the root of the scan rate. Therefore, the approximate Q_s and Q_d values are estimated by the total voltammetric charge Q_t (charge stored, C g^{-1}) versus the reciprocal square root of the scan rate plot, and eq 8 measures the charge of both Q_s and Q_d in total charge contribution (see Figure 5d),⁶⁰

$$Q_t = Q_s + kv^{-1/2} \quad (8)$$

where Q_s can be evaluated from the intercept of plot Q_t vs $v^{-1/2}$ as shown in Figure 5d, and k is a constant. Accordingly,

the stored charge proportion of I_{surface} and I_{bulk} contributions for the S-CP series electrodes at a scan rate of 5 mV s^{-1} is shown in Figure 5e. Orange and blue areas represent the capacitive and diffusive charge storage contribution in total current, respectively. The coexistence of orange and blue regions indicates that the electrodes show combined capacitive and battery-type behaviors. Furthermore, it is found that the charge contribution from the bulk process (I_{bulk}) is dominated by an increase in the thickness of the sample, which suggests that the deposited mass of the material influences the charge storage mechanism. The charge contribution diagram for the S-CP-4 series electrode measured at scan rates of 5– 50 mV s^{-1} is provided in Figure 5f, and graphs of other S-CP series electrodes are given in Figure S3, which illustrate that the capacitive contribution increases with the scan rate. This suggests that the capacitive contribution is rampant at a high

scan rate and contributes more to the total capacitance of the prepared electrodes.

The S-CP series electrodes' GCD curves at a current density of 1 mA cm^{-2} are demonstrated in Figure 6a. The GCD curves exhibit an almost symmetrical triangular shape, which suggests the extrinsic pseudocapacitive behavior of the material. The GCD curve of the S-CP4 electrode indicates the longest charging–discharging time compared to other electrodes, which specifies that the S-CP4 electrode exhibits the maximum charge storage capability. Figure 6b shows the charge–discharge curves of the S-CP4 electrode at various current densities ($1\text{--}5 \text{ mA cm}^{-2}$). The curves of S-CP1, S-CP2, S-CP3, and S-CP5 electrodes are illustrated in Figure S4 a–d. The measured specific capacitances (capacities) are shown in Figure 6c; the S-CP4 electrode demonstrates maximum specific capacitance (capacity) of 1147 F g^{-1} (631 C g^{-1}) at a current density of 1 mA cm^{-2} compared to S-CP1 ($71 \text{ F g}^{-1}/39 \text{ C g}^{-1}$), S-CP2 ($265 \text{ F g}^{-1}/146 \text{ C g}^{-1}$), S-CP3 ($593 \text{ F g}^{-1}/326 \text{ C g}^{-1}$), and S-CP5 ($141 \text{ F g}^{-1}/78 \text{ C g}^{-1}$) electrodes. The measured specific capacitances (capacities) of S-CP series electrodes at various current densities are illustrated in Figure S5 (see ESI). The obtained specific capacitance of the S-CP4 electrode is comparable with previously reported ones. The detailed comparison of cobalt phosphate-based electrodes (S-CP4) in terms of preparation method, morphology, specific capacitance, and capacitive retention with available literature data is tabulated in Table S2 (see ESI). Among them, nanowire-like $\text{Co}_3(\text{PO}_4)_2$ was prepared by Xi et al. using a solvothermal process that achieved a specific capacitance of 1174 F g^{-1} at the current density of 2 A g^{-1} .³¹ Shao et al. prepared $\text{Co}_3(\text{PO}_4)_2 \cdot \text{H}_2\text{O}$ nanoflakes via a hydrothermal route and reported a maximum 1578.7 F g^{-1} specific capacitance at a current density of 5 A g^{-1} .³³ Sankar et al. obtained 1174 F g^{-1} specific capacitance for the hydrothermally synthesized $\text{Co}_3(\text{PO}_4)_2$ at a 0.25 A g^{-1} current density.³⁵ Tian et al. synthesized flowerlike $\text{Co}_{11}(\text{HPO}_3)_8(\text{OH})_6$ by the solvothermal route and obtained a specific capacitance of 1532.2 F g^{-1} at the current density of 1 A g^{-1} .⁴¹ According to the literature survey, only a few articles reported higher specific capacitance than that of the present work; the reason for the maximum specific capacitance achieved in some reported work is the usage of nickel foam as the conducting backbone.^{31,33,35,41} Nickel foam as the conducting support adds self-charge storage capacity to the electrode material through conversion of a surface atom to NiO and $\text{Ni}(\text{OH})_2$ during electrochemical testing.⁶¹ Nevertheless, the SS substrate used in the present work does not contribute to the electrochemical reaction to increase the capacitance; thus, the capacitance obtained in this work is solely based on the hydrous, amorphous cobalt phosphate material.

The EIS analysis is further studied to evaluate impedance involved in electrochemical processes of the S-CP series in the 10 mHz to 1 MHz frequency range at OCP, and the graph of the Nyquist plot is shown in Figure 6d. Magnified Nyquist plot and fitted Randles circuit using ZView-impedance software are shown as an inset of Figure 6d. The fitting parameters of the equivalent circuit consist of parameters of solution resistance (R_s), charge transfer resistance (R_{ct}), Warburg impedance (R_w), and constant phase element (CPE), which are given in Table S3. R_s is the intercept on the horizontal axis containing electrolyte resistance, contact resistance among the current collector and the active substances, and internal electrode resistance. The quasi-semicircle signifies the R_{ct} determined by

the electrostatic interactions and faradic redox process, which proceeds at the electrode and electrolyte interface. The slope of the straight line specifies R_w , signifying the charge diffusion kinetics process within the active material.^{62–65} The S-CP4 electrode demonstrates minimum R_s , R_{ct} , and R_w (0.7, 0.174, and 0.445Ω , respectively) values in comparison with S-CP1, S-CP2, S-CP3, and S-CP5 electrodes (Table S3, see ESI). Thus, the EIS result demonstrates that the S-CP4 electrode illustrates good capacitive behavior due to the quick charge transport rate (low R_s and R_{ct}) owing to the preparation of binder-free hydrous cobalt phosphate material over the SS substrate. Moreover, the excellent charge storage ability and low impedance demonstrate the candidacy of the binder-free S-CP4 electrode as a positive electrode (cathode) in hybrid supercapacitor devices.

3.4. Hybrid Aqueous Supercapacitor (HAASC) Device Performance. The practical feasibility of hydrous and amorphous cobalt phosphate electrode is investigated by fabricating a HAASC device with S-CP4 as a cathode and rGO as an anode (S-CP4//KOH//rGO) in an aqueous 1 M KOH electrolyte, and the actual working is illustrated schematically in Figure 7a. In the present study, the S-CP4 thin-film electrode was operated within a positive $0\text{--}0.6 \text{ V}$ vs Hg/HgO potential range, whereas rGO displays superior electrochemical performance in a negative 0 to -1.0 V vs Hg/HgO operating potential window in the 1 M KOH electrolyte as demonstrated in Figure 7b. The preparation of rGO electrode is given in Note S1 and the morphological, structural, and electrochemical analyses of the rGO electrode are given in Figures S6 and S7. The distinct operating potential windows of S-CP4 and rGO electrodes are suitable for assembling the HAASC device to achieve a wider voltage range for hybrid devices. Also, to obtain the superlative performance of a hybrid supercapacitor device, the charge balance between the S-CP4 electrode and the rGO electrode was achieved by mass-balancing using the charge balance eq S3 (Note S3, see ESI).

The supercapacitive performance of the HAASC device was first tested using CV and GCD analysis at various potentials to fix an optimum working potential window of the HAASC device at a scan rate of 50 mV s^{-1} and a current density of 5 mA cm^{-2} in a 1 M KOH electrolyte (Figure S8a,b, see ESI). Hence, prominent redox contributions were seen in a potential window of $1.2\text{--}1.6 \text{ V}$, while potential window extended up to 1.7 V reflected a sudden surge in current after 1.6 V due to the aqueous electrolyte splitting.⁶⁶ Therefore, a working voltage of 1.6 V is preferred for further electrochemical measurements. Figure 7c displays CV curves of the HAASC device at various scan rates of $5\text{--}100 \text{ mV s}^{-1}$. The curves illustrate the ideal capacitive nature and are maintained even at a higher 100 mV s^{-1} scan rate, revealing outstanding electrochemical reversibility of the aqueous device. Furthermore, the GCD profiles of the HAASC device were probed at various current densities of $3\text{--}7 \text{ mA cm}^{-2}$ and are plotted in Figure 7d. GCD curves are not perfectly triangular; however, the discharge curve does not show any initial potential drop (IR drop), signifying a negligible energy loss of the aqueous device. The measured specific capacitances of the HAASC device from GCD curves versus current densities are demonstrated in Figure 7e. The HAASC device demonstrates the highest 126 F g^{-1} specific capacitance at a current density of 3 mA cm^{-2} , and it reduces up to 113 F g^{-1} (7 mA cm^{-2}) and demonstrates an excellent rate capability of 89.6% of the HAASC device even at maximum current density. The SE and SP are measured using

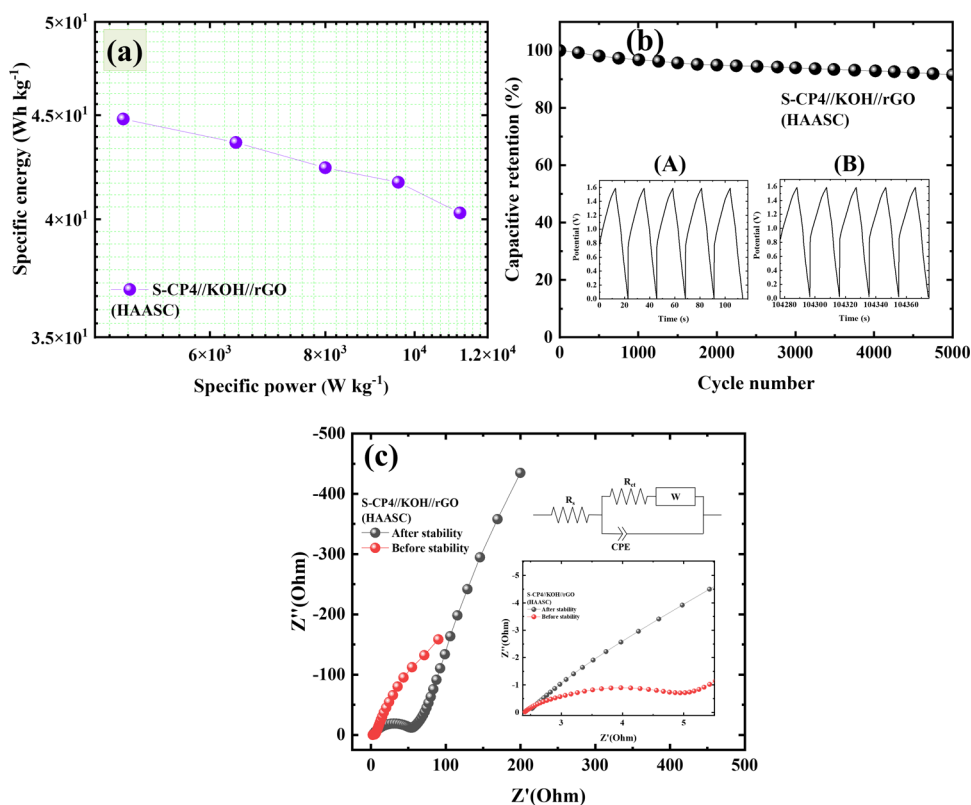


Figure 8. (a) Ragone plot of the HAASC device, (b) capacitive retention vs cycle number plot of the HAASC device, and (c) before and after stability Nyquist plots of the HAASC device.

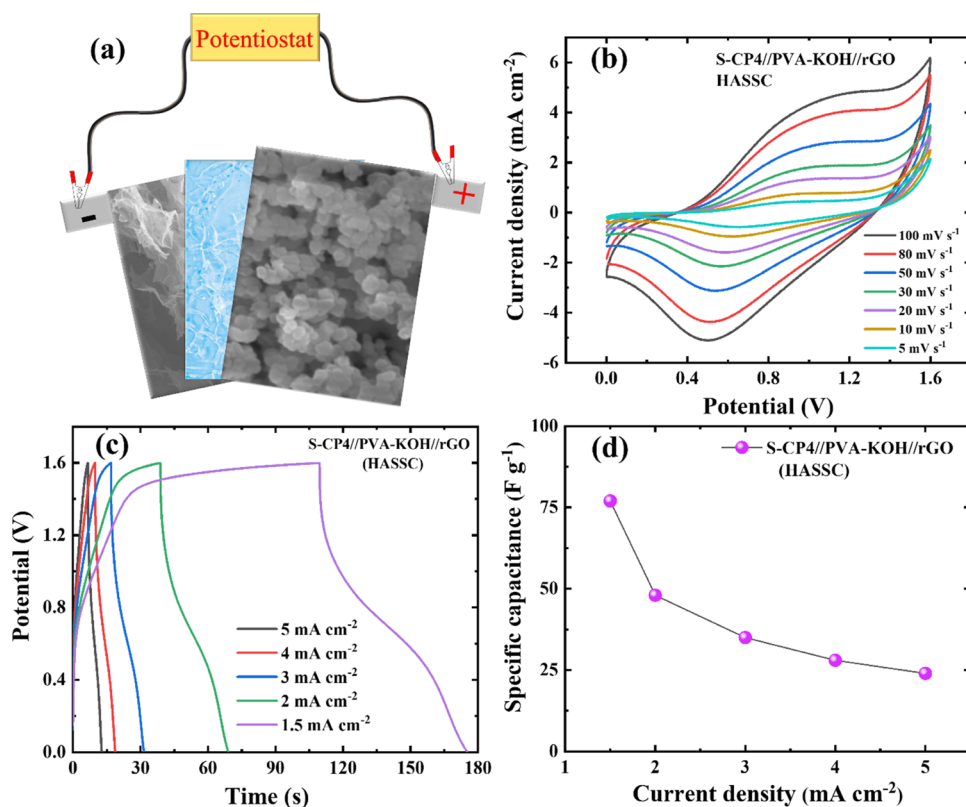


Figure 9. (a) Schematic of the solid-state device, (b) CV curves of HASSC device at different scan rates from 5 to 100 mV s^{-1} , (c) GCD curves of the HASSC device at different current densities from 1.5 to 5 mA cm^{-2} , and (d) specific capacitance of the HASSC device at different current densities from 1.5 to 5 mA cm^{-2} .

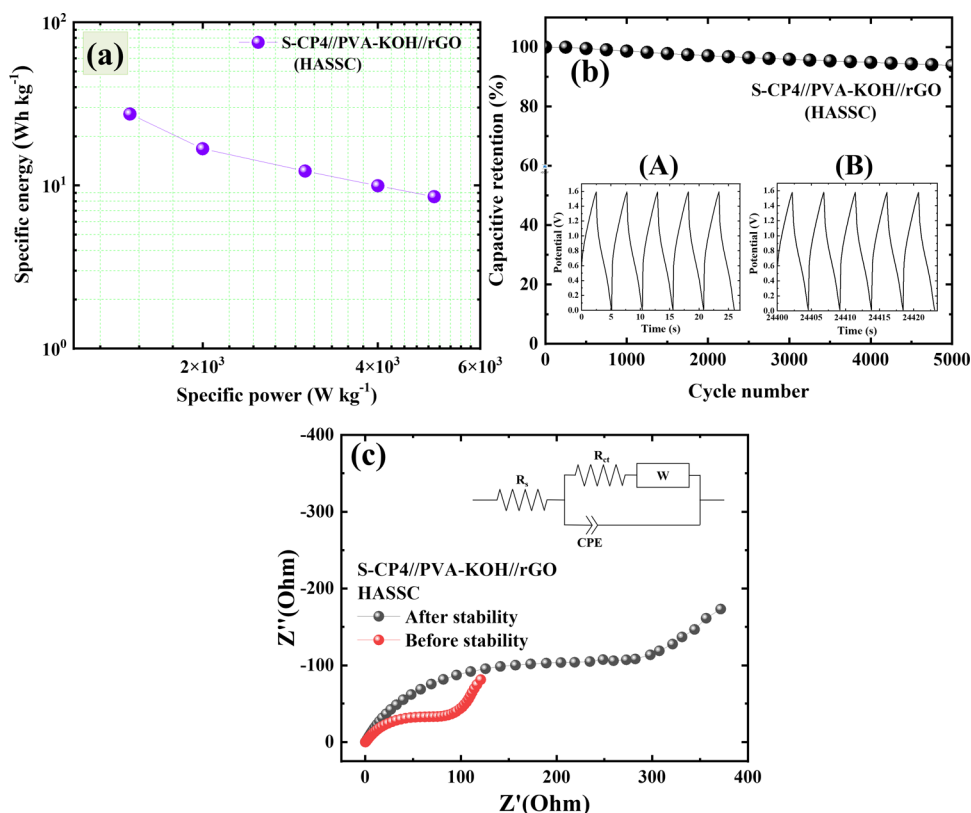


Figure 10. (a) Ragone plot of the HASSC device, (b) capacitive retention vs cycle number plot of the HASSC device, and (c) before and after stability Nyquist plots of the HASSC device.

equations S4 and S5 (see ESI) and plotted in a Ragone plot (Figure 8a). The HAASC device shows a high SE of 44.8 Wh kg⁻¹ at a 4.8 kW kg⁻¹ SP and maintains a 40.2 Wh kg⁻¹ of SE at a maximum 11.2 kW kg⁻¹ SP.

The cyclic durability of the HAASC device is investigated by the GCD cycles at a current density of 7 mA cm⁻² over 5000 GCD cycles, and the capacitive retention of the HAASC device is demonstrated in Figure 8b. The HAASC device revealed capacitive retention up to 92% after 5000 cycles; the initial (A) and final (B) five cycles of stability demonstrate symmetric potential–time response in the inset of Figure 8b. The GCD curves retain maximum symmetry, which can be attributed to the charge equilibrium between the cobalt phosphate (cathode) electrode and the rGO (anode) electrode. The amorphous, hydrous cobalt phosphate electrode provides a minimum diffusion length for electrolyte ions. In contrast, the rGO electrode collects charge through electrochemical double-layer capacitance and delivers quick electron transfer for reversible and fast faradic reactions. The before and after durability test Nyquist plots of HAASC are displayed in Figure 8c, and both spectra indicate angles higher than 45°, demonstrating the capacitive behavior of the HAASC device. In an equivalent circuit, before stability, the R_s , R_{ct} , and R_w are found to be 2.17, 3.50, and 0.038 Ω , respectively. After stability, all values are increased slightly to 2.44, 56, and 0.14 Ω , respectively, ascribed to the enhancement of the minimum electrochemically active surface oxidation layer (Table S5, see ESI). The excellent supercapacitive HAASC device performance is accredited to the use of greatly conductive aqueous electrolyte and the reciprocity effect among two asymmetric electrodes.⁶⁷

3.5. Hybrid All-Solid-State Supercapacitor (HASSC) Device Performance.

The HASSC device was fabricated using S-CP4 and rGO electrodes, with a PVA-KOH gel electrolyte as a separator to avoid leakage problems and sustain the flexible nature of the device. The schematic of the HASSC device is illustrated in Figure 9a and photographs of device fabrication are shown in Figure S9a,b. To keep both electrodes reversible, the potential window varied from 1.2 to 1.7 V using CV and GCD curves at a 50 mV s⁻¹ constant scan rate and 5 mA cm⁻² current density (Figure S10a,b, see ESI). Similar to the HAASC, the HASSC device also maintained the CV and GCD curve shape up to 1.6 V with good reversibility in electrochemical reactions. However, while expanding the potential window to 1.7 V, electrochemical reactions resulted in an irreversible form. Therefore, the potential window of 0–1.6 V is selected for further HASSC device study. Figure 9b demonstrates the HASSC device CV curves at 5–100 mV s⁻¹ scan rates. Also, curves upheld their nature and reversibility at low and high scan rates, as demonstrated in Figure 9b. Furthermore, the GCD curves at distinct 1.5–5 mA cm⁻² current densities are illustrated in Figure 9c; the curves show a nontriangular shape that can be due to charge storage from the faradic reactions. During the charging–discharging process, a slight IR drop is observed, representing resistance due to the PVA-KOH gel electrolyte.^{68,69} The specific capacitances of the HASSC device are evaluated from GCD measurements at distinct current densities and plotted in Figure 9d, and a maximum specific capacitance of 77 F g⁻¹ is achieved at a lower current density of 1.5 mA cm⁻² and 24 F g⁻¹ specific capacitance at a high 5 mA cm⁻² current density. Figure 10a demonstrates the HASSC device Ragone plot, which estimates the device's practical potential. As displayed in the Ragone

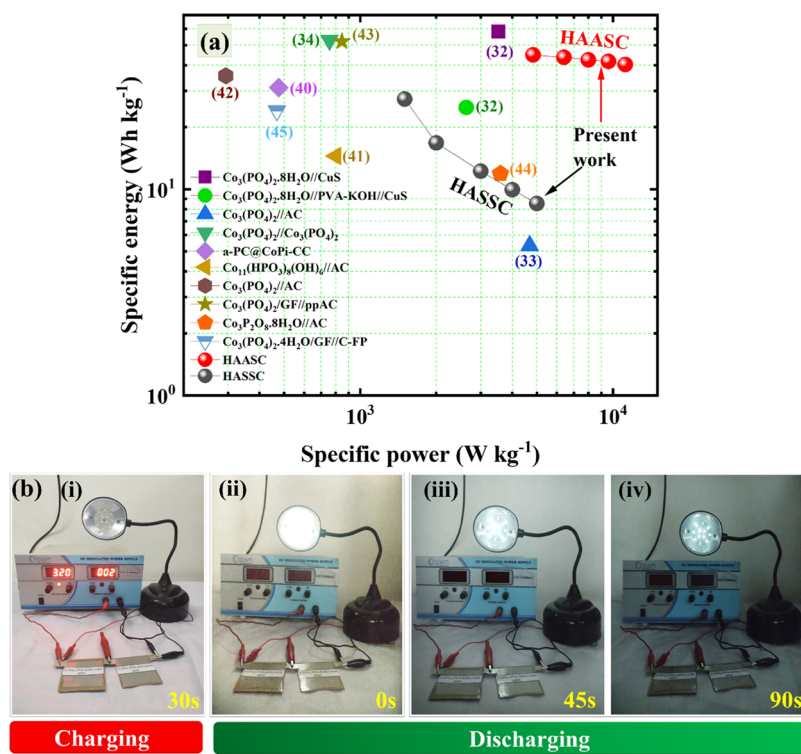


Figure 11. (a) Comparative Ragone plot of HAASC and HASSC devices with an available literature survey and (b) demonstration of the HASSC device by a glowing LED table lamp.

plot, the HASSC device reached 27.3 Wh kg^{-1} SE at 1.5 kW kg^{-1} SP and maintained up to 8.5 Wh kg^{-1} SE at 5 kW kg^{-1} SP. In practical application, the long-term cyclic durability of the solid-state device is another critical requirement, and the cyclic stability of the HASSC device is investigated at a current density of 7 mA cm^{-2} (Figure 10b); the first five cycles (A) and last five cycles (B) of the typical GCD profiles are shown as an inset of the figure. The first and last five stability cycles demonstrate symmetrical potential–time response and show 94% capacitive retention after 5000 successful cycles, suggesting superior cycling stability. Excellent stability of the HASSC device is obtained because of the strong coupling between cobalt phosphate and the rGO material. To further evaluate the charge transfer behavior and ion-diffusion properties, EIS measurements were conducted before and after the durability test, and the HASSC device's Nyquist plots are illustrated in Figure 10c. Before charging–discharging stability cycles, the R_s value of 0.26Ω was recorded, which is very close to the after-stability R_s value of 0.16Ω , indicating good ion diffusion, excellent conductivity, and interaction between the substrate and materials. Moreover, after 5000 stability cycles, the R_{ct} value increases from 92 to 314Ω , demonstrating decreased conductivity due to surface oxidation (equivalent fitting parameters are shown in Table S6).

To examine the practical application of the fabricated device, the energy storage capacity and power output ability are important measurements for evaluating the device. In this study, both the fabricated aqueous (HAASC) and solid-state (HASSC) asymmetric supercapacitor devices deliver impressive specific energy (HAASC = 44.8 and HASSC = 27.3 Wh kg^{-1}) and specific power (HAASC = 4.8 and HASSC = 1.5 kW kg^{-1}) against the reported cobalt phosphate-based hybrid devices, as shown in the Ragone plot (Figure 11a). The

detailed comparison of HAASC and HASSC device performance with the available literature data is summarized in Table S7 (see ESI) with specific capacitance, SE, SP, and capacitive retention. In comparison with previous reports, it is observed that the HAASC device exceeds the specific power while maintaining specific energy comparable to that of reported cobalt phosphate-based aqueous hybrid supercapacitor devices. Nevertheless, HASSC displays moderate SE and SP compared to aqueous hybrid supercapacitor devices. Only a few articles^{32,34,43} described a slightly higher SE than the present work; however, the specific power is compromised in achieving the high specific energy. The high specific energy is reported for aqueous asymmetric $(\text{Co}_3(\text{PO}_4)_2 \cdot 8\text{H}_2\text{O})/\text{CuS}$,³² symmetric $(\text{Co}_3(\text{PO}_4)_2)/\text{Co}_3(\text{PO}_4)_2$,³⁴ and composite-based hybrid $(\text{Co}_3(\text{PO}_4)_2)/\text{GF}/\text{ppAC}$ ⁴³ supercapacitor devices, where these devices are fabricated using pseudocapacitive materials as electrodes. On the other hand, in the present work, cobalt phosphate provides facile charge transfer kinetics, which provides excellent specific power without sacrificing much specific energy owing to the mesoporous, amorphous, and hydrous nature of the pseudocapacitive cathode. Furthermore, to evaluate the feasibility of the HASSC device, two series-connected devices were charged for 30 s at 3.2 V and successfully lighted up 12 white light-emitting diode table lamps for 90 s, as displayed in Figure 11b(i–iv). Furthermore, the supercapacitive performance of the solid-state hybrid device (HASSC) at different bending angles was studied, and CV curves at the 0, 45, 90, 135, and 175° bending angles are shown in Figure S11a. It is found that, at distinct bending angles, a very negligible difference among the CV curves is observed. The excellent 89% capacitive retention is maintained even at a bending angle of 175° (Figure S11b), confirming the excellent flexibility of the HASSC device. The photographs of

the flexible HAASC device at various bending angles are shown in Figure S11c(i–v). These results highlighted the applicability of fabricated HAASC devices in flexible, portable electronic devices.

Overall, the some benefits of SILAR-synthesized, binder-free, amorphous, hydrous cobalt phosphate electrode are accountable for the excellent electrochemical capacitive performance, which are as follows. (1) The mesoporous structure and amorphous nature of cobalt phosphate electrodes demonstrate a large surface area. (2) Binder-free synthesis by the facile SILAR method elucidates minimum electrochemical resistance for rapid charge transfer in an electrochemical process. (3) The hydrous nature of the material is beneficial for accessing aqueous electrolytic ions freely. (4) Moreover, the defect-rich amorphous material does not display alterations in strain during the charge–discharge process as in crystalline structures and proposes long-term durability. Thus, amorphous, hydrous, clustered spherical particles and the mesoporous nature of cobalt phosphate display maximum capacitive performance in terms of high SP and SE with exceptional durability.

4. CONCLUSIONS

The present study introduces a SILAR synthesis method to prepare hydrous, amorphous, binder-free, cobalt phosphate thin films. The mesoporous, clustered spherical particles of cobalt phosphate are grown on a flexible SS substrate. The electrochemical testing demonstrates that cobalt phosphate electrodes with optimum mass loading exhibit higher specific capacitance (capacity) of 1147 F g⁻¹ (630.7 C g⁻¹) at a 1 mA cm⁻² current density. Moreover, HAASC and HAASC devices assembled using best-performing Co₃(PO₄)₂·nH₂O as a cathode and rGO as anode display specific capacitances of 126 and 77 F g⁻¹, respectively. Also, both HAASC and HAASC devices deliver high SE (HAASC = 44.8 and HAASC = 27.3 Wh kg⁻¹) and SP (HAASC = 4.8 and HAASC = 1.5 kW kg⁻¹) with outstanding 92 and 94% capacitive retention after 5000 charging–discharging cycles, respectively. Moreover, the two HAASC series devices can power up a table lamp, indicating wide-range applications in short-powered electronic appliances. The results concluded that the hydrous, amorphous cobalt phosphate thin-film electrode with an optimum mass loading is an exceptional candidate as a cathode (positive electrode) for hybrid supercapacitor devices with a high specific power. Moreover, the SILAR process is an excellent synthesis method for the binder-free preparation of hydrous, amorphous, mesoporous cobalt phosphate in thin-film form.

■ ASSOCIATED CONTENT

SI Supporting Information

The Supporting Information is available free of charge at <https://pubs.acs.org/doi/10.1021/acs.energyfuels.2c02202>.

EDS spot FE-SEM image and EDS spectra of S-CP4; CV curves of S-CP1, S-CP2, S-CP3, and S-CP5 electrodes; plots of the log of current density versus the log of scan rate for S-CP1–S-CP5 electrodes; contribution of I_{surface} and I_{bulk} current density at distinct 5–100 mV s⁻¹ scan rates of S-CP1, S-CP2, S-CP3, and S-CP5 electrodes; GCD curves of S-CP1, S-CP2, S-CP3, and S-CP5 electrodes; X-ray diffraction patterns of GO and rGO; FE-SEM image of rGO material; rGO electrode's CV and GCD curves at various scan rates

and current densities; specific capacitance of rGO electrode at different current densities; capacitive retention versus cycle number plot of the rGO electrode; before and after stability Nyquist plot of the rGO electrode; CV curves of the HAASC device at a scan rate of 50 mV s⁻¹ in various potential windows; HAASC device GCD curves at a current density of 5 mA cm⁻² in different potential windows; HAASC device fabrication photographs; CV curves of the HAASC device in different potential windows at 50 mV s⁻¹ scan rate and GCD curves of the HAASC device at 5 mA cm⁻² current density in different potential windows; CV curves of the HAASC device at distinct bending angles; plot of capacitive retention at various bending angles; photographs of the HAASC device at different bending angles; tables of SILAR preparative parameters; EIS fitting parameters; and literature study, synthesis process of GO, rGO; device fabrication process; calculations for specific capacitance, capacity, mass balance, specific energy, and specific power density (PDF)

■ AUTHOR INFORMATION

Corresponding Authors

Dattakumar S. Mhamane – Department of Chemistry, Sangameshwar College (Autonomous), Solapur 413001, India; Email: dkumar.mhamane@gmail.com

Umakant M. Patil – Centre for Interdisciplinary Research (CIR), D. Y. Patil Education Society (Deemed to be University), Kolhapur 416006, India; Email: umakant.physics84@gmail.com

Authors

Vinod V. Patil – Centre for Interdisciplinary Research (CIR), D. Y. Patil Education Society (Deemed to be University), Kolhapur 416006, India; School of Chemical Sciences, Punyashlok Ahilyadevi Holkar Solapur University, Solapur 413255, India

Sachin S. Pujari – Centre for Interdisciplinary Research (CIR), D. Y. Patil Education Society (Deemed to be University), Kolhapur 416006, India

Shraddha B. Bhosale – Centre for Interdisciplinary Research (CIR), D. Y. Patil Education Society (Deemed to be University), Kolhapur 416006, India

Sambhaji S. Kumbhar – Centre for Interdisciplinary Research (CIR), D. Y. Patil Education Society (Deemed to be University), Kolhapur 416006, India

Vinayak G. Parale – Department of Material science and Engineering, Yonsei University, Seoul 03722, South Korea

Jayavant L. Gunjekar – Centre for Interdisciplinary Research (CIR), D. Y. Patil Education Society (Deemed to be University), Kolhapur 416006, India; orcid.org/0000-0003-2642-1295

Hyung-Ho Park – Department of Material science and Engineering, Yonsei University, Seoul 03722, South Korea; orcid.org/0000-0001-5540-5433

Chandrakant D. Lokhande – Centre for Interdisciplinary Research (CIR), D. Y. Patil Education Society (Deemed to be University), Kolhapur 416006, India; orcid.org/0000-0001-6920-6005

Mukund G. Mali – School of Chemical Sciences, Punyashlok Ahilyadevi Holkar Solapur University, Solapur 413255, India

Complete contact information is available at:
<https://pubs.acs.org/10.1021/acs.energyfuels.2c02202>

Notes

The authors declare no competing financial interest.

ACKNOWLEDGMENTS

The authors are thankful to the Department of Science and Technology, Science and Engineering Research Board (DST-SERB), New Delhi, India, for financial support through research projects sanction no. CRG/2019/005730 and CRG/2019/006059. Also, H.-H.P. and V.G.P. announce that this work was supported by the National Research Foundation of Korea (NRF) grant funded by the Korean government (MSIT) (No. 2020R1A5A1019131).

REFERENCES

- (1) Jiang, K.; Weng, Q. Miniaturized energy storage devices based on 2D materials. *ChemSusChem* **2020**, *13*, 1420–1446.
- (2) Ho, M. Y.; Khiew, P. S.; Isa, D.; Tan, T. K.; et al. A Review of Metal Oxide Composite Electrode Materials For Electrochemical Capacitors. *Nano* **2014**, *09*, 1430002–1430026.
- (3) Yu, L.; Chen, G. Z. Supercapatteries as High-Performance Electrochemical Energy Storage Devices. *Electrochem Energy Rev.* **2020**, *3*, 271–285.
- (4) Wang, F.; Wu, X.; Yuan, X.; Liu, Z.; Zhang, Y.; Fu, L.; Zhu, Y.; Zhou, Q.; Wu, Y.; Huang, W. Latest advances in supercapacitors: from new electrode materials to novel device designs. *Chem. Soc. Rev.* **2017**, *46*, 6816–6854.
- (5) Wang, G.; Zhang, L.; Zhang, J. A review of electrode materials for electrochemical supercapacitors. *Chem. Soc. Rev.* **2012**, *41*, 797–828.
- (6) Qi, D.; Liu, Y.; Liu, Zhiyuan.; Zhang, Li.; Chen, X. Design of Architectures and Materials in In-Plane Micro-supercapacitors: Current Status and Future Challenges. *Adv. Mater.* **2017**, *29*, 1602802–1602820.
- (7) Yan, J.; Li, S.; Lan, B.; Wu, Y.; Lee, P. See. Rational Design of Nanostructured Electrode Materials toward Multifunctional Supercapacitors. *Adv. Funct. Mater.* **2020**, *30*, 1902564–1902593.
- (8) Pujari, S. S.; Patil, V. V.; Patil, A. S.; Parale, V. G.; Park, H. H.; Gunjekar, J. L.; Lokhande, C. D.; Patil, U. M. Amorphous, hydrous nickel phosphate thin film electrode prepared by SILAR method as a highly stable cathode for hybrid asymmetric supercapacitor. *Synth. Met.* **2021**, *280*, 116876–116887.
- (9) Mackanic, D. G.; Chang, T. H.; Huang, Z.; Cui, Y.; Bao, Z. Stretchable electrochemical energy storage devices. *Chem. Soc. Rev.* **2020**, *49*, 4466–4495.
- (10) Muzaffar, A.; Ahamed, M. B.; Deshmukh, K.; Thirumalai, J. A review on recent advances in hybrid supercapacitors: Design, fabrication and applications. *Renewable Sustainable Energy Rev.* **2019**, *101*, 123–145.
- (11) Chen, C.; Zhang, N.; He, Y.; Liang, B.; Ma, R.; Liu, X. Controllable Fabrication of Amorphous Co-Ni Pyrophosphates for Tuning Electrochemical Performance in Supercapacitors. *ACS Appl. Mater. Interfaces* **2016**, *8*, 23114–23121.
- (12) Huang, J.; Li, H.; Zhu, Y.; Cheng, Q.; Yanga, X.; Li, C. Sculpturing metal foams toward bifunctional 3D copper oxide nanowire arrays for pseudo-capacitance and enzyme-free hydrogen peroxide detection. *J. Mater. Chem. A* **2015**, *3*, 8734–8741.
- (13) Jadhav, S. B.; Malavekar, D. B.; Bulakhe, R. N.; Patil, U. M.; In, I.; Lokhande, C. D.; Pawaskar, P. N. Dual-Functional Electrodeposited Vertically Grown Ag-La₂O₃ Nanoflakes for Non-Enzymatic Glucose Sensing and Energy Storage Application. *Surf. Interfaces* **2021**, *23*, 101018–101026.
- (14) Chodankar, N. R.; Pham, H. D.; Nanjundan, A. K.; Fernando, J. F. S.; Jayaramulu, K.; Golberg, D.; Han, Y. K.; Dubal, D. P. True Meaning of Pseudocapacitors and Their Performance Metrics: Asymmetric versus Hybrid Supercapacitors. *Small* **2020**, *16*, No. 2002806.
- (15) Patil, U. M.; Nam, M. S.; Sohn, J. S.; Kulkarni, S. B.; Shin, Ryung.; Kang, S.; Lee, S.; Kim, J. H.; Jun, S. C. Controlled electrochemical growth of Co(OH)₂ flakes on 3D multilayered graphene foam for high performance supercapacitors. *J. Mater. Chem. A* **2014**, *2*, 19075–19083.
- (16) Patil, A. S.; Gunjekar, J. L.; Lokhande, C. D.; Patil, U. M.; Sadavar, S. V.; Padalkar, N. S.; Shinde, R. B.; Wagh, M. M.; Bagi, J. S. Nanocrystalline copper-chromium-layered double hydroxide with tunable interlayer anions for electrochemical capacitor application. *Synth. Met.* **2020**, *264*, 116371–116379.
- (17) Yu, X.-Y.; Yu, L.; Wu, H.; Lou, X. Formation of Nickel Sulfide Nanoframes from Metal-Organic Frameworks with Enhanced Pseudocapacitive and Electrocatalytic Properties. *Angew. Chem., Int. Ed.* **2015**, *54*, 5331–5335.
- (18) Mirghni, A. A.; Madito, M.; Oyedotun, K.; Masikhwa, T.; Ndiaye, N.; Ray, S.; Manyala, N. A high energy density asymmetric supercapacitor utilizing a nickel phosphate/graphene foam composite as the cathode and carbonized iron cations adsorbed onto polyaniline as the anode. *RSC Adv.* **2018**, *8*, 11608–11621.
- (19) Kale, S. B.; Lokhande, A. C.; Pujari, R. B.; Lokhande, C. D. Cobalt sulfide thin films for electrocatalytic oxygen evolution reaction and supercapacitor applications. *J. Colloid Interface Sci.* **2018**, *532*, 491–499.
- (20) Shao, Y.; El-Kady, M.; Sun, J.; Li, Y.; Zhang, Q.; Zhu, M.; Wang, H.; Dunn, B.; Kaner, R. Design and Mechanisms of Asymmetric Supercapacitors. *Chem. Rev.* **2018**, *118*, 9233–9280.
- (21) Wang, T.; Chen, H. C.; Yu, F.; Zhao, X. S.; Wang, H. Boosting the cycling stability of transition metal compounds-based supercapacitors. *Energy Storage Mater.* **2019**, *16*, 545–573.
- (22) Ramulu, B.; Nagaraju, G.; Sekhar, S. C.; Hussain, S. K.; Narsimulu, D.; Yu, J. S. Synergistic Effects of Cobalt Molybdate@ Phosphate Core-Shell Architectures with Ultrahigh Capacity for Rechargeable Hybrid Supercapacitors. *ACS Appl. Mater. Interfaces* **2019**, *11*, 41245–41257.
- (23) Gür, T. M. Review of electrical energy storage technologies, materials and systems: challenges and prospects for large-scale grid storage. *Energy Environ. Sci.* **2018**, *11*, 2696–2767.
- (24) Raccichini, R.; Varzi, A.; Passerini, S.; Scrosati, B. The role of graphene for electrochemical energy storage. *Nat. Mater.* **2015**, *14*, 271–279.
- (25) Saraf, M.; Natarajan, K.; Mobin, S. M. Emerging Robust Heterostructure of MoS₂-rGO for High-Performance Supercapacitors. *ACS Appl. Mater. Interfaces* **2018**, *10*, 16588–16595.
- (26) Zhang, L. L.; Zhou, R.; Zhao, X. S. Graphene-based materials as supercapacitor electrodes. *J. Mater. Chem.* **2010**, *20*, S983–S992.
- (27) Li, X.; Xiao, X.; Li, Q.; Wei, J.; Xue, H.; Pang, H. Metal (M = Co, Ni) phosphate-based materials for high-performance supercapacitors. *Inorg. Chem. Front.* **2018**, *5*, 11–28.
- (28) Li, H.; Yu, H.; Zhai, J.; Sun, L.; Yang, H.; Xie, S. Self-assembled 3D cobalt phosphate octahydrate architecture for supercapacitor electrodes. *Mater. Lett.* **2015**, *152*, 25–28.
- (29) Pang, H.; Wang, S.; Shao, Weifang.; Zhao, S.; Yan, B.; Li, X.; Li, S.; Chen, J.; Du, W. Few-layered CoHPO₄·3H₂O ultrathin nanosheets for high performance of electrode materials for supercapacitors. *Nanoscale* **2013**, *5*, 5752–5757.
- (30) Theerthagiri, J.; Thiagarajan, K.; Senthilkumar, B.; Khan, Z.; Senthil, R. A.; Arunachalam, P.; Madhavan, J.; Ashokkumar, M. Synthesis of Hierarchical Cobalt Phosphate Nanoflakes and Their Enhanced Electrochemical Performances for Supercapacitor Applications. *ChemistrySelect* **2017**, *2*, 201–210.
- (31) Xi, Y.; Dong, B.; Dong, Y.; Mao, N.; Ding, L.; Shi, L.; Gao, R.; Liu, W.; Su, G.; Cao, L. Well-Defined, Nanostructured, Amorphous Metal Phosphate as Electrochemical Pseudocapacitor Materials with High Capacitance. *Chem. Mater.* **2016**, *28*, 1355–1362.
- (32) Katkar, P. K.; Marje, S. J.; Pujari, S. S.; Khalate, S. A.; Lokhande, A. C.; Patil, U. M. Enhanced Energy Density of All-Solid-State Asymmetric Supercapacitors Based on Morphologically Tuned

Hydrous Cobalt Phosphate Electrode as Cathode Material. *ACS Sustainable Chem. Eng.* **2019**, *7*, 11205–11218.

(33) Shao, H.; Padmanathan, N.; McNulty, D.; O'Dwyer, C.; Razeeb, K. M. Supercapattery Based on Binder-Free $\text{Co}_3(\text{PO}_4)_2 \cdot 8\text{H}_2\text{O}$ Multilayer Nano/Microflakes on Nickel Foam. *ACS Appl. Mater. Interfaces* **2016**, *8*, 28592–28598.

(34) Mao, H.; Zhang, F.; Liu, X.; Qiu, J.; Li, Bing.; Jin, Z. Synthesis of cobalt phosphate nanoflakes for high-performance flexible symmetric supercapacitors. *J. Mater. Sci. Mater. Electron.* **2018**, *29*, 16721–16729.

(35) Sankar, K. V.; Lee, S. C.; Seo, Y.; Ray, C.; Liu, S.; Kundu, A.; Jun, S. C. Binder-free cobalt phosphate one-dimensional nanograsses as ultrahigh-performance cathode material for hybrid supercapacitor applications. *J. Power Sources* **2018**, *373*, 211–219.

(36) Pang, H.; Liu, Y.; Li, J.; Ma, Y.; Li, G.; Ai, Y.; Chen, J.; Zhang, J.; Zheng, H. Cobalt phosphite microarchitectures assembled by ultralong nanoribbons and their application as effective electrochemical capacitor electrode materials. *Nanoscale* **2013**, *5*, 503–507.

(37) Lee, D. H.; Kang, M.; Paek, S. M.; Jung, H. Study on the Electrochemical Property of Microporous Cobalt Phosphite [$\text{Co}_{11}(\text{HPO}_3)_8(\text{OH})_6$]. *Bull. Korean Chem. Soc.* **2016**, *37*, 192–199.

(38) Wang, S.; Pang, H.; Zhao, S.; Shao, W.; Zhang, N.; Zhang, J.; Chen, J.; Li, S. $\text{NH}_4\text{CoPO}_4 \cdot \text{H}_2\text{O}$ microbundles consisting of one-dimensional layered microrods for high performance supercapacitors. *RSC Adv.* **2014**, *4*, 340–347.

(39) Pang, H.; Yan, Z.; Wang, W.; Chen, J.; Zhang, J.; Zheng, H. Facile fabrication of $\text{NH}_4\text{CoPO}_4 \cdot \text{H}_2\text{O}$ nano/microstructures and their primarily application as electrochemical supercapacitor. *Nanoscale* **2012**, *4*, 5946–5953.

(40) Kim, T.; Prasad, A.; Chhetri, K.; Ojha, G. P.; Kim, H.; Chae, S. H.; Dahal, B.; Lee, B. M.; Mukhiya, T.; Kim, H. Y. Phytic acid controlled in situ synthesis of amorphous cobalt phosphate/carbon composite as anode materials with a high mass loading for symmetrical supercapacitor: amorphization of the electrode to boost the energy density. *Nanoscale Adv.* **2020**, *2*, 4918–4929.

(41) Tian, Y.; Lian, X.; Wu, Y.; Guo, W.; Wang, S. The morphology controlled growth of $\text{Co}_{11}(\text{HPO}_3)_8(\text{OH})_6$ on nickel foams for quasi-solid-state supercapacitor applications. *CrystEngComm.* **2020**, *22*, 5218–5225.

(42) Duraisamy, N.; Arshid, N.; Kandiah, K.; Iqbal, J.; Arunachalam, P.; Dhanaraj, G.; Ramesh, K.; Ramesh, S. Development of asymmetric device using $\text{Co}_3(\text{PO}_4)_2$ as a positive electrode for energy storage application. *J. Mater. Sci. Mater. Electron.* **2019**, *30*, 7435–7446.

(43) Mahmoud, B.; Mirghni, A. A.; Oyedotun, K. O.; Momodu, D.; Fasakin, O.; Manyala, N. Synthesis of cobalt phosphate-graphene foam material via co-precipitation approach for a positive electrode of an asymmetric supercapacitors device. *J. Alloys Compd.* **2020**, *818*, No. 153332.

(44) Li, J. J.; Liu, M. C.; Kong, L.-B.; Shi, M.; Han, W.; Kang, L. Facile synthesis of $\text{Co}_3\text{P}_2\text{O}_8 \cdot 8\text{H}_2\text{O}$ for high-performance electrochemical energy storage. *Mater. Lett.* **2015**, *161*, 404–407.

(45) Mirghni, A. A.; Momodu, D.; Oyedotun, K. O.; Dangbegnon, J. K.; Manyala, N. Electrochemical analysis of $\text{Co}_3(\text{PO}_4)_2 \cdot 4\text{H}_2\text{O}$ /graphene foam composite for enhanced capacity and long cycle life hybrid asymmetric capacitors. *Electrochim. Acta* **2018**, *283*, 374–384.

(46) Pathan, H. M.; Lokhande, C. D. Deposition of metal chalcogenide thin films by successive ionic layer adsorption and reaction (SILAR) method. *Bull. Mater. Sci.* **2004**, *27*, 85–111.

(47) Shaikh, A. A.; Waikar, M. R.; Sonkawade, R. G. Effect of different precursors on electrochemical properties of manganese oxide thin films prepared by SILAR method. *Synth. Met.* **2019**, *247*, 1–9.

(48) Hu, J.; Kang, Z.; Li, F.; Huang, X. Graphene with three-dimensional architecture for high-performance supercapacitor. *Carbon* **2014**, *67*, 221–229.

(49) Latif, I. A.; Merza, S. H. Fabrication of Functionalize Reduce Graphene Oxide and Its Application in Ampicillin Detection. *J. Nanosci. Nanotechnol.* **2016**, *6*, 24–33.

(50) Liu, S.; Lee, S. C.; Patil, U.; Shackery, I.; Kang, S.; Zhang, K.; Park, J. H.; Chung, K. Y.; Jun, S. C. Hierarchical MnCo-layered

double hydroxides@ $\text{Ni}(\text{OH})_2$ core-shell heterostructures as advanced electrodes for supercapacitors. *J. Mater. Chem. A* **2017**, *5*, 1043–1049.

(51) Malavekar, D. B.; Lokhande, V. C.; Mane, V. J.; Ubale, S. B.; Patil, U. M.; Lokhande, C. D. Enhanced energy density of flexible asymmetric solid state supercapacitor device fabricated with amorphous thin film electrode materials. *J. Phys. Chem. Solids* **2020**, *141*, No. 109425.

(52) Li, Q.; Xu, Y.; Zheng, S.; Guo, X.; Xue, H.; Pang, H. Recent Progress in Some Amorphous Materials for Supercapacitors. *small* **2018**, *14*, 1800426–1800444.

(53) Kim, K. H.; Jeong, J. M.; Lee, S. J.; Choi, B. G.; Lee, K. G. Protein-directed assembly of cobalt phosphate hybrid nanoflowers. *J. Colloid Interface Sci.* **2016**, *484*, 44–50.

(54) Wen, H.; Cao, M.; Sun, G.; Xu, W.; Wang, D.; Zhang, X.; Hu, C. Hierarchical three-dimensional cobalt phosphate microarchitectures: Large-scale solvothermal synthesis, characterization, and magnetic and microwave absorption properties. *J. Phys. Chem. C* **2008**, *112*, 15948–15955.

(55) You, X.; Zhu, L. Synthesis, crystal structure and characterization of an organically templated cobalt phosphate supramolecule. *IJC-A* **2010**, *49A*, 1478–1482.

(56) Marje, S. J.; Patil, V. V.; Parale, V. G.; Park, H. H.; Shinde, P. A.; Gunjalkar, J. L.; Lokhande, C. D.; Patil, U. M. Microsheets like nickel cobalt phosphate thin films as cathode for hybrid asymmetric solid-state supercapacitor: Influence of nickel and cobalt ratio variation. *Chem. Eng. J.* **2021**, *429*, No. 132184.

(57) Chodankar, N. R.; Dubal, D. P.; Patil, S. J.; Seeta Rama Raju, G.; Karekar, S. V.; Huh, Y. S.; Han, Y. K. $\text{Ni}_2\text{P}_2\text{O}_7$ micro-sheets supported ultra-thin MnO_2 nanoflakes: A promising positive electrode for stable solid-state hybrid supercapacitor. *Electrochim. Acta* **2019**, *319*, 435–443.

(58) Pujari, S. S.; Kadam, S. A.; Ma, Y. R.; Katkar, P. K.; Marje, S. J.; Khalate, S. A.; Lokhande, A. C.; Patil, U. M. Facile Synthesis of Microstrip-Like Copper Phosphate Hydroxide Thin Films for Supercapacitor Applications. *J. Electron. Mater.* **2020**, *49*, 3890–3901.

(59) Perera, S. D.; Rudolph, M.; Mariano, R. G.; Nijem, N.; Ferraris, J. P.; Chabal, Y. J.; Balkus, K. J., Jr. Manganese oxide nanorod-graphene/vanadium oxide nanowire-graphene binder-free paper electrodes for metal oxide hybrid supercapacitors. *Nano Energy* **2013**, *2*, 966–975.

(60) Perera, S. D.; Ding, X.; Bhargava, A.; Hovden, R.; Nelson, A.; Kourkoutis, L. F.; Robinson, R. D. Enhanced Supercapacitor Performance for Equal Co–Mn Stoichiometry in Colloidal $\text{Co}_{3-x}\text{Mn}_x\text{O}_4$ Nanoparticles, in Additive-Free Electrodes. *Chem. Mater.* **2015**, *27*, 7861–7873.

(61) Xing, W.; Qiao, S.; Wu, X.; Gao, X.; Zhou, J.; Zhuo, S.; Hartono, S. B.; Jurcakova, D. H. Exaggerated capacitance using electrochemically active nickel foam as current collector in electrochemical measurement. *J. Power Sources* **2011**, *196*, 4123–4127.

(62) Zhang, J.; Wang, X.; Ma, J.; Liu, S.; Yi, X. Preparation of cobalt hydroxide nanosheets on carbon nanotubes/carbon paper conductive substrate for supercapacitor application. *Electrochim. Acta* **2013**, *104*, 110–116.

(63) Deshmukh, P. R.; Pusawale, S. N.; Jamadade, V. S.; Patil, U. M.; Lokhande, C. D. Microwave assisted chemical bath deposited polyaniline films for supercapacitor application. *J. Alloys Compd.* **2011**, *509*, 5064–5069.

(64) Hao, Q.; Xia, X.; Lei, W.; Wang, W.; Qiu, J. Facile synthesis of sandwich-like polyaniline/boron-doped graphene nano hybrid for supercapacitors. *Carbon* **2015**, *81*, 552–563.

(65) Johra, F. T.; Jung, W. G. Hydrothermally reduced graphene oxide as a supercapacitor. *Appl. Surf. Sci.* **2015**, *357*, 1911–1914.

(66) Chodankar, N. R.; Dubal, D. P.; Kwon, Y.; Kim, D. H. Direct growth of FeCo_2O_4 nanowire arrays on flexible stainless-steel mesh for high-performance asymmetric supercapacitor. *NPG Asia Mater.* **2017**, *9*, 419.

(67) Shao, Y.; El-Kady, M. F.; Sun, J.; Li, Y.; Zhang, Q.; Zhu, M.; Wang, H.; Dunn, B.; Kaner, R. B. Design and Mechanisms of Asymmetric Supercapacitors. *Chem. Rev.* **2018**, *118*, 9233–9280.

(68) Chatterjee, M.; Saha, S.; Das, S.; Pradhan, S. K. Advanced asymmetric supercapacitor with NiCo₂O₄ nanoparticles and nanowires electrodes: A comparative morphological hierarchy. *J. Alloys Compd.* **2020**, *821*, 153503–153514.

(69) Dubal, D. P.; Chodankar, N. R.; Gund, G. S.; Holze, R.; Lokhande, C. D.; Romero, P. G. Asymmetric Supercapacitors based on Hybrid CuO@Reduced Graphene Oxide@Sponge versus Reduced Graphene Oxide@Sponge Electrodes. *Energy Technol.* **2015**, *3*, 168–176.



INTELLECTUAL
PROPERTY INDIA

PATENTS | DESIGNS | TRADE MARKS
GEOGRAPHICAL INDICATIONS



सत्यमेव जयते

क्रमांक : 022124199
SL No :



भारत सरकार
GOVERNMENT OF INDIA
पेटेंट कार्यालय
THE PATENT OFFICE
पेटेंट प्रमाणपत्र
PATENT CERTIFICATE
(Rule 74 of The Patents Rules)

पेटेंट सं. / Patent No. : 430650
आवेदन सं. / Application No. : 202021041651
फाइल करने की तारीख / Date of Filing : 25/09/2020
पेटेंटी / Patentee : DR. VISHWANATH VITHAL BHOSALE
आविष्कारक (जहां लागू हो) / Inventor(s) : 1.DR. UMAKANT MAHADEV PATIL 2.MR. SACHIN
SHIVAJI PUJARI 3.PROF. CHANDRAKANT DNYANDEV
LOKHANDE 4.DR. VISHWANATH VITHAL BHOSALE

प्रमाणित किया जाता है कि पेटेंटी को, उपरोक्त आवेदन में यथाप्रकटित "AMORPHOUS NICKEL PHOSPHATE THIN FILM ELECTRODE BY CHEMICAL METHOD FOR SUPERCAPACITOR APPLICATION" नामक आविष्कार के लिए, पेटेंट अधिनियम, 1970 के उपबंधों के अनुसार आज तारीख सितम्बर 2020 के पच्चीसवें दिन से बीस वर्ष की अवधि के लिए पेटेंट अनुदत्त किया गया है।

It is hereby certified that a patent has been granted to the patentee for an invention entitled "AMORPHOUS NICKEL PHOSPHATE THIN FILM ELECTRODE BY CHEMICAL METHOD FOR SUPERCAPACITOR APPLICATION" as disclosed in the above mentioned application for the term of 20 years from the 25th day of September 2020 in accordance with the provisions of the Patents Act,1970.



अनुदान की तारीख : 28/04/2023
Date of Grant :

पेटेंट नियंत्रक
Controller of Patent

टिप्पणी - इस पेटेंट के नवीकरण के लिए फीस, यदि इसे बनाए रखा जाना है, सितम्बर 2022 के पच्चीसवें दिन को और उसके पश्चात प्रत्येक वर्ष में उसी दिन देय होगी।

Note - The fees for renewal of this patent, if it is to be maintained will fall / has fallen due on 25th day of September 2022 and on the same day in every year thereafter.



**D. Y. PATIL EDUCATION SOCIETY
DEEMED TO BE UNIVERSITY, KOLHAPUR**

(Deemed to be University Declared u/s 3 of the UGC Act 1956 vide Notification No. F.9-26/2004-U.3 dt. 01-09-2005 of the GOI)

Accredited by NAAC with 'A' Grade

869, 'E', D. Y. Patil Vidyanagar, Kolhapur-416 006

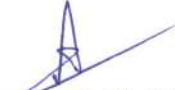
Phone No. : (0231) 2601235-36, Fax: (0231) 2601595

Web: www.dypatilunikop.org, E-mail: info@dypatilkolhapur.org

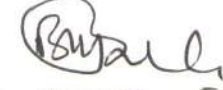
CERTIFICATE

This is to certify that

Mr. S. S. Pujari has presented his
research work in the University Anveshan 2018
held on December 5, 2018.


Dr. Arvind Gulbake
Convener


Prof. C.D.Lokhande
Chairman


Dr. V.V.Bhosale
Registrar



Rayat Shikshan Sanstha's

Estd.: June 1992

PROF. DR. N. D. PATIL MAHAVIDYALAYA, MALKAPUR-PERID

Tal: Shahuwadi, Dist: Kolhapur - 415101

Affiliated to Shivaji University, Kolhapur

NAAC Reaccredited - 'B' Grade (CGPA - 2.82)

Certificate ID: 2TDIKK-CE000071

CERTIFICATE OF PARTICIPATION

This is to certify that Mr./Ms./Dr. **PUJARI SACHIN SHIVAJI** of **D. Y. Patil Education Society (Deemed to be University), Kolhapur** has participated in International Web-Seminar on '**Novel Applications of Nanomaterials**' organized by **Internal Quality Assurance Cell (IQAC)** of Prof. Dr. N. D. Patil Mahavidyalaya, Malkapur in association with **Department of Chemistry and Physics** on **18th July 2020**.

Dr. Mohan Sangale
Organizing Secretary

Prof. Kshitij Kharat
Co-coordinator

Dr. Somnath Panade
Coordinator

Dr. Sunil Helkar
Principal & Convenor



Madha Taluka Shikshan Prasarak Mandal's



K. N. Bhise Arts, Commerce and Vinayakrao Patil Science College,

Vidyanagar, Bhosare (Kurduwadi) Dist-Solapur (M.S.)

(NAAC Accredited 'B' Grade)

Faculty of Science, IQAC and Solapur University, Solapur

Organized

National Seminar on

Modern Approaches in Sciences

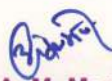
(MAS-2019)
(28 Jan. 2019)

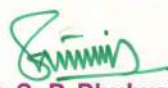


CERTIFICATE

This is to certify that Prof./Dr./Mr./Ms. Pujari Sachin Shivaji of D.Y. Patil
University, Kolhapur participated as a research student/delegate/resource person/chair
person/referee and presented paper/poster entitled _____

in National Seminar held at K. N. Bhise Arts, Commerce and Vinayakrao Patil Science College, Vidyanagar, Bhosare (Kurduwadi).


Dr. A. M. More
Convener


Mr. S. P. Phulwale
Organizing Secretary


Prin. Dr. R. R. Patil
Director

Digitally signed by Dr. A. M. More
DN: cn=Dr. A. M. More, o=K. N. Bhise Arts, Commerce and Vinayakrao Patil Science College, ou=K. N. Bhise Arts, Commerce and Vinayakrao Patil Science College, email=am.more@knbhise.edu.in



Rayat Shikshan Sanstha's

D. P. BHOSALE COLLEGE, KOREGAON

Dist- Satara, Maharashtra, India- 415501

Reaccredited by NAAC with 'A' Grade (CGPA - 3.12) ISO 9001-2015 Certified

e-Certificate

This is to certify that Dr./Mr./Mrs. **PUJARI SACHIN SHIVAJI**

from **D. Y. Education Society (Deemed to be University), Kolhapur**

successfully participated in the **International Web-Seminar on "Recent Trends in Nanostructured Materials Based Devices and Their Applications"** organized by Department of Physics and IQAC in Collaboration with Electra Solar Energy System Pvt. Ltd, MIDC, Koregaon, Dist-Satara on 18th July, 2020.

Dr. V. S. Jamadade
Convenor

Dr. B. S. Lokde
IQAC Coordinator

Dr. V. S. Sawant
Principal



SANJAY GHODAWAT UNIVERSITY Kolhapur

Empowering Lives Globally !

(Approved by UGC & Govt.of Maharashtra)

Certificate

This is to certify that

Prof. / Dr. / Mr. / Ms. Sachin Shivaji Pujari, Ph.D. Scholar

of D.Y. Patil Education Society Kolhapur has participated in National Seminar on

“Emerging Nano Materials for Renewable Energy”

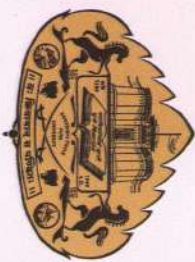
held on Monday, 26th December, 2022 and organized by Sanjay Ghodawat University, Kolhapur.

Dr. Sambhaji M. Pawar
Convener

Dr. Pallavi D. Bhange
Convener

Dr. Sarita P. Patil
Co-ordinator

Prof. Dr. Arun S. Patil
Vice-Chancellor



**NATIONAL CONFERENCE ON
ADVANCED MATERIALS
SYNTHESIS, CHARACTERIZATION AND APPLICATIONS
(AMSCA - 2018)**

PARTICIPATION CERTIFICATE

This is to certify that Mr./Ms./Dr. SACHIN SHIVAJI PUJARI affiliated to

CIR, D.Y. PATIL EDUCATION SOCIETY, KOLHAPUR has presented oral / poster/
participated in the *National Conference on Advanced Materials Synthesis, Characterization
and Applications (AMSCA - 2018)* organized by Department of Physics, Savitribai Phule Pune
University during December 14-15, 2018.

Prof. S. W. Gosavi

Chairman, AMSCA-2018
Department of Physics,
Savitribai Phule Pune University

Dr. S. D. Sarale

Convener, AMSCA-2018
Department of Physics,
Savitribai Phule Pune University



**4th International Conference on Physics of Materials and
Materials Based Device Fabrication
(4th ICPM-MDF-2019)**

Organized by,
DEPARTMENT OF PHYSICS, SHIVAJI UNIVERSITY, KOLHAPUR
(UGC-DRS-I & II, ASIST-I, DSA-I & II, DST-FIST-I & II,
DST-PURSE Sponsored Department)

CERTIFICATE

This is to certify that Prof./Dr./Mr./Ms. *Sachin Shivaji Pujari*.....
of *D. Y. Patil Education Society, Kolhapur*..... has worked as resource person
 chaired the session presented poster participated worked as local organizing committee member
in the 4th International Conference on Physics of Materials and Materials Based Device Fabrication (4th ICPM-MDF-2019) held at
Department of Physics, Shivaji University, Kolhapur (Maharashtra), India during January 10-11, 2019. His/Her contribution to the
conference is highly appreciated.



Dr. A.V. Moholkar
Dr. A.V. Moholkar
Convener, ICPMMDF-2019



**International Conference on
Smart Materials and Nanotechnology (ICSMN-2020)**

Organized by

Department of Engineering Physics and Chemistry

SKN Sinhgad College of Engineering, Pandharpur

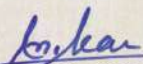
Accredited by NAAC with 'A' Grade

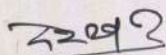


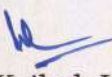
Certificate

This is to certify that Prof/Dr/Mr/Ms/Mrs SACHIN SHIVAJI PUJARI of D.Y. PATIL EDU. Soci. Kolhapur has presented poster/oral scientific presentation in International Conference on **Smart Materials and Nanotechnology (ICSMN-2020)** at **SKN Sinhgad College of Engineering, Pandharpur - 413304, Maharashtra, India** held during 02-04 January, 2020.

Title of Paper: "Study of Copper phosphate, Hydroxide Thin film for Supercapacitor Application."


Prof. Anil I. Nikam
Co-convener


Dr. Sampat G. Deshmukh
Convener


Dr. Kailash J. Karande
Chairperson



Agricultural Development Trust's
**Shardabai Pawar Mahila Arts, Commerce and Science
College, Shardanagar, Baramati.**

NAAC Re-Accredited 'A' Grade College Affiliated to Savitribai Phule Pune University.

CERTIFICATE

This is to certify that, *Mr. Sachin Shivaji Pujari*
from

“D. Y. Patil Education Society (Deemed University), Kolhapur”

has attended

an International Web-Conference organized by Department of Physics on **“Advanced Nanostructured Materials for Energy Generation, Storage and Smart Applications”**
on 09th - 10th October 2020.

Dr. T. P. Gujar
Organizing Secretary

Mr. S. N. Belpatre
Coordinator

Mr. R. B. Deshmukh
Co-Convener

Dr. S. J. Sathe
Convener



CERTIFICATE OF PARTICIPATION

This is to certify that Mr. Sachin Pujari has attended the Asian e-Conference on 'Engineered Science' 2020 which was held online on 5-6 December 2020.

Organizer

ES Publisher, USA

Prof. C. D. Lokhande Endowment Charitable Trust

In association with P. S. G. V. P. Mandal's Arts, Commerce and Science college
Shahada, Dist. Nandurbar, India



Rayat Shikshan Sanstha's

D. P. Bhosale College, Koregaon

Tal. Koregaon Dist. Satara (MS) India – 415 501

Reaccredited by NAAC with 'A' Grade (CGPA 3.12)



e-Certificate of Participation

This is to certify that, **PUJARI SACHIN SHIVAJI** of **D. Y. Patil Education Society Kolhapur** participated in the **National Level One Day Online Workshop on "Intellectual Property Rights"** under **National IPR Awareness Mission** organized by Research Committee, IPR Cell in Association with IQAC, D. P. Bhosale College, Koregaon, Dist- Satara and Collaboration with Office of Controller General of Patents & Design Office, Mumbai, Govt. of India on 12-08-2022.

Dr. V. S. Jamadade
Convener

Dr. B. S. Lokde
IQAC Coordinator

Dr. V. S. Sawant
Principal

D. Y. Patil Education Society, (Deemed to be University)

NAAC 'A' Grade and NIRF 97 (2018)

Kolhapur, Maharashtra



CERTIFICATE

This is to certify that

Mr./Ms. *Sachin Pujari*..... from..... *D.Y.P.U., Kolhapur*.....
has participated as Invited Speaker in “**One Day Workshop on Biodiversity Conservation and Biodiversity Act 2002**” held on 15th February, 2019 organized by Department of Stem Cell and Regenerative Medicine, Centre for Interdisciplinary Research, D. Y. Patil Education Society (Deemed to be University), Kolhapur, M.S. India.

(Signature)
Registrar

(Dr. V. V. Bhosale)

(Signature)
Director

(Dr. C.D. Lokhande)

(Signature)

Organizing Secretary

(Dr. Meghnad Joshi)



K. L. E. Society's

**Shri Kadasiddheshwar Arts College And H. S. Kotambri Science Institute,
Vidyanagar, Hubballi-580031, Karnataka**

Accredited At 'A' Grade With 3.18 CGPA By NAAC

**Unnata Bharata Abhiyan: Participating Institute
IQAC Initiative**

**National Webinar Series-2020
(10th July to 23rd July 2020)**

Certificate of Participation

This is to certify that Mr. SACHIN SHIVAJI PUJARI of D. Y. Patil Education Society (Deemed to be University), Kolhapur has participated in National Webinar on **“Density Functional Theory- In the absence of Spectrometers”** organized by the Department of Physics, K.L.E. Society's S. K. Arts College and H. S. Kotambri Science Institute, Vidyanagar, Hubballi on 22nd July 2020.

**(Dr. C. S. Hiremath)
Convenor & HoD**

**(Prof. S. N. Emmi)
IQAC Coordinator**

**(Dr. Uma V. Nerle)
Principal**



D.Y. PATIL EDUCATION SOCIETY

(DEEMED TO BE UNIVERSITY) KOLHAPUR, MAHARASHTRA

Reaccredited by NAAC with "A" Grade



This is to certify that Mr./Ms./Mrs/Dr./Prof. SACHIN SHIVAJI PUJARI has participated in the two-days webinar on "Emerging Trends and Clinical Challenges in Cancer Treatment" Conducted on cancer day 4th to 5th Feb 2021 by Department of Medical Physics, Center for Interdisciplinary Research.

Prof. C. D. Lokhande
Convener

Dr. Padmaja Pawaskar
Organizing Coordinator

Dr. K. Mayakannan
Organizing Secretary



Government of India
Ministry of Commerce and Industry
Department for Promotion of Industry and Internal Trade
Office of the Controller General of Patents, Designs and Trade Marks

CERTIFICATE

This is to certify that, **MR. PUJARI SACHIN SHIVAJI** of **D. Y. PATIL EDUCATION SOCIETY**
KOLHAPUR has successfully participated in IP Awareness/Training program under
NATIONAL INTELLECTUAL PROPERTY AWARENESS MISSION

on August 12, 2022

Organized by
Intellectual Property Office, India

Date: August 22, 2022




(Prof. (Dr) Unnat P. Pandit)
CONTROLLER GENERAL OF
PATENTS, DESIGNS & TRADE MARKS